Depositional History and Palaeoenvironments of the Lake Mulurulu Lunette, Willandra Lakes World Heritage Area, New South Wales

---

By
Tegan E. Smith

A thesis submitted for the degree of
Doctor of Philosophy
of the Australian National University

April 2019

Declaration

Except where otherwise acknowledged in the text, this thesis represents original research by the author.

Tegan Smith

April 2019

Approx. 73 000 words

Dedicated to my unborn baby, at 6 months gestation at the time this thesis was first submitted...for providing the final deadline needed to get the thesis completed

Love Mum xxx.

Acknowledgements

My thanks are given firstly to my primary supervisor, Prof. Rainer Grün for his guidance, encouragement and support in this research. Appreciation is also extended to my advisory committee members for their feedback and advice; in particular Dr John Magee, for his thorough and informative feedback on my thesis draft, and Dr Steve Eggins for stepping-in to review the revised thesis. A huge thank you goes to Rainer, John and Steve for being there when I needed them!

My very sincere and appreciative thanks go to the Elders Council of the Three Traditional Tribal Groups. Thank you for welcoming me and permitting me an amazing opportunity to learn about and appreciate your beautiful Country. I am honoured to have had the pleasure.

Thanks also go to the Cultural Officers, Daryl Pappin and Cally Doyle, for your help, cultural advice and guidance in the field; it was a pleasure working with you. Other field assistants provided valuable guidance, enthusiastic help and good company too; Damien Kelleher, Wayne Cook, Katarina Sporcic and in particular, Ian Moffat.

For allowing me access to their properties, for touring me around a shearing shed in shearing season, and for occasionally showing up to my camp-site with a ute-full of cold beers after my eskies had warmed, massive thanks go to Reese at Mulurulu Station and Tim at Spring Hill Station.

I received a huge amount of advice and training in analytical techniques throughout my PhD, for which I am eternally grateful. Enormous thanks to Dr Kathryn Fitzsimmons for training me in OSL dating; Prof. Ian Williams, who advised on SHRIMP sample preparation and analysis; Dr Graham Mortimer for help with wet chemistry; Dr Rachel Wood for guidance and training on radiocarbon dating and Bayesian analysis; and Dr Hilary Stuart-Williams for advice and guidance on preparing and analysing samples with CF-IRMS.

A special note of gratitude goes to Geoscience Australia for supporting me in completing my thesis while employed at GA. In particular, the then GA Chief Scientist Dr Clinton Foster is thanked for his enthusiastic encouragement.

Thank you to all the amazing friends I have made at the Research School of Earth Sciences over the years, particularly my previous office-mate, Renaud Johannes-Boyau. Thanks also to Tazz and Sarlae – Tazz for accommodating me in his office during my final couple of months of writing, and Sarlae in general for her friendship and moral support.

Lastly, to my husband, Cluan, your unwavering support and belief in me has been a part of this from the start. From moving to Canberra with me in the first place so that I could start this PhD, to marrying me, buying a house with me and knocking me up, all whilst my weekends were consumed with study; thank you for undertaking this adventure with me.

Abstract

The Willandra Lakes form a dry lake system consisting of a number of ancient, formerly perennial, lakes in the western Murray basin. The area has significant scientific value, providing detailed palaeoenvironmental records of arid, ice-age Australia as well as a rich and unique archaeological record. Lake Mungo, resting place of Australia's oldest dated aboriginal remains, is a terminal lake where studies of the lake system are concentrated. Lake Mulurulu, a flow-through lake in the northern part of the system, is relatively understudied despite abounding potential and a differing hydrological regime.

A range of geochronological techniques, combined with stratigraphic and isotope palaeoecological methods, inform the palaeoenvironmental history for the Lake Mulurulu lunette. A comprehensive suite of quartz optically stimulated luminescence (OSL) ages is combined with detailed sedimentological analyses to build a chronostratigraphic framework. Mussel shells and fish otoliths are radiocarbon dated, and wombat teeth are analysed for electron spin resonance (ESR) and uranium series dating. Oxygen isotope analyses on fish otoliths and wombat teeth are used in an attempt to ascertain high-resolution palaeoenvironmental records for the area.

The quartz was well suited for OSL dating. Very little evidence for partial bleaching was observed, though sediment mixing proved to be relatively common. A small aliquot multi-grain OSL methodology allowed the identification of sediment mixing and grain transport across unit boundaries. Many samples were found to be very young (< 200 years), and were disproportionately affected by recuperation issues, low precision and high overdispersion.

Dating reveals the Mulurulu lunette comprises five major units. Unit A, dating from 60 to over 110 ka, is clay and carbonate rich with a thick palaeosol, and is equivalent to the Golgol Unit at Lake Mungo. Unit B is a clean quartz sand representing an early lake full stage,

initiating around 60 ka and ending around 40 ka at the southern end of the lunette and around 32 ka at the northern end of the lunette. Unit C comprises a pelletal clay representing a drying phase, dated to 40-32 ka and 32-28 ka at the southern and northern ends of the lunette, respectively. Unit D is a 28-17 ka quartz sand representing another lake full stage. A thin, previously unrecognised, pelletal clay layer at the southern end of the lunette caps this unit. Unit E comprises laminated quartz sands derived from reworked lunette materials dating to less than 200 years old, indicating a significant amount of recent lunette remobilisation. Unconsolidated mobile sands are present on the crests and leeward side of the dunes.

Oxygen isotope analyses of fish otoliths provided evidence of flood events and potentially a lake drying signal that was not expected in this flow-through lake. The oxygen isotope analyses of wombat teeth on the other hand, proved less successful for gaining insight into high-resolution palaeoenvironmental events.

This research provides a new chronology of deposition for the Lake Mulurulu lunette. This forms a similar but distinctive local hydrological history compared to the previous regional understanding, built primarily on the events recorded at Lake Mungo, a terminal lake situated further downstream.

Table of contents

List of figures

List of tables

List of appendices

Chapter 1. Introduction

1.1. Aims

The primary aim of this research is to provide a depositional and palaeoenvironmental history of Lake Mulurulu in the Willandra Lakes World Heritage Area, over the last glacial-interglacial cycle (~150 ka). Previous studies of the Willandra Lakes system have been concentrated at Lake Mungo—resting place of Australia's oldest dated aboriginal remains. Lake Mulurulu, in the northern part of the system, is relatively understudied despite abounding potential and a differing hydrological regime. This research aims to rectify that disparity.

By characterising and dating the stratigraphic layers of, and faunal materials within, the lunette, a depositional and palaeoenvironmental history of the lake is constructed, and compared with the existing knowledge on the history of the other lakes in the system; primarily, Lake Mungo. It is hypothesised that the differing hydrological regime at Lake Mulurulu, being a flow-through lake located higher upstream in the system, will result in a complimentary but distinctive record of wetting and drying events to that recorded in the sediments of Lake Mungo, which as a terminal lake, is likely to be more sensitive to intermittent aridity events. It is predicted the depositional history and palaeoenvironments of the Lake Mulurulu lunette will record fewer drying events during the last 150 ka, and during drying events, little-to-no indications of short-term lake level fluctuations, and less indication of salinity stress than is recorded at Lake Mungo. This hypothesis and prediction is tested by addressing the following questions:

- What are the sedimentological and stratigraphic characteristics of the depositional units of the Mulurulu lunette, when were they deposited, and what palaeoenvironments do they represent?

- What palaeoclimatic signals can be identified in faunal materials from the Mulurulu lunette, and what time period do they represent?

- How does the depositional and palaeoenvironmental history recorded in the Lake Mulurulu lunette sediments and faunal materials, particularly indicators of drying and salinity, relate to the record in the Lake Mungo lunette, and how do they compare in the context of the broader region and palaeoclimate?

1.2. Approach

The above stated aims of this research are addressed through the use of multiple techniques, including various geochronological methods, isotopic analyses of faunal materials, and stratigraphic descriptions to construct a palaeoenvironmental history of Lake Mulurulu as recorded in its lunette. The focus is on OSL dating of quartz in sediments characterised to determine the broad-scale palaeoenvironment. To compliment this work, a small number of oxygen isotope analyses are conducted on two types of faunal materials, in order to compare high resolution palaeoenvironmental information with the broad-scale garnered from the stratigraphic work. In measuring isotopes, two different measurement techniques are utilised, allowing the techniques to be compared. Direct dating is attempted on the faunal materials, to provide a geochronological context for the isotopic results, plus a comparison to the OSL results for the surrounding sediments.

Four different dating techniques are utilised in this study: optically stimulated luminescence (OSL), electron spin resonance (ESR), uranium-series (U-series) and radiocarbon (^{14}C) dating. This multi-dating approach was applied for two reasons. Primarily because a number of different types of materials are being dated (quartz sediments, bioapatite, aragonite and calcite), which are suited to different types of techniques, but also because the utilisation of independent dating methods for materials from the same strata allows for comparisons and tests of the reliability of the techniques. Figure 1.1 shows the applicable dating range for each of these techniques and their overlap with the time period represented in the Lake Mulurulu lunette sediments.

The terminology used in quoting ages varies depending on the dating technique. OSL, ESR and U-series ages are generally reported using ka, meaning ‘thousands of years ago’. Radiocarbon dates are reported as BP (or cal. BP), meaning ‘before present’, where ‘present’ denotes 1950 (further discussed in Section 5.1).

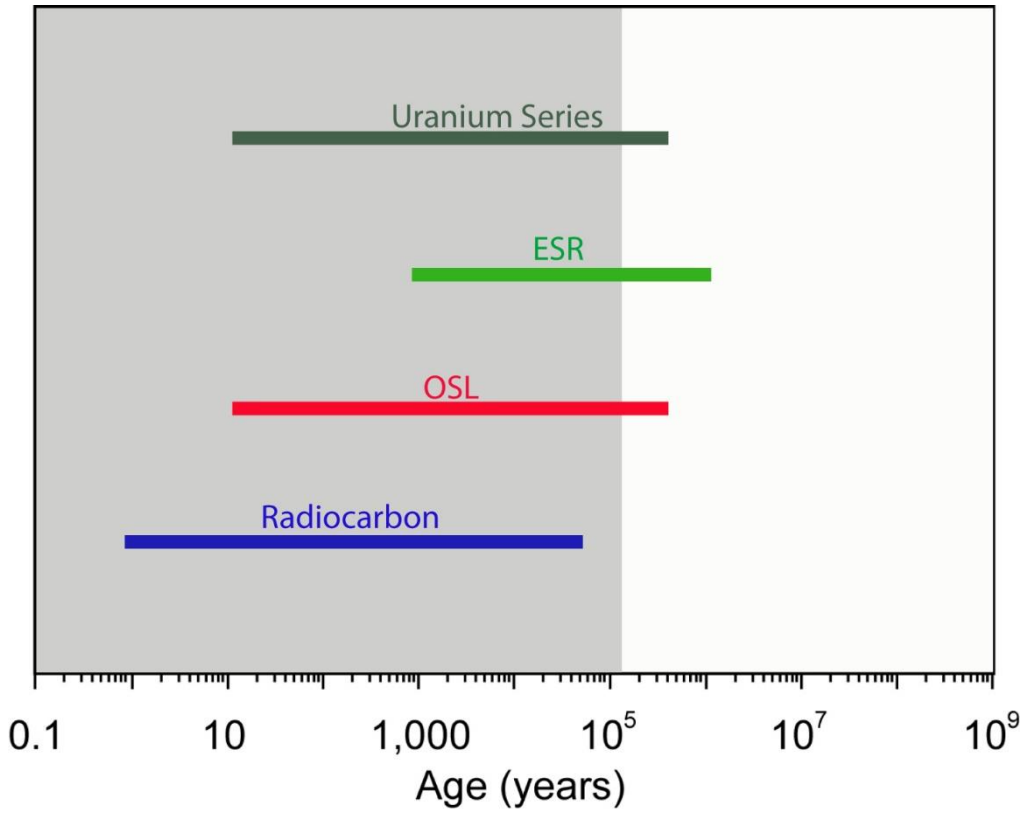

Figure 1.1. Applicable dating ranges of the techniques utilised in this study. The shaded area represents the period of time represented by the sediments of the Lake Mulurulu lunette. Note the logarithmic scale. (Adapted from Grün 2006, his Fig 1).

1.3. Thesis structure

After outlining the aims, approaches and techniques for the research, and structure for this thesis, in Chapter 1, Chapter 2 sets the scene, providing a history of research in the Willandra Lakes and implications for studies at Lake Mulurulu. Firstly, the regional setting of Lake Mulurulu is outlined, including the Murray-Darling Basin, the Lachlan Catchment and the Willandra Lakes. The local modern climate is also described. Next, an introduction to Willandra human and archaeological remains is followed by a synopsis of lunette geomorphology, and previous work on the sedimentology and stratigraphy of Willandra Lakes lunettes, including at Lake Mulurulu. The chapter finishes off with a lake level curve for the Willandra system, and a summary of Lake Mulurulu's hydrological positioning relative to the other lakes.

Chapter 3 details the sedimentological and stratigraphic work characterising the depositional units at Lake Mulurulu. It details the initial field reconnaissance such as aerial photography and foot surveys, plus methods such as stratigraphic logging, drilling, thin section analysis,

and surveying. Results and interpretations are provided for each of the stratigraphic units, and cross sections of the lunette are presented at a series of transect sites. The chapter finishes off with a stratigraphic summary of the depositional units of the Mulurulu lunette.

An investigation in to the use of oxygen isotopes in biogenic materials as a palaeoenvironmental proxy at Lake Mulurulu is presented in Chapter 4. The chapter includes background information about the technique, the materials, (fish otoliths and wombat teeth) and the methods—Sensitive High Resolution Ion Micro Probe (SHRIMP), Laser Ablation-Inductively Coupled Plasma Mass Spectrometry (LA-ICPMS) and Continuous-flow Isotope Ratio Mass Spectrometry (CF-IRMS). The results are presented for each sample type, inferences regarding environmental information are made, and the suitability of these types of materials as providers of palaeoenvironmental records is discussed.

Chapter 5 provides information on the chronology of human occupation at Lake Mulurulu, through radiocarbon dating of charcoal, mussel shells and fish otoliths (including the otoliths analysed in Chapter 4). The materials are described and a background on radiocarbon dating is provided. The results are presented and discussed in the context of previous radiocarbon dating work in the Willandra Lakes.

Attempts at dating wombat teeth (analysed in Chapter 4) using ESR and Uranium series methods are described in Chapter 6. For each of these techniques, the background, methods and results are presented, followed by a discussion on the combined US-ESR analysis results. Challenges encountered with this sample set are also discussed.

In Chapter 7, a chronological framework for sediment deposition at Lake Mulurulu is established, through the OSL dating of quartz-rich sediments.

Background information regarding the principles of OSL are discussed in Section 7.1, including the luminescence signal, the SAR protocol, dose distributions (and the external and intrinsic factors that influence them), and age models. The differences between single grain and multi-grain dating techniques are highlighted and the application of OSL dating to Australian sediments is reviewed.

Section 7.2 provides the OSL methods, including the presentation of preheat-plateau and dose-recovery tests, used to determine the settings of the SAR protocol, and also an assessment of the OSL performance with regard to recycling and recuperation rates. The

methodology for determining D_e is detailed, including the aliquot rejection process, error calculation and dose distribution assessment. The factors contributing to dose rate calculation and errors are described, as are the methods for determining OSL ages and errors.

OSL results are presented as a data table in Section 7.3, as well as a discussion of the dose distribution results for each unit, followed by an estimate of the boundary ages for each unit, in the form of a Bayesian analysis.

In Section 7.4 patterns in the OSL dose distributions are discussed, including evidence for mixing—across unit boundaries, in palaeosols, and elsewhere. The low potential for incomplete bleaching and microdosimetry issues are briefly discussed and issues observed in the young samples in the study are highlighted.

The results from the previous chapters are drawn together in Chapter 8. A chronostratigraphic framework for the lunette is provided through a synthesis of the geochronological results and stratigraphic interpretations. This is followed by a narrative description of the depositional and palaeoenvironmental transitions recorded in the landscape of the Mulurulu lunette, in the context of the broader region and environmental regimes.

Chapter 9 provides conclusions, revisiting each of the questions posed in the introduction, and proposes recommendations for further study.

Chapter 2. Setting the scene: a brief history of research in the Willandra Lakes

Throughout the Quaternary, cyclical changes in climate, driven by predictable orbital variations known as Milankovitch cycles (Emiliani 1966), have left a record of cyclical change throughout the Australian landscape. The lake and dune sediments of the Willandra Lakes System form a cornerstone of Australian Quaternary chronostratigraphy, with detailed records of repeated wetting and drying, coupled with a rich Palaeolithic archaeological archive.

Lake Mulurulu is located at the northern end of the Willandra Lakes system. The Willandra Creek is a palaeodistributary of the Lachlan River, the catchment area of which lies within the Murray-Darling Basin. A large amount of work has been carried out in the Willandra Lakes, regarding the Quaternary record, geomorphology and archaeological history of the area. The primary focus of this work has been the Lake Mungo lunette—known as the 'Walls of China'—though focused studies at lakes Arumpo, Garnpung, Leaghur and Mulurulu have complemented this research. The discovery of ancient human remains at Mungo in the late 60s and early 70s led to decades of work at the site, resulting in a repository of knowledge of the stratigraphy and sedimentology of the Mungo lunette, and a proposed hydrological history of the Willandra Lakes system.

2.1. Regional setting and climate

2.1.1. The Murray Darling Basin

The Murray-Darling Basin catchment area covers over one million square kilometres of Victoria, New South Wales, Queensland and South Australia (Figure 2.1). The Murray Basin is a geological depositional system bounded by the foothills of the Mt Lofty and Olary ranges

in the west, and the south eastern highlands of NSW and Victoria in the east and south (Brown & Stephenson 1991). The surface physiography of the Murray Basin consists of fluviatile riverine plain in the east, and aeolian Mallee dune fields in the west (Bowler et al. 2006). The Mallee region is characterised by flat to gently undulating sand plains in the northwest and widespread Quaternary dune fields of four types elsewhere (Brown & Stephenson 1991):

1) The east-west longitudinal dunes of the Woorinen Formation,

2) Remobilised Woorinen sub-parabolic to irregular dunes,

3) Tongue-like dune fields of the Big Desert, Little Desert and Sunset Desert; and,

4) Small source bordering dune fields adjacent to the Murray River.

Lake Mulurulu is flanked by sand plains to the west and north, with linear and irregular sub-parabolic dunes to the east, alluvium associated with the Willandra Creek to the south, and irregular sub-parabolic dunes further to the west and south (Figure 2.2).

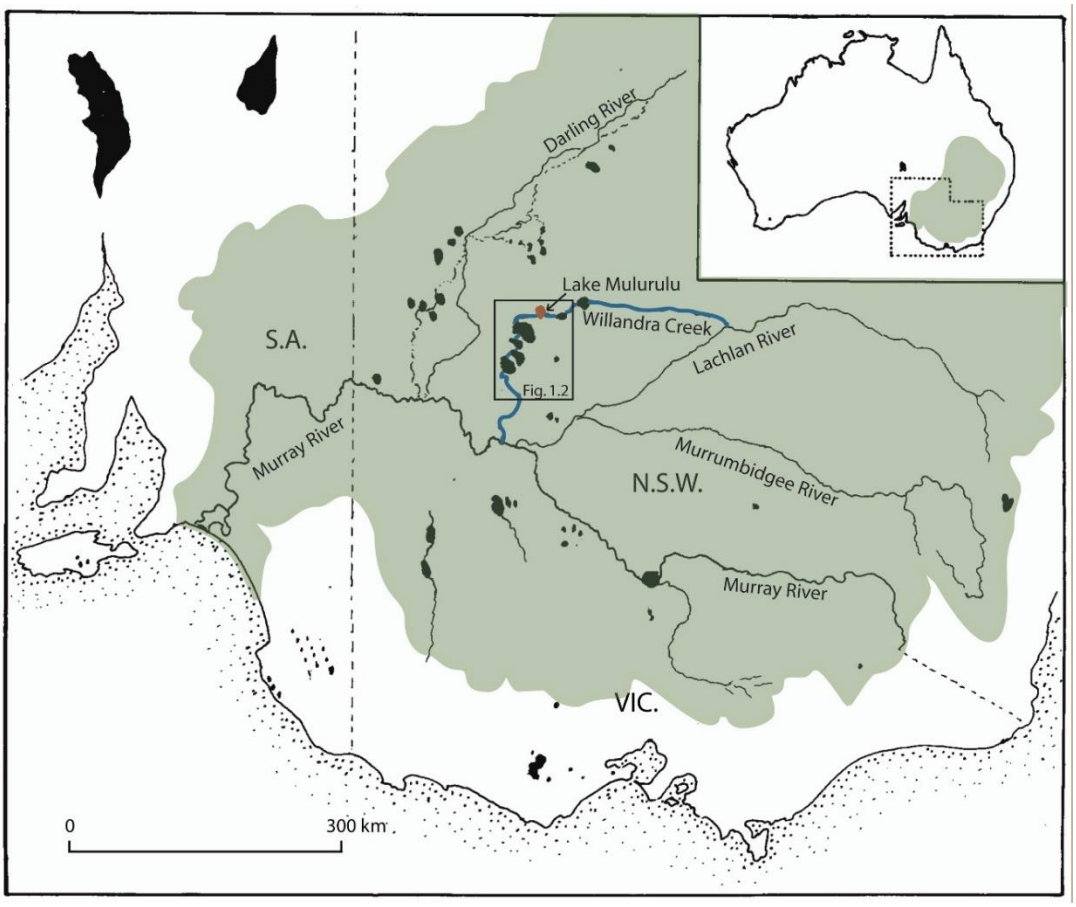

Figure 2.1. The Murray-Darling river system. The shaded area is the Murray-Darling Basin. The black shapes are lakes. The blue line marks the route of Willandra Creek and the red lake is Lake Mulurulu. Box outline shows the location of Figure 2.2. Modified from Bowler (1983, his Fig. 1).

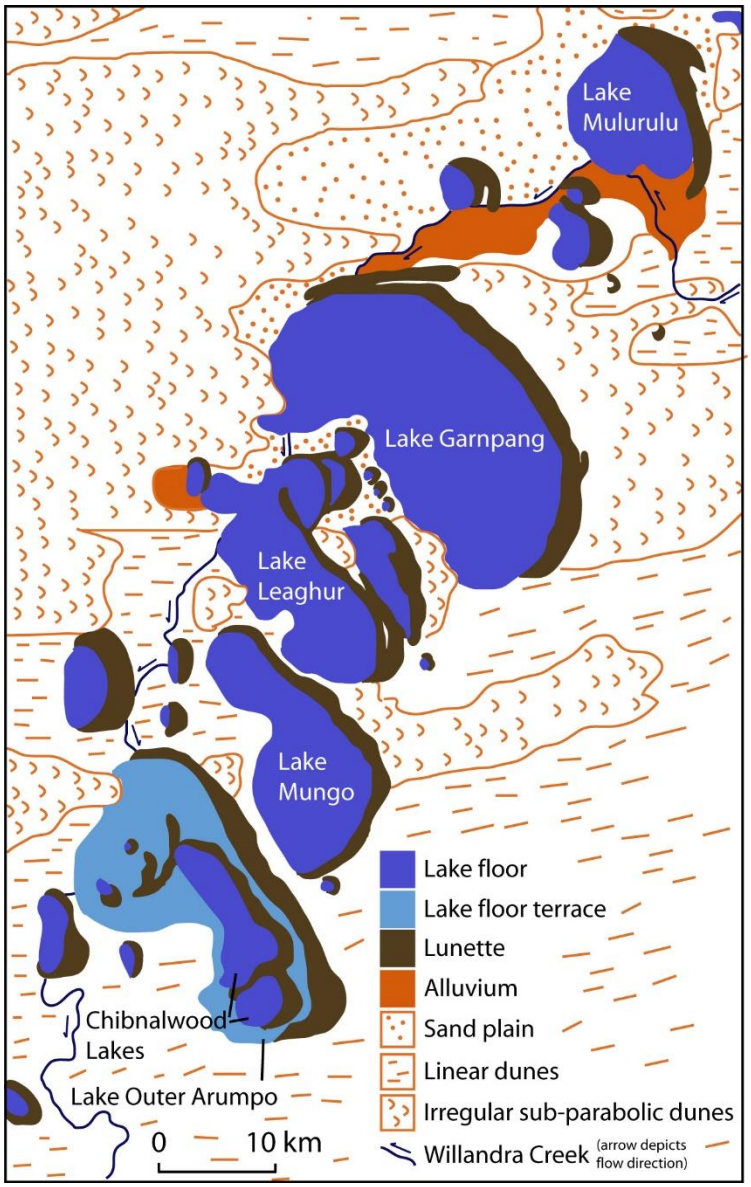

Figure 2.2. Geomorphology map of the Willandra Lakes. Willandra Creek enters Lake Mulurulu from the south and leaves in the south west. Modified from Magee (1991; Fig. 1b), after Bowler (1971); Bowler & Magee (1978).

2.1.2. The Lachlan catchment

The headwaters of the Lachlan River are located in the eastern highlands of southeast Australia and when the Willandra Creek still filled the lakes, the hydrology of the Willandra Lakes system reflected changes in conditions in these highlands, rather than local conditions (Fitzsimmons et al. 2014). During periods of high rainfall and runoff, fluvial sedimentation was dominant in the fluvial corridors of the Murray Darling Basin, while periods of aeolian deposition reflect aridity (Nanson et al. 1992; Lomax et al. 2011). Kemp and Spooner (2007) demonstrated high runoff around 34 ka, through the Ulguthrie palaeochannel system (named

by Kemp 2001), which in the upper Lachlan, generally followed the modern river. In its middle reaches, anabranches divert and re-join, before diverging westward, through the Willandra Lakes to the palaeo-Murrumbidgee. The bank-full discharge was estimated to be 6-8 times greater than the present Lachlan River (Kemp & Spooner 2007). Kemp and Rhodes (2010) compiled ages on rivers of the central Murray Darling Basin with new dates for the Lachlan River and confirmed the synchronous development of large meandering channels around 34 ka, possibly associated with lower evapotranspiration and higher precipitation in the alpine highland catchment (Ayliffe et al. 1998) and periglacial activity at the more moderate elevations of the Ulguthrie headwaters (Barrows et al. 2001). Around the same time, at 32 ± 2.5 ka, the glaciers in the highlands were advancing (Hadley Tarn advance; Barrows et al. 2001). Glacial advance also occurred during the Last Glacial Maximum (LGM), with the Blue Lake Advance (19.1 ± 1.6 ka; Barrows et al. 2001), a period of reduced river channel sedimentation signifying aridity, while large, seasonally active migrating channels were maintained by snowmelt sourced from the Alps (Kemp and Rhodes 2010). Although the LGM was relatively colder and more arid than present day across much the Australian continent (Hesse et al. 2004; Fitzsimmons et al. 2013) and aeolian sedimentation was active in the local dune fields (Lomax et al. 2011), Lake Mungo maintained permanent lake conditions at this time (Bowler et al. 2012).

2.1.3. The Willandra Lakes

The Willandra Creek is a palaeodistributary of the Lachlan River in the Murray-Darling river system (Figure 2.1). It flowed through the Willandra Lakes Region World Heritage Area, located in the Mallee region of the Murray Basin (Figure 2.3). In the Late Quaternary the river maintained more than 1000 km^2 of perennial, mostly freshwater lakes, but its lower section has been dry and inactive for millennia (Bowler et al. 1976). At or shortly before 18.4 ka, channel avulsion diverted runoff from the lower Lachlan away from the Willandra Lakes to the more southern areas of the Lachlan alluvial plains (Kemp et al. 2017). The Willandra Lakes formed an overflow system, with Lake Mulurulu the first lake beyond the limits of historic flooding, connected to the other lakes by the Willandra Creek (Figure 2.2). Lake Mungo, where the majority of previous Willandra Lakes research has been carried out, is a terminal lake, filling only in response to overflow from the neighbouring Lake Leaghur (Figure 2.2).

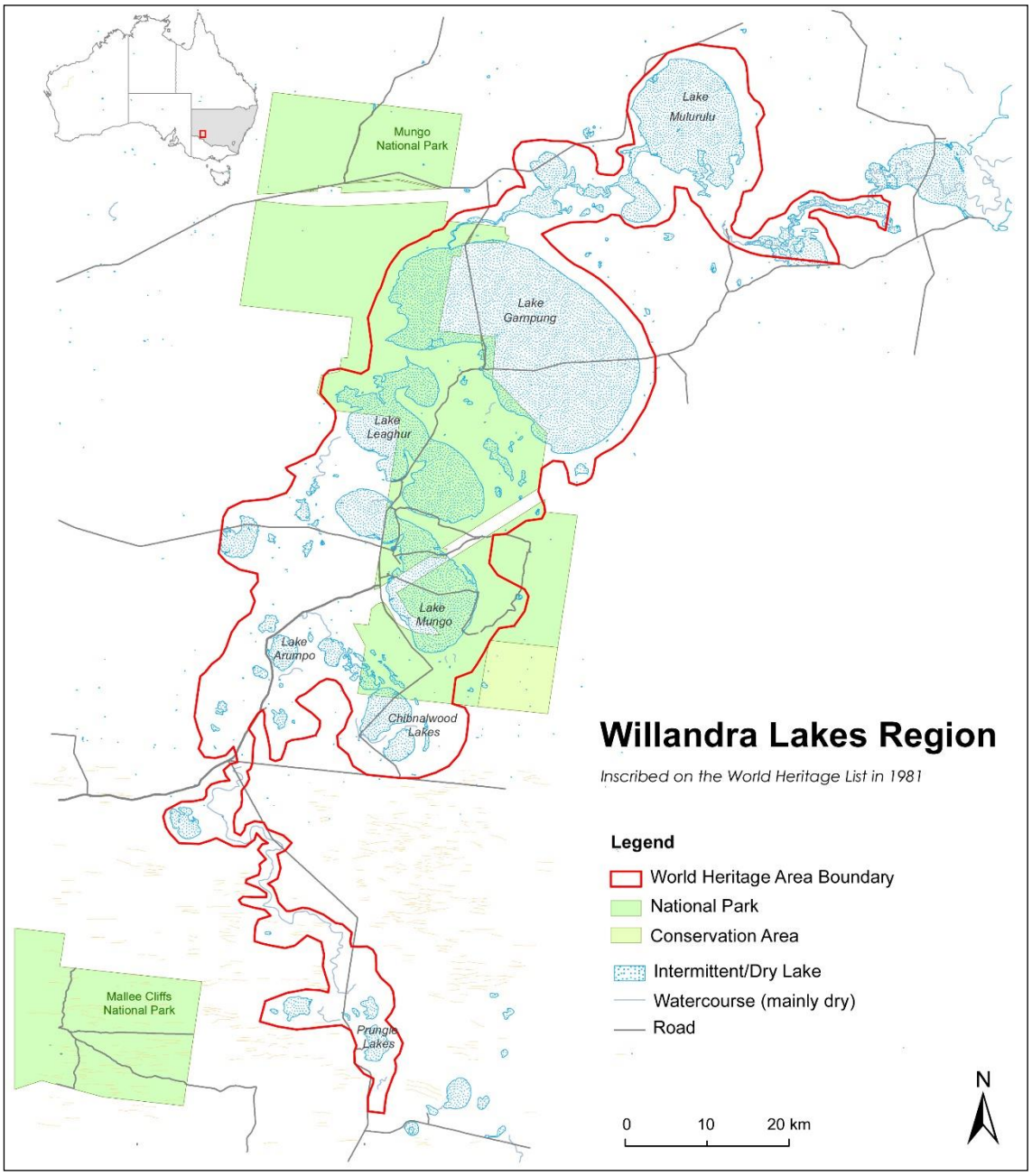

Figure 2.3. Willandra Lakes Region World Heritage Area (Modified from UNESCO 2015).

2.1.4. Local climate

The modern climate of most of the Murray-Darling Basin catchment ranges from semi-arid to sub-humid, and mean annual evaporation is high, significantly exceeding annual rainfall throughout the basin. The dominant year-round wind directions are from the south to southwest (Figure 2.4), which has had a strong influence on the pattern of aeolian dune development and migration in the Murray Basin (Brown & Stephenson 1991). Summer temperatures in the Mallee region are high, and regularly exceed 40°C in summer, while

winters are mild with maxima around 15-17°C (Bowler & Magee 1978). Sixty years (1889-1949) of climate data from the Mildura weather station, ~140 km to the south west of Mulurulu, sourced from the Australian Bureau of Meteorology (Figure 2.5) indicates the area has hot summers, with a mean maximum temperature above 30°C and mild winters with a mean maximum above 15°C, though the mean minimum is around 5°C. A small amount of rain falls year round, with higher precipitation levels and relative humidity in winter than summer (Figure 2.5).

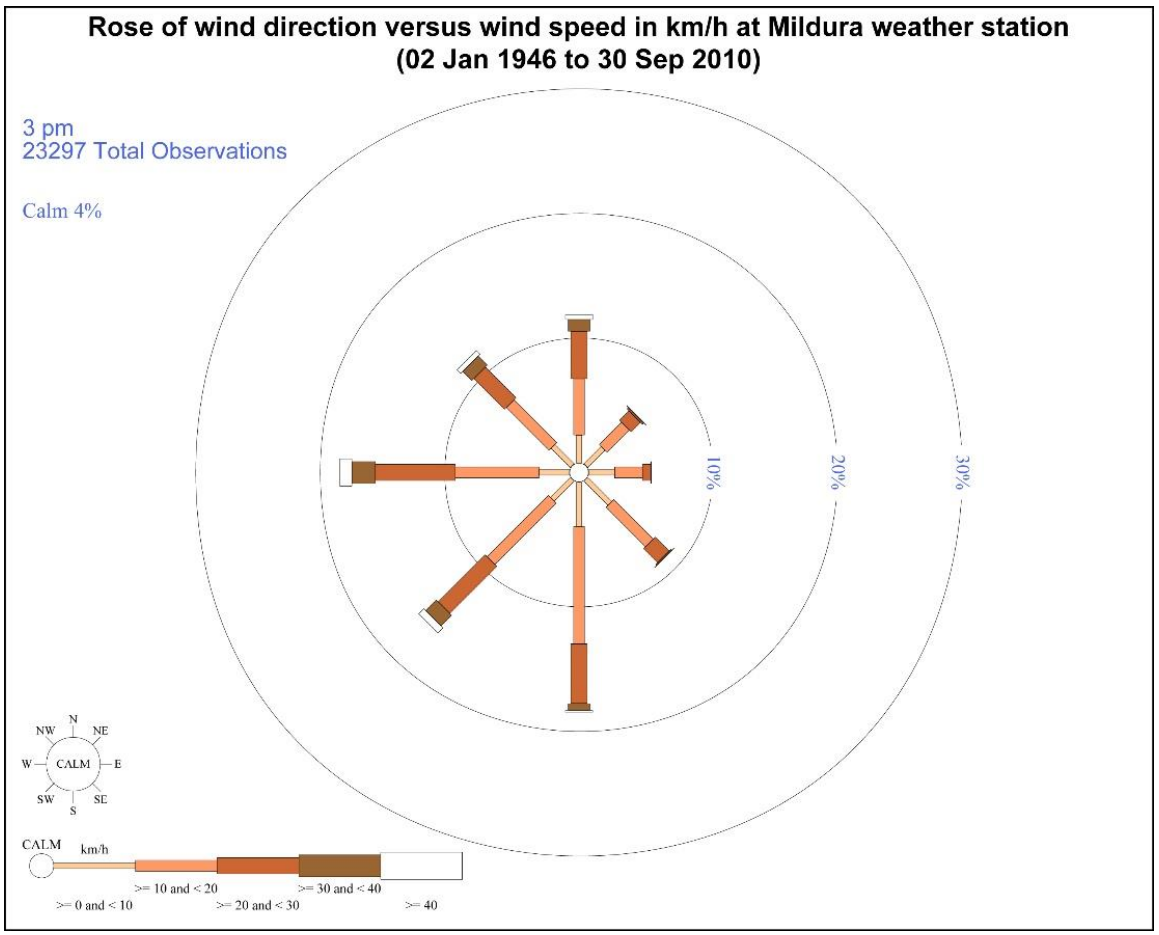

Figure 2.4. Windrose for 1946 to 2010 at Mildura Weather Station (Modified from Bureau of Meteorology 2014).

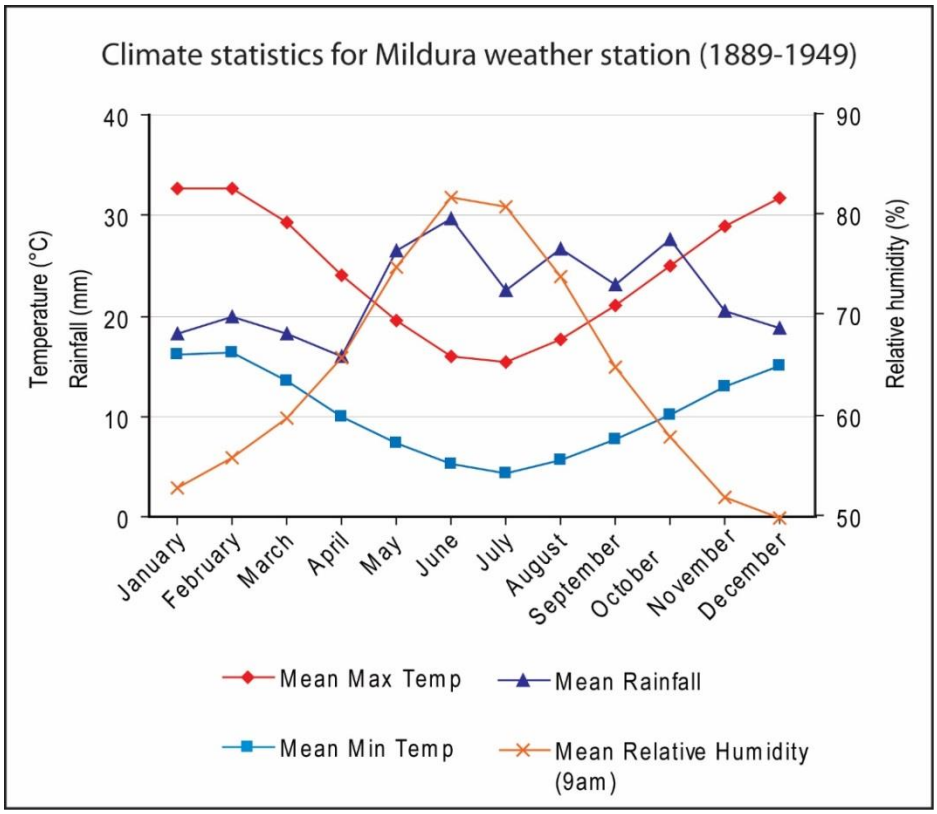

Figure 2.5. Climate data for 1889 to 1949 at Mildura weather station (Bureau of Meteorology 2015b).

2.2. Human Remains

Over 100 human skeletons have been discovered throughout the Willandra Lakes (Gillespie 1997). The first (WLH-1, Mungo 1) and third (LM3, Mungo 3), known as Mungo lady and Mungo Man, respectively, have received the most attention, and garnered the most debate.

WLH-1 was first discovered in 1968, at the southern end of the Lake Mungo lunette, within the Mungo Unit (Section 2.4). The deposit of burnt, carbonate-encrusted bones was identified as cremated human remains in 1969 (Bowler et al. 1970). Deflation in the immediate area meant that determining an age for the remains required reconstructing the pre-deflation sequence. Early estimates based on radiocarbon dates of charcoal from a hearth 15 cm above an equivalent level in the reconstructed stratigraphic sequence, plus collagen and bone apatite from skeletal fragments, dated the burial to 24 500 and 26 500 BP (Bowler et al. 1970; 1972).

LM3 was discovered in 1974, consisting of a near complete skeleton in an eroding grave, also at the south end of the Mungo lunette. The body had been sprinkled with powdered red ochre before the grave, located in the upper part of the Lower Mungo Unit (Section 2.4), was filled in (Bowler & Thorne 1976). A range of age estimates have been determined for Mungo 3,

including initial radiocarbon (^{14}C) ages around 30 ka BP (Bowler & Thorne 1976), thermoluminescence (TL) ages of 45-42 ka (Oyston 1996; Bowler & Price 1998) and a ~60 ka age resulting from a range of techniques carried out by Thorne et al. (1999; see below). The controversial results of the latter age led to a heated academic debate on the reliability and applicability of the dating methods used (e.g. Bowler & Magee 2000; Gillespie & Roberts 2000; Grün et al. 2000).

Thorne et al. (1999) employed a number of dating techniques to arrive at their ~60 ka age estimate for the LM3 burial: Combined electron spin resonance (ESR) and uranium series (U-series) direct dating (see Chapter 6) of the LM3 skeletal material (62 ± 2 ka), optically stimulated luminescence (OSL) dating (see Chapter 7) of the Lower Mungo sediments at a level thought to be stratigraphically equivalent to the LM3 burial (61 ± 2 ka), and U-series dating of a calcitic matrix precipitated on the bones after burial (81 ± 21 ka). This combination of corroborating results led the authors to suggest that the earlier radiocarbon and TL age estimates for LM3 were all erroneously too young. The alternative explanation would be that the new dates were erroneously too old, but while there is a significant level of uncertainty in the age estimates, the authors found it difficult to provide an explanation that could accommodate ages of less than 50 ka. The uncertainty in the age modelling largely arises from different U-mobilisation histories. Significant uranium-leaching (in the range of 65%) would have to have occurred in order to reach apparent ages 20 ky too old, a process that has rarely been recorded in teeth, and where it is recorded, is only on a small scale (Grün et al. 2000).

Bowler and Magee (2000) criticise Thorne et al's (1999) results for not taking in to account field and stratigraphic details at the burial site, suggesting the materials sampled for OSL dating were not stratigraphically equivalent to the level in which the burial was interred. Grün et al's (2000) response to this was that they based their understanding of the stratigraphy provided by Bowler & Thorne (1976) and Bowler (1998), while Bowler and Magee (2000) present a different stratigraphic interpretation, which, though not a valid criticism of Thorne et al.'s methodology, does undermine Thorne et al.'s results. Gillespie and Roberts (2000) cite dose rate considerations and concerns regarding partial bleaching as possible sources for erroneous OSL ages. Grün et al. (2000) respond to this by pointing out that their arguments could equally apply to the previously accepted TL dates of Oysten (1996). So although the ~60 ka date of Thorne et al. (1999) could not be easily explained away, it also could not be easily accepted.

Bowler et al. (2003), went on to provide a thorough reassessment of the age of both burials, using OSL to date sands from the units in which the Mungo 1 and Mungo 3 burials were interred, as well as from overlaying units sealing the graves. Analyses were carried out independently at four separate dating laboratories, resulting in an age for the underlying sands of 42 ± 3 ka and 38 ± 2 ka for the overlying unit, thus constraining the age of the skeleton to 40 ± 2 ka (Bowler et al. 2003). In 2006, Olley et al. corroborated these dates by independently dating preserved grave-infill samples using single-grain OSL. The analyses were carried out on sand grains recovered from sediment blocks impregnated with polyester resin, sampled from burial infill material at the time of the original excavation. The population of grains identified as light-safe yielded an age of 41 ± 4 ka, consistent with the dates of Bowler et al. 2003. Thus, both burials are currently considered to date to approximately 40 ka.

2.3. Archaeological remains

In addition to the human burials, the Willandra Lakes display a rich archaeological record. Cooking hearths, burned and unburned food remains (including middens with remains of fish, eggshells, marsupials and shellfish), stone tools, and debris from their manufacture and repair occur throughout the region, as well as ochre pellets, unworked silcrete nodules, large cores, grinding stones and other tools (Stern et al. 2013). A functional study of grinding stones and fragments from the central part of the Mungo lunette provides evidence of pre-Holocene plant processing and seed grinding activities at the site (Fullagar et al. 2015). The earliest evidence of a human presence at Lake Mungo dates to 46-50 ka (Bowler et al. 2003). This makes the occupation of the area synchronous with, or soon after, the initial occupation of northern and western Australia (various authors in Bowler et al. 2003). Much of the archaeology of the Willandra Lakes was summarised and put into a regional context in a series of papers in a special Mungo edition of Archaeology in Oceania (Allen 1998; Johnston & Clark 1998; Shawcross 1998). Later, fossil track ways of at least 124 human footprints were discovered between Lakes Leaghur and Garnpung, and dated to between, 23-19 ka (Webb et al. 2006). More recently, Stern et al. (2013) provided a record of the interaction of past human activities with the environment through a detailed foot survey documenting the presence of archaeological traces in relation to sedimentary units in a central portion of the Lake Mungo lunette.

2.4. Sedimentology and stratigraphy

2.4.1. Processes of lunette formation

A lunette is a crescentic-shaped dune, formed on the down-wind side of intermittent water bodies and composed at least partially of clay materials. Lake Mulurulu is typical of the lakes of the Murray Basin, in having a lunette on its downwind, eastern and north-eastern shore. Coffey (1909) was the first to describe lunettes, though he didn't call them by that name. He studied lunettes in Texas and called them 'clay dunes'. The term 'lunette' was first coined in Australia by Hills (1940), who described crescentic ridges of silty clay along the eastern shores of lakes and swamps across the plains of northern Victoria. Bowler (1973, p.316) defines clay dunes as "any dune in which clay forms more than about 20%, as well as those consisting predominantly of clay".

Clay dunes form under certain conditions of oscillating wet-dry cycles and strong unidirectional winds, even though the fine-grained nature of clay usually precludes the saltation of individual grains. When a lake floor dries out, the clays shrink and are broken up by salts crystallising within the lake floor sediments, at the capillary fringe of the saline water table. These disrupted lake-floor sediments, and the salts, can be deflated by the wind, and fine-grained particles are removed as dust, while coarser grained particles are abraded and sorted by saltation transport across the lake floor. The resultant sand-sized clay pellets are then transported much like sand grains, and deposited on the down-wind side of the mud flats, where transport may be hindered by an existing dune or vegetation. Later higher moisture conditions cause the hygroscopic salts to absorb moisture and the clay pellets to cohere, preventing further transportation (Coffey 1909; Hills 1940; Price 1963, Bowler 1973; 1983). By this process, clay dunes known as lunettes form on the downwind side of drying lakes. Modern active lunette building occurs in Texas and Africa, whereas in Australia lunettes are mostly relict (Bowler 1973; 1983).

It was the detailed study of active Texan clay dunes (e.g. Huffman & Price 1949; Fisk 1959; Price 1963) that allowed Australia's relic dunes to be related to the processes that formed them (Bowler 1973). Strong easterly and southeasterly winds blow off the Gulf of Mexico for many months of the year, leading to the development of lunettes on the northwestern edge of tidal salt flats and lagoons (LeBlanc and Hodgson 1959). The strong onshore winds also lead to local high tides and these, along with high spring tides, result in periodic flooding of the

lagoons and salt flats, which then dry out due to high evaporation rates (~1900 mm/y; Price 1963). Active lunette building also occurs in Oran, Algeria, where Boulaine (1954 1956 in Bowler 1973) recorded the growth of a clay ridge 1.5 m high following a large flood in 1903, which caused a previously cultivated area to become severely salt-affected. Erosion in the region is controlled by a seasonal oscillation of the water-table. When the water-table falls with summer drying, the surface clays develop the pelletal structure necessary for erosion and transport to the edge of the salt-affected area where they are trapped by vegetation (Boulaine 1956 in Bowler 1973).

Clay dominated dunes are different to quartz dominated dunes in a number of features, such as showing a lack of cross bedding and being steeper on the windward slope than the lee slope in cross section. Also, while barchan dunes (crescentic sand dunes) typically have 'horns' that point downwind, the horns on lunettes point toward the prevailing winds (Figure 2.6; Bowler 1973). The lunettes of the Willandra lakes are compound lunettes which consist of alternating clay and quartz sand units (Figure 2.6), recording oscillations of past hydrologic sequences. As described above, clay pellets are deposited during saline, drying conditions. Quartz sands are deposited during periods of high lake level. The presence of lake waters leads to the development of gravels and beach sands (Bowler 1998 2012). Those beach sands are then reworked onto the dunes by prevailing winds, resulting in quartz sand sediments lacking in gravel and course materials, often with cross bedding and sometimes with biogenic carbonates, above the level of the beach from which the sediments are derived (Bowler 1998).

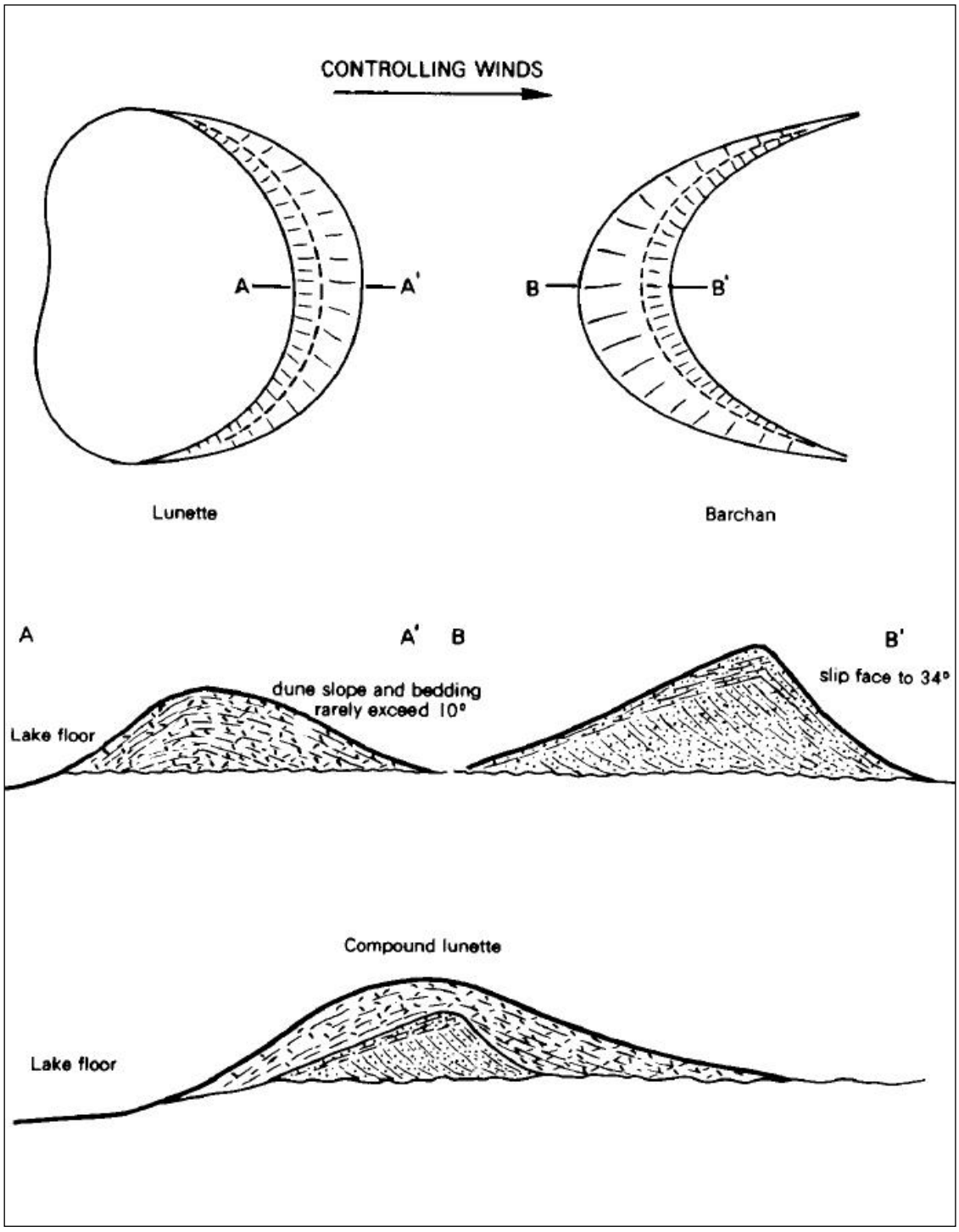

Figure 2.6. Plan and section characteristics of lunettes and barchan (crescentic) dunes. Lunette 'horns' face toward the controlling wind direction, while in barchans, they face away. Additionally barchan dunes show steep slip faces, and are steeper on the lee side of the dune, while clay dunes have very low dips and are steeper on the windward side of the dune. The bottom section is of a compound lunette, with a clay layer overlying a sand dune core. From Bowler (1973, his Fig. 2).

2.4.2. Generalised stratigraphy of the Willandra Lakes lunettes

After decades of work in the area, Professor Jim Bowler (currently honorary professorial fellow at the University of Melbourne) is the definitive authority on the stratigraphy of the lunettes of the Willandra system. Bowler (1998) provided a detailed summary of the stratigraphy and environmental interpretations. Douglas (1996) wrote an Honours thesis under Bowler's supervision, which specifically addressed the land systems and stratigraphy of the Mulurulu lunette, and her results were summarised in Bowler (1998). The dating of the Lake Mungo stratigraphy was refined by Bowler et al. (2003) in response to controversial dates for the Mungo 3 burial (Thorne et al. 1999, see above). A comprehensive chronostratigraphic interpretation of the Willandra Lakes system provided by Bowler et al. (2012) is summarised below.

The combined stratigraphic analyses of the Willandra Lake lunettes indicate an environment that varies from lake-full conditions to oscillating water levels and aridity. The Golgol unit, at the core of the lunettes, suggests multiple earlier lake drying events 100-140 ka or earlier, followed by a long period of stability, when a thick palaeosol developed (Bowler 1998). The return of water to the lakes around 60 ka deposited the clean sands of the Lower Mungo unit onto the lunettes. Further drying commencing around 40 ka resulted in the pelletal-clay (PCD) layers of the Upper Mungo unit. Oscillations between dry and wet phases continued until a more significant wet period commenced around 30 ka, marking the onset of the lower Arumpo unit, which ended with an Upper Arumpo dry phase, indicated by pelletal clays, around 23 ka. The final lake filling period, around the LGM, is diachronous between the lakes. The southern, distal and topographically lowest lake, Lake Outer Arumpo, was the first to dry out, while Lake Mulurulu, as the northern, proximal and topographically highest lake, was conversely the last to dry (Bowler et al. 2012; see below). This transition to more arid ice age conditions was non-linear, punctuated with wet periods driven by high catchment rainfall and runoff. Indeed the wettest period yet recognised in the Willandra Lakes has been recorded at around 24 ka, with a very high lake filling phase known as "Mega-lake Mungo", with a lake volume increase of almost 250%, making the lake up to five metres deeper than at any preceding or subsequent lake full events (Fitzsimmons et al., 2015). This event is evidenced by a previously unrecognised thin red sandy unit related to a laterally extensive pebble beach, identified in the northern portion of the Mungo Lunette (Fitzsimmons et al., 2015) and at the neighbouring smaller Lake Durthong Lunette (Fitzsimmons, 2017).

Many of the lake-level interpretations at Lake Mungo have focussed on the lunette sediments at the southern end of the lake. The definition of the Arumpo Unit, however, comes primarily from the Long Waterhole Gully site at Lake Outer Arumpo (Bowler 1998), while the Mulurulu Unit was defined from sediments at Lake Mulurulu (Douglas 1996; Bowler 1998), and later recognised as equivalent to the Zanci Unit (Bowler et al. 2012). Fitzsimmons et al. (2014) described the depositional history preserved in a central section of the Lake Mungo lunette, where the Lower and Upper Mungo units are thinner and date to 50-40 ka and 34 ka, respectively, while the interbedded sands and clayey sands of the Arumpo and Zanci units are much thicker, poorly differentiated and were deposited around 25-14 ka. They posit that the differences in unit thickness may be a result of spatially variable deposition of sediments along the lunette, or variation in post depositional erosion, either of which may be evidence of changes to the prevailing wind regimes. Fitzsimmons (2017) further investigated this proposition, with a systematic investigation of spatial variability in stratigraphic unit thickness across the Mungo Lunette. The analysis determined the likely prevailing wind orientations over time, with winds shifting from predominantly west-north-westerly over the period ~60-30 ka, to west-south-westerly ~24 ka, before shifting westerly ~24-15 ka.

Table 2.1. A generalised Willandra Lakes lunette stratigraphy (modified after Bowler 1976, Bowler et al. 2012 and Fitzsimmons et al. 2014).provides a summary of descriptions, interpretations and dates of the units of the Willandra Lakes' lunettes and Figure 2.7 shows a profile section of the Lake Mungo lunette.

Table 2.1. A generalised Willandra Lakes lunette stratigraphy (modified after Bowler 1976, Bowler et al. 2012 and Fitzsimmons et al. 2014).

Unit	Characteristics	Estimated age , southern end of lunette (Bowler et al. 2012; luminescence and calibrated radiocarbon)	Estimated age, central lunette (Fitzsimmons et al. 2014, luminescence and calibrated radiocarbon)
Golgol	Calcareous sands or weakly pelletal clays, forming a dune core. Typified by strongly red calcareous soil indicating a depositional hiatus.	At least two phases, with the later dating to ~140,000	
Lower Mungo	Well-sorted quartz sands representing a lake full period	~60,000 – 40,000	50,000-40,000
Upper Mungo	Saline, interbedded sandy clays with ancient red brown soil. This is the surface most closely associated with human occupation at Mungo.	40,000 – 30,000	~34,000
Arumpo	Period of quartz dune building followed by pelletal clay facies, representing oscillations between wet and dry conditions.	30,000 – 23,000	25,000-14,000
Zanci	Predominantly gypseous and pelletal clays. Includes quartz dune phases at some lakes, including what has been referred to as the Mulurulu Unit at Lake Mulurulu.	23,000 – 16,500	

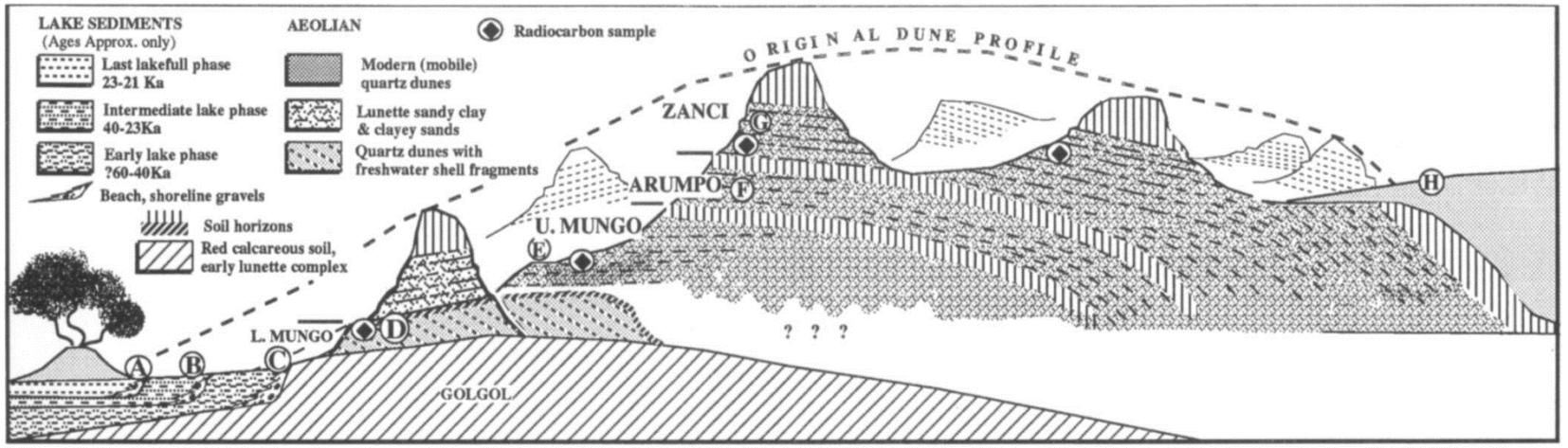

Figure 2.7. A Stratigraphic profile of the Tourist Site at Lake Mungo. From Bowler (1998, his Fig. 4)

2.4.3. Stratigraphy of the Lake Mulurulu lunette

Bowler's stratigraphy described above is largely derived from Lake Mungo and to a lesser extent Lake Outer Arumpo, both of which fill from overflow from Lake Leaghur and may be expected to show similar responses to environmental change. Bowler described only limited stratigraphic sections and units from Lakes Mulurulu and Garnpung. Lakes Mungo and Outer Arumpo are both downstream of Lake Garnpung, which is so much larger than the other lakes that it could buffer the hydrological responses of lakes downstream of it. Lake Mulurulu, on the other hand, is upstream of Lake Garnpung and more proximal to the catchment and as such, can be expected to show less impact of water stress and salinity, and a stronger and prolonged response to wet conditions, compared to other lakes in the Willandra System. Therefore, the stratigraphic sequence at Lake Mulurulu can be expected to differ significantly from the details of Bowler's composite stratigraphic scheme.

Douglas (1996) and Bowler (1998; 2012) divided the stratigraphy of the Lake Mulurulu lunette into five main units. There is a Golgol-equivalent lunette core and two lake-full sand units radiocarbon dated to around 34 ka Cal. BP and 22-18 ka Cal. BP (Bowler et al. 2012). Over these is a laminated sand layer originally deemed the 'Mulurulu Unit' (Bowler 1998), before being redefined as equivalent to the Zanci unit (Bowler et al. 2012). A single pelletal-clay unit (other than the Golgol) was identified, which divided the two lake-full layers and was thought to represent the Upper Arumpo phase. These units are all eroded to varying degrees and are overlain in parts, particularly on the leeward side, by modern, mobile sands derived from that erosion. Additionally, the lunette displays a degree of lateral variation, with simpler stratigraphy in the south and increasing complexity toward the north (Figure 2.8).

A primary cause of lateral variation in the Mulurulu lunette is neotectonic activity. Douglas (1996) recognised crossed shorelines, with extensive cliffing in the northern part of the lunette. A differential of approximately 1 metre from south to north resulted in displacement of the final shoreline. As this deformation event occurred before final lunette building, Bowler (1998) places it between about 17 to 15 ka BP. The Geoscience Australia Neotectonic Features database (Geoscience Australia 2015) lists this as a probable neotectonic event.

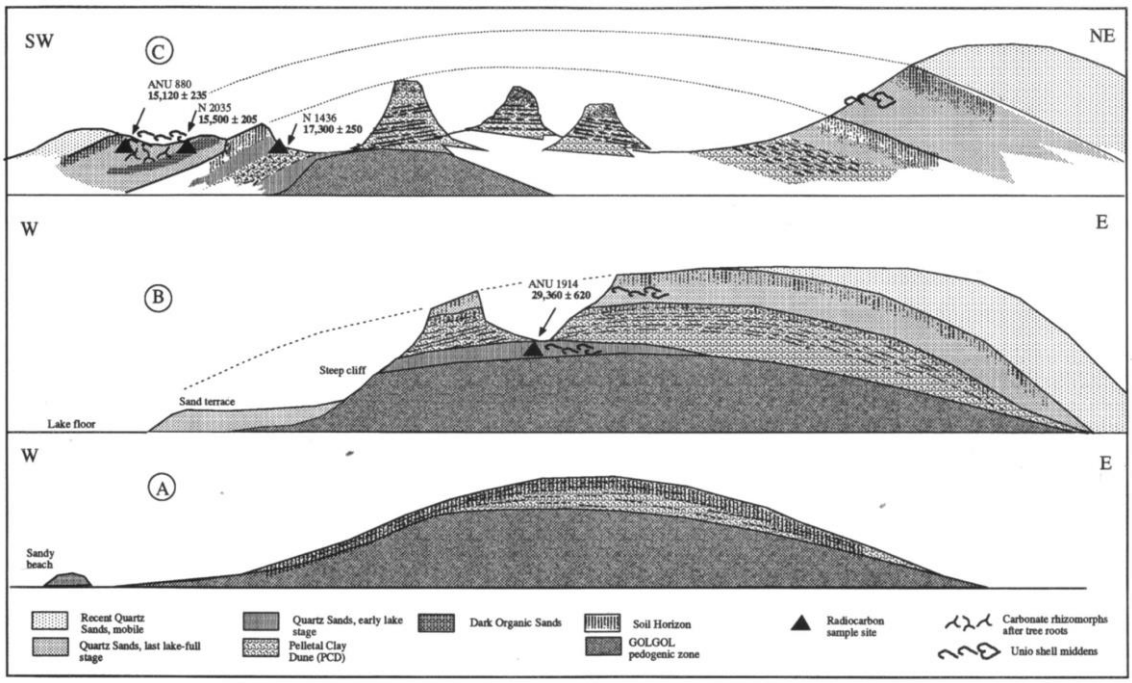

Figure 2.8. Stratigraphic profiles of the Mulurulu lunette. A) the south end of the lunette, B) mid-way along the lunette. C) the North end of the lunette, where the stratigraphy is most complex. From Bowler (1998, his Fig. 15).

A more detailed stratigraphic log from Douglas (1996) is shown in Figure 2.9. In this composite log, the Golgol unit shown in Figure 2.8 is divided into units J to H, consisting of a gypsum-rich unit, a sandy calcareous pelletal clay and a calcareous red palaeosol, respectively. The early lake-full unit consists of G1, white sands, overlying G2, reworked red sands from Golgol soil. The PCD unit is represented as E, which grades into the overlying late lake-full sand unit, here consisting of units D and C, comprising buff quartz sands and a red palaeosol, respectively. The laminated 'Mulurulu Unit' is here shown as B2, overlain by a red soil, B1. The remobilised modern dunes are labelled A.

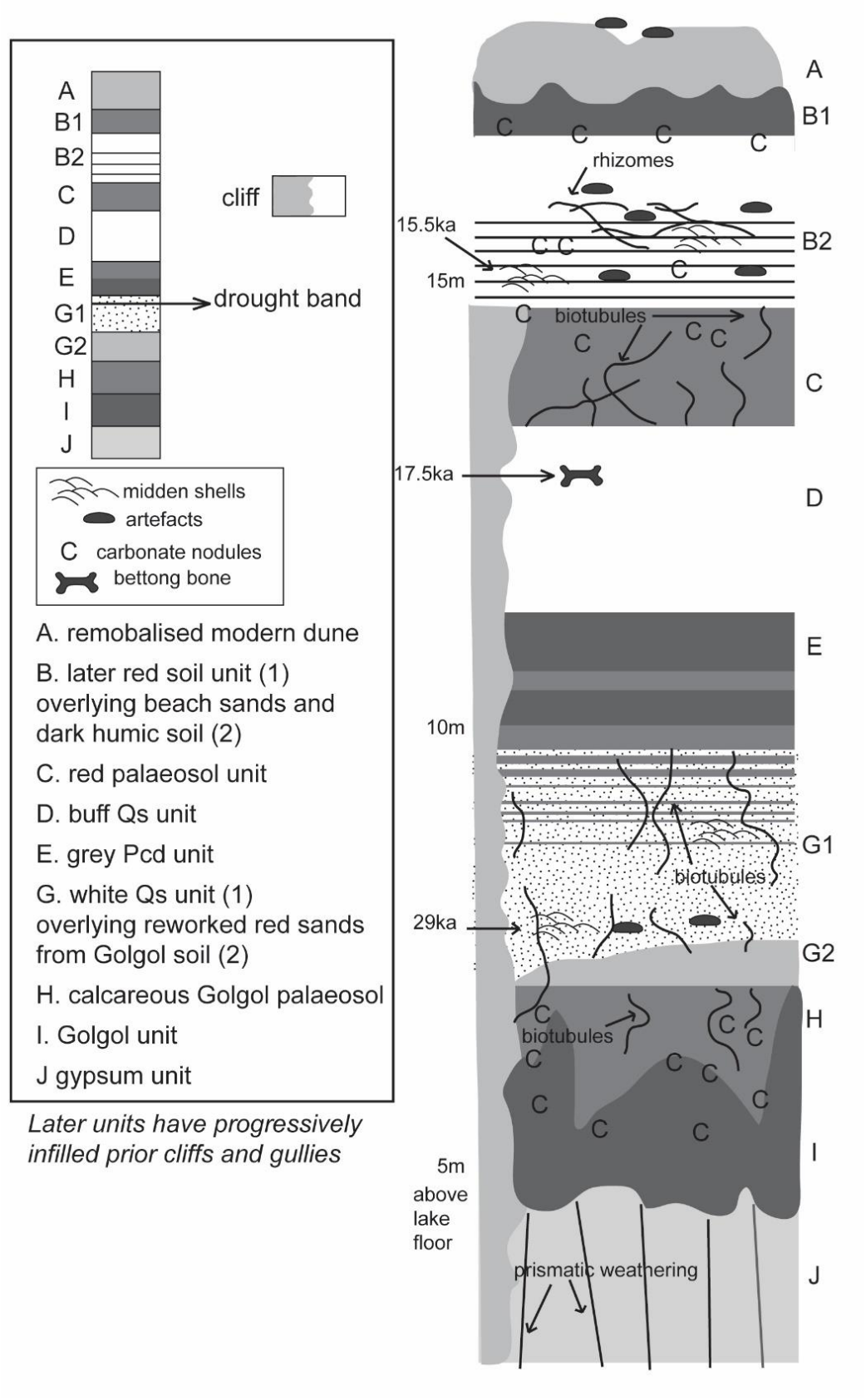

Figure 2.9. Composite stratigraphic log showing the detailed stratigraphy of the Mulurulu lunette. From Douglas (1996; her Fig. 14).

Douglas (1996) also provided a comparative evolution of the Mungo and Mulurulu lunettes, highlighting a lack of one to one correlation between units at the two lunettes, and relatively fewer drying episodes represented at Lake Mulurulu. The more comprehensive and updated chronostratigraphy of the Lake Mulurulu lunette provided in this study provides the opportunity to create a better informed comparison of the evolution of the Mulurulu lunette with the updated understanding of the Mungo lunette provided by Bowler et al. (2012) and Fitzsimmons et al. (2014). See Chapter 8 for discussion on this topic.

2.5. Lake Level reconstructions and lake interactions

The Willandra Lakes form an overflow lake system. Most lakes in the Lake Eyre and Murray-Darling basins are flood-out or terminal lakes, or where coordinated drainage is absent playas are formed as groundwater-controlled systems (Jacobson et al. 1994). In an overflow system consisting of a chain of interconnected lakes such as the Willandra, the response to any particular climatic effect will be felt and expressed differently between lakes of various shape, size and position in the drainage system (Figure 2.10; Bowler et al. 2012). Lakes proximal to the catchment will retain water for longer while lakes more distal to the catchment respond more sensitively to the onset of aridity (Nanson et al. 1992; Hesse et al. 2004). Thus, the greatest impacts of drying events are felt downstream. Indeed, the Prungle Lakes, located well downstream of Outer Arumpo, show strong evidence of water stress and salinity, with abundant gypsum evaporites in the lake floor sequence and gypsum-rich lunettes (Magee 1991). Figure 2.11 shows a composite water level curve for the Willandra system, where the diachronous lake record during the LGM is indicated by A', B' and C', representing deflation events from the progressively drying basin floors of lakes Outer Arumpo to Mungo to Mulurulu, respectively (Bowler et al. 2012).

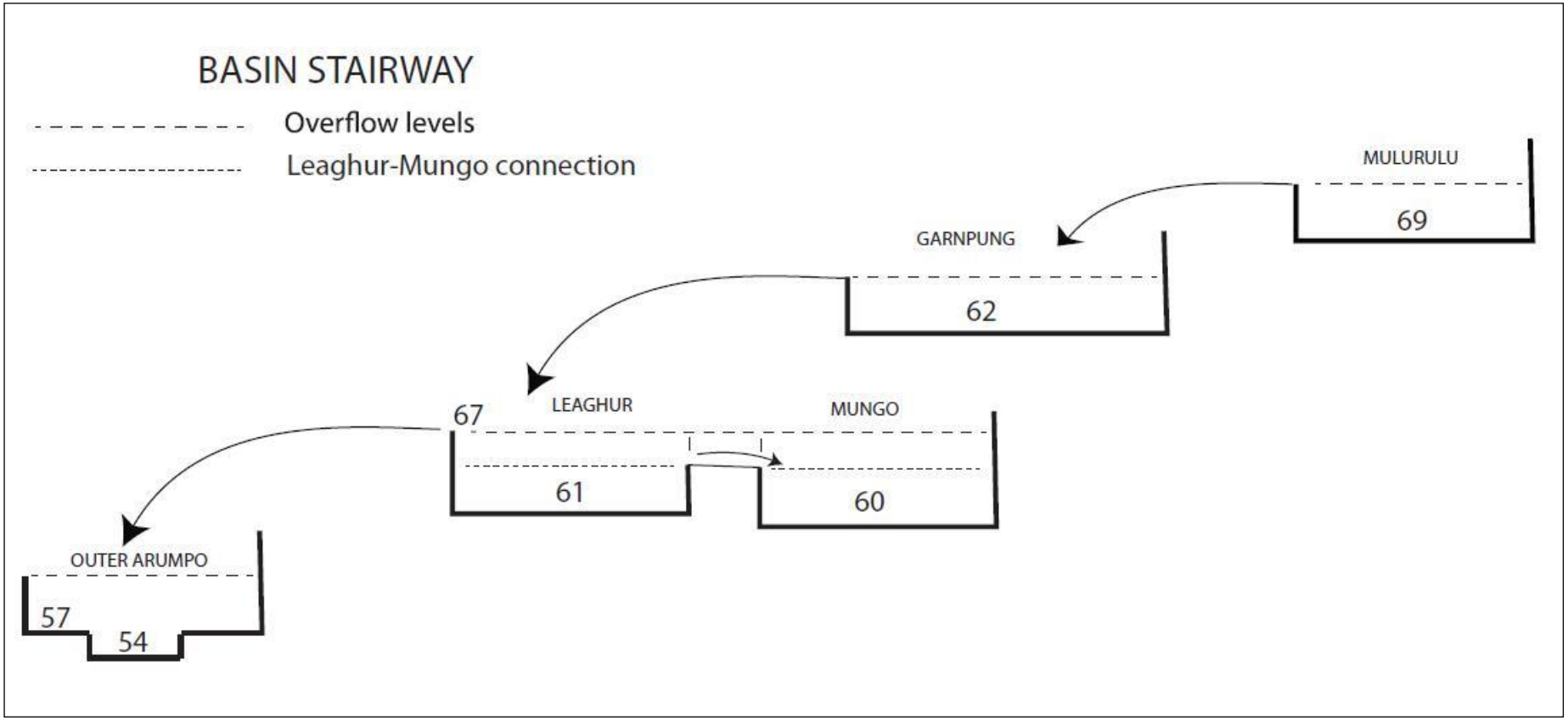

Figure 2.10. Diagrammatic representation of Willandra basins in ‘stairway’, relative to each other. Approximate levels of basin floors in metres AHD, from digital elevation and local surveys From Bowler et al. (2012; Fig. 3).

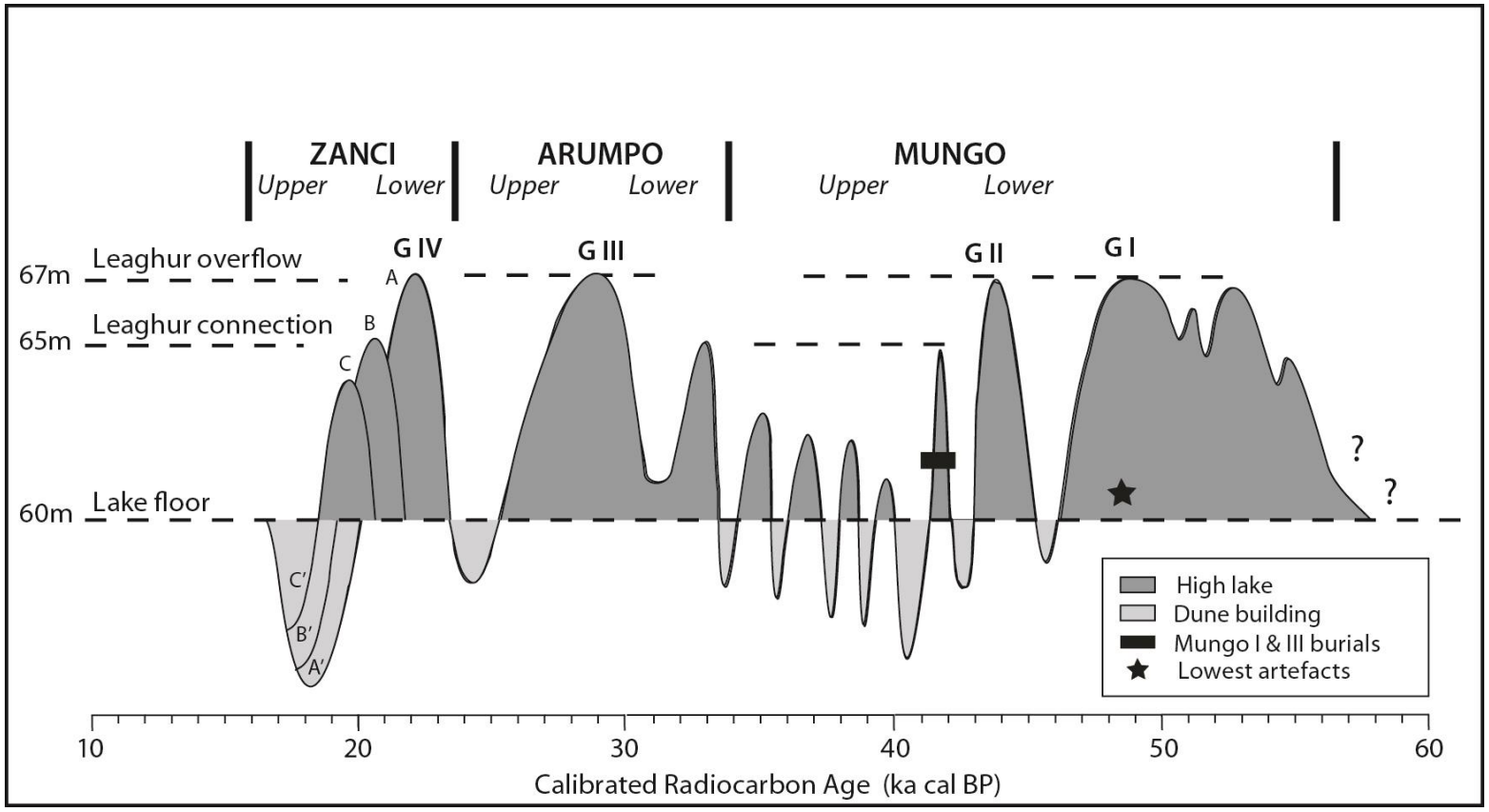

Figure 2.11. Lake level and dune formation summarising data mainly from Lake Mungo. Highest levels associated with gravels developed during high lake stands. LGM drying diachronous between basins A, B and C, representing progressive reduction in levels from Outer Arumpo to Mungo to Mulurulu respectively. A', B' and C' deflation events from progressively drying basin floors. Clay dune A' includes initial deposition on Outer Arumpo, with continued gypseous clay deflation from inner basins Chibnalwood, Inner Arumpo and Bulbugaroo. From Bowler et al. (2012, his Fig. 12).

Chapter 3. Sedimentology and stratigraphy of the Lake Mulurulu lunette

A background covering the existing research into the sedimentology and stratigraphy of the Mulurulu lunette is provided in Section 2.4. This chapter details the methods, results and interpretations of sedimentological and stratigraphic work carried out in this study.

3.1. Field reconnaissance

3.1.1. Aerial photography

On 20 July 2007, Fugro Spatial Solutions took 22 vertical photographs of the Mulurulu lunette at a resolution of 1:10 000 from a fixed wing plane at a height of 1609 m ASL. The flight paths are shown in Figure 3.1.

Digital copies of the aerial photos were stitched together using *Adobe Photoshop* and the resultant image was imported into *ArcGIS* and geo-rectified based on known survey points.

3.1.2. Foot survey and faunal sample collection

Based on the aerial photography, site codes were given to all blow-outs (BOxx) and big gullies (BGxx), numbered in ascending order from north to south. Some other areas were given a different code such as RBO (rear blow outs, behind the main dune) or MSE (mungo style erosion, where single blow outs were not identified but a large area of erosion had left a series of residuals).

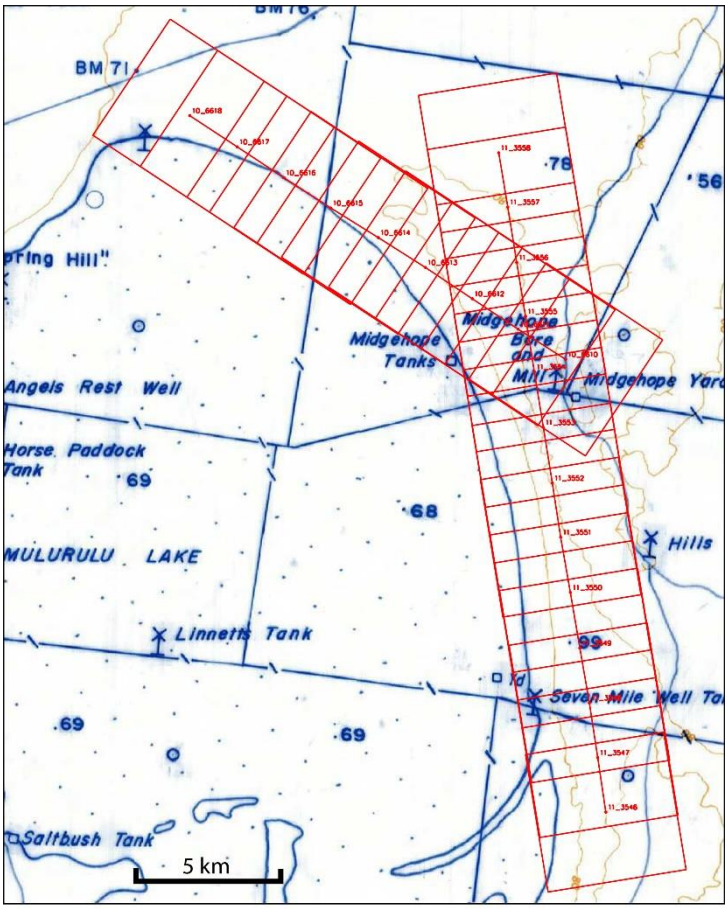

Figure 3.1. Aerial photography flight path. (Image provided by Fugro Spatial Solutions)

The aerial map overlaid with site codes is shown in Figure 3.2. These exposure sites were then surveyed on foot. Each was thoroughly traversed by two or three field workers and faunal samples consisting of isolated mollusc shells, wombat teeth, emu egg shells and fish otoliths were photographed and collected. An orange field tag was labelled and pinned in each sample location.

All field work was undertaken in cooperation with one or both of the designated cultural officers, Daryl Pappin and Cally Doyle, who were present as representatives of the Three Traditional Tribal Groups. Every time a sample was collected or sediment disturbed, the work was carried out under the consultation, guidance, and with explicit agreement from, the cultural officers. As the wombat teeth were to be ESR dated, 10-15 g sediment samples were also collected from each wombat sample location, placed into sample bags and labelled. In addition, a handheld gamma spectrometer was used to measure gamma radiation levels at each wombat sampling location. Additional mollusc shells were collected from twelve sites, and charcoal from five, for radiocarbon dating. Sites were selected based on proximity to

transects (Section 3.2.4.3) and optically stimulated luminescence (OSL) sampling sites (Section 7.2.1). Samples were collected using latex gloves and tweezers. After wrapping the samples in foil, they were placed into plastic bags, sealed closed with adhesive-tape and labelled. Six to eight isolated mollusc shell fragments were collected from each of the twelve sites. In addition to marking the locations of collected samples, other items of interest were photographed and their location recorded, although they were not collected. These included shell middens, heat retainer hearths or significant accumulations of stone artefact materials. All marked locations were later surveyed and added to the *ArcGIS* database. A list of all collected samples and all marked locations is available in Appendix A.

Figure 3.2. Two copies of the aerial photography of the Lake Mululu lunette, with all site codes labelled on one copy.

3.2. Sedimentology and stratigraphy methods

3.2.1. Stratigraphic logging

Stratigraphic exposures were logged at 39 locations at various positions along the length of the lunette. Exposures were typically recorded on the sides of residuals or gullies and were chosen with respect to both location and to facilitate minimal sediment removal. A vertical face for logging was cleaned with a handheld shovel, trowel and paintbrush. Vertical variations in stratigraphic features such as grainsize, sorting, rounding and sphericity were recorded based on the parameters defined in the Geoscience Australia Grain Size Card (Figure 3.3). Dry sediment colour was recorded using a Munsell Soil Colour chart, and other physical and biogenic structures such as laminations and calcretions and rhizomorphs were described. Clay content was identified and estimated using a field texturing 'bolus and ribbon' technique described by (McDonald (1998) and the presence of carbonate was identified through the observation of effervescence in response to the application of a weak (10%) hydrochloric acid solution. Logs were hand drawn in the field on Outcrop Stratigraphic Log Sheets (e.g. Figure 3.4). Sediment samples were taken from each unit at each stratigraphic log site, for oriented thin sections (Section 3.2.3).

Sediments associated with OSL samples (Section 7.2.1) were sub-sampled to approximately 100 g using a cone and quartering technique. These were then further sub-sampled by grain size using hand held mesh sieves at intervals of 840, 590, 212, 106 and 74 µm and each size fraction was weighed. Microsoft Office *Excel* was used to create frequency distributions and QQ probability plots. A further sub-sample was analysed under a binocular microscope to describe grain size, roundness, sphericity and other physical features of the sediments, including dry Munsell colour, using the same methodology described for field stratigraphic logs (above).

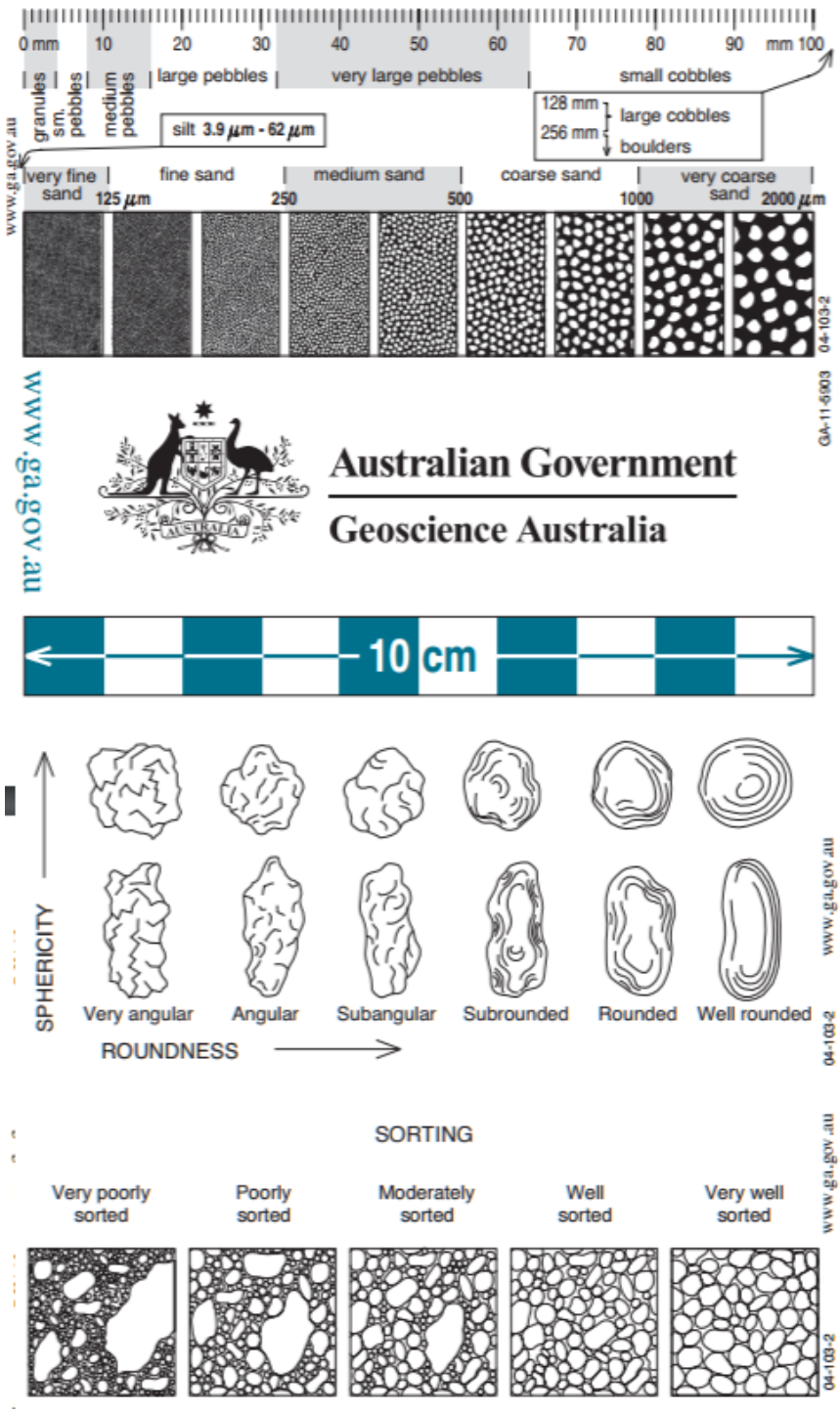

Figure 3.3. Geoscience Australia Grain Size Card used for describing sediment properties.

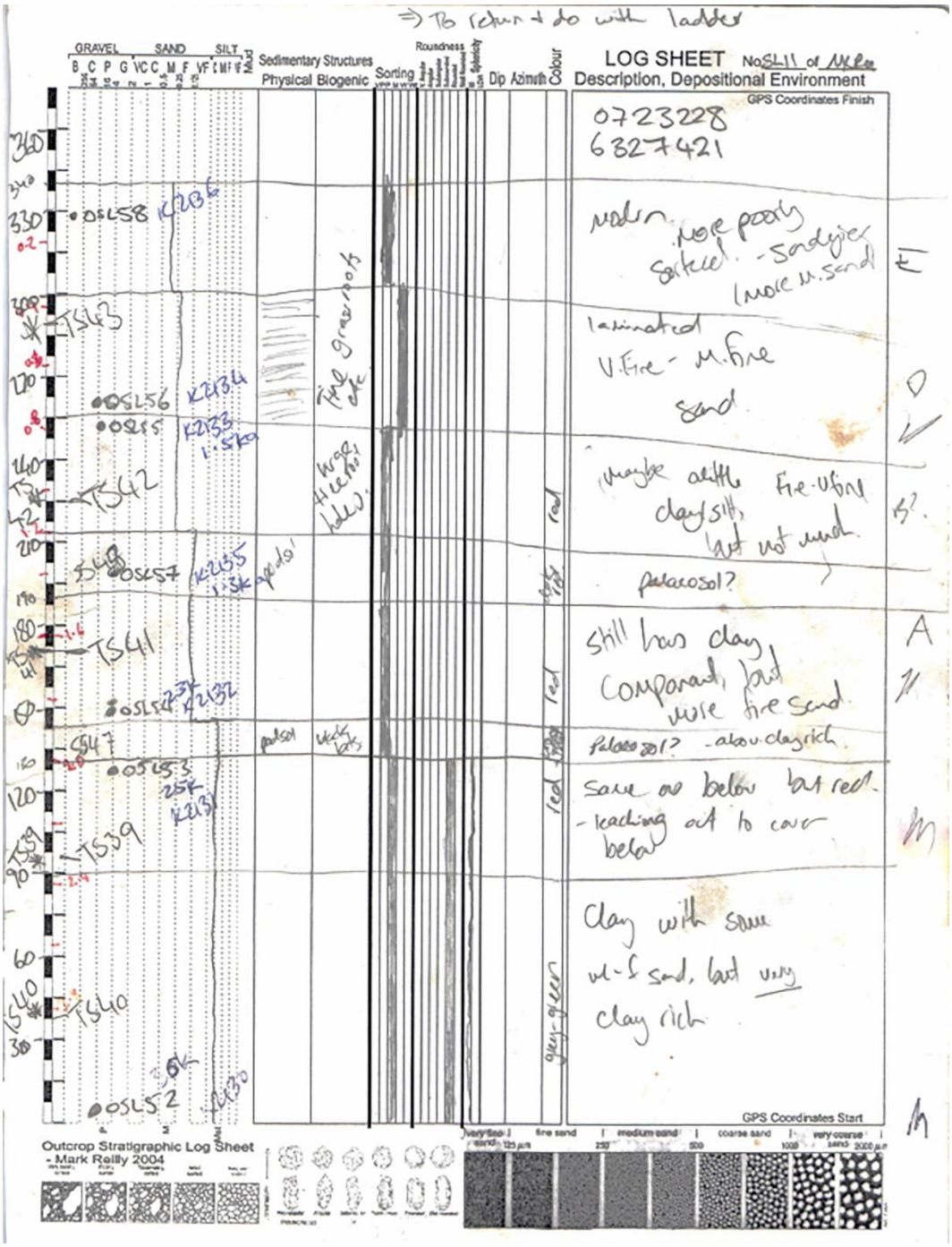

Figure 3.4. Example of an Outcrop Stratigraphic Logsheet. Additional detailed notes were also made in an accompanying notebook.

3.2.2. Drilling

A drill rig with a thin-walled core tube sampler inside hollow auger casing was utilised to determine the internal stratigraphy at three poorly exposed areas of the lunette (Figure 3.5). Four holes were drilled, two at DH01 (16 m, then four metres further down slope, 14 m) and

one each at DH02 (11 m) and DH03 (11.5 m). Core material was logged at the time of drilling, with features such as grainsize, sorting, rounding and colour and clay or carbonate content noted every 20-30 cm and at any obvious contacts, using the same methodology described for field stratigraphic logs (Section 3.2.1). These notes were used to create stratigraphic logs using *Adobe Illustrator*.

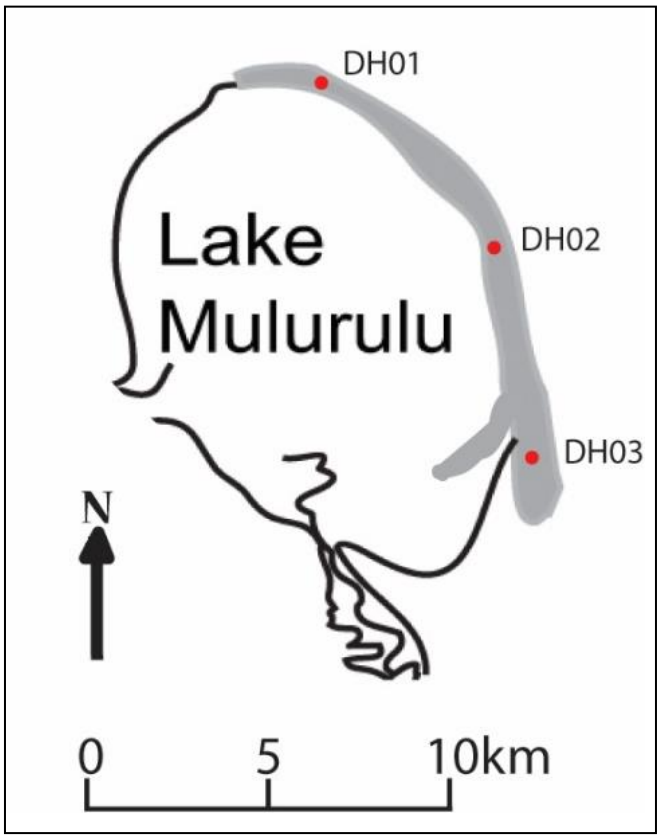

Figure 3.5. A map of Lake Mulurulu showing the locations of the drilling sites. (Map modified from Webb 2006).

3.2.3. Oriented thin sections

Initially, 151 sediment samples were collected from stratigraphic logs (Section 3.2.1), OSL (Section 7.2.1) and transect (Section 3.2.4.3) sites, for oriented thin sections. Where sediments were loose, samples were collected in stainless steel or PVC tubes, which were gently pushed into the sediment (Figure 3.6a). Where necessary, an aluminium foil plug was used to stop the sediment collapsing inside the tube (Figure 3.6b). Once collected, the ends of the tube were stuffed with aluminium foil and adhesive-taped to ensure a tight fit and avoid movement of the sediments inside the tube during transport (Figure 3.6c & d). Where sediments were more coherent, small samples were pried out of the unit using a hand trowel,

and simply wrapped in aluminium foil. All samples were labelled with a sample number and an orientation marker. Due to time and funding limitations, thin sections were prepared from 32 of the 151 samples. These were the samples associated with OSL samples and a few other selected sites. Oriented sediment samples were submitted the ANU School of Geology and Marine Biology thin section laboratory, where they were impregnated with polyester resin. Once set, slices were cut using a rock saw and these sub-samples were again provided to the thin section laboratory, where they were mounted on glass slides, cut and ground to make large (60 x 45 mm), oriented thin sections with cover glass. These were analysed and imaged through a petrographic microscope, noting physical features such as composition, grain-size, roundness and sphericity.

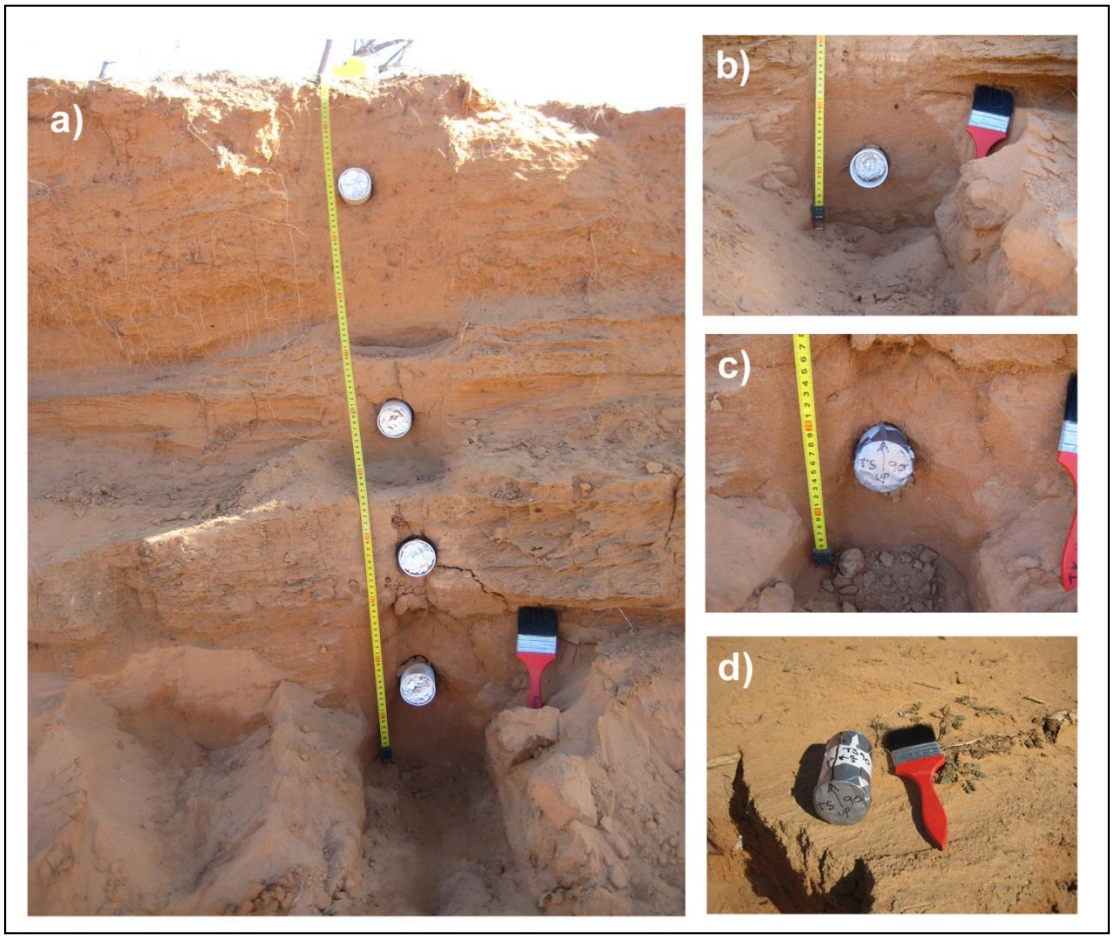

Figure 3.6. Oriented thin section sampling procedure. a) A partially sampled logging section. b) A PVC tube with an aluminium plug is inserted into the sediments. c) Once the tube is full, the end is taped, and the sample labelled with a way-up direction. d) The sample is removed from the sediments, and both ends are taped and labelled

3.2.4. Surveying

3.2.4.1. Differential GPS

Differential GPS (dGPS) stations were positioned at 14 sites on the lake floor along the inside edge of the lunette, approximately 1 km apart and 200 - 500 m from the lunette. A base station (MLRU) was positioned approximately halfway along the lunette, and an aerial and receiver box used to collect satellite information over 24 hours, to determine the GPS location to within millimetres. Thirteen rover stations (ML27- ML39) were set up in turn, and an aerial and receiver box utilised for two hours at each, to determine their location with reference to the base station. The co-ordinates for each dGPS location could thus be determined with high precision. Each was marked with a permanent surveying peg and used for all further surveying in the field area. The dGPS locations are available in Appendix A.

3.2.4.2. Sampling locations

The co-ordinates for all sampling locations (stratigraphic logs, thin section, OSL, and faunal samples) across the lunette were determined using surveying equipment. For each region of the lunette, a total-station was set up on a dGPS marker proximal to the area of interest and a backsight prism setup on a neighbouring dGPS marker. Given that the dGPS markers were at known co-ordinates, they could be used to confirm the accuracy of the total-station. Points of interest on the lunette were surveyed using a prism on a staff, and backsight readings were recorded and checked at the start and end of each surveying session. These were later added to the *ArcGIS* map and located on the aerial photography (Section 3.1).

3.2.4.3. Transects

The survey equipment was also used to record the shape of the lunette by transects across it at seven locations (Figure 3.7). The total-station equipment was set up and backsights used in the same manner as for sampling locations. The topography of a transect of the lunette was recorded, followed by the contacts between stratigraphic units across the same transect. The transect locations were chosen based on getting an even spread across the lunette, stratigraphic exposure and visibility from dGPS markers. PR01, PR02, PR04 and PR05 were sites with stratigraphic exposures, while the other three sites were not. They were also

collection locations for OSL, thin section, loose sediment and radiocarbon samples, plus wombat samples were also collected from PR02 and otoliths from PR01.

Figure 3.8 to Figure 3.11 show aerial photos of transect sites, PR01, PR02, PR04 and PR05 respectively, indicating the sampling locations. The surveying data for each of the six transects were plotted using Microsoft Office *Excel* and *Adobe Illustrator*. For the four transects at which stratigraphy was visible on the surface, a stratigraphic profile was made based on the surface expression of the units. From this, a composite stratigraphic log was created, using estimated depths for an idealised vertical sequence at each site. Sampling locations for OSL, thin sections, faunal materials and drill holes were also recorded on the profiles and composite stratigraphic logs. The stratigraphic logs were then combined to construct an idealised composite stratigraphic log for the entire lunette.

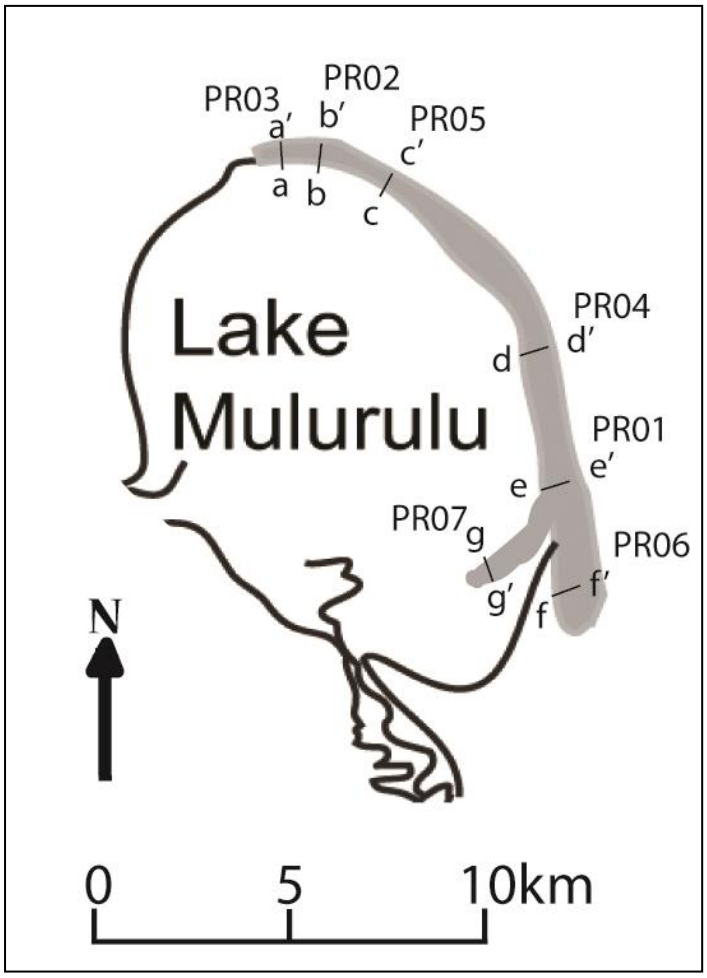

Figure 3.7. Map of Lake Mulurulu showing the locations of the transect sites. (Map modified from Webb 2006).

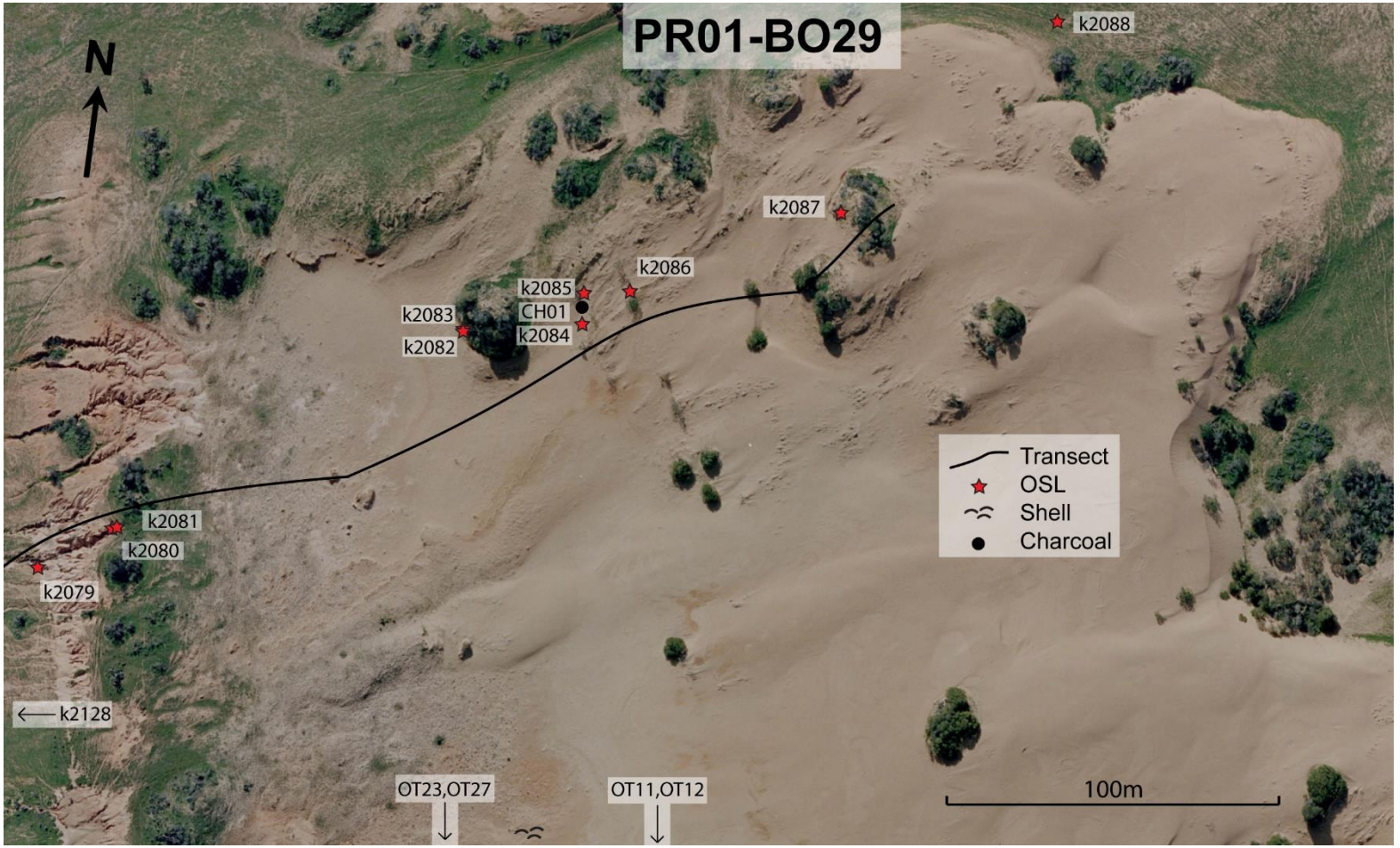

Figure 3.8. Transect site PR01

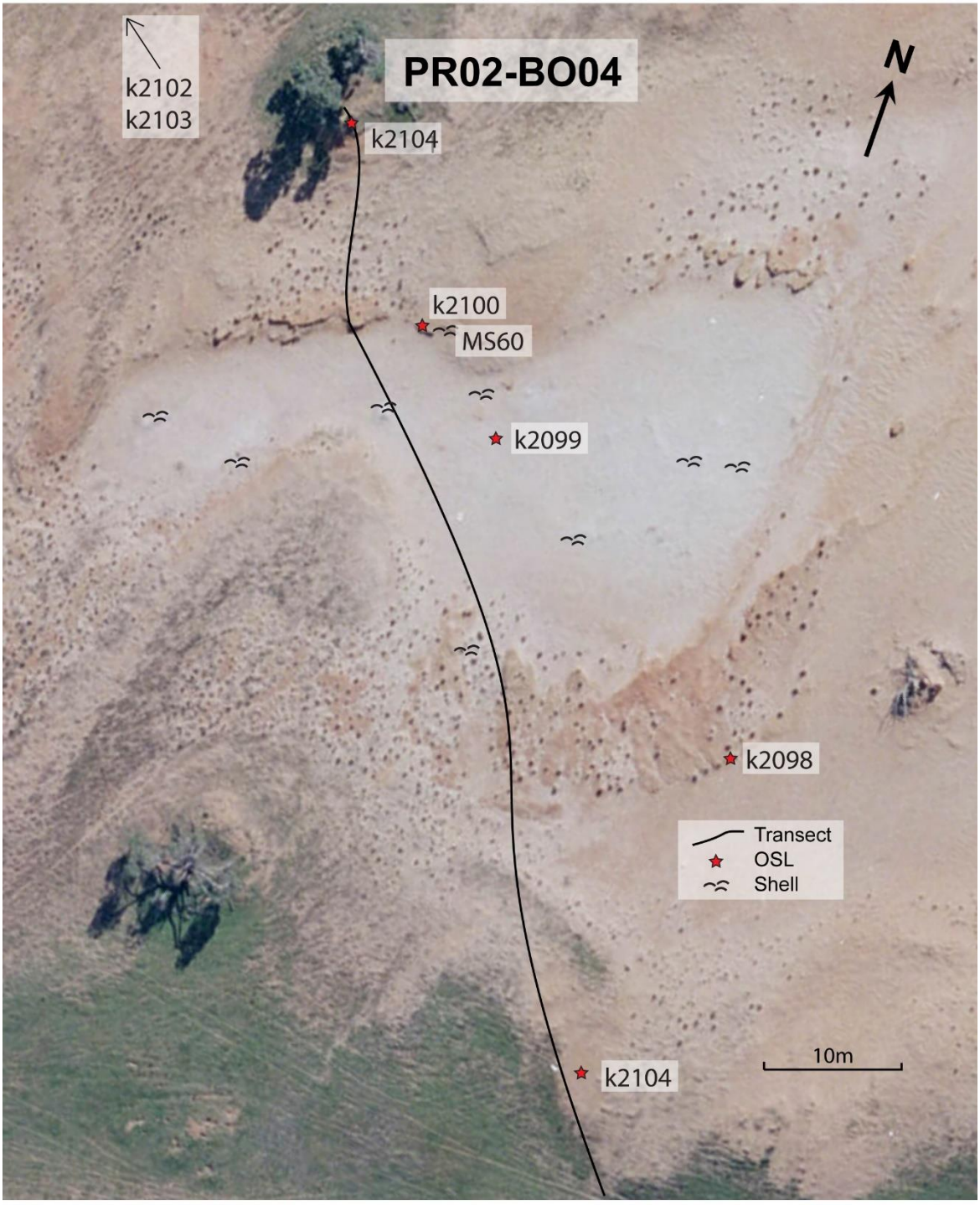

Figure 3.9. Transect site PR02

Figure 3.10. Transect site PR04

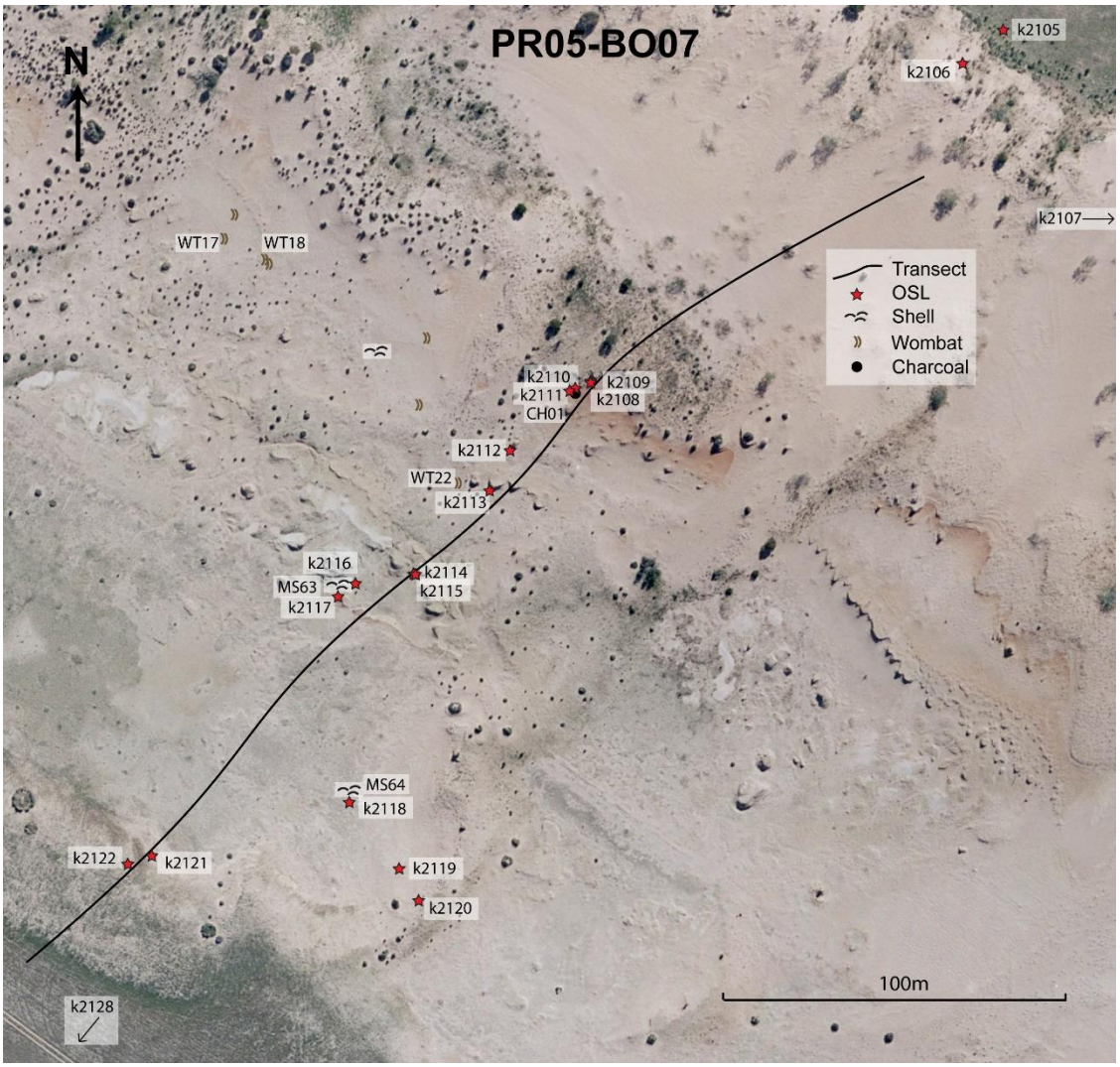

Figure 3.11. Transect site PR05

3.3. Sedimentology and stratigraphy results and interpretations

3.3.1. Stratigraphic units

The stratigraphy of the Mulurulu lunette was divided into five main units, labelled A, B, C, D and E (from oldest to youngest), on the basis of sediment characteristics, including grainsize, sorting and colour, as well palaeosol characterisation and the presence of unconformities at unit boundaries. Few sites exposed a preserved record of all five units; rather each unit is variously eroded in different parts of the lunette, and unconformably overlie different units in different locations. Summary descriptions for each unit are presented here, based on an amalgamation of information from drill core, stratigraphic logs and transect sites. These

individual exposures are each described in Sections 3.3.2, 3.3.3 and 3.3.4. Tables of thin section and sediment descriptions, including Munsell colours, are available in Appendix B and detailed sedimentary descriptions from each sampling location are available in Appendix C. Throughout this discussion, the terms ‘front’ and ‘rear’ are used to describe the lunette from the perspective of standing on the lake bed; thus they represent locations on the windward and leeward sides of the lunette, respectively.

3.3.1.1. Non-lunette locations

Seven samples were collected from beneath the current ground surface, in areas not part of the lunette. Four samples from behind the lunette (e.g. Figure 3.12a), two from the ‘beach edge’ along the front (e.g. Figure 3.12b) and one from the ‘spit’ (Figure 3.12c). Those from behind the lunettes are mostly fine to medium, poorly-sorted sub-rounded sands. The sediments from the spit are similar, though a coarse sand component is also present. The beach, on the other hand, consists of fine to medium, moderately well-sorted, sub-angular to sub-rounded sands with a few clay pellets. All of these sediments are affected to some degree by soil formation, as they were collected within 30 cm of the modern, vegetated ground surface. Only the sample from the spit, however, has evidence of an illuvial clay matrix, indicative of the B-horizon of a true soil.

Figure 3.12. Sampling locations not in the lunette proper. a) behind the lunette at PR02. b) along the 'beach' edge at PR01. c) in the 'spit'. The dotted line highlights the edge of the spit.

3.3.1.2. Unit A 'lunette core'

Description: This unit consists of a mostly poorly sorted, sandy clay, varying in grainsize from silt and clay to coarse sand (Figure 3.13), with abundant clay pellets that form sand-sized grains (Figure 3.14). It forms the basal core of the lunette and is most commonly exposed by gully erosion and in the base of blowouts. At the deepest gully exposure, the unit is two metres thick and it is more than 9 m thick in drill core at DH01. The base of the unit consists of a massive grey-green plastic clay layer, at least 6 m thick. In some areas it is mottled orange/green/grey and it also contains some centimetre-scale sandy horizons. The basal clay layer is capped by a sandy clay layer with a well-developed (2-3 m) palaeosol. It is easily recognisable by a deep brown to reddish yellow colouring (7.5YR 4/6, 5/8, 6/8, 7/6) and abundant secondary carbonates. The sand grains in this layer regularly have both inherited and *in situ* cutans. Illuvial clay forms the matrix between grains, along with disaggregated clay pellets. The extent of calcification varies from secondary carbonate impregnating the clay matrix (Figure 3.14), to fine pisolitic grains, to 1 mm to 5 cm nodules (Figure 3.15). A massive calcrete layer (>1 m thick) is exposed beneath the clay layer at some locations toward the south end of the lunette (Figure 3.16). The palaeosol also varies laterally, with different degrees of secondary carbonate precipitation in different exposures. Rubification is more intense toward the top of the unit. At two locations, gypsum crystals were seen in the nodular region above the massive calcrete (Figure 3.17 and Figure 3.18).

Interpretation: Unit A represents the earliest lunette building phase evident at Lake Mulurulu, while the underlying clay suggests an earlier lake floor on which the lunette has been built. The pelletal clay component of the sandy-clay unit indicates drying of the lake floor (Bowler 1973), and may have hindered the movement of sand particles, preventing rounding or sorting, leaving the sand texturally immature. The calcification and rubification of the unit represents palaeosol development, indicating a stable period in the history of the lunette, when very little deposition occurred, allowing vegetation to grow (Bowler 1998). The thickness and intensification of the palaeosol suggest a very long period of stability for such a thick calcareous soil to develop. The presence of gypsum crystals can indicate very saline groundwater (Schütt 2004), as they grow amongst the sediments when there is evaporation at the capillary fringe of the water table (Magee et al. 1995). Alternatively, they may be a result of pedogenic salt accumulation. Given the elevation above lake level, this is the more likely source for these crystals; possibly introduced into the system as dust and transported into the

soil profile by meteoric water during pedogenesis. The presence of calcrete at the surface of this unit indicates an erosional unconformity. Soil calcification occurs at depth as carbonate minerals are leached from upper to lower soil horizons, so here the topsoil must has been removed before the overlying layers were deposited. Additionally, some exposures contain re-worked red sands, most likely derived from this unit, directly overlying the calcrete.

This unit is most likely equivalent to the Golgol unit of Lake Mungo, which is a similar rubified and calcified PCD unit forming the core of the Lake Mungo, Garnpung and Outer Arumpo lunettes (See Section 8.1.1 for a discussion including geochronological results).

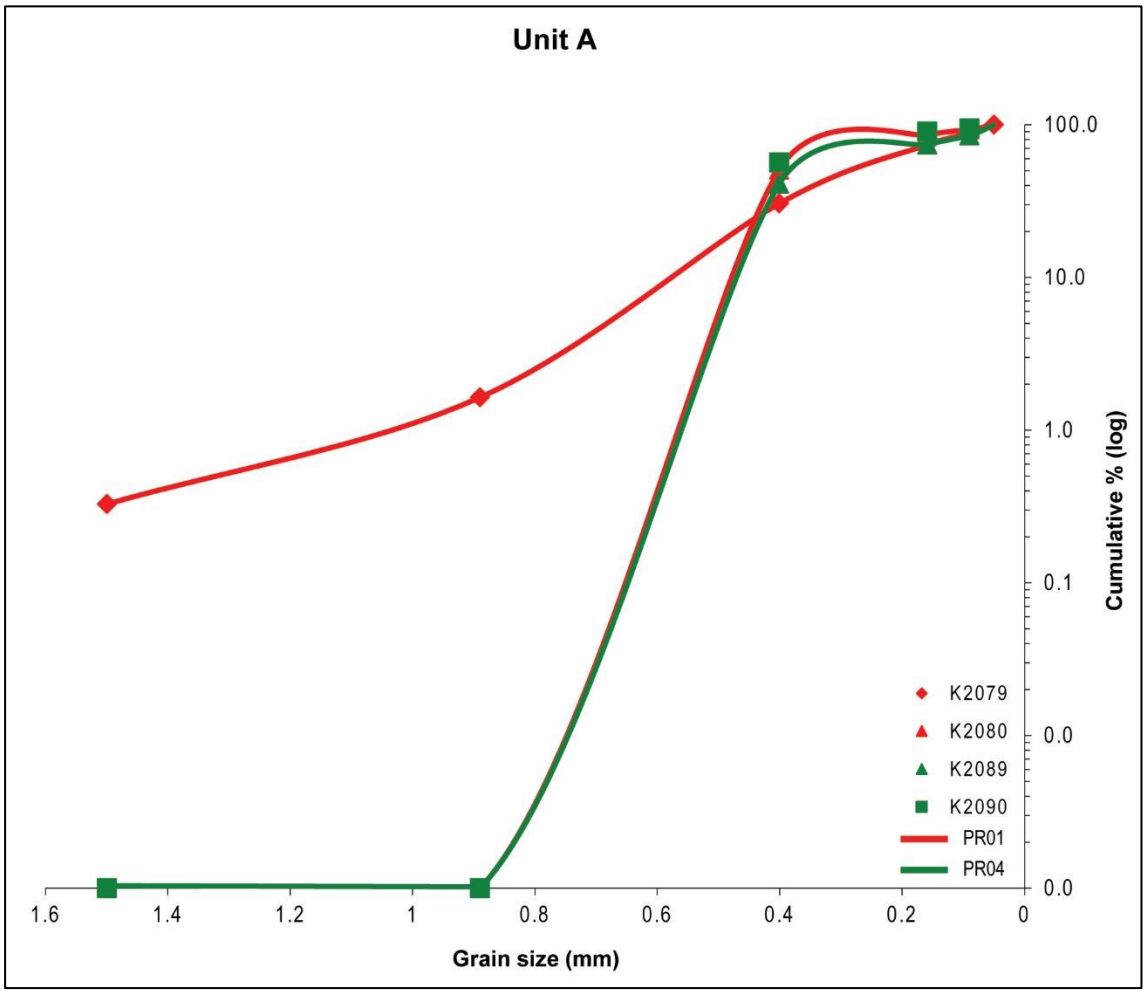

Figure 3.13: Cumulative grain size chart for sediments associated with OSL samples from Unit A. Where clay pellets have maintained coherence, they sieve as sand-sized grains. Detailed sedimentary data for each sample is available in Appendix B.

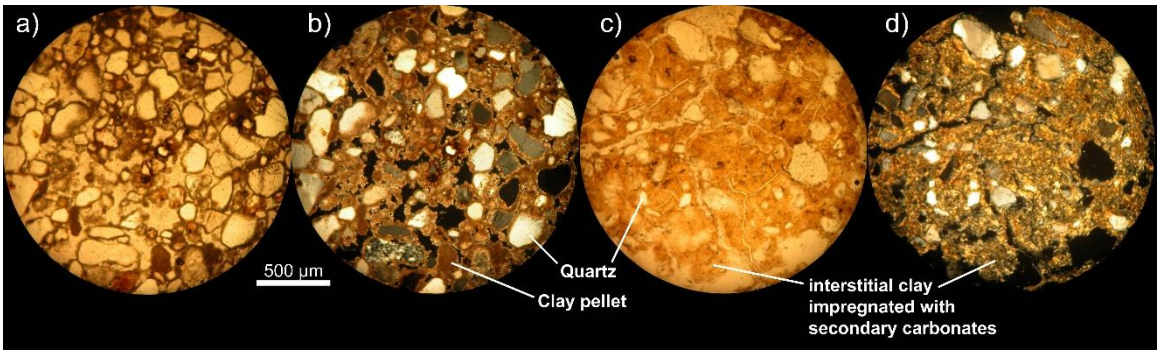

Figure 3.14. Two fields of view thin section TS143 from Unit A at PR01, showing the clay matrix impregnated with secondary carbonates. Images a) and b) are the same field of view, shown in PPL and XPL respectively, as are c) and d).

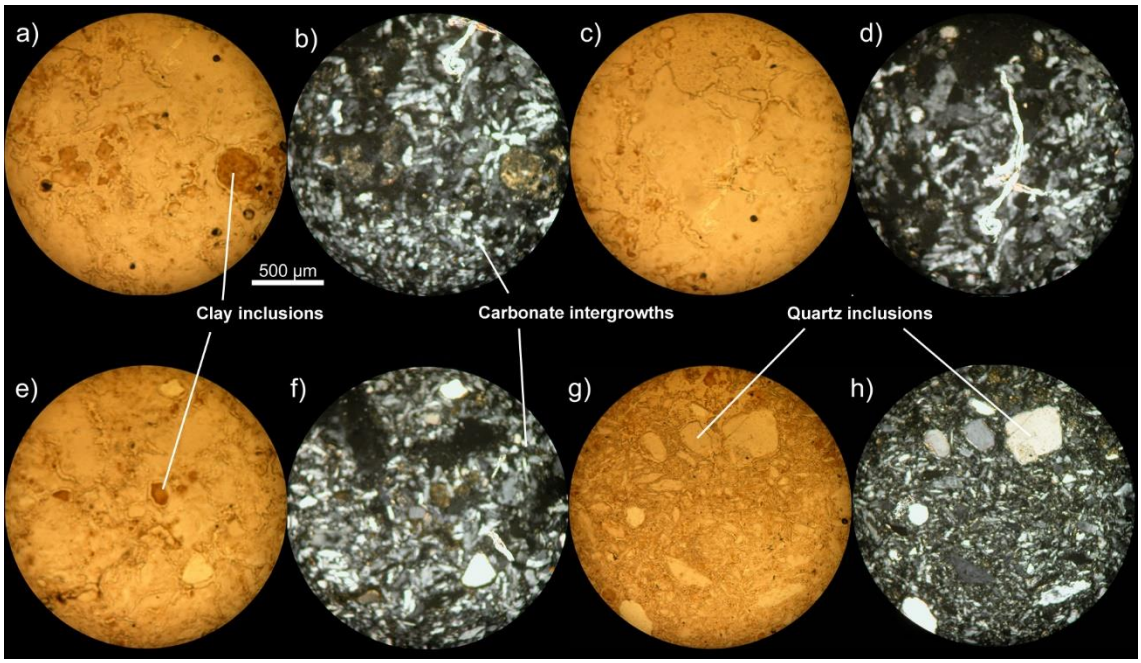

Figure 3.15. Four fields of view thin section TS051, of a carbonate nodule from Unit A, showing the fine grained carbonate intergrowths with quartz and clay inclusions. Images a) & b) are the same field of view, shown in PPL and XPL respectively, as are c) & d), e) & f) and g) & h).

Figure 3.16. Exposure of massive calcrete in gully erosion through Unit A. Calcrete in this picture is about 50 cm thick.

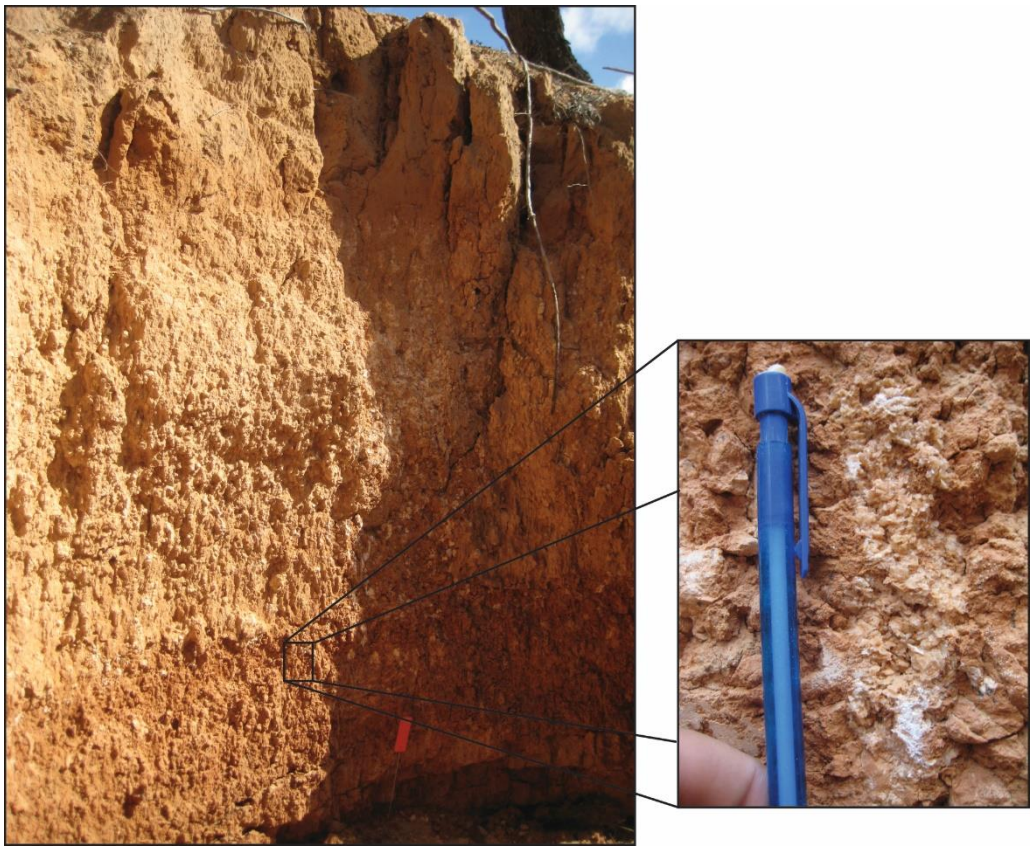

Figure 3.17. Gypsum crystals in Unit A in a gully exposure at Lake Mulurulu. The orange tag in the left picture is approx. 6cm long.

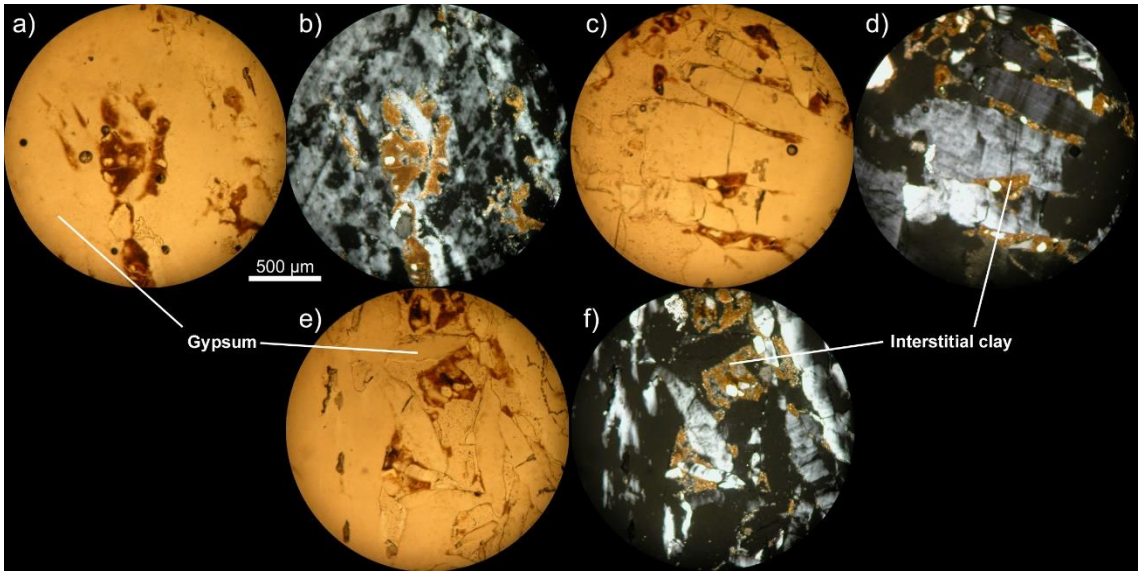

Figure 3.18. Three fields of view thin section TS049, of gypsum crystals from Unit A, the euhedral to subhedral crystals with interstitial clay and fine carbonates. Images a) & b) are the same field of view, shown in PPL and XPL respectively, as are c) & d) and e) & f).

3.3.1.3. Unit B 'lower sand unit'

Description: Unit B unconformably overlies Unit A and is dominated by sub-rounded, mostly moderately to well-sorted, fine to medium, clean quartz sand (Figure 3.19). The base of Unit B includes re-worked red sands, clays and carbonate clasts, intermingled with the more typical clean sand described above. Small (5-20 mm) *in situ* calcrete nodules occur in laterally localised areas (e.g. PR02, but not PR04), above which sediments are rubified. This palaeosol appears to be largely deflated in some areas (e.g. PR04) where the rubified region is only preserved atop residuals. Unionid shell middens are present in a number of locations, including immediately overlying Unit A, in the reworked red sands (PR04; Figure 3.20c) as well as within the clean sand (PR05; Figure 3.20b) and immediately below the rubified palaeosol, amongst the carbonate nodules (PR02; Figure 3.20a).

Interpretation: The clean sand comprising the bulk of the unit, lacking coarse or gravel components, is typical of dune sands developed by deflation from a sandy beach (Bowler 1998). The microbialite clast in TS133 is evidence of an input of materials from shallow water derived sediments (Figure 3.21). This clean sand layer indicates the return of water to the lake, providing the development of a sandy beach from which the material is derived. The reworked sediments at the base of the unit, including red sands with thick inherited cutans and clasts of clay and carbonate (Figure 3.22) are almost certainly derived from the underlying Unit A. The calcrete and rubified sediments toward the top of the unit represent a moderately well developed, discontinuous palaeosol, indicating a period of stability, with reduced sediment input while vegetation colonised the dunes. The faunal material, where distributed in middens, demonstrates aboriginal occupation of the area, indicating the use of the lake environment as a food source. This is the earliest evidence of occupation at Lake Mulurulu, (see Section 5.3 for dating results).

Given that it directly overlies Unit A, considered to be equivalent to the Golgol unit (see above), this sandy unit is thought to correlate with the Lower Mungo sands from Lake Mungo (See Section 8.1.2 for a discussion including geochronological results).

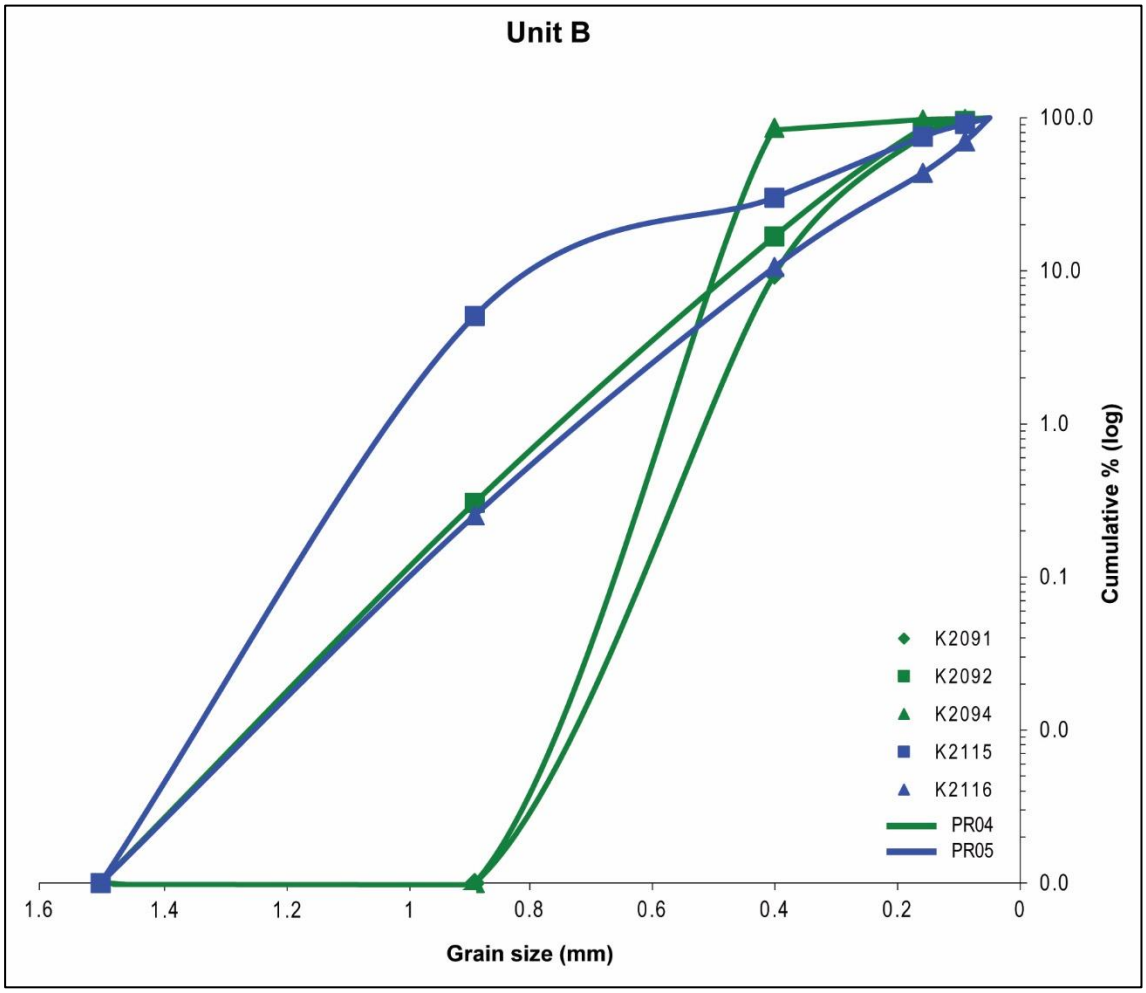

Figure 3.19: Cumulative grain size chart for sediments associated with OSL samples from Unit B. Detailed sedimentary data for each sample is available in Appendix B.

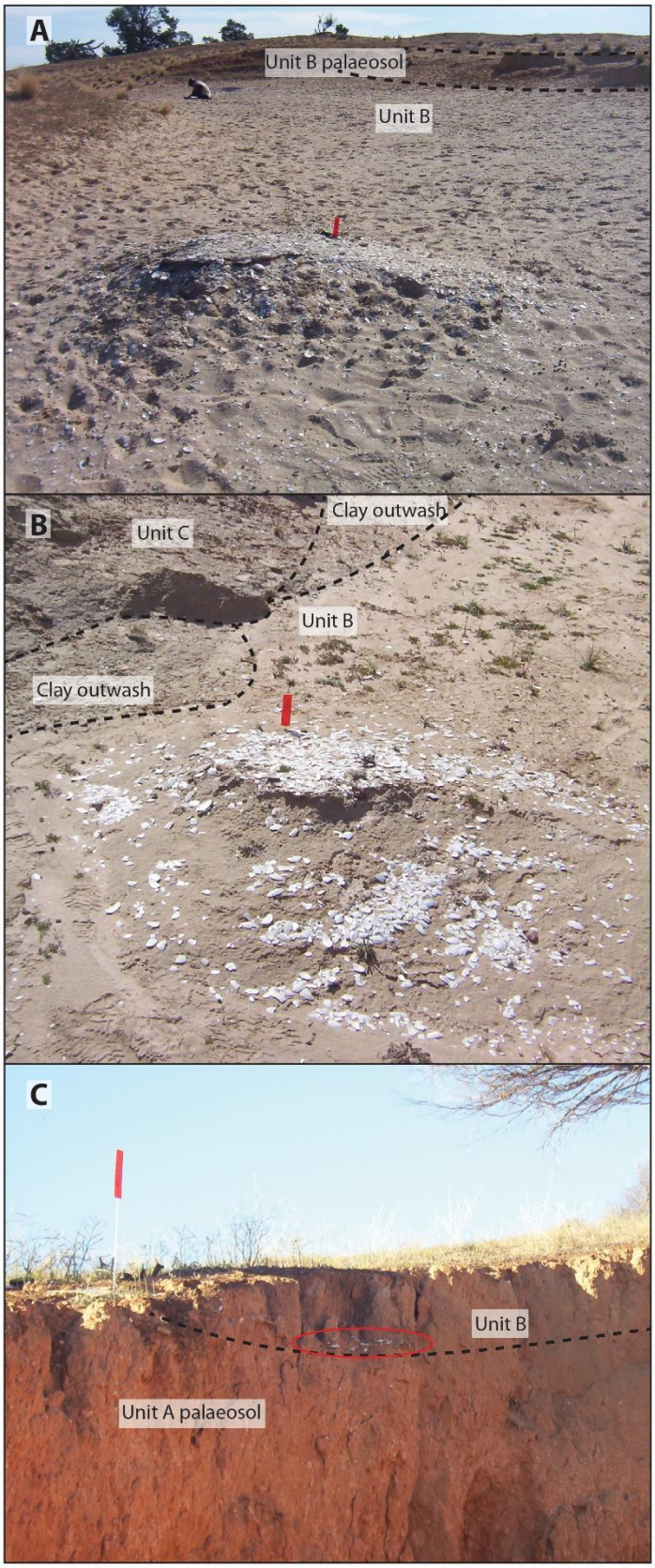

Figure 3.20. Shell middens in Unit B, (A) beneath the palaeosol, (B) amidst the clean sand and (C) immediately above Unit A palaeosol, in the reworked sands.

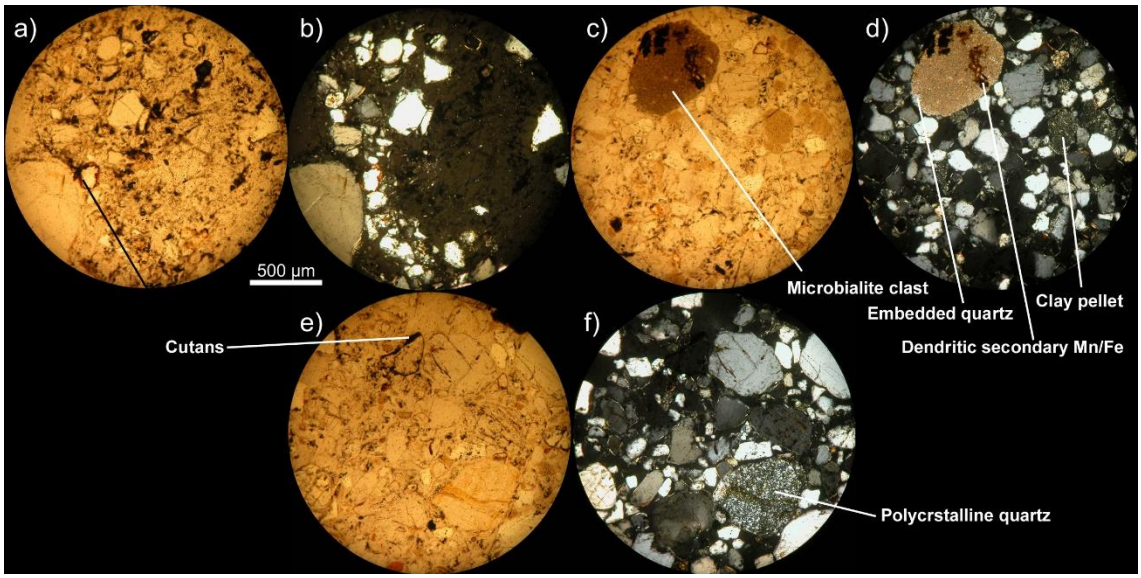

Figure 3.21. Three fields of view thin TS133, section of Unit B sands at PR05. A microbialite clast can be seen in images c) and d). Images a) & b) are the same field of view, shown in PPL and XPL respectively, as are c) & d) and e) & f).

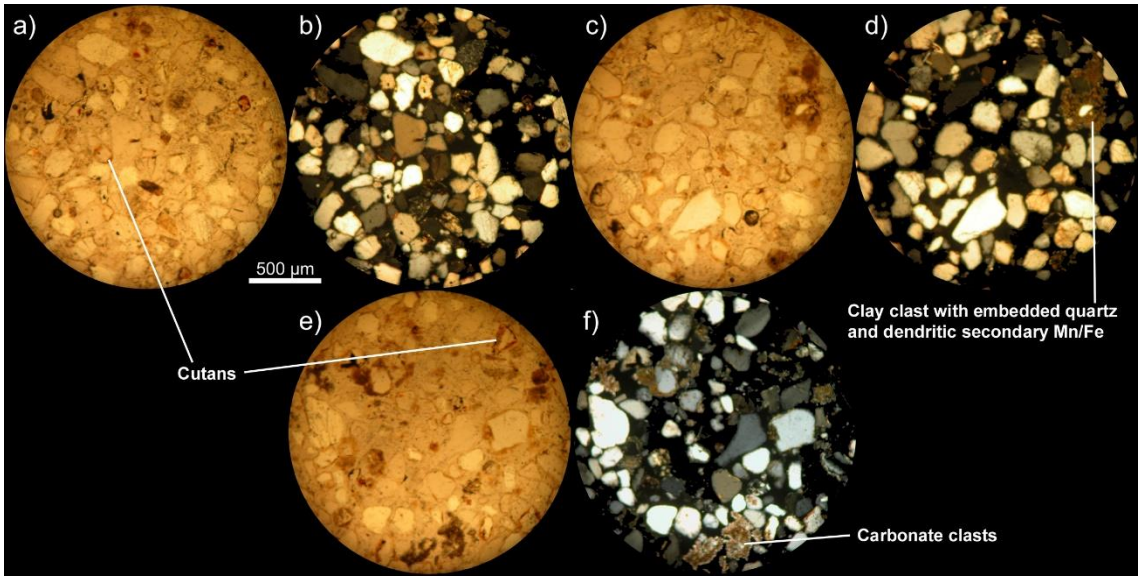

Figure 3.22. Three fields of view thin section TS141, of the reworked sediments at the base of Unit B at PR04, showing clasts of secondary carbonate and clay and many inherited cutans. Images a) & b) are the same field of view, shown in PPL and XPL respectively, as are c) & d) and e) & f).

3.3.1.4. Unit C 'clay unit'

Description: Unit C is a sandy clay layer, consisting of what Bowler (1998) termed 'Pelletal-Clay Dunes' (PCD). The sand component of the layer is generally poorly sorted (Figure 3.23), sub-angular to sub-rounded quartz, often with inherited cutans. Rounded medium sand-sized clay pellets are abundant, dominating the thin sections (Figure 3.24). Gypsum rosettes were also observed in this unit at one location (PR04; Figure 3.25). At least two palaeosols are present (seen in succession at SL11, Figure 3.26) At least two palaeosols are present (seen in succession at SL11, Figure 3.26) but were either never developed or were eroded away at the north end of the lunette where Unit C is unconformably overlain by sand of Unit D.

Interpretation: This unit represents another drying phase, as evidenced by the pelletal clays. The presence of two palaeosols indicates at least two periods of stability occurred, when sediment input decreased, allowing soils to develop (Bowler 1998). There is no depositional evidence of a return to fresh water conditions in between these two periods of vegetation colonisation.

The gypsum is likely to have grown pedogenically after arriving as dust, much like in Unit A. The eroded palaeosol at the northern end represents an unconformity and period of erosion concentrated at the north end of the lunette.

This PCD unit may be equivalent to either the Upper Mungo or Arumpo units at Lake Mungo (Section 2.4). Both of those units contain PCD facies, though the Arumpo unit includes a clean quartz sand phase separating the PCD's of the respective units, which appears to be missing at Mulurulu (See Section 8.1.3 for a discussion including geochronological results).

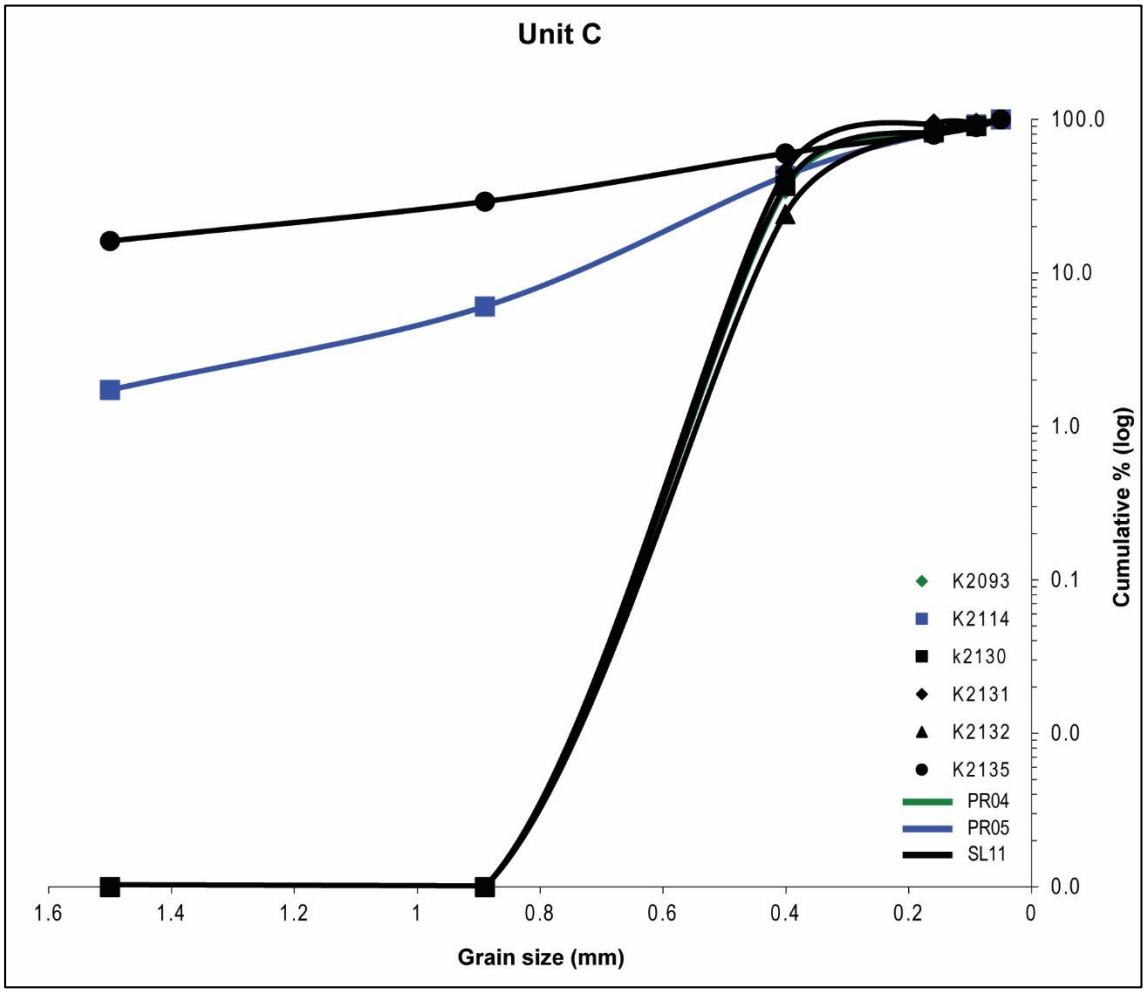

Figure 3.23: Cumulative grain size chart for sediments associated with OSL samples from Unit C. Where clay pellets have maintained coherence, they sieve as sand-sized grains. Detailed sedimentary data for each sample is available in Appendix B.

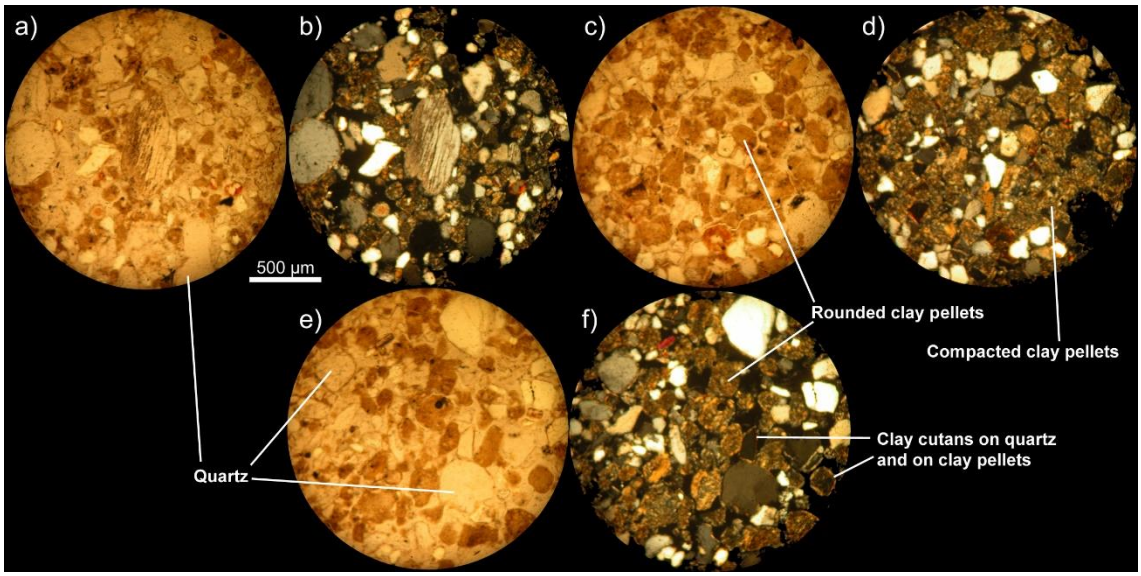

Figure 3.24. Three fields of view thin section TS132, of pelletal clays in Unit C at PR05. Images a) & b) are the same field of view, shown in PPL and XPL respectively, as are c) & d) and e) & f).

Figure 3.25. Gypsum crystals in Unit C at PR04.

Figure 3.26. Palaeosols in Unit C of SL11, in BG01. The two holes in Unit C are the result of OSL sample collection, while the holes in Unit E were pre-existing.

3.3.1.5. Unit D 'upper sand unit'

Description: Unit D has a massive structure and mostly consists of moderately to well-sorted (Figure 3.27), sub-angular to well-rounded, fine to medium sand (Figure 3.28). The unit shows considerable lateral variation, poorly sorted in some areas (DH03) and very well-sorted in others. The unit was either not deposited or was completely removed at some sites (PR02 and PR04), where underlying units are directly in contact with Unit E (see below). Where Unit D occurs, a palaeosol consisting of small (1-2 cm) calcrete nodules, rhizomorphs and rubification is generally present (Figure 3.29). At the south end of the lunette (including PR01) the unit is topped with a thin (<10 cm), laterally continuous clay pellet layer (Figure 3.31A; Figure 3.28). The sands of Unit D contain abundant *Velesunio* shell middens (Figure 3.30), as well as other animal remains, such as bettong teeth (*Bettongia lesueur*) and fish otoliths (*Maquaria ambigua*). Burnt wood occurs near the top of the unit, at a number of locations at the south end (e.g. PR01), and dark humic staining occurs at the north end (PR05) of the lunette (Figure 3.31).

Interpretation: The sandy materials represent a final return of water to Lake Mulurulu, accompanied by aboriginal occupation, as evidenced by the middens. Soil formation, as evidenced by the palaeosol in this unit, requires a period of relative stability, with low sediment input and successful vegetation colonisation (Bowler 1998). Burnt wood may be a result of a modern fire (a burnt goat skull was also seen on the lunette). The consistent presence of the burnt material in the same horizon may be due to the burning of modern tree roots or it may be that the wood was burnt prior to burial and re-exposure.

Given that this is the last lake-full phase recorded at Lake Mulurulu, this unit is probably equivalent to the Zanci unit at Lake Mungo (See Section 8.1.4 for a discussion including geochronological results). At Lake Mungo, however, the Zanci unit is dominated by PCD facies, with discontinuous wet-phase event sand facies, while here at Mulurulu very little PCD development is apparent, apart from the thin clay-rich layer at the southern end of the lunette.

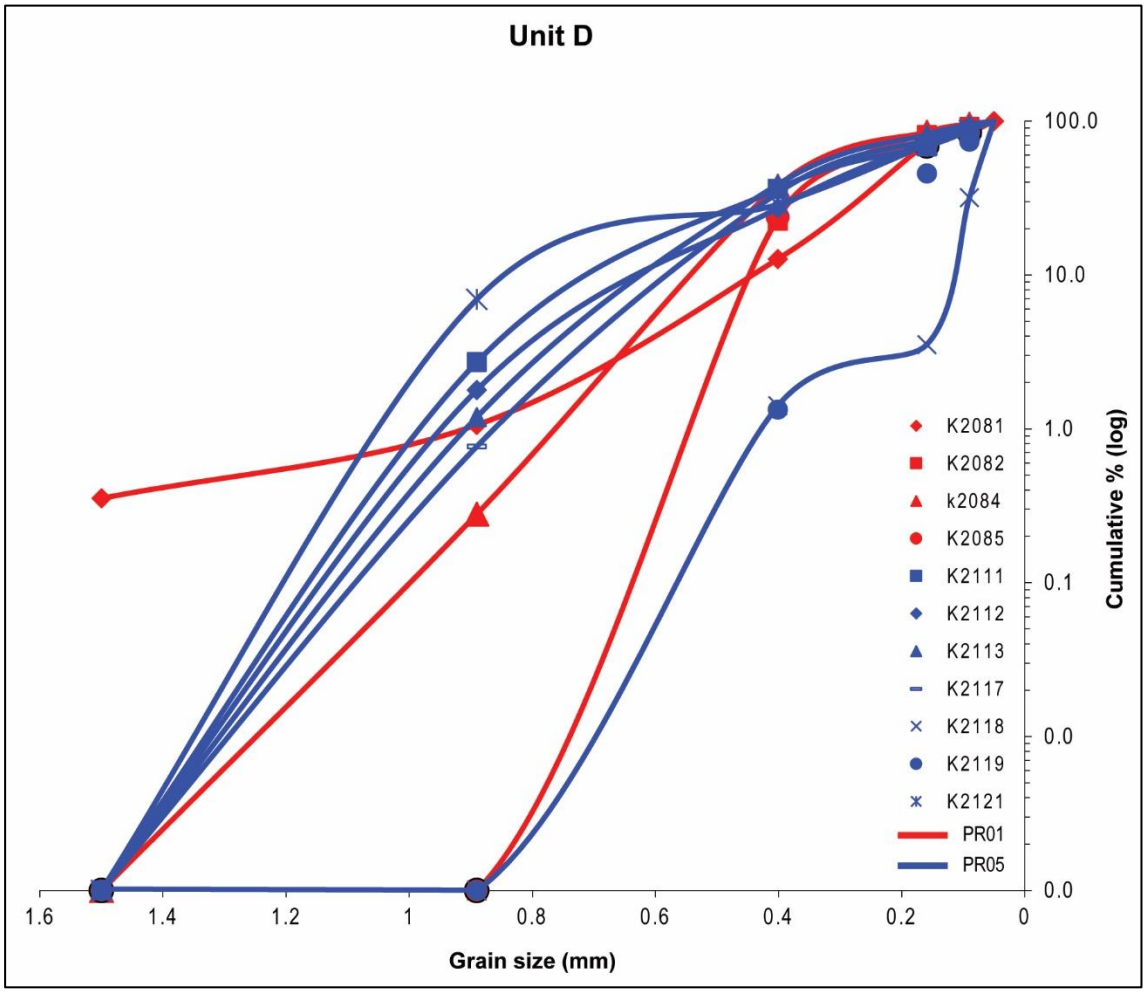

Figure 3.27: Cumulative grain size chart for sediments associated with OSL samples from Unit D. Detailed sedimentary data for each sample is available in Appendix B.

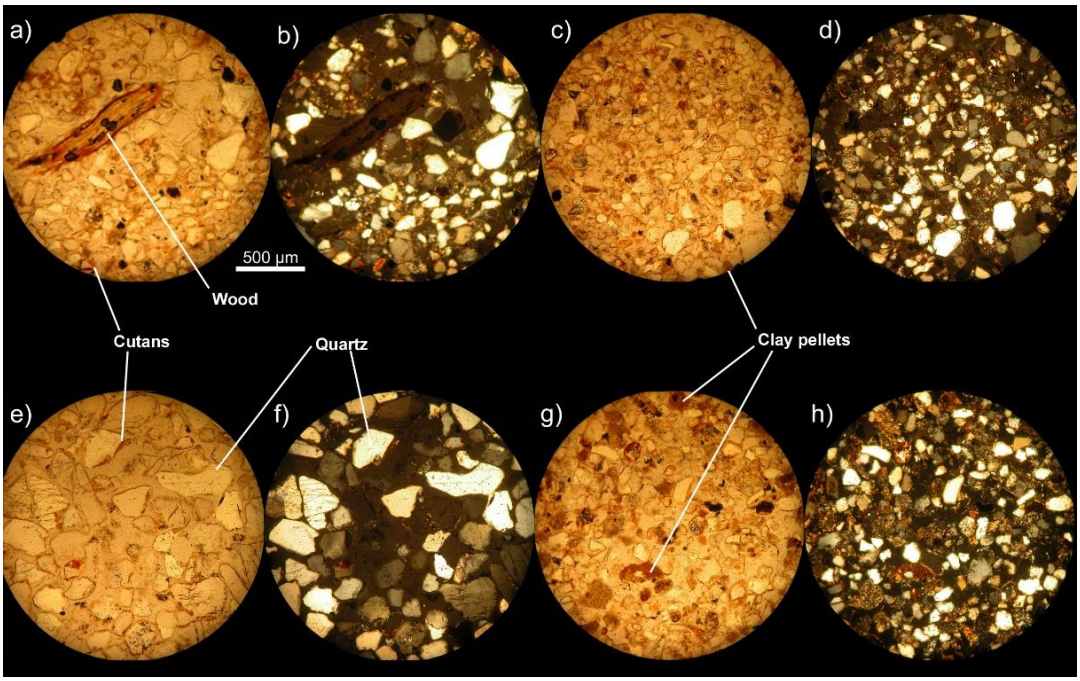

Figure 3.28. Four fields of view thin section TS146, of sands and clay at the top of Unit D at PR01. Images a) & b) are the same field of view, shown in PPL and XPL respectively, as are c) & d), e) & f) and g) & h).

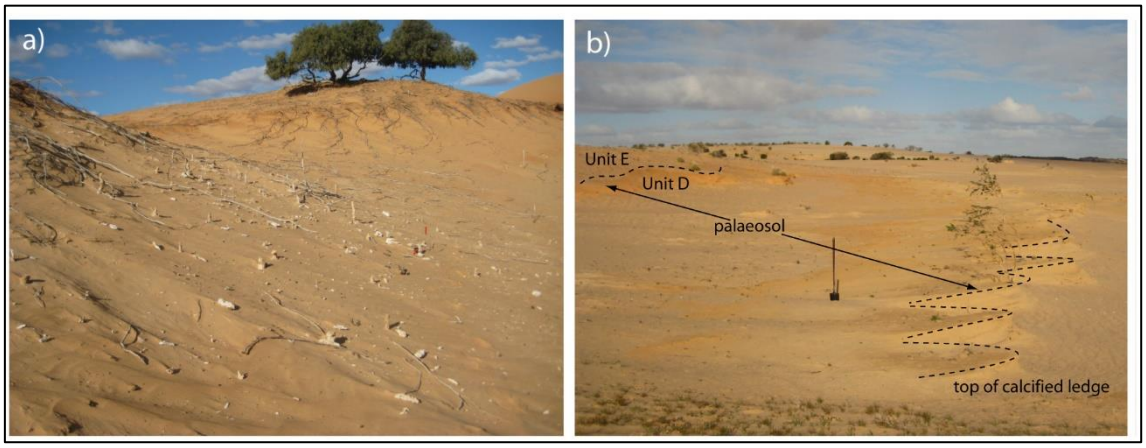

Figure 3.29. a) Carbonate rhizomorphs in Unit D at PR01. b) Palaeosol of Unit D at PR05. The ledge is created by the hard calcified layer. Rubification can be seen to the left, grading to dark red at the top of the unit.

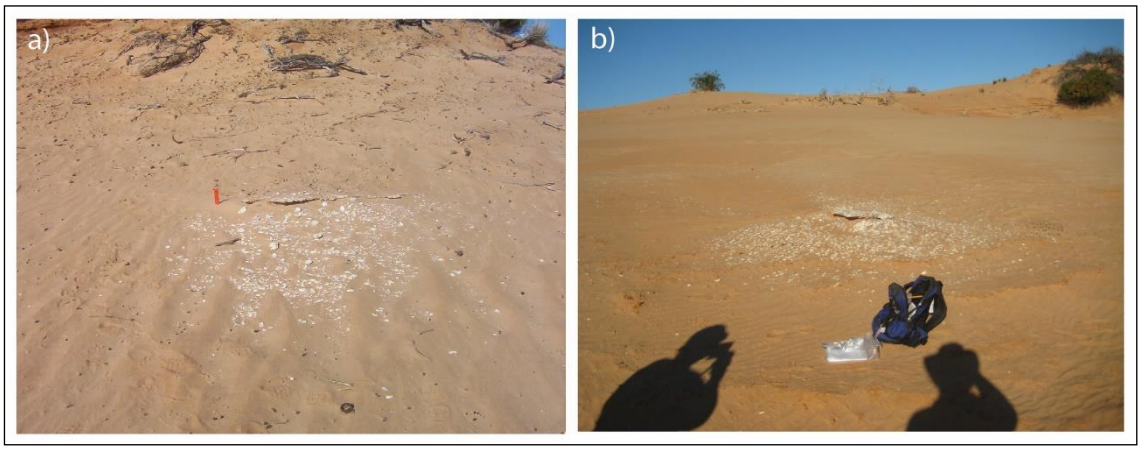

Figure 3.30. Shell middens in Unit D at PR01

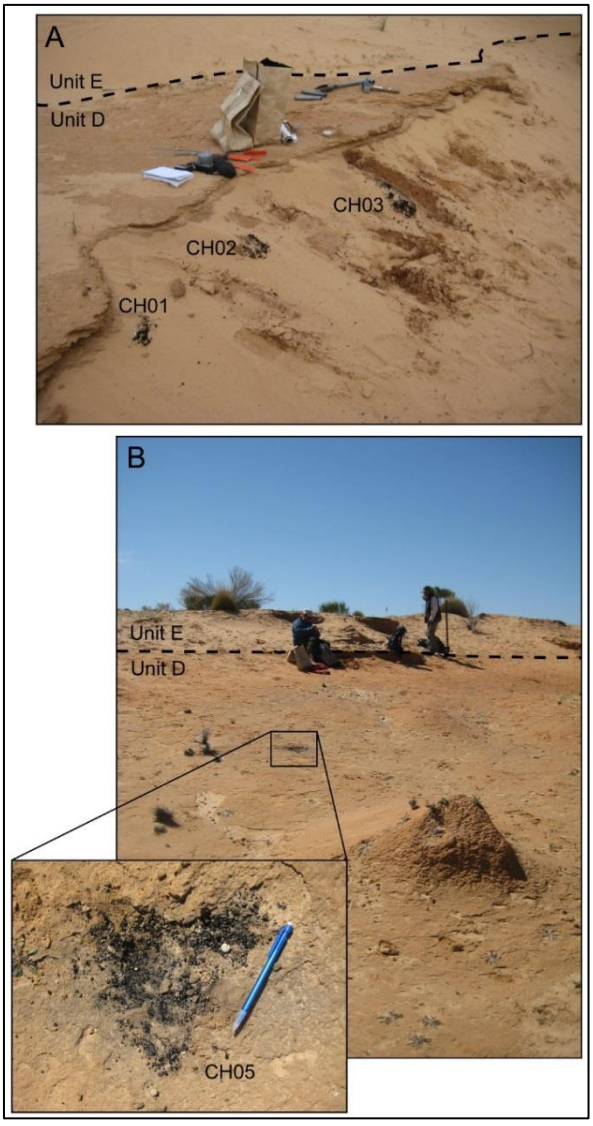

Figure 3.31. Charcoal in Unit D. A: below the thin clay-rich layer at PR01. B: in the rubified palaeosol at PR05.

3.3.1.6. Unit E 'recent sand unit'

Description: Unit E is a thick (up to 8 m), poorly consolidated, sandy unit mantling much of the lunette, especially along the leeward side of the lunette. It unconformably overlies all other layers in various areas, and has been extensively eroded to reveal these contacts. It is of very variable composition, with sub-angular to sub-rounded, very fine to coarse quartz sand, often with inherited cutans. The sediments vary from poorly sorted to well-sorted (Figure 3.32). The unit is commonly laminated, usually horizontally, but also shows evidence of crossbedding and convoluted laminations (Figure 3.33 and Figure 3.34). In other areas the unit is massive, such as in SL11, where relatively thin massive layers (30-40 cm) bracket a laminated layer of similar thickness. Rare clay pellets occur in this unit at a number of locations (Figure 3.35) and in some areas clay laminations are evident (Figure 3.36). No palaeosol is present in this unit and though some grasses and bushes grow in the sandy surface, no true soil development is apparent.

Interpretation: This poorly consolidated unit represents a remobilisation of the lunette sediments. The variety of grains present, including sparse clay pellets and numerous grains with inherited cutans suggests that the source is the eroded units of the lunette. The large scale cross bedding (Figure 3.33a) shows clear aeolian dune development, while the convoluted laminations (Figure 3.33b) suggest some degree of wet sediment deformation.

This is most likely a young unit, representing the remobilisation of lunette sediments at the onset of the current erosional regime. (See Section 8.1.5 for a discussion including geochronological results).

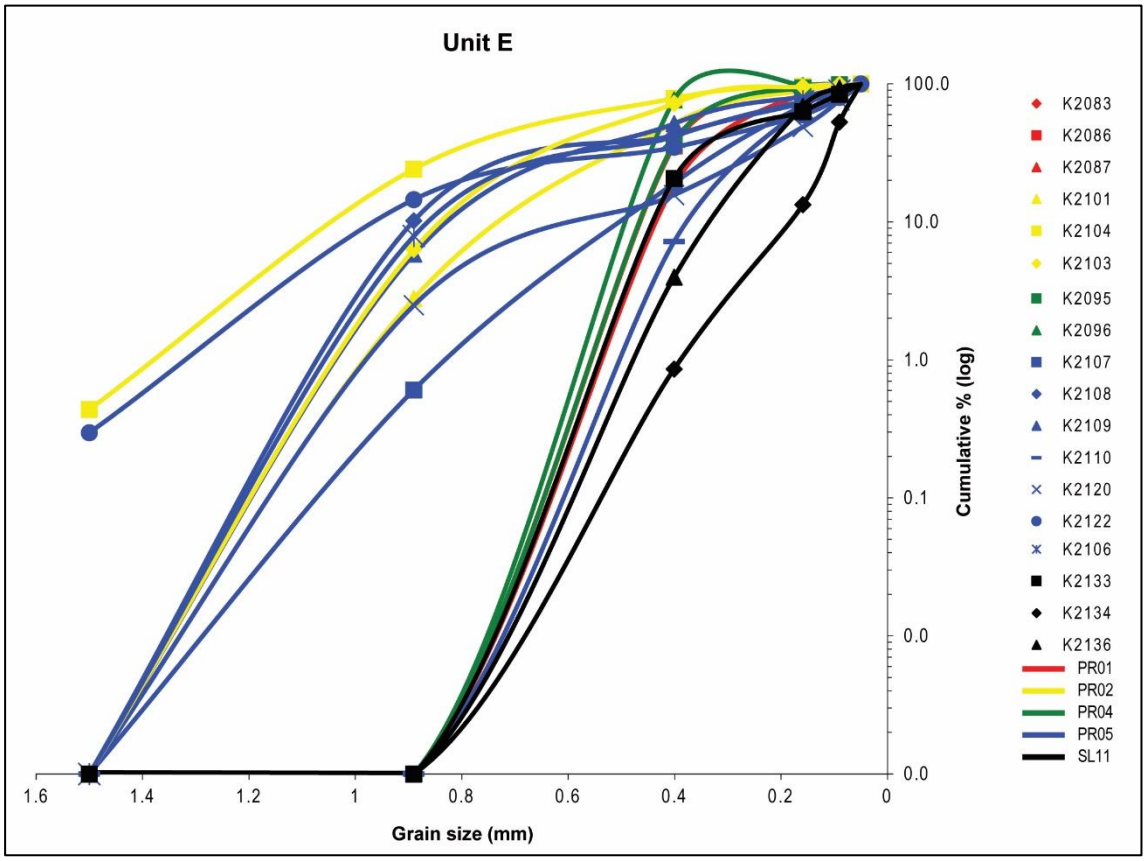

Figure 3.32: Cumulative grain size chart for sediments associated with OSL samples from Unit E. Detailed sedimentary data for each sample is available in Appendix B.

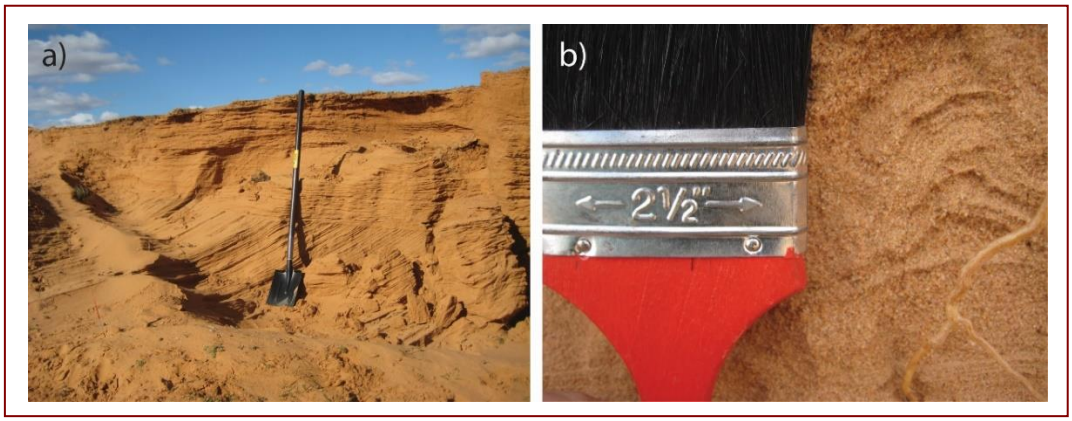

Figure 3.33. Laminations in Unit E showing a) crossbedding and b) convoluted laminations.

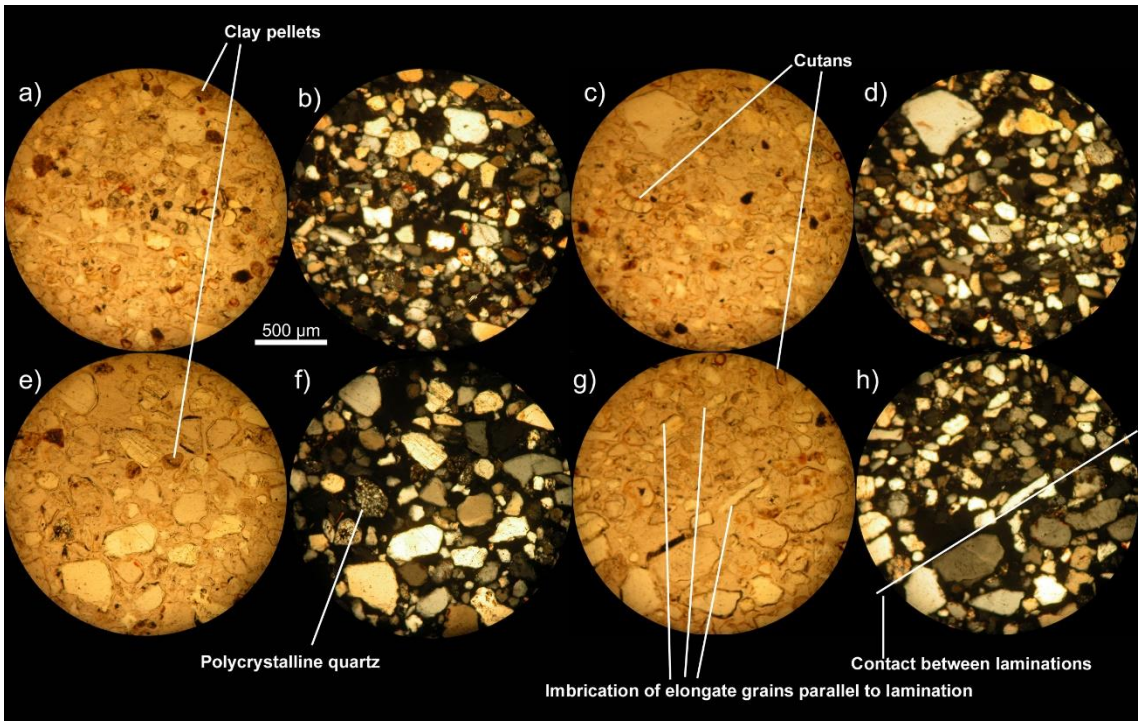

Figure 3.34. Four fields of view thin section TS129, of laminated sands in Unit E at PR05. Images a) & b) are the same field of view, shown in PPL and XPL respectively, as are c) & d), e) & f) and g) & h).

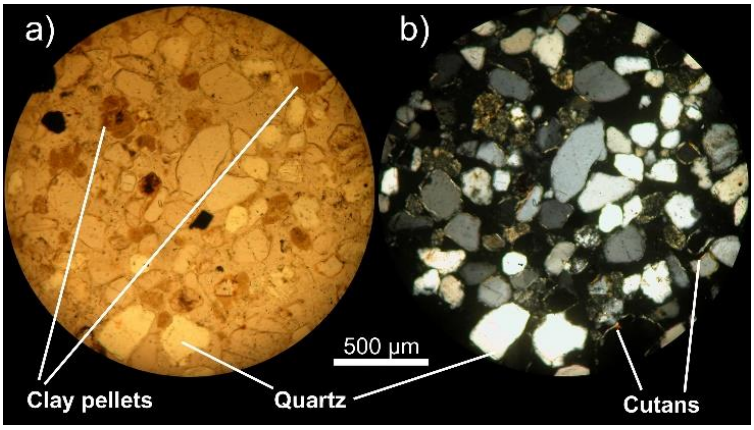

Figure 3.35. One field of view thin section TS138, of sands and clay pellets in Unit E at PR04. Images a) & b) are the same field of view, shown in PPL and XPL respectively.

Figure 3.36. Laminated sands in Unit E.

3.3.1.7. Modern mobile sands

Stratigraphically above the laminated E layer and toward the rear of the lunette, there are modern mobile sands. Blowouts on the windward side of the lunette are scouring out and providing material forming dunes over the crest and down the leeward edge of the lunette (Figure 3.37). The sands are white unconsolidated clean quartz. These represent the most recent sediment deposition, reflecting the current climatic regime. These also occur at Lake Mungo.

Figure 3.37. Mobile sands of the Mulurulu lunette: a) some parts of the lunette are mantled in modern sands while others are not; b) looking east off the lunette over the crest of the modern dune; and c) behind the lunette, looking back at the leeward edge. The progression of the sands can be seen by the partially covered bushes and the twigs of a dead bush sticking out of the sands above.

3.3.2. Drill core descriptions

As described in Section 3.2.2, cores were drilled at three locations on the Mulurulu lunette (Figure 3.5). Figure 3.38 shows the stratigraphic logs of DH01, the drill cores from the north end of the Mulurulu lunette. These cores penetrate from Unit D through C and B and into Unit A. In this location the lower part of Unit A consists of a thick greenish-grey malleable clay. In some areas it is mottled orange/green/grey and it also contains some centimetre scale sandy horizons. The upper three metres consist of moderately sorted sands with a small clay component grading upwards into red, clay-rich, well-sorted quartz sands typical of Unit A exposures. Unit B is a moderately well-sorted quartz sand with re-worked red sand and clays from Unit A at the base. The clay-rich sands of Unit C are a greenish colour and Unit D is present here in the form of poorly sorted reddish sands with carbonate nodules present in the top two metres.

Figure 3.39 shows the stratigraphic logs of DH02a and DH03, the drill cores from PR04 and PR06, respectively. Only Units A and B were seen in DH02a. Unit B includes red grains above the contact with Unit A, indicating reworked material. Some mottled black regions are present in Unit B, at 2.5 m depth.

In DH03, Units A to D were intersected. The reddish clayey sands of Unit A are marbled with white sands at approximately 8 m, 10.3 m and 10.8 m in depth. Unit B is well-sorted fine white sand with no indication of a palaeosol, while Unit C is well consolidated and clay rich. Large (1 – 4 cm) carbonate nodules are abundant in the upper two metres of Unit D.

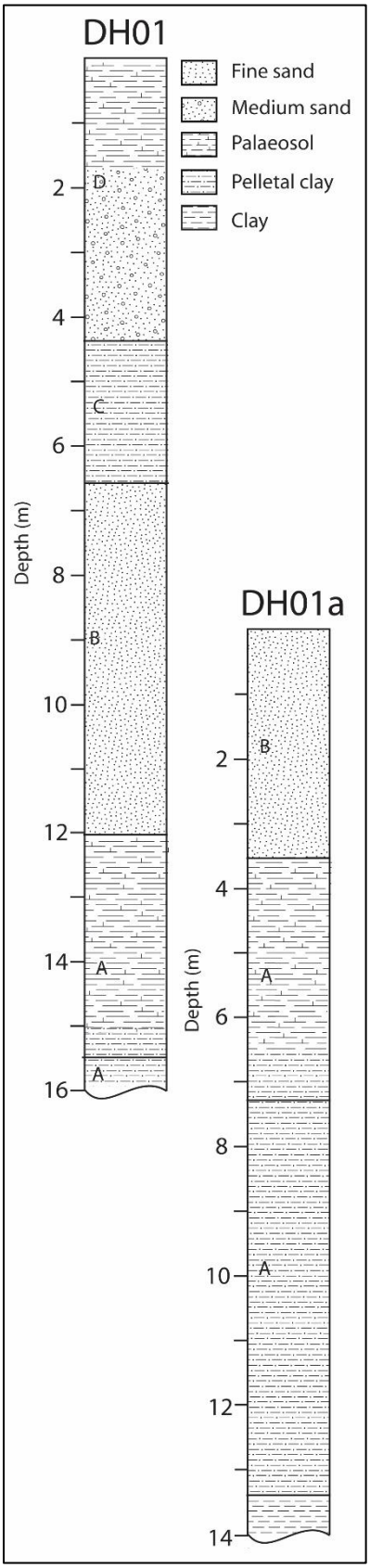

Figure 3.38 Stratigraphic log of DH01

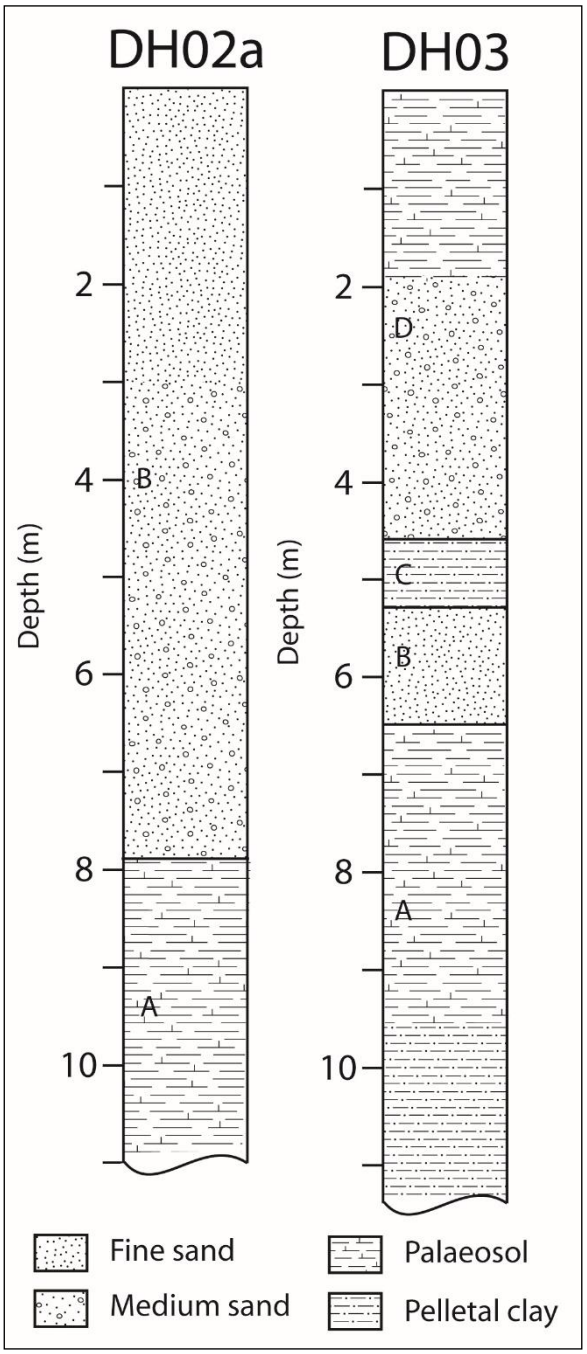

Figure 3.39. Stratigraphic logs of DH02a and DH03

3.3.3. Transects

As described in Section 3.2.4.3, seven transects were surveyed in this study (Figure 3.7) and four of them extensively sampled and described. Figure 3.40 to Figure 3.50 show the surveyed transects. They are presented here in order from north to south and for those where stratigraphy was exposed, a synthetic composite stratigraphic log is created and described. Previous extents have been inferred with dashed lines on the profile images, where sediments have been removed by erosion. These are hypothetical only, and have simply been drawn in a traditional dune shape, linking exposures of the same unit. All sampling locations are marked on both the profiles and stratigraphic logs. Detailed description of the loose sediment and thin section samples are available in Appendices B and C

Figure 3.34 shows the transect at PR03. This northernmost section of the lunette is vegetated and no sediments are exposed. Thus, no stratigraphic profile is created for this transect site.

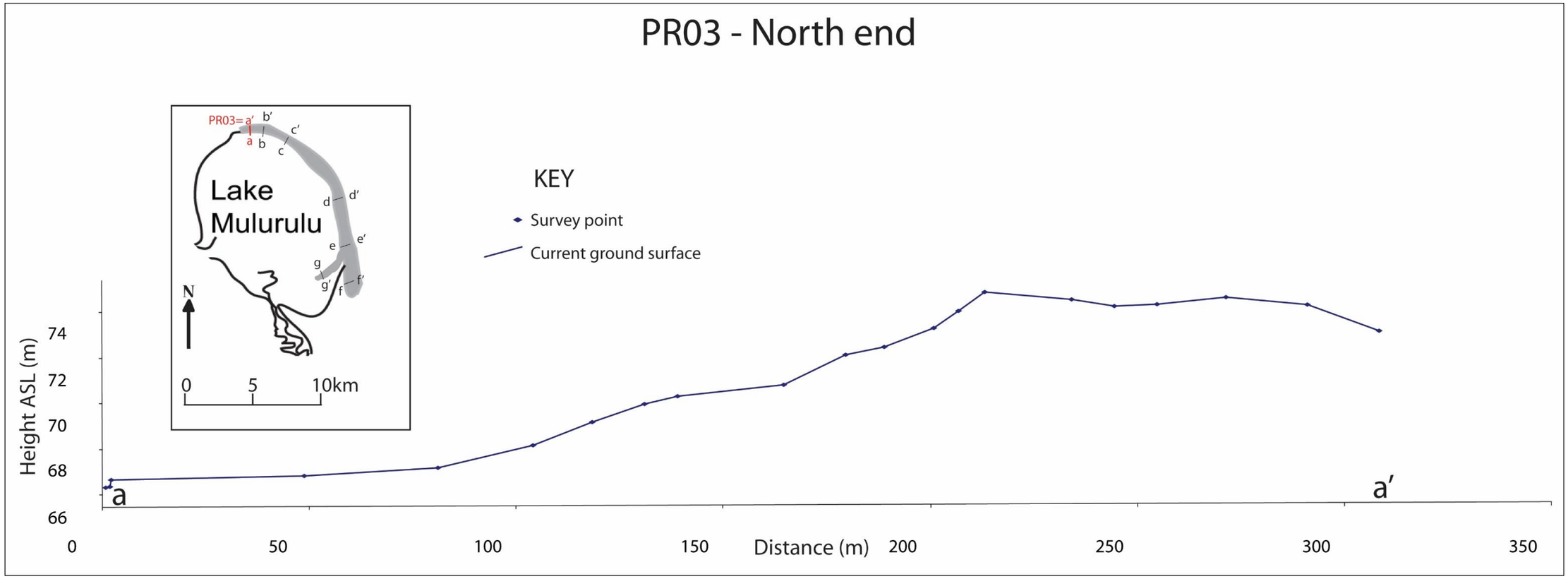

Figure 3.40. PR03, at the north end of the lunette. The ground here is vegetated, with no exposed sediments.

Figure 3.41 and Figure 3.42 show the stratigraphy of PR02. In addition to the samples shown in the figures, an OSL and loose sediment sample (K2102) of poorly sorted, yellowish red sand was collected 30 cm beneath the current ground surface, behind the lunette.

At PR02 Unit B is exposed and directly overlain by Unit E. Unit B consists of a fine grained moderately sorted sub-angular sand with a few clay pellets and possible wurstenquartz. A palaeosol is indicated by rubification and abundant calcrete nodules. Unionid shell middens are abundant where modern erosion has broken through the palaeosol.

Unit E mantles Unit B at both the front and rear of the blowout. It consists of laminated strong brown quartz sands with inherited grain cutans.

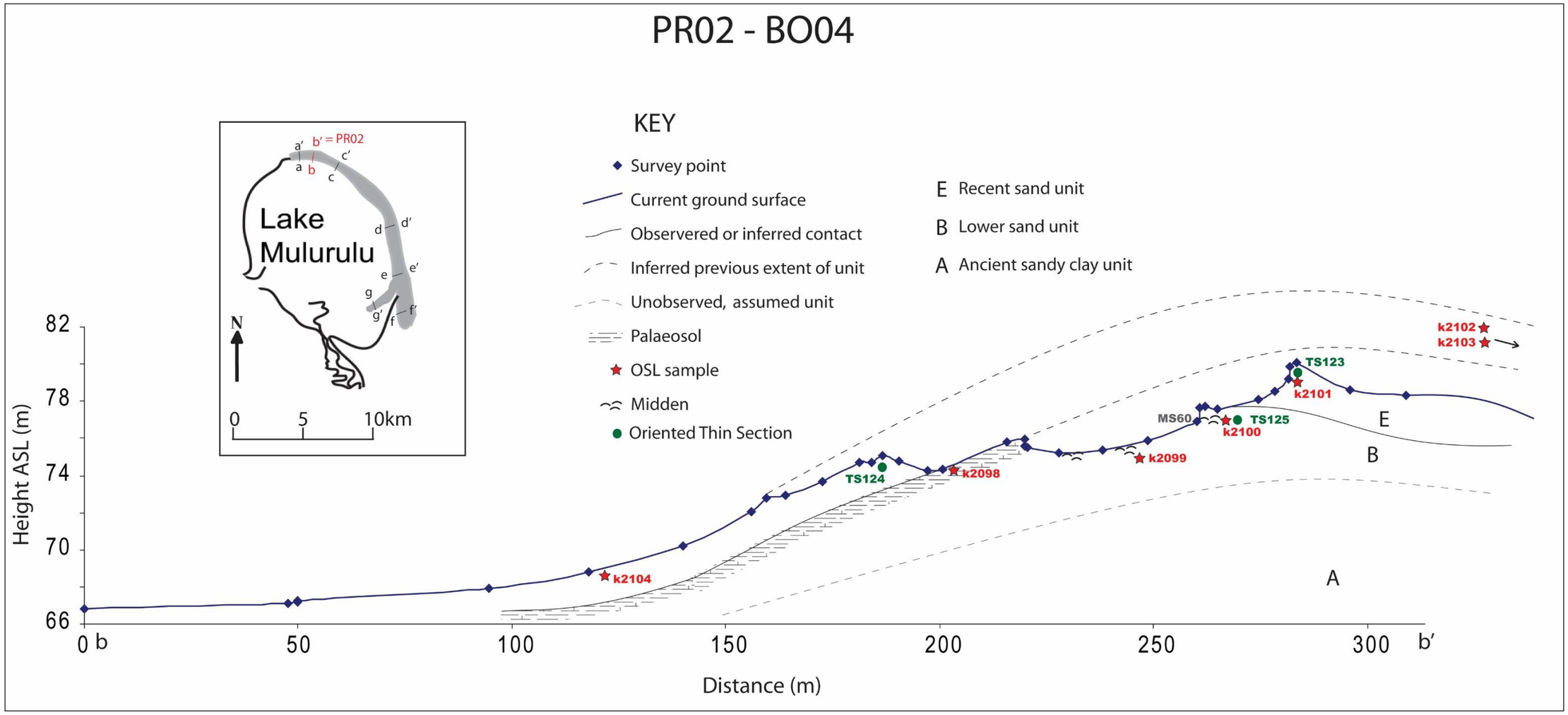

Figure 3.41. PR02, in BO04.

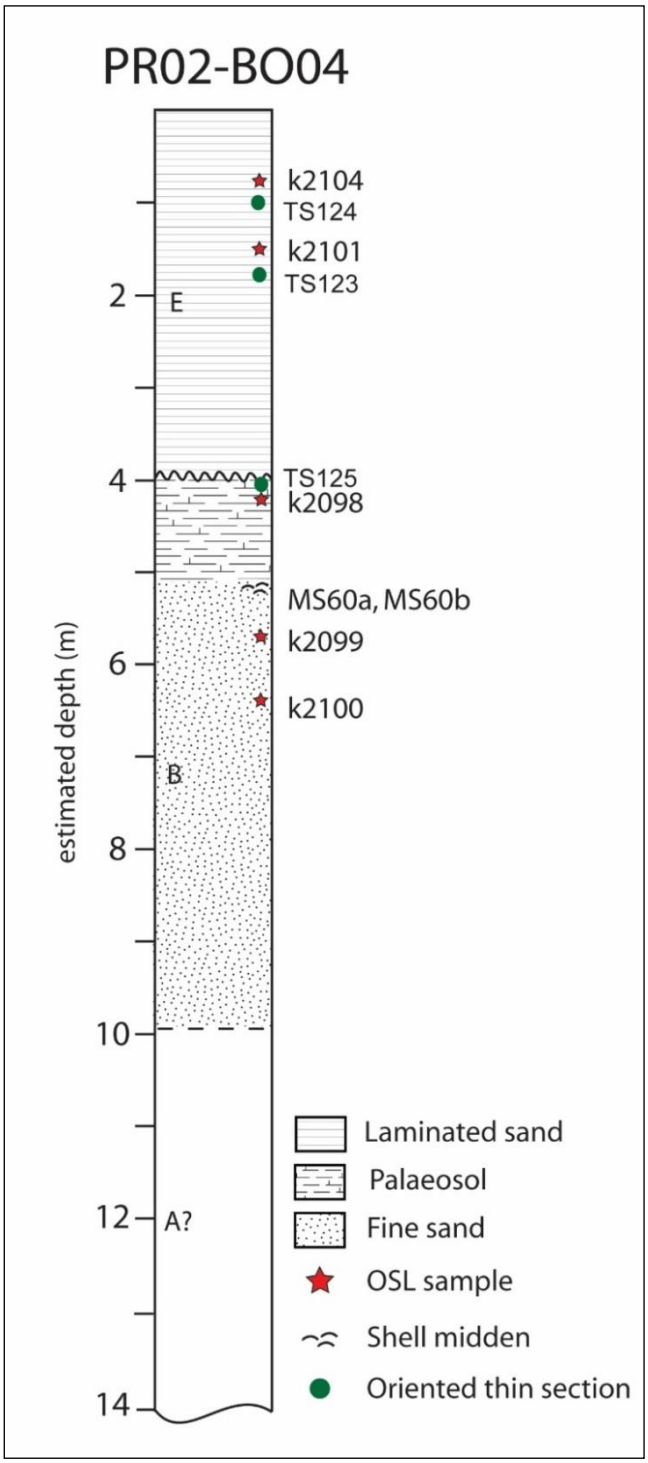

Figure 3.42. Stratigraphic log of an idealised vertical sequence based on exposed sediments in PR02.

Figure 3.43 and Figure 3.44 show the stratigraphy of PR05. In addition to the samples shown in the figures, an OSL and loose sediment sample (K2105) was collected 30 cm beneath the

current ground surface, behind the lunette, and others were collected from the edge of the lake floor (the beach) in front of the lunette (K2127, TS149). Units B to E were present at this site.

Unit B is present as a small exposure in the centre of the blowout. Some indications of a palaeosol are present here, including *in situ* grain cutans. The unit also contains very few clay pellets and at least one reworked microbialite clast (Figure 3.21). One *Unionid* shell midden is present in this blowout, and others are in the same unit in adjacent blowouts.

Unit C is apparent as a yellowish-brown pelletal-clay unit outcropping above Unit B, though only in the rear of the lunette. Clay pellets are abundant in this unit, dominating the thin section (TS132; Figure 3.24).

Unit D overlies Unit C in the rear of the lunette, though it directly overlies Unit B in the front. Sorting of the sediments varies at PR05, with poorer sorting toward the top of the unit with a bimodal population (very fine and medium) in some areas. The lower part of the unit, at the front of the lunette is well-sorted and fine grained. *Unionid* shell middens are present in this area. A palaeosol is present, clearly visible as a zone of secondary carbonate cementation, forming a ‘bench’ with increasing rubification upward toward the contact with Unit E (Figure 3.29). Ooids and shell fragments are also apparent in thin section along with the secondary carbonate cementation. Three patches of charcoal or dark humic staining are present near the top of the unit.

Unit E is present as a thick layer of poorly consolidated sand mostly at the rear of the lunette, and also present along the front of the foredune. The unit connects along a ridge at the eastern side of the blowout, unconformably overlying all other units. The unit is mostly poorly sorted, sometimes laminated, sometimes massive, with sub-rounded to well-rounded quartz sand. A sharp contact exists between a yellowish brown and a reddish yellow layer. Some clay pellets are present, possibly reworked from other units.

The sediments collected from behind the lunette consist of a very fine, well-sorted, sub-rounded, reddish-yellow sand. While those from the ‘beach’ are fine to medium, moderately well-sorted, sub-angular to sub-rounded, strong-brown sand with inherited cutans and a few clay pellets.

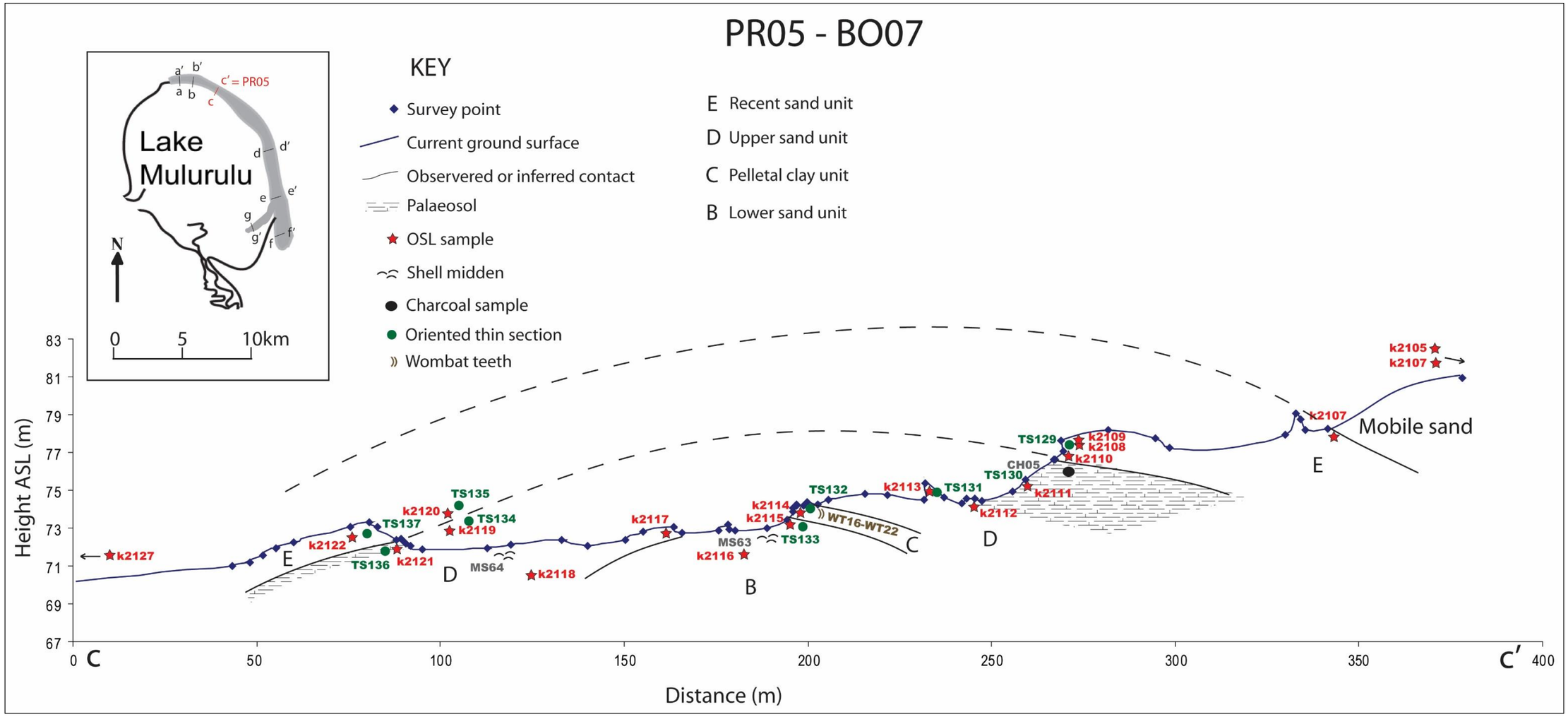

Figure 3.43. PR05, in BO07.

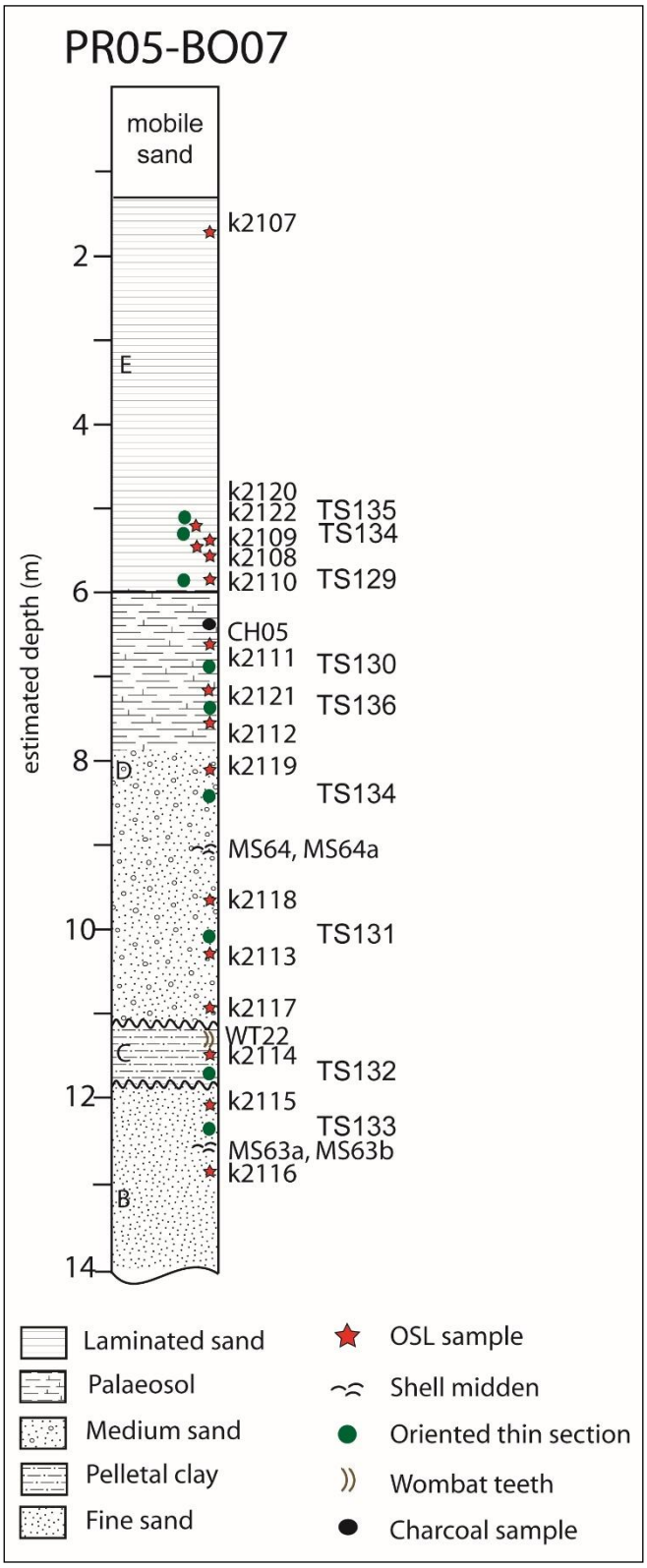

Figure 3.44. Stratigraphic log of an idealised vertical sequence based on exposed sediments in PR05.

Figure 3.45 and Figure 3.46 show the stratigraphy of PR04. Here, Units A, B and C are overlain by Unit E. In addition to the samples shown in the figures, an OSL and loose sediment sample (K2097) was also collected 30 cm beneath the current ground surface behind the lunette.

Unit A is a reddish clayey sand visible in the gully walls with a thick palaeosol present as secondary calcification impregnating a clay matrix as well as carbonate nodules and rubification. Unit B is fine, well-sorted sand, grading to medium sand toward the top of the unit. *Unionid* shell middens are present at the base of unit where the sand is reddish and contains clasts of reworked clay and carbonate from Unit A. Some rubification at the top of the unit suggests a highly eroded palaeosol.

Unit C is a yellowish brown pelletal clay, which has been heavily eroded and is only present at front of lunette. Clumps of heavy minerals (possibly zircon) are present in thin section and gypsum rosettes were observed in the field.

The laminated light yellowish brown sands of Unit E overlie Unit B at the rear of the lunette and include a small portion of remobilised clay pellets.

The sediments from behind the lunette are very fine to medium, poorly sorted, sub-rounded, yellowish red sand.

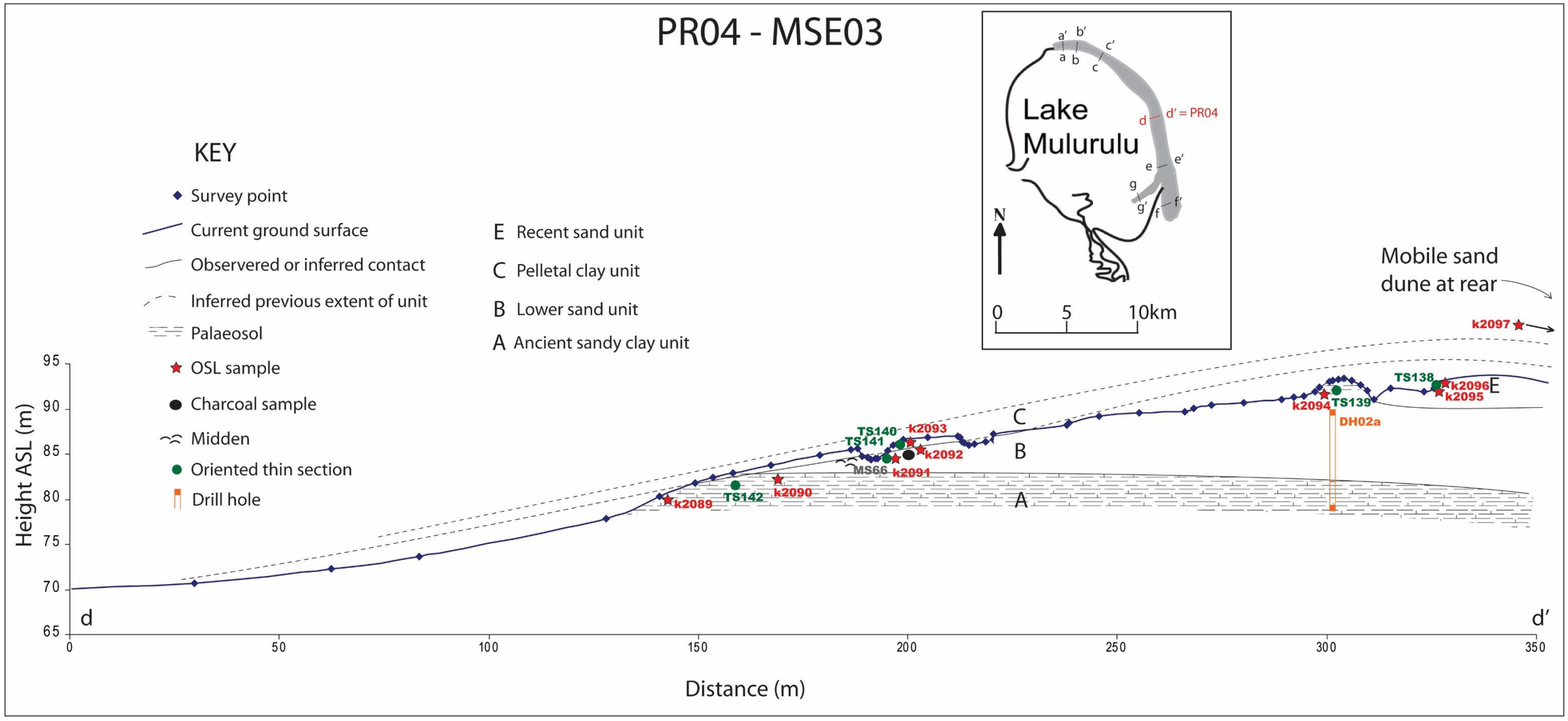

Figure 3.45. PR04, in MSE03

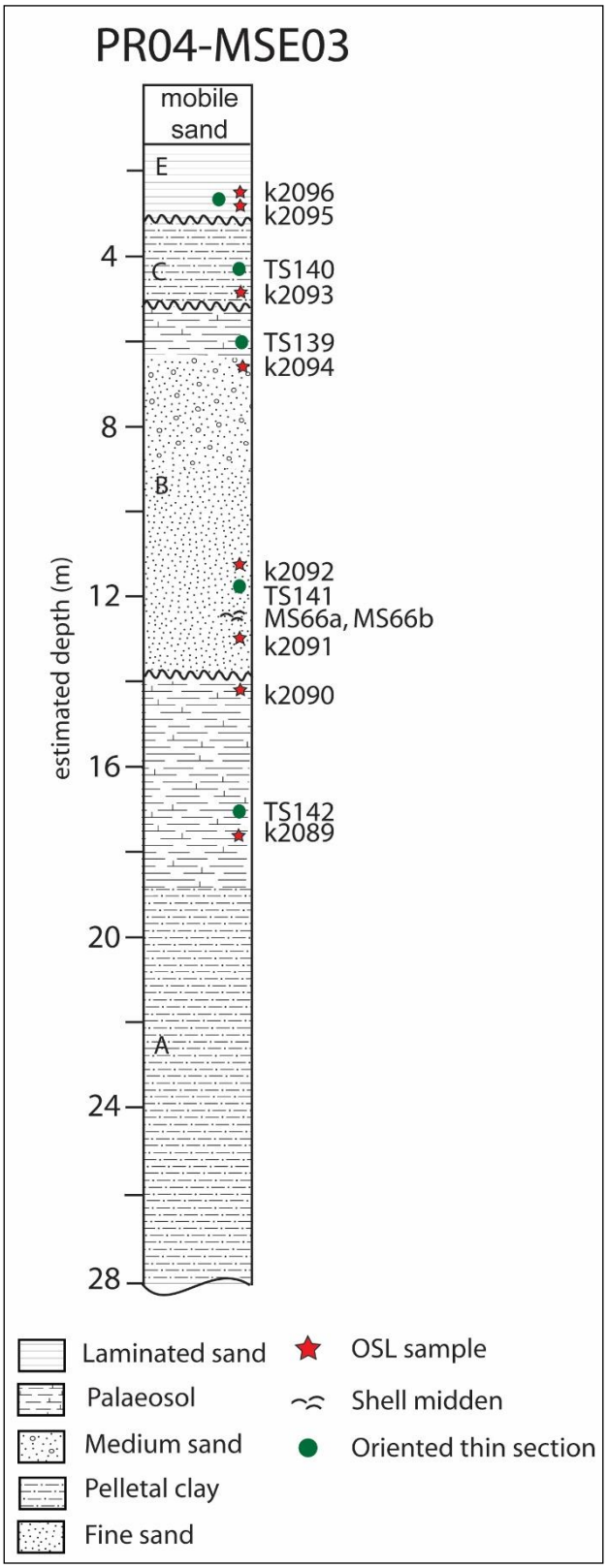

Figure 3.46. Stratigraphic log of an idealised vertical sequence based on exposed sediments in PR04.

Figure 3.47 and Figure 3.48 show the stratigraphy of PR01. In addition to the samples shown in the figures, an OSL and loose sediment sample (K2088) were also collected 30 cm beneath the current ground surface behind the lunette, as well as from the edge of the lake floor (the beach) in front of the lunette (K2128, TS150).

Unit C is not apparent at this location, though all the other major units are present. Unit A is exposed in gullies at the front of the lunette and consists of poorly sorted sand in a clay matrix, impregnated with secondary carbonate. Quartz grains display both *in situ* and inherited cutans in grain embayments. Only a few clay pellets are discernible in this section, though such pellets are likely to have been the original source of the interstitial clay. Carbonate nodules, secondary carbonate matrix and intense rubification all suggest a thick palaeosol.

Unit B is thin at this site, overlying Unit A and visible at the top of gullies. With no Unit C apparent at this location, the similar nature of Units B and D make the contact difficult to discern in the field. Both units consist of moderately sorted strong brown quartz sand. Unit D includes numerous Unionid shell middens (including *Maquaria ambigua* otoliths) and abundant carbonate rhizomorphs and is topped by a 10 cm thick clay-rich layer consisting of both pelletal and illuvial clays. This layer can be clearly correlated across a number of blowouts in the proximity of this transect, though it only occurs at the southern end of the lunette. This clay-rich layer is in turn overlain with a thick succession of laminated Unit E sands.

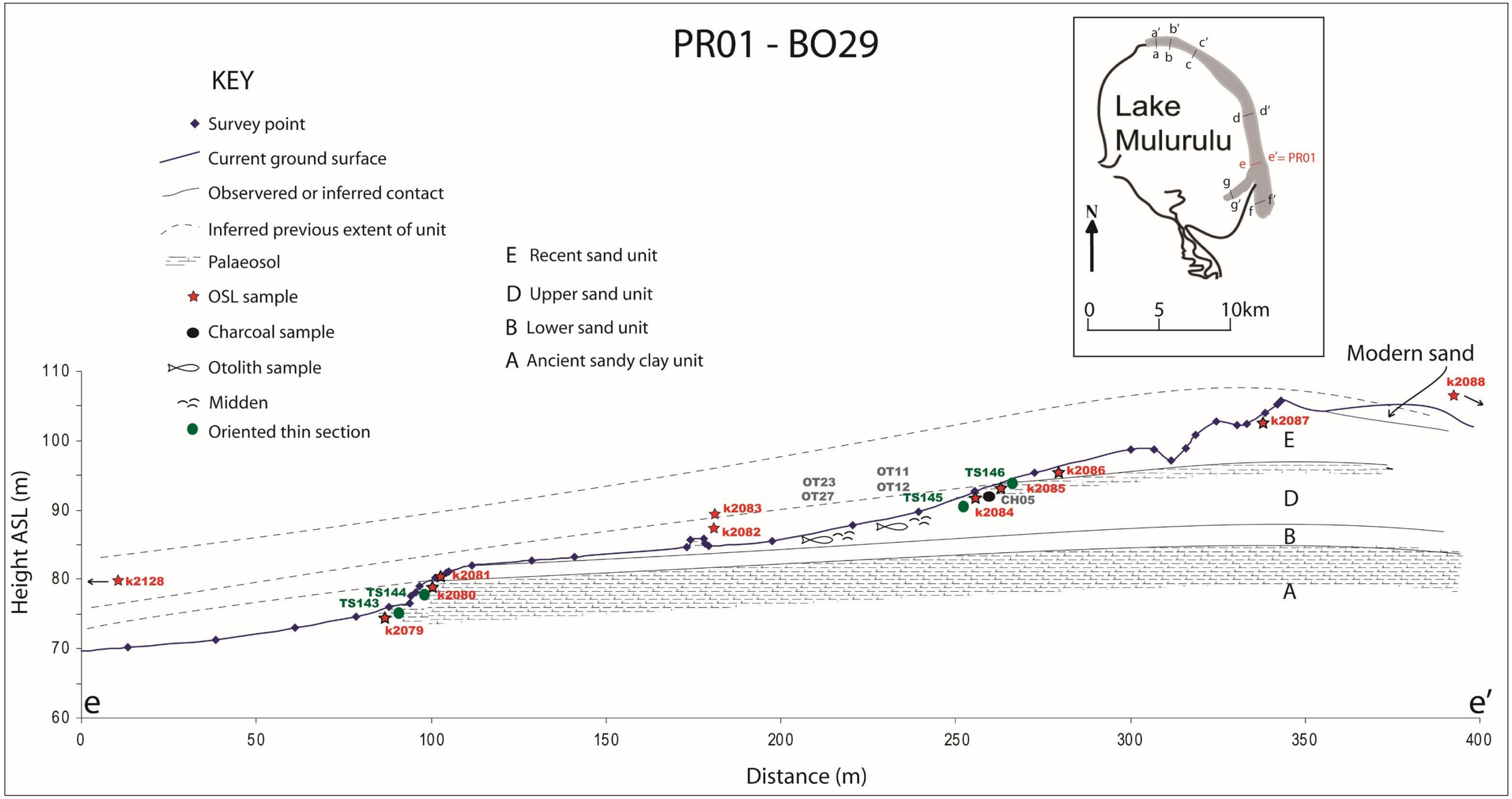

Figure 3.47. PR01, in BO29.

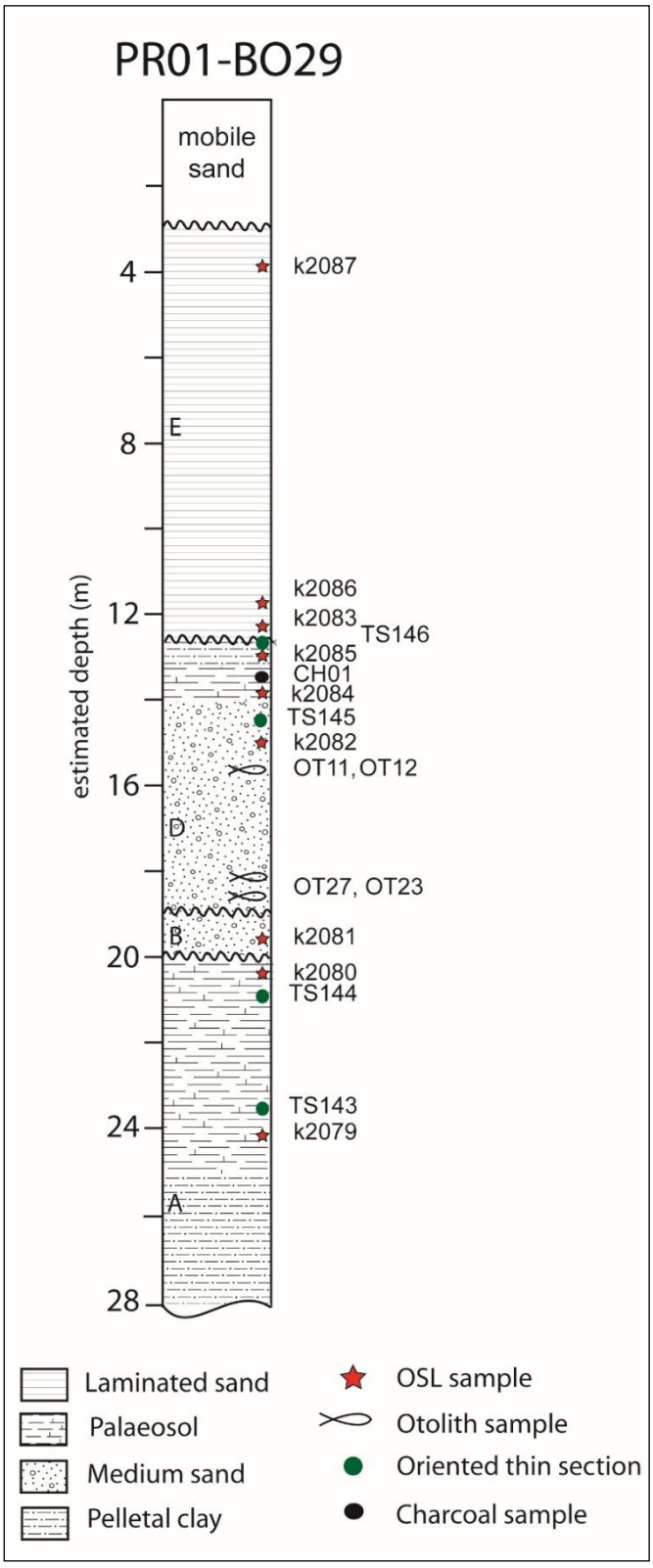

Figure 3.48. Stratigraphic log of an idealised vertical sequence based on exposed sediments in PR01.

Figure 3.49 shows the transect at PRO6, at the south end of the lunette. No stratigraphy was exposed at this site, but a drill core taken here penetrated Units D, C, B and A, as described above in Section 3.3.2.

Figure 3.50 shows the survey transect at ‘the spit’ jutting onto the lake floor from the lunette. Although no stratigraphy was exposed here due to vegetation cover, a thin section and loose sediment sample was collected at the OSL sampling site. The sediments here consist of very fine to coarse, poorly sorted, sub-rounded sand with inherited cutans overprinted with a primary illuvial clay matrix.

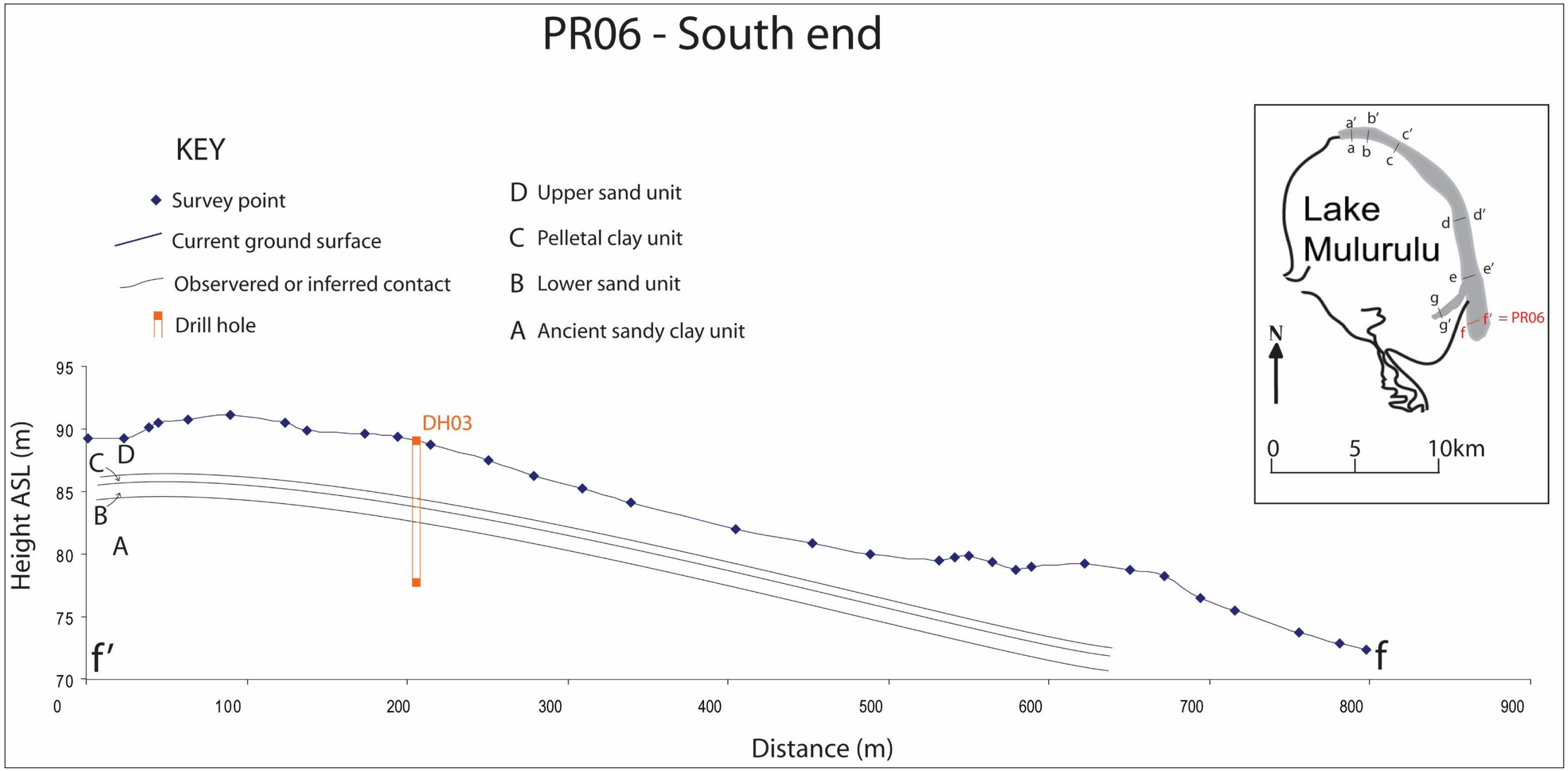

Figure 3.49. PR06, at the south end of the lunette. See Section 3.3.2 for a description of DH03.

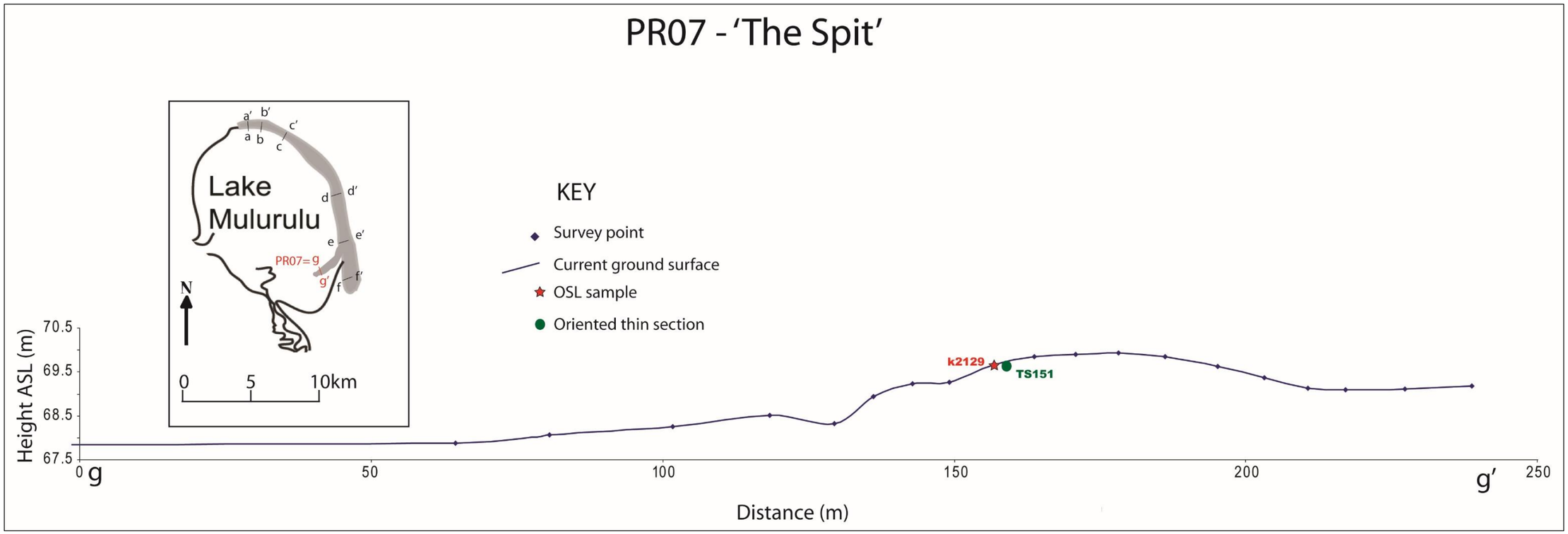

Figure 3.50. PR07, at 'the spit'.

3.3.4. Other sampling locations

In addition to the presented transect lines, OSL, loose sediment and thin sections were collected from a gully (SL11 at BG01 and a blowout in the rear of the lunette (SL44 at RB03). The locations are shown in Figure 3.51.

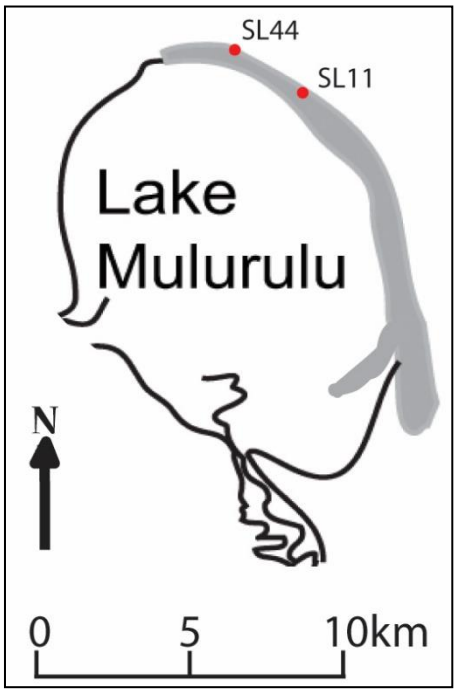

Figure 3.51. Locations of the other sampling sites.

Figure 3.52 shows the stratigraphy of SL11, from the wall of BG01. The gully wall appears to be composed of Unit C sediments overlain by a series of Unit E layers (Figure 3.26A greenish grey clay occurs at the base overlain by a moderately poorly sorted, sub-angular, strong brown sand layer with abundant clay pellets. Two palaeosols are present, highlighted by a higher density of clay materials, apparent as an illuvial clay matrix in thin section.

At SL11, Unit E consists of three layers, a section of massive, strong brown sand unconformably overlying Unit C, followed by a layer of very fine, well-sorted, reddish yellow laminated sands, topped with fine, well-sorted, massive reddish yellow sands. All three layers are poorly consolidated with some inherited cutans and a few clay pellets.

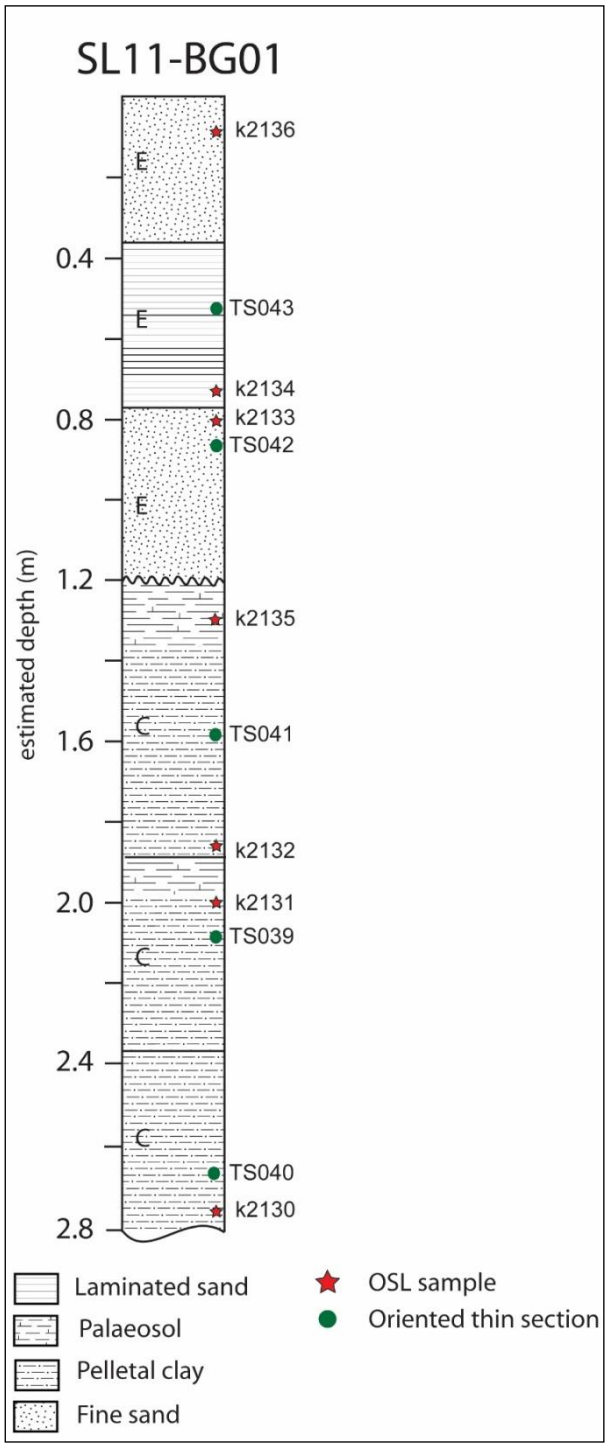

Figure 3.52. Stratigraphic log of sediments exposed in SL11.

Figure 3.53 shows the stratigraphy of SL44, a stratigraphic log taken in the side of a blowout behind the lunette (RB03, see Figure 3.2). The loose sediment samples from this location were accidentally lost before analysis. As such the descriptions here are based on the thin section (TS119) and field observations.

Unit A is present at the base and partway up the side of the blow-out. It consists of moderately sorted, yellowish-red sand with some clay pellets. Carbonate nodules are abundant, including large amounts of nodules deflated onto the floor of the blow-out. This is unit is unconformably overlain by a thick layer of poorly consolidated, laminated sands of Unit E.

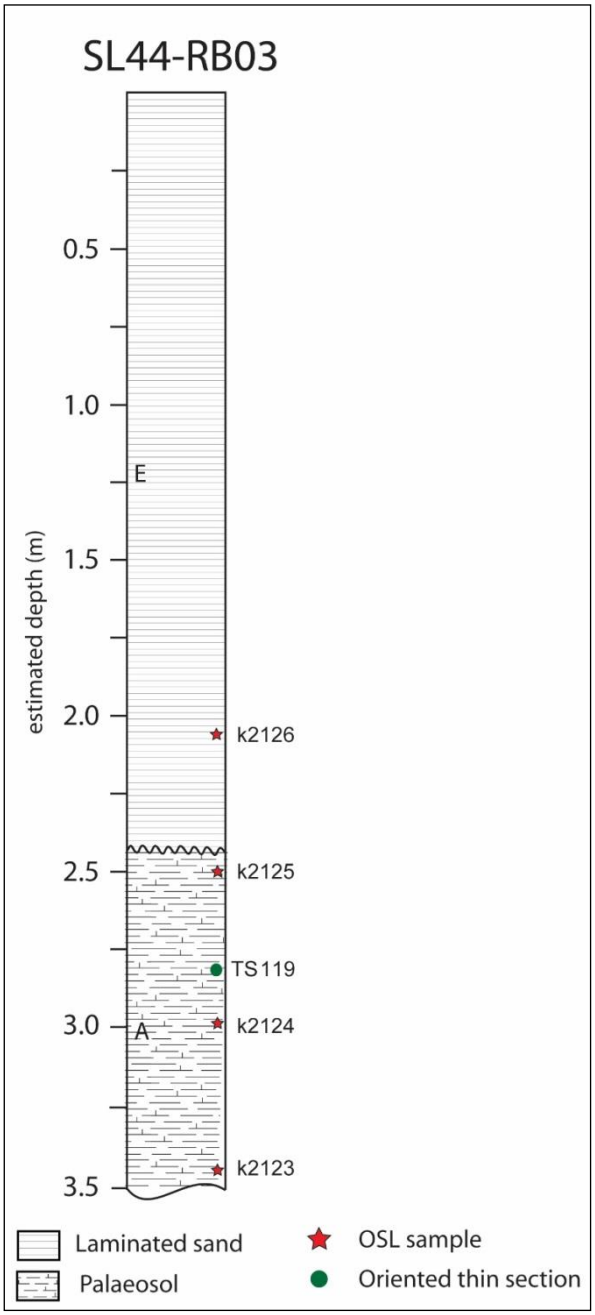

Figure 3.53. Stratigraphic log of sediments exposed in SL44.

3.4. Stratigraphic Summary

Figure 3.54 shows an idealised composite stratigraphic log of the complete sequence of the Lake Mulurulu lunette. This full sequence was not observed at any one site, but is pieced together from all drill cores, transects and sampling locations. All contacts are unconformable and layer E was observed directly overlaying each of the other units in different locations.

The core of the lunette is a pelletal clay, representing an ancient lake drying period. Unit A has a thick (~4 m) palaeosol indicating a long period of stability during which the lunette was vegetated and a soil profile formed. This was followed by a period of erosion, removing the uppermost soil and exposing the carbonate-rich B horizon. A return of water to the lake then provided sandy materials to the lunette. The lowermost part of Unit B contains materials reworked from the underlying palaeosol, mixed with clean sands blown on to the lunette from the lake beaches. This grades upward into clean sands. Aboriginal occupation of the lunette during this period is present in the form of shell middens, the earliest of which are located on the eroded surface of Unit A, buried in the reworked, mixed sands at the base of Unit B. Other shell middens occur stratigraphically higher, in the clean sand. A period of stability led to the development of a palaeosol on this layer, though it is much less well developed than the soil formation in Unit A. This was again followed by a period of erosion, which removed the uppermost parts of Unit B, including the entire palaeosol in some areas. Another pelletal clay unit follows, representing drying of the lake. Unit C has at least two palaeosols in some areas suggesting that a period of stability occurred, perhaps due to a brief return of water to the lake, before further drying and renewed clay pellet development, followed again by stability and soil formation. These palaeosols either never formed, or were eroded away, in some areas of the lunette, before deposition of another sandy unit (Unit D), which represents a sustained return of lake water. Again, shell middens occur in Unit D, indicating aboriginal occupation of the area. A thick palaeosol then developed, during a further period of stabilisation. This layer is capped by a thin pelletal clay, apparent only at the south end of the lunette.

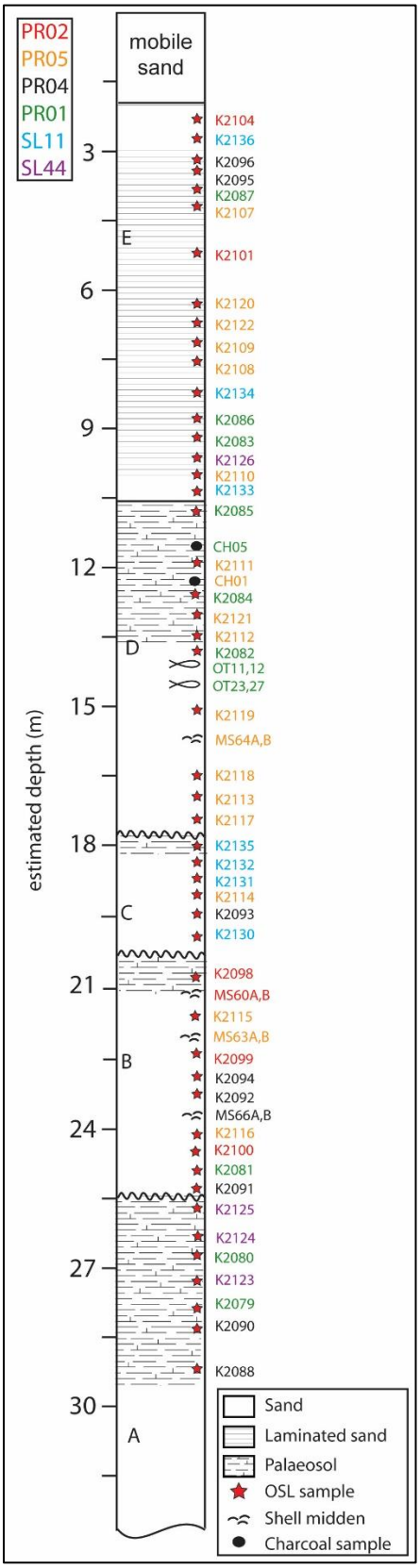

Figure 3.54. The idealised composite stratigraphic log of the Mulurulu lunette

The lack of substantial pelletal clay dunes suggests that the final drying was rapid, with the water table quickly dropping below the level of the lake floor preventing the development of a saline water table and progressive lake-floor lowering by deflation. Therefore clay pellets were not developed and the lake floor was swiftly re-vegetated. Erosional processes then dominated the lunette for some time, exposing all the units at various locations, before they were mantled by re-mobilised sediments, to form the thick laminated sequence presented as Unit E. Finally, recent erosion has led to the creation of the present blow-outs. Aeolian erosion leads to the scouring out of blow-outs and deposition of mobile sand dunes on the downwind side of the lunette, while fluvial erosion due to infrequent rains in the area have led to gully development, washing materials onto the lake floor. A chronological framework for this succession is provided in Chapter 7 and discussed in detail and with comparison to the Mungo lunette, in Chapter 8.

Chapter 4. Understanding the palaeoenvironments at Lake Mulurulu: Oxygen isotopes of wombat incisors and fish otoliths

4.1. Oxygen isotope geochemistry background

Stable isotopes are non-radioactive variants of an element, with different atomic masses, causing fractionation in environmental and biological processes, resulting in a differing isotopic ratio in the end product, relative to the source (Campana 1999). Koch (1998) explains that because natural fractionations are small, isotopic abundances of light stable isotopes are reported as parts per thousand (‰) deviations in isotopic ratio from a standard, using δ notation:

$$\delta X = [\frac{R_{sample}}{R_{standard}} - 1] \times 1000 \qquad (1)$$

where R_{sample} and $R_{standard}$ are the high mass to low mass ratios of the sample and standard, respectively. For oxygen analyses, the isotopes utilised are ^{18}O and ^{16}O. The most common standard reference material for oxygen isotopes from carbonate materials is the Peedee belemnite (PDB), and for other oxygen sources, standard mean ocean water (SMOW). An enrichment of the heavier isotope relative to the standard results in positive δ values, while negative values indicate depletion. Oxygen isotope ratios are hence expressed as ± X ‰ $\delta^{18}O$, where a value of 0 ‰ $\delta^{18}O$ matches the standard.

The oxygen isotopic composition ($\delta^{18}O$) of phosphate and carbonate in biological materials such as bones, teeth and otoliths are regularly used as environmental proxies in archaeological and ecological investigations (e.g., Ayliffe & Chivas 1990; Schoeninger & Moore 1992;

Stuart-Williams & Schwarcz 1997; Patterson 1998; Sponheimer & Lee-Thorp 2000). Environmental $\delta^{18}O$ values vary with geographic and environmental variables and the average $\delta^{18}O$ values of the Earth's oceans have oscillated through time in response to global climate (Section 4.1.1). The isotopes in mineralised animal tissues are derived from the environment in which the animal lived, taken into the animal through processes such as feeding, drinking and respiration (Sections 4.1.2 and 4.1.3). As a result, assuming no diagenesis has occurred (Section 4.1.4) the analysis of $\delta^{18}O$ in animal tissues can provide information regarding temperature, humidity, evaporation and aridity, of the area in which the animal lived. Oxygen from phosphate in wombat (*Lasiorhinus latifrons)* tooth enamel (Section 4.2.1.1) and carbonate in fish otoliths (4.2.1.2), collected from the Lake Mulurulu lunette, form the basis for this study.

4.1.1. Oxygen isotopes in the environment

Oscillations in the average oxygen isotope values of the Earth's ocean over the Quaternary Period (the last ~2.6 million years) reflect changes in global climate conditions. Quasi-cyclic variations in $\delta^{18}O$, with periodicities matching the main components of the glacial-interglacial Milankovitch cycle, are preserved in microfossils from marine cores (Emiliani 1966). This is because the expansion of polar ice caps during glacial periods removes water from the ocean and stores it in ice. Ice is proportionately higher in ^{16}O than the water from which it is derived, leaving the remaining seawater isotopically heavier. When the icesheets subsequently melt, large volumes of isotopically light water are released back into the ocean (Lowe & Walker 2015). Thus the variations in the isotope record indirectly reflect global temperature variations, with 'peaks' of lighter ratios reflecting warmer conditions, high sea level and reduced ice cover. The cyclical variations are used to define marine oxygen isotope stages (MIS) with the even and odd numbered periods generally denoting stadial (warmer) and interstadial (cooler) periods, respectively.

MIS stage 5 (about 130-80 ka) forms an exception to the rule of even-numbered stadials and odd-numbered inter-stadials. This stage is divided in to five sub-stages (5a-5e), with 5b and 5d denoting relatively cooler stadial periods. Glacial-interglacial cycles are generally higher-order than stadial-interstadial cycles. Thus, while the current interglacial period is denoted by

MIS 1, MIS 5e denotes the previous interglacial. MIS 2 is the last glacial maximum (LGM) and the last glacial period covers MIS 2-5d (Figure 4.1).

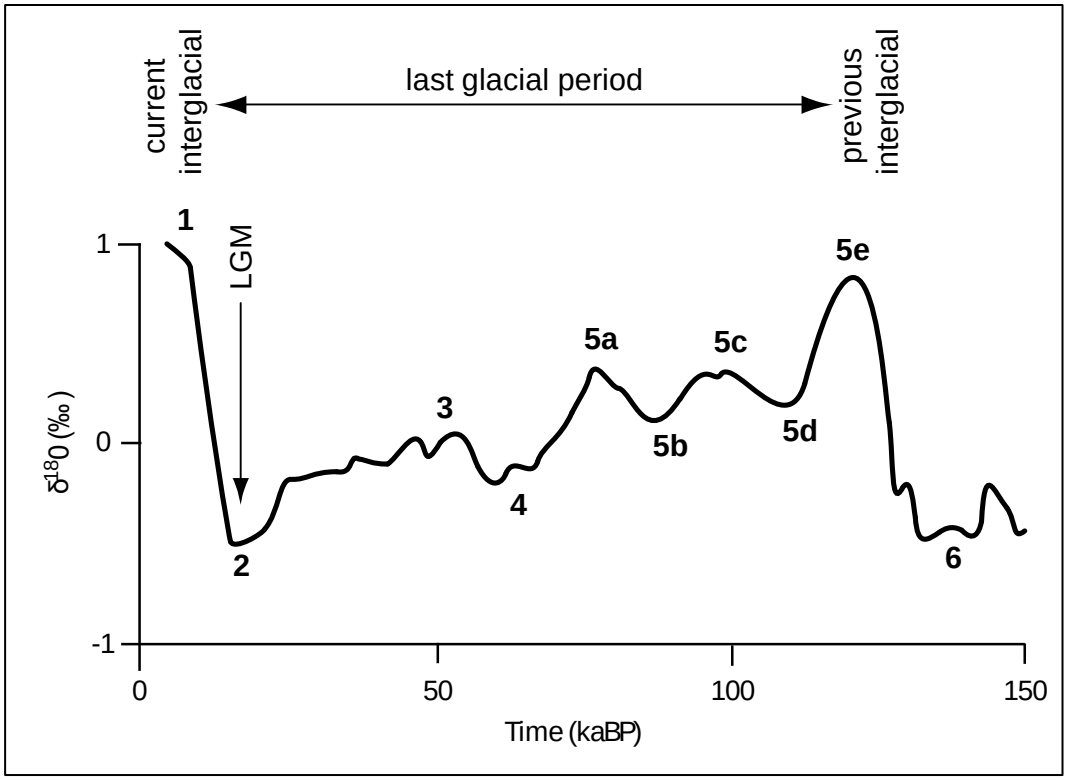

Figure 4.1. A stacked marine oxygen isotope record for the past 150 ka. Numbers represent Marine oxygen isotope stages (MIS). MIS1 is the current interglacial, MIS2 is the last glacial maximum (LGM) and MIS5e is the previous interglacial. Curve after Martinson et al. (1978), MIS numbers after Shackleton & Opdyke (1973).

On a local level, the $\delta^{18}O$ values of meteoric water are largely influenced by climate and geography. Generally, meteoric waters are more depleted in the heavier isotope, ^{18}O, than ocean water (Hoefs 1997), this is because the $\delta^{18}O$ of water is influenced by evaporation, as the lighter ^{16}O isotope evaporates preferentially (Faure & Mensing 2005). Additionally, in a process known as the 'rainout' effect, precipitation becomes more depleted in ^{18}O as it moves further away from the source. These principles combine to create a number of effects on oxygen isotope ratios, which can be summarised as follows:

- Temperature effect: the $\delta^{18}O$ is more negative with colder temperatures
- Latitude effect: the $\delta^{18}O$ is more negative with increasing latitude (temperature and rainout)

- Elevational effect: the $\delta^{18}O$ is more negative with altitude (temperature and rainout)
- Continental effect: the $\delta^{18}O$ is more negative further inland (rainout)
- Seasonal effect: the $\delta^{18}O$ is more negative in winter (temperature)
- Amount effect: the $\delta^{18}O$ is less negative when more precipitation falls (rainout)

At high latitudes, oxygen isotope composition generally trends with the seasons, as summer precipitation is enriched relative to winter. At lower latitudes, seasonal patterns are not as pronounced and instead the amount effect has more influence. In summary, colder environments are likely to have more negative $\delta^{18}O$ values and precipitation becomes more depleted with altitude, latitude and increasing distance from the coast (Rozanski et al. 1993).

In aquatic animals that precipitate their mineralised parts from solution, a large contribution to isotopic ratios of those parts is derived from the water in which they live. Oxygen isotopes in terrestrial animal tissues come from ingested water, both through drinking and incorporated in food as well as respired oxygen, which then makes its way to body water, from which the precipitation of hard-parts occurs. During incorporation of $\delta^{18}O$ into animal tissues, the degree of fractionation is largely influenced by temperature (Grossman & Ku 1986), which though stable in endotherms, varies with the environment in ectotherms.

4.1.2. Oxygen isotopes in aquatic ectotherms (i.e. fish otoliths)

There are two main assumptions involved when interpreting stable isotope measurements in calcareous materials of aquatic animals; 1) precipitation occurs in equilibrium with environmental water and 2) that the empirically determined temperature-fractionation relationship defining equilibrium, is correct (Patterson 1998). (A third assumption for fossil materials is that no diagenesis has occurred, see Section 4.1.4). Thus, fractionation of isotopes during precipitation should result in an isotopic composition of carbonate reflecting the isotopic composition of the water, as predicted according to the temperature of precipitation. Urey et al. (1951) gave the name ‘vital effect’ to the case in which equilibrium does not occur, suggesting that other within-organism fractionations may be altering the expected isotope ratio.

Apart from mammals and birds, all animal phyla are ectothermic (cold-blooded) meaning their body temperature alters with that of the ambient environment. Because of the relationship between temperature and fractionation, this has major implications for the stable isotope analysis of materials from ectothermic animals, including the golden perch otoliths in this study. Because the degree of fractionation depends on the temperature of the environment at the time, complex equations are required to determine the predicted equilibrium isotope values.

Numerous studies have looked into whether or not equilibrium is the norm for aragonitic animal materials in both saltwater (e.g. Grossman & Ku 1986, Kalish 1991, Naylor et al. 2007) and freshwater (e.g. Patterson et al. 1993, Dettman et al. 1999, Wurster & Patterson 2001) environments. In some species, such as molluscs, equilibrium of $\delta^{18}O$ is variable, with some researchers finding equilibrium with the environment (Patterson et al. 1993, Dettman et al. 1999, Wurster & Patterson 2001) while others find disequilibrium (Naylor et al. 2007). Otolith aragonite on the other hand, has been demonstrated to precipitate in (or very close to) isotopic equilibrium with the $\delta^{18}O$ value of environmental water (Kalish 1991 and various authors in Wefer & Burger 1991; Patterson 1998; Campana 1999; Ghosh et al. 2007). This suggests that water is the primary source of the oxygen isotopes (Campana 1999).

In order to determine equilibrium in this way, equations regarding the relationship between carbonate $\delta^{18}O$, water $\delta^{18}O$ and temperature need to be utilised. Three regularly used, and successfully applied, equations are those by Grossman & Ku (1986), Patterson et al. (1993) and Dettman et al. (1999).

Grossman & Ku (1986) studied aragonite precipitation in foraminifera, gastropods and scaphopods from continental margins off Southern California and Texas, USA and Mexico. They proposed the following equation:

$$T°C = 20.6 - 4.34(\delta^{18}O_{ar} - \delta_w), \qquad (2)$$

where $\delta^{18}O_{ar}$ is the $\delta^{18}O$ (PDB) of aragonitic shell and δ_w is the $\delta^{18}O$ (SMOW) of the water minus 0.2‰. The subtraction adjusts the water and carbonate $\delta^{18}O$ measurements to the different scales on which they are measured. It is now thought that this correction should be 0.27‰ (Gonfiantini et al. 1995 in Dettman et al. 1999).

Dettman et al. (1999) studied aragonitic precipitation in Unionid freshwater bivalves in two southern Michigan rivers. They modified Grossman & Ku's equation (2), because the term '($\delta^{18}O_{ar}$-δ_w)' introduced a systematic error for water with $\delta^{18}O$ values below -10‰ (SMOW). They related temperature directly to fractionation factor, yielding a relationship in water of any $\delta^{18}O$ value:

$$10^3 \ln(\alpha) = 2.559(10^6 T^{-2}) + 0.715 \qquad (3)$$

where T is temperature in Kelvin and α is the fractionation between water and aragonite, described by the following equation:

$$\alpha = \frac{(1000 + \delta^{18}O_{ARAGONITE(SMOW)})}{(1000 + \delta^{18}O_{WATER(SMOW)})} \qquad (4)$$

Note that both $\delta 1^8O$ values are relative to SMOW and the aragonite composition must be converted to the PDB scale using an α_{PDB}^{SMOW} value of 1.0309 (Gonfiantini et al. 1995 in Dettman et al. 1999).

Patterson et al. (1993) developed a similar equation, but specifically for aragonitic otoliths of freshwater fish, from six large temperate lakes around the world:

$$10^3 \ln(\alpha) = 18.56(10^3)T^{-1} - 33.49 \qquad (5)$$

where T and α have the same meanings as in equations (3) and (4).

Patterson et al. (1993) applied their equation to data from numerous previous studies (various authors in Patterson et al. 1993), and found that the relationship is applicable in both marine and non-marine settings and that metabolic or generic/species effects were not significant.

Each of the above equations has three unknown parameters; the temperature of precipitation, the $\delta^{18}O$ of the carbonate, and the $\delta^{18}O$ of the ambient water. Therefore, two need to be determined, to predict the third. For fossil samples, the $\delta^{18}O$ of the carbonate can be measured, but one of either the temperature of precipitation, or the $\delta^{18}O$ of the water, needs to be estimated to predict the other. Patterson (1998) suggested that growth activity temperature

tolerances (i.e. the lowest temperature at which aragonite precipitates) for warm-water eurythermic fish can be used to estimate the temperature of precipitation, and hence calculate the $\delta^{18}O$ of environmental water. This is done by assuming the otolith sample location with the highest $\delta^{18}O$ represents the coldest tolerance of the fish. Klein et al. (1996) pointed out that the skeletal $\delta^{18}O$ of molluscs varied with both salinity and temperature and hence they used salinity (Mg/Ca) as a proxy for temperature. Campana (1999) similarly suggested using Sr/Ca ratios, though these can be confounded by salinity changes. Ghosh et al. (2006; 2007) used 'clumped isotopes' to get around the issue of needing to know the isotopic composition of water. They constrain the temperature of carbonate growth based on the isotopic composition of the carbonate alone. Ghosh et al. (2006) documented a relationship between the $^{13}C^{18}O^{16}O$ of standard carbonates, corals and inorganic carbonates, as measured by Δ_{47} value, which is the difference in per mille between the measured 47/44 ratio of the sample and 47/44 ratio expected for that sample if its stable carbon and oxygen isotopes were randomly distributed among all isotopologues, a situation known as 'the stochastic distribution'. The 47 value includes the isotopologues $^{12}C^{17}O^{18}O$ and $^{13}C^{17}O^{17}O$ in addition to $^{13}C^{18}O^{16}O$, and 44 includes $^{12}C^{16}O^{16}O$. Ghosh et al. (2007) went on to apply this technique to aragonitic fish otoliths.

When neither the palaeotemperature nor $\delta^{18}O$ of the ambient water can be determined in order to calculate the other, absolute values cannot be assigned. The relative changes in the $\delta^{18}O$ of the carbonate do, however, still provide environmental information, though the observed measurements may be a result of the interaction between temperature and $\delta^{18}O$ water variations, not a single tracer of one or the other. Relative changes that can be expected to be seen in archaeological otoliths from Lake Mulurulu include more negative values during the LGM relative to Holocene due to lower environmental temperatures, and a negative shift in winter relative to summer. Additionally, as golden perch generally migrate upstream (Section 4.2.1) a gradual negative trend may be seen as the fish moves inland (continental effect), with a shift to more positive values when the fish is residing in a lake undergoing evaporation.

Oxygen isotopes in otoliths have been used in numerous palaeoclimate studies. For example, Patterson (1998) used high resolution analysis of otoliths to contribute to determining North American continental seasonality during the last thousand years. Otoliths of freshwater drum (*Aplodontus grunniens*) collected from middens along the shores of Lake Erie, Ohio, were

radiocarbon dated and microsampled for carbonate $\delta^{18}O$ analysis. Using the known growth activity temperature tolerance of the species, the temperature of precipitation of the otolith samples were constrained, and the $\delta^{18}O$ of the ambient lake water at the time could then be calculated (Patterson 1998). The results were used to infer temperature, evaporation/precipitation and seasonality over the last thousand years of North American climate variations.

4.1.2.1. Previous isotope studies at Lake Mulurulu

Douglas (1996) analysed oxygen isotopes in a bivalve shell from Lake Mulurulu and compared them with those from a biosedimentary algal mat from Lake Mungo. Both samples date from the latter part of the last glacial cycle, yet the Mungo stromatolite $\delta^{18}O$ was approximately 4.5 ‰ heavier than the Mulurulu shell. Douglas ascribed this variation to longer term evaporative processes at the terminal Lake Mungo, compared to the through-flow system of Lake Mulurulu. Boljkovac (2009) analysed six otoliths from the Willandra Lakes, four from Lake Mungo plus two from Lake Mulurulu. Oxygen isotopes were analysed using a Sensitive High-Resolution Ion Micro-Probe (SHRIMP) II and coupled to trace element and strontium isotope measurements analysed using Laser-Ablation Inductively Coupled Plasma Mass Spectrometry (LA-ICPMS). By combining oxygen isotopes with trace element analyses Boljkovac (2009) was able to determine that an overall increase in $\delta^{18}O$ ratios in some samples was likely due to a drying of the lake environment. Flood events were also identified in some samples, represented as sudden increases in isotope ratio compositions. This was the first time $\delta^{18}O$ measurements were carried out on otolith material using SHRIMP. Long et al. (2014) continued this work, comparing $\delta^{18}O$ ratios and trace elements in otoliths from Lake Mungo with those from two otoliths from the current study, from Lake Mulurulu. The results show evidence for lake drying in the isotopes of the Lake Mungo samples but not those from Lake Mulurulu.

4.1.2.2. Oxygen isotope measurements using SHRIMP

A well preserved otolith of *Micropogonias altipinnis* from a Paijan site on the northern margin of the Chicama Valley, Northern Peru was analysed for $\delta^{18}O$ using both conventional

Isotope Ratio Mass Spectrometry (IRMS) and SHRIMP II analyses (QCD; Boljkovac 2009; Aubert et al. 2012). For the conventional analyses, micro-samples were drilled along 43-100 µm wide tracks parallel to the annual growth banding, while SHRIMP analyses were carried out *in situ* on the re-polished specimen. Both techniques produced very similar results, with an average difference of -0.08 ‰ between the SHRIMP measurements and conventional mass spectrometry, possibly due to fractionation differences between the two techniques or the use of different standards (Figure 4.2). There are also slight variations between the two sets of results, possibly due to the difficulty of aligning the SHRIMP sampling points with the micro-drilled tracks and the fact that micro-drilling samples a larger volume of material, which in some cases may constitute more than one growth band.

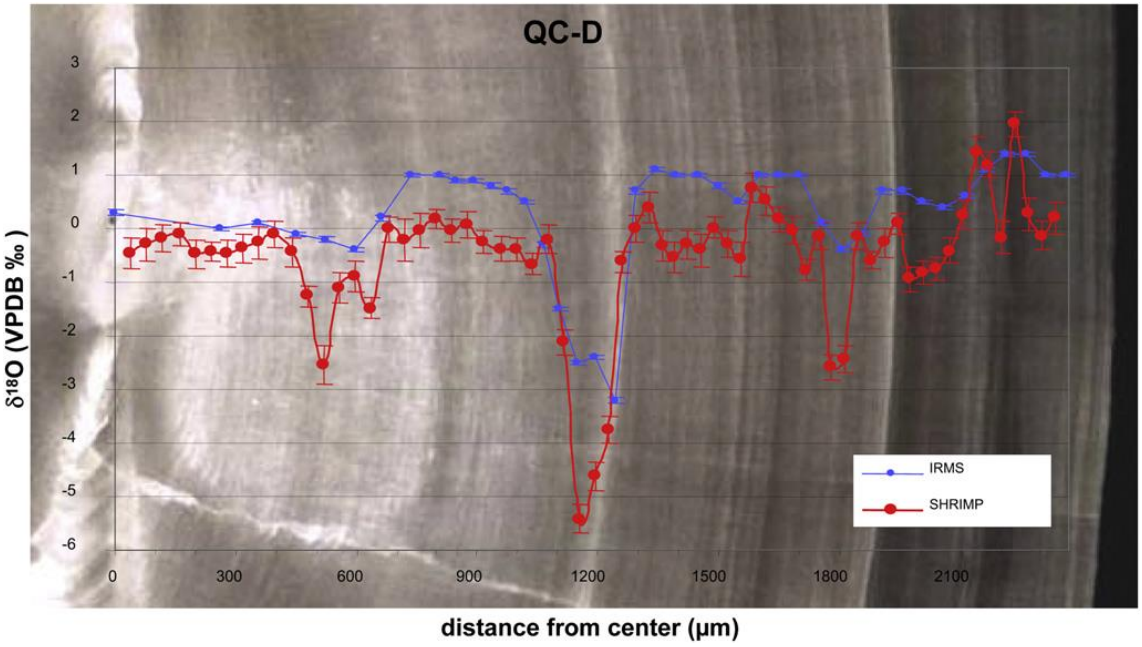

Figure 4.2. QC-D Otolith $\delta^{18}O$ results for SHRIMP II (data points with error bars) and conventional mass spectrometry (Aubert et al. 2012, their Fig. 4).

Both methods facilitate reconstructing the life-history of the fish and as suggested by Aubert et al. (2012), with the cyclic variations in $\delta^{18}O$ values most likely related to seasonal changes in ambient water temperature. One major and two minor excursions are apparent, all of which are of a greater magnitude when measured via SHRIMP, probably due to the higher temporal resolution provided by the *in situ* SHRIMP analyses (Aubert et al. 2012). While the conventional analyses provide better analytical precision than SHRIMP II, temporal resolution is lower and preparation and measurement times are significantly longer. The

preparation and measurement of 42 oxygen isotope analyses took approximately three days. The preparation for the SHRIMP analysis on the other hand (sample mounting and polishing) took approximately two hours, and 65 analyses were carried out in a single day.

4.1.3. Oxygen isotopes in terrestrial endotherms (i.e. wombat teeth)

Mammals are warm blooded, and as such, the above fractionation equations are not required. Although fractionation is temperature dependent (Grossman & Ku 1986), warm-blooded animals maintain their body temperature at a constant level, therefore bioapatite precipitates from cell water at a maintained temperature (usually 37°C for mammals). Depending on the component of bioapatite analysed an offset may need to be applied to determine body water $\delta^{18}O$ values. Mammalian tooth enamel generally contains <1 wt.% carbonate, ~ 96 wt.% calcium phosphate, ~1 wt.% organic material and ~3 wt.% water (Hillson 1986). When precipitated in equilibrium, the oxygen isotope ratio of the carbonate component is approximately 8.4-9‰ higher than in the phosphate component. When making comparisons between results it is important that this offset is applied if required. Given phosphate comprises such a large portion of the enamel material, bulk enamel measurements can be considered as phosphate analyses.

In obligate drinkers $\delta^{18}O$ can provide information on rainfall regimes (Zanazzi & Kohn 2008) whereas in non-obligate drinkers, such as hairy-nosed wombats, $\delta^{18}O$ is derived from leaf-water, and hence gives an indication of relative humidity or aridity (Ayliffe & Chivas 1990). This is because leaf water evaporates from stomata during transpiration, with ^{16}O evaporating preferentially (Farquar and Lloyd 1993). Hence, plants growing in conditions of low humidity have enriched ratios relative to those in high humidity (Barbour et al. 2004). Additionally, factors other than climate may have an effect, as physiological and behavioural adaptations, such as panting and sweating, will influence the fractionation of $\delta^{18}O$ out of the body (Kohn et al. 1998).

Ayliffe and Chivas (1990), who found a strong relationship between phosphate $\delta^{18}O$ values in modern Macropus bone and the relative humidity of the environment, were the first to suggest the use of $\delta^{18}O$ as a palaeoenvironmental proxy in Australian fossil materials. Murphy et al. (2007) found that the relationship between kangaroo tooth enamel $\delta^{18}O$ and relative humidity

varied with mean annual temperature, with a steeper linear relationship at lower temperatures. After analysing modern wombat tooth enamel, Fraser at al. (2008) suggested that although $\delta^{18}O$ analyses of fossil wombat teeth cannot be relied upon to provide quantitative rainfall $\delta^{18}O$ or temperature estimates, they may provide a qualitative indication of relative habitat dryness. They measured $\delta^{18}O$ and $\delta^{13}C$ micro-profiles in modern hairy-nosed wombat teeth from a number of sites around Australia. Figure 4.3 shows the results from two wombats retrieved from Brookfield Conservation Park. Of the sites analysed by Fraser et al. (2008), this site shares environmental conditions most similar to those at the Willandra Lakes. It is a semi-arid inland site in southern Australia with a mixture of mallee eucalypt open woodland, saltbush, sedges and winter/spring grasses.

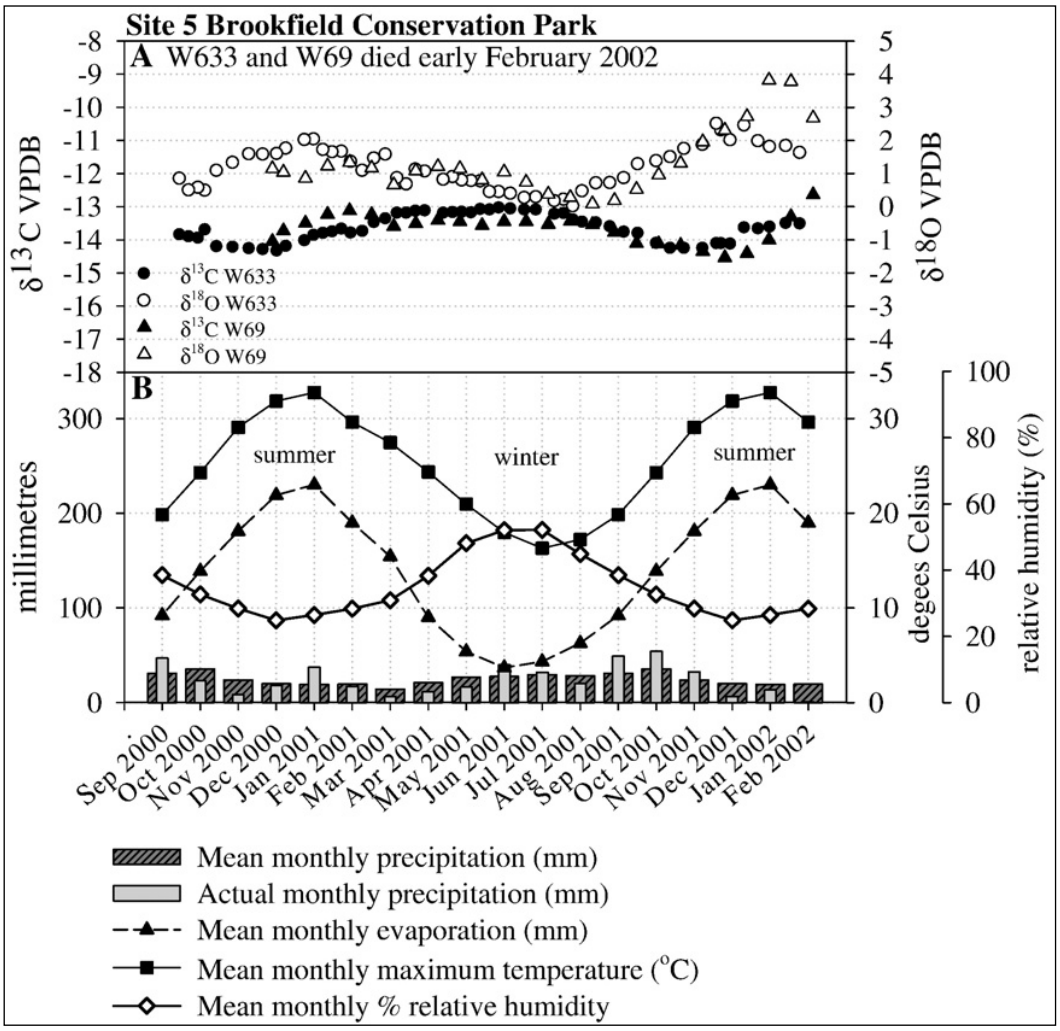

Figure 4.3. A: Carbon and Oxygen microprofiles from two wombat incisors from Brookfield Conservation Park, South Australia. B: Mean monthly climate data for the time period represented by the incisors, based on average growth rate of 0.15mm/day. (Fraser et al. 2008; their Fig. 8).

The $\delta^{18}O$ values display a cyclical pattern, with higher values in the warmer, drier and less humid summer, and lower during the wetter, cooler and more humid winter. Surface water in the area is rare and given plant water $\delta^{18}O$ is negatively correlated with relative humidity (Barbour & Farquhar 2000), Fraser et al. (2008) suggested the $\delta^{18}O$ may be inversely tracking seasonal changes in relative humidity. A similar pattern may be expected in fossil wombat tooth samples from the Lake Mulurulu lunette.

Stable isotopes in Australian marsupial remains have been used in only a few palaeoecological studies. Bone collagen $\delta^{13}C$ and $\delta^{15}N$ values were analysed in Macropus, Sthenurus and Diprotodon by Gröke (1997; 1998). Miller et al. (2005) examined $\delta^{13}C$ values of fossil wombat tooth enamel and found that values became more depleted and confined in range over the time period of approximately 50 to 45 ka. This was similar to the temporal pattern they observed in the $\delta^{13}C$ values of emu eggshells, adding validity to their suggestion that there was a substantial vegetation change during this period. Given there is little substantial evidence for detrimental climate change within the region, they suggested the cause of this change may have been the land-use, primarily increased fire regimes, of early Australians. Prideaux et al. (2009) analysed both $\delta^{13}C$ and $\delta^{18}O$ of *Procoptodon goliah* tooth enamel. The $\delta^{18}O$ results showed it drank more in low-rainfall areas than its grazing contemporaries, similar to modern saltbush feeders. They combined the isotope analysis results with craniodental morphology and dental microwear evidence to suggest the extinction of this giant Pleistocene kangaroo may have been more influenced by human hunting than landscape burning or climatic aridity.

Wombat teeth have not been measured previously using SHRIMP though tooth enamel samples from other animals have. Aubert et al. (2012) used SHRIMP to analyse $\delta^{18}O$ in a steenbok tooth that had previously been microdrilled and analysed via conventional mass spectrometry (Balasse et al. 2002). The conventionally measured analyses were carried out only on the carbonate portion of the enamel, while the SHRIMP measured bulk enamel ratios, which primarily reflects the phosphate signal. As such, the vertical axes in Figure 4.4 are offset by 9 ‰ between the carbonate (conventional analyses) and phosphate (SHRIMP) measurements.

More detailed intra-tooth isotopic variations are clearly visible in the higher spatial resolution SHRIMP analyses (Figure 4.4A). When the shrimp analyses are averaged to represent the same resolution as the microdrilled samples, there is a 1-2 ‰ discrepancy at some locations (Figure 4.4B). The authors suggested this may be due to the differing scales of analysis, with the microdrilled samples averaging the isotopic composition of a sample volume about seven orders of magnitude larger than that sampled by SHRIMP. Alternatively, diagenesis may have occurred in this sample, possibly preferentially affecting the carbonate fraction (see below), resulting in an isotopic offset between the two tooth apatite components.

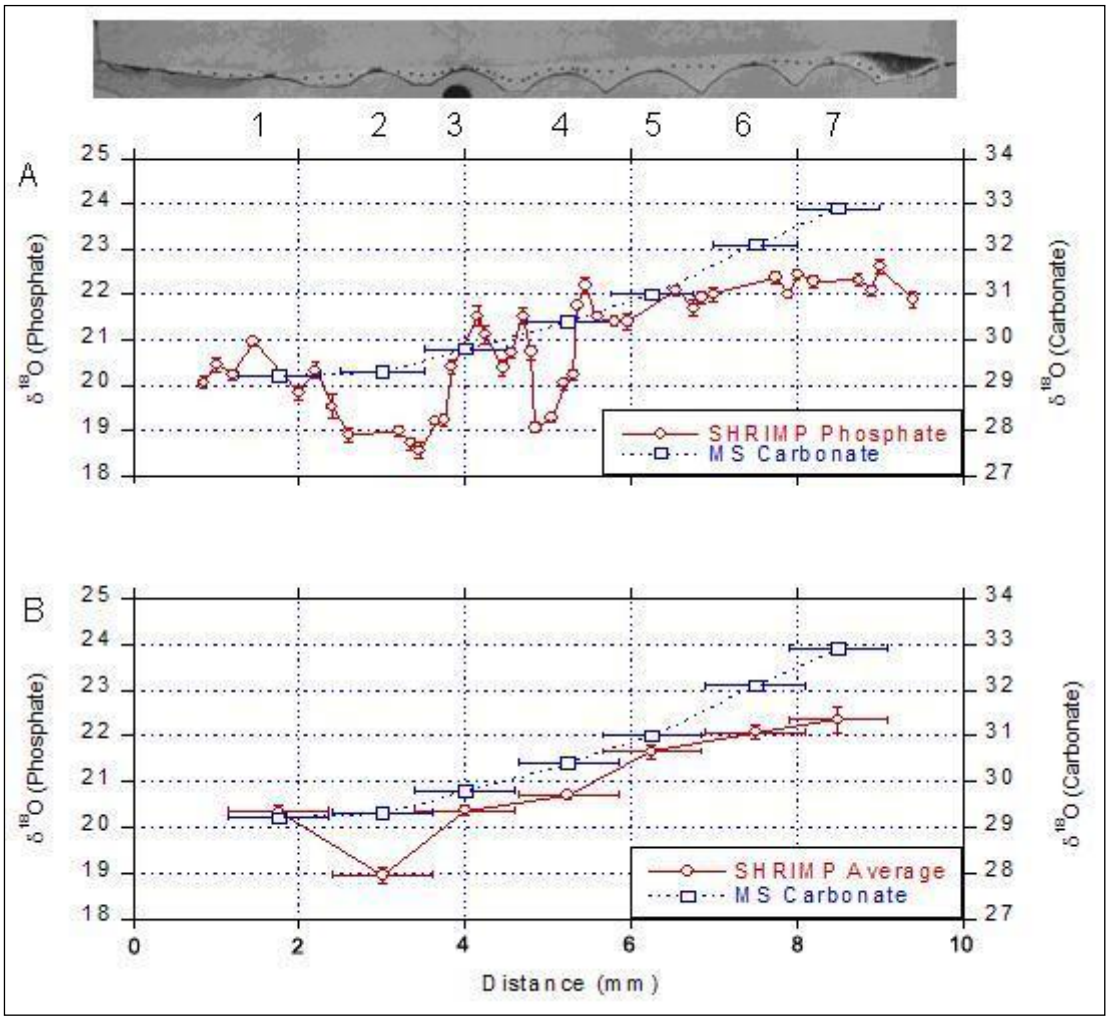

Figure 4.4. A: SHRIMP II profile compared to a micro-drilled profile analysed by conventional mass spectrometry. B: Average SHRIMP II profile compared to the same micro-drilled profile analysed by conventional mass spectrometry (Aubert et al. 2012, their Fig 1)

Aubert et al. (2012) also analysed tooth enamel from deer, bison and a Neanderthal from the Palaeolithic site of Payre. Herbivore teeth from different levels at the Payre excavation site

gave average SHRIMP values equal to those determined via conventional methods for other samples from the same layers. Additionally, the SHRIMP measurements highlighted a general trend toward lighter oxygen along the growth axis of deer teeth and in one sample, quasi-sinusoidal variation that is probably related to seasonality. The Neanderthal tooth showed a similar average value but narrower isotopic range than herbivores from the same archaeological layer. The authors suggested that the more restricted range may be due to the longer human enamel maturation period, or may represent a restricted feeding range and/or more uniform sources of drinking water while the enamel was mineralising.

4.1.4. Diagenesis

An assumption when using the $\delta^{18}O$ composition of fossil materials, whether otoliths, enamel or anything else, as an environmental proxy is that diagenesis has not modified the measured isotopic ratios such that they no longer reflect the environment in which the material formed. Collagen from bone material is relatively susceptible to diagenesis (Lee-Thorpe et al. 1989a; Budd et al. 2000) and normally only retained in bone for less than 20,000 years, unless preserved in a very cold environment (Schroeninger and Moore 1992). Tooth enamel, especially of Quaternary age, is less likely to have undergone diagenesis because its structural integrity and heavily mineralised nature makes it more resistant to contamination and alteration (Lee-Thorpe et al. 1989b; Budd et al. 2000). Luz et al. (1984) suggested phosphate-oxygen bonds are extremely stable in low temperature geological systems, and are essentially unaffected by post-depositional isotopic exchange reactions, even over geological timescales. This conclusion was challenged by Ayliffe et al. (1992) who analysed fossil elephant enamel, dentine, cement and bone and found a larger spread of phosphate $\delta^{18}O$ values in the different skeletal phases, which they interpreted as evidence for post-depositional alteration of primary $\delta^{18}O$ signatures. Ayliffe et al. (1994) then carried out X-ray diffraction analysis on these four skeletal components of fossil elephants and found that the X-ray spectra of the less crystalline phases are similar to that of the enamel, indicating that the dentine, cement and bone recrystallised during diagenesis, while the enamel did not. For this reason enamel is a preferred material for palaeoecological isotope studies.

Although the phosphate component of biological apatite is more resistant to alteration than the carbonate component, carbonate $\delta^{18}O$ is often measured because preparation is simpler and carbon isotopes can then be measured concurrently with oxygen. The precipitation of secondary carbonates can mask the original isotope signature in the material however, so various preparation procedures have been suggested for removing diagenetic carbonate prior to analysis (Koch et al. 1997; Zazzo et al. 2004). Aragonitic materials pose little problem, as diagenesis is evident by the conversion of aragonite into calcite (Koch 1998; Dettman et al. 1999; Kim et al. 1999) and so can be easily recognised and avoided.

4.2. Oxygen isotope geochemistry materials and methods

4.2.1. Sample materials

Two different types of fossil faunal materials were collected from the Lake Mulurulu lunette for isotopic analysis: teeth from the southern hairy-nosed wombat (*Lasiorhinus latifrons*) and teleost fish otoliths (*Maquaria ambigua,* golden perch). Each has different characteristics making them useful for isotope studies. Fish otoliths are carbonate (primarily aragonite), grow in accretionary layers and can be radiocarbon dated. Wombat tooth enamel also grows in accretionary layers and consists of hydroxyapatite, which is suitable for Electron Spin Resonance (ESR) dating. Metabolically inert, accretionary biological materials such as these can provide a continuous record of stable isotope variation for the period over which the material grew.

4.2.1.1. Wombat teeth

Wombats (Vombatidae) are large burrowing marsupials, with a lifespan of around 20 years, during which they may grow to over a metre long and weigh up to 30 kg (Ride 1970). Southern hairy-nosed wombats (*L. latrifrons*) differ from common wombats (*Vombatus ursinus*) in having broader, hairier noses, silkier fur and longer ears (Horsup 2004) and for living in colonies in arid and semi-arid regions of South Australia (Wells 1978a; 1978b). The presence of fossil southern hairy-nosed wombat teeth at Willandra Lakes (Figure 4.5; Scott 1988; Hope 2006) demonstrates they were once distributed more widely around semi-arid

Australia than they are today, as there are no written or oral records of wombats in the Willandra region. Scott (1988) proposed in a Masters thesis that the extinct wombats from the Willandra may constitute a separate species, *L. mungoensis*, based on cranial morphology. The formal description of the species does not appear to have been published, however, and the Willandra specimens are generally considered to be *L. latifrons*. Modern *L. latifrons* are adapted to an arid environment, conserving water through both behavioural strategies and physiological adaptations. They forage at dawn and dusk while escaping the heat of the day in underground tunnels (Ride 1970) where respiratory water loss is significantly reduced by elevated tunnel humidity. They do not sweat, have dry faeces and produce only small volumes of urine (Wells & Green 1998). Together these adaptations allow the wombats to be non-obligate drinkers, gaining water primarily from their food, though their specific drinking habits may be site-dependent (Fraser et al. 2008). They also have a very slow metabolism, 64% of that predicted for a marsupial of the wombats' size (Wells 1978b).

Figure 4.5. a) Wombat teeth *in situ* in the Lake Mulurulu lunette, Willandra Lakes World Heritage Area, NSW. (Photo courtesy of Wayne Cooke 2007). b) The same wombat teeth, after removal from the field.

Wombats are strict herbivores, almost exclusively eating grasses and reeds (Miller et al. 2005), and survive on a low protein diet through a symbiotic relationship with gut micro-bacteria that digest the otherwise indigestible cellulose in their food (Ride 1970). Wombats graze in concentric circles around their warrens, ranging 2.5-4.2 ha (Wells 1978a). Warrens vary in complexity depending on the number of occupants, ranging from simple, single entrance warrens, to three dimensional systems with numerous tunnels and dozens of entrances (Shimmin et al. 2002). Although they usually live in densely populated communities, individual wombats are essentially solitary in behaviour (Ride 1970). Figure 4.6 shows a modern southern hairy-nosed wombat

Figure 4.6. A modern southern hairy-nosed wombat.(http://z.about.com/d/goaustralia/1/0/x/Z/wombat.jpg**)**

Wombat teeth are similar to rodent incisors (Hillson 1986), in that they are rootless and grow continuously. In southern hairy-nosed wombats, only the labiodontal side of each incisor is covered in enamel, and incisor length is 6-8 cm whereas molars are 3-4 cm (Fraser et al. 2008). Tooth enamel is composed of a form of hydroxyapatite [$Ca_{10}(PO_4)_6(OH)_2$] that functions as an essential barrier against mechanical and abrasive stresses on teeth throughout the lifetime of an organism (Fincham et al. 1999). As such it is very tough and resistant, composed of 96-97% inorganic material (Scott & Symons 1974 in Hillson 1986) making it the most highly mineralised structure in the vertebrate body (Fincham et al. 1999). As a result, tooth enamel is relatively resistant to diagenesis and is commonly represented in the fossil record (Lee-thorpe et al. 1989b; Budd et al. 2000). Additionally, wombat remains are favoured for preservation, due to wombats often dying inside their burrows (Miller et al. 2007). Fraser et al. (2008) calculated a modern wombat incisor growth rate of 0.15 mm/day,

such that a full incisor represents 14-16 months growth. By tracing stable isotope ratios along the length of a tooth, following the growth axis, inferences can be made regarding the habitat in which the wombat lived and fed (e.g. seasonality, aridity, diet; see Section 4.1.3).

4.2.1.2. Fish otoliths

The term 'otolith' can be used in a broad sense to mean any type of dense body in the labyrinth (inner ear) of vertebrates (Calstrom 1963). Fish otoliths are particularly useful for ecological and palaeoenvironmental studies (Casteel 1976) as fish grow relatively large otoliths (three in each ear), rather than large numbers of very small otoliths held together by an organic gel (Casteel 1976). Fish otoliths are composed primarily of aragonite, with around 3% organic matrix (Campana 1999). Accretion can exceed one millimetre per year in some species, resulting in visible layers representing daily accretion (various authors in Paterson et al. 1993).

The species of fish most commonly represented by otoliths in the Willandra lakes area is the golden perch (*Maquaria ambigua;* Figure 4.7; Hope 2006). Also known as Murray perch, callop or yellow belly, it is an extant native Australian freshwater fish, which lives in sluggish, often turbid inland rivers (Lake 1978), primarily within the Murray River and its distributaries (Roughly 1957), though allopatric subspecies also exist in surrounding drainage basins (Musyl & Keenan 1992). It is a carnivorous fish that eats crustaceans including yabbies (Cherax), molluscs and fish (Lake 1978). It is a relatively slow-growing species, and although individuals can reach 23 kg and 76 cm in length, they typically weigh less than five kilograms (Lake 1978). It reaches sexual maturity at around three years of age, when it has usually reached about a third of its full size (Roughly 1957). The golden perch reproductive cycle is synchronised with the hydrological regime of the river, spawning after flooding (Williams 1983), usually September to November, but also in March or April if water level is high (Roughly 1957). Adults generally migrate upstream (some as far as 2000 km) while eggs, larvae and very young fish are washed downstream (Lake 1978).

Figure 4.7. A modern golden perch, 800 mm long. (Lake 1978).

Anderson et al. (1999) described the otoliths of the golden perch as large, ovoid and laterally concavo-convex, with a deep groove on the convex proximal surface, relatively elongate with a prominent rostrum, and very irregular or scalloped margins (Figure 4.8). Otoliths in *M. ambigua* continue to grow and deposit distinct, relatively evenly spaced annual rings, even after body growth of the fish has essentially ceased. In addition to being useful for aging fish (Anderson et al. 1999; Pritchard 2004) this permits high-resolution measurement of stable isotope variation for the entire period of the fish's life (e.g. Boljkovac 2009; Long et al. 2014; see Section 4.1.2). Pritchard (2004) compared modern *M. ambigua* otoliths from the Googong Reservoir (in the southern Murray-Darling Basin) with fossil *M. ambigua* otoliths from the Willandra Lakes dating to 17-20 ka Cal. BP. She found that although there were no substantial differences in external otolith dimensions, older age classes were more common in the Pleistocene (up to 43 years compared to up to 26 years in modern counterparts) and otolith increment widths were narrower in the fossil specimens, suggesting slower somatic growth, possibly due to the colder glacial climate. This decreased growth rate combined with increased longevity means that the Pleistocene fish may have reached larger asymptotic sizes than historic records, given the well-known demographic trade-off between these traits (Prichard 2004).

Figure 4.8. Otoliths from the Lake Mulurulu lunette, Willandra Lakes World Heritage Area, NSW.

4.2.2. $\delta^{18}O$ analysis using SHRIMP

4.2.2.1. Sample Preparation

Two wombat teeth and two fish otoliths were selected for $\delta^{18}O$ analysis using SHRIMP. Each was sliced with a diamond saw to expose growth layers, mounted in a 35 mm epoxy resin 'megamount' (Ickert et al. 2008) along with standards (Durango mineral apatite, NBS18 carbonate and NBS19 carbonate) and polished using 3 μm then 1 μm diamond lapping paste. The mounted samples are pictured in Figure 4.9. Before mounting, a small portion from the rostrum of each otolith (~5 mg) was removed for ^{14}C dating (Chapter 5). The mounted samples were photographed in transmitted and reflected light, ultrasonicated, oven-dried at 60ºC and given an aluminium coating approximately 12 nm thick.

Figure 4.9. SHRIMP mounts before the application of the Al coating. A: WT34B. B: Durango mineral apatite standard. C: WT36B. D: OT23. E: NBS18 carbonate standard. F: NBS19 carbonate standard. G: OT27. Scale = 1 cm bars

4.2.2.2. Measurement and Analysis

Isotope ratios were measured *in situ* using the SHRIMP II with a 30 μm spot size, spaced at 25 μm and 250 μm intervals for otoliths and wombat teeth, respectively. Each spot was analysed for 100 s as two blocks of five ten-second measurements using two movable Faraday cup collectors to measure $^{16}O^-$ and $^{18}O^-$. Analysis transects were run perpendicular to growth lines in the otoliths and along the length of wombat tooth enamel. An additional transect was run across a section of each otolith and one of the wombat teeth as a check for reproducibility (Figure 4.10 and Figure 4.11). Standards were measured a number of times at the start of each run and after every four to five spots during the analyses, to permit calibration and normalisation for instrument drift. A detailed description of the SHRIMP II analysis methodology is available in Aubert (2012) and Long (2014).

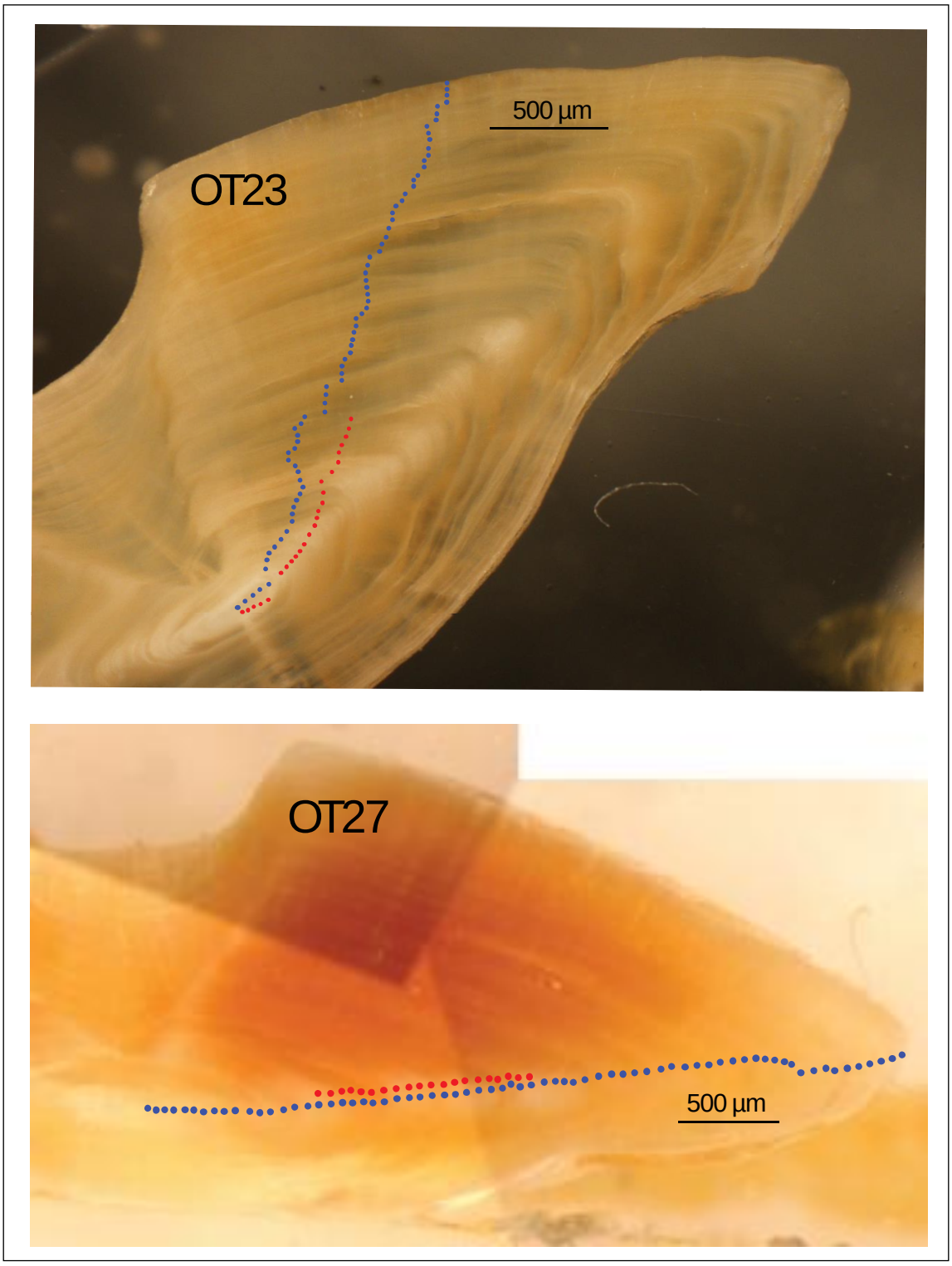

Figure 4.10. SHRIMP analysis locations on fish otoliths. Blue spots are the full transects. Red spots show the replicated portion

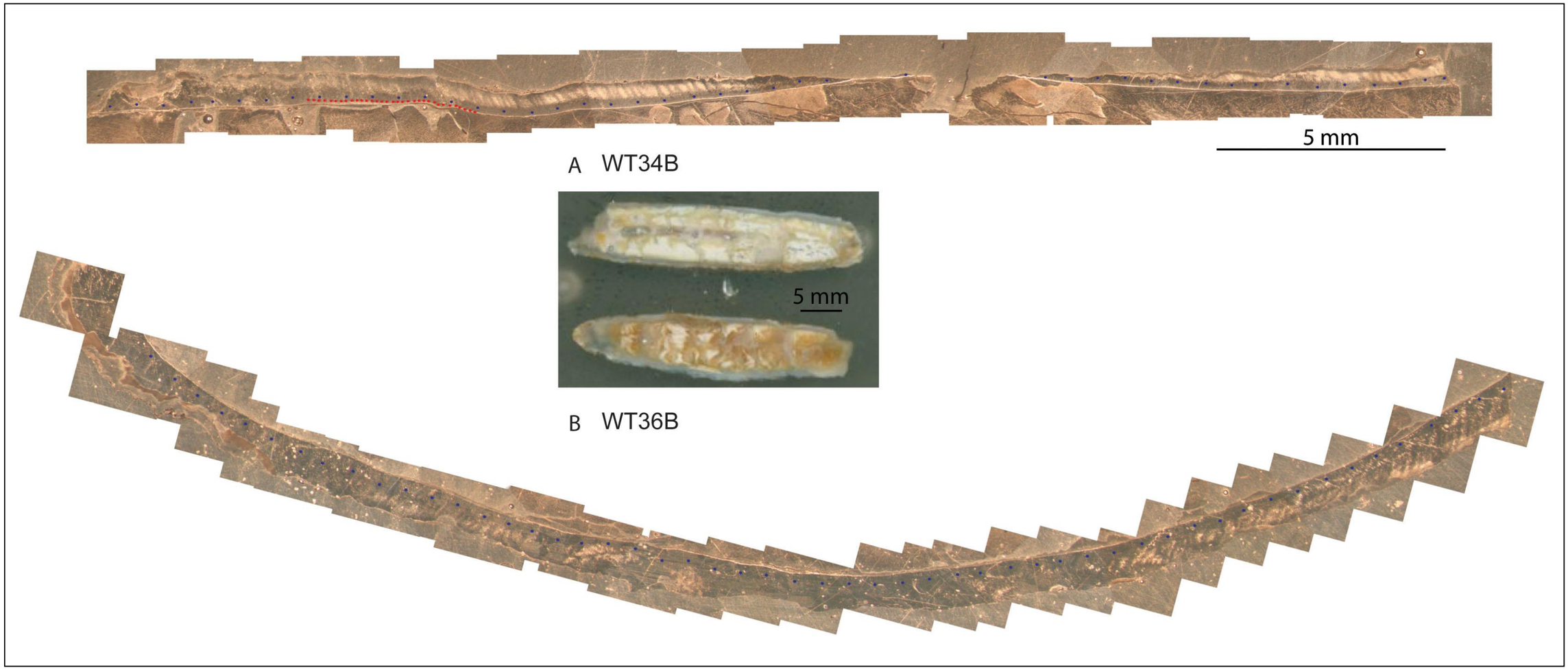

Figure 4.11. SHRIMP analyses on wombat teeth. Blue spots are the full transects. Red spots show the replicated portion

4.2.3. Trace element analysis using Laser Ablation – Inductively Coupled Plasma Mass Spectrometry (LA-ICPMS)

The same sample mounts used for SHRIMP analysis (Section 4.3.2.1) were used for trace element analysis by LA-ICPMS using an ANU HelEx ArF (λ = 193nm) excimer laser-ablation system coupled to a *Varian 820* quadrupole ICPMS. A suite of trace elements were measured including Sr, Ca, Mg, Ba and U. LA-ICPMS analyses were made parallel to the SHRIMP transects across each of the otoliths (Figure 4.10). LA-ICPMS was selected as the method of choice for measuring trace element concentrations in these samples, because the non-destructive methodology allows an assay line to closely follow the previous SHRIMP assay, permitting correlation and comparison of the resultant data sets.

4.2.4. $\delta^{18}O$ analysis of Wombat teeth using Continuous Flow – Isotope Ratio Mass Spectrometry (CF-IRMS)

SHRIMP is not traditionally used for analysing oxygen isotopes in tooth enamel. Destructive methods of isotope ratio mass spectrometry are more commonly used (e.g. Stuart-Williams & Schwarcz, 1997; Balasse et al., 2002; Zazzo et al., 2004; Fraser et al., 2008). Although these methods result in the loss of materials, more comprehensive research in to these techniques for this purpose makes the results more reliable than SHRIMP. For this reason, CF-IRMS was employed in addition to SHRIMP for analysing wombat teeth in this study.

4.2.4.1. Leaching tests

A series of leaching tests were conducted to determine the most effective treatment for removal of diagenetic material while avoiding altering the primary composition of the tooth enamel (Section 4.1; Koch 1997, Nielsen-Marsh & Hedges 2000). Six samples were chosen for this investigation, four wombat teeth (two modern and two fossil) and two mineral standards (Florida Rock Phosphate NIST 120c and Durango mineral apatite).

Tooth enamel was separated and cleaned with a diamond saw. Enamel and Durango mineral apatite were ground with an agate mortar and pestle, while NIST120c was available in powder

form. Each sample was split into 11 sub-samples of approximately 20 mg (40 mg for NIST120c) and labelled a-k. A list of sample numbers and weights is presented in Table 4.1

Table 4.1. Leaching test sub-sample masses

Modern WB503	Mass (mg)	**Modern WB69**	Mass (mg)	**Fossil WT23A**	Mass (mg)	**Fossil WT01G**	Mass (mg)	**Mineral NIST120c**	Mass (mg)	**Mineral Durango**	Mass (mg)
M1-a	19.99	**M2-a**	19.91	**F1-a**	20.05	**F2-a**	20.56	**S1-a**	40.48	**S2-a**	21.88
M1-b	20.12	**M2-b**	19.3	**F1-b**	19.92	**F2-b**	20.19	**S1-b**	41.81	**S2-b**	21.63
M1-c	20.06	**M2-c**	19.99	**F1-c**	20.08	**F2-c**	20.44	**S1-c**	38.67	**S2-c**	20.13
M1-d	20.09	**M2-d**	19.1	**F1-d**	20.08	**F2-d**	20.23	**S1-d**	39.64	**S2-d**	20.97
M1-e	20.03	**M2-e**	20.29	**F1-e**	20.01	**F2-e**	20.28	**S1-e**	40.42	**S2-e**	20.85
M1-f	20.06	**M2-f**	19.36	**F1-f**	19.91	**F2-f**	20.35	**S1-f**	41.07	**S2-f**	21.07
M1-g	20.14	**M2-g**	19.79	**F1-g**	20.02	**F2-g**	19.99	**S1-g**	39.97	**S2-g**	20.84
M1-h	20.08	**M2-h**	19.7	**F1-h**	19.96	**F2-h**	20.15	**S1-h**	40.81	**S2-h**	21.21
M1-i	19.97	**M2-i**	20.95	**F1-i**	19.89	**F2-i**	20.63	**S1-i**	39.57	**S2-i**	20.83
M1-j	19.94	**M2-j**	16.07	**F1-j**	19.98	**F2-j**	20.36	**S1-j**	40.07	**S2-j**	20.44
M1-k	20.08	**M2-k**	20.17	**F1-k**	10.72	**F2-k**	20.26	**S1-k**	41.02	**S2-k**	20.8

To destroy organic matter, 30% H_2O_2 was added to sub-samples a-j at a ratio of 0.04 ml per 1 mg. Subsample k was not treated for organic matter removal. After 24 hours, each of the treated samples was centrifuged for five minutes and the supernatant decanted and discarded. Samples were then rinsed in ultra-high purity water (>18 MΩ), centrifuged and decanted twice, then oven-dried at 60ºC.

Sub-samples a-i were each leached in one of three treatment solutions (0.1 M sodium acetate buffer solution, pH 3.8; 0.1 M acetic acid, pH 2.7; and 1.0 M acetic acid, pH 2.2) for 4, 8 or 24 hours. Subsample j was untreated apart from organic matter removal while sub-sample k remained untreated. Table 4.2 shows each of the treatment strengths and treatment times applied to sub-samples a-i. After treatment, these sub-samples were centrifuged, decanted and rinsed twice, then oven-dried in the same manner following H_2O_2 treatment described above.

Table 4.2. Treatment strengths and times for sub-samples a-i.

	4h	12h	24h
buffer	a	b	c
0.1M	d	e	f
1.0M	g	h	i

All sub-samples were digested in 2 ml 1 M HNO_3 for 24 hours then transferred to 10 ml tubes. A silver nitrate solution of 0.1 g $AgNO_3$ in 1 ml 1 M HNO_3 was added to each

sub-sample followed by drop-wise addition of 1 M NaOH, until a persistent yellow precipitant (silver phosphate) formed. They were left to precipitate overnight, before being centrifuged, decanted, rinsed twice and dried as above.

One or two 2.5-3.5 mg aliquots of each sub-sample were weighed into silver foil cups along with 0.5 mg graphite (see Appendix D for the final weights of each sample). These were dried in a vacuum oven at 82ºC for at least one hour. They were subsequently loaded into a sample tray for pyrolysis and $\delta^{18}O$ measurement by Continuous Flow Isotope Ratio Mass Spectrometry (CF-IRMS). The combustion chamber was set to 1200ºC to produce CO which was introduced via a helium carrier gas to the CF-IRMS fitted with three Faraday cups arranged to measure masses 28 ($^{12}C^{16}O$), 29 ($^{13}C^{16}O$) and 30 ($^{12}C^{18}O$).

At the start of each of two analytical runs, eight beet sugars of known $\delta^{18}O$ composition were measured as consistency standards in addition to two silver phosphate standards (NH4_2 and 2ndFS), which were run in pairs after every 15 sample measurements.

Figure 4.12 shows the results for a modern wombat tooth (M1), fossil wombat tooth (F1) and standard (S2). M1 shows a general trend of increasing $\delta^{18}O$ with treatment time. The 0.1 M acetic acid gives higher ratios than the buffer solution, while the 1.0 m acetic acid gives consistently high ratios. F1 conversely shows a general trend of decreasing ratios with treatment time and treatment strength. The Durango mineral apatite displays a decrease in $\delta^{18}O$ with treatment time even with the weakest treatment (buffer solution). Unfortunately, due to sample loss during preparation, the full results for the untreated, 0.1 M and 1.0 M acetic acid treatments are not available for this sample.

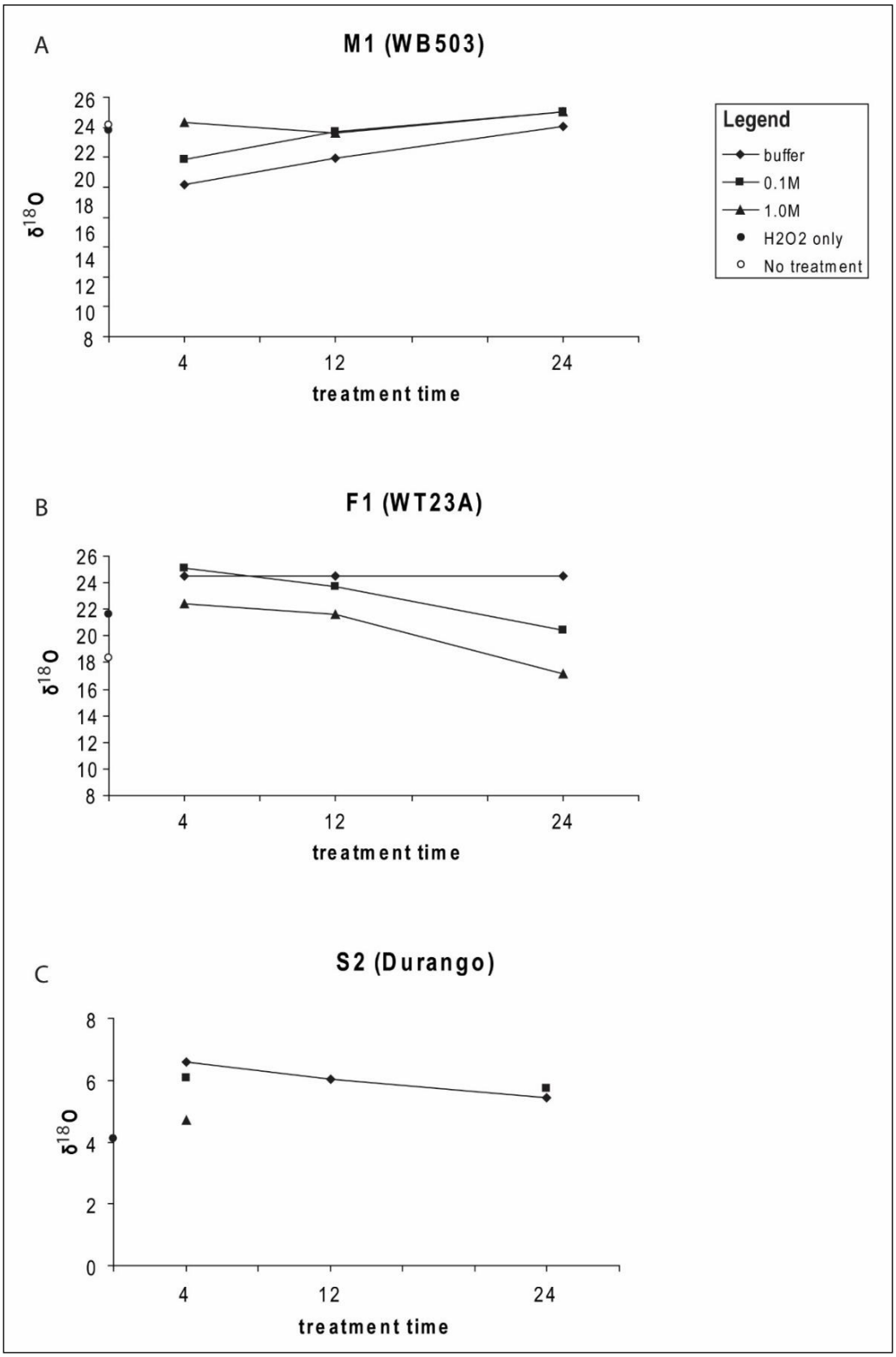

Figure 4.12. Results of leaching treatments for three samples. A: a modern wombat tooth (M1, WB503). B: a fossil wombat tooth (F1, WT23A). C: Durango mineral apatite standard (S2). Note the different scale for S2. Note also that uncertainties are not shown, as they are generally smaller than data point markers.

The fossil sample shows a change in $\delta^{18}O$ with H_2O_2 treatment, whereas the modern sample does not. This is unexpected as modern enamel would be expected to have higher organic matter content. This suggests the fossil tooth may have been contaminated by organic material with a significantly lower $\delta^{18}O$ than the enamel apatite. The decrease in $\delta^{18}O$ in the mineral apatite with treatment time is concerning, as mineral apatite should not contain any diagenetic material. These results could indicate that recrystallisation is occurring, altering hydroxyapatite to brushite (Lee-Thorp & Van Der Merwe 1991). On the other hand, these sub-samples were measured toward the end of the run, where the NH4_2 standard which was run in pairs after every 15 sample measurements shows a significant decrease in measured values (Figure 4.13). It is possible a similar decrease may have affected the measured values of the Durango mineral apatite. This would also explain why the sub-sample treated only with H_2O_2 (black circle in Figure 4.12C) gives a lower value than any of the treatments, as this was the last sample measured in the run. On the other hand, the second standard (2ndFS) continues to provide consistent results during this stage of measurement.

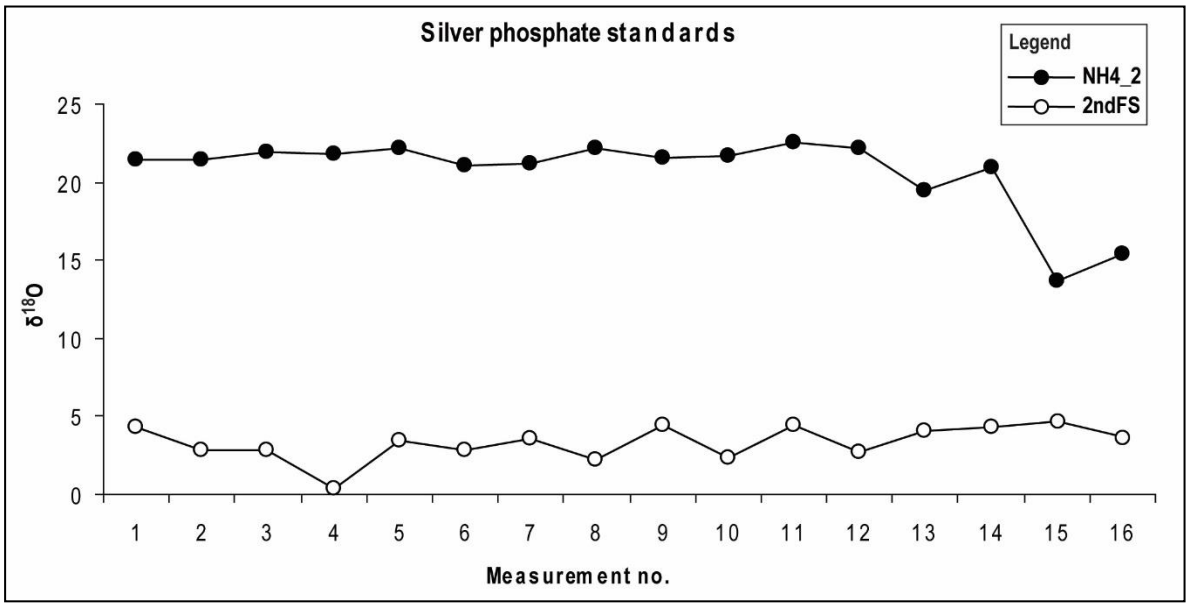

Figure 4.13. Results for silver phosphate standards, NH4_2 and 2ndFS. A pair of each standard was measured after every 15 samples.

Given the change in measured $\delta^{18}O$ becomes stronger with increased treatment time and with treatment strength for both the fossil and modern enamel sub-samples, and since the results for the mineral apatite potentially suggests recrystallisation with stronger treatments, the four-hour buffer solution treatment was selected for the main runs of wombat teeth. This is in

accordance with the findings of Koch et al. (1997) and Nielsen-Marsh & Hedges (2000), who also suggest short treatment times and reduced reagent strengths be applied to biological apatite, to avoid recrystallisation and chemical exchange.

4.2.4.2. Sequential sampling of wombat teeth

Fourteen samples were chosen for sequential sampling along growth increments and $\delta^{18}O$ analysis. Each enamel slice was cleaned and cut with a diamond saw into 6-11 sub-samples. They were cut perpendicular to the growth axis in slices 2-5mm thick (7-30 mg) with most sub-samples representing approximately 3 to 4 weeks growth (Section 4.1.3). These were ground with a mortar and pestle and weighed. The samples were treated in H_2O_2 and given the results of Section 4.2.4.1, leached in 0.1 M sodium acetate buffer solution for four hours. Silver phosphate crystals were precipitated as described in Section 4.2.4.1. The measurement process and settings were also the same as detailed in Section 4.2.4.1.

4.3. Oxygen isotope analysis results

4.3.1. $\delta^{18}O$ analyses of fish otoliths

4.3.1.1. OT23

Figure 4.14 shows the analysis tracks for the $\delta^{18}O$ SHRIMP measurements and the ICP-MS trace element analyses of OT23, as well as the SHRIMP results. The trace element results are presented in Figure 4.15.

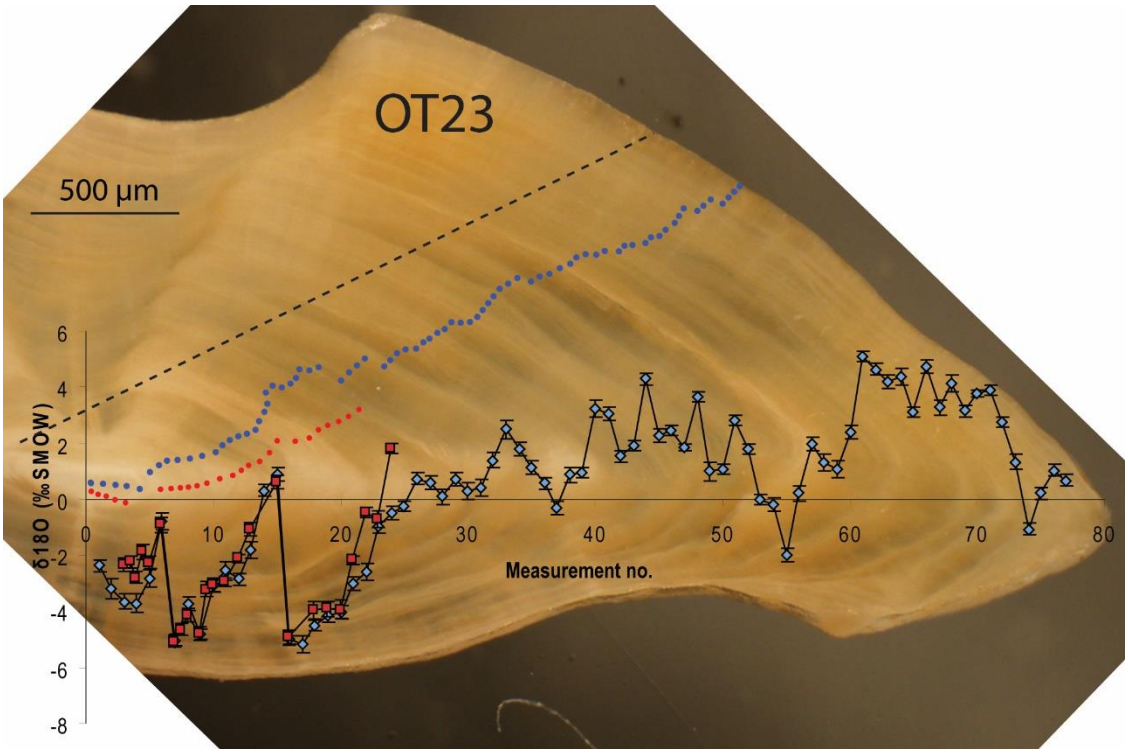

Figure 4.14. SHRIMP results for OT23. Blue spots show locations of individual analyses, for which the results are shown as blue diamonds on the overlying graph. The red spots show a replicate analysis track, for which the results are presented as red squares. The dashed line shows the location of the trace element analyses (Figure 4.15).

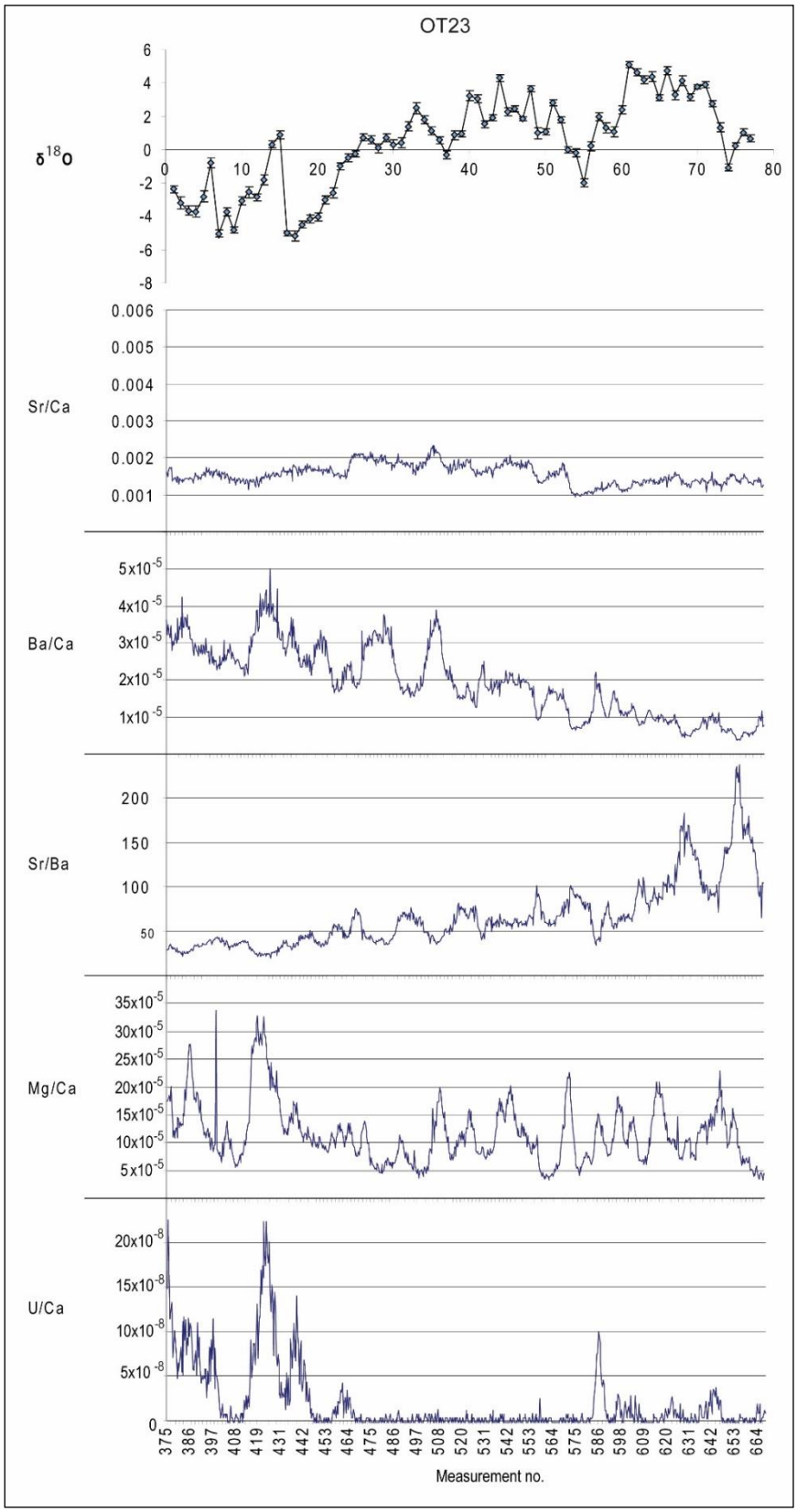

Figure 4.15. Trace element results for OT23. The core to outer edge of the otolith runs from left to right. The oxygen isotope results from Figure 4.14 are also shown for comparison.

The SHRIMP results reveal small scale variations overprinted with a trend of increasing $\delta^{18}O$ with otolith growth spanning a total range of approximately 9 ‰. Sudden decreases of 4 ‰ and 6 ‰ occur at points 7 and 17 respectively, while more gradual drops also occur at points 55 and 75. The replicated analysis section on the otolith (red circles in Figure 4.14) shows good reproducibility with the first transect.

The trace element results display a variety of compositional change with otolith growth. Sr/Ca is roughly constant across the otolith, with values mostly between 0.001 and 0.002 mol/mol. Ba/Ca shows an overall downward trend from approximately 0.0004 to 0.0001 mol/mol, with decreasing size of fluctuations with time. As is to be expected (given constant Sr/Ca), Sr/Ba shows the opposite trend, with an increasing magnitude in fluctuations and an overall increase in the ratio, from less than 50 to over 200 mol/mol. Mg/Ca fluctuates greatly with no overall trend, though the magnitude of the fluctuations decreases significantly one quarter of the way across the sample, and increases slightly after half way. The U/Ca ratio shows there is very little uranium in the sample, though some is present near the start of the transect, as well as a small amount near measurement 586.

4.3.1.2. OT27

Figure 4.16 shows the location of the analysis tracks for the $\delta^{18}O$ SHRIMP measurements and the ICP-MS trace element analyses of OT27, as well as the SHRIMP results. The trace element results are presented in Figure 4.17.

The SHRIMP results for this sample are similar to OT23, with small-scale fluctuations overprinted with a trend of increasing $\delta^{18}O$ with time and a total range of approximately 9 ‰. A sudden decrease from 4.5 ‰ to 0 ‰ occurs around point 52, followed by a sudden increase to nearly 6 ‰ by point 55. A second decrease occurs between points 66-69, resulting in the lowest measured value, at approximately -3 ‰, at the tip of the otolith. Again, the second analysis run on the otolith (red circles in Figure 4.16) demonstrates good reproducibility in the measurements, though it records a stronger decrease in measured ratios around point 26.

Many of the trace element analyses show a large change around three quarters of the way along the otolith. Sr/Ca is roughly constant, with values mostly between 0.001 and 0.002

mol/mol across the first three quarters of the otolith. Values then rise sharply to over 0.005 mol/mol, fluctuate between 0.0035-0.0045 mol/mol then decrease to 0.0025 mol/mol by the end of the assay. Ba/Ca values fluctuate greatly across the first half of the otolith, varying from 0.00002 to over 0.00004 mol/mol. The size of fluctuations then decrease to between 0.00002 and 0.00003 mol/mol before decreasing again to a base level of around 0.00001 mol/mol for the last quarter of the transect. Sr/Ba values are low, mostly below 50 mol/mol across most of the otolith, gradually increase to 100 mol/mol just before the last quarter, then rise sharply to 300 mol/mol and fluctuate from 150 to 250 mol/mol for the remainder of the assay. Mg/Ca values fluctuate from 0.0007 to 0.0015 mol/mol, with two sharp increases followed by gradual decreases, in the first half of the otolith. The magnitude of the fluctuations then greatly increases, with measurements varying between 0.00010 and 0.00035 mol/mol. The U/Ca results reveal there is little uranium in the sample, though some is present near measurement 1107 and toward the end of the transect (outer surface of the otolith).

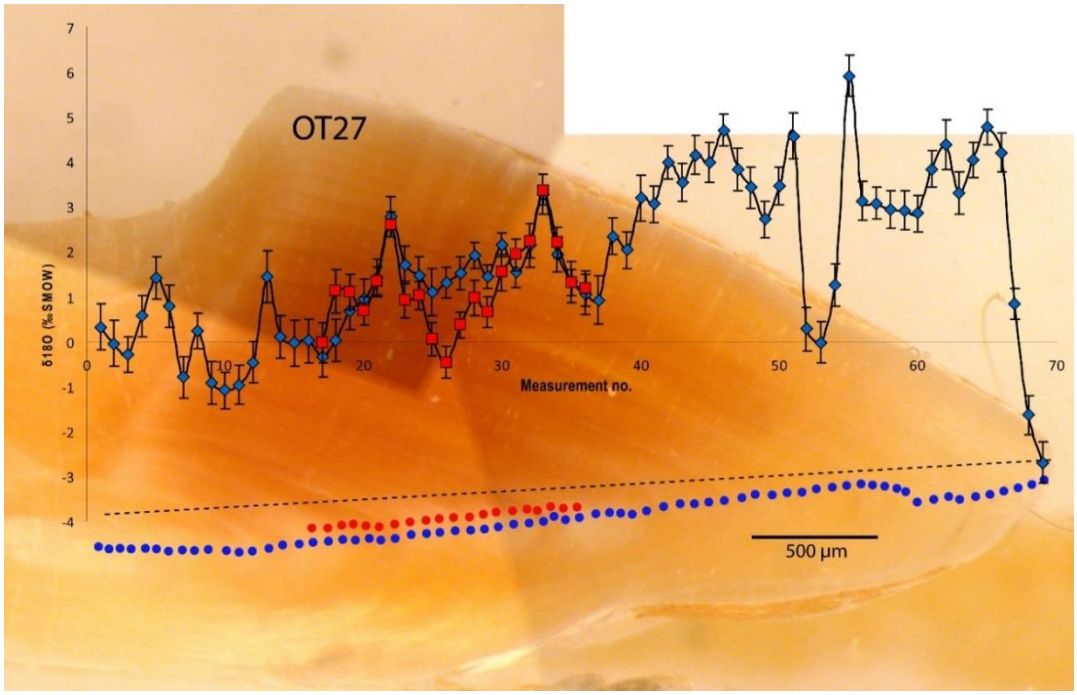

Figure 4.16. SHRIMP results for OT27. Blue spots show locations of individual analyses, for which the results are shown as blue diamonds on the overlying graph. The red spots show a replicate analysis track, for which the results are presented as red squares. The dashed line shows the location of the trace element analyses (Figure 4.17).

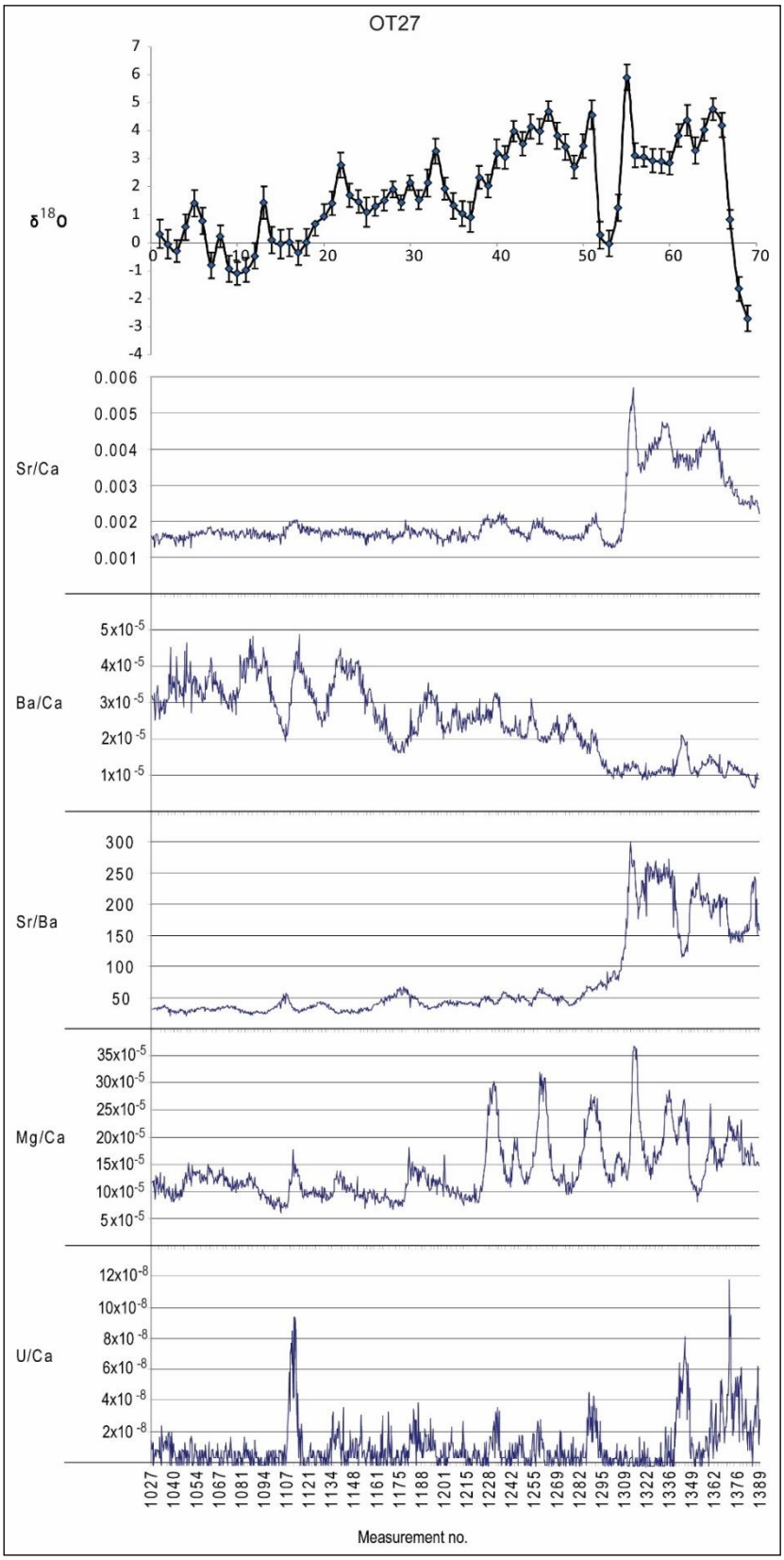

Figure 4.17. Trace element results for OT27. The core to outer edge of the otolith runs from left to right The oxygen isotope results from Figure 4.16 are also shown for comparison.

4.3.2. $\delta^{18}O$ analyses of wombat teeth

4.3.2.1. SHRIMP analyses

Figure 4.18 shows the SHRIMP $\delta^{18}O$ results obtained for the wombat tooth enamel samples. Both samples show a trend of increasing $\delta^{18}O$ values from tooth tip toward the root, thus indicating a relative increase of about 5 ‰ with time (tooth growth). On remeasuring a section of WT34B, however, very different results were obtained, with mostly non-systematically lower isotope ratios than the initial results (red circles in Figure 4.18).

4.3.2.2. Continuous flow-isotope ratio mass spectrometry analyses

Figure 4.19 shows the continuous flow-isotope ratio mass spectrometry (CF-IRMS) $\delta^{18}O$ results for each analysed wombat tooth. Most teeth show some change in $\delta^{18}O$ along the length of a tooth, though a clear seasonal signal is rarely apparent. Figure 4.20 shows the same data displayed as box and whisker plots. A long whisker relative to the length of the box (e.g. WT01D, WT14) indicates that the large range is due to a few outlying values, with most values falling within the range of the box. Almost all samples show a wide range of measured $\delta^{18}O$ values. The maximum range is 14.43 ‰ (WT26A), and the minimum is 1.70 ‰ (WT01E) with an average range of 9.01 ‰

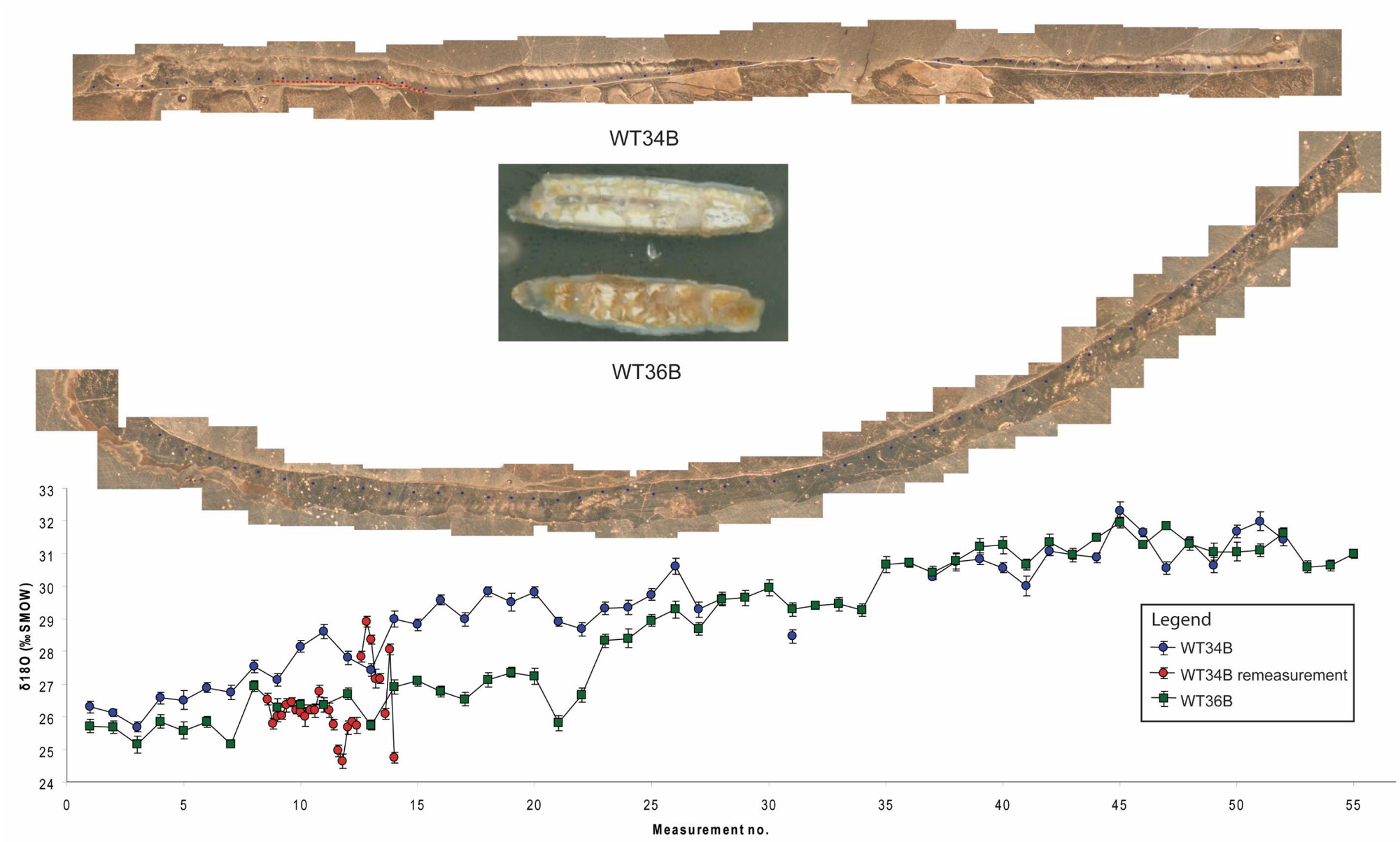

Figure 4.18. SHRIMP $\delta^{18}O$ results obtained along transects of wombat tooth enamel. Blue circles are the results for WT34B and green squares are WT36B. Red circles are the results for the re-measured section of WT34B. Results are plotted as increasing measurement no. with growth direction.

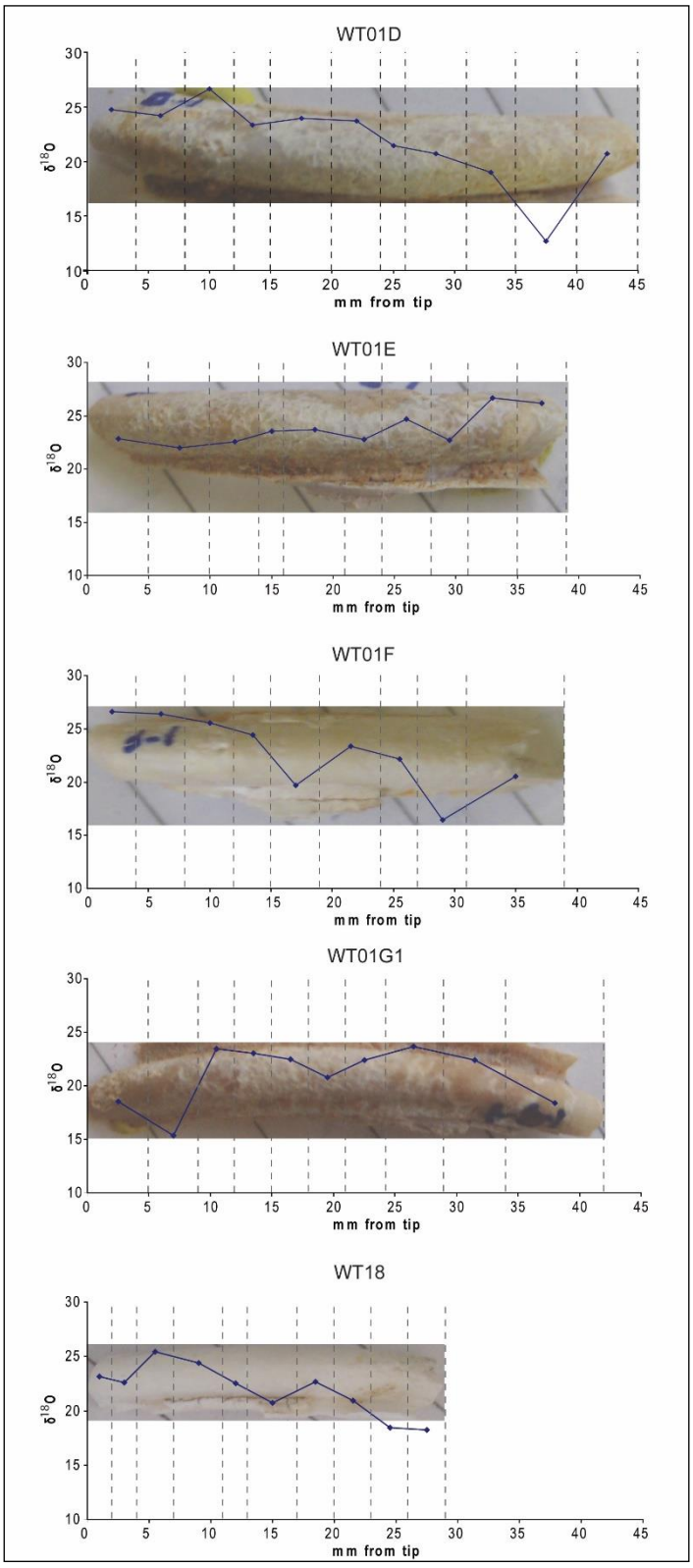

Figure 4.19. Intra-tooth $\delta^{18}O$ results for fossil wombat enamel. Dashed lines indicate where the teeth were sliced.

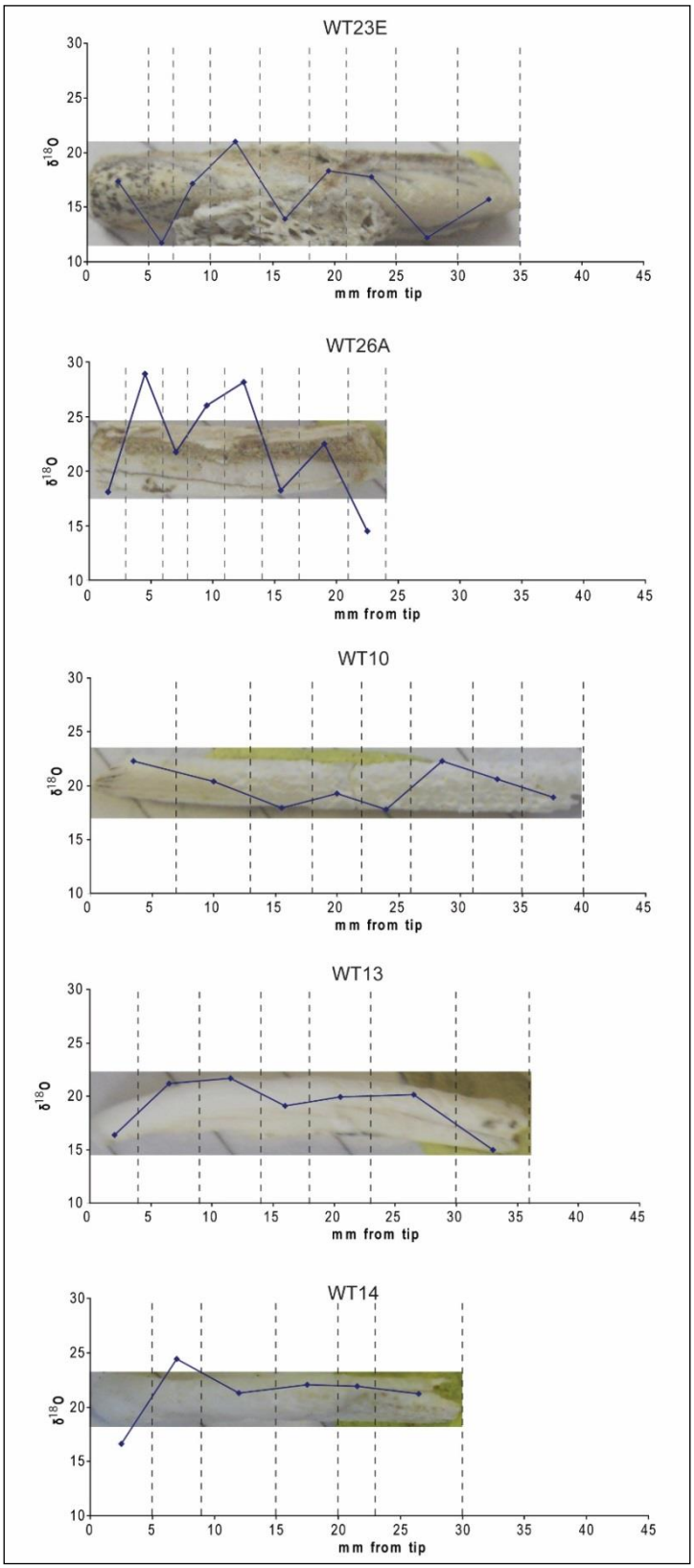

Figure: 4.20 (cont.): Intra-tooth $\delta^{18}O$ results for fossil wombat enamel. Dashed lines indicate where the teeth were sliced.

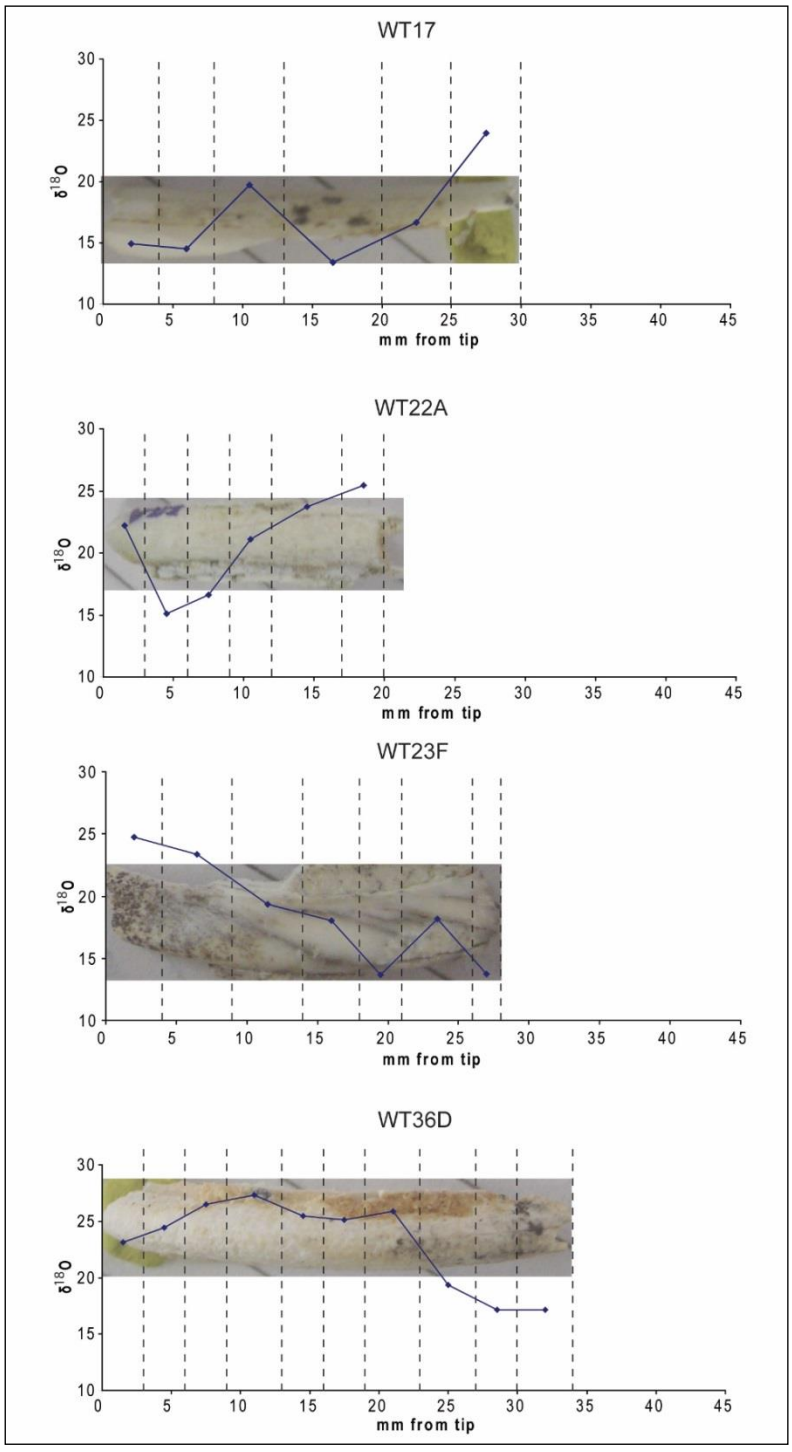

Figure: 4.20 (cont.): Intra-tooth $\delta^{18}O$ results for fossil wombat enamel. Dashed lines indicate where the teeth were sliced.

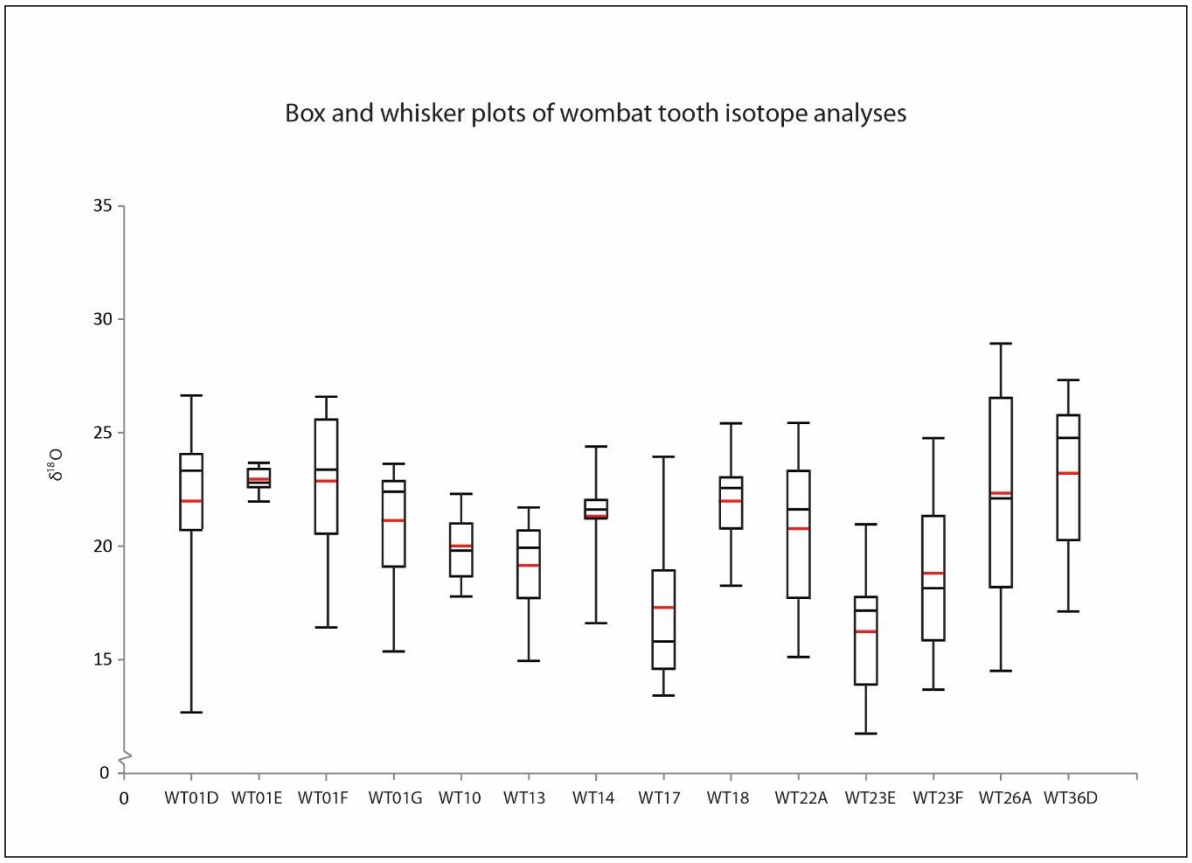

Figure 4.20. Box and Whisker plots of wombat tooth isotope analyses. The red line shows the average value, while the black line inside the box is the median.

4.4. Oxygen isotope geochemistry discussion

4.4.1. $\delta^{18}O$ analyses of fish otoliths using SHRIMP

OT11 and OT12 were originally collected for inclusion in this study, but were provided to K. Boljkovac to include in her Honours research to provide a comparison to the Mungo otoliths she was studying. The results were reported in Boljkovac (2009) and Long et al. (2014; there reported as MLRU11 and MLRU12) and are shown in Figure 4.21 and Figure 4.22, respectively. These otoliths show no trends of increasing or decreasing $\delta^{18}O$ over time, but show what may be seasonal fluctuations and possibly flood events represented by sudden decreases in $\delta^{18}O$. The Sr/Ca ratios are fairly constant in both of these Mulurulu otoliths. In saline waters both $\delta^{18}O$ and Sr/Ca ratios are expected to be higher than in freshwater (Gillanders 2005). As such these signatures suggest that these fish were probably collected

from the lake while it was in direct contact with the Willandra Creek, maintaining a freshwater signal.

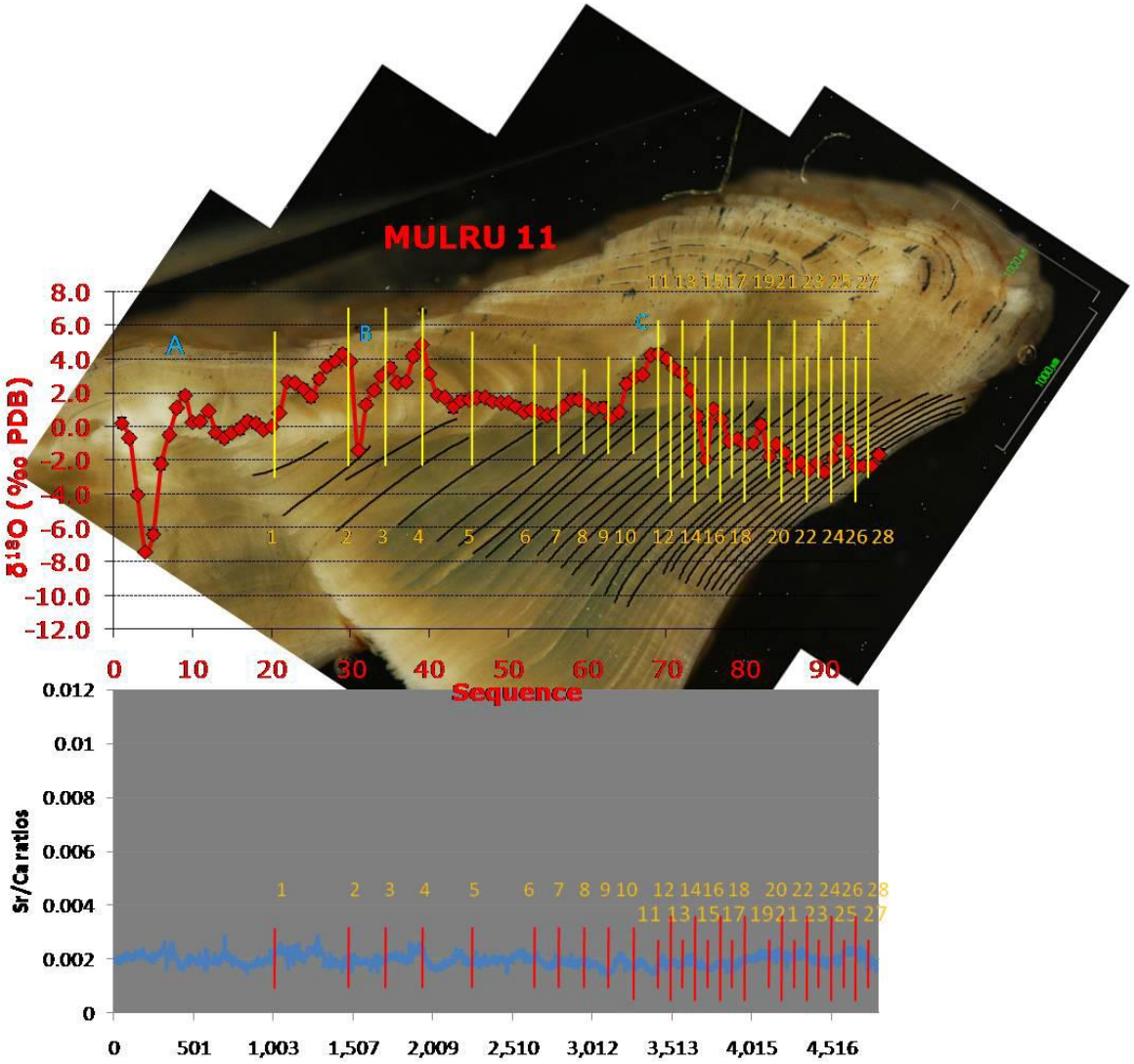

Figure 4.21. $\delta^{18}O$ and Sr/Ca values from transects across MLRU11 (OT11), from Boljkovac 2009).

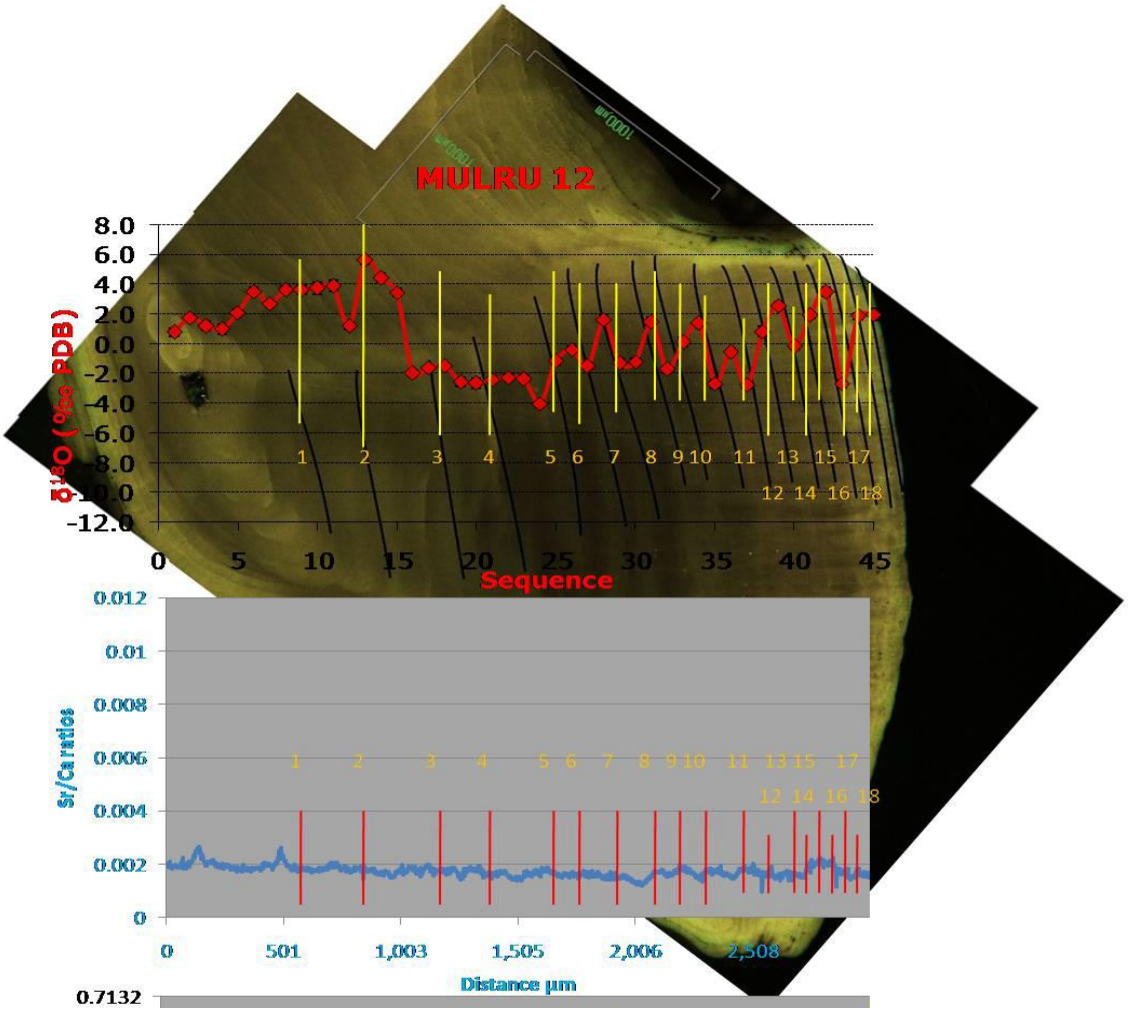

Figure 4.22. $\delta^{18}O$ and Sr/Ca values from transects across MLRU12 (OT12). (Boljkovac 2009).

Direct connection to Willandra Creek is expected to be the most common scenario for Lake Mulurulu, as it is a flow-through lake, higher in the hydrological system that would have dried out and recorded evaporitic conditions only during extreme periods of aridity, when the Willandra Creek ceased to flow. Lake Mungo on the other hand, as a terminal lake, would have been much more sensitive to changes in regional aridity (Bowler et al. 2012). Overflow from Lake Leaghur would cease during periods of low flow in the Willandra Creek, resulting in the periodic drying of Lake Mungo while the other lakes in the system continued to be recharged. Only during the periods of peak flow would the overflow provide a significant recharge of freshwater to Lake Mungo. As a result, many of the otoliths analysed from Lake Mungo show the chemical signature expected from an evaporitic influence (Boljkovac 2009; Aubert et al. 2012; Long et al. 2014). This signature includes gradually increasing $\delta^{18}O$ over

time (overprinted with seasonal variations and/or flooding events) and in many cases, an abrupt increase in Sr/Ca that likely represents the point when the fish entered the evaporitic-influenced lake waters.

OT27, one of the two otoliths from this study (Section 4.3.1.2, Figure 4.16 and Figure 4.17), shows indications of an evaporitic signal at Lake Mulurulu. After remaining fairly constant between 0.01-0.02 mol/mol for the first three quarters of the otolith growth, Sr/Ca values spike, then fluctuate around a much higher value (~0.04 mol/mol). This most likely indicates the fish entering a relatively saline water body. At the same point the Ba/Ca signal also changes, dropping from fluctuating around $2x10^{-5}$ to around $1x10^{-5}$ mol/mol, which could also indicate higher salinity (Gillanders 2005). The oxygen isotope ratios show a consistent positive trend from around -1 ‰ to ~5 ‰ overprinted with variations on the order of ~3 ‰, likely to represent seasonal fluctuations. The sudden decrease in $\delta^{18}O$ values approximately three quarters of the length along the otolith and at the end of the assay may record lake flooding events, perhaps due to periglacial outwash from the highlands. The first of these events occurs just before the shift in Sr/Ca; possibly indicating a flood event that was significant enough to leave a trace in the $\delta^{18}O$ values, but not to change the relative salinity of Lake Mulurulu, which the fish entered shortly after possibly being washed downstream with the flood.

The other otolith from this study, OT23, also shows a trend of increasing $\delta^{18}O$ over time. The two early sudden drops in $\delta^{18}O$ values are likely to represent flood events. The Sr/Ca values in this otolith, however, do not show any indication of entering a more saline environment. The gradual decline in Ba/Ca could indicate a gradual increasing salinity, but could also be a response to gradual temperature change as could the trend of increasing $\delta^{18}O$.

The pattern of oxygen isotopes seen in OT23 and OT27, specifically the trend of increasing $\delta^{18}O$, is more similar to the pattern seen in a number of Lake Mungo otoliths, than the consistent freshwater signal previously recognised in OT11 and OT12 from Lake Mulurulu (Boljkovac 2009; Long et al. 2014). The sudden increase in Sr/Ca values in OT27 suggests entry into a more saline environment. OT11 and OT12 both date to between 19.2-18.8 ka Cal. BP (Boljkovac 2009), while OT23 and OT27 both lived between 20.0-19.2 ka Cal. BP, so there may be a few hundred years separating the two sets of Mulurulu otoliths. The increased

salinity signal observed in OT27 may indicate a short term drying event, well before the final drying of the lake around 17 ka Cal. BP (Section 2.5). Intermittent drying, resulting from seasonal or secular discharge variability, would have impacted terminal lakes like Lake Mungo more profoundly than flow-through lakes such as Lake Mulurulu. It is not unreasonable, however, to assume that drying during some seasons may have been sufficient to produce salinity changes that are recorded in otolith chemistry over short timescales, but sufficient to leave evidence in the stratigraphy of sediments of the Mulurulu lunette (like the laminated clay and sand layers of the Zanci unit at Lake Mungo).

The Sr/Ca chemistry of OT23 does not indicate an entry point into more saline waters. Although the positive trend in $\delta^{18}O$ indicates this fish migrated along a chemical gradient, the gradient need not necessarily be related to salinity. As described in Section 4.1, oxygen isotope values can vary due to a number of factors. The trend toward heavier $\delta^{18}O$ values in otoliths could be due to other geographic factors such as increasing temperature and/or decreasing latitude and altitude. Long et al. (2014) identified two populations of otoliths at Mungo; those with $\delta^{18}O$ isotope compositions starting between -4 and -7 ‰, and those starting between 0 and 2 ‰. OT23 matches the former pattern and OT27 matches the latter. The authors hypothesise two different spawning grounds, one in the Lachlan River from which the fish migrated westward into Lake Mungo, and the other in the Murrumbidgee or Murray Rivers, with the fish migrating from the south west. If the overall trend of increasing values is the result of change in geographical location rather than regional drying, this would require the fish to have migrated downstream from the higher catchment areas of the Lachlan River, whereas a fish migrating inland from the south west would be expected to show a trend of decreasing $\delta^{18}O$. It may be that both populations migrated downstream but started from different spawning grounds in the upstream catchment. As highlighted by Long et al. (2014) detailed O isotopes records from the modern rivers are required to gain further insights into this hypothesis.

4.4.2. $\delta^{18}O$ analyses of wombat teeth

Two wombat teeth were analysed for $\delta^{18}O$ using SHRIMP (Section 4.2.1). Both showed a similar pattern of gradually increasing $\delta^{18}O$ over a range of about 5-6 ‰ (Section 4.3.2.1,

Figure 4.18). Wombats gain most of their ingested water through consumed leaf water, so $\delta^{18}O$ values are likely to represent humidity levels in the local environment, rather than the $\delta^{18}O$ of available meteoric water (Ayliffe & Chivas 1990). Fraser (2005) found that $\delta^{18}O$ in modern wombat tooth enamel becomes more enriched as climate becomes warmer, drier and less humid. Each of these fossil tooth fragments represents approximately five to six months growth, based on a growth rate of approximately 0.15mm/day (Fraser et al. 2008).

It appears these particular tooth fragments did not capture a turning of the seasons but chart a gradual progression to warmer, drier conditions, thus indicating a seasonal shift from winter to summer. These samples both date to approximately 7 ka according to extrapolated ESR ages, well after the LGM, when the climate of the Willandra region was likely to be similar to modern climate, which is reasonably seasonal with hot dry summers and more humid and cooler winters (Section 2.1.4). A further 14 samples were measured for intra-tooth $\delta^{18}O$ using CF-IRMS (Section 4.2.4). The relationship between climate and the $\delta^{18}O$ composition of wombat enamel is discussed further based on samples analysed by both SHRIMP and CF-IRMS below.

A short second SHRIMP transect was run on WT34B, alongside but at higher resolution than the first transect. This yielded generally but not systematically lower $\delta^{18}O$ values (Figure 4.23). Unlike the otolith analyses, which demonstrated high reproducibility (Section 4.3.1), the SHRIMP data obtained on tooth enamel raises concerns about the reproducibility and reliability of these analyses.

The second SHRIMP transect was run very close to the enamel-dentine boundary, and could be the result of diagenetic alteration penetrating into the enamel from the dentine. Dentine is very porous and more liable to contamination than enamel (Ayliffe et al. 1994), and as such provides a pathway for diagenetic alteration to infiltrate a buried tooth. Although enamel is generally resistant to diagenesis, when diagenesis occurs it is concentrated around cracks and near the enamel-dentine junction (Reynard & Balter 2014). This highlights the need to ensure analyses are made near the centre of the tooth enamel, away from areas more likely to have been exposed to alteration. This is one of the strengths of the SHRIMP technique over conventional micro-sampling techniques, as the sampling locations can be very carefully selected and located with high spatial precision.

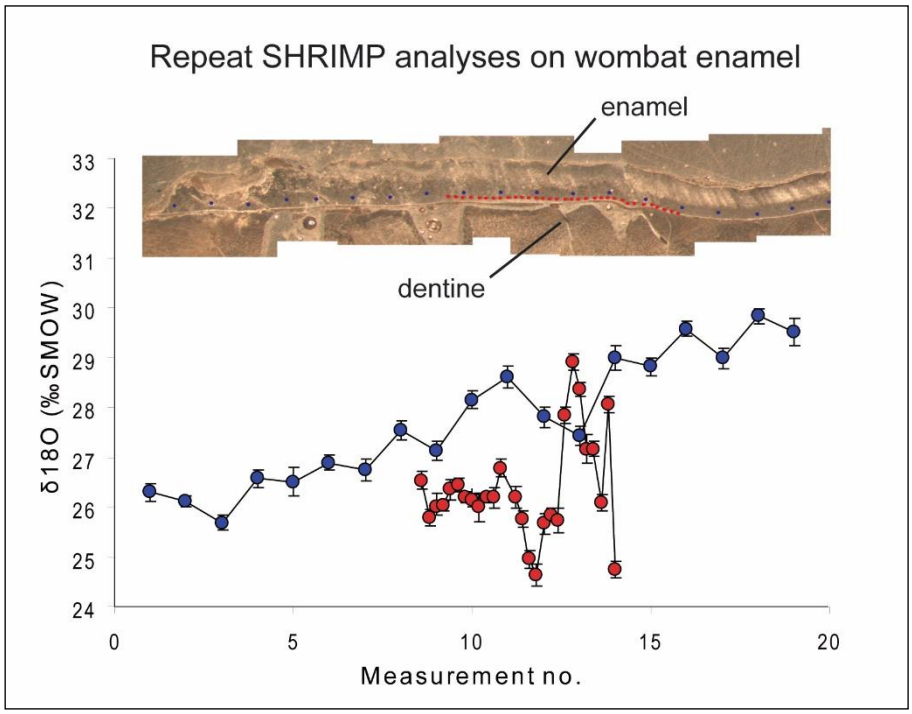

Figure 4.23. Repeated $\delta^{18}O$ analyses on tooth enamel from WT34B, using SHRIMP. The full analysis is shown in Figure 4.11.

Fourteen wombat enamel samples were measured for intra-tooth $\delta^{18}O$ variation using CF-IRMS analysis of powdered enamel slices. Results for each tooth are shown in Figure 4.19 (Section 4.3.2.2). Only four samples show a possible sinusoidal seasonal pattern of variation, WT01G1 (Figure 4.19D), WT13 (Figure 4.19I), WT22A (Figure 4.19M) and WT36D (Figure 4.19N), but even these appear to only show a possible turning point in the $\delta^{18}O$ trend in each case. None record of a full range of seasonal variation with a summer peak and winter trough.

This lack of clear seasonality may be a result of tooth fragments of insufficient length; averaging effects from using powdered slices, or may reflect a lack of seasonality in the environment in which the wombats lived. The tooth fragments ranged in length from 160 to 480 mm, thus preserving 5-16 months of growth, with most teeth representing 6-9 months. Accordingly, they should be long enough to preserve a sinusoidal signal. Each tooth slice was generally 3-4 mm wide, representing ~3-4 weeks of growth although some enamel material was lost through the sawing process. The averaging effect of powdering each enamel slice may have dampened any seasonal signals otherwise present in the enamel. Aubert et al. (2012) found that even micro-milled samples, which are many orders of magnitude smaller

than the 3-4 mm samples used here, are likely to have averaged-out $\delta^{18}O$ values in steenbok tooth enamel, previously measured by Balasse et al. (2002), compared to SHRIMP analyses of the same tooth (Section 4.1.3).

Alternatively, the analyses may be a true representation of the preserved $\delta^{18}O$ of the wombat's environment. Wombats are locally extinct in the Willandra region, so no local modern samples are available for comparison. In a study of modern wombats from a range of environments Fraser et al. (2008) found $\delta^{18}O$ values were generally less variable than the other isotopes that record seasonal changes in the environment, such as $\delta^{13}C$. Fraser et al. (2008) also noted the seasonal climate was recorded in $\delta^{18}O$ oscillations in wombat tooth enamel at some sites but not others (e.g. Figure 4.24). They hypothesised this may result from wombats using different water sources in some environments, drinking relatively $\delta^{18}O$ depleted creek water in the winter and consuming relatively $\delta^{18}O$ enriched leaf water in the summer. This was not confirmed but if correct, a strong seasonal signal in $\delta^{18}O$ may be an indicator of relative water availability more than changing seasonal humidity levels. Accordingly, results indicating a lack of a seasonal $\delta^{18}O$ variation in wombat tooth enamel do not necessarily indicate a lack of a seasonal climate.

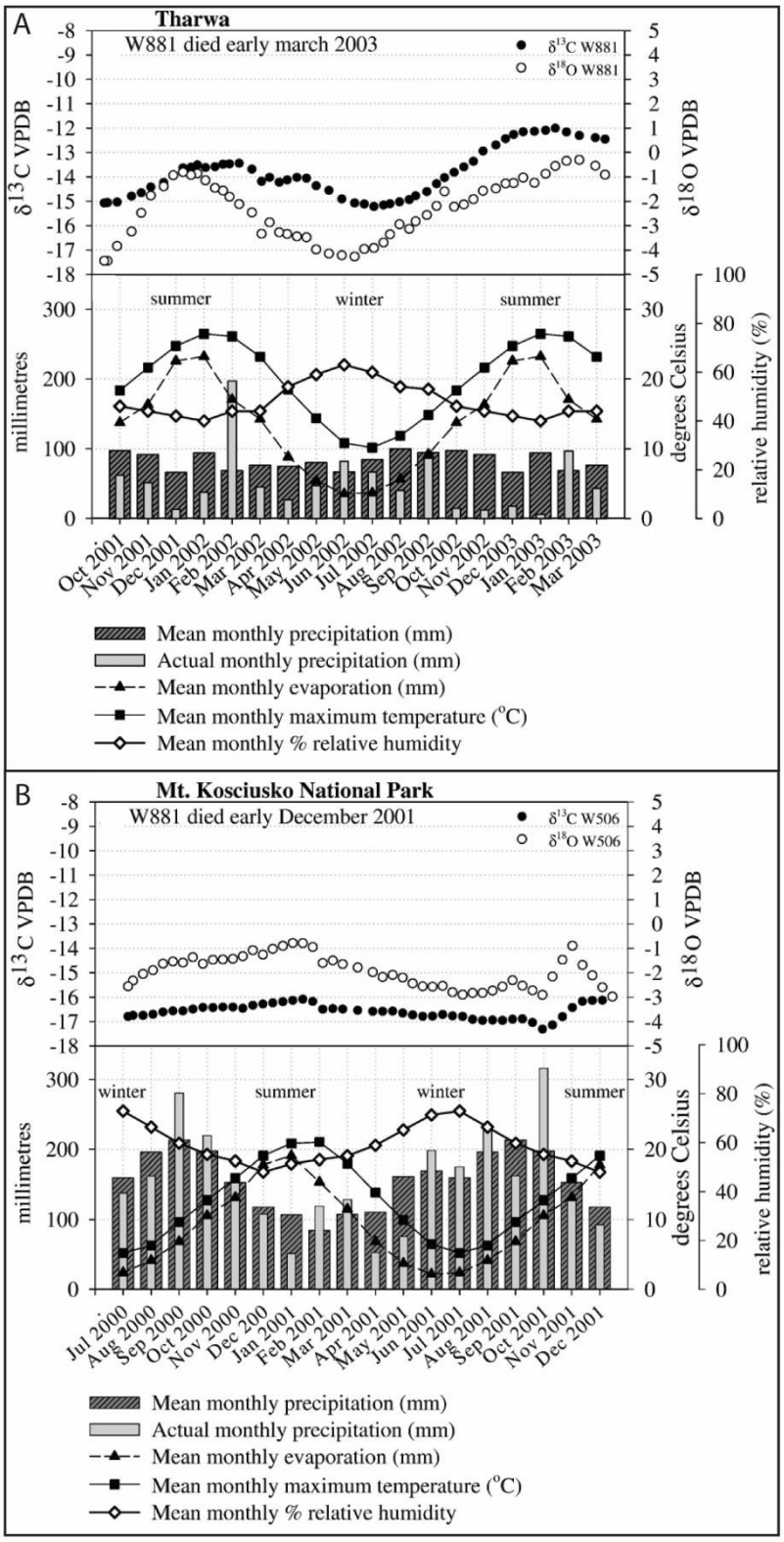

Figure 4.24. Oxygen and carbon isotope ratios in modern wombat teeth, showing an example of intra-tooth variability that reflects the local seasonality at A: Tharwa and another that does not reflect the local seasonality at B: Mt. Kosciusko National Park.

As part of the same study, Fraser (2005) showed that although seasonality was not always recorded, the average $\delta^{18}O$ values of modern wombat teeth correlated with numerous climate variables; negatively with precipitation, relative humidity, and moisture balance, and positively with evaporation and temperature. Figure 4.25 shows box and whisker plots for each sample measured in this study sorted by extrapolated ESR LU age. Three samples have generally lower average values, WT17, WT23E and WT23F, lived before the LGM, during the last stadial period, when temperatures are expected to be lower compared to after the LGM. The two teeth analysed via SHRIMP (above) apparently date to well after the LGM and have average $\delta^{18}O$ values of 29.3 ± 1.8 ‰ and 28.8 ± 2.2 ‰ (WT34B and WT36B, respectively). These values are substantially higher than those measured via CF-IRMS. This is to be expected, as there is a ~9 ‰ offset between enamel phosphate $\delta^{18}O$ and enamel carbonate $\delta^{18}O$ (Aubert et al. 2012) and SHRIMP primarily measures the former, whereas the CF-IRMS analyses measure the latter. Once the SHRIMP isotopes are corrected for this offset, they are close to 20 ‰, which is similar to other post-LGM samples.

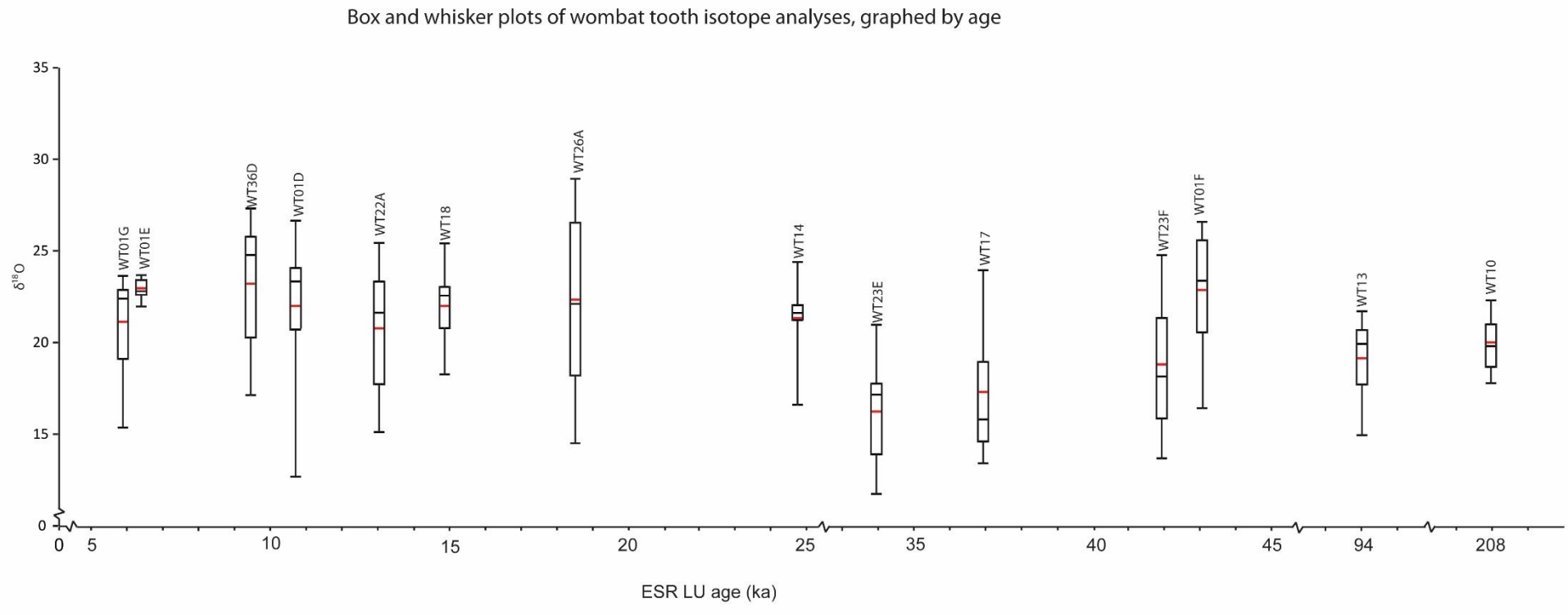

Figure 4.25. Box and whisker plots of $\delta^{18}O$ analyses of wombat tooth enamel samples, graphed by LU-ESR age. The red line represents the mean, while the black line inside the box represents the median. Samples are plotted according to their measured LU-ESR ages. Note the breaks in the axes.

One might expect the magnitude of $\delta^{18}O$ variation to be different during the LGM as well, with differing seasonality relative to the modern day. This does not appear to be reflected in this dataset. However given the analysed tooth fragments are of different length, the magnitude of recorded $\delta^{18}O$ change may simply reflect the length of the tooth fragment. Figure 4.26 demonstrates this is not the case, as there is no relationship between tooth fragment length (in days) and magnitude of tooth $\delta^{18}O$ variation.

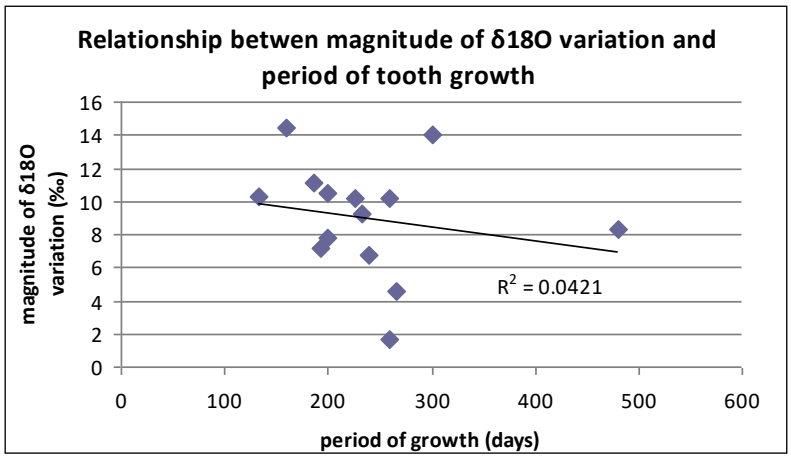

Figure 4.26. The range of $\delta^{18}O$ values in each tooth, plotted against the period of tooth growth represented in the sample.

It must be kept in mind when comparing the pre-and post-LGM wombat teeth, that the ESR dates are not very reliable. However, after repeated attempts to date the wombat teeth via ESR, U-series and radiocarbon dating, these salvaged ESR dates are the best available and should be considered indicative only.

4.5. Oxygen isotope analysis conclusions

Oxygen isotopes were analysed at high spatial resolution along growth layering fish otoliths and wombat teeth. Two samples of each were analysed for $\delta^{18}O$ using SHRIMP and an additional 14 wombat tooth fragments were analysed using CF-IRMS. In addition to $\delta^{18}O$, complementary analyses of trace element ratios (Sr/Ca, Ba/Ca, Sr/Ba, Mg/Ca and U/Ca) were carried out by LA-ICPMS in the two otoliths analysed via SHRIMP.

The chemical analyses of one otolith (OT27) provides evidence for an evaporitic signal at Lake Mulurulu, with a sudden increase in Sr/Ca values and decrease in Ba/Ca, coupled with a

gradual increase in $\delta^{18}O$. This pattern is commonly seen in Lake Mungo otoliths, where drying would have occurred more often as recharge of the terminal lake was dependent on overflow from Lake Leaghur. Previous analyses of Lake Mulurulu otoliths have given produced compositions consistent with freshwater signals, as expected in a flowthrough lake that would only have dried out during conditions of extreme aridity. It is likely the evidence for increased salinity observed in OT27 indicates a short term drying event at Lake Mulurulu, around 20-19 ka Cal. BP, prior to the final drying around 17 ka Cal. BP.

The SHRIMP results for the wombat teeth show gradually increasing $\delta^{18}O$ with a magnitude of about 5-6 ‰. Given each tooth fragment represents a few months growth, the signal probably indicates a gradual progression to warmer and drier conditions, during a seasonal shift from winter to summer. A replicate analysis transect made at higher spatial resolution along one of the two wombat teeth (WT34B) demonstrated very poor reproducibility, possibly due to diagenetic alteration penetrating into the enamel near the enamel-dentine boundary. This contrasts with replicate transect analyses on each of the otolith samples, which show good reproducibility.

The CF-IRMS analyses of wombat tooth fragment are inconclusive. While $\delta^{18}O$ analyses of modern full-length wombat teeth have previously been demonstrated to provide useful climate and environmental signals, these fossil teeth lacked clear indications of seasonality, possibly due to tooth fragments being of insufficient length, averaging effects resulting from analysis of powdered slices of the teeth, or an actual lack of seasonal $\delta^{18}O$ variation which may or may not be due to the lack of a seasonal climate.

Chapter 5. The chronology of human occupation at Lake Mulurulu: Radiocarbon dating of charcoal, mussel shell and fish otoliths

5.1. Radiocarbon dating background

Radiocarbon is a name for the radioactive isotope of carbon (^{14}C). Radioactive elements in the natural environment decay via various decay mechanisms (e.g. α decay, β decay, electron capture, fission etc.) to form daughter isotopes of the same or different elements. The rate of decay for any particular radioactive isotope is expressed as the half-life of the element, that is, the time required for half of the initial radioactive atoms to decay. In practical terms, the parent isotope is completely decayed after about 10 half-lives. By determining the ratio of parent to daughter isotopes in a sample of appropriate material, the age of the sample can be determined, so long as a few criteria are met (Schwarcz 1997):

- The time range being dated is no more than 6 to 10 times the half-life of the parent isotope being used for dating.

- The initial conditions for the sample are known. For instance, if the decay of an element is used to measure time (such as with radiocarbon dating, see below), the amount of the isotope present when initially deposited needs to be known. When using the growth of an isotope to determine age (as with U-series dating, see below) it must be ensured that none of that isotope was present at T = 0, or if some of was present, it must be determined how much.

- Any changes to the amount of each isotope in the sample must be a result of radioactive decay, that is, the sample is a closed system for the isotopes in question.

> True closed systems, with no intrusion or leakage of isotopes into or out of the sample can be difficult to obtain. Open systems, as is the case for many archaeological materials such as bones and teeth, can still be dated but may require modelling of isotope loss or uptake to derive useful age information.

Radiocarbon forms in the upper atmosphere when a neutron from cosmic radiation is absorbed by a nitrogen molecule, causing the ^{14}N to emit a proton, converting it to ^{14}C (Grün 2006). Being radioactive, the ^{14}C molecule then commences its decay back to ^{14}N through the release of β-particles, with a half-life of 5,730 years (Kaplan 2003). A half-life of 5568 ± 40 was used by Libby, one of the founders of radiocarbon dating, and remains the half-life used by archaeologists today (Holdaway et al. 2002). Uncalibrated radiocarbon dates are expressed as years BP, and according the protocol of Stuvier & Polach (1977), a conventional BP date is calculated by:

1. The use of the 5568 year half-life;
2. The assumption that the specific atmospheric ^{14}C activity was constant;
3. the use of oxalic acid as a standard (directly or indirectly);
4. normalisation for isotopic fractionation on a value of $\delta^{13}C = -25$ ‰ (the value of wood relative to the PDB standard);
5. the base year of 1950, with ages given in BP.

Calibrated radiocarbon dates are expressed as cal. BP. These are dates that have been through the calibration process, which involves correcting for the incorrect Libby half-life and the incorrect assumption of constant atmospheric ^{14}C activity (see below).

Carbon dioxide in the atmosphere (a small portion of which is made up of ^{14}C isotopes) is in continual exchange with the hydrosphere and biosphere, but when an organism dies, the exchange ceases, and the decay of ^{14}C continues without further equilibration with the atmosphere (assuming no contamination) (Mulvaney and Kamminga 1999). This decay is used as an atomic clock, to date the death of the organism. As such, radiocarbon dating is applied to organic matter including bones, shells and charcoal, materials, which are often

present at archaeological sites (e.g. various examples in Flood 1999, Mulvaney & Kamminga 1999).

Fractionation of carbon isotopes occurs during the incorporation of carbon into an organism's tissues, and can be assessed and corrected for using $\delta^{13}C$ values (Grün 2006; see Section 4.1 for a discussion on fractionation and δ notation). The half-life of radiocarbon results in less than 1% of the original (already very small amounts) of ^{14}C remaining in a sample after 37,000 years (Mulvaney & Kamminga 1999). The ability to detect these small concentrations (which are particularly liable to contamination, see below) places a limit on the dating range of the radiocarbon technique at around 40 ka. Previously, decay counting methods were used to determine the amount of ^{14}C remaining in a sample by counting the number of β- particles emitted from the sample. These methods have low detection efficiency, especially for old samples. Measurement efficiency can be improved by using accelerator mass spectrometry (AMS) to directly measure all ^{14}C atoms, not just those that decay (Bronk-Ramsey 2008) allowing smaller samples to be used and extending the measurement range of the radiocarbon technique to levels as low as age equivalents around 60-70 ka BP (Higham 2011).

The amount of radiocarbon in the atmosphere has fluctuated over time, such that radiocarbon dates do not correlate linearly with calendar dates (Flood 1999). A calibration curve, known as IntCal13 is usually used to account for variation in radiocarbon production, through correlation with dendrochronology, U-Th-dated marine corals and varves (Reimer et al. 2013). Figure 5.1 shows the calibration curve from 50 to 10 ka Cal. BP. Calibration at the older end of the curve has substantial uncertainty. A similar though not identical curve has been developed specifically for use in the Southern Hemisphere, known as SHCal13 (Hogg et al. 2013). Even for young dates, calibration may result in large errors (where the slope of the curve is shallow), or multiple possible ages (where the curve oscillates between peaks and troughs.

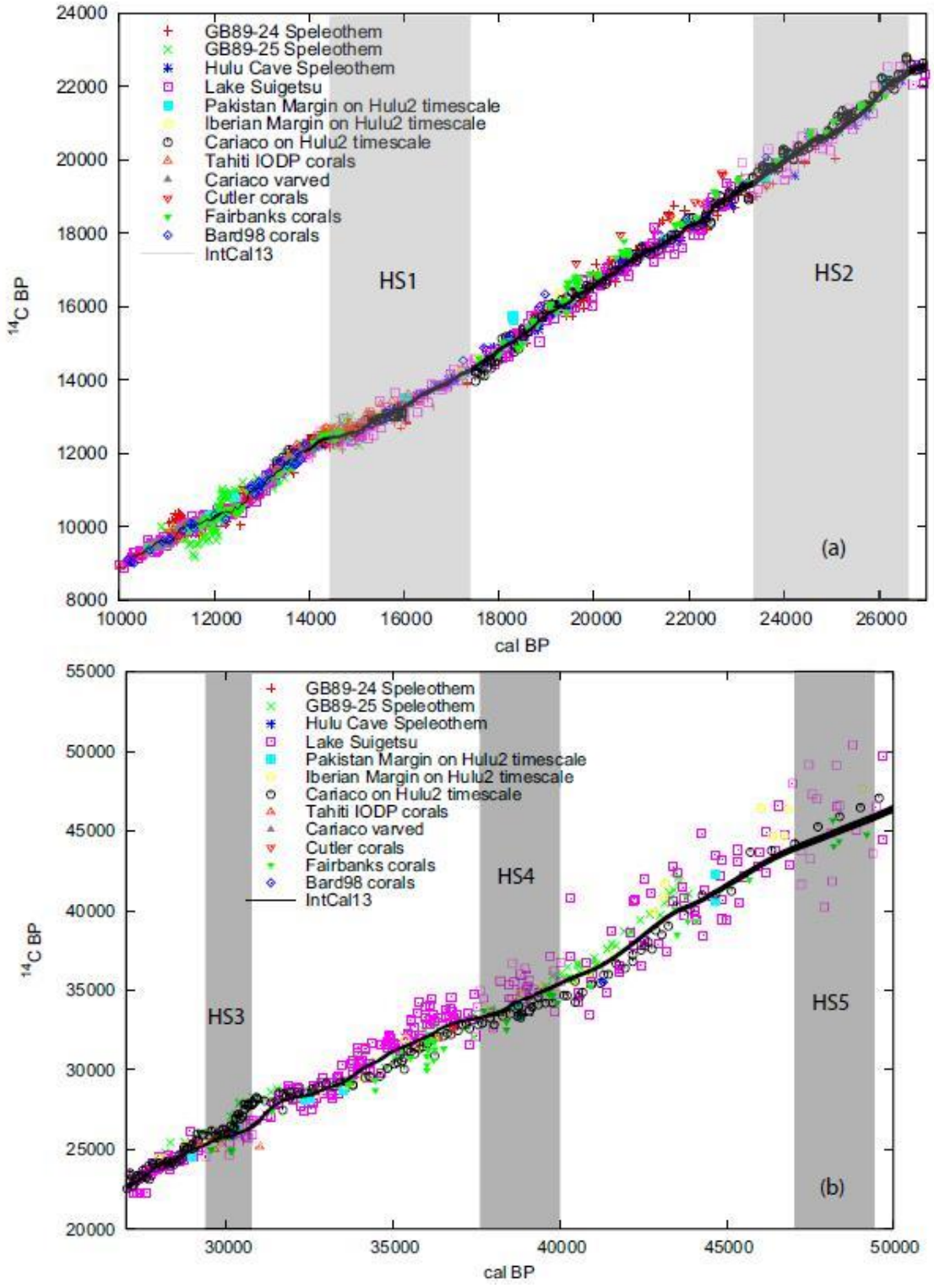

Figure 5.1. The IntCal13 data sets for: a) the period 27–10 ka Cal. BP and b) 50–27 ka Cal. BP (with the approximate timing of Heinrich stadials in the North Atlantic shown as grey boxes). A 1-standard deviation envelope of the IntCal13 curve is also shown. (after Reimer et al. 2013; their Fig. 1).

Carbon contamination is a major issue for radiocarbon dating, as any contamination will contain 'old' or 'young' carbon, and result in respectively older or younger apparent dates. This is a particular problem for samples older than six to seven half-lives of ^{14}C, which have very small amounts of original ^{14}C remaining, as contamination can add a proportionately large amount of young radiocarbon to the sample (Jacobi et al. 2006). Therefore, any date that approaches the measurement limit of the technique should be regarded as a minimum age, unless there is corroborating evidence from stratigraphic context or other dating techniques.

Contamination may occur due to factors such as the dissolution and recrystallisation of hydroxyapatite (Piepenbrink 1989) or from ion exchange with the surrounding soil and atmosphere (Newesely 1989). This can be minimised by utilising samples which are relatively resistant to contamination, or in which alteration would be readily apparent (Section 4.1.4). Additionally pre-treatment techniques are routinely used to remove carbon contaminants from the sample before preparing for analysis (Hedges & Law 1989; Jacobi et al. 2006; Bronk-Ramsey 2008). Charcoal is generally considered to be the most reliable material for radiocarbon dating.

This has not, however, proved to be true in the Willandra Lakes region, where much of the 'charcoal' dated in early archaeological work was in fact various types of plant remains stained black by humic material (Gillespie 1997). Biogenic carbonate materials, such as mussel shells, fish otoliths and emu eggshells, provide the most reliable age estimates via radiocarbon dating in the Willandra region (Gillespie 1998).

Radiocarbon dates from the Willandra Lakes on charcoal, shells and otoliths from Bowler et al. (1970), Clark (1987), Gillespie (1997), Kalish et al. (1997), Bowler (1998), Johnston and Clark (1998), Boljkovac (2009) and unpublished sources were recently compiled by Bowler (2012) and are presented in Figure 5.2. Bowler et al. (2012) noted that most of the shell ages are based on multi-fragment samples with simple pre-treatments and old results that are close to maximum age limits for the available technology at the time they were dated. All otoliths, on the other hand, were measured using AMS on single samples, often with better decontamination procedures, stable isotope correction and smaller uncertainties. Though the predominance of results at the younger end of the age range is probably a consequence of taphonomy, site destruction and opportunistic sample collection (Surovell et al. 2009;

Johnson & Book 2011 in Bowler et al. 2012), the modal clustering of shell and otolith age groups relative to the LGM period is striking and important, demonstrating the presence of water in the lakes during this otherwise arid time (Lomax et al. 2011; Section 2.5)

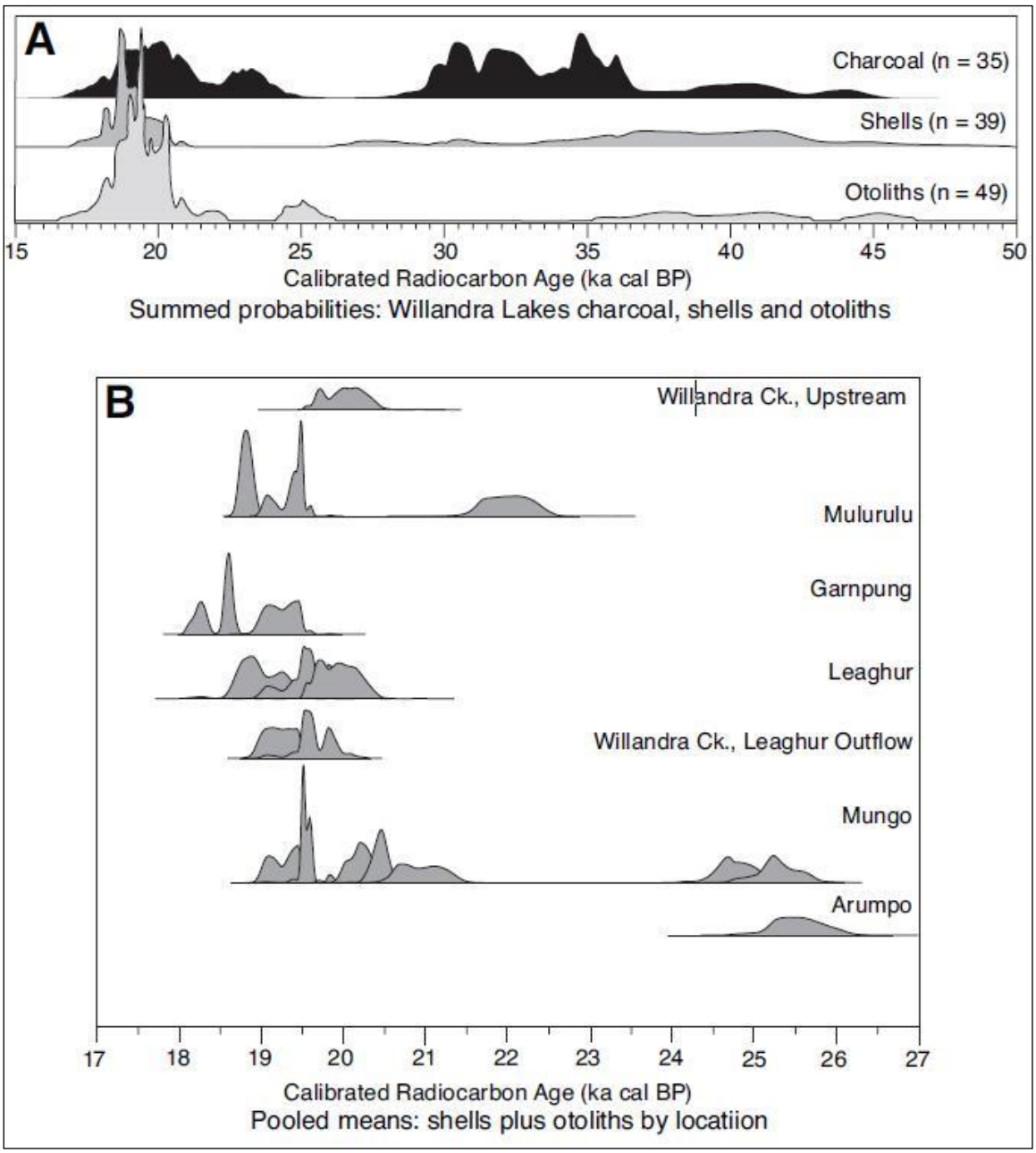

Figure 5.2. Radiocarbon ages for shells and otoliths (from Bowler et al. 2012; their Fig. 6). A. Summed probability distributions (2σ calibrated) for 39 shell and 49 fish otolith radiocarbon ages, calculated with the atmospheric data in Reimer et al. (2009), using *OxCal 4.1* (Bronk-Ramsay 2009). B. Location-based probability distributions of calibrated pooled mean ages for groups of shells and otoliths through the LGM. Peak height is approximately proportional to the number of samples (1-10) in each group, lake-bed shells excluded.

5.2. Radiocarbon dating materials and methods

Three types of sample materials were submitted for dating at the ANU Radiocarbon Dating Laboratory: charcoal to date possible hearth fires, and fish otoliths and mussel shells, to date middens and provide a geochronological context for isotope analyses (Chapter 4). The otoliths are from *Maquaria ambigua* (Macquarie Perch; life history detailed in Section 4.2.1.2). The mussel shells are Hyriidae Unionids, described here.

The Hyriidae are a family of Unionid bivalve molluscs, which live buried in the sand or silt in the bottom of streams throughout Australasia and South America (Child 1968, Williams 1983). *Velesunio* is the most common genus of the Hyriidae family (Child 1968), distributed widely across rivers and wetlands of Australia (Hughes et al. 2004) and is more typical of standing water bodies, such as lakes and billabongs, than of flowing rivers (Williams 1983). Thought to be very long lived, possibly up to 60 years (Walker et al. 2001), they are largely sedentary, dispersing as parasitic larvae attached to the gills of fish (Hughes et al. 2004). Although they are obligate freshwater organisms, Velesunio species can tolerate some degree of salinisation of their home waters, osmoregulating at low salinities, and osmoconforming when salt levels are higher (Williams 1983). *Velesunio ambiguus* are commonly represented in aboriginal shell middens of the Willandra Lakes, though, as with golden perch, there are no modern representatives in the local area, since the final drying of the system. Bivalve shells can be composed of aragonite, calcite or both (Wefer & Berger 1991) though unionids are usually aragonitic (Dettman et al. 1999). Figure 5.3shows examples of fossil and living *Velesunio ambiguus.*

Two charcoal, ten mussel shells (two each from five sites) and two otoliths were submitted to the Australian National University radiocarbon dating laboratory for analysis. Charcoal subsamples of 5-10 mg were pre-treated with an acid-alkali-acid pre-treatment using 1 M HCl and 1M NaOH, then rinsed in Milli-Q H_2O. 2.5-3 mg of each sample was then loaded into quartz tubes with CuO and silver wire. These were converted to CO_2 in a sealed vacuum at 900°C then further converted to graphite by hydrogen reduction in the presence of iron powder at 550°C. Carbonate samples were mechanically cleaned with a handheld drill and leached in a 0.1M HCl pre-treatment, removing at least 10 wt% to remove altered surface material. The cleaned carbonate was then reacted with 85% H_3PO_4 in an evacuated

Vacutainer™, and the CO_2 collected and cryogenically purified and trapped before conversion to graphite as described for charcoal. The pelletised samples were run on the Single Stage Accelerator Mass Spectrometer (SSAMS) at the Australian National University.

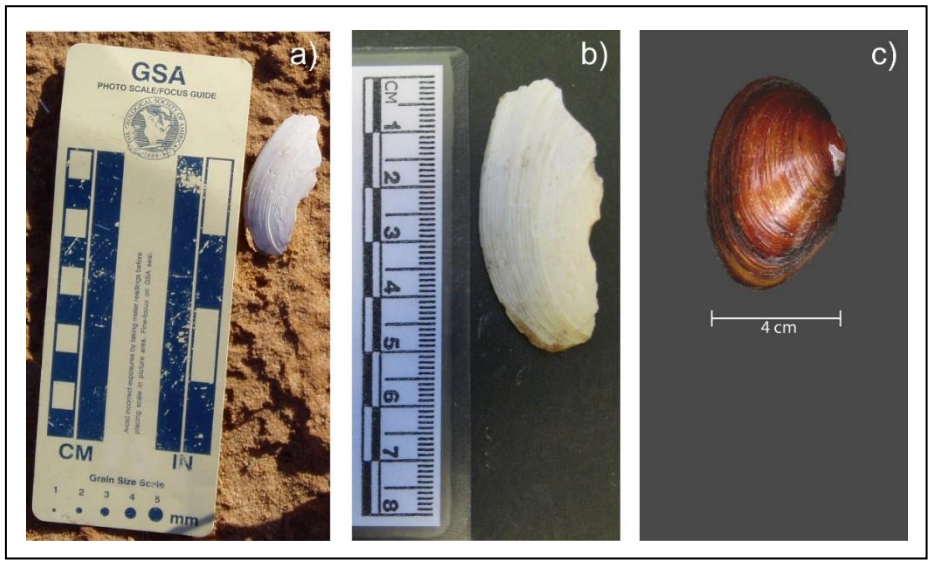

Figure 5.3. a) *Velesunio ambiguus* shell fragment in the Lake Mulurulu lunette. b) The same shell, after removal from the field. c) An example of a modern *Velesunio ambiguus*
(http://www.manandmollusc.net/advanced_introduction/Images/Velesunio-ambiguus.gif**)**

Measurement results were converted to an age in radiocarbon years using the Libby half-life of 5568 years and following the conventions of Stuiver and Polach (1977; Section 5.1). These ages were then converted to calibrated ages using the southern hemisphere radiocarbon curve, SHCal13, of Hogg et al. (2013) through the *OxCal 4*.2 software (Bronk Ramsey 2009a).

OxCal 4.2 was also used to run a Bayesian analysis on the radiocarbon dates (and the OSL dates, see Section 7.3.2). Each of the stratigraphic units from which samples were collected (Units B and D for radiocarbon samples) were modelled as Phases, in which the measured ages are assumed to be unordered and uniformly distributed. A Boundary was placed at the start and end of each Phase. The modelled probability distributions of these Boundaries provide estimates for the start and end of the stratigraphic units. These components were then arranged into a Sequence, assuming that Unit B is older than Unit A due to their relative stratigraphic positions. A General t-type Outlier Model (Bronk Ramsay, 2009b) was used to assess the likelihood of each measurement being consistent. Each date was assigned a prior outlier probability of 5%, unless it was clearly Holocene (i.e. sample CH01), in which case it was excluded from the model by assigning a ‘non’ prior outlier probability in the code.

During the modelling process, the posterior outlier probability is calculated and the date down-weighted accordingly. For example, if the posterior probability is found to be 5%, the date is included in 95% of the model iterations, but if it is found to be 50% it is included in only 50% of model iterations. The *OxCal 4.2* code and output tables are available in Appendix E.

5.3. Radiocarbon dating results

The calibrated radiocarbon ages determined for charcoal (CH), mussel shells (MS) and otoliths (OT) are listed in Table 5.1. Figure 5.4 shows the output of the Bayesian analysis of the results modelled using *OxCal 4.2* (see Appendix E for the run code and table outputs). The sample numbers with question marks are those with a 'non' prior outlier probability, and were not used in the model. Convergence for all samples was very high, at >95% (Appendix E.2). The mussel shells and otoliths fall within two distinct age ranges: approximately 20-17 ka (samples from Unit D) and 40-30 ka (samples from Unit B). The two charcoal samples are much younger, at around 8 ka and less than 300 years. Shells sampled from the same location (a and b) have similar or overlapping age ranges in all cases except for MS66, which shows a discrepancy of 8-4 ka.

Table 5.1. Radiocarbon results, including calibrated ages

Sample	SSAMS ANU#	Unit	$\delta^{13}C$[a]	±	Percent Modern Carbon (pMC)[c]	±	^{14}C age BP[bc]	±	^{14}C age cal. BP[ef] from	to
MS63a	SANU-10325	B	-6.1	0.4	1.83	0.08	32150	370	36975	35095
MS63b	SANU-10326	B	-4.7	0.4	1.84	0.08	32100	360	36855	35082
MS66a	SANU-10330	B	-6.6	0.2	2.87	0.09	28510	250	33228	31601
MS66b	SANU-10331	B	-6.9	0.3	1.37	0.08	34450	470	39986	37229
MS60a	SANU-10323	B	-3.2	0.4	3.64	0.08	26630	190	31127	30508
MS60b	SANU-10324	B	-4.3	0.4	3.53	0.09	26870	200	31230	30691
CH01	SANU-10318	D	-23.7	0.3	97.55	0.30	200	30	292	-2
CH05	SANU-10319	D	-22.6	0.3	40.01	0.19	7360	40	8284	8011
MS64a	SANU-10327	D	-5.5	0.3	13.77	0.12	15930	70	19418	18937
MS64b	SANU-10329	D	-10.8	0.3	15.76	0.13	14840	70	18290	17770
OT23	SANU-10332	D	-9.7	0.4	12.88	0.12	16470	80	20048	19560
OT27	SANU-10321	D	-9.1	0.3	13.30	0.12	16210	70	19743	19251

[a]$\delta^{13}C$ values are the AMS machine quoted values and are used to correct the age. They can differ from IRMS results.
[b]The quoted age is in radiocarbon years using the Libby half-life of 5568 years and following the conventions of Stuiver and Polach (1977).
[c]Radiocarbon concentration is given as percent Modern Carbon and conventional radiocarbon age
[d]Sample preparation backgrounds have been subtracted based on measurements of samples of ^{14}C-free CO_2.
[e]Calibrated using SHCal13, Hogg et al. (2013)
[f]2 sigma range presented

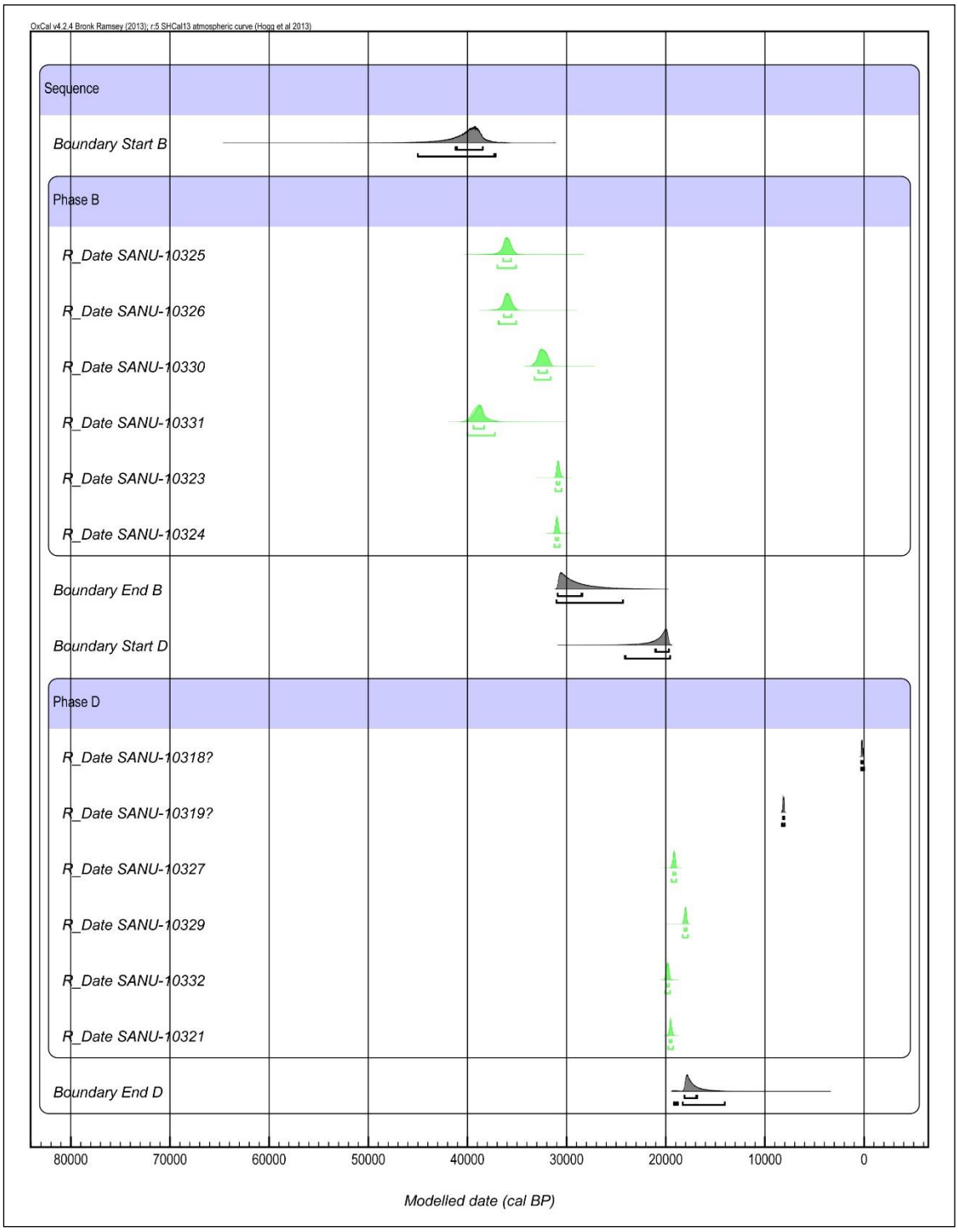

Figure 5.4. Modelled radiocarbon ages calculated using *OxCal 4.2* (Bronk Ramsey 2009a). Phases B and D include samples collected from Units B and D, respectively.

5.4. Radiocarbon dating discussion

Radiocarbon ages for mussel shell and otolith carbonate from this study fall into two date ranges, 20-17 ka Cal. BP and 40-30 ka Cal. BP. These ages largely correlate with previous Willandra Lakes shell and otolith radiocarbon age estimates, summarised in Bowler et al. (2012) and Section 5.1, Figure 5.2. Table 5.2 shows the radiocarbon ages for shell and otolith carbonate from Mulurulu, compiled by Bowler et al. (2012; their Table 1). Prior to the current study, only one sample dated to over 30 ka Cal. BP had been obtained from Lake Mulurulu. This study adds another six (shells) to over 30 ka Cal. BP, and four (two shells and two otoliths) to the 20-17 ka Cal. BP time range. The otolith samples labelled OT11 and OT12 were initially collected for use in this study but provided for dating and analysis by Boljkovac (2009), so that Mulurulu otoliths could be compared with the Mungo otoliths that were the focus of Boljkovac's Honours thesis. These samples have ages very similar to the other otoliths dated from the same site in this study (OT23 and OT27) and have been included in the results presented in Section 5.3.

Table 5.2. Compilation of previous radiocarbon dating results for Lake Mulurulu (Bowler et al. 2012).

Label	Material Dated	Lab. No.	14C age (BP)	1sigma (years)	IntCal09 Age cal. BP (median)	1 sigma (years)
ME1	shell	ANU-880A	15 120	235	18 290	260
-	shell	N-2036	15 400	205	18 630	250
ME1	shell	ANU-880B	15 450	240	18 670	290
OT-04	otolith	SANU-8823	15 500	90	18 710	85
ME3	shell	N-2035	15 500	205	18 720	240
ME3	shell	ANU-948B	15 560	240	18 770	280
3	otolith (7)	OZB-608	15 700	340	18 920	350
OT12	otolith	SANU-8819	15 720	90	18 860	160
OT11	otolith	SANU-8820	15 750	90	18 890	170
1	otolith (23)	OZB-624	16 150	120	19 260	180
1	otolith (11)	OZB-612	16 200	120	19 320	190
1	otolith (9)	OZB-610	16 250	130	19 400	210
ME3 m3/3	otolith (29)	OZB-630	18 350	220	21 890	270
ME8	shell	ANU-1914	29 360	620	33 860	710

Being derived from aquatic fauna, mussel shell and fish otolith radiocarbon ages provide evidence for periods during which the lake was filled with water. The 20-17 ka ages re-confirm the presence of freshwater in the lake during the Last Glacial Maximum, a period otherwise considered more arid than present day across much the Australian continent (Hesse

et al. 2004; Fitzsimmons et al. 2013), with active aeolian deposition in the local dune fields (Lomax et al. 2011). The source of water for the lake is likely to have been altered by changing runoff regimes due to periglacial activity in the elevated headwaters, associated with the peak Blue Lake Glacier advance in the southeast Australian alps at 19.1 ± 1.6 ka (Barrows et al. 2001). Seasonally active migrating Lachlan River channels dating to this period provide evidence for this increased flow (Kemp and Rhodes 2010). The presence of fresh lake water between 40-30 ka Cal. BP, also correlates with glacial activity in the highlands. The Hadley Tarn Advance peaked at 32 ± 2.5 ka (Barrows et al. 2001), while synchronous development of large meandering channels across the Murray-Darling Basin and evidence of high runoff through the Ulguthrie River channel of the Lachlan River occurred around 34 ka (Kemp & Spooner 2007; Kemp & Rhodes 2010).

Radiocarbon ages for these materials, however, do not always correlate with the OSL ages for their interring sediments (Chapter 7). Mussel shell ages at two sites, PR04 and PR05, are younger than OSL ages for sediments thought to be located immediately above the middens from which the shells were derived. Table 5.3 summarises the sample ages in the relevant locations.

Table 5.3. Radiocarbon ages that do not correlate with bracketing OSL ages

				Bracketing OSL samples					
Site	**Fig.**	**Sample**	**^{14}C age (ka Cal. BP)**	**sample above**	**age (ka)**	**error**	**sample below**	**age (ka)**	**error**
PR04	7.5	MS66a	33.2-31.6	K2092	51.6	2.8	K2091	81.3	6.1
		MS66b	40.0-37.2						
PR05	7.6	MS64a	19.4-18.9	K2119	24.3	1.4	K2118	27.1	1.6
		MS64b	18.3-17.8						

One possible explanation for these discrepancies is miscorrelated stratigraphy. Telfer & Thomas (2006) demonstrated that even in apparently simple lunettes, dune structure can be more complex than is readily apparent. At PR05 the radiocarbon samples from MS64 were not collected from immediately between the 'bracketing' OSL samples, but from a nearby location thought to be stratigraphically equivalent to the sand between the dated sediments (Appendix H.3). Sample K2119 was collected from near the top of Unit D in the side of a

blow-out, below the contact with the overlying unit E. The MS64 samples were derived from a shell midden within Unit D deeper within the blow-out. As the contact between units D and E is erosional, the horizon equivalent to MS64 may have been locally removed at the OSL dating site, resulting in an older age for the OSL sample near the "top" of the unit. The radiocarbon ages for the MS64 samples do fall within the range of other Unit D samples at the PR05 site, such as K2121, dated to 17.4 ± 1.0 ka.

The same explanation cannot apply to PR04, however, where the stratigraphic relationship between the middens and OSL samples is clearer (Appendix H.5). Shell sample MS66b does provide an age very close to the maximum age limit of the technique (Section 5.1). It is possible that the radiocarbon ages are minimum estimates only, and the true age of the shell could be substantially older than 40 ka Cal. BP. If this is the case, and the age of the midden is truly bracketed by the OSL ages of 51.6 ± 2.8 and 81.3 ± 6.1 ka, this would suggest very early evidence for aboriginal occupation in the area. Moreover, contamination due to diagenesis is quite common in mussel shells. Unionid shells are composed of aragonite, but remineralisation can lead to post-depositional diagenesis of aragonite into calcite; a process which would result in a young apparent age for the sample. Even when original aragonite is identified, cryptic diagenesis can still occur (Webb et al. 2007). If this is the case, other samples may also be affected and thus may also be providing young apparent ages. On the other hand, a small right-side tail occurs in the probability distribution for K2092 (Appendix H.5), and the thin sectioned sediment (TS 141, Appendix C.3), which is bracketed by the two samples, shows evidence of mixing from below, in the form of carbonate and clay clasts typical of Unit A. Therefore it may be that the apparent age of K2092 is slightly too old.

It is also possible that the samples believed to derive from MS66 may actually be derived from elsewhere. Under the guidance of the Cultural Officer, samples were not directly dislodged from middens but collected from loose material that had already eroded from the interring sediments. At this particular location, the midden was in the wall of a gully and the samples were collected from the loose shells accumulated at the base of the gully, immediately below the *in situ* midden eroding out of the gully wall. The loose samples appeared to be clearly related to the *in situ* midden; however, it is not impossible that they were contaminated with shells from younger middens not visible *in situ* in the stratigraphy.

The two charcoal samples dated to 8 ka Cal. BP and around 0-300 years (Table 5.1, Section 5.3). The near modern sample, CH01, was collected from near the top of Unit D at PR01, just below the capping clay layer (Figure 5.5A). The three charcoal samples here clearly consisted of burnt wood, possibly tree roots. A burnt goats skull seen nearby indicated that a fire has likely occurred in the area post European settlement and may be the source of this of this recent charcoal material. The other sample, CH05, collected from within the palaeosol near the top of Unit D at PR05 (Figure 5.5B) dates to around 8.2 ka Cal. BP. In addition to the charcoal residue, the sediments around the charcoal appear to be discoloured (Figure 5.5B inset). This may represent a baked-sediment hearth, a common archaeological feature in the Willandra Lakes (Stern et al. 2013). If so, this is evidence for human occupation in the area around 8 ka, with a fire having been built on the sediments of Unit D, which would have then formed the ground surface, during palaeosol formation and prior to deposition of Unit E.

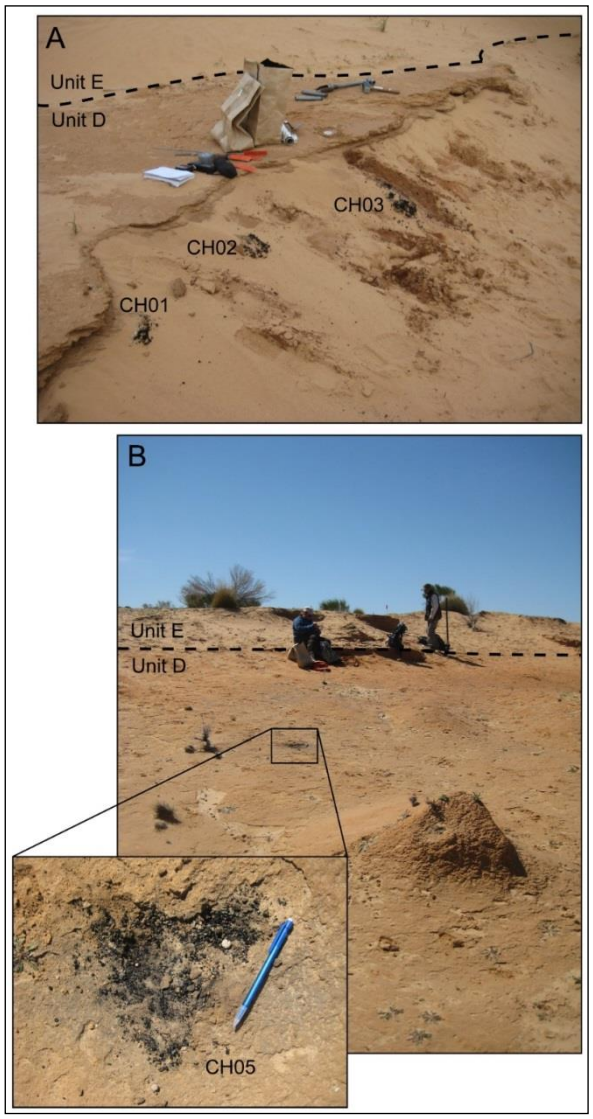

Figure 5.5. Charcoal sampling locations. A: location of CH01, CH02 and CH03, in Unit D at PR01 (CH02 and CH03 were not dated). B: location of CH05 in Unit D at PR05.

5.5. Radiocarbon dating conclusions

Radiocarbon ages on mussel shells and otoliths fall within two age ranges, ~30-40 ka Cal. BP and ~17-20 ka Cal. BP. These age ranges corroborate previous radiocarbon ages from Lake Mulurulu, as summarised by Bowler et al. (2012), though there was previously only one date >30 ka Cal. BP. The presence of freshwater species at these times indicates lake-full periods, and both age ranges correlate with times of increased glacial activity in the Australian Alps and high run-off evidenced by the development of large meandering river channels in the Lachlan and Ulguthrie river systems. Mussel shell ages do not always correlate with

bracketing OSL ages, and there may be a number of reasons for this, including stratigraphic miscorrelation, carbon contamination, measurement limits to radiocarbon dating, or unreliable OSL ages. It is recommended that the radiocarbon results for carbonate materials in this study be considered as minimum age estimates. One of the dated charcoal samples is near-modern, and probably relates to a modern local bushfire event. The other charcoal sample dates to ~8 ka Cal. BP, and if it relates to a baked-sediment hearth, suggests more recent, early Holocene aboriginal occupation in the area.

Chapter 6. U-series and ESR dating of Wombat incisors

6.1. Uranium series dating

6.1.1. Uranium series dating background

Similarly to radiocarbon dating (Chapter 5), uranium series (U-series) dating is based on radioactive decay. However, rather than using a single parent-daughter half-life relationship to calculate age, the radioactive decay chain of the ^{238}U uranium isotope is used. In a decay chain, each isotope decays into other, relatively short-lived daughter isotopes, until eventually, the series terminates with a stable isotope (^{206}Pb, in the case of the ^{238}U decay chain; Figure 6.1).

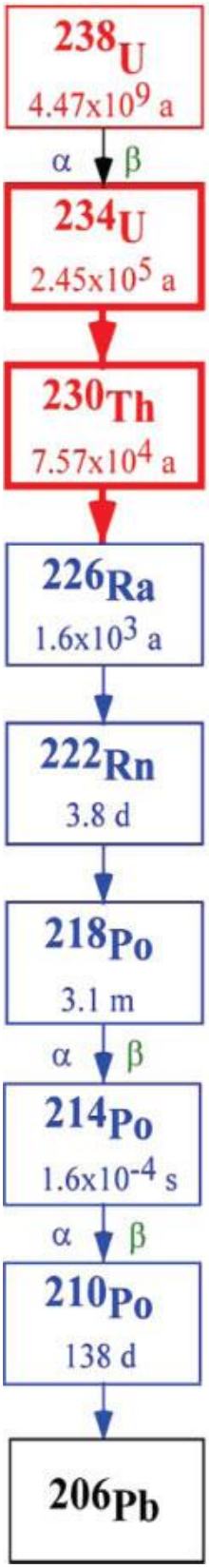

Figure 6.1. A simplified ^{238}U decay chain (adapted from Grün 2006, his Fig. 7).

In Quaternary dating, the decay chain is used for dating under conditions of secular disequilibrium, by measuring the ratio of $^{234}U/^{230}Th$. Once the decay chain reaches equilibrium, the activity (decays per time unit) of all isotopes within the decay chain is the same (Grün 2006). This point is reached after approximately 600 ka for Th/U, putting a limit on the range for U-series dating.

Uranium is generally soluble, whereas the daughter isotope ^{230}Th is insoluble in aqueous media. Thus, minerals precipitated from solution, such as in speleothems and corals, contain uranium but not thorium derived from the source solution. By measuring the ratio of parent (^{234}U) and daughter (^{230}Th) isotopes in a sample, it can be determined how close the isotopic ratio is to the equilibrium value of 1, and hence how long since it was 0 (i.e. when the material precipitated and no daughter isotope was present). Other datable materials, such as teeth and bones, do not contain any uranium when formed, but uptake uranium from environmental waters after burial. These samples are inherently open systems and the nature of the uranium uptake history must be estimated in order to determine age estimates. If no uranium uptake model is applied and a closed-system is assumed, the apparent U-series age would be an underestimate. Any thorium leaching from the sample would also result in an underestimate; however, Th-loss has never been documented in nature. An age overestimate could result if uranium is leached from the bone following uptake and likewise, the presence of detrital thorium could result in overestimation, though this latter issue can be addressed through measuring the presence of ^{232}Th and using it to correct for detrital ^{230}Th (Grün et al. 2014).

Ages from different models can be compared to see how sensitive the ages are to uptake assumptions (Latham 2001). As with ESR dating (Section 6.2.1), the most commonly used models are early uptake (EU) and linear uptake (LU). The EU model assumes a closed system, in which uranium accumulates rapidly from the environment after burial. The alternative linear uptake model (LU) proposed by Ikeya (1982), assumes uranium uptake occurs gradually and constantly over time. The uptake of uranium into fossil bones and teeth is governed by the diffusion of uranyl ions (UO_2^{2+}) which are then adsorbed on to the surface of hydroxyapatite (Millard & Hedges 1996). As described below (Section 6.2.1), a US-ESR methodology can be used to constrain uranium migration histories (Grün et al. 1988) and a DA model determining the spatial distribution of uranium within a sample may further

increase the reliability of this method (Pike & Hedges 2001). Furthermore, the diffusion-absorption-decay (DAD) model proposed by Sambridge et al. (2012) allows for continuous diffusion of U, rather than assuming closure after initial equilibration, as in the DA model. DAD age results are generally older than closed system results derived from the same data, due to the assumption of constant $^{234}U/^{238}U$ ratios at the boundary of the sample, with a greater difference seen in older samples (Sambridge et al. 2012). The application of the DAD model is not straight forward, and regardless of the model applied U-series dating results on bones and teeth are best regarded as minimum age estimates (Grün et al. 2014).

6.1.2. Uranium-series methods

Of the tooth slices measured for U-concentration (Section 6.2.2.4), one was also uranium series dated using an ANU HelEx 193 nm excimer laser ablation system coupled to a *Neptune* multi-collector ICP-MS. Four 132 μm diameter spots were sampled using a 5 Hz laser pulse rate in the tooth slice; three in enamel and one in dentine. ^{238}U, ^{234}U, and ^{230Th} were measured along with ^{232}Th to correct for detrital thorium contamination. A detailed description of the methodology is available in Grün et al. (2014). The U-series dating result is combined with the ESR result using the *DATA* software (Grün 2009b) to provide a US-ESR age for this sample and inform which uptake model is the most appropriate for use on the Willandra wombats.

6.1.3. Uranium series results

The U-series age dating result is shown in Table 6.1. The age was estimated for three enamel spots on the tooth, and the errors for each analysis overlap. The average age is 5.26 ± 0.76 ka. This is a minimum estimate only and gives an indication of when U-uptake may have occurred; it is not a direct date for the tooth.

Table 6.1. Uranium-series results for sample WT22A

Sample no.	Spot no.	Age (ka)	Error (ka)	Average (ka)	Error (ka)
WT22A	9	5.68	1.19	5.26	0.76
	10	4.97	1.03		
	11	5.12	1.01		

The combined US-ESR result for this sample gives an age of ~15 ka. This age is close to but slightly older than the calculated LU ESR age for the sample, of 13.2 ± 0.6 ka. This suggests the linear uptake model is the more appropriate model for use on the Willandra wombats.

6.2. Electron spin resonance dating

6.2.1. Electron spin resonance dating background

6.2.1.1. Introduction to trapped charge dating

Electron spin resonance dating (ESR) dates materials that accumulate trapped electrons due to exposure to ionising radiation (as does luminescence dating, see Chapter 7). The decay of naturally occurring isotopes and daughter isotopes of potassium (K), thorium (Th) and uranium (U), as well as cosmic radiation, produce ionizing radiation in the natural environment. In insulating minerals such as quartz or apatite, electrons occur at two energy levels, the valence band and the conduction band. Environmental radiation causes electrons to be ejected from the valence band and moved to an excited state in the conduction band, leaving a positively charged ‘hole’ near the valence band. Most of the electrons recombine with these holes, while a few become trapped in defects in the crystal lattice (Grün 2006; Figure 6.2).

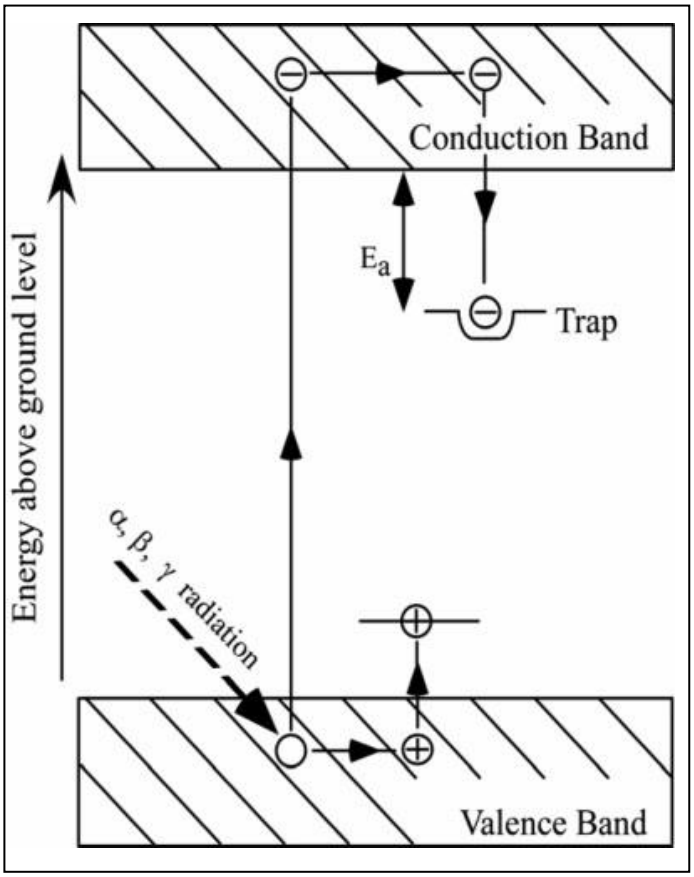

Figure 6.2. The basis for trapped charge dating (ESR and luminescence): trapping of electrons and holes. E_a = activation energy or trap depth. (Grün 2006, his Fig 14).

The activation energy (trap depth from the conduction band), combined with an escape frequency factor, determines the stability of the trapped electrons over time (Aitken 1985). Generally, continued exposure to environmental radiation will lead to an increase in the number of trapped electrons. These types of samples can be dated by determining the amount of trapped electrons a sample contains, while ascertaining the way in which the sample responds to radiation. This allows for the estimation of palaeodose (the amount of radiation to which the sample was exposed) or equivalent dose (the laboratory measured estimation of palaeodose [D_e]). This dose is measured in grays (Gy) which is a measure of the absorbed energy per kilogram (1 Gy= 1 J/Kg[1]; Aitken 1998). The method used to determine D_e depends on the type of traps being utilised for dating and hence, the dating technique (e.g. ESR or OSL). The event being dated is either the initial formation of the material (as with tooth enamel) or a 'zeroing' event, releasing previously trapped electrons thus resetting the 'clock'

to zero. Depending on the types of traps being measured, zeroing may be caused by heating or exposure to light (as with TL and OSL, respectively).

In addition to the equivalent dose, the dose rate ($\dot{D}$) or amount of radiation received per unit time), measured in grays per year (Gy a^{-1}) or grays per thousand years (Gy ka^{-1}), is used to determine a sample age. Assuming a constant dose rate, an age (T) can be calculated using the simple equation (Grün 2006):

$$T = \frac{D_e}{\dot{D}} \qquad (6)$$

Trapped charge dating can be applied to numerous materials, including tooth enamel (Schwarcz 1994). The 'zeroing' event for enamel is tooth formation. ESR dating involves measuring the trapped charge *in situ* (as opposed to measuring the light emitted when trapped electrons are released in OSL, see chapter 7). An ESR spectrometer detects paramagnetic centres created by trapped electrons, and the resulting ESR signal (Figure 6.3) is a reflection of the concentration of trapped electrons in the sample (Rink 1997).

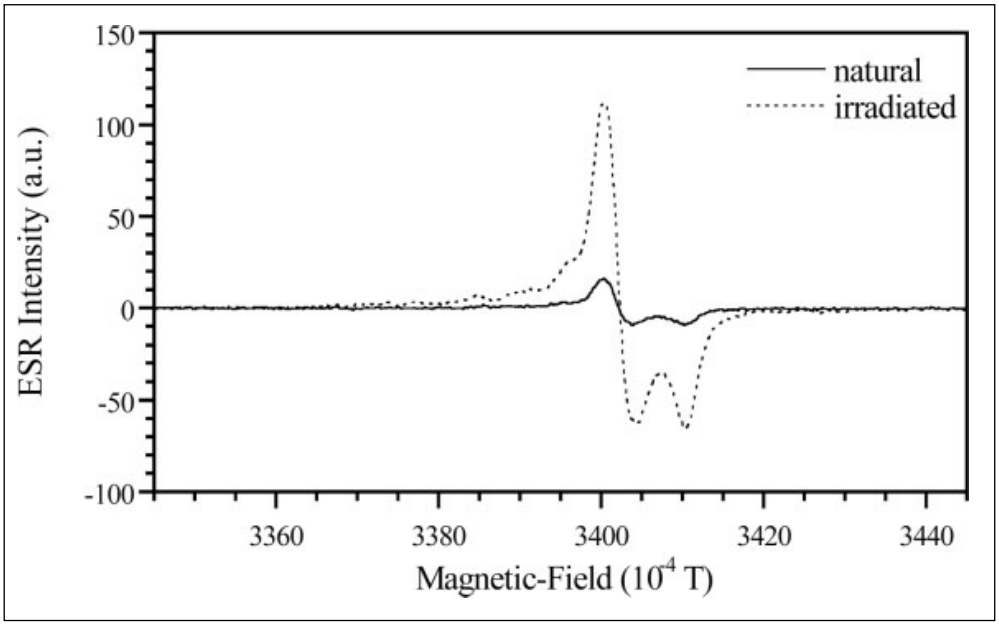

Figure 6.3. Example ESR spectra of tooth enamel. Solid line: natural sample; dotted line: irradiated sample (Adapted from Grün 2006, his Fig. 15).

6.2.1.2. Determining equivalent dose (D_e)

D_e is calculated by measuring the natural intensity of the sample and characterising how the sample responds to radiation. A dose response curve is created using the additive method (as opposed to regeneration method, both described in Chapter 7 for OSL) by repeatedly irradiating the sample in the laboratory, increasing the dose amount each time. The ESR intensity is measured after each dose to create a graph of signal intensity versus applied dose (Figure 6.4). This relationship is then used to extrapolate back to a signal intensity of zero, at which point the intersection on the dose axis indicates the D_e (Grün 1989). The uncertainty on the D_e estimate consists of a combination of systematic and random errors due to factors such as source calibration and curve fitting, errors due to detection limits related to the reproducibility of signal intensity, and interferences of post-sedimentary diagenetic processes, such as recrystallisation (Grün 1989).

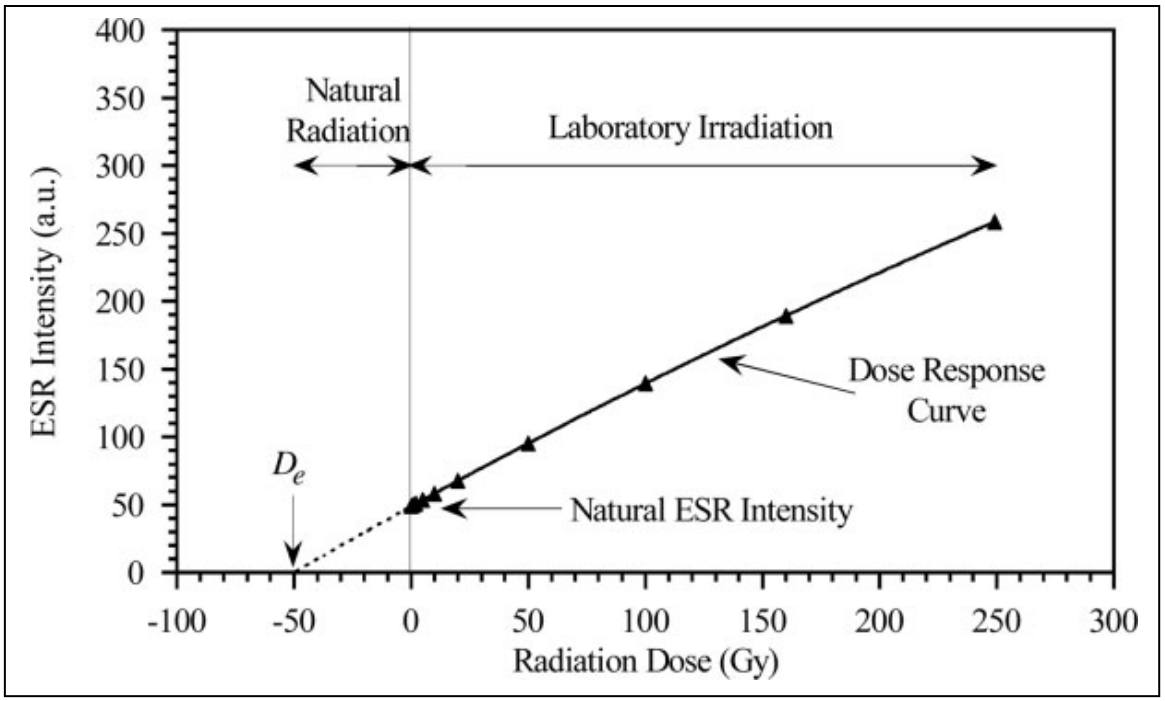

Figure 6.4. An example of a dose response curve. (From Grün 2006, his Fig 16)

6.2.1.3. Estimating dose rate (Ḋ)

The sample dose rate (Ḋ) is an estimate of the rate at which the sample received ionising radiation over the period of burial. This radiation is primarily derived from the radioactive

elements ^{40}K, ^{232}Th & ^{238}U and their daughter products (Aitken 1985). The half-life of the parent isotopes are sufficiently long (~10^9 years) that their natural abundance is effectively constant over the time range of OSL and ESR dating interest. Thus, assuming the decay chains are in secular equilibrium (see Section 6.2.1), the past dose rate can be estimated by measuring the current radiation influx. The total environmental dose rate comprises four forms of radiation: three types of ionising radiation resulting from the decay of radionuclides in sediment; alpha particles (α), which have a very short range (approximately 20-40 μm); beta particles (β; range approximately 2 mm) and gamma rays (γ; range approximately 30 cm); and cosmic ray radiation (Aitken 1985). Due to this range in spatial scale part of the dose rate is derived from within the samples (internal dose), while some is from the interring sediments and cosmic radiation (external dose, Figure 6.4). Internal and external dose rates must be assessed independently, as the concentrations of radioactive elements within the sample are likely to be very different to those in the surroundings. There are two ways of measuring dose rates: direct measurement of elemental concentrations, which are then converted to dose rates by calculations based on published tables (Adamiec & Aitken 1998; Guerin et al. 2011), or by emission counting, either in the lab or the field.

The internal dose rate, primarily from α and β particles, is usually determined by measuring the concentrations of U, Th and K in the sample, by mass spectrometry. Alpha particles are less efficient at producing the trapped charge than β and γ rays, thus an α efficiency value needs to be applied to the results. The α efficiency is the ratio of the intensity generated by a given dose over the intensity generated by an equivalent β or γ dose, which for tooth enamel, is in the range of 0.13 ± 0.02 (Grün & Katzenburger-Apel 1994).

External dose is measured both via elemental concentrations and emission counting, depending on which dose component is being quantified. The external dose from alpha particles is minimised by removing the outer few microns from the sample during the preparation process (e.g. by grinding off the outer layer of tooth enamel and by etching quartz grains in hydrofluoric acid). Small samples, such as teeth or shells, are completely penetrated by external β rays and the affected volume cannot be removed. Schwarcz (1994) provides an example distinguishing between two types of host sediment: smooth, and rough, with the expectation that γ rates measured in a smooth site would be very homogeneous while those in a lumpy site would be very inhomogeneous, on the 30 cm scale relevant to gamma dosimetry.

The examples used by Schwarcz (1994) for smooth and rough sites were sand dunes and cave breccias, but even sand dunes, particularly lunettes sediments, may be inhomogeneous due to the presence of non-sand features such as clay laminations or carbonate concretions. An estimate of the external dose rate from cosmic rays must also be made, which is dependent on the geographic location of the sampling site (latitude, longitude and altitude) and the depth of sample burial (Prescott & Hutton 1994), the latter of which will have changed over time. High energy cosmic rays are attenuated on penetrating the sedimentary layers, with cosmic ray dose rates for practical purposes becoming negligible at a depth greater than 20 m.

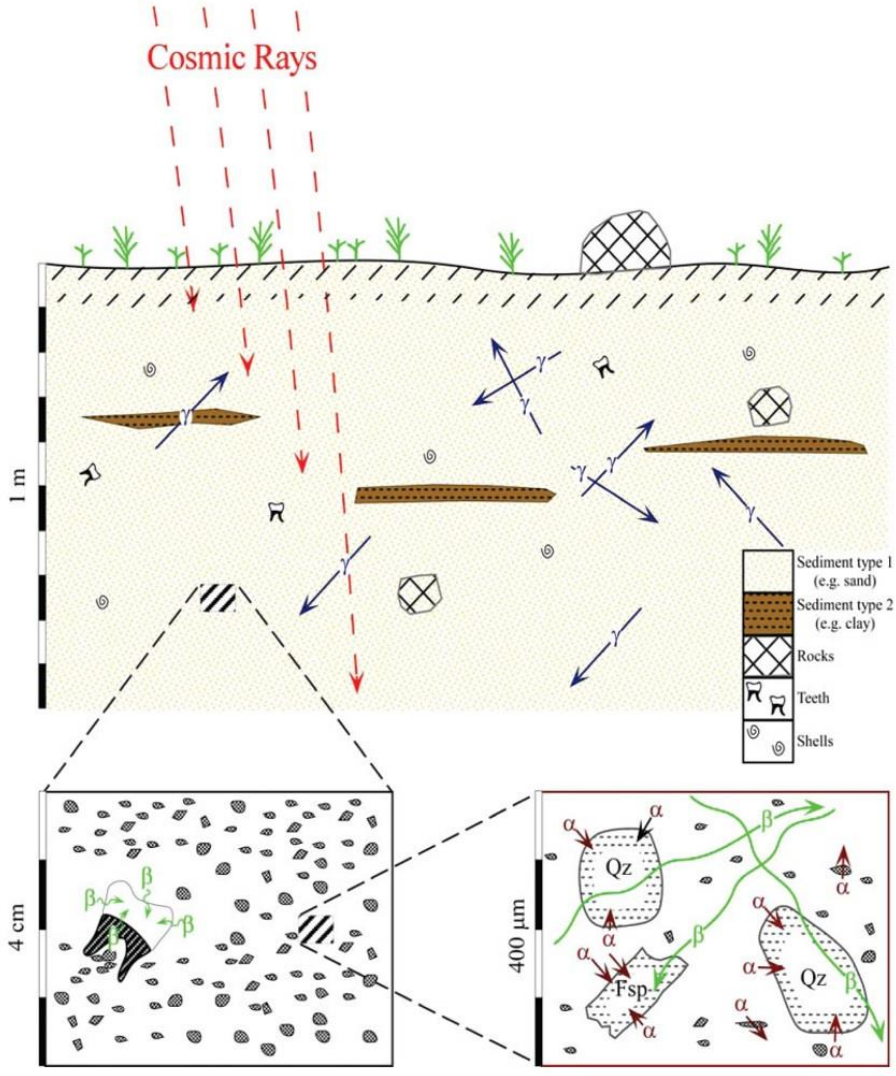

Figure 6.5. Schematic representation of the different external components of natural radiation relevant for dose rate calculations (Qz = quartz, Fsp = feldspar). (from Grün 2006, based on S. Stokes as shown in Aitken 1998: Fig. 2.2

Disequilibrium in the uranium decay series can cause a time-dependant variation in the radiation dose received by the sample. The short half-lives of the daughters in the ^{232}Th decay chain mean that disequilibrium is unlikely to be important for sediments that have been buried for more than 20 years. In the ^{238}U decay chain on the other hand, disequilibria may persist for millennia (Olley et al. 1997). As such the dose rate received due to nuclides from this decay series will vary as a function of time. By calculating the relative contributions of uranium, thorium and potassium to the dose rate of a sample, the impact of disequilibrium can be estimated. For example, Jacobs et al. (2008a), in single-grain OSL analyses of quartz from a middle stone age site at Sibudu, South Africa, determined that the average contributions from uranium and thorium were only $15 \pm 4\%$ and $17 \pm 3\%$ respectively. They came to the conclusion that any effect on the total dose rate of any disequilibrium in the U and Th series would have been negligible at those levels. The same principle applies in ESR dating; if the portion of dose contribution from external uranium and thorium are relatively small (as they are in this study, Section 7.4.3), disequilibrium is unlikely to have much influence on the final age estimate.

Finally, the water content of the surrounding sediment is estimated and incorporated into the calculations, because water is more efficient than sediment or open pore space in absorbing β and γ rays. (e.g. Aitken & Xie 1990). Each external dose rate component needs to be corrected for attenuation due to the presence of water. It is likely that the measured water content (the water content of the sample when collected) is not representative of the historical water content (long-term average water content of the burial sediments). Thus the historical water content needs to be estimated and used to correct the dose rate using the methodology described by Aitken (1998).

Dating of tooth enamel is complicated by the fact that enamel is an open system with regard to uranium and when uranium content is high the dose rate calculation is complicated by uranium uptake into the sample material over time (Grün 2006). For fossil teeth with low uranium levels this is not an issue, and the dose rate is simply calculated from the radioactivity of the surrounding sediments (e.g. Chase et al. 2007). When relatively high levels of uranium are present in the enamel, however, the rate at which the uranium was adsorbed by the tooth will have a large influence on the dose rate. As described above (Section 6.1.1), this problem can theoretically be addressed through modelling, resulting in

the estimation of two possible ages for a sample; a closed system, early uptake (EU) age, and an open system, linear uptake (LU) age. It was initially thought that the true age of the sample would be bracketed by these two dates; however, this is not necessarily the case (Grün et al. 2009a). Grün et al. (1988) suggested combining ESR estimates with the results of uranium series measurements to constrain the uranium migration history of the sample, resulting in a combined ESR/U-series dating method (US-ESR). Soressi et al. (2007) and Peresani et al. (2008) each used US-ESR to date mammal teeth from European Neanderthal sites and found that, though less precise, the results agreed with other methods used at each site (radiocarbon and TL). Pike & Hedges (2001) suggested that the precision of dose rate estimations may be improved by applying a uranium diffusion-adsorption (DA) model, which determines the spatial distribution of uranium within enamel, further characterising uranium uptake and leaching and increasing the reliability of US-ESR dates. Some issues with US-ESR remain unresolved, however, due to thermal stability and the interactions of the different types of CO_2^- radicals in ESR dating (Joannes Boyau & Grün 2011).

6.2.2. Electron Spin Resonance methods

6.2.2.1. Sample Preparation

Initially 58 wombat tooth enamel samples were sliced longitudinally with a handheld diamond saw and half put aside for geochemical analysis (Sections 4.2 and 5.2). The diamond saw and tweezers were used to remove one to two pieces each of enamel and dentine and one slice of enamel and dentine together from each sample. Each sample was given a four digit ESR number and enamel sub-samples were labelled A and B. The thickness of each enamel sub-sample was measured with callipers and the outer surface was removed with the diamond saw to eliminate the portion irradiated by external alpha rays (Section 6.2.1). Dentine and enamel were ground to fine powder in an agate mortar and pestle. Approximately 30 mg of each enamel sub-sample was weighed and placed into a glass tube for ESR analysis. Approximately 50 mg of enamel, 50 mg of dentine and one gram of milled sediment also collected from the wombat sample locations, was sent to the *Genalysis* lab for the measurement of U, Th and K concentration. The slice of enamel and dentine was mounted in blu-tac for *in situ* LA-ICPMS analysis of uranium concentration.

6.2.2.2. Sample Measurement

ESR measurements were carried out on a Bruker ECS 106 spectrometer with a 7 kg magnet and a rectangular 4102 ST cavity. The measurement parameters used were in accordance with the routine procedures for powder samples at the RSES laboratory; accumulation of 100 scans with 0.5 Gpp modulation amplitude, 10.24 ms conversion factor, 20.48 ms time constant, 2048 bit spectrum resolution (resulting in total sweep time of 20.972 s), 120 G sweep and 2 mW microwave power. The natural intensity of all 58 samples was measured before running the samples through a series of 12 laboratory irradiation steps of increasing dose, each followed with a measurement of the resultant ESR intensity according to the additive dose method.

Due to difficulties with the ESR equipment the measurement results are mostly unusable. After all of the measurements were completed, a hard-disk crash resulted in the loss of all data. The samples were re-prepared and run a second time, but the data from the second attempt was also lost, except for measurements of the natural intensities for each sample, which were saved separately early on in the process. By this stage, only fourteen of the 58 samples had unused enamel sample material remaining, so these were measured a third time. Samples were irradiated using an X-Rad 320 biological irradiator with a rotating stage at the John Curtain School of Medical Research, ANU. This machine irradiates samples at a rate of approximately 6 Gy per minute (Grün pers com). Table 6.2provides a list of the measured ESR samples.

Table 6.2. A list of ESR samples

Tooth Code	Field Site	ESR no.
WT01D	RBO02	2493A
WT01E	RBO02	2494A
WT01F	RBO02	2495B
WT01G1	RBO02	2496B
WT10	BO07B	2517A
WT13	BO07B	2520A
WT14	BO07B	2521A
WT17	BO07C	2525A
WT18	BO07C	2526A
WT22A	BO07C	2530A
WT23F	BO07E	2533A
WT23E	BO07E	2534A
WT26A	MSE01	2538A
WT36A	BO21	2554A

6.2.2.3. Estimation of equivalent dose

The amplitudes of the normalised natural intensities and laboratory dose steps were plotted in *Microsoft Office Excel.* As the natural intensities of the samples were relatively low, the dose response curves could be fit by a linear equation for all samples. This fit was then used to extrapolate the D_e values of the samples when intensity equals zero (Figure 6.6). All samples except two (WT10 and WT01G1) have very similar gradients. An average curve was calculated from these dose response curves, which was used to extrapolate a D_e from the measured natural intensities for each of the 58 samples in the study. This allowed the determination of at least rough age estimates for the remaining 44 ESR samples for which dose step intensities were lost. This is possible because the relationship between the natural intensity and the D_e is similar for all samples. Figure 6.7 shows the relationship between natural intensity and D_e for the 14 measured samples. The R^2 values demonstrate an extremely strong relationship (>0.9) regardless of whether the two relative outliers (WT10 and WT01G1 are included. The D_e for each sample was thus extrapolated from the measured natural intensities, using a standard linear equation:

$$y = mx + c \qquad (7)$$

where y = the ESR intensity, m = the gradient of the relationship (average of the 14 measured samples), x = D_e, and c = the y intercept (the natural ESR intensity). By using the average gradient and the natural intensity of each sample, the equation can be solved for x when y=0 to determine an estimate of the D_e of the sample.

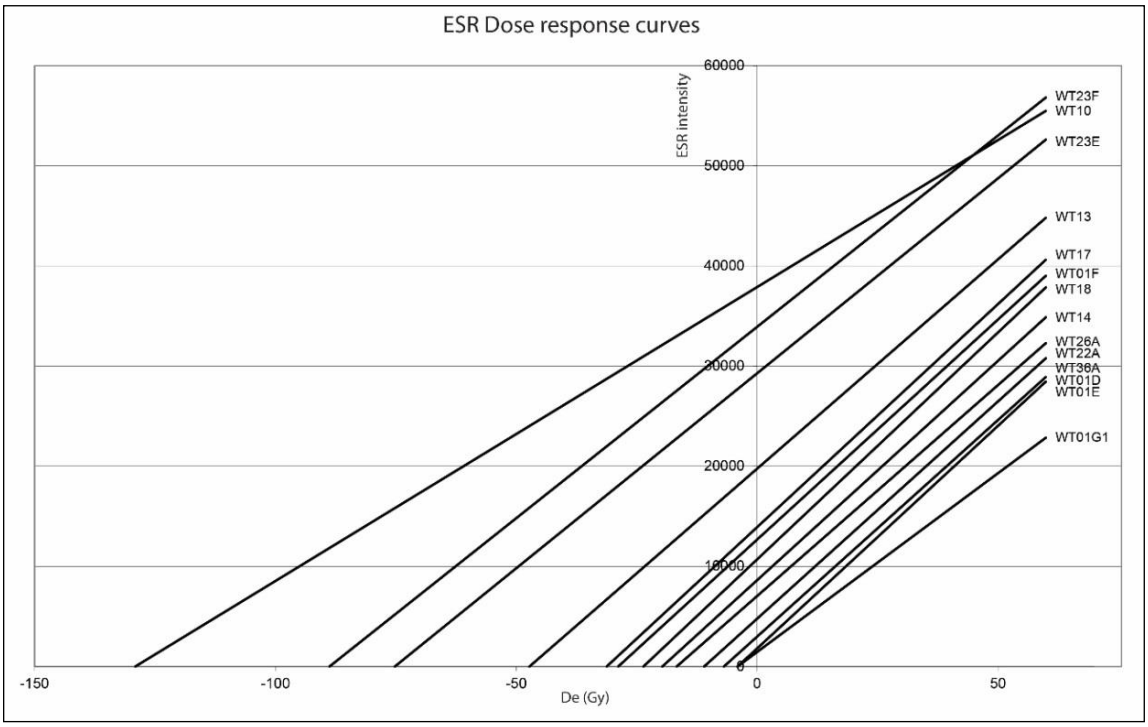

Figure 6.6. ESR dose response curves for measured samples.

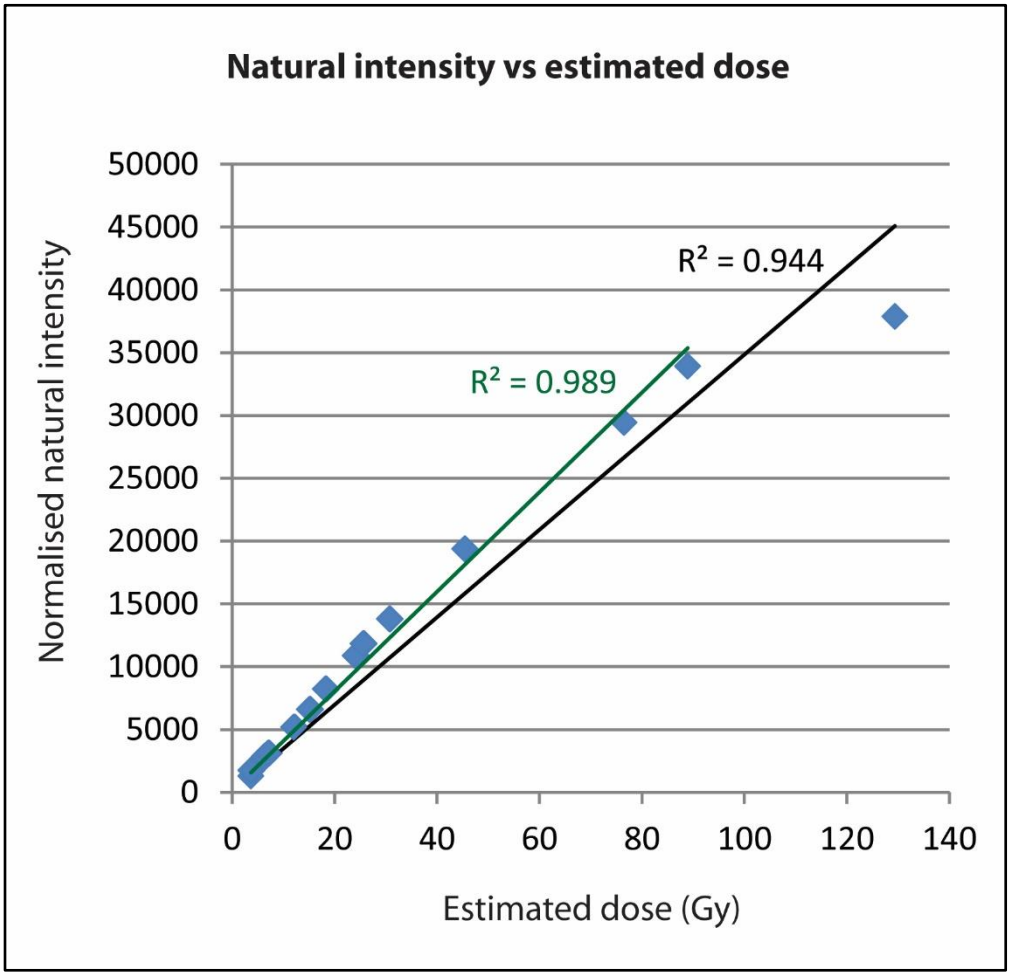

Figure 6.7. Graph of normalised natural intensities versus estimated doses for measured samples. The black trend line and R^2 value is was calculated using all 14 samples while the green trend line and R^2 value ignores the two outlier samples (WT10 and WT01G1).

6.2.2.4. Estimation of dose rate

A number of measurements were combined to derive the overall dose rate estimation for each sample, including external gamma dose, U, Th and K concentrations in the burial sediments and cosmic dose calculations, plus internal contributions from within the enamel. A correction to dose rate was applied based on an estimation of historical moisture content. The error on the dose rate was calculated by summing in quadrature the errors for all dose rate components (Appendix F).

A portable sodium-iodide gamma spectrometer was used to determine the *in situ* gamma ray contribution. The gamma probe was inserted into a hole dug in to the sediment from which

the tooth sample was collected, to a depth of at least 30 cm to accommodate the probe, and gamma counts were recorded for a 20 minute period. The gamma spectrometer was calibrated using the "Oxford Blocks" (Rhodes and Schwenninger 2007). A background measurement was carried out while the probe was immersed in water at Yerrabi Pond in Gungahlin, ACT, with counts recorded for a period of 20 minutes. The dose rate was calculated in *Microsoft Excel*, using the 'threshold' technique of Murray (1981) updated by Mercier and Falguères (2007). An error of 0.05 was used for the gamma dose rates. This is to accommodate a counting error of ~1%, a triple point estimation error ~2%, a temperature related uncertainty in selecting the channel for the threshold energy ~1-2% and an unknown calibration error, probably ~1-3%.

K, Th and U concentrations were measured in the sediments collected along with tooth sample, by ICP--OES (K) or ICP-MS (Th and U) at *Genalysis Laboratories*, in Perth. These concentration values were then converted to dose rates according to the conversion tables of Guerin et al. (2011). A standard fractional error of 0.05 was applied to these calculations.

The cosmic dose rate was calculated using the procedures described by Prescott & Hutton (1994), taking in to account the depth of burial (an estimated pre-erosion depth, ignoring the uppermost, very young Unit E; Section 8.1.5), the density of the overlying material (assumed to be an average of 1.9±0.10 g/cm^3) and the altitude, latitude and longitude of the sampling site. The altitude was measured at each sampling location, while latitude and longitude were approximated to -33 and 143, respectively.

The current water content was measured in sediments collected along with each tooth sample. An error of 30-60% was applied depending on the nature of the sample material (i.e. sand or clay). The historical water content (WF) was estimated as the current water content divided by, 1 minus the current water content. Attenuation factors were applied using the correction factors outlined in Aitken (1985) and taken from Zimmermann (1971).

The internal dose rates were determined by measuring K, Th and U concentrations in bulk enamel and dentine material and converted to dose rates also according to the conversion tables of Guerin et al. (2011). Internal U concentration was measured *in situ* in the tooth slices by LA-ICPMS using an ANU HelEx 193 nm excimer laser ablation system coupled to a *Neptune* multi-collector ICP-MS, operated with a 5 Hz laser pulse rate and 132 μm spot size.

The U concentration was estimated from laser ablation transects that traversed both dentine and enamel in each sample.

6.2.2.5. Electron spin resonance age estimation

Estimated ages were calculated by inputting the D_e values and variables required for estimating dose rates (Appendix F.1) in to the DATA software (Grün 2009b). Early uptake (EU) and linear uptake (LU; Section 6.2.1) ages were estimated for the samples using the measured D_e values and also using D_e values extrapolated from their measured natural intensity using equation (7). All EU and LU results are listed in Appendix F.2. Figure 6.8 shows a comparison of LU age estimates calculated from measured D_e values compared against the LU age estimates calculated using extrapolated D_e values. Most of the younger samples (with LU ages below around 40 ka) provide ages in relatively good agreement, while older sample ages are offset by up to tens of thousands of years, with the extreme example being WT10, for which the extrapolated age is around half the measured age. This particular sample was one for which a substantially different dose response gradient was identified (Figure 6.6). The other was WT01G1, the youngest sample measured, which had measured and estimated ages well within error of each other.

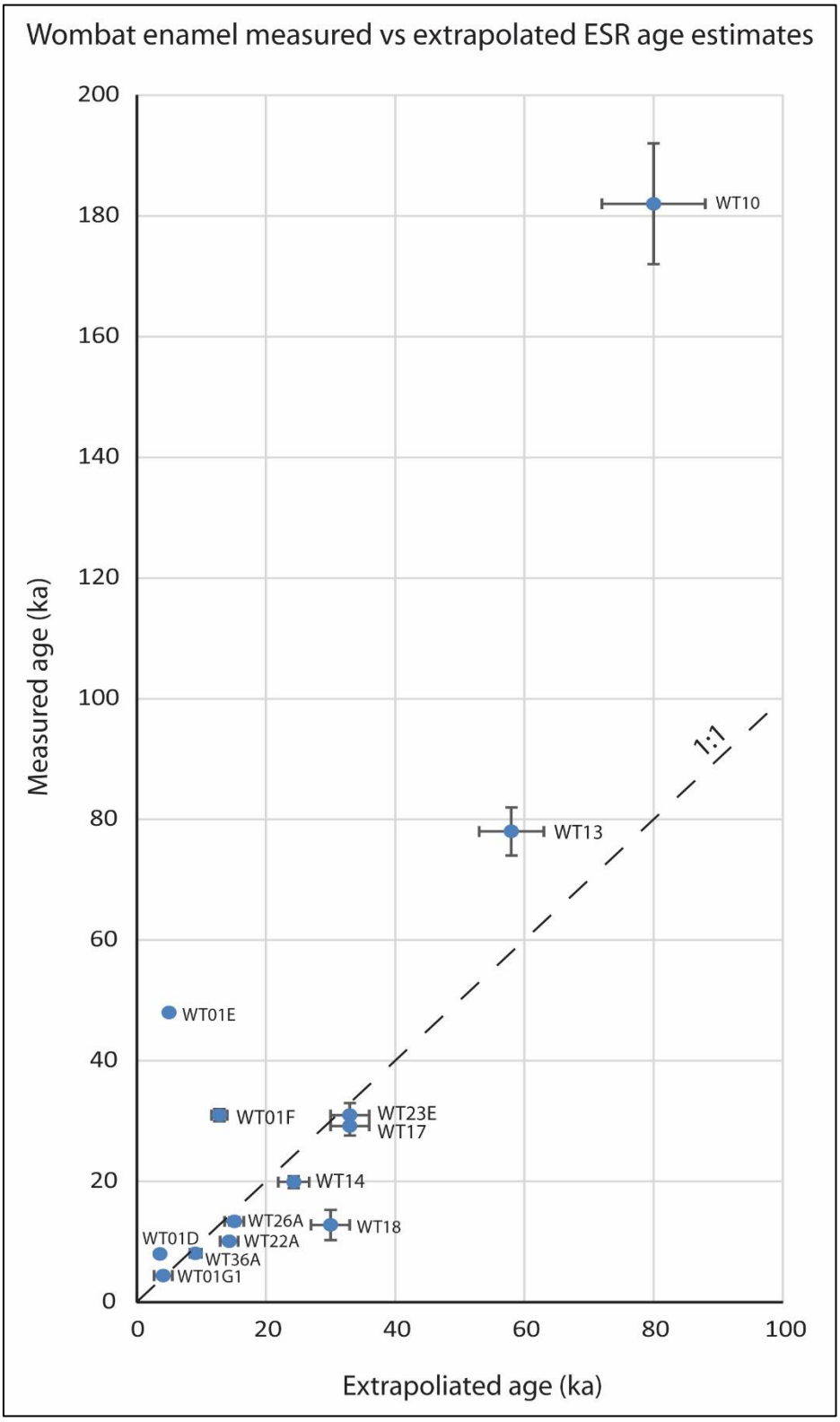

Figure 6.8. Comparison of LU ESR age estimates using measured and extrapolated D_e values.

6.2.3. Electron spin resonance dating results

Figure 6.9 shows the LU ages extrapolated from the measured natural intensities using equation (7) (Section 6.1.2) for all analysed wombat enamel samples. All EU and LU ages are available in Appendix F.2. The difference between the EU and LU age varies from 0 - ~40% of the LU age, though for most samples the difference is small enough to be inconsequential to the age interpretation. Given the results of the U-series analysis (Section 6.1.3), LU ages are presented here. It must be kept in mind that these are salvaged results from minimal data, so are indicative of possible wombat ages only. The results indicate that the oldest wombats may date to around 100 ka (or possibly older, according to a single sample, WT23B), and were present up until around 4 ka.

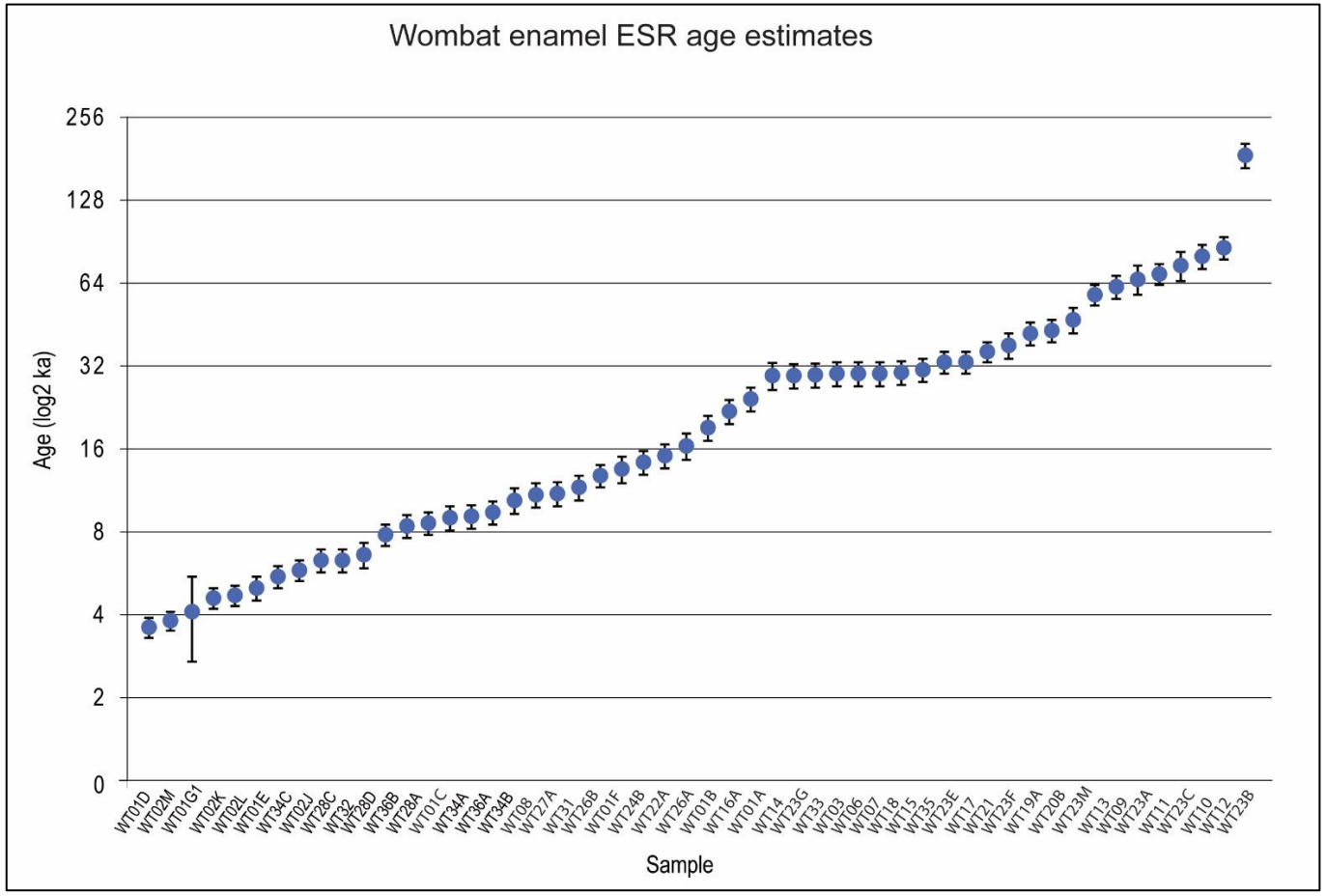

Figure 6.9. Indicative wombat enamel ESR age estimates extrapolated from natural intensities Note the log2 scale.

6.3. Electron spin resonance and uranium series dating discussion

When considered at face value, the distribution of extrapolated ESR ages for all wombat teeth (Figure 6.9, Section 6.2.3) indicates a continuing presence of wombats at Lake Mulurulu from around 100 ka to 4 ka. These ages are indicative only, however, and there are numerous reasons why they should not be accepted at face value. The full ESR measurement data set is available for only fourteen samples. The dose response curves for these allowed an average curve to be calculated, which was used to extrapolate a D_e from the measured natural intensities for each of the 58 samples in the study. The measured and extrapolated ages are not always in agreement (Figure 6.8), indicating the unreliability of the extrapolated age estimates. Additionally, intra-tooth and intra-skull age comparisons also show inconsistent reproducibility of results when using the extrapolated D_e age estimates.

Paired sub-samples were collected from six teeth (Figure 6.10). The extrapolated ESR age estimates for the two sub-samples only overlap for two of the six pairs (WT01G1 and WT02M.). Two pairs provide ages within a few thousand years of each other (WT02J and WT02K), while the other two give ages differing by over 10 kyr. Enamel derived from the same tooth must be the same age, yet these samples have differing natural intensities, possibly due to the differential distribution of anisotropic and non-oriented CO_2^- radicals throughout the tooth enamel (Johannes-Boyau & Grün 2011). This means that when the average dose response curve equation (7) (Section 6.2.1) was used to extrapolate D_e from the natural intensity, the result varied between the sub-samples, resulting in different age estimates.

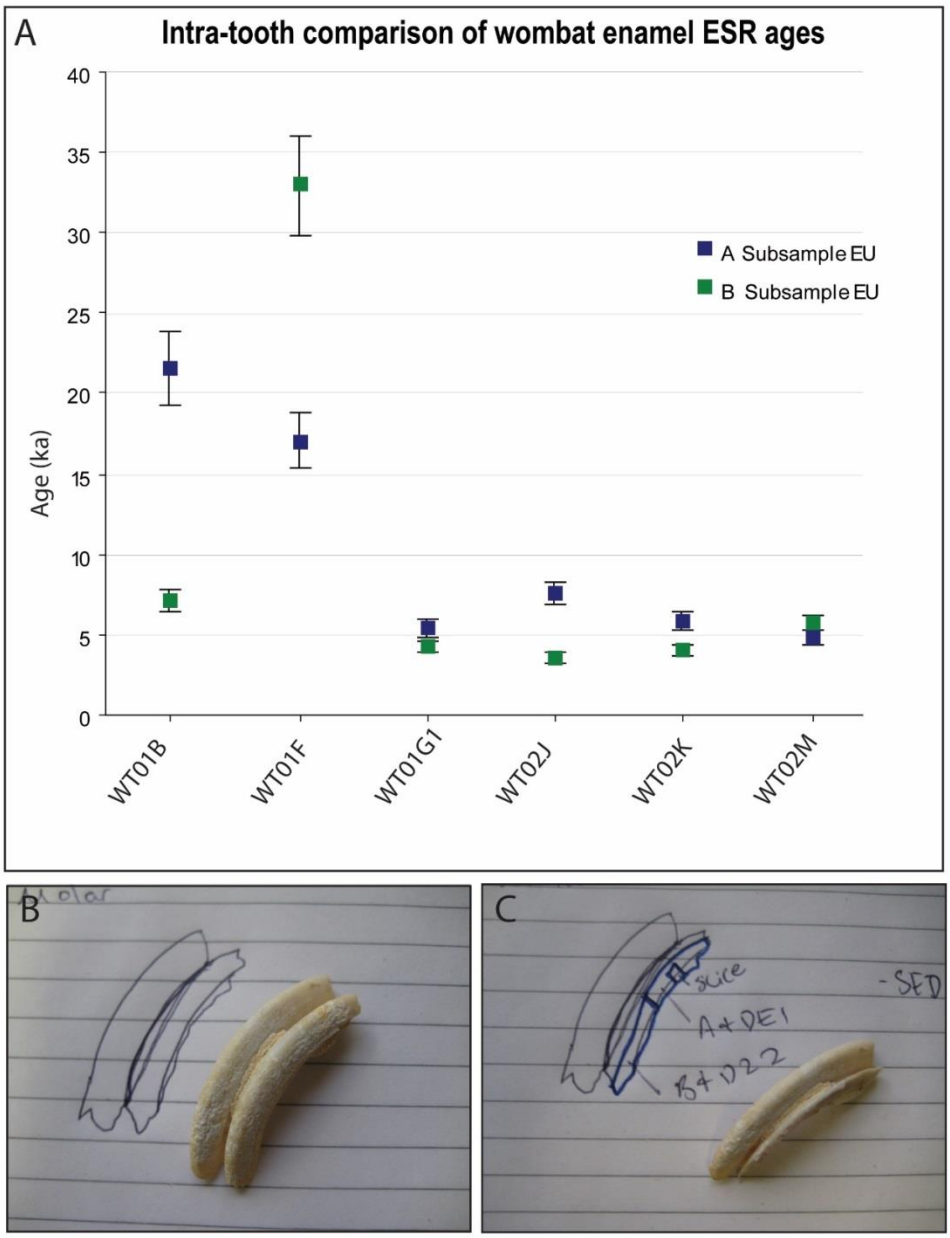

Figure 6.10. A: Intra-tooth comparison of extrapolated ESR age estimations for six wombat teeth for which two sub-samples (A and B) were collected. EU and LU ages are very similar for each of these samples so for clarity, only EU ages are shown here. B: before and C: after images of sub-sampling of WT01B, providing an example of the sub-sampling of the two neighbouring enamel pieces.

The analysed samples also included seven sets of multiple teeth thought to originate from seven skulls (Figure 6.11). Most of the intra-skull age estimates agree within error, justifying to some extent, the approach taken, though two (WT01, Figure 6.11A and WT23 Figure 6.11C) do not. These two appear to be older sets of teeth (note the differing scale on the y-axis for these skulls). These two samples also have a more questionable provenance, as they

included individual teeth found in close proximity to one another that were assumed to be from the same skull, but were not clearly still articulated as a single individual as with other samples, such as WT02 were (Figure 6.12).

Wombats often tend to die in their burrows (Miller et al. 2007), so the age of the interring sediments provides a maximum age for the animal, as the layer must have been pre-existing for the wombat to burrow in to. The wombat remains at Mulurulu were all recovered from two units; the clay-rich C and A Units. This does not mean that the wombats form two age populations however. Shimmin et al. (2002) found *L. latifrons* burrow architecture to depend on geology, with steep burrows in sandy areas and shallow declines in clay and calcrete rich sediments. It may be that the Mulurulu wombats tended to preferentially burrow down through the sandy layers, creating the horizontal warrens throughout the clay layers, which offered more structural stability, resulting in the preferential preservation of remains in these layers. WT01 remains were found in Unit A, which dates from >110 ka to around 60 ka (Section 8.1.1). All the remaining wombat teeth were recovered from Unit C, which includes two components, dating to around 32-29 ka and 40-32 ka (Section 8.1.3). These units thus provide maximum ages for these samples. Two of the 14 measured ESR samples, samples WT10 and WT13, gave much older age estimates, of 208 ± 12 ka and 94 ± 5 ka (LU ages), respectively, suggesting that even the measured ESR estimates may be providing older apparent ages than the true ages of the samples. For most samples, the difference between the EU and LU age is small and has little effect on the age interpretation for the sample. For other samples, such as the apparently old outliers above, the difference is quite large: up to ~40% of the LU age.

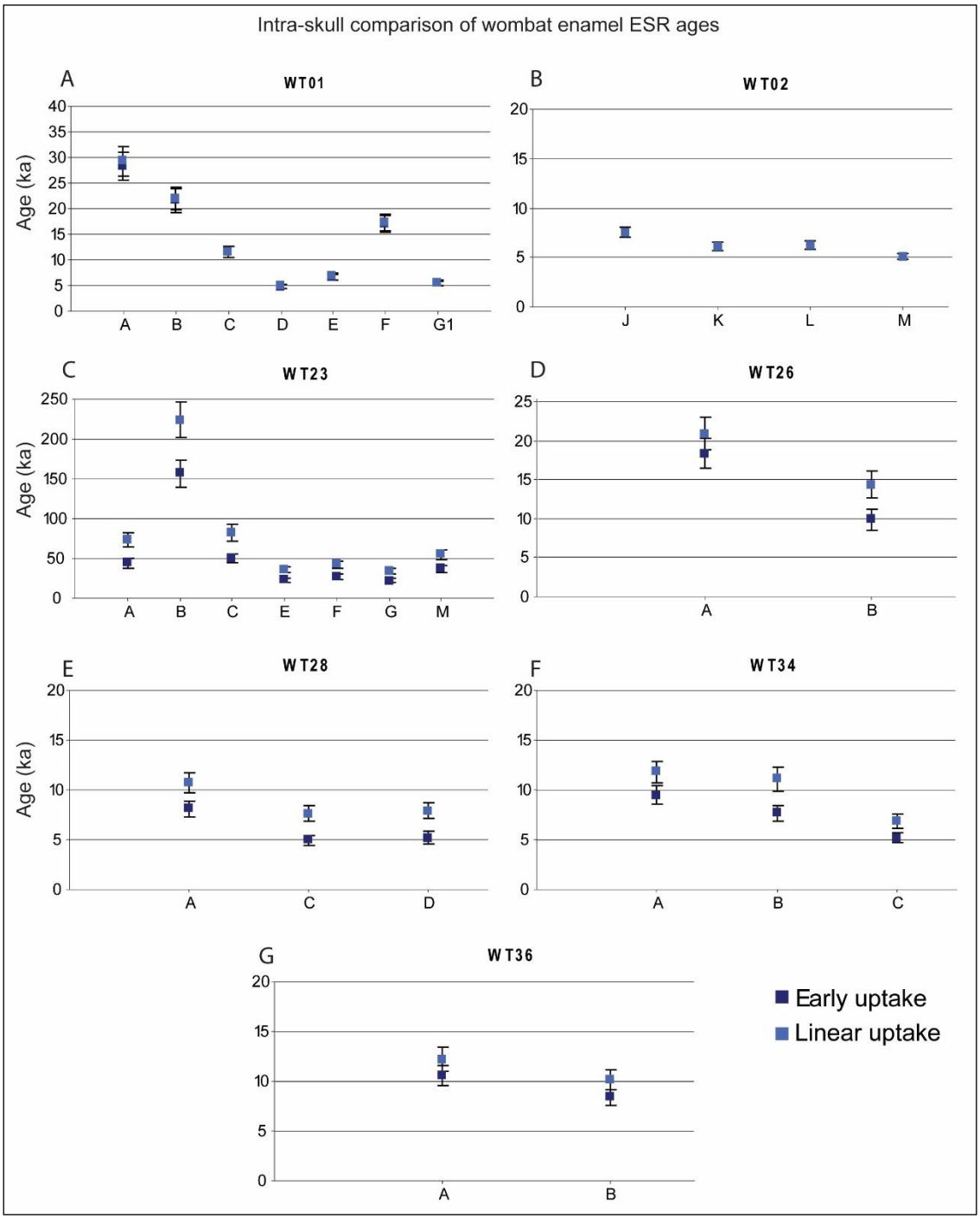

Figure 6.11. Extrapolated ESR age estimates for teeth thought to originate from the same wombat skull. Note the different scale on the y-axis for A and C.

Figure 6.12. Field photos of WT01 and WT02 wombat tooth samples. A: WT01, showing the sample location of WT01B proximal to but not articulated with other WT01 samples. A set of five articulated teeth (also included in WT01) can be seen at the far right of the photo. B: WT02, showing articulated teeth *in situ* with the remains of the wombat skull

Uranium series analyses were run on one tooth to investigate the possible U-uptake history of the sample, calculate a US-ESR age, and to also give an indication as to which of the early or linear uptake models might provide a better age estimate for Willandra wombats. The resulting U-series age is close to the linear uptake ESR age for the sample, suggesting that the LU model provides the better age estimate for these samples

Many of the LU ESR ages, however, are beyond the maximum age limit of ~40-29 ka provided by the OSL age estimates for the Unit C layer in which most of the wombat teeth were interred. The wombats obviously cannot have been burrowing into a layer that did not yet exist. This is a further indication that these salvaged analyses are unreliable. Whether the issue may be a result of extrapolating ages from limited dose response curve data, or something else, perhaps in the many parameters contributing to dose rate estimation, is difficult to assess.

One possibility as to the source of error in the ESR analysis is the X-ray source used to irradiate the samples when creating a dose response curve. Previous work in the ANU ESR laboratory had used a Cs source at the CSIRO. The radioactivity of this source was well known and precisely calculated, allowing for very precise irradiation of ESR samples. This source was decommissioned during the period of analysis of samples in this study, and the final run of 14 samples was instead irradiated with an alternative, X-ray, source at the John Curtin School of Medical Research at ANU. This radiation source has not been so well characterised, though preliminary investigation indicated that the dose it provided was approximately 6 Gy per minute (Grün pers com). This estimate may well be erroneous and if so, the resulting inaccuracies will have propagated throughout the ESR calculations.

6.4. ESR and uranium series dating conclusions

Limited conclusions can be drawn based on the ESR dating results. The data are show poor reproducibility, suggesting low reliability and accuracy for these age estimates. Intra-tooth sampling indicates the natural dose intensity from the tooth enamel cannot be assumed to be directly proportional to the D_e of the sample, undermining the attempt to salvage the data for all 58 samples by using an average dose response curve derived from the 14 measured samples. Although the OSL dating was successful, dating the sediments in which the wombat remains were interred only provides maximum age estimates. A further attempt to directly date wombat samples, using radiocarbon dating on bone material associated with the wombat teeth, was also unsuccessful, as pristine collagen could not be extracted (Rachel Wood pers com).

Chapter 7. The chronology of sediment deposition at Lake Mulurulu lunette: OSL dating of quartz-rich sediment

7.1. Optically stimulated luminescence background

Luminescence dating is a 'trapped charge' dating technique (Section 6.2.1) based on the principle that certain minerals store energy derived from environmental radiation, in a manner proportional to the duration and strength of exposure. In luminescence dating, the intensity of the emission of light due to the release of the trapped electrons is measured to determine how long the trapped energy has been accumulating.

There are two main methods of luminescence dating: thermoluminescence (TL) and optically stimulated luminescence (OSL). TL dating was first proposed by Daniels et al. (1953) and uses light emitted from stored energy released during heating, to estimate how long ago material was last substantially heated. That makes it particularly useful for dating archaeological materials, either heated deliberately (e.g. pottery) or inadvertently (e.g. hearth stones; Duller 2004). Wintle and Huntley (1982) reviewed the use of TL for dating sediments, which estimates when the material was last exposed to sunlight, and hence its burial date. Huntley et al. (1985) then proposed using optical stimulation instead of thermal energy to release the trapped energy and thus began OSL.

Like ESR dating, OSL uses the age equation (6; Section 6.1.1). The estimation of $\dot{D}$ (dose rate) is discussed in detail in Section 6.2.1.3, and is similar for both ESR and OSL dating. An additional consideration for sand grains is that although uranium and thorium may only be present in very low levels within the grains, they are often present at higher levels in iron-oxide or clay grain coatings. Thus the relative contributions of U and Th to the β dose

rate may be higher than seen in clean quartz or tooth enamel. This becomes important if the U-series decay chain is in disequilibrium (see Sections 6.1.1 and 6.2.1).

The Estimation of D_e (equivalent dose) for OSL is discussed in the following sections.

7.1.1. The luminescence signal

Trapped electrons can be evicted through heating (TL) or exposure to light (OSL) and are then diffused and recombined with the holes near the conduction band. Some of the holes are luminescence centres and the energy released during the process is emitted as light (Aitken 1985; Aitken 1998). The more radiation a crystal was exposed to, the more electrons are trapped and the greater the luminescence intensity upon recombination. The luminescence obtained from natural exposure is described as the natural intensity of the sample. It is measured along with the luminescent response to laboratory irradiation, to estimate the dose absorbed by the sample during burial (D_e).

When measured with a photomultiplier, the optically stimulated luminescence signal produces a decay curve. The curve is derived from the sum of multiple exponential decays from multiple components, known as fast, medium or slow based on the length of time taken to decay during stimulation (Bailey et al. 1996; Figure 7.1A). Figure 7.1B & C show a signal with two components as identified by (B) light stimulation at constant intensity and (C) light stimulation ramped at a constant rate (linear modulation).

In this study, the intensity of the light stimulation was constant and the OSL signal from channels within the first two seconds was used to determine D_e, meaning the signal was dominated by the fast component, with small amounts of the medium and slow components.

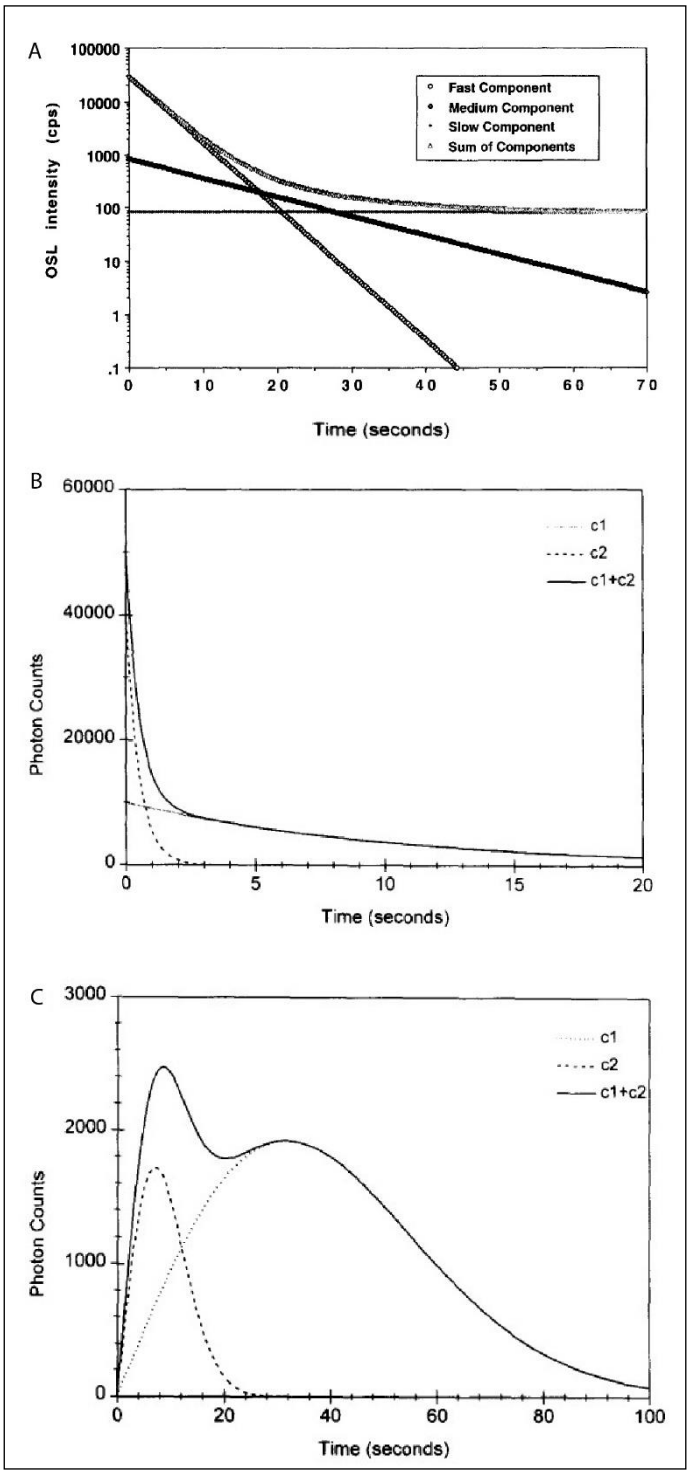

Figure 7.1. A: the multiple components making up a decay curve (Bailey et al. 1996). Examples of luminescence signal output components using B: light simulation at a constant intensity and C: light simulation ramped at a linear rate (Bulur 1996).

7.1.2. The dose response curve and SAR protocol

When calculating the D_e, the luminescent response of the material to lab irradiation is determined by creating a 'dose response curve'. There are two principle techniques for this: the additive dose method, and the regeneration method. Additive dose methods involve exposing multiple sample aliquots of the natural sample to different laboratory doses of radiation, and extrapolating D_e from the results (Wintle 1997). This technique requires a lot of a sample material, and does not account for inter-aliquot variability (Jain et. al. 2003). The regeneration method involves first measuring the natural signal (i.e. resetting the aliquot) prior to several cycles of laboratory irradiation and luminescence signal measurement, from which D_e is interpolated. This technique increases the precision of the results (Wintle 1997). It has been shown, however, that the sensitivity of samples can alter with repeated radiation exposure (Murray & Wintle 2000; Pietsch 2008) and this sensitivity change is not accounted for during the regenerative dose cycles of the regeneration method. These 'multiple aliquot' methods, utilise numerous aliquots to determine a single growth curve, and have been superseded by 'single aliquot' methods, the most widely used of which is the single aliquot regeneration technique (SAR; Murray & Wintle 2000).

In the SAR protocol, the regeneration method is applied repeatedly to each single aliquot of the sample, with changes in sensitivity arising from each dose measurement cycle corrected for, through comparison with a subsequent small test dose (10-20% of the D_e; Murray & Wintle 2000). The first dose in each cycle is denoted by L (luminescence), and the second by T (test). The first cycle measures the natural dose (L_N) and the following test dose (T_N). The doses in the following regeneration cycles are denoted by L_X and T_X, where x is the regeneration step. (L_1, L_2, L_3 etc.). The sensitivity corrected signals are thus denoted as L_N/T_N and L_X/T_X (Duller 2008b).

Additionally, a pre-heat is applied to each sample before measurement. This application of mild heating empties traps with an inadequate lifetime of signal retention, which would not have contributed to the natural signal (Aitken 1997). Unfortunately, electrons released from thermally unstable traps may recombine with luminescence centres, in a process known as recuperation (Wintle & Murray 2006; see below). The transferred electrons may result in a D_e overestimation, so the effect is minimised by determining an appropriate preheat temperature

using a preheat plateau test (see below) and monitored by including a zero dose step in the SAR protocol.

The resultant growth curve is then compared with the natural intensity of the sample, to determine a D_e for each aliquot (Figure 7.2).

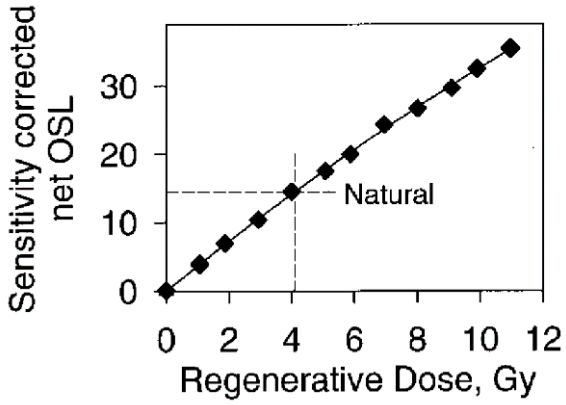

Figure 7.2. Example of a dose response curve using a single aliquot regeneration (SAR) method (modified after Murray & Wintle 2000, their Fig. 2b)

7.1.3. Dose distributions

For each sample, the SAR protocol is applied to a number of aliquots (e.g. 18-24), resulting in distribution of D_e values. This distribution can be viewed graphically in a number of ways. A simple (x,y) scatter plot with aliquot number on the x axis and D_e (in Gy) on the y axis conveys the basic information of estimated dose per aliquot, but does not highlight patterns in the data, and only considers each aliquot individually. Two other ways to graphically present D_e distributions, are as probably density (PD) plots or as radial plots. Examples of each are shown in Figures 7.3 and 7.4, respectively.

PD plots (also known as relative probability plots or weighted histograms), for example, as advocated by Brandon (1996) for viewing fission track dating data, use a Gaussian density function, in which means and standard deviations are calculated from the observed D_e values and their errors, with the functions added pointwise to produce a continuous curve. When there is a single age component present in the data, a symmetrical Gaussian curve is produced (Figure 7.3A). With mixed distributions, multiple peaks are present (Figure 7.3B), wherein

the area beneath each peak should be proportional to the relative size of the component. PD plots have the benefit of providing a clear graphical representation of mixed populations that is easy to describe (i.e. narrow, broad, bimodal, skewed etc.) and indications of pre- or post-depositional impacts on D_e distributions (such as partial bleaching or sediment mixing) are often described in these terms (Sections 7.1.4 and 7.1.6, below). PD plots can be misleading however, due to the temptation to interpret each mode as a discrete age component, when they in fact do not necessarily correspond. Also, good information in the data can be obscured by inappropriate weighting with poor data (Galbraith 1997). Galbraith and Roberts (2012) recommend avoiding PD plots and instead suggest using radial plots.

A radial plot is a graphical method for comparing several estimates that have different precisions. It is a type of (x,y) scatter plot, in which y is the standardised estimate and x measures precision (Galbraith 1990). It is represented on a circular scale so that for any point the corresponding (De) estimate can be read by extrapolating a line from (0,0) through (x,y) (Figure 7.4). Galbraith (1997) explains that estimates forming a statistically concordant population should generally fall within the 2σ error of a radiating line (Figure 7.4B). When there are multiple components, data points will generally fan out, as low precision estimates could belong to any component, while high precision estimates group in to separate components (Figure 7.4C). A radial plot has the benefit that it does not confound true age variation with estimation error, it clearly displays precision of each data point, and any statistical outliers are easy to spot (Galbraith 1990; 1997).

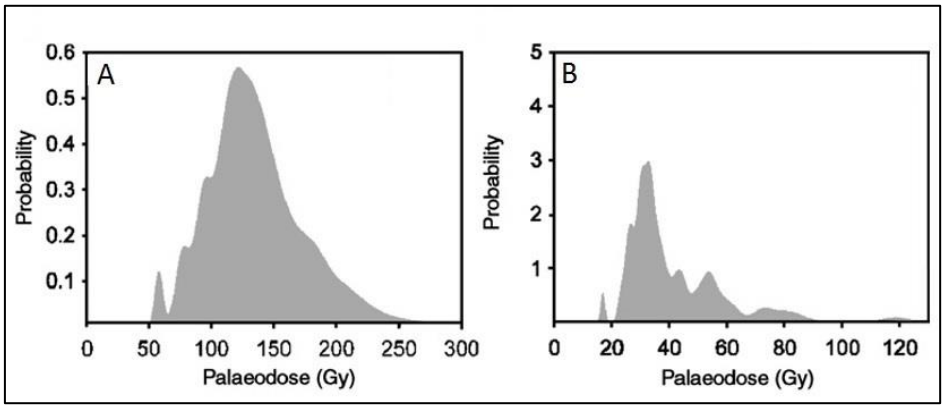

Figure 7.3. Examples of probability distribution plots. A) a near-Gaussian distribution with a central modal peak. B) a multimodal distribution with a right skew. Modified from Lomax et al. (2007, Fig 2).

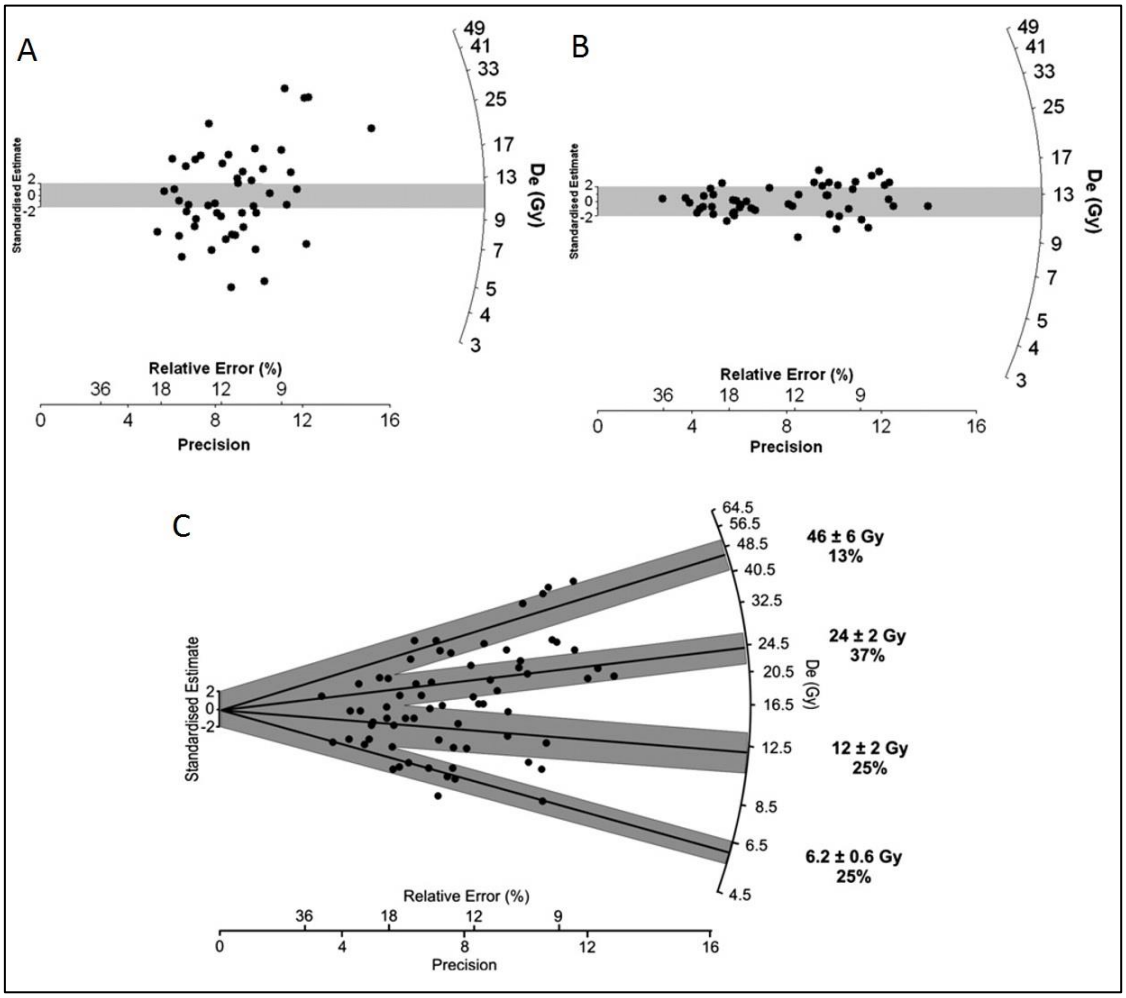

Figure 7.4. Examples of radial plots. A) a scattered distribution with most data points falling outside the 2δ error. B) a concordant population with most points falling within the 2δ error. C) a multi-component distribution, with four populations identified using a finite mixture model (Section 7.1.6). Modified from Lomax et al. (2011, Figs 2 and 4).

7.1.4. External factors influencing D_e distributions

Each of the above described graphical displays provides a way to view the distribution of D_e values calculated for the aliquots of a given sample. In practice, natural quartz samples rarely yield D_e estimates that are statistically concordant with respect to their in-aliquot standard errors (Galbraith & Roberts 2012). The three main external factors contributing to dispersed D_e distributions are partial bleaching, an inhomogeneous beta dose, and sediment mixing (Jacobs et al. 2008b; Galbraith & Roberts 2012).

7.1.4.1. Partial bleaching

All grains being fully bleached prior to deposition is a major assumption of the age equation (6). Different components of the OSL signal bleach at different rates; the signal of the fast-dominated component is reduced within seconds of exposure, while the slow-dominated component can take several hours to days (various authors in Olley 2006). Fuchs et al. (2007) pointed out that though partial bleaching is frequent in fluvial sediments, it is not usually an issue for aeolian material. Additionally, bioturbation and sediment mixing may expose buried grains to light, causing them to be partially bleached, but not re-zeroed (Bateman et al. 2003

Incomplete bleaching is unusual in Australian aeolian dune sands. Olley (2006) found no evidence of partial bleaching in wind-blown dune sediments from Lake Mungo; sediments directly analogous to those analysed in this study. Iron-oxide coatings on quartz grains do, have the potential to prevent complete resetting of the quartz OSL signal (Lomax et al. 2007) and heavily iron-oxide coated grains are likely to be less-well bleached than those less heavily coated (Singhvi et al. 1986). Where this type of iron staining is the result of *in situ* pedogenesis, however, it does not impede bleaching prior to burial (Roberts et al. 1994).

Microscopic investigation of sedimentary grains in this study revealed many samples for which quartz grains had primary cutans. Primary iron-coatings in grain embayments indicate that a previous iron-coating on the grain remained at least partially intact during transport, before being buried in a later location, where it may potentially develop a secondary iron-coating. Samples in this study showed varying degrees of wear in primary cutans indicating that some grains may have been transported with iron-coatings at least partially intact.

To test the ability for iron-coatings to impede bleaching prior to burial, Lomax et al. (2007) assessed the bleachability of etched and non-etched quartz. Both samples were aeolian iron-coated samples from western Murray Basin palaeodunes. Although resetting of the OSL signal was slower in non-etched quartz than etched quartz (Figure 7.5), even the iron-coated grains were bleached to a negligible signal within 120s, which should be sufficient to bleach aeolian quartz OSL signals during transport and deposition. They concluded that incomplete bleaching as an external source of scatter is therefore not likely in these Murray Basin aeolian

dune sands. The same is likely to be the case for the Willandra Lakes samples analysed in the present study, thus significant impacts from partial bleaching is not expected to be a problem in these samples.

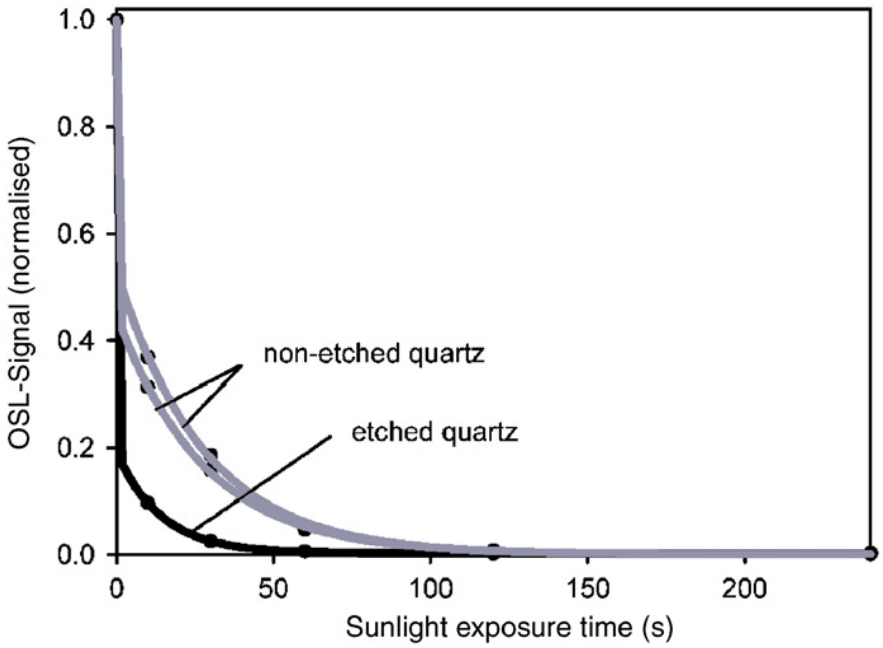

Figure 7.5. Decrease of signal intensity of an etched and non-etched quartz with different sunlight exposure times (10, 30, 60, 120 & 240 s). (Lomax et al. 2007, their Fig. 3).

7.1.4.2. Microdosimetry

Scattered or broad D_e distributions can often be attributed to grains that were buried at the same time, but which received different beta doses afterwards (Jacobs et al. 2008b; Murray & Roberts 1997; Olley et al. 1997). All grains from within the sample will have received the same gamma dose, as gamma rays can penetrate 30 cm through sediments (Aitken 1985). The short travel distance of beta rays (~2 mm), however, means that in heterogeneous sediment, some grains may receive a small beta dose while others receive a substantial beta dose, depending on whether they are within 2 mm of radiogenic materials, such as potassium rich clays. Conversely, materials with low radioactivity, such as carbonates, may insulate grains from beta rays. Olley et al. (1997) demonstrated that the beta dose contribution to individual grains can vary greatly. Differences in dose rate derived from different sediment fractions become increasingly significant as the number of grains examined decreases. Thus, the effects

of sediment heterogeneity are averaged out when using a large number of grains, making beta-heterogeneity less of an issue in multi-grain aliquots.

7.1.4.3. Sediment mixing

A major cause of broad or bimodal distributions is sediment mixing. Mixing may occur through pedoturbation or bioturbation, and will result in a positive or negative skew, depending whether older or younger material has been mixed in. Figure 7.6 shows some of the possible theoretical D_e distributions resulting from mixed sediments. Note that a sample contaminated with a small amount of older material, gives a similar distribution (a positive skew) to a poorly bleached, undisturbed sample.

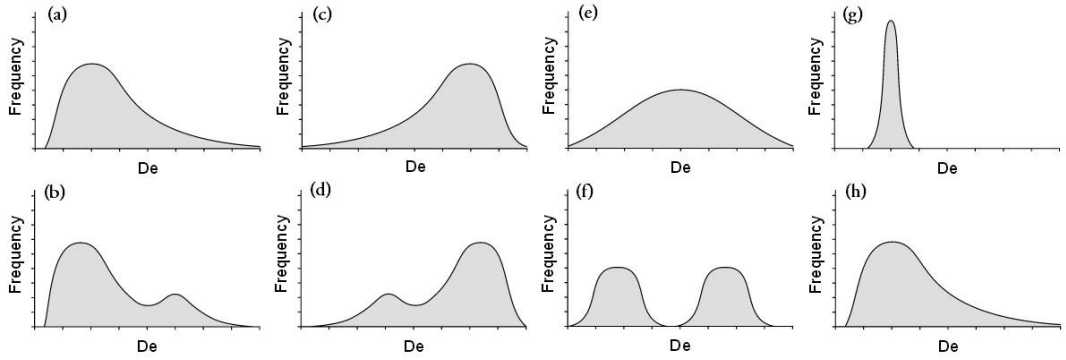

Figure 7.6. The hypothetical effects of bioturbation on D_e distribution compared to a well bleached undisturbed sample and a poorly bleached undisturbed sample. (a, b) A sample into which older material has been mixed giving rise to a high D_e tail or skewed bimodal distribution. (c, d) A sample into which younger and exhumed material has been mixed giving rise to a low D_e tail or skewed bimodal distribution. (e, f) A sample in which mixing has caused near homogeneity giving a wide range of D_e values with a low frequency at any single value or 2+definable peaks. (g) Undisturbed well bleached sample with a small D_e distribution and high reproducibility. (h) Undisturbed poorly bleached sample with tail of higher D_e values reflecting antecedent OSL signal (after Bateman et al. 2003).

When vertical mixing processes occur, a long tail can be expected in the D_e distribution (Murray & Roberts 1997). Bateman et al. (2003) pointed out that while a positive tail may be attributable to a contribution from older grains (Figure 7.6a,b) or partial bleaching of undisturbed sediments (Figure 7.6h); a negative tail can only be attributed to a contribution from younger grains (Figure 7.6c,d). Multiple discrete populations (Figure 7.6f) are more likely in mixed aeolian deposits, where episodic periods of aridity deposited well bleached grains (Roberts et al. 2000). Additionally, under conditions of episodic phases of

pedoturbation, discrete definable peaks are likely to form, whereas intense or prolonged mixing results in a broad distribution (Bateman et al. 2003). Lomax et al. (2011) investigated broad dose distributions from dune sands in the western Murray Basin, South Australia. They found that despite issues arising from post-depositional mixing, OSL ages were in chronostratigraphic order within errors, independent of the mean estimate used for the palaeodose.

7.1.5. Intrinsic factors influencing D_e distributions

Intrinsic factors, such as recuperation, sensitivity, and overdispersion can also influence D_e distributions.

7.1.5.1. Recuperation

Recuperation (also known as thermal transfer) is an effect created during heating, in which charge is transferred from light insensitive traps to OSL traps, which will then contribute to the photoluminescence of the sample when OSL is measured (Aitken & Smith 1988). Optically stable, but thermally unstable traps may contain a dose at deposition, and if this component is large, then recuperation can have a considerable effect, especially in younger samples (Murray & Roberts 1997). The thermal transfer of charge occurs during pre-heating (Rhodes & Bailey 1997) and the result is that equivalent dose estimates will be larger than expected; a result which can be mistakenly attributed to partial bleaching (Roberts et al. 2000). Rhodes & Bailey (1997) were able to account for relatively high D_e values observed in recent glaciogenic sediments in terms of anomalously high recuperation, rather than partial bleaching. Roberts et al. (2000) demonstrated that non-zero doses apparent in 'zero-dose' quartz grains previously bleached by sunlight, measured, stored in light-safe conditions then measured again were also a result of recuperation rather than incomplete bleaching. Rhodes (2000) suggested the use of a pre-heat plateau test, to select a pre-heat temperature that minimises recuperation effects. As mentioned above, the SAR protocol includes a zero-dose measurement on each aliquot at each dose step, in order to monitor any recuperation that may have occurred during the previous pre-heat step of the procedure.

7.1.5.2. Sensitivity change

Sensitivity change is the term used to describe the tendency for a grain to show change in the intensity of the luminescence signal when it is stimulated under different conditions, such as in the field and in the laboratory. If this is not corrected for, repeated measurements could result in inconsistent signal response, disproportionate to the laboratory dose. The SAR protocol includes a test dose step, to provide a sensitivity correction to the measured D_e. The corrected luminescence signals are expressed as L_X/T_X, where x represents the dose step in the SAR protocol. In order to test the accuracy of the SAR sensitivity correction, Murray & Wintle (2003) suggested using a dose recovery test, in which the SAR is applied to bleached samples which have since been given a known dose, to monitor the accuracy of the resulting apparent D_e. The dose recovery is expressed as the ratio between the apparent dose and applied laboratory dose, which should ideally be close to unity (Murray & Wintle 2003). A routine check on the sensitivity correction is also usually included in the SAR protocol, in the form of a recycled dose, in which one of the earlier regenerative dose steps is repeated at the end of the protocol. If the sensitivity correction is working, then the luminescence signals of the repeated dose should be the same. If the signal differs by more than ~10%, something about the procedure or the sample is inappropriate and the aliquot should be rejected (Duller 2008b)

7.1.5.3. Overdispersion

The term overdispersion is used to describe a situation in which the dose estimates for individual aliquots from the same sample are spread more widely than expected from their measurement uncertainties alone (Roberts et al. 2000). It is measured as the spread in D_e values remaining when all other measurement uncertainties have been taken in to account (Jacobs et al. 2012). It is typical even for fully-bleached undisturbed quartz grains and should be considered when D_e distributions for natural samples are assessed for the effects of external factors of depositional and post depositional disturbance (Jacobs et al. 2012). Even in samples thought or known to have been well bleached at the time of deposition, overdispersion values of 9-22% have been reported (various authors in Jacobs et al. 2008a). This led Galbraith et al. (2005) and Olley et al. (2004) to conclude that overdispersion of 20%

is in most cases consistent with a single component D_e distribution thus allowing the central age model of Galbraith et al. (1999) to be used to calculate the D_e value (Jacobs et al. 2008a).

7.1.6. Age models

Once the D_e estimates have been determined for each aliquot, statistical age models can be applied to identify a representative D_e value for the sample, from the mixed dose population. These models include the central age model (CAM; Galbraith et al 1999), minimum age model (MAM; Galbraith, et al. 1999) and finite mixture model (FMM; Galbraith 2005). The choice of model to use for a particular set of D_e values depends on the context of the stratigraphy and sedimentology of the sample (Bailey & Arnold 2006).

The central age model of Galbraith et al. (1999) calculates the weighted mean of a set of D_e values, while also taking overdispersion in to account, which is solved for by maximum likelihood analysis. A CAM is appropriate for deriving a representative D_e in the case where the distribution of D_e values exhibits lognormal statistical properties, i.e. there has been no post-depositional disturbance For sediments that have undergone post-depositional disturbance, a central age model applied to the full data set will provide an average value with little bearing on the target event (Jacobs et al. 2008a). The model also assumes complete bleaching, and will overestimate D_e in partially bleached sediments (Olley et al. 2004).

For sediments that include partially bleached grains, or are mixed with older material, a MAM, which estimates the D_e value for the lowest dose population in the sample, may be more appropriate (Galbraith et al. 1999). This model should only be applied when the lowest dose population is likely to represent the true depositional age of the sediments. Being able to determine this in practice requires a sound knowledge of the stratigraphic context of the sample (e.g. Bateman et al 2003, Jacobs et al. 2006).

Another approach to mixed distributions is to use a FMM (Galbraith. 2005). This model calculates a D_e value and uncertainty for each dose component identified in the model. A single one of these components is then selected to as the most likely to reflect the true depositional age of the sediments. Understanding the field context of the samples is important in explaining why different components exist and in justifying why one is preferred as the

target event. (Galbraith et al. 2005; Jacobs et al. 2008b). Although very useful in analysing single-grain datasets (Jacobs et al. 2008a), the finite mixture model is not applicable to multi-grain data (Arnold and Roberts 2009).

The averaging effect of multi-grain aliquots (Section 7.1.7) rules out the use of FMM for reliably identifying discrete component ages in this study. A minimum age model can be applied to data with a positive skew, though this is most appropriate for partially bleached samples, which is unlikely in this study region (Section 7.1.8). For relatively undisturbed samples, a central age model can be applied (Galbraith et al. 1999). When a mixed distribution is identified, supporting stratigraphic and sedimentological information can be used to provide a rationale for excluding outliers or selecting a particular sub-population of aliquots as most likely to represent the burial dose, and apply a CAM to these. Modelling by Arnold and Roberts (2009) suggested that the most favourable types of multi-component mixtures for obtaining reliable burial dose estimates are those composed of 2-3 discrete parent components with relative ranges >1 and each exhibiting a log-normal distribution with a relative dispersion value of <30%. These are likely to be analogous to fully bleached grain populations affected by only a small to moderate amount of inherent overdispersion. For example, where OSL samples originate from either side of a unit boundary that represents a significant depositional hiatus, a mixed dose distribution may result from post deposition grain transport across the unit boundary. The component ages are likely to have a large difference in average dose, resulting in identifiable populations in a radial plot and a broad or bimodal PD plot. Identification of sediment mixing in the field or in thin-sections can then support a decision to exclude aliquots likely to be dominated by grains from the contaminating unit, and only apply the CAM calculation to aliquots more likely to better represent the true burial dose of the target stratigraphic unit.

7.1.7. Single-grain and multi-grain dating methods

Dating single grains individually, rather than dating aliquots of multiple grains, can help in addressing many of the issues described in Sections 7.1.4 and 7.1.5, as affected individual grains can be rejected from analyses. Unfortunately, Single-grain analyses were not routinely carried out at the ANU OSL laboratory at the time this study was conducted (2008), and the

laboratory was better equipped for multi-grain dating. Instead small multiple-aliquot samples, consisting of approximately 20 grains in the 125-180 µm size fraction were measured using a 1 mm mask (Section 7.2.2).

The ability for single-grain and multiple-grain measurements to identify D_e dose populations has been compared in both natural (e.g. Murray & Roberts 1997) and simulated samples (e.g. Arnold & Roberts 2009). If all the grains within an aliquot are homogeneous, then multiple-grain aliquots should give the same D_e estimate as single grain analyses of the same sample. In reality though, all quartz grains within a sample are rarely homogeneous and while single-grain methods allow anomalous grains to be rejected, the signals from these grains are averaged when multiple grains are measured together. The fewer grains present in the multi-grain aliquot, the less likely it is that the aliquot will include anomalous grains, but the greater effect the anomalous grains have on the overall D_e measurement when they are present (Bateman et al. 2003; Arnold & Roberts 2009).

In the first application of single-grain OSL dating, Murray & Roberts (1997) applied additive dose and regenerative dose single aliquot protocols to aeolian quartz from an archaeological deposit at Allen's Cave, located on the semi-arid Nullarbor Plain in southern Australia. They found that 5% of the grains produced about 57% of the summed natural luminescence output of 120 grains, indicating that while the estimate of D_e is not biased by grain sensitivity for single-grain measurements, the multiple-grain D_e estimates must be heavily weighted to the D_e in the brightest grains. The resulting D_e estimates (21.8 ± 1.1 Gy and 23.8 ± 1.0 Gy, respectively) were in agreement with 13 multiple grain regeneration dose single aliquot measurements on 1 mg (~700 grains) sub-samples (23.9 ± 0.3 Gy), nine multiple grain additive dose single aliquot measurements in 1 mg sub-samples (22.4 ± 0.7 Gy) and one previously published multiple aliquot additive dose estimate (of 23.5 ± 0.6 Gy), using 5 mg sub-samples. All values were in agreement with a weighted mean of 23.7 ± 0.3 Gy, resulting in an age estimate of 10.2 ± 0.4 ka, also in excellent agreement with ^{14}C dates for an overlying hearth.

Examples such as this, where multi-grain analyses give results within error of the single-grain dating results, occur when samples are fully bleached at deposition and there are no complications from post depositional mixing or other forms of contamination. A finite

mixture model can be used to identify discrete dose components in mixed samples, but Arnold and Roberts (2009) point out that the finite mixture model is only appropriate to single-grain data sets, not multi-grain, even for small aliquots. For example, Russel & Armitage (2012), attempted to apply the finite mixture model as suggested by Jacobs et al. (2008a) to single-grain and small-aliquot (~14-20 grains) data and found differences between the two sample sets attributable to grains that contribute to the OSL signal in small aliquots, which would be rejected in single grain analyses. While the single grain analyses identified three grain age populations, the multi-grain data only identified one population, due to the presence of rogue grains and averaging effects inherent in multi-grain measurements.

In multi-grain dating, aliquot size is important. When multiple D_e populations are present in a multi-grain aliquot, representing younger or older intrusive grains along with the *in situ* grains, the signatures of minor sedimentary mixing may be obscured, and the presence of intrusive grains may therefore become 'masked', in the final D_e estimates of individual aliquots. Arnold and Roberts (2009) used simulated D_e datasets to generate theoretical distributions of single grain D_e values, which were randomly mixed together to simulate multi-grain aliquot D_e distributions containing a known number of mixing components and corresponding burial doses. Their results suggested that the identification of genuine (not phantom) dose components in a mixed distribution is strongly dependent on the relative range between the mean dose values of the parent distributions. Also, the number of phantom components increased as the relative range between the parent dose components increased.

Duller (2008a) provides a review of the use of single grain and multi-grain methods in glacial, fluvial and aeolian Quaternary environments. He suggests that in aeolian materials, partial bleaching is relatively uncommon, so is unlikely to result in issues arising from the averaging effect of multi-grain aliquots. Post-depositional mixing, however, may make burial dose more difficult to discern when not using single grains. Bateman et al. (2003) compared D_e results for three different aliquot sizes (9.6 mm, ~2300 grains; 4 mm, ~400 grains; and single grains) when sampling bioturbated sediments from inside a Holocene krotovina (infilled gopher burrow) along with neighbouring, undisturbed sediments, in Lee County, Texas. The mean D_e estimate from inside the burrow was 4% higher than outside for the 9.6 mm aliquots, 25% higher for the 4 mm aliquots and 28% higher for the single grain samples. The heterogeneity in D_e was masked in larger aliquots, though the 4 mm aliquot (~400 grains) results approach

that of the single grain results. These results are encouraging for the 1 mm aliquots (~20 grains) used in the current study, which are likely to result in minimal masking of heterogeneous signals.

As discussed above, partial bleaching is unlikely to be an issue for the sediments used in this study. Given that multi-grain analyses were to be conducted, extra care was taken when sampling to avoid issues from post-depositional mixing (such as ant nests, and rabbit and wombat burrows) and a careful record of stratigraphic context (particularly palaeosols) was made for all samples.

7.1.8. OSL dating of Australian sediments

Luminescence dating is regularly applied to geomorphological (e.g. Rendell et al. 1994; Fitzsimmons et al. 2007) and archaeological studies (e.g. Roberts et al. 1994; Olley et al. 2006). OSL has been successfully applied in a range of Australian contexts, such as in northern Australia, and central and southeast Australia, including previous studies at the Willandra Lakes. Australian arid-zone sands appear to be particularly well suited to OSL dating, due to long transport histories resulting in ample opportunity for sensitisation and thorough bleaching.

In northern Australia a significant piece of OSL dating work was carried out at Jinmium Rock Shelter, a site previously thought to provide evidence for early human occupation, prior to 50 ka and possibly over 100 ka, based on TL dates (Fullagar et al. 1996). Spooner (1998) raised questions over the antiquity of these dates and Roberts et al. (1998) used OSL dating to demonstrate the deposit to be much younger, at less than 10 ka. They suggest previously unidentified partial bleaching as the reason for the previous age overestimations. The study utilised multiple aliquot, multi-grain single aliquot and single grain dating work, and Galbraith et al's (1999) seminal paper on the experimental design and statistical models employed on the samples from the site remains the key reference on CAM methodology.

Some of the earliest evidence for human occupation in Australia also comes from northern Australian OSL dates, including Roberts et al's (1994) optical dates of ~53-60 ka for human arrival at Deaf Adder Gorge, which in this case corroborated previous TL dates of 50-60 ka

(Roberts et al. 1990). More recently, Wood et al. (2016) dated human occupation at Riwi in the Kimberly of Western Australia to 46.4-44.6 cal kBP using a combination of radiocarbon and OSL dating, and Veth et al. (2017) announced new OSL evidence for human occupation on Barrow Island around 50 ka. OSL evidence continues to push-back the timing of the earliest occupation of Australia, with human presence at the Madjedbebe rock shelter in the Northern Territory dated to ~65 ka (Clarkson et al. 2017) and the earliest evidence for expansion in to central Australia provided by ~49 ka dates for human occupation at Warratyi rock shelter (Hamm et al., 2016).

Geomorphological and palaeoclimate studies have been a focus for OSL dating in central and southeastern Australia. Fitzsimmons et al. (2007), for example, determined the timing of linear dune activity in the Strzelecki and Tirari Deserts of Australia and were able to correlate dune reactivation with arid conditions occurring in other parts of the country. Kemp & Rhodes (2010) dated palaeochannels and source bordering dunes in the southern Murray-Darling Basin, and were able to correlate the timing of large sediment loads and high bank-full discharge levels with periods of glacial advance and thus high-run-off from the Australian Alps. In the southeastern Murray Basin, Fitzsimmons et al. (2010) used OSL to construct a chronology of recent lake shoreline sediments at Lake George, demonstrating three distinct periods of permanent lake conditions, broadly synchronous with comparable records of Holocene climatic variability across southeastern Australia.

As described in Chapter 2, a number of OSL studies have been conducted in the Willandra Lakes, including Thorne et al.'s (1999) controversial age of ~60 ka for the Lower Mungo unit and Bowler et al's (2003) ~40 ka age for same unit, corroborated by Olley et al's (2006) 41±4 ka age for burial infill at the LM3 burial site (Section 2.1). The fossil track ways site between Lakes Leaghur and Garnpung was dated to 23-19 ka using OSL (Webb et al. 2006; Section 2.2) and Fitzsimmons et al. (2014) provided a comprehensive OSL chronology for the units of the Lake Mungo lunette (Section 2.4.2). These studies have demonstrated that the quartz-rich sediments from the region are well suited to OSL dating, exhibiting bright, rapidly decaying signals typical of highly sensitive quartz dominated by the fast component, a high proportion of luminescent grains relative to sediments from other environments, and negligible IRSL signals (Fitzsimmons et al. 2014).

Many factors of Australian sediments are favourable for OSL dating. Australian sediments often have a long transport history, with sediments from the Lake Eyre Catchment (which covers one sixth of the continent) being derived from bedrock as far as 1000 km distant (Pell et al. 2000). The OSL component composition of quartz grains appears to depend on transportation distance, with grains with longer transport histories and thus multiple cycles of exposure and burial, being more dominated by the fast OSL component (Pietsch et al. 2008; Fitzsimmons 2011; Jeong & Choi 2012). OSL preferentially samples electrons held in light sensitive traps. These traps are those most likely to have been emptied by exposure to sunlight (bleached) during sediment transport, thus being effectively re-set at the time of deposition (Murray & Roberts 1997). Aeolian sediments in particular have abundant opportunity for bleaching and sensitisation. Fitzsimmons et al. (2010) found aeolian material from Lake George in New South Wales to be an order of magnitude more sensitive than sediments from other depositional contexts within the same catchment. Clean Australian aeolian quartz is expected to be well bleached (Olley et al. 2006, Bowler et al. 2003), so a single population from a single depositional event should therefore be expected to produce narrow, unskewed, normal D_e distributions.

7.2. OSL dating methods

7.2.1. OSL Sampling

Fifty-eight OSL samples were collected from numerous locations along the lunette. Most of the OSL samples were collected at or near transect sites (Section 3.3.3) and where possible, from near the top and base of each stratigraphic layer. Stainless steel tubes, 10 cm long with a diameter of 3.5 cm, were hammered into vertical sections of sediment using a steel anvil and metal mallet. Opaque rubber caps were placed onto the ends of the tubes, and the entire tube covered in adhesive-tape and labelled. A metal hand auger was used to remove further sediment from the sample hole, making it at least 30 cm deep. Approximately 10-15 g of the excavated sediment was placed in a sample bag, taped closed and labelled with the same number as the OSL sample tube. A gamma spectrometer was used to measure gamma radiation levels inside the sample hole.

7.2.2. Sample Preparation

Sand samples were opened in a dark laboratory under yellow-orange sodium vapour lamps and filtered red light. Two to three centimetres from the ends of each sample tube were weighed and placed into a plastic container (wet ends). The central 4-6 cm of the sediment used for D_e estimation was transferred to lightproof bags. These samples were prepared according to the protocol in Figure 7.7 with the aim of isolating pure quartz sand. This procedure was carried out under controlled red lighting and included clay and carbonate removal, wet sieving, organics removal, heavy mineral separation, HF etching and dry sieving as explained in greater detail below (Figure 7.7).

The accompanying loose-sediment sample was also placed into a plastic container, weighed and labelled (H_2O sample). The wet ends and H_2O samples were oven dried at 121ºC and re-weighed to ascertain the moisture content for dose rate determination (Section 7.2.6). Following drying, the wet ends were milled in a tungsten carbide mill and sub-sampled using a cone and quartering technique. Sub-samples of 0.5-1 g were sent to *Genalysis*, Perth for U, Th (ICP-MS) and K (ICP-OES) content analysis.

The OSL samples were placed into beakers and submerged in distilled water. The fine (clay) component was removed by stirring and decanting. Carbonates were dissolved by placing the samples in excess 10% HCl and stirred every 4-12 hours until effervescence ceased to occur upon the addition of more HCl. The remaining HCl was decanted and the sample rinsed four times with distilled water. Wet sieving was undertaken using a series of sieves with mesh sizes of 300, 210, 180, 125 and 90 μm. The size fractions of 90-125 μm, 125-180 μm, 180-210 μm, 210-300 μm and >300 μm were placed into open ziplock bags in a 60°C oven to dry. The modal size fraction was selected for dating and placed into 30% H_2O_2 for 24 hours to dissolve organic matter, then rinsed in distilled water four times and air dried at 40ºC.

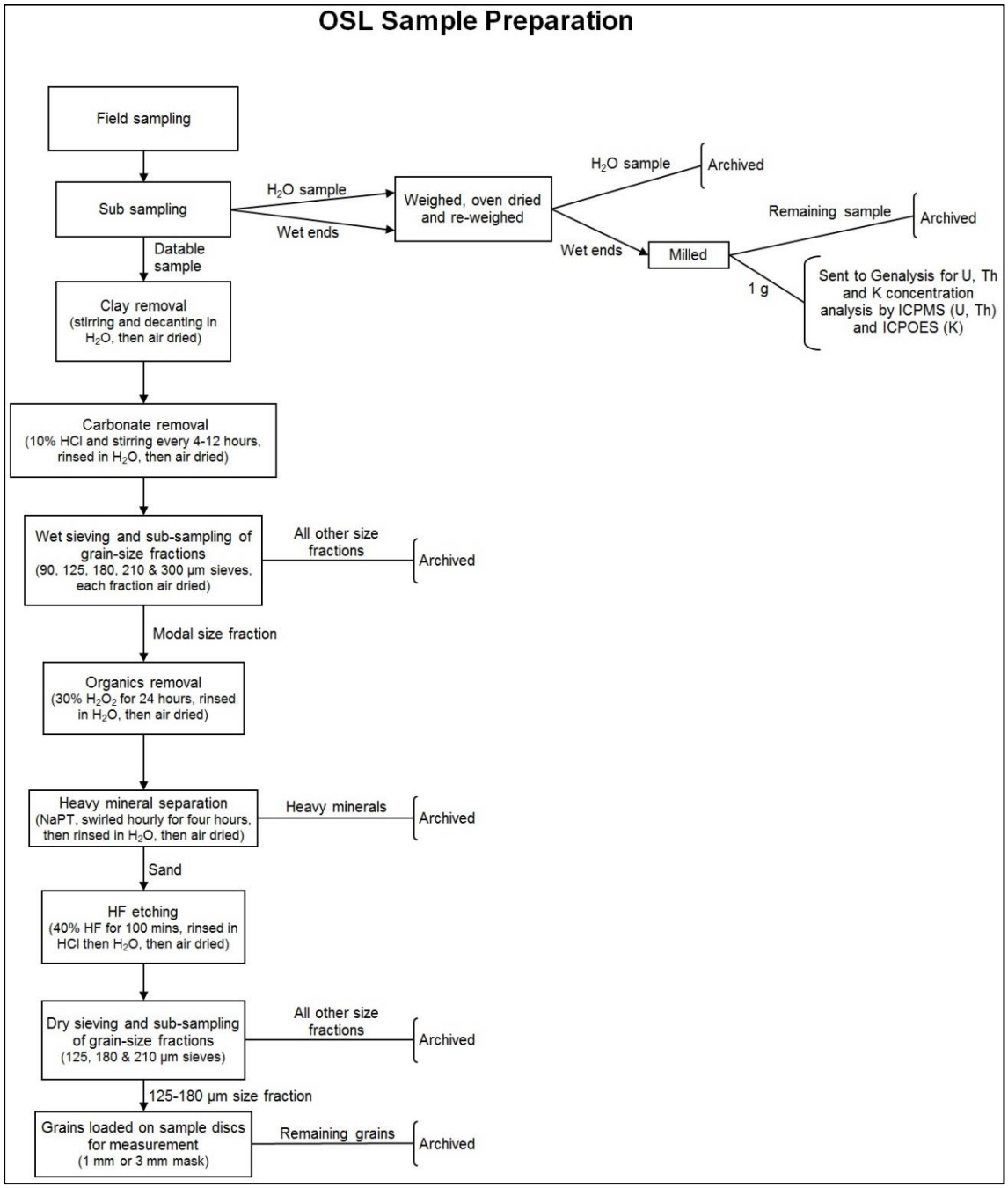

Figure 7.7. Flow chart of OSL sample preparation procedure. See text for further details.

Heavy minerals were separated from the quartz-rich sand using a separatory flask. Dry datable sample was added to 100-150 ml of sodium polytungstate (NaPT; with a specific gravity of 2.68 ± 0.02 g/cm^3). The flask was swirled hourly for four hours to facilitate separation, and heavy minerals were flushed from the base. These were collected in the filter paper, dried and archived. The remaining sample was transferred into a beaker, rinsed four times in distilled water to remove the NaPT, and dried in a 40°C oven.

Three grams of the dry sample was etched in 40% HF for 100 minutes, rinsed in HCl to remove fluoride salts, further rinsed multiple times in water, then air-dried. Grain diameters of the original quartz were reduced during etching, thus the resulting purified quartz was dry sieved into <125 μm, 125-180 μm and 180–210 μm size fractions, placed into light-proof containers and double bagged in light-proof bags.

The final 125-180 μm size fraction was used for OSL measurement for all aliquots. Single layers of grains were mounted onto 9.8 mm diameter stainless steel discs using a spray-on silica oil adhesive, applied through masks of varying diameter. A 3 mm diameter mask (approx. 200 grains) was used for all routine initial estimates of equivalent dose (referred to here as DeLIA for D_e Luminescence Initial Estimate; Schwenninger et al. 2007). Further measurements for D_e, pre-heat plateau (6.1.2.3) and dose recovery (6.1.3.3) tests made use of smaller aliquots comprising about 20 grains (Figure 7.8), mounted using a 1 mm diameter mask.

7.2.3. Sample measurement

7.2.3.1. Equipment

Measurements were carried out on one of two Risø instruments: a TL-DA-15 (Risø A) and a TL-DA-12 (Risø B). The system set up was similar to that described in Fitzsimmons (2007) and Bøtter-Jensen et al. (2000) and a schematic diagram is shown in Figure 7.9. In both systems, samples were stimulated with blue-green LED arrays, providing approximately 16-20 mW/cm^2 with a peak-stimulation wavelength of 470 Δ 20 nm. This light was filtered using Schott GG420 long pass filters to remove wavelengths below 420 nm. TEMPT-484 IR diodes emitting 800 Δ 80 nm provided IRSL stimulation. Coated U340 optical filters allowed

the transmission of a UV emission band at 240-360 nm. EMI 9235 QA photomultiplier tubes converted photons emitted from the sample to an electric signal. Luminescence counts from the photomultiplier were integrated over 0.1 s intervals). A calibrated $^{90}Sr/^{90}Y$ radiation source was used to irradiate samples. The dose rate of the radiation source in Risø B is five times slower than that of Risø A. As such, it is useful for giving smaller irradiation doses and was used primarily for samples with smaller expected dose values (<20 Gy) due to younger expected ages.

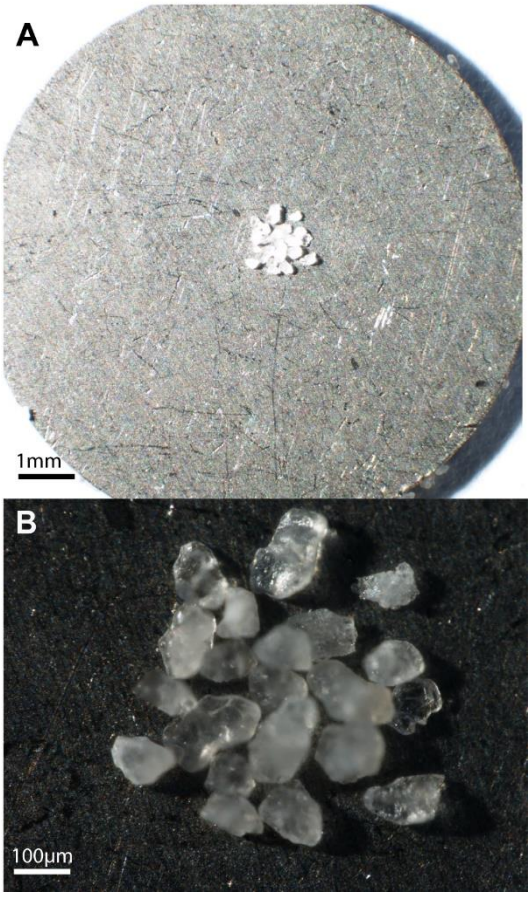

Figure 7.8. 125-180 µm sand grains from sample K2133, mounted using the 1 mm diameter mask.

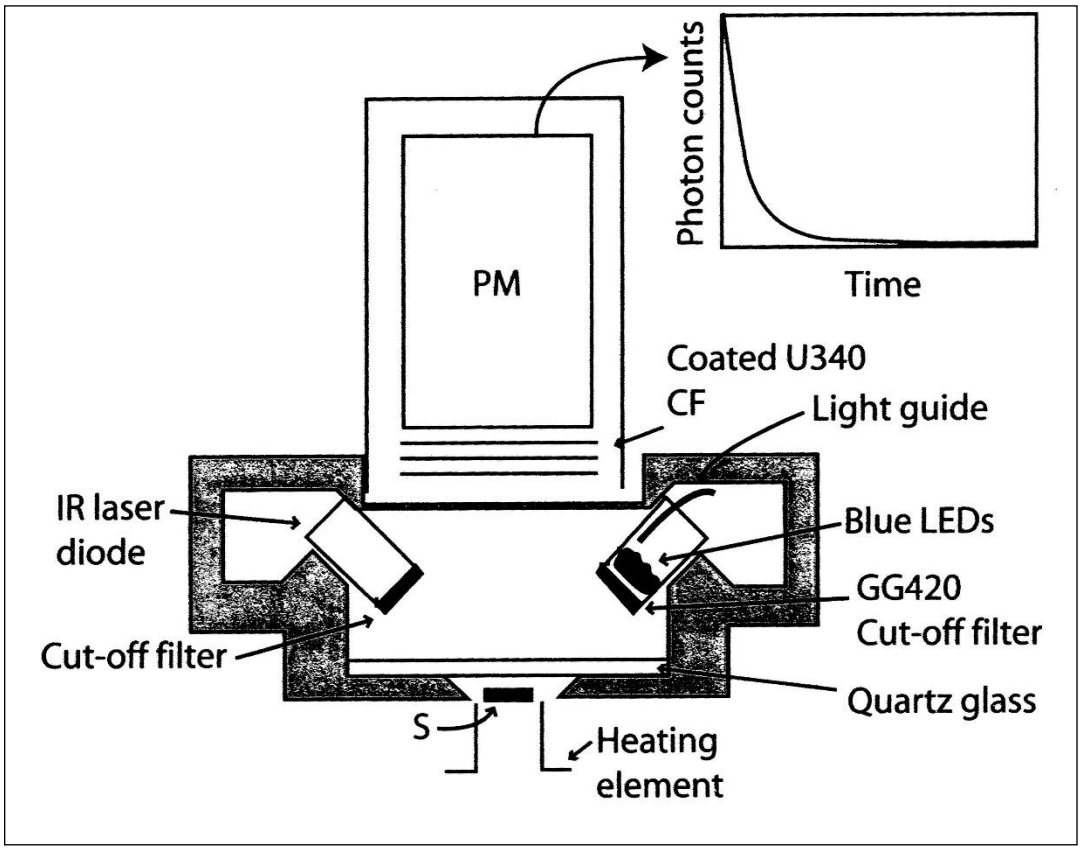

Figure 7.9. OSL instrumentation. Optical stimulation is provided by blue-green LEDs directed onto the sample (S). Luminescence is emitted from S (the sample) and passed through colour filters (CF) into the photomultiplier (PM), which in turn produces an output of photon counts against time. (Fitzsimmons 2007, her Fig. 5.2, adapted from Bøtter-Jensen et al. 2000.)

7.2.3.2. The SAR Protocol

The initial DeLIA measurement is conducted to evaluate an approximate D_e value using an abbreviated SAR protocol comprising four irradiation dose steps of 3, 10, 30 and 100 Gy. Following analysis of the DeLIA results, a full SAR protocol was run for 18 aliquots of each sample using the schema summarised in Table 7.1 (Murray & Wintle 2003; Wintle & Murray 2006). Each protocol included four regeneration steps bracketing the approximate D_e identified during the DeLIA assessment, followed a 0 Gy regeneration step (to monitor recuperation) and finally a repeat of the first regeneration dose to check recycling of the OSL signal. As a precaution, IR stimulation at 50°C preceded each OSL measurement to release any potential signals from feldspars not fully removed during HF etching. Before each OSL

measurement, samples were pre-heated to a temperature identified during pre-heat plateau tests.

Table 7.1. Summary of the SAR protocol

Step	Treatment	Observation
1	Natural or regenerative dose, D_i*	-
2	Pre-heat (PH_1) for 10s#	-
3	IR stimulation and IRSL measurement	I_i£
4	OSL stimulation and OSL measurement at 125°C	L_i**
5	Test dose, D_T##	-
6	Pre-heat (PH_2) for 10s#	-
7	IR stimulation and IRSL measurement	R_i£
8	OSL stimulation at 125°C	T_i££

Source: Modified from Murray & Wintle (2003; 2006)
* For the natural sample, i=1, D_i=0 Gy.
# PH_1 = 240°C, PH_2 = 220°C, determined using pre-heat plateau tests (Section 7.2.3.3).
£ I_i and R_i are IRSL signals.
** L_i is the OSL signal
D_T was a dose approximately 10-20% of the D_e as estimated from the DeLIA.
££ Ti is the OSL response to D_T.

7.2.3.3. Determining pre-heat temperature

The pre-heat temperatures used in steps two (preheat before the regenerative dose measurement) and six (preheat before the test dose measurement) were chosen based on measurement of pre-heat plateaus. Two samples were selected for pre-heat plateau tests, one with a low D_e (~5 Gy) and one with a higher D_e (~50 Gy). From the results of the DeLIA analyses, these were thought to be adequate to cover the range of D_es apparent across the Mulurulu sample set. Analyses were thus carried out on samples K2081 and K2129, using six pre-heat temperatures at 20ºC intervals ranging between 180-280ºC with two or three aliquots per temperature, respectively.

The results of the pre-heat plateau tests are shown in Figure 7.10. At 280ºC, K2129 gave an anomalously high D_e value for one aliquot, while at 260ºC, K2081 gave an anomalously low result. All of the aliquots for both samples showed recuperation values of less than 2% and recycling ratios close to unity. Although no clear plateau was detected in K2081, most preheat combinations yield acceptable results, and a high pre-heat temperature is desirable to ensure the sufficient release of electrons from unstable recombination centres (Murray & Wintle

2000), thus the more stringent preheating condition of 240ºC was chosen as the highest temperature that did not give anomalous results for samples in either dose range. In order to ensure removal of any potential ultra-fast component from the test dose, a stringent cut-heat temperature was desired, and was thus set at 220 ºC , 20ºC below the pre-heat temperature for the dose measurement, as recommended by Murray and Wintle (2003). In hindsight, this relatively high cut-heat temperature may have inadvertently contributed to the high recuperation rate seen in young samples in this study (discussed in Sections 7.2.4.2 and 7.4.4).

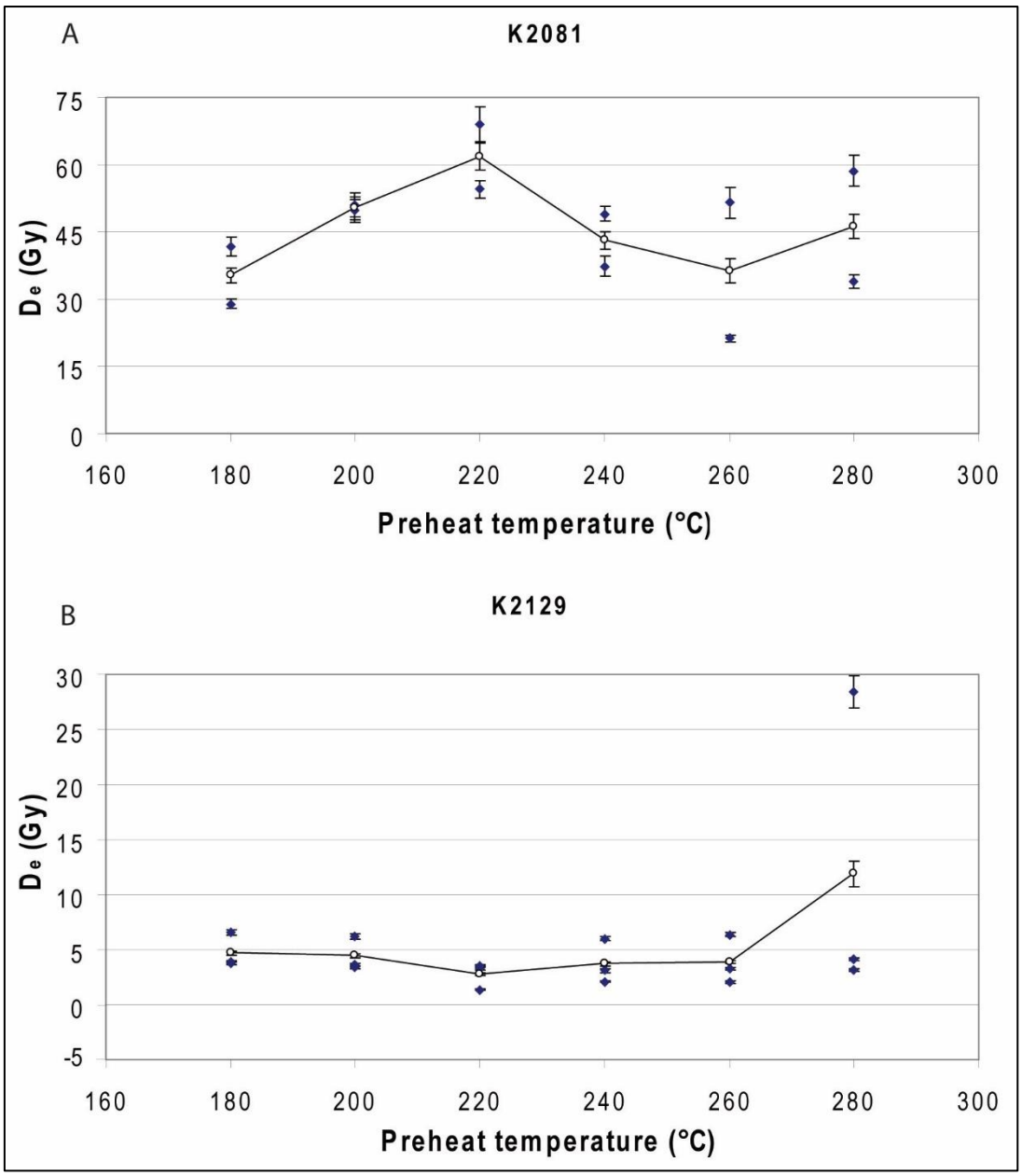

Figure 7.10. Pre-heat plateau tests on two samples with different natural D_e values.

7.2.3.4. Dose-recovery tests

Three samples in this study were subjected to dose recovery tests to assess their suitability for the SAR protocol. Samples were split into two sub-sets of aliquots, with one set bleached by natural sunlight for 7 hours and the other by laboratory stimulation with blue-green LEDs. They were then given a dose roughly equivalent to their natural dose followed by the SAR protocol. Dose recovery is expressed as a ratio between the apparent dose and known applied laboratory dose. The results are shown Table 7.2. and Figure 7.11.

Dose recovery was within 2% for five of the six sub-samples and within 6% for the laboratory bleach of K2129. Figure 7.11 shows the apparent dose distributions for all six sub-samples, all showing near-Gaussian distributions.The degree of dose recovery does not appear to be related to the method of bleaching. It is unknown why the laboratory bleach sample of K2129 exhibited a lower dose recovery, at 6% from unity. All of the dose recovery aliquots showed recuperation values of less than 2% and recycling ratios close to unity, indicating that the grains were otherwise well suited to the SAR protocol measurements. It is likely that the larger relative deviation from unity is the result of a small absolute variation in dose recovery in such a low dose sample.

Murray and Wintle (2003) suggested that while dose recovery tests do not provide a full assessment of sample behaviour, they do provide a useful test to indicate suitability of samples for the SAR protocol. The results from the tests in this study are more consistent than those presented by Murray & Wintle (2003) and it is proposed that the Mulurulu samples are generally well suited to the SAR protocol, since five of the six samples tested showed evidence of good dose recovery.

Table 7.2. Results from dose recovery tests

Sample Code	Bleaching method	Applied dose (Gy)	Apparent Dose (Gy)	Dose recovery ratio
K2116	Natural	48.38	48.25 ± 0.80	1.00 ± 0.02
	Laboratory	48.38	47.54 ± 0.66	0.98 ± 0.01
K2121	Natural	17.63	17.59 ± 0.50	1.00 ± 0.03
	Laboratory	19.00	18.85 ± 0.28	0.99 ± 0.01
K2129	Natural	4.41	4.36 ± 0.15	0.99 ± 0.04
	Laboratory	4.75	5.03 ± 0.11	1.06 ± 0.02

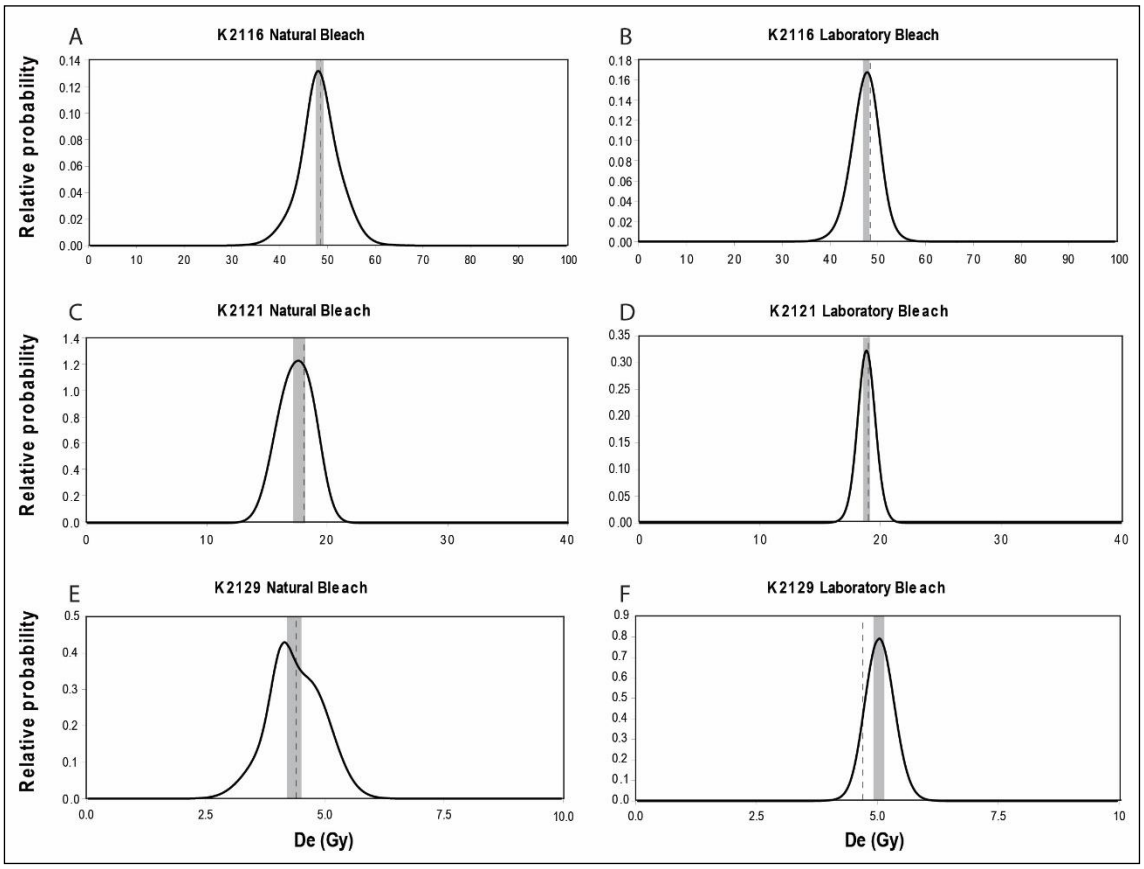

Figure 7.11. Probability distribution function results of dose recovery tests. The shaded area represents the Central Age Model D_e for the apparent dose and the dashed line is the laboratory administered dose.

7.2.4. Assessing the OSL performance

7.2.4.1. Recycling Ratios

In order to check for appropriate sensitivity correction and reproducibility in dose-response, recycling ratios were measured by including a repeat of the first regenerative dose at the end of the SAR protocol (Section 7.2.3.2). Aliquots in which the two measurements of the regenerated dose varied by more 10% were rejected (Section 7.2.5.1). The average recycling ratio for all accepted aliquots is 1.00 ± 0.08. The variability reflected in the standard deviation mainly occurs in the samples run on Risø B. The average recycling ratio for Risø A aliquots is 1.01 ± 0.05, while for Risø B it is 1.00 ± 0.10. Not only do Risø B samples show twice the standard deviation in accepted aliquots, it also had a 12 times higher rejection rate based on this criteria (ten rejected aliquots with poor recycling on Risø A and 120 rejected aliquots

with poor recycling on Risø B). This suggests that the sensitivity correction applied based on the test dose results in the SAR protocol was not always adequate for these samples. This may be due to the very young age of the majority of samples run on Risø B, many of which had very low D_e values, often <0.02 Gy. The test dose value for each sample was intended to be approximately 10-20% of the D_e as estimated from the DeLIA. In such young samples, it would only take one or more bright grains within the population of young grains on the 3 mm mask used in the DeLIAs to give erroneously high results, causing an inappropriately high test dose to be used in the full SAR runs. Also, the first and replicate regenerative dose steps used on the young samples were very low, and a small absolute variation in L_x/T_x could result in a high relative difference.

7.2.4.2. Recuperation

Recuperation was measured by including a zero dose step and OSL measurement within the SAR protocol (Section 7.2.3.2). Recuperation is expressed as the ratio of the sensitivity-corrected intensity of the zero dose and natural OSL signals. The recuperation ratios for each sample are given in Appendix G.1. Figure 7.12 shows the recuperation plotted against D_e for all accepted aliquots. Although most aliquots yielded ratios of less than 4%, there is a clear relationship of higher ratios in aliquots with lower D_e. Where low D_e values were expected, samples were run preferentially on Risø B. It is not known whether the higher ratios at low D_e values are due to an instrumental issue with Risø B, or related specifically to young samples. It seems likely that the relatively high cut-heat (220°C, Section 7.2.3.3) may have contributed to the high recuperation rates for samples run on Risø B. The majority of recuperation ratios greater than 10% were in aliquots yielding D_e values of less than 0.02 Gy. The size of the test dose for these samples was very small, resulting in noisy decay curves for both the natural and test dose measurements, leading to high uncertainties in the recuperation ratios. Additionally, any signal arising from the zero dose step will represent a significant fraction of the natural OSL in these low D_e samples.

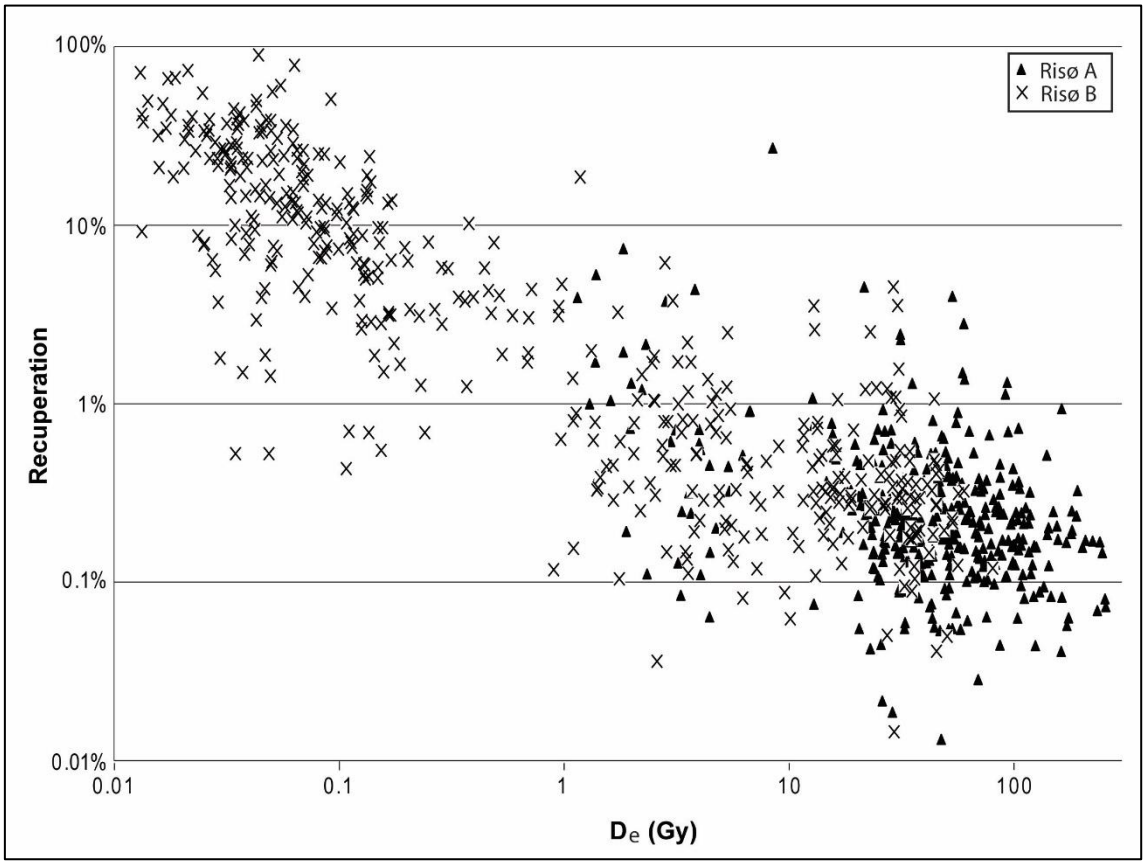

Figure 7.12. Plot of recuperation against D_e for each aliquot. Recuperation is calculated as the zero dose sensitivity corrected OSL signal expressed as a percentage of the sensitivity corrected natural signal. Note the logarithmic scale on both axes.

7.2.5. Estimation of D_e

Each aliquot yielded a dose-response curve from which the natural D_e can be interpolated (Murray & Wintle 2003). This curve is derived from the sensitivity-corrected OSL decay signal from the natural and regenerated doses, with the assumption that the OSL signal arises solely from the most easily bleached fast component (Singarayer & Bailey 2003). The intensity of each OSL signal was determined using *Luminescence Analyst v3.24* software (Duller 2007), by integrating the signal from the first 10 channels (1 second) and subtracting channels 11-20 as background. D_e values were calculated only for aliquots that were not rejected after applying a series of rejection criteria. D_e values and their errors were calculated for each accepted aliquot, resulting in a dose distribution for each sample. These distributions were graphically displayed using probability-density plots in an *Excel* spreadsheet and radial plots using *Radialplotter v8.3.* A single D_e value for each sample was calculated within the

Radialplotter v8.3 software, usually via a central age model (Vermeesh 2009; Galbraith et al. 1999). Not all accepted aliquots were always included in the CAM calculation, depending on the nature of the dose distribution and stratigraphic context of the sample.

7.2.5.1. Aliquot rejection process

.In an attempt to ensure good signals and reliable dose-response curves, five rejection criteria were employed:

1. Saturated aliquots and aliquots where the natural signal was out of range of the highest regeneration dose in the dose-response curve. (Here, only minimum dose estimates are possible).
2. Aliquots in which the recycled dose signal was >10% different from the first dose step signal
3. Aliquots where the test dose to the natural OSL signal (T_N) was within the 3σ error of the background signal.
4. Aliquots in which the error in test dose was >30%
5. Aliquots in which the error in D_e was >30%

An additional criterion for rejection was initially tested. An attempt was made to reject aliquots for which the medium or slow components were not fully bleached (Bailey 2000). This was determined by analysing D_e using two different integrations for each aliquot, using the fast channels 1-5 and slower channels 11-15, respectively. Channels 30-100 were used for background. It was proposed that aliquots for which the difference between the two D_e values was greater than the combined 2σ error, would be rejected on the basis of including a slow component. This technique led to rejection of 203 of the 1044 aliquots (almost 20%). It was evident, however, that removing these aliquots from the CAM calculations did not improve the quality of the data. Most revealingly, it did not decrease the CAM values for the samples (as would be expected if these aliquots really did include incompletely bleached slow or medium components). Therefore, this criterion was removed from the routine rejection criteria.

The majority of sample aliquots yielded OSL signals with rapid decay to background within 10 s and mostly within 3 s. Figure 7.13A-C gives some examples of such decay curves at varying intensities. Figure 7.13D shows an unacceptable decay curve, in which the OSL signal is less than three times the background.

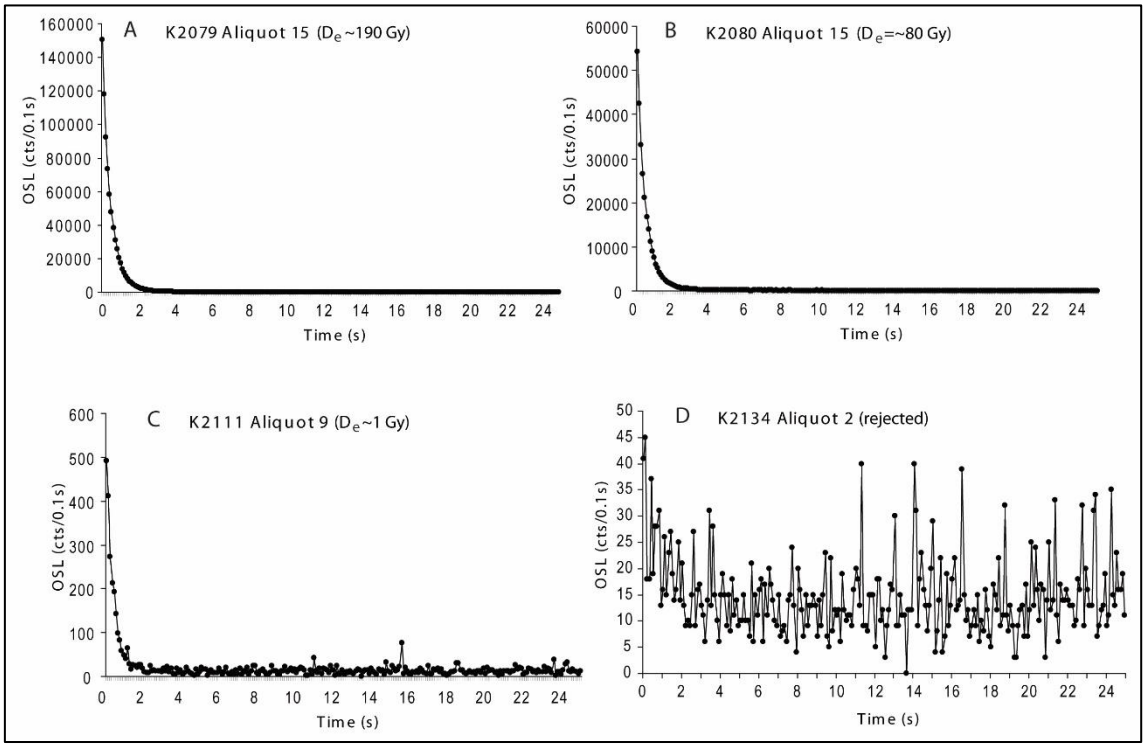

Figure 7.13. Some examples of decay curves. Note the differing scales on the y-axis.

A total of 221 of the 1044 aliquots (21.2%) were rejected based on the listed criteria. Table 7.3 indicates the number and percentages of aliquots rejected for each rejection criterion, grouped by Risø reader. They have been grouped this way because generally younger samples were run on Risø B, while older samples were run on Risø A and different types of rejections can be expected for samples of different ages, such as low signal to background ratio or natural signal being out of range of the highest dose step. Some aliquots may have had multiple reasons for rejection, but samples were rejected sequentially, i.e. aliquots rejected due to criterion 1 were not assessed for criteria 2-5 etc.

Table 7.3. Summary of number of samples rejected and reasons for rejection.

Rejection Criterion	Risø A		Risø B		Total Rejected
	no. rejected	% of Risø A rejections	no. rejected	% of Risø B rejections	
1. out of range	26	70.3%	3	1.63%	**29**
2. recycling ratio (>10%)	10	27.0%	120	65.2%	**130**
3. <3σ above background	0	0.00%	7	3.80%	**7**
4. σTd >30%	1	2.70%	54	29.4%	**55**
5. σD_e >30%	0	0.00%	0	0.00%	**0**
Total rejected	**37**		**184**		**221**
total accepted	**395**		**428**		**823**
% rejected	**8.56%**		**30.07%**		**21.17%**

The first criterion for rejection, due to signals greater than the highest regenerative dose in the dose-response curve, led to 29 rejections, with most (26) occurring in Risø A samples. They account for almost three quarters (70.3%) of all Risø A rejections. The most common reason for rejection in Risø B samples was poor recycling ratio with 120 rejections, plus a further ten in Risø A. Poor signal to background ratio was not apparent in any Risø A samples, but led to seven rejections in Risø B, while error in the test dose led to one rejection in Risø A and 54 in Risø B. Error in D_e did not lead to any rejections. This does not mean that no samples had a D_e error greater than 30%, as this was the last criterion applied, so there may have been some rejected in the previous rejection criteria.

Overall, there were many more rejections of Risø B aliquots (30.1%) than Risø A aliquots (8.6%). These aliquots were particularly susceptible to poor recycling ratios and high errors in the test dose (and possibly also errors in D_e). These young samples were also disproportionately affected by other intrinsic factors, such as overdispersion and recuperation (Section 7.2.4.2).

It is necessary to reject aliquots based on these types of criteria because they may give unreliable D_e values. Figure 7.15 shows examples of an acceptable dose-response (A) and two rejected curves; a saturated curve (B), and a nonsensical curve from a sample with poor signal to background ratio (C). Dose response curve generation and fitting is discussed further in Sections 7.1.2 and 7.2.5.2.

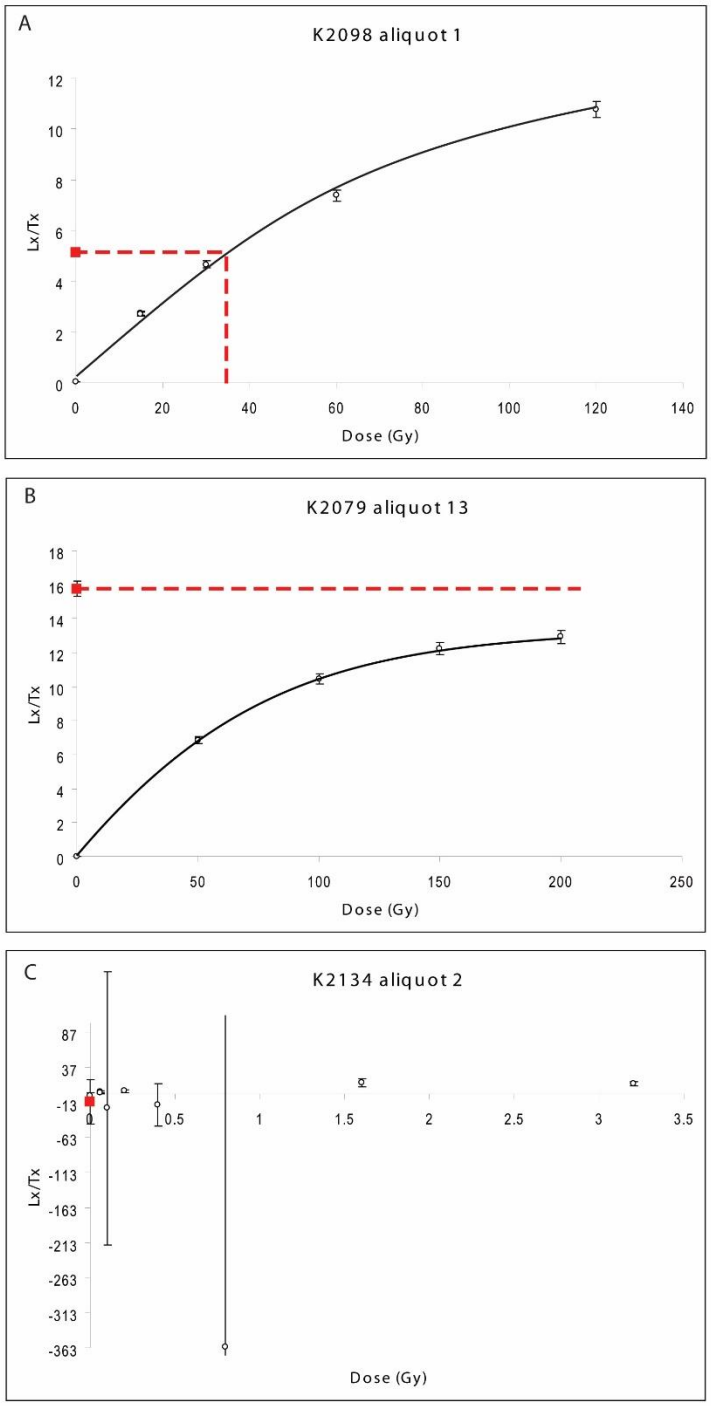

Figure 7.14. Dose-response curves. The red square represents the natural luminescence of the sample. A: An acceptable dose-response curve. B: A curve in which the natural signal is greater than the highest regenerative dose in the dose-response curve. C: A nonsensical dose-response curve from the aliquot in D, rejected due to the poor signal to background ratio.

7.2.5.2. Calculation of error on D_e

The uncertainty associated with the D_e is composed of random error and a systematic error.

The random error applied to each aliquot is derived from two sources: the uncertainty associated with the OSL measurements, which in turn has two components, plus uncertainty associated with a dose response curve fitting error.

Galbraith (2002) provides an equation (his equation 3) to calculate the random uncertainty for each OSL measurement (L_N, T_N, L_X and $T_{X)}$ associated with photon counting statistics. This error is added in quadrature to an instrumental error to produce the uncertainty on L_N/T_N and L_X/T_X. An instrumental error of 1.6% was used for all measurements made on both Risø readers used in this study, based on measurements previously made for both Risø A and Risø B.

The dose response curve fitting error is based on the average deviation between the measured value and that predicted by the fit to the dose response curve. This is known as the 'fitting residual'. The square root of the averaged sum of the squared fitting residuals creates an error that is added in quadrature to the error in L_X/T_X (and L_N/T_N) described above. The upper and lower limits of L_N/T_N is then interpolated on to the dose response curve to transform this combined error in to the 1σ limits on the D_e estimate in Gy (Duller 2007).

The systematic error consists of a 2% uncertainty added in quadrature to the random error, in the final D_e estimate for each sample, to account for uncertainty in the calibration of the beta source in the Risø reader.

7.2.5.3. Dose Distributions and component selection

The unrejected aliquots provided a range of D_e values for each sample. These were expressed as PD plots, using *Microsoft excel* and as radial plots, using *RadialPlotter v8.3* to identify patterns of mixing or partial bleaching (Section 7.1). Unfortunately the functionality for *RadialPlotter to* export to .pdf was not working, so all radialplots were saved as .png files, resulting in lower resolution raster graphics. These graphical displays were used in conjunction with stratigraphic and sedimentological information to interpret the D_e

distributions. Where the radial plots identified a single age component, with most aliquots falling within the 2σ range on the radial plot, a central age model (Galbraith et al. 1999) was applied to all aliquots, using the central age calculation functionality within *Radialplotter*. Individual outliers were removed when one or two aliquots were substantially different to the primary population used for CAM calculation, and in mixed samples, to the extent possible with multi-grain aliquots, the appropriate component for CAM calculation was selected based on rationale provided by the stratigraphic context of the sample. A discussion of each of the 58 samples, including the rationale for each outlier removal, is described in detail in Section 7.3.1.

7.2.6. Estimation of dose rate

A number of measurements were combined to derive the overall dose rate estimation for each sample, including external gamma dose, U, Th and K concentrations in the sample sediments and cosmic dose calculations. Corrections to dose rate were applied based on beta attenuation factors and estimation of historical moisture content. Numerical values for all dose rate components are shown in Appendix G2. The error on the dose rate was calculated by summing in quadrature the errors for all dose rate components, taking in to account a range of age uncertainties detailed in Appendix G3.

A portable sodium-iodide gamma spectrometer was used to determine the *in situ* gamma ray contribution. The gamma probe was inserted into the hole from which the OSL sample was collected, deepened to at least 30 cm to accommodate the probe, and gamma counts were recorded for a 20 minute period. The gamma spectrometer was calibrated using the "Oxford Blocks" (Rhodes and Schwenninger 2007). A background measurement was carried out while the probe was immersed in water at Yerrabi Pond in Gungahlin, ACT, with counts recorded for a period of 20 minutes. The dose rate was calculated in *Microsoft Excel*, using the 'threshold' technique of Murray (1981) updated by Mercier and Falguères (2007). The gamma count error was determined by calculating the sum of the measurement counts minus the sum of the background counts, plus 0.5, and also the square root of the sum of measurement counts plus the sum of background counts. The latter was divided by the

former, and the result multiplied by the dose rate for the gamma measurement to arrive at the measurement uncertainty

K, Th and U concentrations were measured in the sediments collected along with the OSL sample, by ICP--OES (K) or ICP-MS (Th and U) at *Genalysis Laboratories*, in Perth. These concentration values were then converted to dose rates according to the conversion tables of Guerin et al. (2011). A standard fractional error of 0.05 was applied to these calculations.

The cosmic dose rate was calculated using the procedures described by Prescott & Hutton (1994) taking in to account the depth of burial, the density of the overlying material (assumed to be an average of 1.9±0.10 g/cm^3) and the altitude, latitude and longitude of the sampling site. As the depth of overburden will have changed over time, an estimated pre-erosion depth, subtracting the uppermost, very young Unit E, was calculated for samples from Units A-D. For Unit E samples, current depth was used. The altitude was measured at each sampling location, while latitude and longitude were approximated to -33 and 143, respectively.

Beta attenuation was calculated for U, Th and K contributions to the beta dose rate, using the beta attenuation factors of Mejdahl (1979) for grains in the 125 to180 µm size range. A standard fractional error of 0.05 was applied to these calculations.

The current water content was measured in sediments collected along with each OSL sample. An error of 30-60% was applied depending on the nature of the sample material (i.e. sand or clay). The historical water content (WF) was estimated as the current water content divided by, 1 minus the current water content. Attenuation factors were applied using the correction factors outlined in Aitken (1985) and taken from Zimmermann (1971).

7.2.7. OSL age estimation

Ages were calculated using the age equation ([6]; Section 6.2.1) in *Microsoft excel*. This simply divides the D_e of each sample by the dose rate of each sample, each calculated as described in Sections 7.2.5 and 7.2.6. To calculate the uncertainty on the age, first the D_e error (including the 2% systematic error) was multiplied by $dAge/dD_e$ (one divided by dose rate) and the dose rate error was multiplied by dAge/dDR (D_e divided by the square of the dose

rate). The results were added together in quadrature to determine the overall error for each age determination.

In order to provide age ranges for the dated depositional units, Bayesian statistics were applied using *OxCal 4.2*, (Bronk Ramsey 2009a). The model methodology was the same as described for the radiocarbon analyses (Section 5.2). As described by (Rhodes et al. 2003), the application of Bayesian methods to OSL is not straightforward, as the age uncertainties on different OSL samples are not fully independent. Before entering the age estimates in to *OxCal*, the systematic error associated with the beta source was stripped out of the uncertainty calculation (i.e. ages were recalculated as above, but using the D_e error provided by the CAM calculation in *Analyst*, without incorporating this 2% systematic error) and ages were converted in to years before 1950 by multiplying the ka age by 1000, then subtracting 60 years. Prior outlier probability was applied as for radiocarbon dates, with six samples given null probability due to being Holocene in age (Appendix E). Additionally, one sample, K2091, was given a prior outlier probability of 0.5, due to a lack of confidence in this OSL age due to a high degree of sediment mixing (Appendix H.5). The *OxCal 4.2* code and output tables are available in Appendix E. Note that the output tables are generated directly from OxCal and the systematic error has not been recombined with the age uncertainties calculated by the software. All dates being compared in the analysis were measured at the same laboratory, so the impact of removing the systematic error should be minimal. Also, for the purposes of this research, the Bayesian analysis is used primarily as a visualisation aide, with regard the broad timing of deposition of the stratigraphic units at Lake Mulurulu.

7.3. OSL dating results

Table 7.4 shows the dose rate ($\dot{D}$), equivalent dose (D_e) and calculated age for each sample. The notes column includes factors that should be considered when determining the reliability of the age estimate, such as high overdispersion, high recuperation or few aliquots. Values used to calculate dose rate are presented in Appendices G.2 and G.3. The rationale for determining the D_e results are provided for each sample in Appendix H and the results for each unit are discussed in Section 7.3.1, below.

Table 7.4. OSL results for all samples

Sample	Site	Unit	Thin section	Ḋ (Gy/ka)	Ḋ error	D_e (Gy)	D_e error	Age (ka)	Age error	n	Risø	Notes
K2079	PR01	A	TS143	1.18	0.07	127.00	19.17	107.32	17.37	14	A	**
K2080	PR01	A	TS144	1.21	0.07	71.30	2.71	58.95	3.94	18	A	
K2081	PR01	B		1.28	0.06	54.20	3.38	42.50	3.27	18	A	*
K2082	PR01	D	TS145	0.97	0.04	16.97	0.90	17.57	1.16	18	A	
K2083	PR01	E		0.70	0.03	0.13	0.03	0.18	0.04	11	B	** ^
K2084	PR01	D	TS145	0.65	0.03	3.84	0.35	5.92	0.59	18	A	*
K2085	PR01	D	TS146	0.88	0.06	0.16	0.01	0.18	0.02	16	B	
K2086	PR01	E	TS146	0.62	0.03	0.10	0.03	0.16	0.04	11	B	**
K2087	PR01	E		0.59	0.02	0.04	0.01	0.07	0.01	8	B	** ^
K2088	PR01			1.27	0.06	0.11	0.02	0.09	0.01	6	B	* #
K2089	PR04	A	TS142	1.26	0.06	n/a	n/a	n/a	n/a	0	A	#
K2090	PR04	A	TS142	1.25	0.07	137.80	10.28	110.21	10.03	17	A	*
K2091	PR04	B	TS141	1.10	0.05	89.10	5.40	81.33	6.07	18	A	*
K2092	PR04	B	TS141	0.97	0.03	50.20	2.15	51.61	2.82	18	A	
K2093	PR04	C	TS140	2.06	0.11	77.50	3.29	37.58	2.59	18	A	
K2094	PR04	B	TS139	0.72	0.03	38.90	2.52	54.31	4.16	17	A	*
K2095	PR04	E	TS138	0.81	0.04	0.06	0.01	0.07	0.01	10	B	* ^
K2096	PR04	E	TS138	0.74	0.07	0.05	0.01	0.07	0.01	11	B	* ^
K2097	PR04			1.16	0.05	2.49	0.61	2.15	1.29	15	B	**
K2098	PR02	B		0.99	0.05	31.90	1.36	32.38	2.11	18	B	
K2099	PR02	B		0.72	0.03	33.60	1.55	46.57	3.41	18	B	
K2100	PR02	B	TS125	0.83	0.04	49.50	2.41	59.79	2.91	18	A	
K2101	PR02	E	TS123	0.63	0.03	0.19	0.11	0.30	0.33	7	B	** ^ #
K2102	PR02			0.83	0.04	4.23	0.49	5.12	0.59	18	B	*
K2103	PR02	E		0.54	0.05	0.03	0.01	0.05	0.01	16	B	** ^
K2104	PR02	E	TS124	0.58	0.02	0.03	0.00	0.05	0.01	9	B	* ^ #
K2105	PR05	E		1.31	0.24	0.05	0.00	0.04	0.01	11	B	^
K2106	PR05	E		0.89	0.05	0.03	0.01	0.04	0.01	4	B	* ^ #
K2107	PR05	E		0.97	0.05	0.03	0.00	0.03	0.02	9	B	^ #
K2108	PR05	E		0.77	0.04	0.28	0.12	0.36	0.16	9	B	** #
K2109	PR05	E		0.72	0.03	0.12	0.05	0.16	0.07	8	B	** #
K2110	PR05	E	TS129	0.94	0.05	0.12	0.01	0.13	0.05	10	B	^
K2111	PR05	D	TS130	0.81	0.04	1.02	0.14	1.26	1.10	15	B	**
K2112	PR05	D		0.80	0.04	18.10	1.25	22.49	2.35	18	B	*
K2113	PR05	D	TS131	0.97	0.04	30.70	1.17	31.66	2.27	18	A	
K2114	PR05	C	TS132	1.70	0.08	43.40	2.09	25.54	1.69	18	B	
K2115	PR05	B	TS133	0.77	0.03	26.37	1.08	34.43	1.95	18	A	
K2116	PR05	B		1.02	0.05	54.10	2.19	53.00	3.20	18	A	
K2117	PR05	D		0.88	0.03	24.70	1.12	28.14	1.63	17	A	
K2118	PR05	D		1.37	0.07	37.10	1.25	27.13	1.60	18	A	
K2119	PR05	D	TS134	1.10	0.05	26.73	0.96	24.33	1.43	18	A	
K2120	PR05	E	TS135	0.92	0.04	0.05	0.01	0.05	0.01	18	B	* ^
K2121	PR05	D	TS136	0.85	0.04	14.71	0.50	17.38	0.99	18	B	
K2122	PR05	E	TS137	0.77	0.03	0.09	0.01	0.11	0.01	9	B	* #
K2123	SL44	A		0.98	0.04	89.70	6.74	91.36	7.97	17	A	*
K2124	SL44	A	TS119	0.83	0.04	26.60	2.95	31.97	3.79	18	B	*

Sample	Site	Unit	Thin section	Ḋ (Gy/ka)	Ḋ error	D_e (Gy)	D_e error	Age (ka)	Age error	n	Risø	Notes
K2125	SL44	A		0.68	0.03	0.13	0.01	0.18	0.01	11	B	** ^
K2126	SL44	E		0.71	0.03	0.03	0.00	0.04	0.01	14	B	* ^
K2127	PR05			1.22	0.08	6.28	0.83	5.15	0.76	17	B	**
K2128	PR01			0.94	0.07	3.31	0.62	3.52	0.72	15	B	*
K2129	PR07		TS151	1.28	0.07	4.06	0.34	3.16	0.32	18	B	*
K2130	SL11	C	TS040	2.38	0.13	95.10	6.77	39.88	3.62	18	A	*
K2131	SL11	C	TS039	1.71	0.08	39.30	1.78	22.93	1.47	18	A	
K2132	SL11	C	TS041	1.11	0.07	30.90	1.53	27.81	2.28	17	A	
K2133	SL11	E	TS042	1.29	0.06	2.35	0.27	1.83	0.23	8	A	* #
K2134	SL11	E	TS043	1.16	0.06	0.14	0.01	0.12	0.01	4	B	#
K2135	SL11	C		2.15	0.11	2.74	0.44	1.27	0.22	18	A	**
K2136	SL11	E		1.07	0.08	0.08	0.01	0.08	0.01	10	B	

Notes:
*overdispersion >20%.
**overdispersion >50%.
^average recuperation for sample >10% (recuperation for each aliquot is shown in Appendix G1).
#n <10

7.3.1. OSL results for each unit

In this section, the OSL results are presented for each unit, discussing commonalities and differences in D_e distributions between samples, thus characterising the OSL response of the units. The D_e results for individual samples are systematically discussed in detail in Appendix H, where the dose distributions are presented as radial plots as well as PD plots, outliers are identified and the rationale for assessing the D_e for each sample is presented. While the samples are grouped by unit here, in the appendix the samples are grouped together by sampling site, as the stratigraphic context plays a large role in determining the D_e component most likely to relate to burial dose in the multi-component samples. Additionally, the context for each individual sample, including photographs of each sample collection location, plus their location on aerial photography, in the transects, and in the stratigraphic logs are also available in Appendix H. A Bayesian analysis is applied to the OSL age results to determine age ranges for each unit in Section 7.3.2.

7.3.1.1. Unit A

Seven samples from across three sites were collected from Unit A for OSL dating. The results are shown in Table 7.5 (and together with all other OSL dating results in Table 7.4). No result

could be determined for sample K2089, as all aliquots were rejected due to saturation. Samples K2124 and K2125 both show evidence of post-depositional mixing (see Section 7.4.1.2 and Appendix H.2) and are not representative of the depositional age of Unit A. The dose distributions for the remaining four samples from Unit A are shown in Figure 7.15.

Table 7.5. OSL results for Unit A (excerpt from Table 7.4).

Sample	Site	Unit	Thin section	Ḋ (Gy/ka)	Ḋ error	D_e (Gy)	D_e error	Age (ka)	Age error	n	Risø	Notes
K2079	PR01	A	TS143	1.18	0.07	127.00	19.17	107.32	17.37	14	A	**
K2080	PR01	A	TS144	1.21	0.07	71.30	2.71	58.95	3.94	18	A	
K2089	PR04	A	TS142	1.26	0.06	n/a	n/a	n/a	n/a	0	A	#
K2090	PR04	A	TS142	1.25	0.07	137.80	10.28	110.21	10.03	17	A	*
K2123	SL44	A		0.98	0.04	89.70	6.74	91.36	7.97	17	A	*
K2124	SL44	A	TS119	0.83	0.04	26.60	2.95	31.97	3.79	18	B	*
K2125	SL44	A		0.68	0.03	0.13	0.01	0.18	0.01	11	B	** ^

Notes:
*overdispersion >20%.
**overdispersion >50%.
^average recuperation for sample >10% (recuperation for each aliquot is shown in Appendix G.1).
#n <10

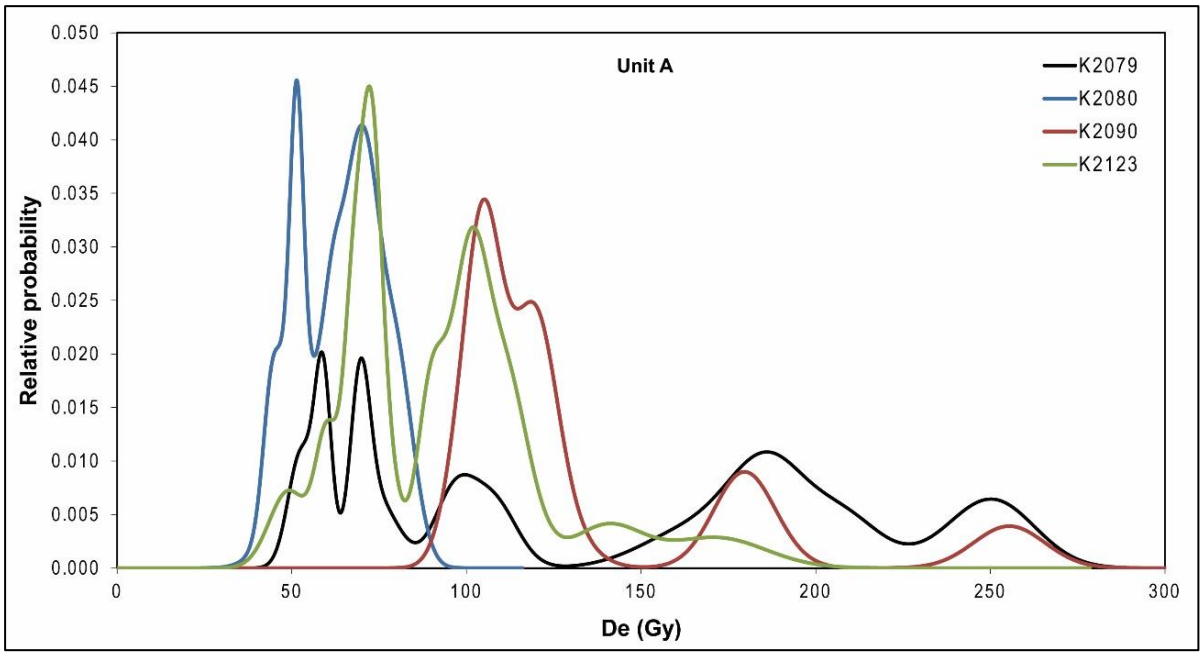

Figure 7.15. Probability density plots of D_e for accepted aliquots in Unit A samples. The dose distributions are discussed in more detail, including presentation of radial plots and rationale for identifying outliers, for each sample individually by sample site in Appendix H.

The four remaining samples provide broad D_e distributions with multiple peaks, all above 50 Gy and in some cases over 100 Gy. Even after removal of one outlying extremely young

aliquot (Appendix H.6) sample K2079 gives a particularly broad D_e range, with a multi-modal distribution ranging to from ~50-280 Gy. K2090 has a similarly long right tail. The multiple D_e populations (probably resulting from post-depositional mixing, see Section 7.4.1) and the fact that both of these samples had multiple aliquots rejected due to saturation (Appendix H.6 and H.5, respectively), means that the CAM ages >100 ka for these samples should be considered as minimum estimates only. Samples K2080 and K2123 both have bimodal distributions. The higher peak is considered to be most likely to relate to the true burial dose in K2080 (Section 7.4.1, Figure 7.24, Appendix H.6). There is no stratigraphic argument as to which of the population reflects the true depositional age in K2123 (Section 7.4.1, Figure 7.26, Appendix H.2), so the calculated age is based on a CAM applied to all aliquots. The reliable age estimates for Unit A range from ~60->110 ka (Table 7.5).

7.3.1.2. Unit B

Nine samples from across four sites were collected from Unit B for OSL dating. The results are shown in Table 7.6 (and together with all other OSL dating results in Table 7.4). Quartz from Unit B proved generally very well suited to OSL dating, with only one rejected aliquot (from K2094) across all Unit B samples.

Table 7.6. OSL results for Unit B (excerpt from Table 7.4).

Sample	Site	Unit	Thin section	Ḋ (Gy/ka)	Ḋ error	D_e (Gy)	D_e error	Age (ka)	Age error	n	Risø	Notes
K2081	PR01	B		1.28	0.06	54.20	3.38	42.50	3.27	18	A	*
K2091	PR04	B	TS141	1.10	0.05	89.10	5.40	81.33	6.07	18	A	*
K2092	PR04	B	TS141	0.97	0.03	50.20	2.15	51.61	2.82	18	A	
K2094	PR04	B	TS139	0.72	0.03	38.90	2.52	54.31	4.16	17	A	*
K2098	PR02	B		0.99	0.05	31.90	1.36	32.38	2.11	18	B	
K2099	PR02	B		0.72	0.03	33.60	1.55	46.57	3.41	18	B	
K2100	PR02	B	TS125	0.83	0.04	49.50	2.41	59.79	2.91	18	A	
K2115	PR05	B	TS133	0.77	0.03	26.37	1.08	34.43	1.95	18	A	
K2116	PR05	B		1.02	0.05	54.10	2.19	53.00	3.20	18	A	

Notes:
*overdispersion >20%.

The PD plots of dose distributions from Unit B samples are shown in Figure 7.16. Samples from PR02 (Figure 7.16A) all approach Gaussian distributions and have low overdispersion (Appendix H.1). Samples from PR04 were not so well behaved (Figure 7.16B), where Sample

K2092 is Gaussian, but K2091 and K2094 have multiple peaks suggesting sediment mixing (Section 7.4.1, Figure 7.26, Appendix H.5). K2091 in particular is unlikely to represent a true depositional dose (See Appendix H.5). Figure 7.16C shows the results for the other three Unit B samples, from PR01 and PR05. K2115 and K2116 provide Gaussian distributions with low overdispersion. K2081 is a fairly broad distribution, but the dispersion is only a little over 20% (Appendix H.6). The reliable ageestimates for Unit B range from ~32-~60 ka (Table 7.6).

7.3.1.3. Unit C

Six samples from across three sites were collected from Unit C for OSL dating. The results are shown in Table 7.7 (and together with all other OSL dating results in Table 7.4). Sample K2135 provided a very young age, with a multi-modal D_e distribution indicative of bioturbation attributable to palaeosol development (Section 7.4.1, Appendix H.4). The dose distributions of the other five samples from Unit C are shown as PD plots in Figure 7.17.

Table 7.7. OSL results for Unit C (excerpt from Table 7.4).

Sample	Site	Unit	Thin section	Ḋ (Gy/ka)	Ḋ error	D_e (Gy)	D_e error	Age (ka)	Age error	n	Risø	Notes
K2093	PR04	C	TS140	2.06	0.11	77.50	3.29	37.58	2.59	18	A	
K2114	PR05	C	TS132	1.70	0.08	43.40	2.09	25.54	1.69	18	B	
K2130	SL11	C	TS040	2.38	0.13	95.10	6.77	39.88	3.62	18	A	*
K2131	SL11	C	TS039	1.71	0.08	39.30	1.78	22.93	1.47	18	A	
K2132	SL11	C	TS041	1.11	0.07	30.90	1.53	27.81	2.28	17	A	
K2135	SL11	C		2.15	0.11	2.74	0.44	1.27	0.22	18	A	**

Notes:
*overdispersion >20%.
**overdispersion >50%.

Unit C samples tend to have bimodal or multi-modal distributions. K2093 and K2130 both have higher D_e values and a long right tail, indicating the incorporation of older material in to the sample (Section 7.4.1, Appendices H.4 and H.5). The other three samples provide lower D_e values and younger ages. Although they are also multi-modal and in some cases may contain younger grain populations incorporated in to clay desiccation cracks (Section 7.4.1), they each have low overdispersion and provide reliable CAM age estimates (Appendices H.3 and H.4). The reliable age estimates from Unit C range from ~40-~23 ka (Table 7.7).

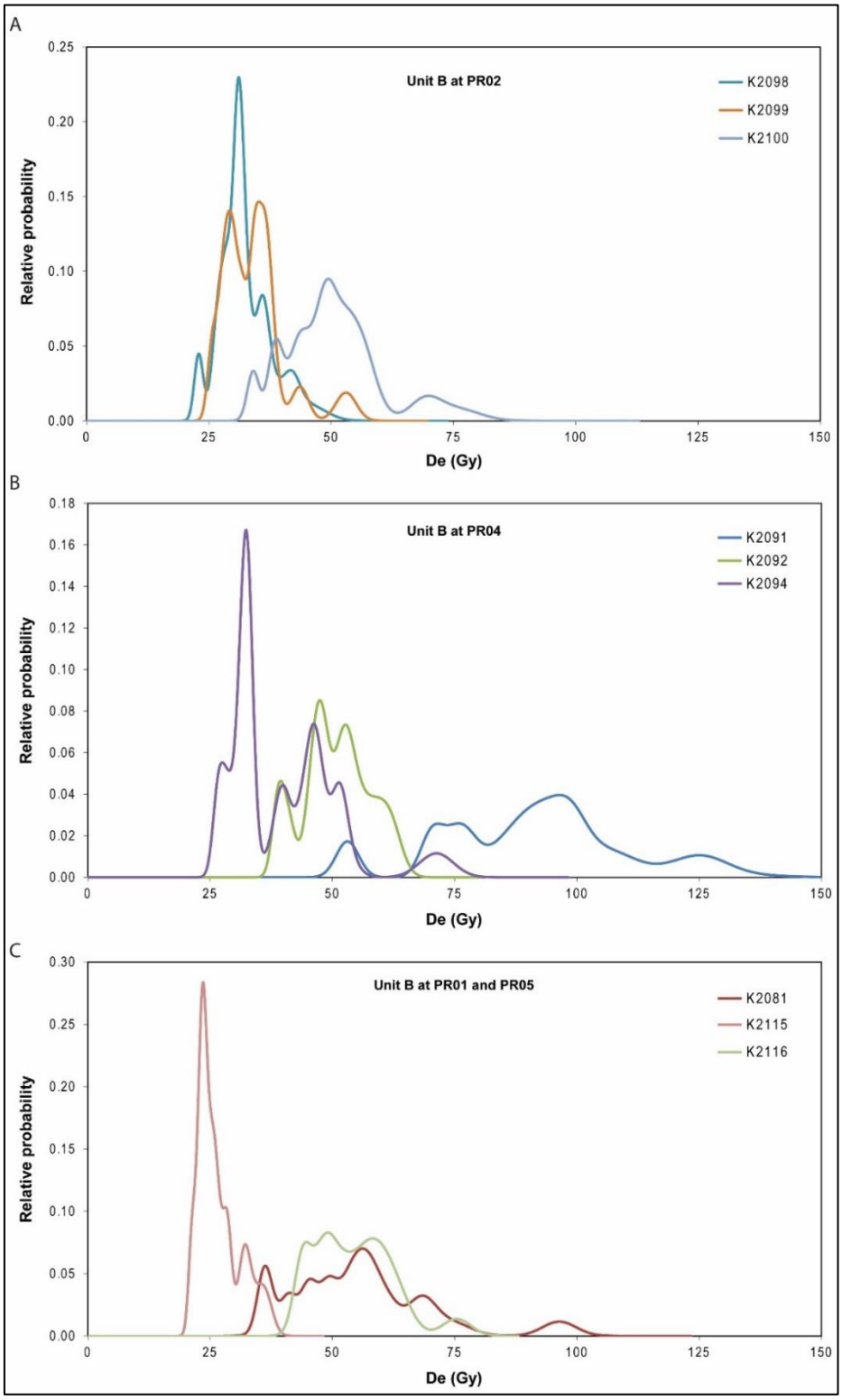

Figure 7.16. Probability density plots of D_e for accepted aliquots in Unit B samples. Samples are displayed across three sub-figures for clarity. A: samples from PR02. B: Samples from PR04. C: Samples from PR01 and PR05. The dose distributions are discussed in more detail, including presentation of radial plots and rationale for identifying outliers, for each sample individually by sample site in Appendix H.

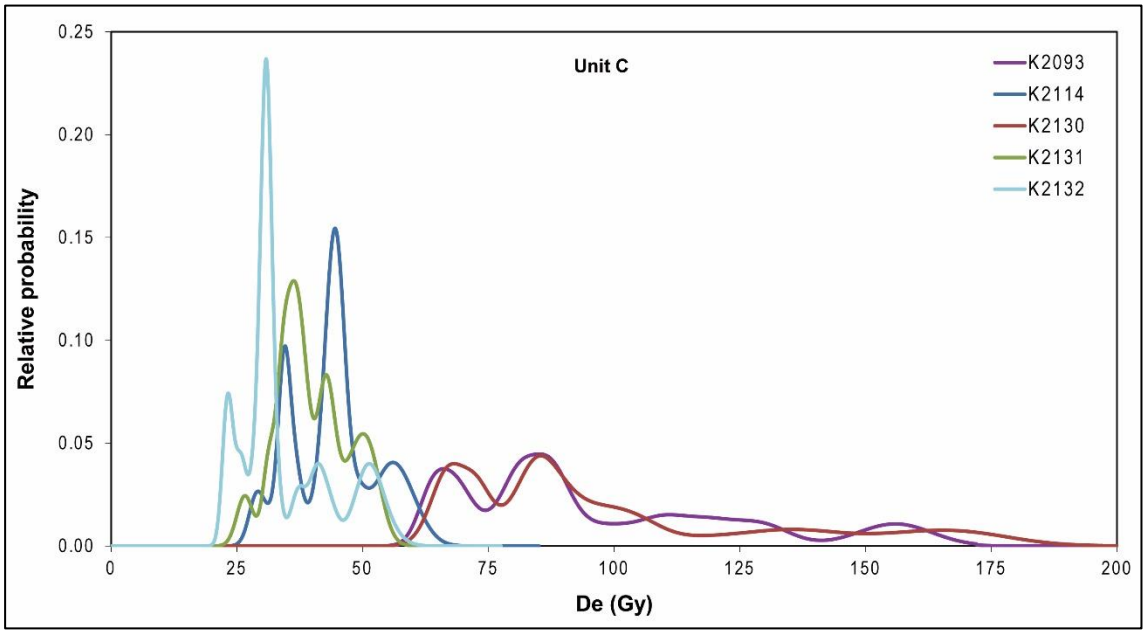

Figure 7.17. Probability density plots of D_e for accepted aliquots in Unit C samples. The dose distributions are discussed in more detail, including presentation of radial plots and rationale for identifying outliers, for each sample individually by sample site in Appendix H.

7.3.1.4. Unit D

Ten samples from across two sites were collected from Unit D for OSL dating. The results are shown in Table 7.8 (and together with all other OSL dating results in Table 7.4). Unit D samples gave variable results. Samples K2084 and K2085 from PR01 (Appendix H.6) and K2111 and K2112 from PR05 (Appendix H.3) gave indications of post-depositional disturbance and sediment mixing (Section 7.4.1). Three of these (K2111, K2084 and K2085), collected from within the Unit D palaeosol, show evidence of pedoturbation that has obscured the true depositional dose of the samples. These are not presented with the other Unit D samples in Figure 7.18.

Sample K2112 provides a multimodal distribution, but as can be seen in Figure 7.18A the peaks all fall within the same range as two other samples from the unit: K2082 and K2121 (from PR01, Appendix H.6, and PR05, Appendix H.3, respectively). Of the remaining four Unit D samples, two have clear central peaks while two are more multi-modal (Figure 7.18B). None-the-less these samples all have low overdispersion and provide reliable CAM estimates (Appendix H.3). The reliable age estimates from Unit D range from ~17.5-~30 ka (Table 7.8).

Table 7.8. OSL results for Unit D (excerpt from Table 7.4).

Sample	Site	Unit	Thin section	Ḋ (Gy/ka)	Ḋ error	D_e (Gy)	D_e error	Age (ka)	Age error	n	Risø	Notes
K2082	PR01	D	TS145	0.97	0.04	16.97	0.90	17.57	1.16	18	A	
K2084	PR01	D	TS145	0.65	0.03	3.84	0.35	5.92	0.59	18	A	*
K2085	PR01	D	TS146	0.88	0.06	0.16	0.01	0.18	0.02	16	B	
K2111	PR05	D	TS130	0.81	0.04	1.02	0.14	1.26	1.10	15	B	**
K2112	PR05	D		0.80	0.04	18.10	1.25	22.49	2.35	18	B	*
K2113	PR05	D	TS131	0.97	0.04	30.70	1.17	31.66	2.27	18	A	
K2117	PR05	D		0.88	0.03	24.70	1.12	28.14	1.63	17	A	
K2118	PR05	D		1.37	0.07	37.10	1.25	27.13	1.60	18	A	
K2119	PR05	D	TS134	1.10	0.05	26.73	0.96	24.33	1.43	18	A	
K2121	PR05	D	TS136	0.85	0.04	14.71	0.50	17.38	0.99	18	B	

Notes:
*overdispersion >20%.
**overdispersion >50%.

7.3.1.5. Unit E

Twenty one samples from across six sites were collected from Unit E for OSL dating. The results are shown in Table 7.9 (and together with all other OSL dating results in Table 7.4) and the PD distibutions are displayed in Figure 7.19. The samples from Unit E have proven very susceptible to issues such as high overdispersion, high recouperation and high aliquot rejection rates. The issues facing these samples are discussed in detail in Section 7.4.4. See Appendix H for individual sample results. All samples provide very young ages (mostly <200 years) from low value D_e distributions (mostly <1 Gy).

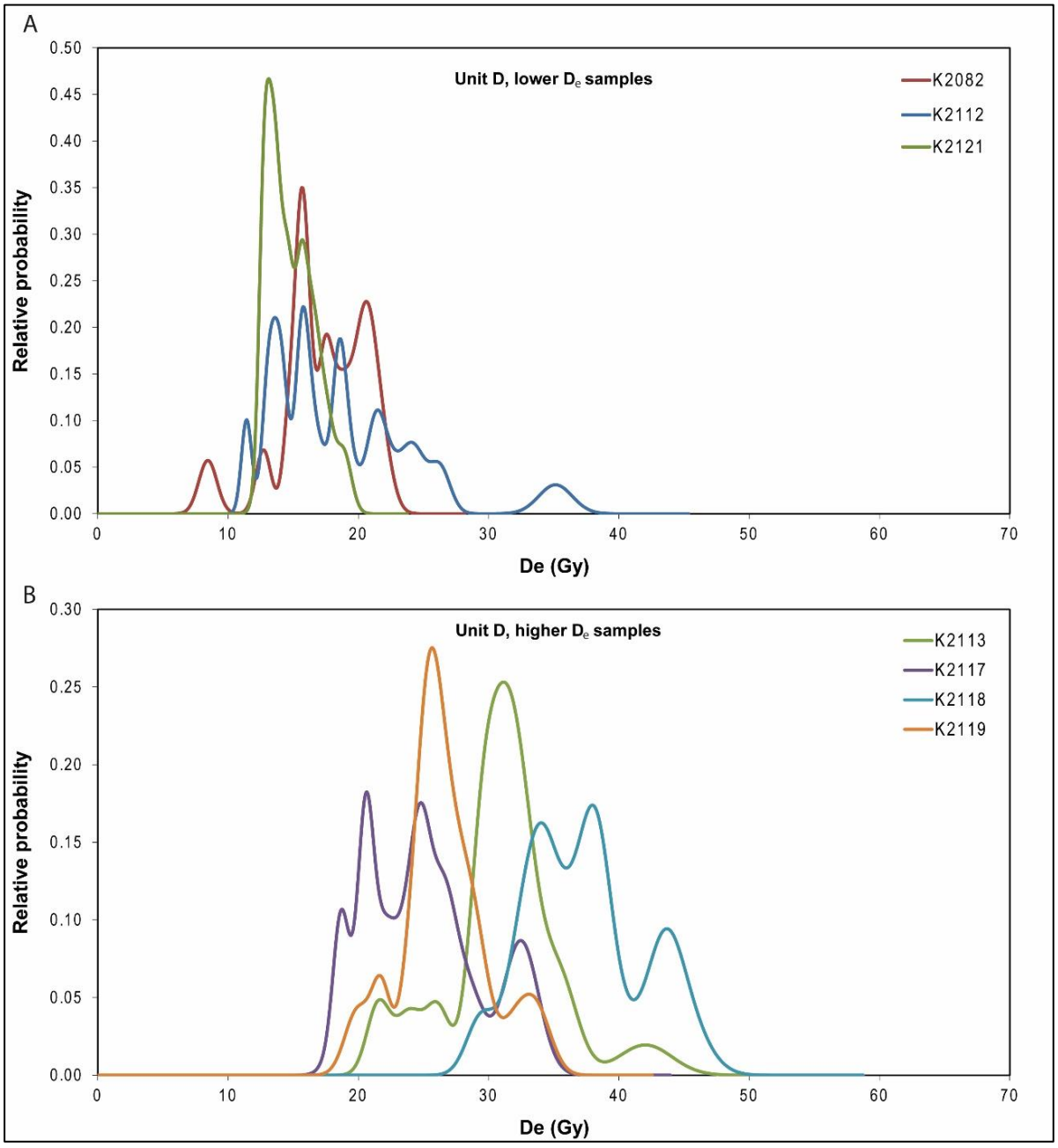

Figure 7.18: Probability density plots of D_e for accepted aliquots in Unit D samples. Samples are displayed across two sub-figures for clarity. A: lower D_e samples (modal value <20 D_e). B: higher D_e samples (modal value >20 D_e). The dose distributions are discussed in more detail, including presentation of radial plots and rationale for identifying outliers, for each sample individually by sample site in Appendix H.

Table 7.9. OSL results for Unit E (excerpt from Table 7.4).

Sample	Site	Unit	Thin section	Ḋ (Gy/ka)	Ḋ error	D_e (Gy)	D_e error	Age (ka)	Age error	n	Risø	Notes
K2083	PR01	E		0.70	0.03	0.13	0.03	0.18	0.04	11	B	** ^
K2086	PR01	E	TS146	0.62	0.03	0.10	0.03	0.16	0.04	11	B	**
K2087	PR01	E		0.59	0.02	0.04	0.01	0.07	0.01	8	B	** ^
K2095	PR04	E	TS138	0.81	0.04	0.06	0.01	0.07	0.01	10	B	* ^
K2096	PR04	E	TS138	0.74	0.07	0.05	0.01	0.07	0.01	11	B	* ^
K2101	PR02	E	TS123	0.63	0.03	0.19	0.11	0.30	0.33	7	B	** ^ #
K2103	PR02	E		0.54	0.05	0.03	0.01	0.05	0.01	16	B	** ^
K2104	PR02	E	TS124	0.58	0.02	0.03	0.00	0.05	0.01	9	B	* ^ #
K2105	PR05	E		1.31	0.24	0.05	0.00	0.04	0.01	11	B	^
K2106	PR05	E		0.89	0.05	0.03	0.01	0.04	0.01	4	B	* ^ #
K2107	PR05	E		0.97	0.05	0.03	0.00	0.03	0.02	9	B	^ #
K2108	PR05	E		0.77	0.04	0.28	0.12	0.36	0.16	9	B	** #
K2109	PR05	E		0.72	0.03	0.12	0.05	0.16	0.07	8	B	** #
K2110	PR05	E	TS129	0.94	0.05	0.12	0.01	0.13	0.05	10	B	^
K2120	PR05	E	TS135	0.92	0.04	0.05	0.01	0.05	0.01	18	B	* ^
K2122	PR05	E	TS137	0.77	0.03	0.09	0.01	0.11	0.01	9	B	* #
K2126	SL44	E		0.71	0.03	0.03	0.00	0.04	0.01	14	B	* ^
K2133	SL11	E	TS042	1.29	0.06	2.35	0.27	1.83	0.23	8	A	* #
K2134	SL11	E	TS043	1.16	0.06	0.14	0.01	0.12	0.01	4	B	#
K2136	SL11	E		1.07	0.08	0.08	0.01	0.08	0.01	10	B	

Notes:
*overdispersion >20%.
**overdispersion >50%.
^average recuperation for sample >10% (recuperation for each aliquot is shown in Appendix G.1).
#n <10

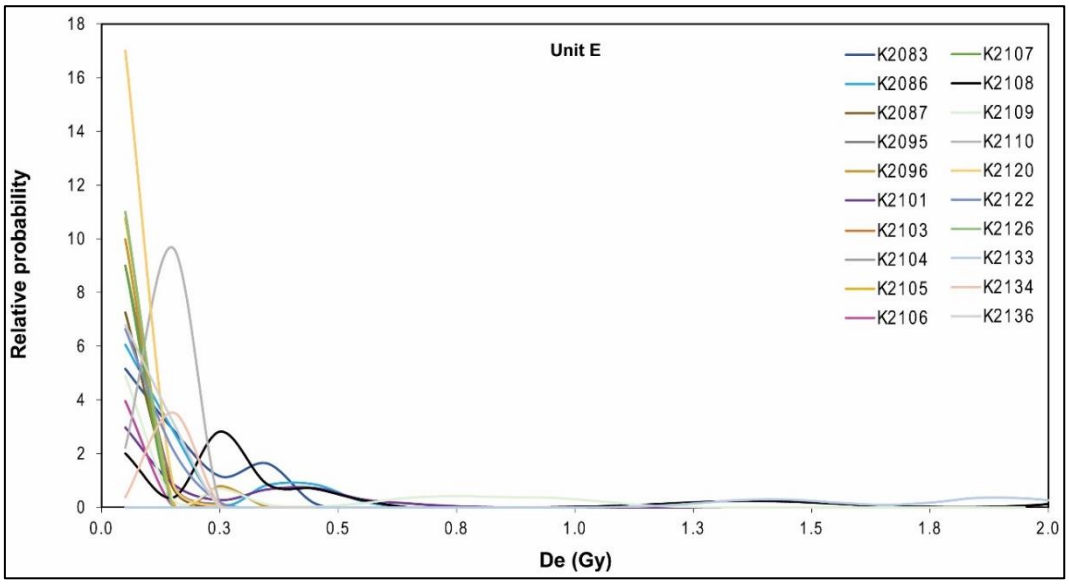

Figure 7.19. Probability density plots of D_e for accepted aliquots in Unit E samples. The dose distributions are discussed in more detail, including presentation of radial plots and rationale for identifying outliers, for each sample individually by sample site in Appendix H.

7.3.1.6. Other OSL samples

Six samples from across five sites were collected from other sample materials ('the spit', 'the beach' and behind the dunes in the pre-dune surface) for OSL dating. The results are shown in Table 7.10 (and together with all other OSL dating results in Table 7.4) and the PD distibutions are displayed in Figure 7.20. These samples all give very similar results to one another, with very multi-modal distributions ranging from <1 to ~10 Gy. Age estimates are all within the last 6 ka, but it is unlikely this reflects the true depositional age of the samples, as the original depositional D_e populations have probably been masked through pedogenic processes (Section 7.4.1.2).

Table 7.10. OSL results for other samples (excerpt from Table 7.4).

Sample	Site	Unit	Thin section	Ḋ (Gy/ka)	Ḋ error	D_e (Gy)	D_e error	Age (ka)	Age error	n	Risø	Notes
K2088	PR01			1.27	0.06	0.11	0.02	0.09	0.01	6	B	* #
K2097	PR04			1.16	0.05	2.49	0.61	2.15	1.29	15	B	**
K2102	PR02			0.83	0.04	4.23	0.49	5.12	0.59	18	B	*
K2127	PR05			1.22	0.08	6.28	0.83	5.15	0.76	17	B	**
K2128	PR01			0.94	0.07	3.31	0.62	3.52	0.72	15	B	*
K2129	PR07		TS151	1.28	0.07	4.06	0.34	3.16	0.32	18	B	*

Notes:
*overdispersion >20%.
**overdispersion >50%.
#n <10

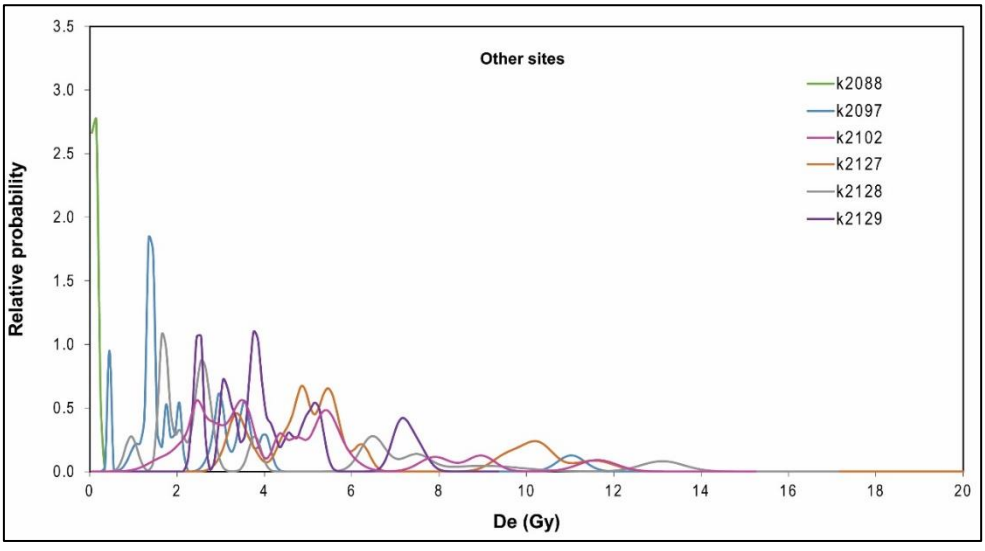

Figure 7.20. Probability density plots of D_e for accepted aliquots in samples from other sampling sites. The dose distributions are discussed in more detail, including presentation of radial plots and rationale for identifying outliers, for each sample individually by sample site in Appendix H.

7.3.2. Bayesian analysis of OSL Results

Figure 7.21 and Figure 7.22 show the results of the Bayesian analysis run on the OSL data in *OxCal 4.3.2* (Bronk Ramsey 2009a). The sample numbers with question marks are those with 'non' for prior outlier probability, and were not used in the model. Shaded histograms are the posterior distributions while outlines are the priors. Those samples identified as outliers (i.e. for which the posterior outlier probability exceeded that of the prior) are coloured olive green (moderate outliers: K2112 and K2080), or red (extreme outlier: K2091) (Bronk Ramsey 2009b). Convergence values for individual samples were mostly acceptable (>85% and mostly >90%; Appendix E), apart from those identified as outliers above (K2112, K2080 and K2091). Estimated age ranges for the start and end dates for each unit were also modelled, and are shown between the phases (units). Convergence is lower for boundaries where the model is less constrained, due to being based on only a few samples. Unit E was not included as the data are of very low precision yet very clearly indicate that the entire unit is very modern. The dating results from Unit C overlap substantially with Units D and B, indicating that this lithostratigraphic unit may not form a single time-unit and may be diachronous as interpreted. Therefore, Unit C was run as an independent sequence and is shown separately in Figure 7.21. The output tables with numerical estimates for each of these age ranges is provided in Appendix E.

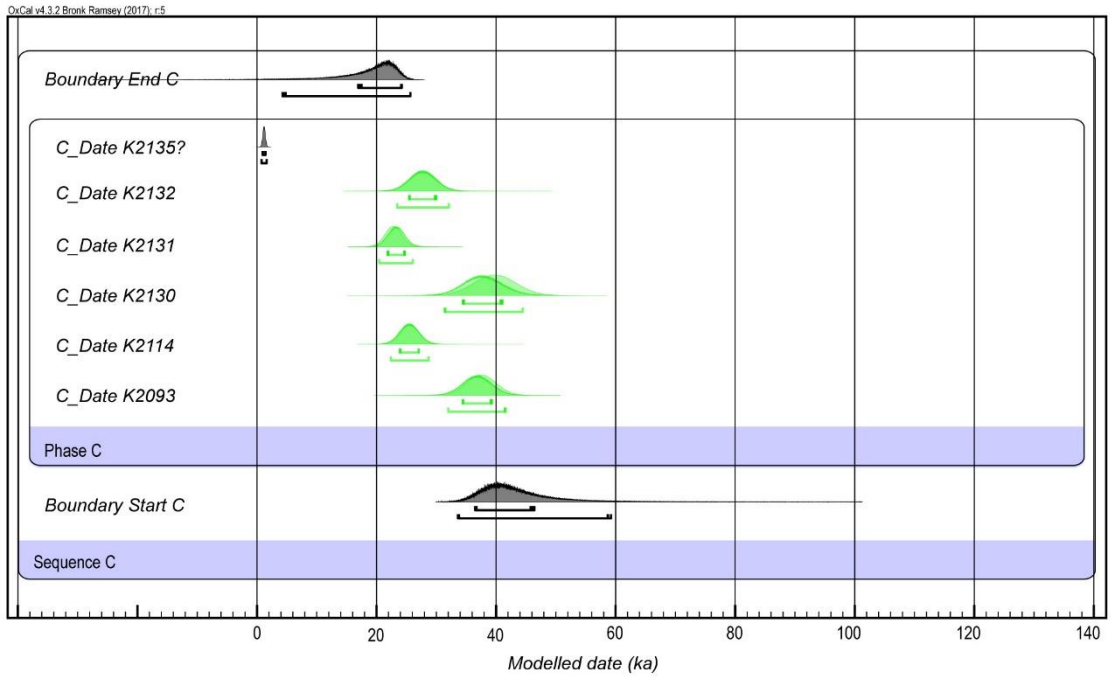

Figure 7.21. Modelled OSL ages for Unit C. Calculated using *OxCal 4.3.2* (Bronk Ramsey 2009a). The modelled ages for Units A, B and D are available in Figure 7.22.

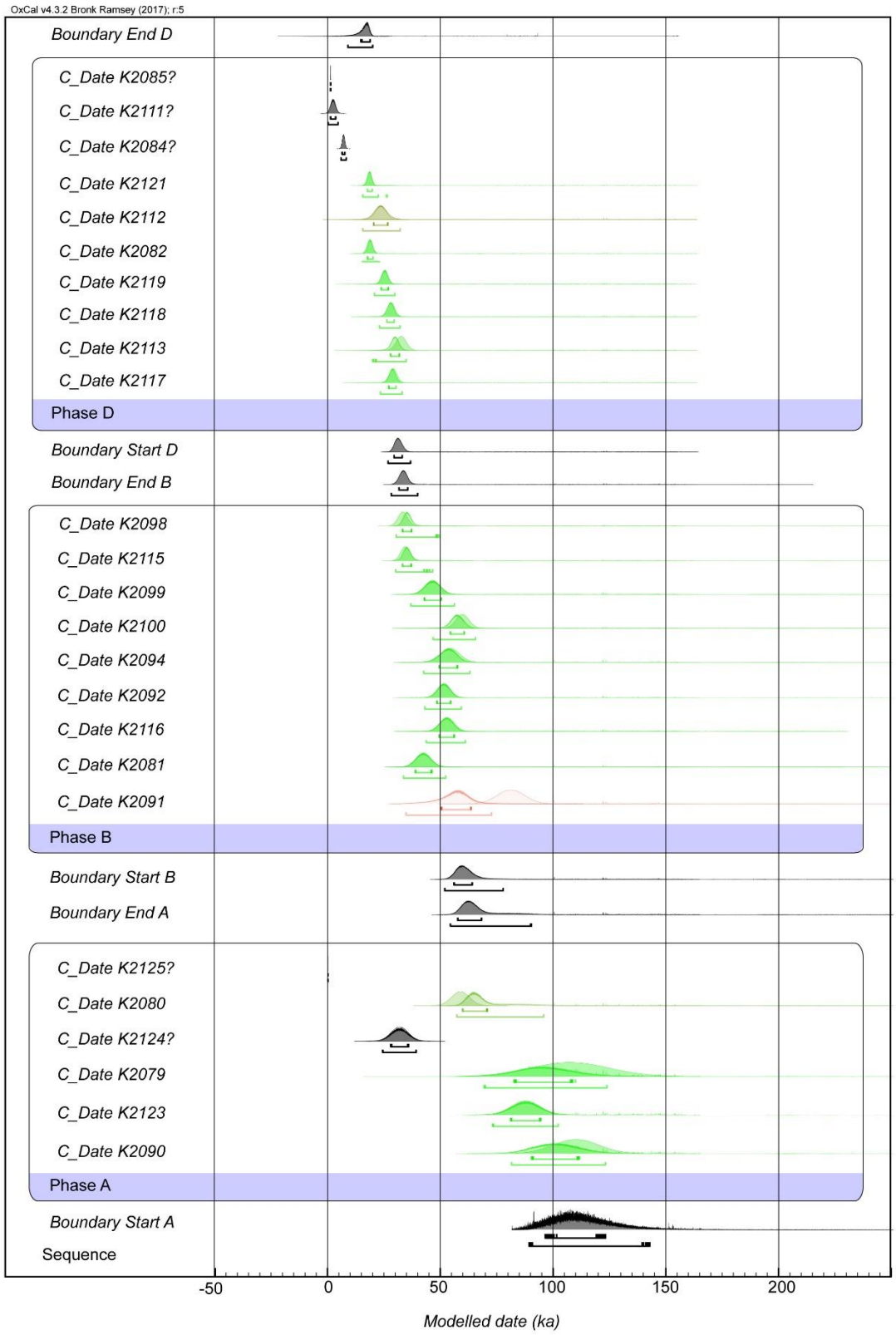

Figure 7.22. Modelled OSL ages for Units A, B and D. Red, olive green and grey samples were identified as outliers. Calculated using *OxCal 4.2* (Bronk Ramsey 2009a). The modelled ages for Unit C are available in Figure 7.21

7.4. OSL dating discussion

Aeolian quartz from the Willandra Lakes is expected to possess properties favourable for OSL dating (Bowler et al. 2003; Olley et al. 2006; Fitzsimmons et al. 2014), such bright, rapidly decaying signals typical of highly sensitive quartz dominated by the fast component and a high proportion of luminescent grains (Section 7.1.8). Figure 7.23 presents an example of a reliable result from each unit, B, C D and E in the Mulurulu lunette, with 'reliable' meaning the PD plot is near-Gaussian and most points on the radial plot fall within the 2σ error. Not all samples, however, were so well behaved. A number of extrinsic factors, such as sediment mixing, heterogeneous microdosimetry and incomplete bleaching, can cause skewed, broad, scattered, bimodal or multi-modal distributions (Section 7.1). In some cases the aliquot population representing the true depositional age of the sample can still be estimated. The evidence for and approaches to addressing these issues are discussed below. The age results for each unit and sampling site are discussed in Chapter 8, to provide an overall chronology of deposition for the lunette in an environmental context.

7.4.1. Evidence for mixing

7.4.1.1. Grain transport across unit boundaries

Mixing of grains from different age populations can result in broad Dose distributions or distributions with multiple peaks (Section 7.1.4.3). The genuine component, representing the true depositional age of the unit, can still potentially be identified in these cases, particularly if the relative range between the mean dose values of the parent distributions is broad (Arnold and Roberts 2009). When single grains are used, a finite mixture model can be applied to identify the age components (Jacobs et al. 2008a). In this study, however, small multiple grain aliquots were utilised, for which the finite mixture model is inappropriate (Arnolds & Roberts 2009). Instead, where multiple populations can be discerned in the radial plot, stratigraphic context is used to estimate which population is likely to represent a closer approximation of the depositional age of the unit. This method allows for the potential identification of grain transport across unit boundaries.

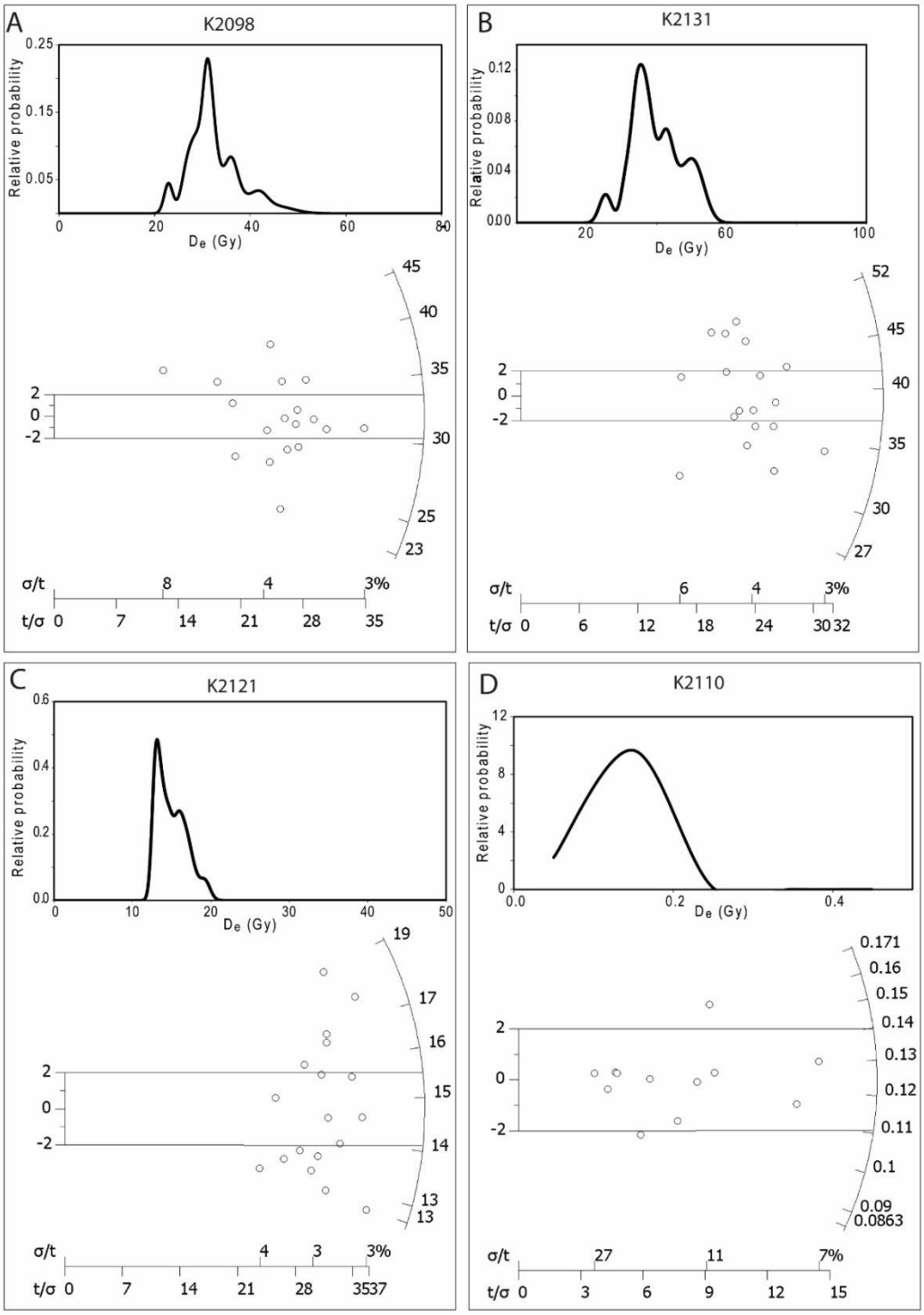

Figure 7.23. Examples of reliable D_e distributions from the Mulurulu lunette. A: Sample K2098, Unit B from PR02. B: Sample K2131, Unit C from SL11. C: Sample K2121, Unit D from PR05.D: Sample K2110, Unit E from PR05.

Sediment transport across boundaries was identified in a number of samples. Sediments have the potential to cross unit boundaries, both downwards, via bioturbation or through cracks via

gravity, but also upwards, via bioturbation by ants, for instance. Sample K2080 from Unit A provides an example. Most exposures of Unit A consist of a very thick palaeosol, so most samples from this unit display some degree of *in situ* mixing. Nonetheless, mixing resulting from grain transport across the unit boundaries was easily discernible in the dose distribution of sample K2080 (Figure 7.24). Sample K2079 was sampled from the base of the exposure in a gully wall at PR01 (Figure 7.24A). Of the 14 unrejected aliquots for this sample, one has a substantially lower D_e than the others (Figure 7.24D). Having been collected from the base of the gully, this is most likely a result of contamination from young material recently carried in to the gully. The remaining aliquots also have a broad distribution with multiple possible peaks. The averaging effect of multi-grain aliquots means that these peaks cannot be reliably determined to represent discrete depositional episodes. Sample K2080 was collected from near the top of Unit A, at the same site as K2079 (Figure 7.24A), slightly further up the gully. K2080 includes five outlying aliquots (Figure 7.24C) that most likely result from the mixing of sediments from below. These aliquots fall between 95-150 Gy, within the range of the underlying K2079 sample (Figure 7.24D), collected from deeper within the palaeosol within the same unit. This indicates that bioturbation within the palaeosol, for example, via ant activity, is likely to have moved grains upwards in the soil profile. Once the outlying aliquots are removed, the resulting distribution is clearly bimodal (Figure 7.24C). The younger population has similar central D_e value (~50 Gy) to sample K2081, collected from the immediately overlying Unit B (Figure 7.24A and B). This indicates that some transport of sediments may have occurred downwards, across the unit boundary. Thus, the population of aliquots forming the older population in K2080 can be discerned as most likely to be representative of the true depositional age of the sample.

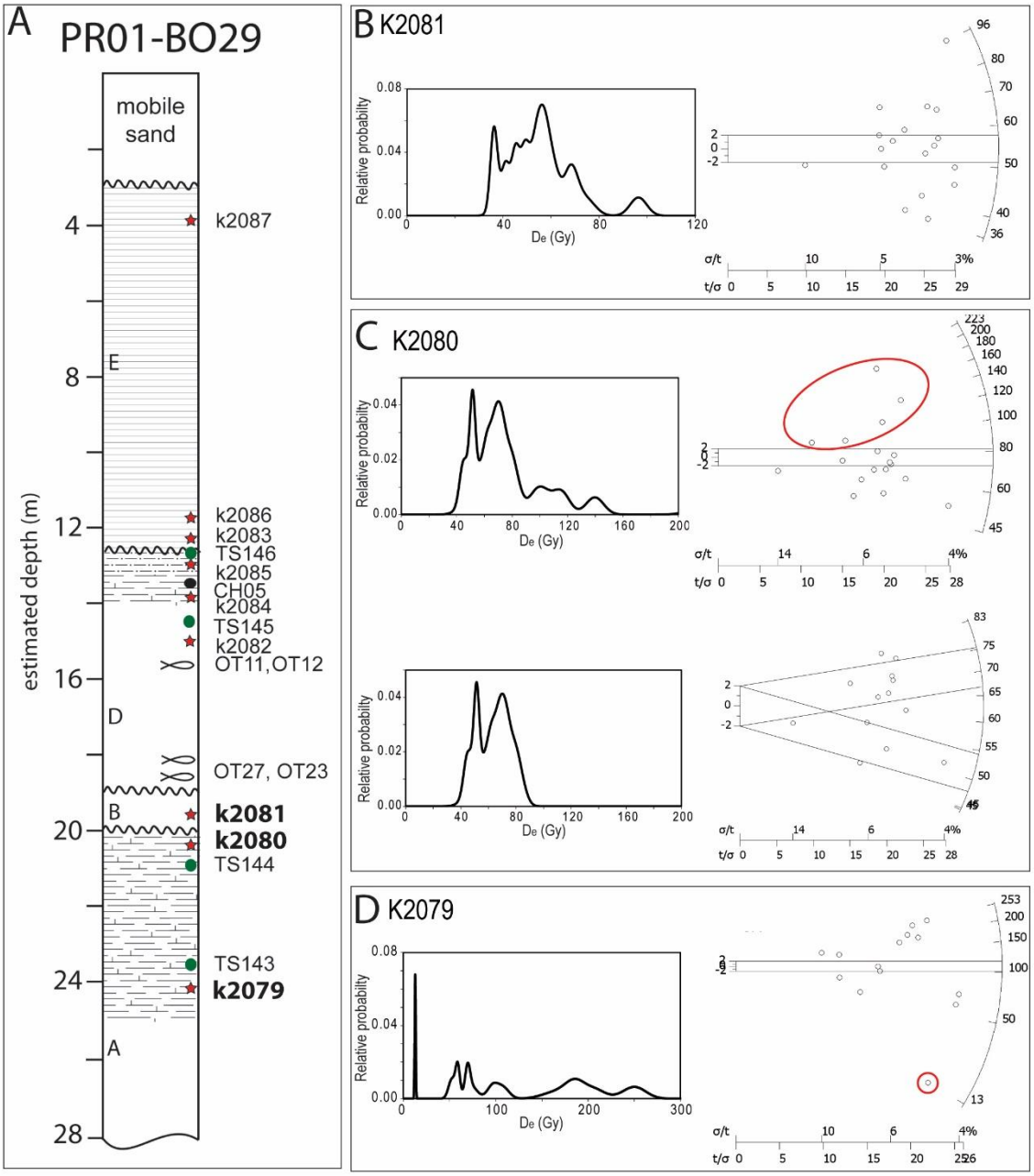

Figure 7.24. Samples from Unit A with evidence for grain transport across unit boundaries. A: Stratigraphic log from PR01 at BO29, indicating the sampling locations of K2079, K2080 and K2081 in Units A and B. B: Sample K2081 from Unit B. C: K2080, with five older aliquots likely derived from mixing from below or partial bleaching, plus bimodal peaks, the younger of which is likely to represent transport of grains from the overlying Unit B (shown in inset B). The first set of plots show the results with all aliquots included, while the second set highlights the bimodal distribution once the five outlying aliquots are removed. D: Sample K2079, with one outlying very young aliquot. Red circles indicate outliers.

Similar evidence of grain transport, but from Unit A to Unit B, was seen at PR04 in samples K2091 and K2092. Grain transport into the clay-rich Unit C was seen in sample K2114 from PR05 and sample K2093 from PR04, as well as in to the clay layer capping Unit D in sample K2085 at PR01. These are likely to be the result of dessication cracks in the clay providing a pathway for grains to intrude, as observed in dry ephemeral lake beds by Olley (unpublished data in Roberts et al. 2000). Although Unit E was often finely laminated, grain transport across unit boundaries was observed in locations without laminations. Transport from Unit E to Unit D was seen in Sample K2111 from PR05 and transport of grains from underlying layers in to Unit E samples collected from the base of the unit at PR05 was seen in samples K2108 and K2109. See Appendix H.3 for detailed descriptions of each of these cases.

Where multiple populations are apparent, an attempt is made to identify and determine the likely cause of each population and select the appropriate target population based on stratigraphic context. Although the population is still likely to be influenced by averaging effects, the CAM is applied to only those aliquots deemed to be most likely to relate to the target population, in order to calculate the closest possible estimate of D_e in these multi-grain, mixed samples.

7.4.1.2. Mixing in palaeosols

Four samples gave results of very young ages, <1.5 ka, collected from very close to the top of stratigraphic layers with typically older ages. These consist of two samples from Unit D (K2085 from PR01 [Appendix H.6] and K2111 from PR05 [Appendix H.3]), and one each from Units C (K2135 from SL11 [Appendix H.4]) and A (K2125 from SL44 [Appendix H.2]). All four of these samples were collected from the top of a palaeosol, overlain by Unit E in each case, and provide evidence of sediment mixing. K2085 was discussed above, where modern grains have fallen into desiccation cracks in the clay layer capping Unit D. The young population of grains in the other three samples may be a result of bioturbation when the palaeosol formed, prior to the relatively recent deposition of the overlying Unit E. Alternatively, the young population of grains may be a result of grain transport across the unit boundary, from Unit E into the uppermost part of the dated unit. Either way, the age estimates

resulting from these samples do not represent the true depositional ages of the units and were not used in chronostratigraphic interpretations.

Three other samples, collected from deeper within palaeosols, also provide evidence for post-depositional mixing. K2084 (Unit D, PR01, Figure 7.25A), K2112 (Unit D, PR05, Figure 7.25B) and K2124 (Unit A, SL44, Figure 7.25C) give CAM ages of <6 ka, ~22.5 ka and ~32 ka, respectively. In these cases, the mixed populations of grains do not appear to be due to the incorporation of Unit E materials, but due to *in situ* bioturbation. The OSL results for these samples give very similar results to the samples from modern soil profiles (Figure 7.25D, E and F) with PD plots with multiple peaks and radial plots in which the majority of aliquots fall outside the 2-σ error of the CAM weighted mean. Unlike cases of additional grain populations resulting from grain migration across unit boundaries (see above), it is not possible to estimate the true depositional age for these three samples from this data.

Many of the samples collected from beneath the current ground surface, rather than from the lunette, show somewhat similar patterns to one another, with evidence of mixing, probably due to modern bioturbation (Figure 7.25D, E and F). These samples were collected from, at most, 30 cm below the ground. The PD plots suggest multiple peaks and the radial plots are scattered with few data points within the 2σ error range. All samples give CAM age results within the last few thousand years, from around 5 to 2 ka. A minimum age model (MAM) could be applied to these samples, but would be unlikely to result in an approximation of the true depositional age in this case. The MAM is appropriate for samples showing a right tail due to partial bleaching, where the younger part of the signal is likely to reflect the true age of the sample. These samples were collected with the aim of dating the ground surface on which the lunette has been built. It is likely that the sampling pits were not dug deeply enough to penetrate beneath the current soil profile. The results indicate a large modern component, likely mixed into the sediments by modern soil forming processes. As such, the attempt to date the pre-existing ground surface was unsuccessful.

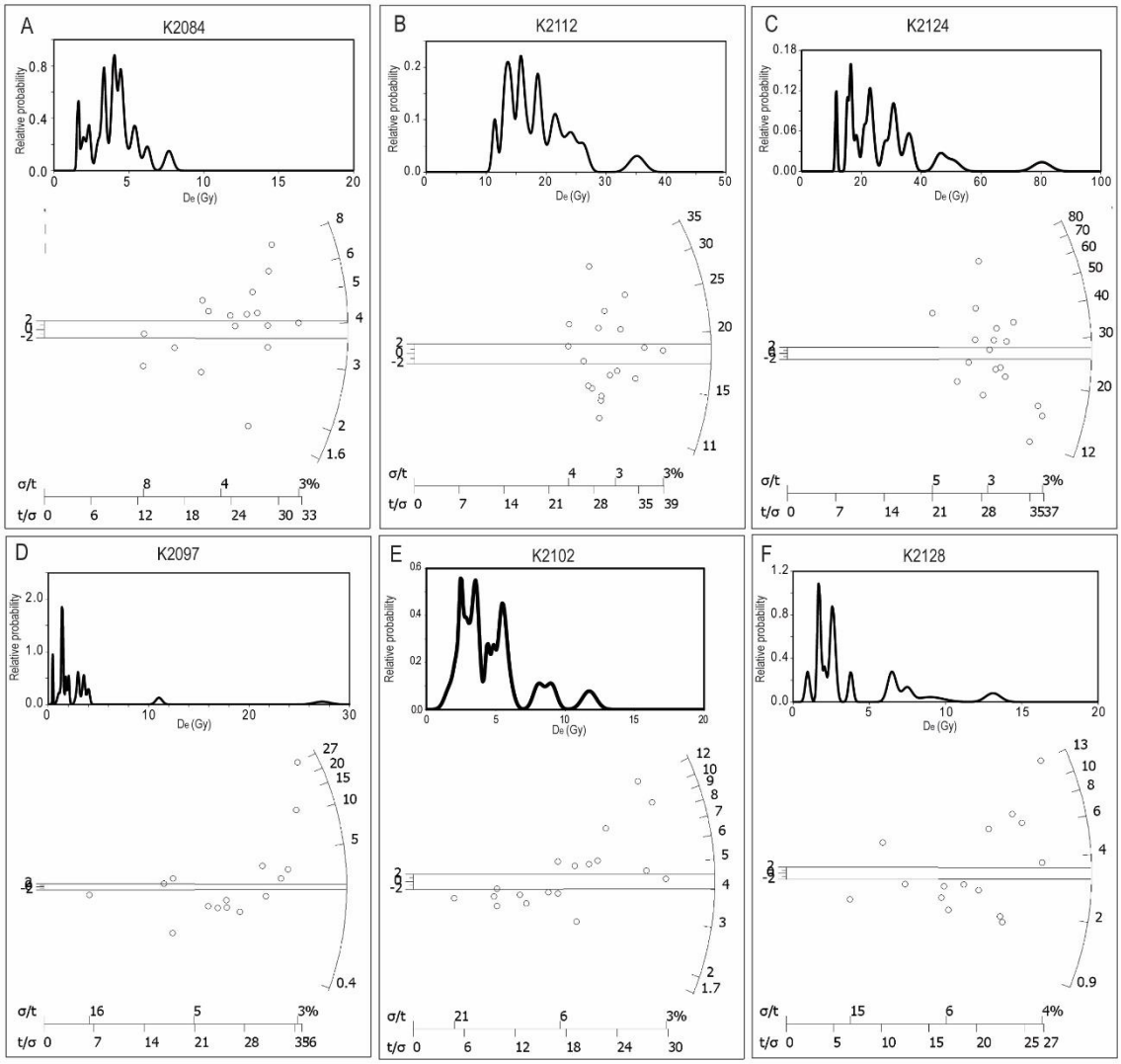

Figure 7.25. Examples of mixed-population samples. A-C are samples from within palaeosols and D-F are samples from within the current soil profile. A: Sample K2084, Unit D palaeosol at PR01. B: Sample K2112, Unit D palaeosol at PR05. C: Sample K2124, Unit A palaeosol at SL44. D: Sample K2097, behind the dune at PR04. E, Sample K2102, behind the Dune at PR02. F, Sample K2128, from the beach ridge at PR01.

7.4.1.3. Other mixed samples

Two samples gave indication of multiple grain populations, for which the source of the unique components could not be determined. Sample K2094 was collected from near the top of a sand residual in Unit B at PR04 and K2123 was collected from the side of a small pit dug in the Unit A sands of a blowout at SL44. In both cases the majority of aliquots are split roughly evenly across two dominant peaks (Figure 7.26). Without any stratigraphic argument

for which population reflects the true age of deposition of each sample, the CAM analysis is applied to all accepted aliquots.

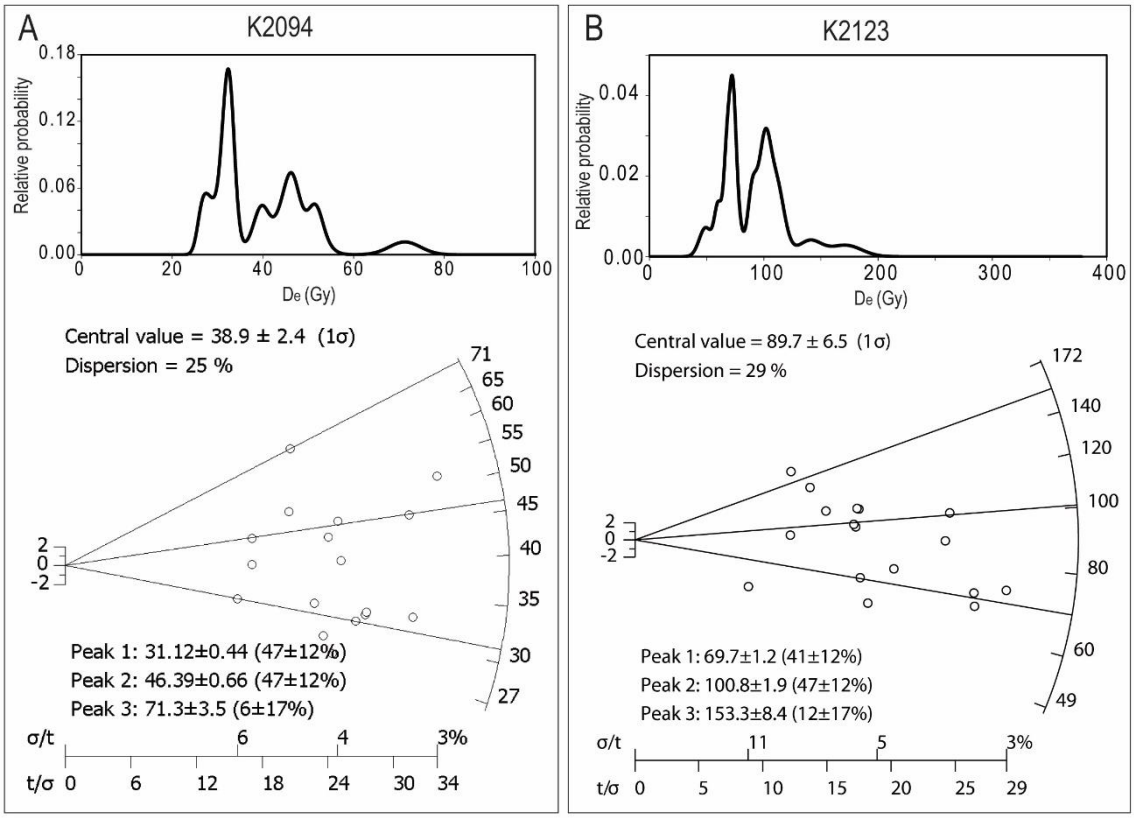

Figure 7.26. Examples of samples with mixed distributions without a clear explanation. A, Sample K2094, from Unit B at PR04. B, Sample K2123, from Unit A at SL44.

7.4.2. Incomplete bleaching

Numerous samples had a right 'tail' (e.g. Figure 7.27). In some cases this can be indicative of partial bleaching (Section 7.1.4.1). This is unlikely for these samples, not only because it's unexpected in quartz from this region, but because the effect of partial bleaching on 70-100 Gy doses will be negligible. To ensure that samples showed no evidence of partial bleaching and that the fast OSL component was indeed the dominant component measured for age estimations, tests were conducted to isolate and remove the medium and slow components from the analysis (see Section 7.2.5.1). No significant change was seen in D_e values after the removal of the medium and slow components. It is therefore concluded that bleaching was strong enough to reset all components in most cases, as expected for aeolian sediments from

arid Australia (Bowler et al. 2003; Olley et al. 2006, Fitzsimmons et al. 2014). In instances where a substantial slow or medium component had a visually identifiable effect on the decay curve, the relevant aliquot was rejected from analysis (see Section 7.2.5).

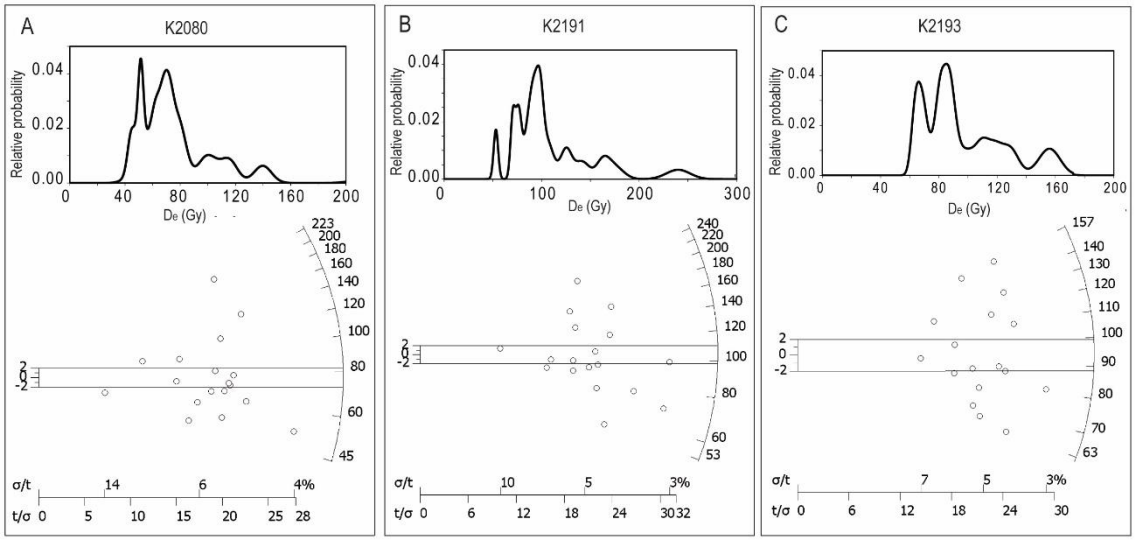

Figure 7.27. Examples of samples with a small portion of aliquots with higher D_e values than the main population, resulting in right tails. A: Sample K2080, Unit A from PR01. B, Sample K2091, Unit B from PR04. C: Sample K2093, Unit C from PR04.

7.4.3. Potential microdosimetry issues

Grains that were buried at the same time can potentially receive different beta doses after burial, which results in scattered D_e distributions (Jacobs et al. 2008b; Murray & Roberts 1997; Olley et al. 1997). The differing doses may be derived from internal sources, due to uneven uranium and thorium present within the grains or in iron coatings. Alternatively, the differing dose can derive from external sources, such as the uneven distribution of beta sources in the surrounding sediments. The differences in dose rate derived from different sediment fractions become increasingly significant as the number of grains examined decreases (Olley et al. 1997), thus in large aliquots, the effect of beta-heterogeneity is reduced, as it gets averaged out across the grains. In this study, the 1 mm aliquots usually contained around 20 grains, so while some averaging can be expected, with so few grains there is still the potential for a small amount of contamination from bright grains to dominate the OSL signal. Murray & Roberts (1997) found that in aeolian samples from the Nullarbor Plain, 5% of the grains produced about 57% of the summed natural luminescence output of

120 grains. Assuming this ratio is similar in the Mulurulu quartz, a single grain could sometimes contribute up to 50% of the measured signal. It is therefore worth investigating whether any of the mixed dose distributions may have resulted from heterogeneous doses.

The internal uranium and thorium contributions to total dose rates (i.e. that portion of the total dose rate attributable to U and Th within the sample grains) in this study are an average of 7.45% and 6.04%, respectively. Even the maximum contributions of 10.69% and 14.84%, respectively, are low enough to be of little concern. Potassium levels, on the other hand, made an average contribution of 34.24% of the total dose rate received, and contributed almost 50% for some samples. The potassium present in clay material provides a source of beta radiation that may result in a heterogeneous beta dose. Conversely, where carbonates are present, these may insulate grains from beta radiation. Both clay and carbonate materials were present in numerous samples (Appendix C). The samples with significantly scattered D_e aliquot results were K2084, K2111, K2112, K2135 and K2124.

K2084 was collected from high in Unit D, immediately below the clay layer at PR01. For this sample, the potassium contribution to the dose rate was 29.23%. Although this is not above average for the samples in this study, it is likely to be derived from clay minerals migrating down from the overlying pelletal clay layer, meaning that the clays are unlikely to be evenly distributed, leading to heterogeneous dose rate contributions to measured quartz. The clay content may also have changed through time, with the clays gradually washing further down in to the sand. Having been sampled from near the top of this unit, within a palaeosol, it is also highly likely that sediment mixing also contributed to the scattered distribution of D_e values (see above).

Samples K2111 and K2112 were both collected from within the rubified area of Unit D at PR05. The potassium contributions to the total dose rates for these samples were 35.19% and 36.81%, respectively, which is just above average. The layer from which they were collected does not contain clay pellets; though some grain cutans may contain small amounts of clay contributing to the slightly elevated K level. The sample does, however, contain numerous carbonate nodules, which may also lead to heterogeneous beta doses due to the shielding nature of the carbonates. The iron-oxide coatings on the grains, which provide the reddish colour to the sediments, have the potential to provide a source of uranium; however, the

uranium contribution to total dose rate for these samples was fairly minor, at an average of 6.10% and 7.16%, respectively. It is more likely, having been sampled from a palaeosol, that the scattered nature of the D_e results is due to post-depositional mixing of the sediments (see above).

Sample K2135 was collected from the top of Unit C, within the upper palaeosol at SL11. Unit C is a pelletal clay unit, and for this sample, the potassium contribution to the total dose rate is 41.71%, which is relatively high. As such, it is likely that heterogeneous dose rates due to the distribution of clays around the quartz grains may have played a significant role in the scattered results for this sample. On the other hand, the sample comes from a palaeosol, which is likely to have undergone post-depositional mixing. The strikingly young age estimate (~1.3 ka) provides support for mixing as the cause of the scattering, as a large amount of material may have been incorporated into this otherwise >20 ka unit, when it formed the soil layer of the ground surface, before the relatively recent deposition of Unit E during the last couple of centuries.

Sample K2124 was collected from within the wall of a large blow-out at SL44. The thin section collected from just above this location (TS119) shows grains with cutans and ferri-argillans, indicative of soil development (Figure 7.28). Uranium, likely derived from the iron-oxide coatings on the grains, makes a 10.09% contribution to the total dose rate for this sample. Although not high enough to be of significant concern, it is one of the highest uranium contributions seen in this study. More importantly, deep embayments on grain edges contain remnant cutans, indicating that the sand has been reworked from a prior soil profile. Thus sediment mixing is likely to be significant for this sample (see above).

All of the above samples, which have significantly scattered D_e results, are samples derived from palaeosols. The scattered distributions are not directly linked to samples with unusually high dose contributions from potassium beta radiation, which suggests that the cause of the observed scattering is most likely to be the result of post-depositional bioturbation of the soil profile, as described above (Section 7.4.1.2).

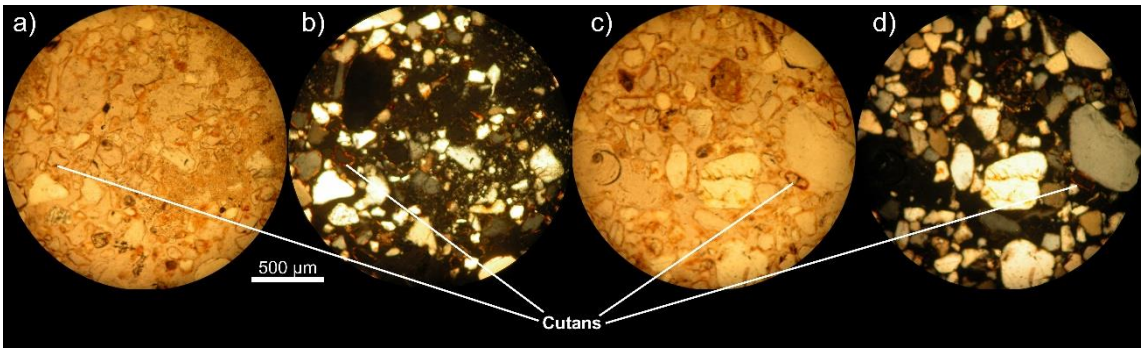

Figure 7.28. Two fields of view from TS119, thin section from Unit A at SL44, showing the cutans visible as orange grain coatings in PPL, with a high refractive index in XPL. Images a) and b) are the same field of view, shown in PPL and XPL respectively, as are c) and d).

7.4.4. Issues with young samples

Samples collected from Unit E (and some samples from palaeosols, see above) gave consistently young ages (<0.2 ka). These samples were disproportionately affected by issues of recuperation, low precision, high errors and high overdispersion. The very young age of these sediments means that the natural signals are particularly low, so any signal arising during the zero dose step represents a significant fraction of the natural OSL luminescence. Indeed, numerous Unit E aliquots displayed recuperation greater than 10%, many over 50% and three over 100% (see Section **Error! Reference source not found.**, Figure 7.12). They were also likely impacted by high test dose signal to background ratios, as the test dose used was 20% of the natural dose, which in these young samples could approach background levels.

The recuperation results shown in Section 7.1.5.1 show that recuperation ratios of greater than 10% were common in the samples with low equivalent doses (<1 Gy; Figure 7.12). It is quite likely that the high recuperation rates are a result of the high pre-heat temperature for the test dose in the SAR protocol. Recuperation ratios were also generally higher for samples measured on Risø B than Risø A; however, this is most likely an artefact of samples with younger expected D_e values being measured on this machine (due to its weaker radiation source). This indicates that luminescence signals originating from recuperation are likely to be making a significant contribution to the measured luminescence in these young samples, resulting in erroneously high apparent doses. The age estimates, although they are only on the

order of a few hundred years, are likely to be overestimated, rendering them effectively indistinguishable from modern samples. As such, rather than assigning numerical ages to these samples, they are instead simply considered to be ‘very recent’.

Thus, the precise age estimates determined for these samples are unreliable, particularly when this issue is combined with high overdispersion and low precision. Nonetheless, even taking in to account the low precision of these age estimates, it is clear that these samples all represent relatively recent deposition, likely within the last 200 years with some being effectively modern.

7.5. OSL dating conclusions

A comprehensive suite of quartz samples was dated from across the Mulurulu lunette. Small (1 mm) multi-grain aliquots were measured using a SAR protocol, and many samples provided narrow dose distributions and a reliable CAM estimate for D_e. None-the-less multiple age populations were common in samples collected from palaeosols and near unit boundaries. These populations are unlikely to be the result of partial bleaching or beta-heterogeneity, but rather, appear to have occurred through sediment mixing. Indeed, many of the palaeosol samples provided dose distribution patterns similar to samples from below the modern ground surface, impacted by pedological sediment mixing. For mixed samples near unit boundaries, finite mixture modelling cannot reliably identify discrete grain populations in these multi-grain aliquot samples. Instead, interpretation of the dose distribution with regard to the stratigraphic context of the sample often allowed the population most likely to reflect the burial dose to be targeted for CAM analysis.

Ages have been calculated for stratigraphic profiles from six sites spanning the Mulurulu lunette, incorporating the five stratigraphic units. Bayesian analyses of the results provide the broad boundary ages for each of the units (provided rounded to the nearest thousand years to avoid artificial apparent precision, as the uncertainties do not include the systematic error on D_e (Sections 7.2.5.2 and 7.2.7):

- Unit A: From 123-96 to 68-58 ka.
- Unit B: From 64-56 to 34-30 ka.
- Unit C: From 46-37 to 24-17 ka.
- Unit D: From 31-28 to 18-14 ka.

The dating results from Unit C overlap substantially with Units D and B, indicating that this lithostratigraphic unit may not form a single time-unit and may be diachronous as interpreted. Unit E was not included in the Bayesian analyses, as the dates are unreliable and imprecise (high recuperation, high overdispersion, high relative errors), yet likely to all be very young, probably deposited within the last 200 years.

Chapter 8. The depositional history and palaeoenvironments of Lake Mulurulu in time and sediment context

In Section 8.1, the dating results are discussed, combining OSL and radiocarbon ages, to provide age estimates for each unit and an overall chronology of deposition for the Mulurulu lunette. This is followed by a depositional and palaeoenvironmental history of Lake Mulurulu in Section 8.2, which synthesises the chronological, sedimentological and isotopic evidence presented in the previous chapters, to provide a narrative description of the depositional and palaeoenvironmental transitions recorded in the landscape of the Mulurulu lunette, in the context of the broader region and environmental regimes.

8.1. Chronostratigraphy of the Lake Mulurulu lunette

Figure 8.1 shows a composite stratigraphic log and an age-depth graph using estimated depths for a schematic composite sequence of the Mulurulu lunette. In this figure, all results are shown regardless of analytical reliability. Figure 8.2 shows the same age-depth graph for the composite log of the lunette, but with problematic samples discussed in Chapter 7 and Appendix H highlighted. Samples that are crossed out were discarded during the Bayesian modelling (Section 7.3.2). These are all samples collected from palaeosols. Samples in brackets were given low weight through the outlier analysis and contributed proportionately lower to the Bayesian analysis results.

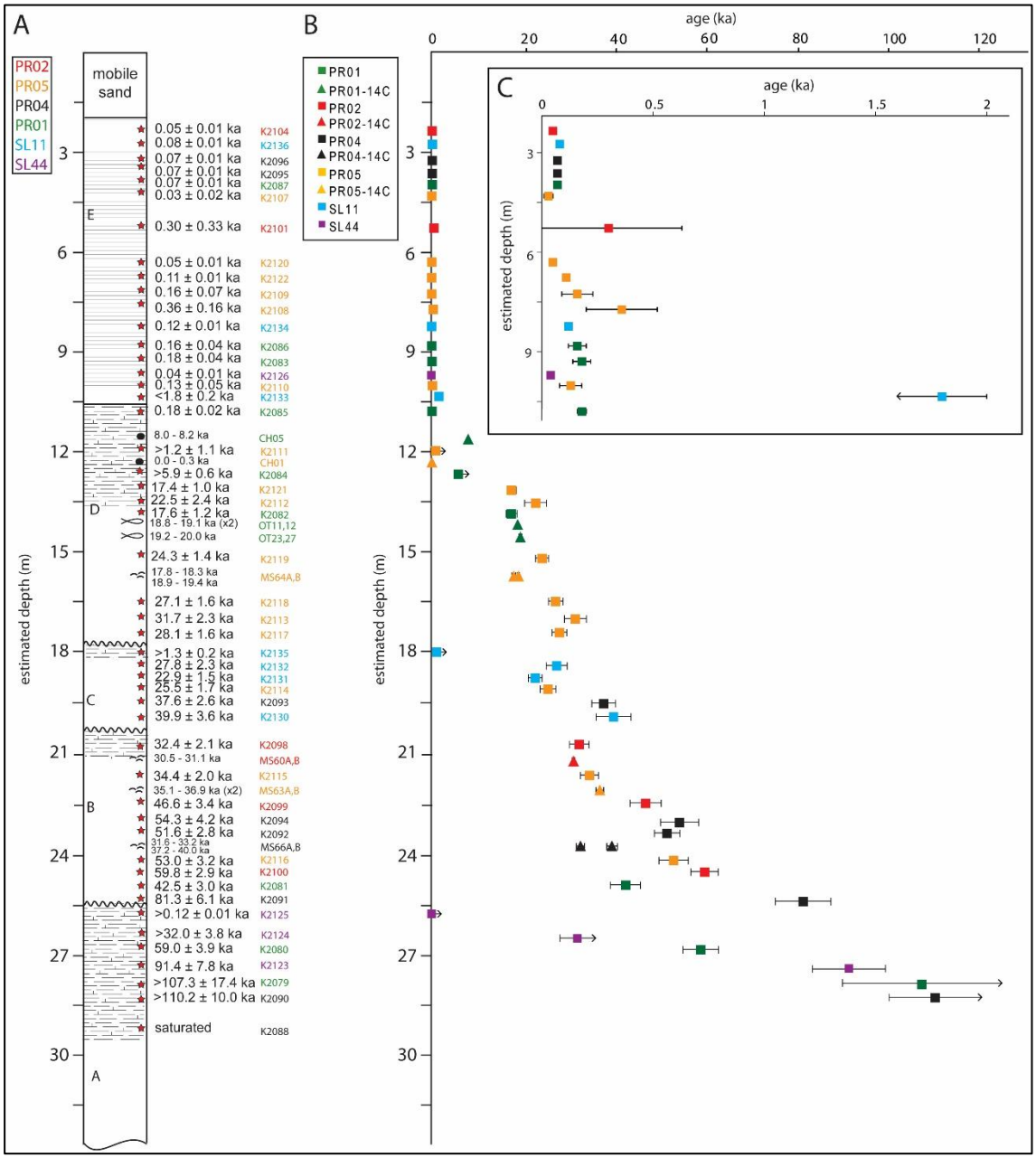

Figure 8.1. Composite stratigraphic log (A) and age-depth graph (B) for the Mulurulu lunette. Squares are OSL ages and Triangles are radiocarbon. A different colour is used for each sampling area. Inset (C) shows Unit E samples with a different x axis scale.

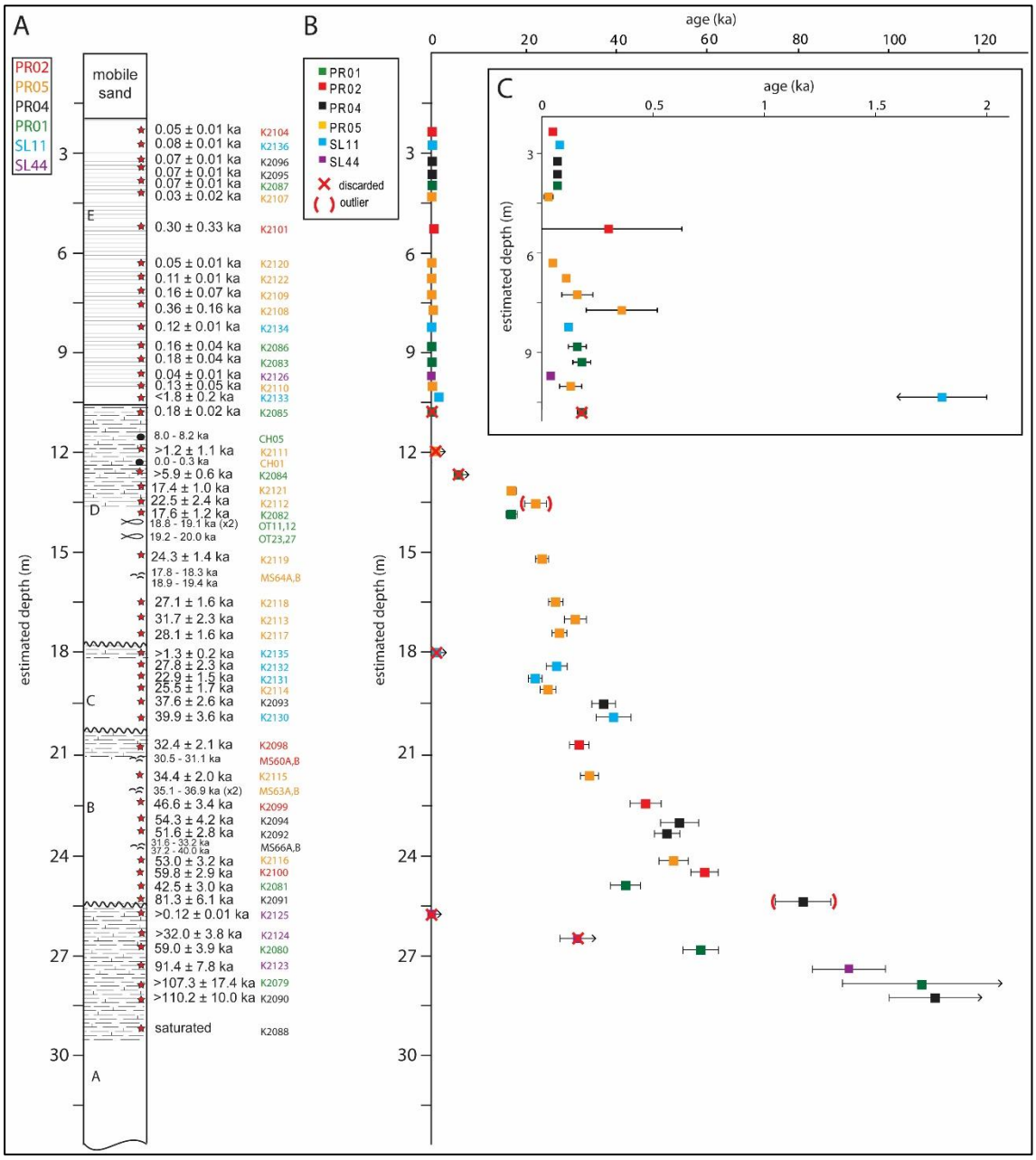

Figure 8.2. Reproduction of Figure 8.1, but with radiocarbon results removed, to show an age-depth graph of all OSL dating results for the lunette. Red crosses indicate ages that were deemed not representative of the true depositional age of the sample, while those in brackets had issues identifying the primary population and were identified as outliers in the outlier analysis when doing the Bayesian modelling of unit ages in *OxCal 4.2* (Bronk Ramsey 2009a; 2009b).

Excepting Unit E and some radiocarbon ages, sample age increases with depth with very few inversions. It must be kept in mind, however, that in this idealised stratigraphic log, age estimates, in addition to palaeosols and proximity to contacts, were utilised in estimating the

relative depths of samples collected at different sampling sites. The figure indicates relatively consistent deposition on the Mulurulu lunette from over 80 ka up until at least 18 ka, despite unconformable contacts and at least four palaeosol development phases (around 80-60 ka, 34 ka, 23 ka, and 18 ka). There is also a very thick, relatively modern unit deposited within the last 200 years.

8.1.1. Unit A

The oldest lunette unit present at Lake Mulurulu is Unit A. This unit was represented as Unit I in Douglas (1996; Section 2.4). It represents the initial stage of lunette formation, over what was previously a fluvial system, as indicated by palaeochannel traces (Douglas 1996). It can be correlated to the 'Golgol' unit from Lake Mungo (Bowler 1998), which was described as sandy clays with a deep red calcareous soil, characterised by calcrete and red colouration. Bowler & Price (1998) dated the unit to >100 ka at Lake Mungo, which Bowler (1998) pointed out meant it represented a deflational period, preceded by a lake-full phase, during the penultimate glacial cycle. Although there may have been some offset in the timing of this early drying of Lake Mulurulu and Lake Mungo, due to the relative antiquity of this unit, the difference is unlikely to be resolvable using OSL dating techniques.

Described and interpreted in Section 3.3.1.2, the upper limit on the age of this sandy clay unit could not be determined due to the presence of saturated aliquots. At PR01, four of 18 aliquots were rejected from K2079 due to saturation. K2080 was collected from higher in the unit, but showed evidence of sediment mixing, with at least two, and possibly three, populations. All 18 aliquots of sample K2089, collected from deep within Unit A at PR04, were rejected due to saturation, while for the sample from higher in the unit at this location (K2090) one aliquot was rejected due to saturation and a CAM estimate of the remaining aliquots results in an age of ~110 ka. The other site at which Unit A was dated is SL44 in a blowout in the rear of the lunette. Sample K2123 was collected from a small pit dug into the floor of the blow-out and resulted in a bimodally distributed PD plot. Unfortunately, the lack of stratigraphic context for this sample makes it difficult to assess the cause of the two populations, and hence no particular population can be selected to represent the 'true age' of

the sample. Likewise, sample K2124, from the side of the blow-out, indicates extensive mixing, with a very broad dose distribution, ranging from 12 to 80 Gy.

The dating of this unit was plagued with issues, such as saturation and mixing. Ages range from over 100 ka (PR04 and PR01) and 90 ka (SL44) to around 60 ka (PR01), but due to the number of saturated aliquots removed from these samples, most of these can be considered minimum estimates only. *OxCal 4.2* gave a depositional range for this unit from around 123-96 to 68-58 ka. The mixing issues are likely to be due to the very thick palaeosol in this unit (Section 7.4.1.2). The evidence of this palaeosol is readily apparent in thin sections and sediment samples, with abundant illuvial clays, extensive primary and secondary cutan development and the presence of carbonate nodules, which were also visible in the field. During the long period of stability and palaeosol development that generated this extensive alteration, pedogenic and bioturbitic processes may have caused the movement of grains up and down the turbated section, mixing older grains with younger grains, resulting in the variety of D_e values observed in the sample populations. This is a known problem in palaeosols (Bateman et al. 2003) and is the reason palaeosols are avoided when OSL sampling. At this site, however, the thickness of the palaeosol and the inability to dig trenches resulted in palaeosol sampling being the only option for this unit. It is highly likely that the ~60 ka age for the upper boundary of Unit A is erroneously young due to this in-mixing of younger grains.

8.1.2. Unit B

Unit B is a clean sand unit with re-worked red sands at the base, overlying Unit A. This unit is represented at all four exposed transect sites and is overlain with a PCD (Unit C) which has either been removed, or was not deposited at the far southern end of the lunette, where Unit B is immediately overlain by Unit D. The unit is described and interpreted in Section 3.3.1.3. Douglas (1996) designated this unit as Unit G, with Unit G1 comprised of the re-worked red sands at the base of the unit and Unit G2 comprised of clean sands.

Most of the more reliable age estimates fall between around 60 to 30 ka, and *OxCal 4.2* gave a depositional range for this unit of around 64-56 to 34-30 ka, making it roughly equivalent to the Mungo period of Bowler et al. (2012). One sample, K2091, gave a much older age, closer

to 80 ka. This sample was collected from within the re-worked red sand layer immediately above Unit A. The presence of older aliquots in this sample are indicative of the mixing in of older material from Unit A (see above), Four aliquots gave D_e estimates over 140 Gy (similar to the CAM D_e of the underlying sample from Unit A, K2090) and though these aliquots were removed before CAM calculation, it is likely that at least some similarly ancient grains were included in the remaining aliquots, skewing the results toward an older age. This sample was thus considered an outlier with regard to modelling the age of the unit.

At PR04, two samples bracket a shell midden in Unit B, and the two radiocarbon ages from the midden are around 33 and 40 ka Cal. BP. The upper sample, K2092 from above the midden, gives an OSL age of around 52 ka, suggesting an age inversion at this site. The radiocarbon results are at the limit of radiocarbon dating via the technique used, and because of this, combined with the potential for diagenetic alteration, the result of 40 ka Cal. BP is a minimum age only. As such, the age inversion can be explained through a combination of radiocarbon measurement limits and OSL sediment mixing; putting the age of the shell midden between 50 to 40 ka.

Shells derived from Unit B at PR02 and PR05, both at the north end of the lunette, were also radiocarbon dated, giving results around 31 and 37 ka Cal. BP respectively. At these sites the radiocarbon ages fall within the error of corroborating OSL ages, each derived from reliable CAM estimates from normally distributed data (K2098 and K2115). These shell middens therefore date to the latest Mungo or earliest Arumpo time of Bowler et al. (2012) and appear to be from the same period as a shell midden with an age of 33.86 ± 0.71 ka Cal. BP from Lake Mulurulu, reported in Bowler et al. (2012).

8.1.3. Unit C

Unit C is a pelletal clay unit described and interpreted in Section 3.3.1.4. This unit marks a drying phase and was labelled as Unit E by Douglas (1996). *OxCal 4.2* gave a depositional range for this unit of around 46-37 to 24-17 ka, indicating a wide range of overlap with the under- and overlying Units B and D. The most parsimonious explanation for this is that the unit actually consists of two components; one in the southern and central portions of the lunette, dating to around 40-35 ka, correlating with Bowler et al.'s (2012) Mungo drying

phase; and the other in the central and northern portions of the lunette, dating to around 32-29 ka. These are seen in contact with one another at SL 11, while the earlier PCD is present at PR04 (K2093) and the later one at PR05 (K2114). This suggests earlier drying, commencing at around 40 ka, is preserved at the southern end of the lunette, while sand deposition of Unit D continued at the northern end of the lunette, up until the earliest part of the Arumpo period (see above). Fitzsimmons et al. (2014) found similarly spatially variable deposition of sediments along the Mungo lunette, which they attributed to variation in the prevailing wind regimes.

As mentioned above, the shell middens from PR02 and one from PR04 date to the earliest Arumpo lake full phase, as do the uppermost sediments of Unit B at PR02 and PR05. The only other samples to give an age range within the lower Arumpo lake full phase is K2113, a problematic sample from Unit D that gives an apparently older age than the underlying Unit C sample (K2114). Thus, no reliable age estimates were found for the middle part of the Arumpo lake full phase. Sediments dating to this period may have been eroded; however, the Unit C palaeosols at SL11 appear conformable. This suggests early drying (late Mungo phase) followed by stability with little to no QSD deposition at the site of SL11 (while deposition continued at the north end of the lunette; early Arumpo Phase), then further drying and reactivation of lake clays (middle Arumpo phase).

8.1.4. Unit D

Unit D is a quartz sand unit topped with a rubified and sometimes calcified palaeosol, described and interpreted in Section 3.3.1.5. Unit D was sampled at the south end of the lunette (PR01) where it directly overlays Unit B; and at the north end (PR05) where the PCD Unit C separates the two sandy layers. Douglas (1996) also referred to the clean sands of this unit as Unit D, designating the palaeosol as Unit C.

As mentioned above, although Unit D appears to cover the range of the Arumpo period at PR05, this is due mostly to one sample, K2113, the estimated age range for which is older than the underlying Unit C sample K2114. The age ranges for these two samples do not quite overlap, but almost meet at 29 ka, indicating a possible estimated age for this contact. Likewise, two other samples, K2117 and K2118, provide ages similar to that of K2114, but

must be stratigraphically younger. Deposition therefore likely started around 29 ka, mid Arumpo phase, and continued throughout the Zanci period, where it is recorded at both PR01 and PR05. *OxCal 4.2* gave a depositional range for this unit of around 31-28 to 18-14 ka, which fits with this interpretation.

A final drying of this unit is recorded as a thin but continuous PCD layer capping Unit D at the south end of the lunette. This drying was previously thought to be unrepresented at lake Mulurulu (Douglas 1996; Bowler 1998), but the thin-section of this layer clearly shows that it contains clay pellets (Figure 3.28). An attempt was made to OSL date this thin PCD layer (K2085), where it outcrops at PR01; however the result was a modern age indistinguishable from the typical results of Unit E sands, suggesting that the quartz gathered from this clay-rich sample was actually modern sand blown in to the desiccation cracks in the clay. The youngest reliable OSL age from beneath the clay layer at PR01 is K2082, with an age of around 17.6 ± 1.2 ka. This is almost identical to the youngest reliable OSL age from PR05, of 17.4 ± 1.0 ka in sample K2121.

Radiocarbon ages of otoliths and shells from this layer all give ages around 20-18 ka Cal. BP. Bowler et al. (2012) collated radiocarbon dating results of shells and otoliths from Lake Mulurulu, resulting in 14 samples dating to between 22-18 ka Cal. BP (Zanci), in addition to the one older sample mentioned above.

Two samples from Unit D gave OSL ages younger than 17 ka, one from PR01 (K2084) and the other from PR05 (K2111), with age results of 65.9± 0.06 and 1.2 ± 1.1 ka, respectively. Both are sampled from the palaeosol section of the unit, and while the latter gives an almost entirely modern age, the former gives a very scattered distribution, suggesting very high levels of sediment mixing. Both of these samples are therefore not representative of the true age of Unit D and were not used in the Bayesian modelling.

8.1.5. Unit E

Unit E is a thick unit of finely laminated quartz sands, described and interpreted in Section 3.3.1.6. Bowler (1998) and Douglas (1996) appear to have interpreted this unit to represent the last lake full phase of Mulurulu, designating the unit as Unit B in Douglas (1996). It

seems likely that this unit is also the 'post Zanci blanket' identified by Dare Edwards (1979). The unit, however, consistently gives modern ages, suggesting that it was deposited within the last couple of hundred years. The unit contains rare stray clay pellets, carbonate nodules and re-worked rubified grains and likely represents the remobilisation of the lower units during the current erosional regime. The unit is itself eroded, forming cliffs and pedestals in various locations, presumably supplying much of the sand for the modern mobile dunes flanking the leeward side of the lunette. Prior to this research, it was assumed that the modern mobile sand dunes at Mulurulu represented the remobilisation of sediments after European arrival; possibly due to sheep grazing in the region. This work suggests, however, that far more material than previously realised has been mobilised in the last 200 years; enough to deposit the very thick laminated layer that forms a large portion of the exposures on the Mulurulu lunette; in addition to the mobile sands.

8.1.6. Summary

Table 8.1 provides a summary of the Mulurulu units and their estimated ages from this study. Detailed sediment descriptions can be found in Appendix C.

Table 8.1. Summary of the stratigraphic units of the Lake Mulurulu lunette.

Unit	Characteristics	Estimated age
A	Clay and carbonate rich poorly sorted sands with evidence of disaggregated clay pellets and a thick rubified palaeosol with gypsum rosettes.	>110->60 ka
B	Moderately to well-sorted quartz sand with inconsistent palaeosol development	60-40 (southern end) 60-32 (northern end)
C	Medium to fine grained sandy pelletal clay with rare gypsum rosettes.	40-35 (Southern end) 32-28 (northern end)
D	Moderately to well-sorted quartz sand. Rubified and calcified (carbonate nodules and rhizomorphs) palaeosol. Capped by thin (~10cm) PCD at south end of lunette.	28-17 ka
E	Thick unit of poorly consolidated quartz sands. Usually but not always laminated. Some re-worked clay pellets.	<200 years

8.2. Depositional history and palaeoenvironments at Lake Mulurulu

Figure 8.3A presents the *OxCal* Bayesian analysis results for boundary ages for each unit at Lake Mulurulu compared with the Willandra Lakes lake level curve of Bower et al. (2012; See Figure 2.6 for the full-size version of the curve). Figure 8.3B juxtaposes the timing of other palaeoenvironmental and archaeological records from the Willandra Lakes and broader region, on the same timescale as the unit boundaries in Figure 8.3A. These records include pedogenesis at Lake Mungo (Fitzsimmons et al 2014), ages for earliest human remains and stone artefacts at Lake Mungo (Bowler et al. 2003), high fluvial activity levels in the Lachlan catchment (Kemp & Rhodes 2010), increased precipitation levels in the Murray Darling Basin, as evidenced in speleothem growth at Naracoorte Caves (Ayliffe et al. 1998) and marine oxygen isotope stages over the last glacial-interglacial cycle (adapted from Martinson et al. 1987).

Prior to 110 ka the lake at Mulurulu commenced drying, leading to clay pellet formation on the lake floor and initiating clay dune formation. This formed the Unit A core of the Mulurulu lunette over flood plain sediments. This is the earliest evidence of clay-dune building at Lake Mulurulu, and suggests a change in climatic conditions, causing the previously stable perennial lake to dry out for what may have been the first time. This process was likely driven by regional aridity. A hiatus in speleothem growth at Naracoorte Caves indicates a net water deficit and thus a relatively arid period across the Murray-Darling Basin, around 155-120 ka (Ayliffe et al. 1998). Previously published age estimates of Willandra Lakes records of this drying event consist of TL ages of the Golgol unit at Lake Mungo ranging between 180 and 98 ka, with uncertainties up to 30% (Bowler & Price 1998) and one OSL minimum age estimate of >141 ka (Fitsimmons et al. 2014). Although the onset of this depositional phase across the Willandra Lakes is poorly constrained, it probably predated the last interglacial and was prolonged, continuing throughout MIS 5.

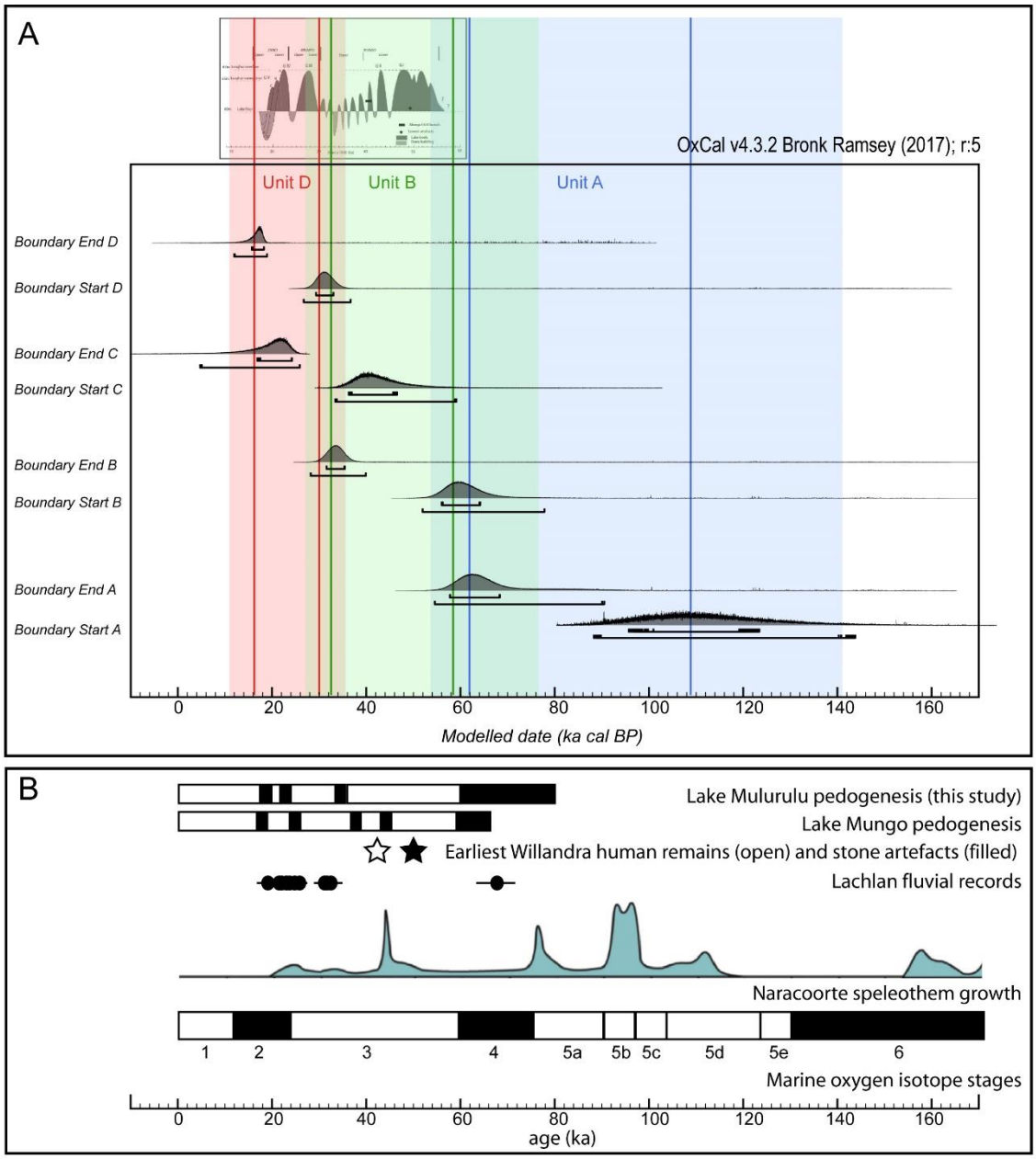

Figure 8.3. A: Bayesian modelling results for boundary ages for Units A (dry lake), B (lake full), C (dry lake) and D (lake full), compared with the Willandra lake-level curve (Bowler et al. 2012, full size image in Figure 2.6). Shaded areas show the 95% confidence intervals for Units A (blue), B (green) and D (red), while the vertical lines show the ranges using the peaks of the modelled ages. Unit C overlaps with both Units B and D; see Section 8.1.3 for discussion. B. Other palaeoenvironmental and archaeological records. Lake Mungo pedogenesis from Fitzsimmons et al. (2014), Ages for earliest human remains and stone artefacts from Bowler et al. (2003), Lachlan fluvial records from Kemp & Rhodes (2010), Naracoorte speleothem growth from Ayliffe et al. (1998). Marine oxygen isotope zones adapted from Martinson et al. (1987).

Arid conditions and uni-directional winds allowed a thick clay-rich dune to continue to be deposited until as recently as 70 ka. It is possible that episodic wetting and drying may have occurred, but if it did, any stratigraphic evidence of this, such as thin laminated sand and clay layers, have been destroyed through pedogenic processes. This pedogenesis occurred during the protracted period of stability that followed. During this time, the dunes were colonised by vegetation, as evidenced by the formation of the deep red calcareous soil. Sometime during MIS 4, vegetation ceased holding the soil in place, and erosional processes stripped the soil back to the resistant calcareous horizon, reworking the red iron-rich upper-most sandy soil in the process. This apparent vegetation loss correlates with another period of net water deficit recorded in speleothems at Naracoorte (Ayliffe et al 1998).

Throughout this low-water level phase, the Willandra Creek wound channels through the previous lake floor (Douglas 1996), until rising fresh water returned to the lake, around 60 ka. Around this time, the other lakes in the system also commencing filling (Bowler et al. 2012). OSL dates for the Lower Mungo unit at Lake Mungo range from, ~62-42 ka, (Bowler et al. 2003) and ~50-40 ka (Fitzsimmons et al. 2014). Throughout MIS 3, quartz beaches built up on the shores of the lake along the edge of the Mulurulu lunette, and the saltation of these beach sands deposited the Unit B sandy dunes over the pre-existing clay dune. This period also correlates with a period of reduced aeolian dune activity in the region (Lomax et al. 2011) and increased effective precipitation in the lower Murray Darling Basin (Ayliffe et al. 1998). Shell middens in this layer corroborate the sedimentological evidence for fresh water, and also indicate the presence of humans in this environment. One midden at the base of the layer may suggest human activity as long ago as 50-40 ka. This is a similar age to the earliest dated stone artefacts at Lake Mungo, which indicate that humans were present in the landscape from around 50-46 ka (Bowler et al. 2003).

Lake Mungo commenced oscillating between wet and dry periods (Upper Mungo unit) around 40 ka. Mulurulu remained full, with quartz sands of Unit B continuing to be deposited along the full length of the lunette until after 40 ka. Not long after this, the lake commenced drying out, first evidenced at the southern end of the lunette with the deposition of the clay-rich Unit C over the Unit B quartz sands, while sandy beaches still fed sandy dunes at the northern end of the lunette and shell middens continued to be produced until around 32 ka. Unlike the Upper Mungo unit there is no evidence of oscillating wet and dry periods leading to laminated

sand and clay layers in Unit C at Lake Mulurulu. The distal positioning of Lake Mungo in the Willandra system, as an overflow lake from Lake Leaghur, makes it more sensitive to hydrologic variations, only filling during periods of particularly high water, while the proximal lakes in the system, as evidenced by Lake Mulurulu here, continued to be constantly recharged. A period of stability around 35-30 ka permitted the formation of a soil profile in the clay-rich Unit C layer at the southern end of the lunette, while sand continued to be deposited on Unit B at the north end. This period correlates with high-run-off, demonstrated by high discharge in large meandering palaeochannels throughout the central Murray Darling Basin (Kemp & Rhodes 2010). This was probably associated with higher precipitation in the alpine highland catchment and periglacial activity related to glacial advance around this same period (Barrows et al. 2001). The remaining water from the northern end of the lake gradually dried out by 28 ka adding the second clay-rich layer of Unit C, over the sands at the northern end, with the two clay layers directly overlaying each other in the central portion of the lunette. The north-south heterogeneity in the timing of deposition of Unit C could reflect the stratigraphic impact of an early event on the neotectonic tilting axis that later created the crossed shorelines (see below). If so, no geomorphic expression of this earlier event appears to have been preserved. Wombats were also occupying the region sometime during or following the deposition of this clay-rich layer.

Around 28 ka lake water again returned and remained at Lake Mulurulu throughout the Arumpo and Zanci periods of Lake Mungo. This includes the Arumpo drying phase 25-23 ka, during which lake levels oscillated at lake Mungo (Bowler et al. 2012), evidence of which is not apparent at lake Mulurulu. The Unit D sand accumulated across the entire Mulurulu lunette throughout this time period. The lake remained wet throughout most of MIS 2 and during the LGM, as evidenced by middens containing mussel shells and fish otoliths. Around 24 ka just prior to the LGM, Lake Mungo experienced a very high lake filling phase, up to 5 m deeper than any preceding or subsequent lake-full events, representing a lake volume increase of almost 250% (Fitzsimmons et al. 2015). Evidence of this was not recorded at Lake Mulurulu, though field work for this study was carried out before the reporting of that event, so the evidence may be there, just not recognised or investigated. Oxygen isotopes in otoliths collected from both lakes Mungo (Boljkovac 2009; Long 2014) and Mulurulu do record evidence for periodic fresh-water flushing of the lake system, though no otoliths from the

region have been dated to the time of this ‘mega-lake’. Fitzsimmons et al. (2015) suggest this ‘mega-lake’ was caused by a pulse of high catchment rainfall combined with neotectonic activity that may have warped the lake basin. This neotectonic tilting during this wet phase also created crossed strandlines at Lake Mulurulu, recognised by Douglas (1996), when uplift raised the level of the outlet channel and tilted the lake-floor to the northeast, realigning the strand line, building the ‘spit’ in the south and cutting a new beach platform into the northern dunes. This period also correlates with increased fluvial activity in the Lachlan Catchment (Kemp & Spooner 2007,; Kemp & Rhodes 2010), increased snow melt associated with periglaciation and the Blue Lake Glacial Advance in the alpine highlands (Barrows et al. 2001).

Despite the high levels of fluvial activity, potentially triggered by reduced vegetation cover leading to more run-off (Kemp & Rhodes 2010) as well as periglacial activity in the highlands (Barrows et al. 2001), the local region was experiencing an arid phase throughout the LGM, with active aeolian dune building (Lomax et al. 2011). The final drying of Lake Mulurulu occurred swiftly sometime around 17 ka, with the only record being a thin pelletal clay-rich layer at the south end of lunette, indicating that the water table dropped very quickly. There is some evidence recorded in otolith geochemistry that temporary drying of Lake Mulurulu may have occurred around 19 ka. This signal has been observed in a number of Lake Mungo otoliths (Boljkovac 2009), corroborating the abundant stratigraphic evidence of episodic drying of that lake, but this is the first time it been recorded at Lake Mulurulu. This suggests that although drying at Lake Mulurulu may not be strongly episodic enough to record stratigraphic evidence, there was still some degree of oscillation in water levels as the lake dried out.

After this final drying, a long period of stability and soil formation ensued. Perennial lake water has not since returned to the lake; Bowler (2008) suggests the channel was diverted upstream, leading to development of the present Lachlan channel. This conclusion was corroborated by Kemp et al. (2017), with geomorphological, geophysical and sedimentological evidence suggesting a diversion of runoff from the Willandra Lakes to the more southern areas of the Lachlan alluvial plains at or shortly before 18.4 ka. In studying the present lake floor and low sand shoreline, however, Douglas (1996) concluded that short, episodic flooding has continued intermittently during Holocene times. The current erosional

phase appears to have been initiated probably less than 200 years ago, after European colonisation of the region. The very thick young Unit E was deposited onto the lunette, mantling the eroded layers beneath. This unit is itself heavily eroded, forming striking laminated residuals, and supplying modern sand to the mobile dunes flanking the lee-side of the Mulurulu lunette.

Chapter 9. Conclusions and recommendations

9.1. Conclusions from this research

The primary aim of this research was to provide a depositional and palaeoenvironmental history of Lake Mulurulu in the Willandra Lakes World Heritage Area, over the last 150 ka. Three questions were posed in Chapter 1, to address this aim, and test the hypothesis that the differing hydrological regime at Lake Mulurulu would result in a complimentary but distinctive record of wetting and drying events to that recorded in the sediments of Lake Mungo, with fewer drying events, little-to-no indications of short-term lake level fluctuations, and less indication of salinity stress.

Multiple techniques were utilised in the pursuit of answering these questions, including various geochronological methods, isotopic analyses of faunal materials, and stratigraphic descriptions. The focus was on OSL dating of quartz in sediments characterised to determine the broad-scale palaeoenvironmental history. To compliment this work, a small number of oxygen isotope analyses were conducted on two types of faunal materials, fish otoliths and wombat teeth, in order to compare small-scale palaeoenvironmental information with the broad-scale garnered from the stratigraphic work. In measuring isotopes, two different measurement techniques were utilised; SHRIMP and CF-IRMS, allowing the techniques to be compared. Attempts were made to directly date faunal materials using radiocarbon and ESR dating, to provide a geochronological context for the isotopic results, plus a comparison to the OSL results for the interring sediments. By characterising and dating the stratigraphic layers of, and faunal materials within, the lunette, a palaeoenvironmental history of the lake was constructed, and compared with the existing knowledge on the history of the other lakes in the system; primarily, Lake Mungo. Through this work, the three questions posed in Chapter 1 were addressed:

What are the sedimentological and stratigraphic characteristics of the depositional units of the Mulurulu lunette, when were they deposited, and what palaeoenvironments do they represent?

Five main units comprise the Lake Mulurulu lunette, with following features:

- Unit A: A clay and carbonate rich poorly sorted sand with evidence of disaggregated clay pellets and a thick rubified palaeosol. The unit dates from >60 to >110 ka and is time equivalent to the Golgol unit at Lake Mungo. It forms the core of the lunette and represents an early drying and deflation period.

- Unit B: A moderately to well-sorted quartz sand with inconsistent palaeosol development. The unit commenced depositing around 60 ka and ceased around 40 ka at the southern and central portions of the lunette, continuing until 32 ka at the northern end. It is time equivalent to the Lower and part of the Upper Mungo units at Lake Mungo and represents a long lake-full period, with the southern end of the lake commencing drying before the northern.

- Unit C: A medium to fine grained sandy pelletal clay. The unit dates from 40 to 32 ka in the central portion of the lunette, where the record of lake drying commenced earlier, and to 32 to 29 ka at the northern end of the lunette, indicating later lake drying in this area. It is time equivalent to the latter part of the Upper Mungo unit at Lake Mungo.

- Unit D: A moderately well-sorted quartz sand with a rubified and calcified palaeosol at the north end of the lunette and capped by a thin pelletal clay layer at the south. The unit dates from 28 to 17 ka and is time equivalent to the Arumpo and Zanci units of Lake Mungo. The unit represents a later lake-full phase, with no evidence of drying during the Arumpo period, and a very short-lived drying phase at the end of the Zanci period.

- Unit E: A thick unit of poorly consolidated quartz sands with some re-worked clay pellets, usually but not always laminated. This unit dates to less than 200 years and is derived from the erosion and re-working of the other lunette layers. It reflects the

recent relatively arid conditions in the region, with erosional processes possibly initiated or exacerbated by the impact of sheep grazing.

Other materials not named as defined units in this study include the mobile modern sand flanking the crests and lee-side of the lunette, which was not dated, and the beach ridges and southern 'spit', for which the OSL dating was unsuccessful due to modern soil forming processes and bioturbation.

The chronostratigraphic context for the depositional units was provided primarily through OSL dating, with complementary radiocarbon dating of mussel shells. Additional conclusions about the use of these techniques can be drawn from this work.

The OSL dating demonstrated that these aeolian sediments are well suited to the technique, with very little partial bleaching identified. Small (~20 grain) multi-grain aliquots were utilised, resulting in very little evidence for heterogeneous beta-dosing, though sediment mixing was a common issue. In most cases, interpretation of dose distributions with regard to the stratigraphic context of the samples allowed the identification of the grain populations most likely to represent the true burial dose of sediments in mixed samples. Grain transport across unit boundaries was identified and the relevant population selected for estimating equivalent dose. In other cases, such as in palaeosols with extensive internal sediment mixing, the mixing was too thorough to allow a single datable population to be identified. Issues were identified with very young samples, including low precision, high recuperation rates and high overdispersion. In this case, however, the low precision results achieved were sufficient for demonstrating the age of the unit to be very recent relative to rest of the dated lunette building episodes. OSL dating provided a geochronological framework to date the five stratigraphic units identified within the lunette. Overlap in age between units indicated heterogeneous deposition along the length of the lunette. All depositional periods overlapped within the 2σ error of the modelled dates for the boundaries of the unit ranges, indicating nearly continuous deposition. Palaeosols on most of the units, however, indicate that depositional hiatuses did in fact occur, but the OSL dating is not precise enough to identify the exact timing or duration of these episodes.

Radiocarbon dating carried out on mussel shells resulted in ages in two clusters: 20-17 ka Cal. BP and 40-30 ka Cal. BP. These ages largely corroborate previous radiocarbon dates at Lake

Mulurulu as well as elsewhere in the Willandra Lakes. The radiocarbon dating was successful, though a few mussel shell dates did not directly agree with the OSL dates for the interring sediments. The most likely causes of discrepancies are incorrect stratigraphic correlations, potential carbonate diagenesis or dating results at the limit of the technique representing minimum ages only.

What palaeoclimatic signals can be identified in faunal materials from the Mulurulu lunette, and what time period do they represent?

Palaeoclimatic signals were investigated in fish otoliths and wombat teeth, using stable oxygen isotopes as an environmental proxy.

SHRIMP analyses of two otolith samples showed a pattern of gradually increasing $\delta^{18}O$, overprinted with occasional fluctuations. This could potentially indicate a gradual drying trend and occasional flooding events. Alternatively it may indicate that the fish migrated along a chemical gradient, not necessarily related to salinity, but possibly due to other geographic factors such as decreasing latitude and/or altitude. One of the otoliths (OT27), however, showed a sudden increase in Sr/Ca indicative of entry into more saline waters. This is a pattern seen commonly in otoliths of a similar age from Lake Mungo, but this is the first time it has been seen in a sample from Lake Mulurulu, where previously analysed otoliths have shown no indication of saline stress. The SHRIMP analysis of oxygen isotopes in aragonitic fish otoliths proved highly successful, with re-analysis of the same otoliths demonstrating very high reproducibility of results. The oxygen isotope analyses were particularly informative once combined with trace element analyses carried out along the same transect of the otoliths using LA-ICPMS.

Radiocarbon dating of the fish otoliths resulted in ages around 19-20 ka Cal. BP. These ages fall within a cluster of previous radiocarbon dates at Lake Mulurulu as well as elsewhere in the Willandra Lakes. The date of 19.7-19.2 ka Cal. BP for OT27 suggests a short term drying event, well before the final drying of the lake around 17 ka Cal. BP. This suggests that drying during some seasons may have been sufficient to produce salinity changes that are recorded in otolith chemistry over short timescales, but insufficient to leave evidence in the stratigraphy of sediments of the Mulurulu lunette.

CHAPTER 9. CONCLUSIONS AND RECOMMENDATIONS

Oxygen isotope analyses of wombat tooth enamel were carried out on two samples using SHRIMP and 14 samples using CF-IRMS. The SHRIMP analyses showed gradually increasing $\delta^{18}O$ along the growth axis of the tooth enamel, probably related to changing environmental humidity with a change of seasons. A re-run section on one of the teeth demonstrated poor reproducibility, possibly due to diagenetic alteration, as the re-run section was closer to the dentine-enamel junction than the original assay. The CF-IRMS measurements were conducted on powdered slices of tooth enamel, resulting in much lower resolution analysis than that provided via SHRIMP. A seasonal signal could only be identified in four of the 14 samples, and whether this low occurrence was due to insufficient tooth fragment length, or a true lack of seasonality in the majority of samples was not discernible.

The direct dating of wombat teeth via ESR and U-series dating was largely unsuccessful. The ESR dating was plagued with technical issues, unrelated to the sample materials (repeated hard-disk crashes, decommissioning of equipment etc.). Enough data was salvaged to provide rough indicative ages, but numerous features of the results indicate that these ages are unreliable: different ages for sub-samples of the same tooth, different ages for teeth from the same skull, and many ages older than the interring sediments into which the wombats had presumably burrowed. An attempt was also made to date wombat bone associated with the teeth, via radiocarbon dating, but unfortunately no pristine collagen material was able to be recovered. These issues meant that only a questionable geochronological framework was established for these samples.

How does the depositional and palaeoenvironmental history recorded in the Lake Mulurulu lunette sediments and faunal materials, particularly indicators of drying and salinity, relate to the record in the Lake Mungo lunette, and how do they compare in the context of the broader region and palaeoclimate?

The palaeoenvironmental history of Lake Mulurulu shares similarities with, but is distinct from, Lake Mungo. Although the two major lake-filling events at Lake Mulurulu are broadly time-equivalent to similar events at Lake Mungo, the record of lake-drying is very different.

The OSL dating of Unit A is not of sufficient resolution to determine a discrepancy between the timing of this drying event at Lake Mulurulu relative to Lake Mungo. In both cases the drying was slow, leading to the development of a thick clay-rich layer, and suggests a change

in the prevailing regional climate, as it forms the earliest evidence of clay dune building across the Willandra Lakes. This arid phase is likely to be related to warming leading in to the MIS 5e interglacial event.

Lake Mungo exhibits alternating lamina of sand and clay-rich facies during the drying phases of the Upper Mungo, Arumpo and Zanci units. In contrast at Lake Mulurulu, the pelletal clay-rich layers (Unit A and Unit C) do not generally display this indicator of oscillating lake levels. This is as predicted due to Lake Mulurulu's direct connection to the Willandra creek and positioning higher in the Willandra over-flow system. None-the-less, salinity indicators do occur in both Units A and C, in the form of gypsum rosettes, as well as clay pellets.

The drying phases of Mungo and Mulurulu were somewhat decoupled during much of the last glacial cycle. While it was thought that the drying of Lake Mulurulu may lag behind that of Lake Mungo, being the first to fill and last to dry during each broad scale wet-dry cycle (Bowler et al. 2012), it appears that in fact the timing of drying events at Lake Mulurulu was very different to Lake Mungo, drying out very gradually during the Upper Mungo phase, not at all during the Arumpo phase, and very swiftly during the Upper Zanci phase.

The gradual drying during the Upper Mungo phase occurred first in the south end of the lunette (commencing ~40 ka), while the north end continued to receive input of clean quartz beach sands up until ~32 ka. This period (~34-32 ka) was a time of high discharge in the meandering palaeochannels of the Murray Darling Basin (Kemp & Rhodes 2010), possibly supplying the water source for the Willandra Creek. The northern end of the lake gradually dried out around 32-28 ka adding the second clay-rich layer of Unit C. This phase of drying correlates with the end of the Upper Mungo dry phase at Lake Mungo, around 30 ka. Lake Mungo underwent repeated cycles of inundation and drying, while Lake Mulurulu experienced this gradual south to north desiccation.

The clean quartz sands of Unit D were deposited across the Mulurulu lunette throughout the Arumpo and Zanci periods. Thus Lake Mulurulu shows no evidence of drying during the Upper Arumpo drying event at Lake Mungo (25-23 ka). Although the period leading in to the LGM was regionally relatively arid (Lomax et al. 2011), increased fluvial activity was again recorded in the Lachlan catchment possibly due to reduced vegetation cover leading to run-off (Kemp & Rhodes 2010). Thus this fluvial input meant Lake Mulurulu remained sufficiently

charged to maintain a lake presence while Lake Mungo underwent oscillating wetting and drying.

The final drying following the LGM occurred around 17 ka. This occurred at both lakes Mungo and Mulurulu, though probably earlier at Mungo, and again, accompanied with interbedded quartz and clay-rich laminae, that do not occur at Lake Mulurulu. Indeed, there is very little pelletal clay development at Lake Mulurulu during this drying period, indicating that Lake Mulurulu dried relatively quickly. A fish otolith from Lake Mulurulu dated to ~19 ka shows evidence of entering a water body with saline conditions shortly prior to death. So although oscillating water levels are not recorded in the stratigraphy at Mulurulu like they are at Mungo, the less extreme events of Mulurulu may be recorded in the high resolution biological materials from the lake.

Previous work on the lunette chronology at Lake Mulurulu comprises a total of 14 radiocarbon dates (summarised in Bowler et al., 2012, see Section 5.1). Although Bowler et al. (2012) incorporated Mulurulu in to their Willandra lake level curve, .the only time Lake Mulrulu has previously formed a focus of detailed research was during Douglas' 1996 honours work. That work utilised an even more limited set of radiocarbon dates to compare three exposures at Lake Mulurulu with the existing stratigraphic understanding of the Lake Mungo Lunette—an understanding that has since been revised and in parts, superceeded, with far more comprehensive unit mapping and OSL dating at Lake Mungo than was available at that time (e.g. Bowler et al., 2012; Stern et al. 2013; Fitzzimmons et al., 2014; 2015 and Fitzsimmons 2017). Until now, similar revision and updating of the Lake Mulurulu stratigraphy had been lacking.

Combining detailed stratigraphic work with a robust geochronological framework has allowed a palaeoenvironmental history to be created for the Lake Mulurulu lunette. This work adds to the existing knowledge of the Willandra Lakes system. It provides an augmented view of the history of wetting and drying in the region, as recorded at a flow-through lake in the upstream portion of the lake system, as opposed to the more hydrologically sensitive Lake Mungo in the southern portion of the system, which has been the focus of studies in the region to date. It demonstrates that as predicted, Lake Mulurulu has a differing arid response compared to Lake

Mungo, experiencing fewer drying events, little-to-no indications of short-term lake level fluctuations, and less indication of salinity stress.

9.2. Recommendations for future work

A number of recommendations for future work at Lake Mulurulu emerge from additional questions raised through this research. There is a lot of information to be gained through targeted OSL dating programs, further isotopic investigations and investigations in to the relationship between the evolution of the landscape and the presence of human occupation on the lake lunette.

- Targeted dating of Unit A
    - The dune core, representing the initiation of drying in the Willandra Lakes would benefit from targeted OSL work, using a methodology devised specifically for old samples nearing saturation of luminescence centres. This work would be valuable at Lake Mulurulu as well as elsewhere in the Willandra Lakes.
- Comprehensive characterisation and dating of Unit C
    - The diachronous nature of the Unit C results, and the overlapping age range with both Units B and D, raises questions about the timing and nature of the 40-28 ka drying period at Lake Mulurulu. Clarification of the timing of deposition, plus focussed stratigraphic work to characterise the lateral variation in the unit and its stratigraphic relationship with the underlying and overlying units B and D would help to provide a better understanding of this drawn-out drying phase.
- Clarification of the timing of deposition of Unit E
    - Focussed work devised specifically for dating young samples would be beneficial for providing reliable dates for Unit E. Evidence of sheep tracks and rabbit burrows in the lunette indicate that European settlement contributes to some extent to the erosional landscape seen in this region. Was the current

deflation of the lunette initiated due to the impact of European settlement? Or simply exacerbated by it? Confirmation that the onset of deposition of Unit E corresponds with the timing of European settlement would support the former conclusion.

- Single-grain dating
    - Any future OSL dating work at Mulurulu should utilise single grain dating methods. Although the quartz-rich sediments at Lake Mulurulu were largely well suited to the technique, post-depositional mixing was a common occurrence. Due to the averaging effects of multi-grain aliquots, discrete burial dose components could only be estimated and not accurately modelled in mixed samples. This recommendation is largely redundant now as over the nine years that have elapsed since the OSL analyses in this study were carried out, single grain dating has continued to become more routine and ubiquitous.
- A comprehensive otolith geochemistry study
    - The otolith geochemistry analyses were very successful, but very few samples were studied. Currently, one of the four otoliths analysed from Lake Mulurulu show evidence of saline conditions. In contrast all but one of thirteen otoliths from Lake Mungo demonstrate a salinity increase prior to the death of the fish (Long et al. 2014). The one otolith in this study that shows a saline signal indicates that there may be more, and that otoliths can carry a record of saline stress that is not indicated in the stratigraphy. A comprehensive set of analyses from Lake Mulurulu would provide a comparison for the sample set from Lake Mungo. Is the rate of one in four otoliths for saline signals representative of the population of unsampled otoliths? Or did this study happen to sample a rare one?
- Stable isotope analyses of fossil Wombat teeth
    - Fraser (2005) demonstrated that geochemical analyses of wombat teeth can provide useful environmental proxies. The few tooth fragments in this study

that provided a seasonal signal demonstrate the potential for these proxies to be preserved in fossil teeth. Targeted selection of long fossil tooth fragments, combined with a suite of other isotopes in addition to oxygen, such as carbon and nitrogen, would provide a more detailed picture of the wombats' environment, than that provided through analysing oxygen alone. The issues with dating the wombat enamel in this study were with the ESR equipment, not the sample material, so wombat teeth in theory should be able to be dated by ESR. The abundance of wombat samples from the Willandra Lakes still hold much promise as a record of geochemical palaeoenvironmental information.

- A study in to human and landscape interactions.
    - Investigation in to the archaeological traces at Lake Mulurulu, beyond dating a small number of shell middens, was outside the scope of the current study. Many studies at Lake Mungo have investigated how humans interact with the lake environment over time as the landscape and environmental conditions change (e.g. Johnston & Clark 1998, Stern et al. 2013, Long et al. 2014, and Fitzsimmons et al. 2015). Lake Mulurulu is replete with evidence of past human occupation, including hundreds of, middens, stone tools, and stone fireplaces, in need of further study.

..

References

Adamiec, G. & Aitken, M. 1998. Dose-rate conversion factors: update. *Ancient TL*. 16, 37-50.

Aitken, M.J. 1985. *Thermoluminescence Dating,* Academic Press, London

Aitken, M. J. 1997. Luminescence Dating. In. R. E. Taylor. & M. J. Aitken (eds.).*Chronometric Dating in Archaeology*. Springer: New York.

Aitken M. J. 1998. *An introduction to optical dating: the dating of Quaternary* sediments by the use of photon-stimulated luminescence. Oxford University Press: New York.

Aitken, M. J. & Smith, B. W. 1988. Optical dating: recuperation after heating. *Quaternary Science Reviews*.7: 387-393.

Aitken, M. J. & Xie, J. 1990. Moisture correction for annual gamma dose. *Ancient TL*. 8: 6-9.

Allen, H. 1998. Reinterpreting the 1969-1972 Willandra Lakes archaeological surveys. *Archaeology in Oceania*. 33, 207-220.

Anderson, J. R., Morison, A. K. & Ray, D. J. 1992. Validation of the use of thin-sectioned otoliths for determining the age and growth of golden perch, *Macquaria ambigua* (Perciformes : Percichthyidae), in the Lower Murray-Darling Basin, Australia. *Australian Journal of Marine and Freshwater* Research. 43, 1103-1128.

Arnold, L. J. & Roberts, R. G. 2009. Stochastic modelling of multi-grain equivalent dose (D_e) distributions: implications for OSL dating of sediment mixtures. *Quaternary Geochronology*. 4: 204–230

Aubert, M., Williams, I. S., Boljkovac, K., Moffat, I., Moncel, M-H., Dufour, E. & Grün, R. 2012. *In situ* oxygen isotope micro-analysis of faunal material and human teeth using

a SHRIMP II: a new tool for palaeo-ecology and archaeology. *Journal of Archaeological Science.* 39: 3184-3194

Ayliffe, L. K. & Chivas, A. R. 1990. Oxygen isotope composition of the bone phosphate of Australian kangaroos: potential as a palaeoenvironmental recorder. *Geochimica et Cosmochimica Acta*. 54, 2603-2609.

Ayliffe, L.K., Marianelli, P.C., Moriarty, K.C., Wells, R.T., McCulloch, M.T., Mortimer, G.E. & Hellstrom, J.C. 1998. 500 ka precipitation record from southeastern Australia: Evidence for interglacial relative aridity. *Geology.* 26: 147-150.

Ayliffe, L. K., Chivas, A. R. & Leakey, M. G. 1994. The retention of primary oxygen isotope compositions of fossil elephant skeletal phosphate *Geochimica et Cosmochimica Acta*.58: 291-529

Ayliffe, L. K., Lister, A. M. & Chivas, A. R. 1992. The preservation of glacial-interglacial climatic signatures in the oxygen isotopes of elephant skeletal phosphate. *Palaeogeography, Palaeoclimatology, Palaeoecology*. 99: 179-191

Bailey, R.M. 2000. The interpretation of quartz optically stimulated luminescence equivalent dose versus time plots. *Radiation Measurements*. 32:129-140.

Bailey R. M. & Arnold L. J. 2006. Statistical modelling of single grain quartz De distributions and an assessment of procedures for estimating burial dose. *Quaternary Science Reviews*. 25: 2475-2502.

Balasse, M., Ambrose, S. H., Smith, A. B. & Price, T. D. 2002. The seasonal mobility model for prehistoric herders in the south-western cape of South Africa assessed by isotopic analysis of sheep tooth enamel. *Journal of Archaeological Science*. 29: 917-932.

Barbour M. M. & Farquhar, G. D. 2000. Relative humidity- and ABA-induced variation in carbon and oxygen isotope ratios of cotton leaves. *Plant Cell Environment*. **23:** 473-485.

Barbour, M. Roden, J., Farquhar, G. & Ehrlinger, J. 2004. Expressing leaf water and cellulose oxygen isotope ratios as enrichment above source water reveals evidence of a Peclet Effect. *Oecologia*. 138: 426-435.

Barrows, T. T., Stone, J. O. Fifield, K., and Cresswell, R. G. 2001. Late Pleistocene Glaciation of the Kosciuszko Massif, Snowy Mountains, Australia. *Quaternary Research* 55, 179–189.

Bateman, M. D., Frederick, C. D., Jaiswal, M. K. & Singhvi, W. K. 2003. Investigations into the potential effects of pedoturbation on luminescence dating. *Quaternary Science Reviews.* **22:** 1169-1176.

Boljkovac, K. 2009. *In situ SHRIMP $\delta^{18}O$ and laser ablation ICP-MS Sr/Ca and $^{87}Sr/^{86}Sr$ measurements in fossil otoliths for palaeoclimate reconstructions at the Willandra Lakes World Heritage Area*. Unpublished BSc (Honours) thesis, Research School of Earth Sciences, Australian National University: Canberra.

Bøtter-Jensen, L., Bulur, E., Duller, G. A. T. & Murray, A. S. 2000. Advances in luminescence instrument systems. *Radiation Measurements*. 32: 523-528.

Bowler, J. M. 1971. Pleistocene salinities and climatic change: evidence from lakes and lunettes in south-eastern Australia. In: D.J. Mulvaney and J. Golson (eds.), *Aboriginal Man and Environment in Australia*. Australian National University Press, Canberra. pp. 47 65.

Bowler, J. M. 1973. Clay dunes: their occurrence, formation and environmental significance. *Earth-Science Reviews*. 9. 315-338

Bowler, J. M. 1983. Lunettes as indices of hydrologic change: a review of the Australian evidence. *Proceeding of the Royal Society of Victoria.* 95, 147-168.

Bowler, J. M. 1998. Willandra Lakes revisited: environmental framework for human occupation. *Archaeology of Oceania*. 33, 120-155.

Bowler, J. M., Jones, R., Allen, H. & Thorne, A. G. 1970. Pleistocene human remains from Australia: a living site and human cremation from Lake Mungo, Western New South Wales. *World Archaeology.* 2: 39–60

Bowler, J.M., Thorne, A.G. & Polach, H.A. 1972. Pleistocene Man in Australia: Age and Significance of the Mungo Skeleton. *Nature*. 240: 48-50.

Bowler, J. M., and Thorne, A. G. (1976). Human remains from Lake Mungo: Discovery and excavation of Lake Mungo III. In R. L. Kirk and A. G. Thorne, (eds.) *The Origin of the Australians*. Australian Institute of Aboriginal Studies: Canberra. pp. 127-138

Bowler, J. M. & Magee, J. W. 1978. Geomorphology of the Mallee region in semi-arid and northern Victoria and western New South Wales. *Proceedings of the Royal Society of Victoria.* 90, 70-88.

Bowler, J. M. & Magee, J. W. 2000. Redating Australia's oldest human remains: a sceptic's view. *Journal of Human Evolution.* 38. 719-726.

Bowler, J. M. & Price, D. M. 1998. Luminescence dates and stratigraphic analyses at Lake Mungo: review and new perspectives. *Archaeology of Oceania*. 33, 156-168.

Bowler, J. M., Hope, G. S., Jennings, J. N., Singh, G. & Walker, D. 1976. Late Quaternary climates of Australia and New Guinea. *Quaternary Research.* 6, 359-394.

Bowler, J. M., Johnston, H., Olley, J. M., Prescott, J. R., Roberts, R. G., Shawcross, W. & Spooner, N. A. 2003. New ages for human occupation and climatic change at Lake Mungo, Australia. *Nature*. 421. p837-840.

Bowler, J. M., Kotsonis, A. & Lawrence, C. R. 2006. Environmental evolution of the Mallee region, Western Murray Basin. *Proceedings of the royal Society of Victoria.* 118, 161-210,

Bowler, J. M., Gillespie, R., Boljkovac, K., Johnson. H. (2012) Wind v Water: Glacial Maximum records from the Willandra Lakes. In: S.G. Haberle & B. David (eds.) *Peopled Landscapes: Archaeological and Biogeographic Approaches to Landscapes. Terra Australis 34*. Canberra: ANU E-Press. pp. 271-296.

Brandon. M. T. 1996. Probability Density Plot for Fission-Track grain-age samples. *Radiation Measurements*. 26: 663-676.

Bronk Ramsey, C. 2008. Radiocarbon dating: revolutions in understanding. *Archaeometry*. 50, 249–275.

Bronk Ramsey, C. 2009a. Bayesian analysis of radiocarbon dates. *Radiocarbon.* 51: 337-360.

Bronk Ramsey, C. 2009b. Dealing with outliers and offsets in radiocarbon dating. *Radiocarbon,* 51: 1023-1045.

Brown, C. M. & Stephenson, A. E. 1991. Geology of the Murray Basin Southeastern Australia. *BMR Bulletin*. 235.

Brown, P. 2000. The first Australians: the debate continues. *Australasian Science.* 21, 28-31.

Budd, P., Montgomery, J., Berreiro, B. & Thomas, R. G. 2000. Differential diagenesis of strontium in archaeological human dental tissues. *Applied Geochemistry*. 15: 687-694.

Bulur, E. 1996. An alternative technique for optically stimulated luminescence (OSL) experiment. *Radiation Measurements*. **26:** 701-709.

Bureau of Meteorology. 2014. Rose of Wind direction versus Wind speed in km/h (13 Jun 1889 to 31 Dec 1949) .http://www.bom.gov.au/clim_data/cdio/tables/pdf/windrose/IDCJCM0021.076077.3pm.pdf. (last accessed 7 July 2015).

Bureau of Meteorology. 2015. Climate statistics for Australian locations: Summary statistics Mildura Post Office. http://www.bom.gov.au/climate/averages/tables/cw_076077.shtml (last accessed 7 July 2015).

Calström, D. 1963. A Crystallographic study of vertebrate otoliths. *Biological Bulletin.* 125, 441-463.

Campana, S. E. 1999. Chemistry and composition of fish otoliths: pathways, mechanisms and applications. *Marine Ecology Progress Series.* 188, 263-297.

Casteel, R. W. 1976. *Fish Remains in Archaeology and Paleo-environmental Studies.* Academic Press. London.

Child, C. 1968. *Australian Pond and Stream Life*. Cheshire-Lansdowne: Melbourne. pp 99.

Chase, P. G., Debénath, A., Dibble, H. L., McPherron, P., Schwarcz, H. P., Stafford Jr., T. W. & Tournepiche, J-F. 2007. New dates for the Fontéchevade (Cherante, France) *Homo* remains. *Journal of Human Evolution*. 52, 217-221.

Clark, P.M. 1987. *Willandra Lakes World Heritage Area archaeological resources study*. Unpublished report, Western Lands Commission, New South Wales Department of Planning, Sydney

Clarkson, C., Jacobs, Z., Marwick, B., Fullagar, R., Wallis, L., Smith, M., Roberts, R. G., Hayes, E., Lowe, K., Carah, X., Florin, S. A., McNeil, J., Cox, D., Arnold, L. J., Hu, Q., Huntley, J., Brand, H. E. A., Manne, T., Fairbairn, A., Shulmeister, J., Lyle, L., Salinas, M., Page, M., Connell, K., Park, G., Norman, K., Murphy, T. & Pardoe, C. Human occupation of northern Australia by 65,000 years ago. *Nature*. 547, 306-310.

Coffey, G. N. 1909. Clay dunes. *Journal of Geology*. 17, 754-755.

Cupper, M. L. 2006. Luminescence and radiocarbon chronologies of playa sedimentation in the Murray Basin, southeastern Australia. *Quaternary Science Reviews.* 25: 2594-2607.

Curnoe, D. & Thorne, A. 2000. The Mungo Man: new dates, old ideas? *Australasian Science.* 21, 24-27.

Daniels, F., Boyd, C. A. & Saunders, D. F. 1953, Thermoluminescence as a research tool. *Science*. 117, 343-349.

Dare-Edwards, A. J. 1979. *Late Quaternary Soils on Clay Dunes of the Willandra Lakes, New South Wales*. Unpublished PHD Thesis. The Australian National University.

Dettman, D. L., Reische, A. K. & Lohmann, K. C. 1999. Controls on the stable isotope composition of seasonal growth bands in aragonitic fresh-water bivalves (unionidae). *Geochimica et Cosmochimica Acta*. 63, 1047-1057.

Douglas, K. 1996. *Land Systems and Stratigraphy of Lake Mulurulu: Examination of Quaternary Palaeoenvironments*. Unpublished Honours Thesis. University of Melbourne.

Duller, G. A. T. 2004. Luminescence dating of Quaternary sediments: recent advances. *Journal of Quaternary Science.* 19, 183-192.

Duller, G.A.T. Assessing the error on equivalent dose estimates derived from single aliquot regenerative dose measurements. Ancient TL, 25: 15–24 2007.

Duller, G.A.T. 2008a. Single-grain optical dating of Quaternary sediments: why aliquot size matters in luminescence dating. *Boreas*, 37: 589-612.

Duller, G.A.T. 2008b. *Luminescence Dating: guidelines on using luminescence dating in archaeology. English Heritage*: Swindon.

Emiliani, C. 1966. Paleotemperature analysis of Caribbean cores P6304-8 and P6304-9 and a generalized temperature curve for the past 425,000 years. *The Journal of Geology*, 74: 109-124.

Farquar G. D. & Lloyd, K. 1993. Carbon and Oxygen isotope effects in the exchange of carbon dioxide between terrestrial plants and the atmosphere. In L. Ehrlinger, A. E. Hall & G. D. Farquar (eds.). *Stable Isotopes and Plant Carbon-Water Relations*. Academic Press; San Diego. 47-70.

Faure, G. & Mensing, T. M. 2005. *Isotopes Principles and Applications, 3rd Edition*. John Wiley & Sons inc: New Jersey.

Fincham, A. G., Moradian-Oldak, J. & Simmer, J. P. 1999. The Structural Biology of the Developing Dental Enamel Matrix. *Journal of Structural Biology.* 126:270-299

Fisk, H.N. 1959. Padre Island and the Laguna Madre flats, coastal south Texas. In: Russell, R.J. (ed). *Second Coastal Geography Conference*. Louisiana State University: Washington D.C.

Fitzsimmons, K. 2007. *The late Quaternary history of aridity in the Strzelecki and Tirari Desert Dunefields, South Australia*. Unpublished PhD thesis: The Australian National University.

Fitzsimmons, K.E. 2011. An assessment of the luminescence sensitivity of Australian quartz with respect to sediment history. *Geochronometria*. 38: 199-208.

Fitzsimmons, K. E., 2017. Reconstructing palaeoenvironments on desert margins: new perspectives from Eurasian loess and Australian dry lake shorelines. *Quaternary Science Reviews*. 171. 1-19.

Fitzsimmons, K. E., Rhodes, E. J., Magee, J. W. & Barrows T. T. 2007. The timing and linear dune activity in the Strzelecki and Tirari Deserts, Australia. *Quaternary Science Reviews.* 26, 2598-2616.

Fitzsimmons, K. E., Rhodes, E. J. & Barrows, T. T. 2010. OSL dating of southeast Australian quartz: A preliminary assessment of luminescence characteristics and behaviour. *Quaternary Geochronology.* 5: 91–95.

Fitzsimmons, K. E., Cohen, T. J., Hesse, P. P., Jansen, J., Nanson, G.C., May, J.-H., Barrows, T.T., Haberlah, D., Hilgers, A., Kelly, T., Larsen, J., Lomax, J., Treble, P. (2013) Late Quaternary palaeoenvironmental change in the Australian drylands: a synthesis. *Quaternary Science Reviews* 74, 78-96.

Fitzsimmons, K.E., Stern, N. & Murray-Wallace, C.V. (2014) Depositional history and archaeology of the central Lake Mungo lunette, Willandra Lakes, southeast Australia. *Journal of Archaeological Science* 41, 349-364

Fitzsimmons, K.E., Stern, N., Murray-Wallace, C.V., Truscott, W. & Pop, C. 2015. The Mungo mega-lake event, semi-arid Australia: non-linear descent into the last ice age,

implications for human behaviour. *PLoS ONE.* 10(6): e0127008. doi:10.1371/journal. pone.0127008

Flood, J. 1999. *Archaeology of the Dreamtime: the story of prehistoric Australia and its* people. Harper Collins: NSW.

Fraser, R. 2005. *A study of stable carbon, nitrogen and oxygen isotopes in modern Australian marsupial herbivores, and their relationships with environmental conditions.* Unpublished PhD thesis. The Australian National University.

Fraser, R. A., Grün, R., Privat, K. & Gagan, M. K. 2008. Stable-isotope micro profiling of wombat tooth enamel records seasonal changes in vegetation and environmental conditions in eastern Australia. *Palaeogeography, Palaeoclimatology, Palaeoecology.* 269, 66-77.

Fuchs, M., Woda, C. & Bürkert, A. 2007. Chronostratigraphy of a sediment record from the Hajar mountain range in north Oman: implications for optical dating of insufficiently bleached sediments. *Quaternary Geochronology.* 2, 202-207.

Fullagar, R. L. K., Price, D. M. & Head, L. M. (1996).Early human occupation of northern Australia: archaeology and thermoluminescence dating of Jinmium rock-shelter, Northern Territory. *Antiquity* 70, 751–773.

Fullagar, R., Hayes, E., Stephenson, B., Field, J., Matheson, C., Stern, N. & Fitzsimmons, K. 2015. Evidence for Pleistocene seed grinding at Lake Mungo, south-eastern Australia. *Archaeology in Oceania.* 50. 3-19.

Geoscience Australia. 2015. Neotectonic feature search. http://www.ga.gov.au/earthquakes/staticPageController.do?page=neotectonics (last accessed 7 June 2017).

Galbraith, R. 1990, The radial plot: graphical assessment of spread in ages. *Nuclear Tracks Radiation Measurements.* 17, 207-214

Galbraith, R. F. 1997. The trouble with “probability density” plots of fission track ages. *Radiation Measurements*. 29: 125-131.

Galbraith, R. 2002. A note on the variance of background-corrected OSL count. *Ancient TL*. 20, 49-51.

Galbraith, R. F. 2005. *Statistics for Fission Track Analysis.* Chapman & Hall: London

Galbraith R.F., & Roberts, R.G. 2012. Statistical aspects of equivalent dose and error calculation and display in OSL dating: An overview and some recommendations.

Galbraith, R. F., Roberts, R.G., Laslett, G. M., Yoshida, H. & Olley, J. M. 1999. Optical dating of single and multiple grains of quartz from jinmium rock shelter, northern Australia, part 1, Experimental design and statistical models. *Archaeometry*. 41: 339-364.

Galbraith, R. F., Roberts, R. G., Yoshida, H. 2005. Error variation in OSL palaeodose estimates from single aliquots of quartz: a factorial experiment. *Radiation Measurements* 39: 289-307.

Ghosh, P., Adkins, J., Affek, H., Balta, B., Guo, W., Schauble, E. A., Schrag, D. & Eiler, J. M. 2006. ^{13}C-^{18}O bonds in carbonate minerals: a new kind of paleothermometer. *Geochimica et Cosmochimica Acta*. 70, 1439-1456.

Ghosh, P., Eiler, J., Campana, S. E. & Feeney, R. F. 2007. Calibrations of the carbonate 'clumped isotope' paleothermometer for otoliths. *Geochimica et Cosmochimica Acta*. 71

Gillanders, B. M. 2005. Otolith chemistry to determine movements of diadromous and freshwater fish. *Aquatic Living Resources*. 18: 291-300.

Gillespie, R. 1997. Burnt and Unburnt Carbon: dating charcoal and burnt bone from the Willandra Lakes, Australia. *Radiocarbon*. 39: 239-250.

Gillespie, R. 1998. Alternative timescales: a critical review of Willandra Lakes dating. *Archaeology in Oceania*. 33: 169-182.

Gillespie, R., Roberts, R. G. 2000. On the reliability of age estimates for human remains at Lake Mungo. *Journal of Human Evolution.* 38. 727-732.

Grossman, E. L. & Ku, T-L. 1986. Oxygen and carbon isotope fractionation in biogenic aragonite: temperature affects. *Chemical Geology (Isotope Geoscience Section)*. 59, 59-74.

Grün, R., Schwarcz, H. P. & Chadam, J. M. 1988. ESR dating of tooth enamel: coupled correction for U-uptake and U-series disequilibrium. *Nuclear Tracks and Radiation Measurements*. 14, 237-241.

Grün, R. 1989. Electron spin resonance (ESR) dating. *Quaternary International*. 1, 65-109.

Grün, R. 2006. Direct dating of human fossils. *Yearbook of Physical Anthropology.* 49, 2-48.

Grün, R., Spooner, N. A., Thorne, A., Mortimer, G., Simpson, J. J., McCulloch, M., Taylor, L. & Curnoe. 2000. Age of the Lake Mungo 3 skeleton, reply to Bowler & Magee and to Gillespie & Roberts. *Journal of Human Evolution.* 38. 733-741.

Grün, R. & Katzenburger-Apel, O. 1994. An alpha irradiator for ESR dating. *Ancient TL*. 12: 35-38.

Grün, R. 2009a. The relevance of parametric U-uptake models in ESR age calculations. *Radiation Measurements*.44: 472-476 –

Grün, R. 2009b. The DATA program for the calculation of ESR age estimates on tooth enamel. *Quaternary Geochronology*. 4: 231-232.

Grün, R., Eggins, S., Kinsley, L., Moseley, H. & Sambridge, M. 2014. Laser ablation U-series analysis of fossil bones and teeth. *Palaeogeography, Palaeoclimatology, Palaeoecology*. 416: 150–167.

Guerin, G., Mercier, N. & Adamiec, G. 2011. Dose-rate conversion factors: update. *Ancient TL*. 29: 5-8.

Hamm, G., Mitchell, P., Arnold, L. J., Prideaux, G. J., Questiaux, D., Spooner, N. A., Levchenko, V. A., Foley, E. C., Worthy, T. H., Stephenson, B., Coulthard, V., Coulthard, C., Wilton, S. & Johnston, D. 2016. Cultural innovation and megafauna interaction in the early settlement of arid Australia. *Nature*. 539. 280-283.

Hedges, R. E. M. & Law, I. A. 1989. The radiocarbon dating of bone. *Applied Geochemistry*. 4: 249-253.

Hesse, P. P., Magee, J. W. & van der Kaars, S. 2004. Late Quaternary climates of the Australian arid zone: a review, *Quaternary International*, 118–119: 87-102,

Higham, T. 2011. European Middle and Upper Palaeolithic radiocarbon dates are often older than they look: problems with previous dates and some remedies. *Antiquity*, 85: 235-249.

Hills, E. S. 1940. *The lunette, a new land form of aeolian origin*. The Australian Geographer. 3,15-21.

Hillson, S. 1986. *Teeth*. Cambridge University Press: Cambridge.

Hoefs, J. 1997. *Stable Isotope Geochemistry*. Springer-Verlag: Berlin.

Hogg, A. G., Hua, Q., Blackwell, P. G., Niu, M., Buck, C. E., Guilderson, T. P., Heaton, T. J., Palmer, J. G., Reimer, P. J., Reimer, R. W., Turney, C. S. M. & Zimmerman, S. R H. SHCal13 Southern hemisphere calibration, 0-50,000 years cal. BP. *Radiocarbon*. 55: 1889-1908.

Holdaway, R. M, Roberts, R. G., Beavan-Athfield, N. R., Olley, J. M. & Worthy, T.H. 2002. Optical dating of quartz sediments and accelerator mass spectrometry ^{14}C dating of bone gelatine and moa eggshell: a comparison of age estimates for non-archaeological deposits in New Zealand. *Journal of the Royal society of New Zealand.* 32, 463-505

Hope, J. 2006 Megafauna and other fossils. In Lawrence, H. (Ed.) *Mungo over Millennia: the Willandra Landscape and its People.* Maygog publishing. TAS.

Horsup, A. 2004. Recovery plan for the northern hairy-nosed wombat *Lasiorhinus krefftii* 2004-2008. Report to the Department of Environment and Heritage, Canberra. Environmental Protection Agency/Queensland Parks and Wildlife Service, Brisbane.

Huffman, G.G. & Price, W.A. 1949. Clay dune formation near Corpus Christi, Texas. *Journal of Sedimentary Petrology*. 19: 118-127.

Hughes, J., Baker, A. M., Bartlett, C., Bunn, S., Goudkamp, K. & Somerville, J. 2004. Past and present patterns of connectivity among populations of four cryptic species of freshwater mussels *Velesunio* spp. (Hyriidae) in central Australia. *Molecular Ecology*. 13, 3197-3212.

Huntley D. J., Godfrey-Smith, D. I. & Thewalt, M. L. W. 1985. Optical dating of sediments. *Nature*. 313**:** 105-107.

Iacumin, P. Bocherens, H., Delgado Huertas, A., Mariotti, A & Longinelli, A. 1997. A stable isotope study of fossil mammal remains from the Paglicci cave, Southern Italy. N and C as palaeoenvironmental indicators. *Earth and Planetary Science Letters.* 148, 349-357.

Ickert, R. B., Hiess, J., Williams, I. S., Holden, P., Ireland, T. R., Lanc, P., Schram, N., Foster, J. J. & Clement, S. W. 2008. Determining high precision, in situ, oxygen isotope ratios with a SHRIMP II: Analyses of MPI-DING silicate-glass reference materials and zircon from contrasting granites. *Chemical Geology.* 257: 114–128

Ikeya, M. 1982. A model of linear uranium accumulation for ESR age of Heidelberg (Mauer) and Tuataval Bones. *Japanese Journal of Applied Physics.* 21, 690-692.

Jain, M., Bøtter-Jensen, L. & Singhvi, A. K. 2003. Dose evaluation using multiple-aliquot quartz OSL: test of methods and a new protocol for improved accuracy and precision. *Radiation Measurements*. 37: 67-80.

Jacobi, R. M., Higham, T. F. G. & Bronk Ramsey, C. 2006.AMS radiocarbon dating of Middle and Upper Palaeolithic bone in the British Isles: improved reliability using ultrafiltration. *Journal of Quaternary Science.* 21, 557-273.

Galbraith & Roberts 2012

Jacobs, Z., Wintle, A. G., Roberts, R. G. & Duller, G. A. T. 2008a. Equivalent dose distributions from single grains of quartz at Sibudu, South Africa: context, causes

and consequences for optical dating of archaeological deposits. *Journal of Archaeological Science*. 35: 1808-1820.

Jacobs, Z., Wintle, A. G., Duller, G. A. T., Roberts, R. G. & Wadley, L. 2008b. New ages for the post-Howiesons Poort, late and final Middle Stone Age at Sibudu, South Africa *Journal of Archaeological Science*. 35: 1790-1807

Jacobs, Z., Roberts, R. G., Nespoulet, R., El Hajraoui M. A. & Debénath, A. 2012. Single-grain OSL chronologies for Middle Palaeolithic deposits at El Mnasra and El Harhoura 2, Morocco: implications for Late Pleistocene human–environment interactions along the Atlantic coast of northwest Africa. *Journal of Human Evolution*. 62: 377–394.

Jacobson, G., Ferguson, J. and Evans, W.R. 1994 In M. R. Rosen (ed) *Paleoclimate and Basin Evolution of Playa Systems*. Special Paper 289. Geological Society of America: Colorado. pp 81-96.

Johnston, H. & Clark, P. 1998. Willandra Lakes Archaeological Investigations 1968-98. *Archaeology in Oceania*. 33, 105-119.

Jeong, G. Y. & Choi, J-H. 2012. Variations in quartz OSL components with lithology, weathering and transportation. *Quaternary Geochronology*. 10: 320-326.

Joannes-Boyau, R.. & Grün R. (2011) A comprehensive model for CO_2^- radicals in fossil tooth enamel: Implications for ESR dating. *Quaternary Geochronology* 6, 82-97.

Kalish, J. M. 1991. ^{13}C and ^{18}O isotopic disequilibria in fish otoliths: metabolic and kinetic effects. *Marine Ecology Progress Series*. 75: 191-203.

Kalish, J. M., Miller, G. H., Tuniz, C., Pritchard, J. C., Rosewater, A. & Lawson, E. 1997. Otoliths as recorders of palaeoenvironments: comparison of radiocarbon age and isoleucine epimerization in Pleistocene golden perch *Macquaria ambigua* otoliths from Willandra Lakes. In: Conference Handbook, Sixth Australasian Archaeometry Conference, Australian Museum, Sydney, 10-13 February 1997.

Kaplan, I. R. 2003. Age dating of environmental organic residues. *Environmental Forensics*. 4, 95-141.

Kemp, J. 2001 The Hydrology, Geomorphology and Quaternary Palaeochannels of the Lachlan Valley, New South Wales,. PhD Thesis, Australian National University, Canberra.

Kemp, J., Pietsch, T., Gontz, A. & Olley, J. 2017. Lacustrine-fluvial interactions in Australia's Riverine Plains. *Quaternary Science Reviews*. 166. 352-362.

Kemp, J. & Rhodes, E.J. 2010. Episodic fluvial activity of inland rivers in southeastern Australia: Palaeochannel systems and terraces of the Lachlan River. *Quaternary Science Reviews*. 29. 731-752

Kemp, J. & Spooner, N. A. 2007. Evidence for regionally wet conditions before the LGM in southeast Australia: OSL ages from a large palaeochannel in the Lachlan Valley. *Journal of Quaternary Science* 22: 423-427

Kim, K. H., Tanaka, T., Nakamura, T., Nagao, K., Youn, J. S. Kim, K. R. & Yun, M. Y. 1999. Palaeoclimatic and chronostratigraphic interpretations for strontium, carbon and oxygen isotopic ratios in molluscan fossils of Quaternary Seoguipo and Shinyangri Formations, Cheju Island, Korea. *Palaeogeography, Palaeoclimatology, Palaeoecology.* 154, 219-235.

Klein, R. T., Lohmann, K. C. & Thayer, C. W. 1996. Bivalve skeletons record sea-surface temperature and $\delta^{18}O$ via Mg/Ca and $^{18}O/^{16}O$ ratios. *Geology*. 24. 415-418.

Koch, P. L. 1998. Isotopic reconstruction of past continental environments. *Annual Review of Earth and Planetary Science.*23, 573-613.

Koch, P. L., Tuross, N. & Fogel, M. L. 1997. The effects of sample treatment and diagenesis on the isotopic integrity of carbonate in biogenic hydroxyapatite. *Journal of Archaeological Science*. **24:** 417-429.

Kohn, M. J., Schoeninger, M. J. & Valley, J. W. 1998. Variability in oxygen isotope compositions of herbivore teeth: reflections of seasonality or developmental physiology? *Chemical Geology*. 152, 97-112.

Latham, A. 2001. Uranium-Series Dating. In: D. Brothwell & A. Pollard (eds.). *Handbook of Archaeological Sciences.* John-Wiley and Sons: New York. pp 63-72.

Lake, J. S. 1978. *Australian Freshwater Fishes*: *an illustrated field guide*. Thomas Nelson Australia Pty Ltd. VIC.

LeBlanc, R.J. & Hodgson, W.D. 1959. Origin and development of the Texas shoreline. In: Russell, R.J. (ed). *Second Coastal Geography Conference*. Louisiana State University: Washington D.C.

Lee-Thorpe, J. A., van der Merwe, N. J. & Brain, C. K. 1989a. Isotopic evidence for dietary differences between two extinct baboon species from Swartkrans. *Journal of Human Evolution.* 18, 183-190.

Lee-Thorp, J. A. & van der Merwe, N. J. 1991. Aspects of the chemistry of modern and fossil biological apatites. *Journal of Archaeological Science.* 18: 343-354.

Lee-Thorpe, J. A., Scaly, J. C. & van der Merwe, N. J. 1989b. Stable Carbon isotope ratio differences between bone collagen and bone apatite, and their relationship to diet. *Journal of Archaeological Science.* 16, 585-599.

Lomax, J., Hilgers, A., Twidale, C. R., Bourne, J. A. & Radtke, U. 2007. Treatment of broad palaeodose distributions in OSL dating of dune sands from the western Murray Basin, South Australia. *Quaternary Geochronology*. 2: 51–56

Lomax, J., Hilgers, A., & Radtke, U. 2011. Palaeoenvironmental change recorded in the palaeodunefields of the western Murray Basin, South Australia - New data from single grain OSL-dating. *Quaternary Science Reviews*, 30, 723-736.

Long, K., Stern, N., Williams, I. S., Kinsley, L., Wood, R., Sporcic, K., Smith, T., Fallon, S., Kokkonen, H., Moffat, I. & Grün, R. 2014. Fish otolith geochemistry, environmental

conditions and human occupation at Lake Mungo, Australia. *Quaternary Science Reviews.* 88: 82-95.

Lowe, J. J. & Walker, M. J. C., 2015. *Reconstructing Quaternary Environments* (3nd Ed.) Routledge: Oxon and New York.

Luz, B., Kolodney, Y & Horowitz, M. 1984. Fractionation of oxygen isotopes between mammalian bone-phosphate and environmental drinking water. *Geochimica et Cosmochimica Acta*. 48: 1689-1693.

Magee, J. W. 1991. Late Quaternary lacustrine, groundwater, aeolian and pedogenic gypsum in the Prungle Lakes, southeastern Australia. *Palaeogeography, Palaeoclimatology, Palaeoecology*, 84: 3-42

Magee, J. W., Bowler, J. M., Miller, G. H. & Williams, D. L. G. 1995. Stratigraphy, sedimentology, chronology and palaeohydrology of Quaternary lacustrine deposits at Madigan Gulf, Lake Eyre, South Australia. *Palaeogeography, Palaeoclimatology, Palaeoecology.* 113: 3-42.

Martin, L., Mercier, N., Incerti, S., Lefrais, Y., Pecheyran, C., Guérin, G., Jarry, M., Bruxelles, L., Bon, F. & Pallier, C. 2015. Dosimetric study of sediments at the beta dose rate scale: characterization and modelization with the DosiVox software. *Radiation Measurements* (in press). 8p.

Martinson, D., Pisias, N.G., Hays, J.D., Imbrie, J., Moore, T.C. Jr. & Shackleton, N.J. 1987. Age dating and the orbital theory of the Ice Ages: development of a high-resolution 0 to 300,000-year chronostratigraphy. *Quaternary Research.* 27,1-29.

McDonald, R.C., Isbell, R.F., Speight, J.G., Walker, J., & Hopkins, M.S. 1998. *Australian Soil and Land Survey Field Handbook.* Australian Collaborative Land Evaluation Program: Canberra.

Mejdahl, V. 1979. Thermoluminescence dating: beta-dose attenuation in quartz grains. *Archaeometry*. 21, 61-72.

Mercier, N. & Falguères, C. 2007. Field gamma dose-rate measurement with a NaI(Tl) detector re-evaluation of the "threshold" technique. *Ancient TL.* 25: 1-4.

Millard, A. R. & Hedges, R. E. M. 1996. A diffusion-adsorption model of uranium uptake by archaeological bone. *Geoochimica et cosmochimica acta*. 60: 2139-2152.

Miller, G. H., Fogel, M. L., Magee, J. W., Gagan, M. K., Clarke, S. J. & Johnson, B. J. 2005. Ecosystem collapse in Pleistocene Australia and a human role in megafaunal extinction. *Science.* 309. 287-309.

Miller, G. H., Magee, J. W., Fogel, M. L. & Gagan, M. K. 2007. Detecting human impacts on the flora, fauna and summer monsoon of Pleistocene Australia. *Climate of the Past*. 3, 463-473.

Mulvaney, J. & Kamminga, J. 1999. *Prehistory of Australia*. Allen & Unwin Pty. Ltd. NSW.

Murphey, B. P., Bowman, D. M. J. S. & Gagan, M. K. 2007. Sources of carbon isotope variation in kangaroo bone collagen and tooth enamel. *Geochimica et Cosmochimica Acta*. 71, 3847-3858.

Murray, A.S. 1981. *Environmental radioactivity studies relevant to thermoluminescence dating*. Unpublished DPhil Thesis, Oxford University, Oxford.

Murray, A. S. & Roberts, R. G. 1997. Determining the burial time of single grains of quartz using optically stimulated luminescence. *Earth and Planetary Science Letters.* 152: 163–180

Murray, A. S. & Wintle, A. G. 2000. Luminescence dating of quartz using an improved single-aliquot regenerative-dose protocol. *Radiation Measurements*. 32, 57-73.

Murray, A. S., & Wintle, A. G. 2003. The single aliquot regenerative dose protocol: potential for improvements in reliability. *Radiation Measurements*. 37: 377-381.

Musyl, M. K. & Keenan, C. P. 1992. Population Genetics and Zoogeography of Australian Freshwater Golden Perch, *Macquaria ambigua* (Richardson 1845) (Teleostei :

Percichthyidae), and Electrophoretic Identification of a New Species from the Lake Eyre Basin. *Australian Journal of Marine and Freshwater Research.* 43, 1585-601.

Nanson, G. C., Price, D. M. & Short, S. A., Wetting and drying of Australia over the past 300 ka, *Geology*, 20(9), 1992, 791-794.

Naylor, J. R., Manighetti, B. M., Neil, H. L. & Kim, S. W. 2007. Validated estimation of growth and age in the New Zealand abalone *Haliotis iris* using stable oxygen isotopes. *Marine and Freshwater Research.* 58, 354-362.

Newesely, H. 1989. Fossil bone apatite. *Applied Geochemistry*. 4, 233-245.

Nielsen-Marsh, C. M. & Hedges, R. E. M. 2000. Patterns of diagenesis in bone II: effects of acetic acid treatment and the removal of diagenetic CO_3^{2-}. *Journal of Archaeological Science.* 27: 1151-1159.

Olley, J. M., Pietsch, T. & Roberts, R. G. 2004. Optical dating of Holocene sediments from a variety of geomorphic settings using single grains of quartz. *Geomorphology.* 60: 337-358.

Olley, J. M., Roberts, R. G., Yoshida, H. & Bowler, J. M. 2006. Single-grain optical dating of grave-infill associated with human burials at Lake Mungo, Australia. *Quaternary Science Reviews.* 25, 2469-2474.

Olley, J. M., Roberts, R. G., & Murray, A. S. 1997. Disequilibria in the uranium decay series in sedimentary deposits at Allen's cave, Nullarbor Plain, Australia: implications for dose rate determinations. *Radiation Measurements*. 27: 433-443.

Oyston, B. 1996. Thermoluminescence age determinations for the Mungo III Human Burial, Lake Mungo, southeastern Australia. *Quaternary Science Reviews*. 15: 739-749

Palmqvist, P., Gröcke, D. R., Arribas, A. & Farina, R. A. 2003. Paleoecological reconstruction of a lower Pleistocene large mammal community using biogeochemical ($\delta^{13}C$, $\delta^{15}N$, $\delta^{18}O$, Sr:Zn) and ecomorphological approaches. *Paleobiology*. 29, 205-229.

Pate, F. D. 1994. Bone chemistry and paleodiet. *Journal of Archaeological Method and Theory*. 1, 161-209.

Patterson, W. P. 1998. North-American continental seasonality during the last millennium: high resolution analysis of sagittal otoliths. *Palaeogeography, Palaeoclimatology, Palaeoecology.* 138. 271-303.

Patterson, W. P., Smith, G. R. & Lohmann, K. C. 1993. Continental Paleothermometry and Seasonality Using the Isotopic Composition of Aragonitic Otoliths of Freshwater Fishes. In P. K. Swart, K. C. Lohmann, J. McKenzie & S. Savin (eds) Climate Change in Continental Isotopic Records. *American Geophysical Union Monograph*. 78, 191-202.

Pell, S. D., Chivas, A. R. & Williams, I. S. 2000. The Simpson, Strzelecki and Tirari Deserts: development and sand provenance. *Sedimentary Geology.* 130: 107–130.

Peresani, M., Cremaschi, M., Ferraro, F., Falguéres, C., Bahain, J.-J., Gruppioni, G., Sibilia, E., Quarta, G., Calcagnile, L. & Dolo, J-M. 2008. Age of the final Middle Palaeolithic and Uluzzian levels at Fumane Cave, Northern, Italy, using ^{14}C, ESR, $^{234}U/^{230}Th$ and thermoluminescence methods. *Journal of Archaeological Science.* 35, 2986-2996.

Piepenbrink, H. 1989. Examples of chemical changes during fossilisation. *Applied Geochemistry*. 4, 273-280.

Pietsch, T. J., Olley, J. M. & Nanson, G.C. 2008. Fluvial transport as a natural luminescence sensitiser of quartz. *Quaternary Geochronology*. 3: 365-376.

Pike, A. W. G. & Hedges, R. E. M. 2001. Sample geometry and U uptake in archaeological teeth: implications for U-series and ESR dating. *Quaternary Science Reviews*. 20: 1021-1025.

Prescott J. R. & Hutton, J. T. 1994. Cosmic ray contributions to dose rates for luminescence and ESR dating: large depths and long term variations. *Radiation Measurements.* **23:** 497-500.

Price, W.A. 1963. Physiochemical and environmental factors in clay dune genesis. *Journal of Sedimentary Petrology*. 33: 766-778.

Price, T. D., Bentley, R. A. Lünig, J., Gronenborn, D. & Wahl, J. 2001. Prehistoric human migration in the Linearbandkeramik of Central Europe. *Antiquity.* 75, 593-603.

Prideaux, G., Ayliffe, L. K., DeSantis, L. R. G., Schuberte, B. W., Murray, P. F., Gagan, M. K. & Cerling, R. E. 2009, Extinction implications of a chenopod browse diet for a giant Pleistocene kangaroo. *Proceedings of the National Academy of Sciences*. 106: 11646-11650

Pritchard, J.C. 2004. *Linking fish growth and climate across modern space and through evolutionary time: otolith chronologies of the Australian freshwater fish, golden perch (Macquaria ambigua, Percichthyidae)*, Unpublished PhD thesis, The Australian National University.

Podlesak, D. W., Torregrossa, A-M., Ehrleringer, J. R., Dearing, M. D., Passey, B. H. & Cerling, T. E. 2008. Turnover of oxygen and hydrogen isotopes in the body water, CO_2, hair, and enamel of a small mammal. *Geochimica et Cosmochimica Acta.* 72, 19-35.

Ride, W. D. L. 1970. *A Guide to the Native Mammals of Australia*. Oxford University Press: Melbourne.

Reimer, P. J. Baillie, M. G. L., Bard, E., Bayliss, A., Beck, J. W., Blackwell, P. G., Bronk Ramsey, C., Buck, C. E., Burr, G. S., Edwards, R.L., Friedrich, M., Grootes, P. M., Guilderson, T. P., Hajdas, I., Heaton, T. J. Hogg, A. G., Hughen, K. A., Kaiser, K. F., Kromer, B., McCormac, F. G., Manning, S. W., Reimer, R. W., Richards, D. A., Southon, J. R., Talamo, S., Turney, C. S. M., van der Plicht, J. & Weyhenmeyer, C. E. 2009. IntCal09 and Marine09 Radiocarbon Age Calibration Curves, 0-50,000 Years cal. BP. *Radiocarbon*. 51: 1111-1150.

Reimer, P. J., Bard, E., Bayliss, A., Beck, J. W., Blackwell, P. G., Bronk Ramsey, C., Buck, C. E., Cheng, H., Edwards, R. L., Friedrich, M., Grootes, P. M., Guilderson, T. P., Haflidason, H., Hajdas, I., Hatté, C., Heaton, T. J., Hoffmann, D. L., Hogg, A. G.,

Hughen, K. A., Kaiser, K. F., Kromer, B., Manning, S. W., Niu, M., Reimer, R. W., Richards, D. A., Scott, E. M., Southon, J. R., Staff, R. A., Turney, C. S. M. & van der Plicht, J. 2013 IntCal13 and Marine13 Radiocarbon Age Calibration Curves 0–50,000 Years cal. BP. *Radiocarbon*. 55: 1869-1887.

Rendell, H.M., Lancaster, N. & Tchakerian, V. P. 1994. Luminescence dating of late quaternary aeolian deposits at Dale Lake and Cronese Mountains, Majove Desert, California. *Quaternary Geochronology*. 13, 417-122.

Reynard, B. & Baltre, V. 2014. Trace elements and their isotopes in bones and teeth: diet, environments, diagenesis, and dating of archeological and paleontological samples. *Palaeogeography, Palaeoclimatology, Palaeoecology*. 416: 4-16.

Rhodes, E. J. 2000. Observations of thermal transfer OSL signals in glacigenic quartz. *Radiation Measurements.* 32: 595-602.

Rhodes, E. J. & Bailey, R. M. 1997. The effect of thermal transfer on the zeroing of the luminescence of quartz from recent glaciofluvial sediments. *Quaternary Science Reviews.* 16: 291-298

Rhodes, E.J., Bronk Ramsey, C., Outram, Z., Batt, C., Willis, L., Dockrill, S. & Bond, J. 2003. Bayesian methods applied to the interpretation of multiple OSL dates: high precision sediment ages from Old Scatness Broch excavations, Shetland Isles. *Quaternary Science Reviews.* 22, 1231-1244.

Rhodes, E.J. & Schwenninger, J-L. 2007. Dose rates and radioisotope concentrations in the concrete calibration blocks at Oxford. *Ancient TL*. 25, 5-9.

Rink, W. J. 1997. Electron spin resonance (ESR) dating and ESR applications in Quaternary science and Archaeometry. *Radiation Measurements*. 27, -75-1025.

Roberts, R. G. 1997. Luminescence dating in archaeology: from origins to optical. *Radiation Measurements*. 27: 819-892.

Roberts R, Bird M, Olley J, Galbraith R, Lawson E, Laslett G, Yoshida H, Jones R, Fullagar R, Jacobsen G, Hua Q. 1998. Optical and radiocarbon dating at Jinmium rock shelter in northern Australia. *Nature* 393, 358–362.

Roberts, R.G., Jones, R. & Smith, M.A. 1990. Thermoluminescence dating of a 50,000 year-old human occupation site in northern Australia. *Nature*, 345, 153-156.

Roberts, R. G., Jones, R., Spooner, N. A., Head, M. J., Murray, A. S. & Smith, M. A. 1994. The human colonisation of Australia: Optical dates of 53,000 and 60,000 years bracket human arrival at deaf adder gorge, Northern Territory. *Quaternary Geochronology*. 13, 575-583.

Roberts, R. G., Galbraith, R. F., Yoshida, H., Laslett, G.M. & Olley, J. M. 2000. Distinguishing dose populations in sediment mixtures: a test of single-grain optical dating procedures using mixtures of laboratory-dosed quartz. *Radiation Measurements*. 32: 459-465

Roughly, T. C. 1957. *Fish and Fisheries of Australia*. Angus and Robertson. NSW.

Rozanski, K., Araguas-Araguas, L. & Gonfiantini, R. 1993. *Isotopic patterns in modern global precipitation*. American Geophysical Union: USA.

Russell, N. J. & Armitage, S. J. 2012. A comparison of single-grain and small aliquot dating of fine sand from Cyrenaica, northern Libya. *Quaternary Geochronology*. 10: 62-67.

Sambridge, M., Grün, R. & Eggins, S. 2012. U-series dating of bone in an open system: The diffusion-adsorption-decay model. *Quaternary Geochronology.* 9: 42-53.

Schroeninger, M. J. & Moore, K. 1992. Bone stable isotope studies in archaeology. *Journal of World Prehistory.* 6, 247-296.

Schütt, B. 2004. The chemistry of playa-lake sediments as a tool for the reconstruction of Holocene environmental conditions – a case study from the central Ebro basin. In: W. Smykatz-Kloss & P. Felix-Henningsen (eds.). Paleoecology of Quaternary drylands. *Lecture Notes in Earth Sciences*. 102: 5-30.

Schwarctz, H. P. 1994. Current challenges to ESR dating. *Quaternary Geochronology.* 13, 601-605.

Schwarcz, H. P. 1997. Uranium Series Dating. In. R. E. Taylor. & M. J. Aitken (eds.) *Chronometric Dating in Archaeology*. Springer: New York.

Schwenninger, J-L., Bridgland, D. R., Howards, A. J. & White, T. 2007. Pleistocene Sediments from the Trent Valley: Optically Stimulated Luminescence (OSL) Dating, Scientific dating report. Research Department Report Series no. 57/2007

Scott, G. G. 1988. *Taxonomy and Diagnostic Osteology of Extant Hairy-Nosed and Common Wombats*. Unpublished Masters Thesis, Department of Prehistory and Anthropology, The Australian National University, Canberra

Shackleton, N. J. & Opdyke, N. D. 1973. Oxygen isotope and palaeomagnetic stratigraphy of Equatorial Pacific Core V-28-238: oxygen isotope temperatures and ice volumes on a 10^5year and 10^6 year scale. *Quaternary Research.* 3:39-55.

Shimmin, G. A., Skinner, J. & Baundinette, R. V. 2002. The warren architecture and environment of the southern hairy-nosed wombat *(Lasiorhinus latifrons). Journal of the Zoological Society of London*. 258, 469-477.

Shawcross, W. 1998. Archaeological excavations at Mungo. *Archaeology in Oceania*. 33, 183-200.

Singarayer, J. S. & Bailey, R. M. 2003. Further investigations of the quartz optically stimulated luminescence components using linear modulation. *Radiation Measurements*. 37: 4-5.

Singhvi, A. K., Deraniyagala, S. U. & Sengupta, A. 1986. Thermoluminescence dating of Quaternary red-sand beds: a case study of coastal dunes in Sri Lanka. *Earth and Planetary Science Letters*. 80: 139-144.

Soressi, M., Jones, H. L., Rink, W. J., Maureille, B. & Tillier, A-M. 2007. The Pech-de-l' Azé I Neandertal child: ESR, uranium-series, and AMS ^{14}C dating of its MTA type B context. *Journal of Human Evolution.* 52, 455-466.

Stern, N., Tumney, J., Fitzsimmons, K. & Kajewski, P. 2013. Strategies for investigating human responses to changes in environment at Lake Mungo in the Willandra Lakes, southeast Australia. In D. Frankel, J. Webb and S. Lawrence (eds.) *Archaeology in Technology and Environment*. Routledge, London. Pp.31-50.

Stuart-Williams, H. L. Q. & Schwarcz, H. P. 1997. Oxygen isotopic determination of climatic variation using phosphate from beaver bone, tooth enamel and dentine. *Geochimica et Cosmochimica Acta*. 61. 2539-2550.

Stuvier, M. & Polach, H. A. 1977. Discussion: reporting of ^{14}C data. *Radiocarbon*. 19: 355-363.

Thorne, A., Grün, R., Mortimer, G., Spooner, N. A., Simpson, J. J., McCulloch, M., Taylor, L. & Curnoe, D. 1999. Australia's oldest human remains: age of the Lake Mungo 3 skeleton. *Journal of Human Evolution.* 36. 291-612.

UNESCO. 2015. Willandra Lakes Region – Map of the inscribed property. http://whc.unesco.org/en/list/167/multiple=1&unique_number=185 (last accessed 7 July 2015)

Urey, H. C., Lowenstam, H. A., Epstein, S. & McKinney, C. R. 1951. Measurement of paleotemperatures and temperatures of the Upper Cretaceous of England, Denmark and the southeastern United States. *Bulletin of the Geological Society of America.* 62, 399-416.

Vermeesch, P. 2009, RadialPlotter: a Java application for fission track, luminescence and other radial plots, Radiation Measurements, 44: 409-410

Veth, P., Ward, I., Manne, T., Ulm, S., Ditchfield, K., Dortch, J., Hook, F., Petchey, F., Hogg, A., Questiaux, D., Demuro, M., Arnold, L., Spooner, N., Levchenko, V., Skippington, J., Byrne, C., Basgall, M., Zeanah, D., Belton, D., Helmholz, P., Bajkan, S., Bailey, R., Placzek, C. & Kendrick, P. 2017. Early human occupation of a maritime desert, Barrow Island, North-West Australia, *Quaternary Science Reviews*, 168: 19-29

Walker, K.F., Byrne, M., Hickey, C.W. & Roper, D.S. 2001. Freshwater mussels (Hyriidae) of Australasia. In: G. Bauer & K. Wachtler (eds.), *Ecology and Evolution of Freshwater Mussels Unionioda* Springer Verlag: Berlin. pp. 5–31.

Wang, Y., Cerling, T. E. & MacFadden, B. J. 1994. Fossil horses and carbon isotopes: new evidence for Cenozoic dietary, habitat, and ecosystem changes in North America. *Palaeogeography, Palaeoclimatology, Palaeoecology.* 107, 269-279.

Webb, S., Cupper, M.L. & Robins, R. 2006. Pleistocene human footprints from the Willandra Lakes, southeastern Australia. *Journal of Human Evolution.* 50: 405-413.

Webb, G. E., Price, G. J., Nothdurft, L. D., Deer, L. & Rintoul, L. 2007. Cryptic meteoric diagenesis in freshwater bivalves: implications for radiocarbon dating. *Geology*. 35: 803-806.

Wefer, G. & Berger, W. H. 1991. Isotope paleontology: growth and composition of extant calcareous species. *Marine Geology*. 100, 207-248.

Wells, R. T. 1978a. Field observations of the hairy-nosed wombat, *Lasiorhinus latifrons* (Owen). *Australian Wildlife Research*. 5, 299-303.

Wells, R. T. 1978b.Thermoregulation and activity rhythms in the hairy-nosed wombat, *Lasiorhinus latifrons* (Owen), (Vombatidae). *Australian Journal of Zoology*. 26: 639-651.

Wells, R. T. & Green, B. 1998. Aspects of water metabolism in the southern hairy-nosed wombat *Lasiorhinus latifrons*. In *Wombats*. 61-66.

Williams, W. D., 1983. *Life in Inland Waters*. Blackwell Scientific Publications. VIC.

Wintle, A. G. 1997. Luminescence dating: laboratory procedures and protocols. *Radiation Measurements.* 27, 769-817.

Wintle, A. G. & Huntley, D. J. 1982. Thermoluminescence dating of sediments. *Quaternary Science Reviews.* 1, 31-53.

Wintle, A. G. & Murray, A. S. 2006. A review of quartz optically simulated luminescence characteristics and their relevance in single-aliquot regeneration dating protocols. *Radiation Measurements.* 41, 369-391.

Wood, R., Jacobs, Z., Vannieuwenhuyse, D., Balme, J., O'Connor, S. & Whitau, R. 2016. Toward an accurate and precise chronology for the Colonization of Australia: the example of Riwi, Kimberley, Western Australia. *PLoS One*. 11 (9): e0160123.

Wurster, C. M. & Patterson, W. P. 2001. Seasonal variation in stable oxygen and carbon isotope values recovered from modern lacustrine freshwater molluscs: Paleoclimatalogical implications for sub-weekly temperature records. *Journal of Paleolimnology*. 26, 205-218.

Zanazzi, A. & Kohn, M. J. 2008. Ecology and physiology of White River mammals based on stable isotope ratios of teeth. *Palaeogeography, Palaeoclimatology,* Palaeoecology. 257, 22-37.

Zazzo, A., L´ecuyer, C., Sheppard, S. M. F., Grandjean, P. & Mariotti, A. 2004. Diagenesis and the reconstruction of paleoenvironments: A method to restore original _^{18}O values of carbonate and phosphate from fossil tooth enamel. *Geochimica et Cosmochimica Acta.* 68: 2245-2258.

Zimmermann, D.W.1971. Thermoluminescence dating using fine grains from pottery. *Archaeometry*. 13, 29-52.

Appendix A. List of surveying and GPS co-ordinates

Site	Name	No.	Easting	Northing	Altitude	Notes
NORTH	DH01	1362	721076.023	6328644.155	81.745	Drill hole
NORTH	DH01A	1363	721249.041	6328553.716	72.895	Drill hole
MID	DH02A	1234	724581.605	6324735.289	89.593	Drill hole
MID	DH02B	1235	724593.737	6324696.909	95.007	Drill hole
South	DH03	1266	725863.199	6318372.493	89.057	Egg shell
BO007A	ES01	1296	721731.451	6328272.685	72.077	Egg shell
BO07E	ES02	1330	722401.595	6327779.778	72.229	Egg shell
BO07E	ES03	1331	722402.382	6327800.456	72.517	Egg shell
BO07E	ES04	1325	722434.351	6327857.043	77.402	Egg shell
BO07E	ES05	1326	722437.080	6327866.818	77.557	Egg shell
BO07E	ES06	1327	722476.567	6327822.828	80.175	Egg shell
BO07E	ES07	1328	722461.819	6327780.606	79.226	Egg shell
MSE01	ES08	1282	722778.242	6327701.514	75.822	Egg shell
MSE02	ES09	1279	723121.484	6327542.007	87.506	Egg shell
BO18	ES10	2008	725326.118	6323276.486	77.825	Egg shell
BO18	ES11	2007	725305.135	6323285.722	73.164	Egg shell
BO18	ES12	2006	725302.574	6323285.659	74.897	Egg shell
BO19	ES13	2015	725165.156	6323074.280	85.659	Egg shell
BO21	ES14	2031	725151.404	6322544.875	84.633	Egg shell
BO21	ES15	2032	725158.130	6322550.083	84.939	Egg shell
BO22	ES16	1247	725190.791	6322313.667	89.686	Egg shell
BO27	ES17	1252	725267.460	6321296.014	91.087	Egg shell
BO28	ES18	1261	725345.616	6320629.370	87.309	Egg shell
BO07C	IS01	1319	722056.043	6328149.734	72.215	Isolated shell
Lake floor	ML27	dGPS	724067.448	6323603.737	66.551	differential GPS survey mark
Lake floor	ML28	dGPS	724249.146	6322550.331	66.485	differential GPS survey mark
Lake floor	ML29	dGPS	724448.944	6321455.306	66.563	differential GPS survey mark
Lake floor	ML30	dGPS	724634.348	6320374.302	66.660	differential GPS survey mark
Lake floor	ML31	dGPS	724733.819	6319450.664	66.926	differential GPS survey mark
Lake floor	ML32	dGPS	723319.012	6325499.354	66.650	differential GPS survey mark
Lake floor	ML33	dGPS	723025.976	6326323.269	66.839	differential GPS survey mark
Lake floor	ML34	dGPS	722564.138	6327236.776	68.470	differential GPS survey mark
Lake floor	ML35	dGPS	721831.392	6327905.711	68.501	differential GPS survey mark
Lake floor	ML36	dGPS	721478.849	6328102.024	68.199	differential GPS survey mark
Lake floor	ML37	dGPS	720490.459	6328532.763	67.190	differential GPS survey mark
Lake floor	ML38	dGPS	719445.489	6328830.571	66.824	differential GPS survey mark
Lake floor	ML39	dGPS	718729.567	6328732.222	66.945	differential GPS survey mark
Lake floor	MLRU	dGPS	723899.254	6324576.583	66.564	differential GPS survey mark
BO01	MS01	1358	718416.467	6329111.694	77.391	Mussel Shell
BO03	MS02	1347	719049.133	6329094.921	76.473	Mussel Shell
BO03	MS03	1348	719051.960	6329093.299	75.911	Mussel Shell
BO03	MS04	1350	719050.878	6329100.676	76.685	Mussel Shell

Site	Name	No.	Easting	Northing	Altitude	Notes
BO03	MS05	1349	719056.190	6329099.364	75.974	Mussel Shell
BO03	MS06	1351	719072.026	6329106.087	75.810	Mussel Shell
BO03	MS07	1352	719073.705	6329107.469	75.907	Mussel Shell
BO03	MS08	1353	719078.682	6329110.764	76.074	Mussel Shell
BO03	MS09	1354	719083.710	6329098.477	75.592	Mussel Shell
BO03	MS10	1355	719109.497	6329102.871	76.737	Mussel Shell
BO03	MS11	1356	719109.933	6329106.995	76.838	Mussel Shell
BO04	MS12	1344	719349.943	6329062.919	76.893	Mussel Shell
BO04	MS13	1343	719341.500	6329068.386	76.759	Mussel Shell
BO04	MS14	1341	719367.292	6329067.751	76.457	Mussel Shell
BO04	MS15	1340	719380.004	6329069.409	75.954	Mussel Shell
BO04	MS16	1338	719403.763	6329061.756	75.293	Mussel Shell
BO04	MS17	1337	719409.092	6329061.066	75.025	Mussel Shell
BO04	MS18	1339	719390.504	6329052.799	75.611	Mussel Shell
BO04	MS19	1345	719743.064	6329007.363	76.854	Mussel Shell
BO07A	MS20	1294	721668.626	6328263.640	70.875	Mussel Shell
BO07C	MS21	1321	722045.812	6328083.928	71.467	Mussel Shell
BO07C	MS22	1322	722048.889	6328024.311	70.851	Mussel Shell
BO07D	MS23	1323	722245.334	6327882.890	72.120	Mussel Shell
BO07E	MS24	1333	722380.606	6327790.079	71.317	Mussel Shell
BO07E	MS25	1332	722382.264	6327791.307	71.425	Mussel Shell
MSE01	MS26	1288	722529.901	6327739.850	77.458	Mussel Shell
BG02	MS27	GPS	6327174.000	723426.000	85.400	Mussel Shell
BG06	MS28	1274	723772.518	6326208.451	85.366	Mussel Shell
BG06	MS29	1271	723811.570	6326086.749	81.242	Mussel Shell
BG06	MS30	1272	723821.810	6326074.493	81.177	Mussel Shell
BG06	MS31	1273	723832.712	6326075.441	81.411	Mussel Shell
BG07	MS33	1269	723967.493	6326085.071	86.173	Mussel Shell
BO11	MS36	1980	724404.960	6325410.032	84.356	Mussel Shell
BG09	MS37	1237	724272.687	6325106.301	79.789	Mussel Shell
BG14	MS38	1233	724447.862	6324727.537	82.897	Mussel Shell
BG14	MS39	1232	724451.146	6324724.044	82.566	Mussel Shell
BG15	MS40	1238	724565.285	6324399.196	82.940	Mussel Shell
BG15	MS41	1239	724564.779	6324390.278	82.611	Mussel Shell
BG18	MS42	1242	724736.183	6323929.648	83.684	Mussel Shell
BG19	MS43	1244	724957.277	6323000.093	81.231	Mussel Shell
BG20	MS45	1243	724992.152	6322911.080	80.573	Mussel Shell
BG26	MS50	1251	725214.707	6321232.910	87.189	Mussel Shell
BO29	MS51	1253	725320.385	6320866.043	87.253	Mussel Shell
BO29	MS52	1255	725295.936	6320805.515	85.807	Mussel Shell
BO29	MS53	1254	725299.733	6320801.899	85.982	Mussel Shell
BO29	MS54	1256	725338.355	6320777.915	88.202	Mussel Shell
BO29	MS55	1257	725343.690	6320782.518	88.700	Mussel Shell
BO29	MS56	1258	725360.331	6320764.905	90.387	Mussel Shell
BO29	MS57	1259	725363.156	6320772.272	90.673	Mussel Shell
BO29	MS58	1260	725386.515	6320723.185	90.600	Mussel Shell
BG32	MS59	1264	725404.849	6319546.932	80.714	Mussel Shell
BO04	MS60	1932	719375.895	6329076.611	77.050	Mussel Shell
BO29	OSL01	2035	725164.834	6320962.554	74.865	OSL sample
BO29	OSL02	2036	725190.344	6320970.550	81.349	OSL sample
BO29	OSL03	2036	725190.344	6320970.550	81.759	OSL sample
BO29	OSL04	2037	725300.882	6321023.790	89.736	OSL sample
BO29	OSL05	2038	725301.257	6321023.808	90.611	OSL sample

Site	Name	No.	Easting	Northing	Altitude	Notes
BO29	OSL06	2039	725338.322	6321026.080	92.740	OSL sample
BO29	OSL07	2040	725338.879	6321035.875	93.865	OSL sample
BO29	OSL08	2041	725353.088	6321036.538	95.829	OSL sample
BO29	OSL09	2042	725418.332	6321061.006	102.507	OSL sample
BO29	OSL10	GPS	725484.000	6321121.000		OSL sample
MSE03	OSL11	1967	724422.746	6324716.265	80.229	OSL sample
MSE03	OSL12	1968	724451.498	6324729.642	82.386	OSL sample
MSE03	OSL13	1969	724452.280	6324729.624	82.576	OSL sample
MSE03	OSL14	1970	724454.299	6324730.396	83.414	OSL sample
MSE03	OSL15	1971	724454.844	6324730.678	83.917	OSL sample
MSE03	OSL16	1972	724581.412	6324742.575	91.820	OSL sample
MSE03	OSL17	GPS	724629.000	6324737.000		OSL sample
MSE03	OSL18	GPS	724629.000	6325736.000		OSL sample
MSE03	OSL19	GPS	724861.000	6324633.000		OSL sample
BO04	OSL20	1928	719408.344	6329027.873	73.635	OSL sample
BO04	OSL21	1929	719381.518	6329064.525	75.310	OSL sample
BO04	OSL22	1930	719373.121	6329077.371	76.925	OSL sample
BO04	OSL23	1931	719364.989	6329100.582	79.404	OSL sample
BO04	OSL24	GPS	719249.000	6329153.000		OSL sample
BO03	OSL25	1936	719445.366	6328830.553	64.983	OSL sample
BO04	OSL26	1927	719391.275	6328991.907	73.276	OSL sample
BO07	OSL27	GPS	722233.000	6328241.000		OSL sample
BO07	OSL28	1953	722221.508	6328231.510	79.144	OSL sample
BO07	OSL29	1954	722315.500	6328186.606	79.500	OSL sample
BO07	OSL30	1952	722116.241	6328141.128	75.715	OSL sample
BO07	OSL31	1951	722116.049	6328141.010	76.024	OSL sample
BO07	OSL32	1950	722111.556	6328139.364	75.301	OSL sample
BO07	OSL33	1949	722109.958	6328138.773	75.027	OSL sample
BO07	OSL34	1948	722093.133	6328121.868	73.051	OSL sample
BO07	OSL35	1947	722087.276	6328110.518	73.037	OSL sample
BO07	OSL36	1946	722066.332	6328086.716	72.664	OSL sample
BO07	OSL37	1945	722065.735	6328086.779	72.290	OSL sample
BO07	OSL38	1944	722049.304	6328083.772	71.257	OSL sample
BO07	OSL39	1943	722044.260	6328080.419	71.656	OSL sample
BO07	OSL40	1940	722047.425	6328022.083	70.488	OSL sample
BO07	OSL41	1941	722061.638	6328003.378	71.417	OSL sample
BO07	OSL42	1942	722067.127	6327994.281	72.120	OSL sample
BO07	OSL43	1955	721991.255	6328006.986	70.770	OSL sample
BO07	OSL44	1956	721984.706	6328004.700	71.582	OSL sample
RB03	OSL45	2064	720549.804	6329008.283	78.353	OSL sample
RB03	OSL46	2063	720545.531	6329018.697	80.076	OSL sample
RB03	OSL47	2062	720545.901	6329024.209	81.099	OSL sample
RB03	OSL48	2062	720545.901	6329024.209	81.399	OSL sample
BO07 beach	OSL49	2094	721765.437	6327750.984	67.274	OSL sample
BO29 beach	OSL50	2091	724744.491	6320914.179	67.180	OSL sample
Spit	OSL51	2068	723976.512	6317542.739	69.641	OSL sample
BG01	OSL52	1959	723226.406	6327421.511	81.147	OSL sample
BG01	OSL53	1959	723226.406	6327421.511	82.347	OSL sample
BG01	OSL54	1959	723226.406	6327421.511	82.497	OSL sample
BG01	OSL55	1959	723226.406	6327421.511	83.447	OSL sample
BG01	OSL56	1959	723226.406	6327421.511	83.747	OSL sample
BO29	PR01	1598	724779.426	6320751.620	67.075	topography

Site	Name	No.	Easting	Northing	Altitude	Notes
BO29	PR01	1599	724780.584	6320752.029	67.144	topography
BO29	PR01	1600	724780.789	6320752.102	67.276	topography
BO29	PR01	1601	724793.937	6320757.309	67.558	topography
BO29	PR01	1602	724833.992	6320776.573	68.045	topography
BO29	PR01	1603	724878.809	6320798.461	68.708	topography
BO29	PR01	1604	724925.081	6320821.031	68.299	topography
BO29	PR01	1605	724960.219	6320839.247	68.333	topography
BO29	PR01	1606	725050.355	6320883.097	69.387	topography
BO29	PR01	1607	725086.077	6320901.107	69.589	topography
BO29	PR01	1608	725103.941	6320911.351	70.135	topography
BO29	PR01	1609	725126.672	6320924.439	71.339	topography
BO29	PR01	1610	725145.150	6320938.529	73.011	topography
BO29	PR01	1611	725157.801	6320950.526	74.693	topography
BO29	PR01	1612	725164.225	6320957.476	75.934	topography
BO29	PR01	1613	725169.806	6320960.549	76.608	topography
BO29	PR01	1614	725170.616	6320960.310	77.604	topography
BO29	PR01	1615	725173.182	6320959.546	78.106	topography
BO29	PR01	1616	725174.876	6320959.562	79.098	topography
BO29	PR01	1617	725179.800	6320961.260	80.261	topography
BO29	PR01	1618	725182.748	6320962.886	80.875	topography
BO29	PR01	1619	725183.434	6320963.235	81.166	topography
BO29	PR01	1620	725189.026	6320967.137	82.069	topography
BO29	PR01	1621	725210.929	6320969.865	82.755	topography
BO29	PR01	1622	725225.477	6320972.633	83.275	topography
BO29	PR01	1623	725264.201	6320978.827	84.576	topography
BO29	PR01	1624	725265.927	6320978.793	85.710	topography
BO29	PR01	1625	725269.371	6320980.724	85.800	topography
BO29	PR01	1626	725269.572	6320981.166	85.124	topography
BO29	PR01	1627	725270.494	6320981.647	84.744	topography
BO29	PR01	1628	725287.102	6320990.443	85.491	topography
BO29	PR01	1629	725309.317	6321000.355	87.758	topography
BO29	PR01	1630	725327.109	6321008.978	89.822	topography
BO29	PR01	1631	725341.433	6321016.709	92.586	topography
BO29	PR01	1632	725341.602	6321016.814	92.827	topography
BO29	PR01	1633	725355.420	6321027.253	95.390	topography
BO29	PR01	1634	725389.147	6321030.525	98.766	topography
BO29	PR01	1635	725395.681	6321032.865	98.715	topography
BO29	PR01	1636	725400.676	6321034.709	97.221	topography
BO29	PR01	1637	725405.520	6321035.393	98.972	topography
BO29	PR01	1638	725408.618	6321036.363	100.759	topography
BO29	PR01	1639	725412.852	6321040.676	102.867	topography
BO29	PR01	1640	725416.975	6321044.533	102.232	topography
BO29	PR01	1641	725418.987	6321046.731	102.403	topography
BO29	PR01	1642	725422.510	6321050.597	103.977	topography
BO29	PR01	1643	725425.055	6321052.896	105.291	topography
BO29	PR01	1644	725424.595	6321055.428	105.847	topography
BO29	PR01	1645	724780.659	6320752.047	67.132	start of beach
BO29	PR01	1646	725164.342	6320957.616	75.949	base of intense gully erosion
BO29	PR01	1647	725180.538	6320961.673	80.441	top of calcrete in A
BO29	PR01	1648	725183.818	6320963.968	81.078	A-B contact
BO29	PR01	1649	725191.867	6320969.423	82.203	top of intense gully erosion
BO29	PR01	1650	725264.299	6320978.294	84.591	base of B palaeosol

Site	Name	No.	Easting	Northing	Altitude	Notes
						(colour)
BO29	PR01	1651	725269.624	6320981.122	85.209	base of B palaeosol (colour)
BO29	PR01	1652	725326.978	6321008.790	89.764	base of B palaeosol (colour)
BO29	PR01	1653	725341.734	6321016.695	92.769	B-C contact
BO29	PR01	1654	725346.556	6321022.429	93.814	C-D contact
BO29	PR01	1655	725348.626	6321023.556	94.206	D-E contact
BO29	PR01	1656	725400.532	6321035.202	97.241	E-D contact
BO29	PR01	GPS	724777.000	6320754.000		topography
BO29	PR01	GPS	725435.000	6321062.000		topography
BO29	PR01	GPS	725444.000	6321061.000		topography
BO29	PR01	GPS	725485.000	6321059.000		topography
BO29	PR01	GPS	725511.000	6321054.000		topography
BO29	PR01	GPS	725550.000	6321054.000		topography
BO29	PR01	GPS	725572.000	6321045.000		topography
BO04	PR02	1660	719427.485	6328874.503	67.101	topography
BO04	PR02	1661	719427.012	6328876.802	67.212	topography
BO04	PR02	1662	719427.099	6328876.887	67.283	topography
BO04	PR02	1663	719411.475	6328918.719	67.924	topography
BO04	PR02	1664	719405.572	6328941.636	68.823	topography
BO04	PR02	1665	719398.923	6328962.761	70.210	topography
BO04	PR02	1666	719393.958	6328977.833	72.049	topography
BO04	PR02	1667	719392.869	6328981.276	72.788	topography
BO04	PR02	1668	719391.503	6328985.246	72.966	topography
BO04	PR02	1669	719388.862	6328993.623	73.660	topography
BO04	PR02	1670	719386.253	6329001.746	74.716	topography
BO04	PR02	1671	719385.468	6329004.535	74.687	topography
BO04	PR02	1672	719384.476	6329007.149	75.077	topography
BO04	PR02	1673	719384.460	6329011.059	74.782	topography
BO04	PR02	1674	719384.167	6329018.109	74.270	topography
BO04	PR02	1675	719383.811	6329021.436	74.334	topography
BO04	PR02	1676	719382.012	6329036.668	75.834	topography
BO04	PR02	1677	719381.074	6329040.837	75.939	topography
BO04	PR02	1678	719381.046	6329040.966	75.613	topography
BO04	PR02	1679	719380.795	6329041.427	75.485	topography
BO04	PR02	1680	719378.503	6329048.276	75.190	topography
BO04	PR02	1681	719374.534	6329057.969	75.393	topography
BO04	PR02	1682	719370.380	6329067.469	75.878	topography
BO04	PR02	1683	719364.468	6329077.936	76.942	topography
BO04	PR02	1684	719364.523	6329078.348	77.630	topography
BO04	PR02	1685	719364.129	6329079.581	77.750	topography
BO04	PR02	1686	719363.744	6329082.759	77.609	topography
BO04	PR02	1687	719365.580	6329093.155	78.074	topography
BO04	PR02	1688	719366.422	6329097.577	78.570	topography
BO04	PR02	1689	719365.556	6329100.504	79.234	topography
BO04	PR02	1690	719365.460	6329100.979	79.834	topography
BO04	PR02	1691	719364.306	6329102.323	80.071	topography
BO04	PR02	1692	719367.621	6329115.965	78.621	topography
BO04	PR02	1693	719365.175	6329128.901	78.304	topography
BO04	PR02	1694	719426.995	6328876.815	67.205	start of beach
BO04	PR02	1695	719390.071	6328987.716	73.347	E-D2 contact
BO04	PR02	1696	719386.649	6329001.538	74.609	E-D2 contact
BO04	PR02	1697	719385.992	6329003.231	74.690	E-D2 contact

Site	Name	No.	Easting	Northing	Altitude	Notes
BO04	PR02	1698	719384.004	6329019.111	74.258	E contact with top of D1 palaeosol
BO04	PR02	1699	719380.795	6329041.071	75.519	D1 palaeosol (bottom of colour)
BO04	PR02	1700	719364.724	6329077.236	76.849	D1 palaeosol (bottom of colour)
BO04	PR02	1701	719364.783	6329081.211	77.626	E contact with top of D1 palaeosol
BO04	PR02	1702	719366.407	6329096.301	78.311	E-D2 contact
BO04	PR02	GPS	719366.000	6329148.000		topo - rear 1
BO01	PR03	1705	718272.352	6328870.484	67.397	topography
BO01	PR03	1706	718272.078	6328871.275	67.444	topography
BO01	PR03	1707	718272.081	6328871.688	67.719	topography
BO01	PR03	1708	718269.186	6328918.432	67.878	topography
BO01	PR03	1709	718266.656	6328950.449	68.228	topography
BO01	PR03	1710	718264.960	6328973.399	69.203	topography
BO01	PR03	1711	718262.239	6328987.534	70.203	topography
BO01	PR03	1712	718259.879	6328999.969	70.991	topography
BO01	PR03	1713	718258.353	6329007.880	71.327	topography
BO01	PR03	1714	718255.621	6329033.281	71.810	topography
BO01	PR03	1715	718255.172	6329048.089	73.116	topography
BO01	PR03	1716	718254.828	6329057.662	73.479	topography
BO01	PR03	1717	718252.960	6329069.469	74.289	topography
BO01	PR03	1718	718252.036	6329075.399	75.046	topography
BO01	PR03	1719	718251.574	6329081.719	75.851	topography
BO01	PR03	1720	718249.205	6329102.529	75.519	topography
BO01	PR03	1721	718247.006	6329112.622	75.240	topography
BO01	PR03	1722	718248.362	6329122.895	75.318	topography
BO01	PR03	1723	718252.173	6329138.913	75.586	topography
BO01	PR03	1724	718254.586	6329158.677	75.260	topography
BO01	PR03	1725	718254.548	6329175.988	74.114	topography
MSE03	PR04	1728	724049.329	6324587.867	67.319	topography
MSE03	PR04	1729	724060.790	6324589.648	67.321	topography
MSE03	PR04	1730	724062.715	6324590.255	67.496	topography
MSE03	PR04	1731	724156.052	6324620.221	68.252	topography
MSE03	PR04	1732	724192.986	6324630.789	68.664	topography
MSE03	PR04	1733	724240.102	6324645.913	69.122	topography
MSE03	PR04	1734	724280.027	6324662.244	69.939	topography
MSE03	PR04	1735	724317.096	6324677.517	70.695	topography
MSE03	PR04	1736	724347.262	6324690.547	72.307	topography
MSE03	PR04	1737	724366.730	6324699.337	73.597	topography
MSE03	PR04	1738	724408.923	6324714.965	77.892	topography
MSE03	PR04	1739	724420.545	6324720.756	80.297	topography
MSE03	PR04	1740	724428.411	6324723.558	81.759	topography
MSE03	PR04	1741	724432.339	6324725.817	82.358	topography
MSE03	PR04	1742	724436.915	6324727.255	82.939	topography
MSE03	PR04	1743	724445.719	6324729.128	83.727	topography
MSE03	PR04	1744	724456.830	6324732.499	84.900	topography
MSE03	PR04	1745	724464.192	6324733.949	85.465	topography
MSE03	PR04	1746	724465.994	6324733.776	85.640	topography
MSE03	PR04	1747	724467.212	6324733.090	84.801	topography
MSE03	PR04	1748	724468.549	6324732.788	84.690	topography
MSE03	PR04	1749	724469.523	6324732.550	84.412	topography
MSE03	PR04	1750	724470.716	6324732.534	84.450	topography

Site	Name	No.	Easting	Northing	Altitude	Notes
MSE03	PR04	1751	724471.331	6324732.369	84.547	topography
MSE03	PR04	1752	724473.803	6324731.838	85.320	topography
MSE03	PR04	1753	724475.144	6324731.674	85.939	topography
MSE03	PR04	1754	724477.632	6324731.754	86.617	topography
MSE03	PR04	1755	724483.114	6324734.119	86.824	topography
MSE03	PR04	1756	724490.078	6324735.871	86.951	topography
MSE03	PR04	1757	724490.754	6324735.627	86.837	topography
MSE03	PR04	1758	724491.354	6324735.492	86.379	topography
MSE03	PR04	1759	724491.873	6324735.232	86.267	topography
MSE03	PR04	1760	724493.012	6324735.132	85.955	topography
MSE03	PR04	1761	724494.496	6324735.103	86.111	topography
MSE03	PR04	1762	724496.994	6324735.494	86.409	topography
MSE03	PR04	1763	724498.864	6324735.857	86.634	topography
MSE03	PR04	1764	724498.997	6324735.871	87.236	topography
MSE03	PR04	1765	724515.719	6324740.978	88.202	topography
MSE03	PR04	1766	724516.004	6324741.228	88.506	topography
MSE03	PR04	1767	724523.185	6324743.093	89.231	topography
MSE03	PR04	1768	724533.146	6324742.727	89.582	topography
MSE03	PR04	1769	724544.423	6324742.568	89.674	topography
MSE03	PR04	1770	724546.602	6324742.321	90.113	topography
MSE03	PR04	1771	724550.929	6324742.329	90.391	topography
MSE03	PR04	1772	724558.664	6324742.857	90.736	topography
MSE03	PR04	1773	724567.776	6324743.740	91.054	topography
MSE03	PR04	1774	724570.767	6324744.033	91.250	topography
MSE03	PR04	1775	724573.338	6324744.244	91.433	topography
MSE03	PR04	1776	724575.902	6324744.202	91.915	topography
MSE03	PR04	1777	724577.157	6324744.235	92.377	topography
MSE03	PR04	1778	724579.515	6324744.190	92.982	topography
MSE03	PR04	1779	724580.453	6324744.001	93.169	topography
MSE03	PR04	1780	724581.814	6324744.108	93.282	topography
MSE03	PR04	1781	724583.134	6324744.129	93.399	topography
MSE03	PR04	1782	724585.049	6324744.138	93.179	topography
MSE03	PR04	1783	724587.026	6324744.285	92.637	topography
MSE03	PR04	1784	724588.789	6324744.331	92.066	topography
MSE03	PR04	1785	724590.508	6324744.279	91.097	topography
MSE03	PR04	1786	724594.313	6324744.645	92.236	topography
MSE03	PR04	1787	724603.495	6324741.093	91.867	topography
MSE03	PR04	1788	724606.568	6324738.757	92.246	topography
MSE03	PR04	1789	724607.172	6324738.377	92.711	topography
MSE03	PR04	1791	724060.928	6324589.786	67.326	start of beach
MSE03	PR04	1792	724410.343	6324715.146	78.037	base of gully/start of exposure
MSE03	PR04	1793	724428.438	6324723.289	81.724	A-C contact
MSE03	PR04	1794	724433.041	6324725.764	82.032	A-C contact
MSE03	PR04	1795	724440.986	6324726.656	82.374	A-B-C contact
MSE03	PR04	1796	724443.646	6324725.525	82.355	A-B contact
MSE03	PR04	1797	724443.936	6324725.677	82.739	B-C contact
MSE03	PR04	1798	724452.427	6324729.277	82.822	A-B contact
MSE03	PR04	1799	724452.618	6324729.712	83.343	B-C contact
MSE03	PR04	1800	724467.090	6324733.217	85.042	B-C contact
MSE03	PR04	1801	724474.615	6324731.734	85.640	B-C contact
MSE03	PR04	1802	724489.617	6324735.677	86.749	B-C contact
MSE03	PR04	1803	724499.595	6324736.449	87.061	B-C contact
MSE03	PR04	1804	724515.701	6324741.030	88.237	C-D contact

Site	Name	No.	Easting	Northing	Altitude	Notes
MSE03	PR04	1805	724525.578	6324743.253	89.381	C-D contact
MSE03	PR04	1806	724574.981	6324744.387	91.681	C-D contact
MSE03	PR04	1807	724590.301	6324743.752	91.137	C-D contact
MSE03	PR04	1808	724590.721	6324743.718	90.971	C-E contact
MSE03	PR04	1809	724606.376	6324738.454	92.210	B-E contact
MSE03	PR04	1810	724607.351	6324738.685	92.526	B-C contact
BO07	PR05	1814	721955.776	6327976.895	71.020	Topography
BO07	PR05	1815	721959.305	6327980.540	71.214	Topography
BO07	PR05	1816	721961.711	6327983.128	71.560	Topography
BO07	PR05	1817	721963.935	6327986.603	71.965	Topography
BO07	PR05	1818	721967.432	6327989.914	72.229	Topography
BO07	PR05	1819	721980.226	6327998.816	73.065	Topography
BO07	PR05	1820	721983.912	6328002.212	73.303	Topography
BO07	PR05	1821	721986.002	6328003.163	73.083	Topography
BO07	PR05	1822	721990.319	6328006.420	72.370	Topography
BO07	PR05	1823	721991.043	6328007.306	72.438	Topography
BO07	PR05	1824	721991.726	6328007.681	72.325	Topography
BO07	PR05	1825	721992.110	6328007.932	72.195	Topography
BO07	PR05	1826	721993.448	6328008.552	72.084	Topography
BO07	PR05	1827	721995.704	6328010.729	71.905	Topography
BO07	PR05	1828	722006.996	6328025.794	71.934	Topography
BO07	PR05	1829	722011.206	6328031.197	72.132	Topography
BO07	PR05	1830	722020.389	6328042.271	72.349	Topography
BO07	PR05	1831	722024.900	6328048.011	72.077	Topography
BO07	PR05	1832	722030.872	6328056.815	72.378	Topography
BO07	PR05	1833	722034.332	6328060.677	72.819	Topography
BO07	PR05	1834	722040.822	6328065.889	73.036	Topography
BO07	PR05	1835	722042.344	6328067.333	72.767	Topography
BO07	PR05	1836	722049.752	6328073.893	72.865	Topography
BO07	PR05	1837	722051.505	6328075.887	73.181	Topography
BO07	PR05	1838	722051.814	6328076.139	72.933	Topography
BO07	PR05	1839	722053.223	6328077.165	72.880	Topography
BO07	PR05	1840	722060.051	6328082.452	72.992	Topography
BO07	PR05	1841	722064.226	6328085.691	73.425	Topography
BO07	PR05	1842	722065.549	6328086.837	73.875	Topography
BO07	PR05	1843	722065.636	6328086.879	74.054	Topography
BO07	PR05	1844	722066.165	6328087.306	74.225	Topography
BO07	PR05	1846	722066.348	6328087.274	74.175	topography
BO07	PR05	1847	722067.910	6328088.595	74.162	topography
BO07	PR05	1848	722068.752	6328089.145	74.388	topography
BO07	PR05	1849	722070.615	6328091.193	74.242	topography
BO07	PR05	1850	722072.456	6328093.327	74.519	topography
BO07	PR05	1851	722080.893	6328099.120	74.799	topography
BO07	PR05	1852	722085.929	6328102.522	74.767	topography
BO07	PR05	1853	722093.009	6328109.655	74.471	topography
BO07	PR05	1854	722092.995	6328110.143	75.397	topography
BO07	PR05	1855	722096.963	6328113.600	74.630	topography
BO07	PR05	1856	722100.219	6328117.199	74.340	topography
BO07	PR05	1857	722100.942	6328118.262	74.541	topography
BO07	PR05	1858	722102.193	6328120.171	74.540	topography
BO07	PR05	1859	722103.268	6328122.134	74.429	topography
BO07	PR05	1860	722108.246	6328129.017	74.944	topography
BO07	PR05	1861	722110.609	6328131.807	75.543	topography

Site	Name	No.	Easting	Northing	Altitude	Notes
BO07	PR05	1862	722115.649	6328138.004	76.595	topography
BO07	PR05	1863	722116.321	6328140.902	77.043	topography
BO07	PR05	1864	722115.551	6328138.399	76.610	topography
BO07	PR05	1865	722115.663	6328140.865	77.640	topography
BO07	PR05	1866	722124.446	6328150.344	78.186	topography
BO07	PR05	1867	722136.202	6328156.242	77.753	topography
BO07	PR05	1868	722139.726	6328158.295	77.232	topography
BO07	PR05	1869	722151.282	6328166.936	77.198	topography
BO07	PR05	1870	722167.147	6328174.525	77.960	topography
BO07	PR05	1871	722169.657	6328176.000	79.080	topography
BO07	PR05	1872	722170.810	6328176.392	78.738	topography
BO07	PR05	1873	722172.061	6328176.850	78.212	topography
BO07	PR05	1874	722172.061	6328176.865	78.209	topography
BO07	PR05	1875	722177.720	6328179.641	78.268	topography
BO07	PR05	1876	722209.221	6328198.679	80.945	topography
BO07	PR05	1877	721989.595	6328005.765	72.408	D2-E contact
BO07	PR05	1878	721990.353	6328006.456	72.349	D1-D2 contact (top of D1 palaeosol)
BO07	PR05	1879	722041.843	6328066.758	72.782	D1-B contact
BO07	PR05	1880	722065.531	6328086.837	73.866	B-C contact
BO07	PR05	1881	722068.149	6328088.689	74.187	Base of C palaeosol (colour)
BO07	PR05	1882	722070.691	6328091.166	74.245	C-E contact
BO07	PR05	1883	722091.915	6328108.187	74.459	D-E contact
BO07	PR05	1884	722093.053	6328109.790	74.606	Base D1 palaeosol (calcrete)
BO07	PR05	1885	722100.195	6328117.437	74.388	D1-E
BO07	PR05	1886	722102.920	6328121.595	74.417	D1-E
BO07	PR05	1887	722107.241	6328128.097	74.795	Base D1 palaesol (colour)
BO07	PR05	1888	722115.597	6328138.057	76.615	D1-D2 contact
BO07	PR05	1889	722148.105	6328163.463	77.146	D2-E contact
BO07	PR05	1890	722167.918	6328173.784	78.018	D2-E contact
BO07	PR05	1891	722173.024	6328176.725	78.122	D2-E contact
BO07	PR05	GPS	721757.000	6327754.000		Topo-beach
South end	PR06	1894	726051.214	6318430.541	89.228	topography
South end	PR06	1895	726036.422	6318413.729	89.215	topography
South end	PR06	1896	726023.797	6318404.773	90.145	topography
South end	PR06	1897	726018.921	6318401.159	90.454	topography
South end	PR06	1898	726004.402	6318389.152	90.771	topography
South end	PR06	1899	725984.628	6318372.484	91.126	topography
South end	PR06	1900	725960.404	6318347.970	90.542	topography
South end	PR06	1901	725916.378	6318332.639	89.667	topography
South end	PR06	1902	725896.776	6318324.293	89.318	topography
South end	PR06	1903	725876.952	6318317.152	88.703	topography
South	PR06	1904	725843.262	6318306.151	87.491	topography

Site	Name	No.	Easting	Northing	Altitude	Notes
South end	PR06	1905	725815.643	6318298.022	86.293	topography
South end	PR06	1906	725786.467	6318291.919	85.254	topography
South end	PR06	1907	725755.845	6318289.958	84.119	topography
South end	PR06	1908	725689.211	6318285.027	82.048	topography
South end	PR06	1909	725642.259	6318280.653	80.924	topography
South end	PR06	1910	725605.368	6318280.038	80.003	topography
South end	PR06	1911	725561.871	6318278.165	79.535	topography
South end	PR06	1912	725552.733	6318276.812	79.804	topography
South end	PR06	1913	725543.544	6318275.850	79.902	topography
South end	PR06	1914	725529.534	6318274.473	79.405	topography
South end	PR06	1915	725513.849	6318275.726	78.727	topography
South end	PR06	1916	725504.806	6318275.651	79.007	topography
South end	PR06	1917	725471.383	6318271.608	79.232	topography
South end	PR06	1918	725443.686	6318267.065	78.782	topography
South end	PR06	1919	725422.106	6318264.080	78.212	topography
South end	PR06	1920	725397.334	6318281.762	76.529	topography
South end	PR06	1921	725376.487	6318277.796	75.532	topography
South end	PR06	1922	725336.861	6318268.190	73.784	topography
South end	PR06	1923	725313.208	6318255.967	72.926	topography
South end	PR06	1924	725297.270	6318250.937	72.365	topography
spit	PR07	2069	724042.712	6317719.046	67.877	topography
spit	PR07	2070	724043.588	6317701.391	68.073	topography
spit	PR07	2071	724042.777	6317678.890	68.251	topography
spit	PR07	2072	724043.592	6317660.745	68.509	topography
spit	PR07	2073	724043.944	6317648.846	68.329	topography
spit	PR07	2074	724044.122	6317641.554	68.942	topography
spit	PR07	2075	724044.360	6317634.237	69.239	topography
spit	PR07	2076	724044.467	6317627.540	69.258	topography
spit	PR07	2077	724044.585	6317619.292	69.661	topography
spit	PR07	2078	724045.878	6317611.342	69.853	topography
spit	PR07	2079	724045.964	6317603.803	69.904	topography
spit	PR07	2080	724045.860	6317596.012	69.928	topography
spit	PR07	2081	724047.187	6317586.957	69.850	topography
spit	PR07	2082	724047.669	6317577.197	69.620	topography
spit	PR07	2083	724047.946	6317568.583	69.376	topography
spit	PR07	2084	724049.616	6317560.031	69.130	topography

Site	Name	No.	Easting	Northing	Altitude	Notes
spit	PR07	2085	724052.109	6317552.302	69.092	topography
spit	PR07	2086	724052.403	6317541.296	69.117	topography
spit	PR07	2087	724052.848	6317529.003	69.173	topography
MSE03	SL001	1790	724586.507	6324723.200	92.971	Stratigraphic log
BO02	SL002	1357	718525.923	6329111.903	77.097	Stratigraphic log
BO04	SL003	1342	719348.719	6329077.116	77.112	Stratigraphic log
BO04	SL004	1336	719430.269	6329034.833	75.653	Stratigraphic log
RB05	SL005	1293	721382.840	6328943.765	81.035	Stratigraphic log
BO007A	SL006	1295	721724.760	6328285.458	73.778	Stratigraphic log
BO007B	SL007	1311	721942.621	6328203.310	72.678	Stratigraphic log
BO07E	SL008	1324	722386.012	6327860.040	76.135	Stratigraphic log
MSE01	SL009	1285	722581.612	6327710.324	77.425	Stratigraphic log
MSE02	SL010	1278	722949.422	6327463.694	76.773	Stratigraphic log
BG01	SL011	1959	723226.406	6327421.511	81.147	Stratigraphic log
BG04B	SL012	1962	723814.582	6326433.886	86.162	Stratigraphic log
BG05	SL013	GPS	723823.000	6326286.000	88.800	Stratigraphic log
BG06	SL014	1270	723805.803	6326093.638	80.367	Stratigraphic log
BO11	SL015	1236	724319.556	6325435.596	90.397	Stratigraphic log
BG09	SL016	1973	724278.450	6325100.922	78.179	Stratigraphic log
BO13	SL018	1999	724750.352	6324454.996	85.349	Stratigraphic log
BO14	SL019	2002	724838.392	6324130.927	86.508	Stratigraphic log
BO15	SL020	GPS	724878.000	6323984.000		Stratigraphic log
BO17	SL021	2005	725109.020	6323508.804	77.985	Stratigraphic log
BO17	SL022	2009	725082.200	6323288.792	86.644	Stratigraphic log
BO19	SL023	2016	725072.827	6322975.661	83.839	Stratigraphic log
BG19	SL024	1996	724957.449	6323000.727	79.834	Stratigraphic log
BO21	SL025	2030	725166.479	6322516.788	88.110	Stratigraphic log
BO22	SL026	2020	725202.186	6322303.689	92.439	Stratigraphic log
BO23	SL027	2021	725194.867	6322053.725	87.074	Stratigraphic log
BO23	SL028	2027	725229.645	6321938.699	90.923	Stratigraphic log
BG	SL029	2022	725125.453	6321750.191	78.940	Stratigraphic log
BO	SL030	2023	725239.458	6321495.175	92.153	Stratigraphic log
BO28	SL031	2024	725326.374	6321197.355	91.854	Stratigraphic log
BO29	SL033	2043	725345.361	6320607.728	91.199	Stratigraphic log
BO30	SL034	2045	725348.103	6320185.035	87.025	Stratigraphic log
BO31	SL035	2046	725310.712	6319973.566	81.943	Stratigraphic log
BG	SL037	2044	725210.914	6320192.742	78.438	Stratigraphic log
BG	SL038	2049	725272.726	6319466.321	75.991	Stratigraphic log
BO03	SL039	GPS	719139.000	6329286.000	77.800	Stratigraphic log
BO04	SL041	1933	719408.346	6329082.080	75.867	Stratigraphic log
RB02	SL043	2060	720355.469	6329246.779	80.900	Stratigraphic log
RB03	SL044	2062	720545.901	6329024.209	79.699	Stratigraphic log
BO12	SL046	1983	724572.282	6325181.307	84.836	Stratigraphic log
BO10	SL047	1963	724024.316	6326036.624	89.755	Stratigraphic log
BO07E	TS116	GPS	722295.000	6328040.000		Thin section
BO07E	TS117	GPS	722295.000	6328040.000		Thin section
BO07E	TS118	GPS	722295.000	6328040.000		Thin section
RB01	TS122	2059	720115.700	6329242.791	82.440	Thin section
BO04	TS125	GPS	719408.000	6329081.000		Thin section
BO03	TS126	GPS	719139.000	6329286.000		Thin section
RB02	WT01	2061	720360.076	6329266.148	79.198	Wombat tooth
BO007B	WT02	1310	721897.430	6328235.987	71.443	Wombat tooth
BO007B	WT03	1309	721902.334	6328228.519	71.726	Wombat tooth

Site	Name	No.	Easting	Northing	Altitude	Notes
BO007B	WT04	1308	721905.080	6328227.446	73.566	Wombat tooth
BO007B	WT05	1307	721905.672	6328227.879	73.565	Wombat tooth
BO007B	WT06	1306	721906.844	6328228.131	73.652	Wombat tooth
BO07B	WT07	1305	721912.383	6328224.382	72.274	Wombat tooth
BOO7B	WT08	1304	721913.147	6328224.381	72.277	Wombat tooth
BO007B	WT09	1303	721889.140	6328221.107	71.545	Wombat tooth
BO007B	WT10	1302	721888.255	6328221.177	71.466	Wombat tooth
BO007B	WT11	1301	721887.923	6328220.839	71.494	Wombat tooth
BO007B	WT12	1300	721887.882	6328220.543	71.491	Wombat tooth
BO007B	WT13	1299	721888.086	6328220.221	71.547	Wombat tooth
BO007B	WT14	1298	721867.013	6328207.228	71.552	Wombat tooth
BO007B	WT15	1297	721859.979	6328208.753	71.385	Wombat tooth
BO007C	WT16	1313	722014.711	6328188.585	72.486	Wombat tooth
BO007C	WT17	1314	722011.813	6328181.684	72.153	Wombat tooth
BO07C	WT18	1315	722023.333	6328175.120	72.386	Wombat tooth
BO07C	WT19	1316	722024.524	6328174.524	72.389	Wombat tooth
BO07C	WT20	1318	722069.233	6328153.634	72.833	Wombat tooth
BO007C	WT21	1317	722067.038	6328134.664	73.119	Wombat tooth
BO007C	WT22	1320	722078.044	6328112.452	73.103	Wombat tooth
BO07E	WT23	1329	722402.792	6327762.053	72.326	Wombat tooth
BO07E	WT24	1361	722401.798	6327760.006	73.142	Wombat tooth
MSE01	WT25	1286	722570.139	6327754.421	83.242	Wombat tooth
MSE01	WT26	1284	722611.924	6327739.099	81.385	Wombat tooth
MSE01	WT27	1283	722616.278	6327734.799	81.487	Wombat tooth
MSE01	WT28	1280	722853.367	6327552.368	76.065	Wombat tooth
MSE01	WT29	1281	722792.218	6327597.209	76.047	Wombat tooth
BO11	WT30	1981	724408.327	6325438.791	88.312	Wombat tooth
BO11	WT31	1982	724385.535	6325442.382	88.091	Wombat tooth
BO14	WT32	2000	724786.174	6324242.101	81.739	Wombat tooth
BO14	WT33	2001	724783.955	6324216.102	84.411	Wombat tooth
BO19	WT34	2013	725061.221	6323018.558	85.811	Wombat tooth
BO19	WT35	2014	725069.025	6323026.863	85.308	Wombat tooth
BO21	WT36	1248	725142.714	6322489.610	87.333	Wombat tooth

Appendix B. Tables of thin sections and loose sediment samples

Appendix B.1: Summary of thin section descriptions

site	profile	Unit	TS no.	grainsize	sorting	roundness[1]	sphericity	clay pellets	cutans[2]	other notes
BO29	PR01	A	**143**	silt to v. coarse	poor	SA	low	few	P	Interstitial clay matrix and impregnated with secondary carbonate.
			144	v.fine to coarse	poor	SR	moderate	few	P & I	Secondary carbonate matrix. Micritic carbonate.
		D	**145**	v.fine to medium	mod well	SR	moderate	none	I	clast of carbonate impregnated clay soil. High relief phase in small amounts
		C/D	**146**	v.fine-silt	well	SA-SR	moderate	many	P & I	Clay layer at top, sand below
		beach	**150**	fine to medium	mod poor	SA-SR	moderate	none	I	
BO04	PR02	B	**125**	fine	moderate	SA	moderate	few	I	Possible wurstenquartz. High relief phase. Some clay pellets with complex extinction domains and some with uniform illumination
		E	**123**	silt to coarse	poor	SA-SR	mod to low	none	I	Cracked atz with Fe stains.
			124	silt to coarse	poor	SA	moderate	none	I	Cutans thick . mm-scale laminations of 100 µm grains.
MSE03	PR04	A	**142**	silt to medium sand	v. poor	SA-SR	moderate	disaggregated	P	Dense clay matrix impregnated with secondary carbonates. Dissagregated clay pellets.
		B	**141**	fine	Mod well	SR	subrounded	none	I	Clasts of dense secondary carbonate. Clast of reddish clay containing Fe-Mn dendritic nodules.
			139	medium	well	SR	moderate	v. few	I	
		C	**140**	fine to medium	mod well	SA-SR	moderate	abundant	I	clay pellets irregular and ragged, heavy minerals
		E	**138**	fine to medium	mod well	WR	mod	few	I	
BO07	PR05	B	**133**	fine to coarse	moderate	SR-WR	moderate	v. few	P	Microbialite clast with quartz grains cemented into matrix and dendritic secondary Mn/Fe. Cutans opaque.
		C	**132**	v.fine to coarse	moderate	SR	moderate	abundant	I	Qtz with zoned extinction. Some clay pellets with complex extinction domains and some with uniform illumination. Cutans of Fe and clay
		D	**130**	very fine to coarse	poor	SR	moderate	none	P & I	
			131	fine to medium	moderate	SA-SR	moderate	few	I	some secondary carbonate cementation plus ooids and shell fragment (beach zone)

APPENDIX B. TABLES OF THIN SECTIONS AND LOOSE SEDIMENT SAMPLES

site	profile	Unit	TS no.	grainsize	sorting	roundness [1]	sphericity	clay pellets	cutans [2]	other notes
			134	silt to fine	well	SA-SR	moderate	none	I	
			136	v fine to coarse	moderate	SR	high to low	none	I	bimodal population 300-500 and 30-50 µm. Large clast of Fe-oxide cemented quartz sand.
		E	**129**	fine and coarse	well within laminations	WR	mod to low	v. few	I	Laminations (fine = 150-200 µm, course = 0.5-1mm) with some imbrication of of eleongate grains.
			135	v.fine to coarse	moderate	SR-WR	mod to low	v. few	I	Some carbonate clasts. Possible wurstenquartz.
			137	silt to v. coarse	v.poor	SR	high	v. few	I	Ferri-argillans
		Beach	**149**	fine to medium	well	SA-SR	moderate	v. few	I	
BG01	SL11	C	**039**	fine to medium	moderate	SA	moderate	abundant	P	
			040	fine to medium	mod poor	SA	moderate	abundant	P	Pellets rounded 200-300 µm. Fe oxides.
			041	v. fine to medium	mod poor	SR	moderate	abundant	P	clay matrix
		E	**042**	medium and silt	mod poor	SA-SR	moderate	few	I	Bimodal grainsize. Ferri-argillans
			043	v. fine to silt	well	SR	moderate	rare	I	
RB03	SL44	A	**119**	v.fine to medium	moderate	SA	moderate to low	v. few	P & I	primary ferri-argillans preferentially coating smaller grains
Spit	PR07		**151**	v.fine to coarse	poor	SR	moderate	none	P & I	Illuvial clay matrix. Dense Fe-oxide. Bone fragment
gypsum		A	**049**	v. coarse		A	low	none		Euhedral to subhedral gypsum crystals with interstitial clay and fine carbonates
Carbonate nodule		A	**051**	fine to medium		WR	low	none		Fine grained carbonate intergrowths with quartz and clay inclusions

[1] – SA = sub-angular. SR = sub-rounded. WR = well rounded
[2] – P = primary. I = illuvial

Appendix B2: Summary of sediment sample descriptions

site	profile	Unit	OSL no.	Munsell Colour name	Musell colour code	grainsize	sorting	roundness	sphericity
BO29	PR01	base A	**K2079**	Reddish Yellow	7.5YR 6/8	medium to silt	poor	sub-angular	mod-low
BO29	PR01	top A	**K2080**	Strong Brown	7.5YR 4/6	fine to silt	poor	sub-rounded	moderate
BO29	PR01	Base B	**K2081**	Strong Brown	7.5YR 5/6	fine to very fine	moderately well	sub-rounded	moderate
BO29	PR01	Mid D	**K2082**	Strong Brown	7.5YR 5/8	fine to very fine	moderate	sub-rounded	low
BO29	PR01	E	**K2083**	Reddish Yellow	7.5YR 6/6	fine to very fine	moderate	sub-rounded	moderate
BO29	PR01	D	**K2084**	Strong Brown	7.5YR 5/8	medium to fine	moderate	sub-rounded	low
BO29	PR01	top of D	**K2085**	Strong Brown	7.5YR 4/6	fine to silt	moderate	sub-rounded	moderate
BO29	PR01	lower E	**K2086**	Strong Brown	7.5YR 5/6	medium to fine	moderately well	sub-rounded	moderate
BO29	PR01	Upper E	**K2087**	Reddish Yellow	7.5YR 6/8	medium to fine	moderately well	sub-rounded	moderate
BO29	PR01	Behind dune	**K2088**	Strong Brown	7.5YR 4/6	medium to silt	poor	sub-rounded	moderate
MSE03	PR04	Base of A	**K2089**	Reddish Yellow	7.5YR 7/6	very fine to silt	poor	sub-rounded	moderate
MSE03	PR04	Top of A	**K2090**	Strong Brown	7.5YR 5/8	fine to silt	poor	sub-rounded	moderate
MSE03	PR04	Base of B	**K2091**	Strong Brown	7.5YR 5/6	fine	moderately well	sub-rounded	moderate
MSE03	PR04	Mid B	**K2092**	Reddish Yellow	7.5YR 6/6	fine	well	sub-rounded	moderate
MSE03	PR04	C	**K2093**	Yellowish Brown	10YR 5/4	fine to silt	poor	sub-rounded	moderate
MSE03	PR04	Top of B	**K2094**	Yellow	10YR 7/6	medium to fine	moderate	sub-rounded	moderate
MSE03	PR04	below contact in E	**K2095**	Light Yellowish Brown	10YR 6/4	fine	well	sub-rounded	moderate
MSE03	PR04	above contact in E	**K2096**	Light Yellowish Brown	10YR 6/4	fine	well	sub-rounded	moderate
MSE03	PR04	Behind dune	**K2097**	Yellowish Red	5YR 4/6	very fine	poor	sub-rounded	moderate
BO04	PR02	E (top of dune)	**K2101**	Strong Brown	7.5YR 5/8	medium to fine	poor	well rounded	moderate
BO03	PR02	Behind dune	**K2102**	Yellowish Red	5YR 4/6	medium to very fine	poor	sub-rounded	moderate
BO03	PR02	E (top of dune)	**K2103**	Strong Brown	7.5YR 5/8	medium to fine	poor	sub- to well rounded	moderate
BO04	PR02	E (front of dune)	**K2104**	Strong Brown	7.5YR 5/8	course to medium	poor	sub- to well rounded	moderate
BO07	PR05	Behind dune	**K2105**	Reddish Yellow	7.5YR 6/6	very fine	well	sub-rounded	moderate
BO07	PR05	E (in rear of dune)	**K2106**	Yellowish Brown	10YR 5/6	course to very fine	poor	sub-rounded	moderate
BO07	PR05	top E	**K2107**	Brownish Yellow	10YR 6/6	fine to very fine	moderately poor	sub-rounded	moderate
BO07	PR05	below contact in E	**K2108**	Yellowish Brown	10YR 5/8	course to very fine	very poor	moderate to well rounded	moderate
BO07	PR05	above contact in E	**K2109**	Reddish Yellow	7.5YR 6/6	medium to very fine	very poor	moderate to well rounded	moderate
BO07	PR05	bottom E	**K2110**	Reddish Yellow	7.5YR 6/6	fine to very fine	moderately well	sub-rounded	moderate
BO07	PR05	top D	**K2111**	Strong Brown	7.5YR 5/6	medium to very	poor	sub-rounded	moderate

site	profile	Unit	OSL no.	Munsell Colour name	Musell colour code	grainsize	sorting	roundness	sphericity
						fine			
BO07	PR05	D palaeosol	**K2112**	Light Yellowish Brown	10YR 6/4	fine to very fine	moderately poor	sub-rounded	moderate
BO07	PR05	bottom D (palaeosol)	**K2113**	Light Yellowish Brown	10YR 6/4	medium to fine	moderate	sub-rounded	moderate
BO07	PR05	C	**K2114**	Yellowish Brown	10YR 5/4	fine to silt	poor	sub-angular	moderate
BO07	PR05	top B	**K2115**	Light Yellowish Brown	10YR 6/4	medium to very fine	moderate	sub-rounded	moderate
BO07	PR05	B under midden	**K2116**	Light Yellowish Brown	10YR 6/4	fine	well	sub-rounded	moderate
BO07	PR05	B	**K2117**			medium to very fine	moderately poor	sub-angular	moderate
BO07	PR05	D (under midden)	**K2118**	Light Yellowish Brown	10YR 6/4	very fine	well	sub-rounded	moderate to high
BO07	PR05	D (above midden)	**K2119**	Light Yellowish Brown	10YR 6/4	very fine	well	sub-rounded	moderate to low
BO07	PR05	E (top of side dune)	**K2120**	Light Yellowish Brown	10YR 6/4	fine to very fine	moderate	sub-rounded	moderate
BO07	PR05	D (base of foredune)	**K2121**	Reddish Yellow	7.5YR 6/6	fine	moderate	well rounded	moderate to high
BO07	PR05	E (top of foredune)	**K2122**	Light Yellowish Brown	10YR 6/4	course to very fine	very poor	sub-rounded	moderate to low
BO07	PR05	beach edge	**K2127**	Strong Brown	7.5YR 4/6	fine to very fine	moderate	sub-angular	moderate
BO29	PR01	beach edge	**K2128**	Strong Brown	7.5YR 4/6	fine to very fine	moderate	sub-angular	moderate
spit	PR07	Spit	**K2129**	Strong Brown	7.5YR 4/6	course to very fine	poor	sub-rounded	moderate to low
BG01	SL11	C (thick clay)	**K2130**	Yellowish Brown	10YR 5/4	very fine to silt	moderate	well rounded	moderate
BG01	SL11	C (palaeosol?)	**K2131**	Strong Brown	7.5YR 5/8	fine to silt	poor	sub-rounded	moderate
BG01	SL11	Within C	**K2132**	Strong Brown	7.5YR 5/6	very fine to silt	poor	sub-rounded	moderate
BG01	SL11	E	**K2133**	Strong Brown	7.5YR 4/6	fine to very fine	moderate	well rounded	moderate
BG01	SL11	E	**K2134**	Reddish Yellow	7.5YR 6/6	very fine to silt	well	moderately	moderate
BG01	SL11	Top of C	**K2135**	Strong Brown	7.5YR 4/6	medium to silt	very poor	moderately	moderate
BG01	SL11	E	**K2136**	Reddish Yellow	7.5YR 6/6	fine	well	sub-rounded	moderate

Appendix C. Sedimentary sample descriptions

Appendix C.1. Sediment descriptions from PR02 at BO04

Unit B

Thin sections

TS125 (near K2100)

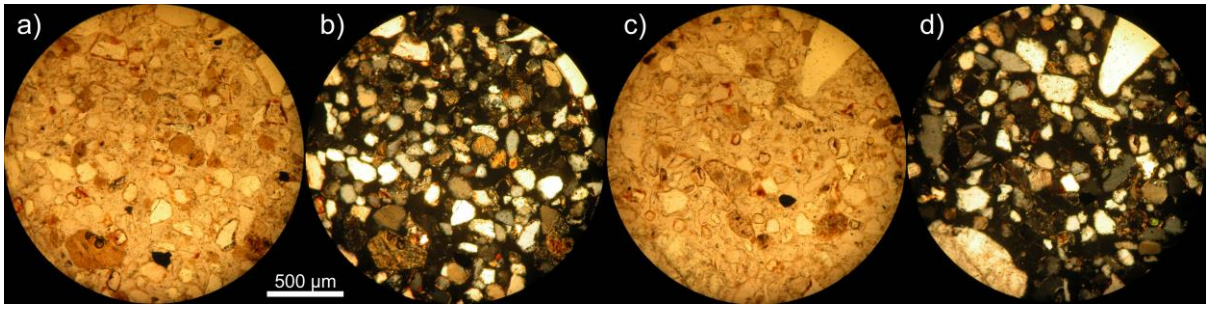

Moderately sorted mostly 100-200 µm (though up to 1mm) sub-angular quartz with moderate sphericity. Cutans are variable in nature and thickness (possible mixed sources of grain coatings). Possible wurstenquartz (top left of a&b). High relief green grain in lower right of c&d. Large very well rounded clay grains, some with complex extinction domains and some with uniform illumination (two difference sources of clay pellets).

Field observations

Exposed as a blow-out area, where broken through paleosol. Filled with shell middens. Paleosol includes rubification and calcrete nodules. Upper parts of paleosol nearby, lots of Fe, especially in cracks.

Summary Description

Stratigraphy

Moderately sorted sand with very few clay pellets.

Pedostratigraphy

Rubification and calcrete nodules

Biostratigraphy

Unionid shell middens

Unit E

Loose Sediments

K2101

Strong brown (7.5YR 5/8) medium to fine, poorly sorted, well rounded grains with moderate sphericity.

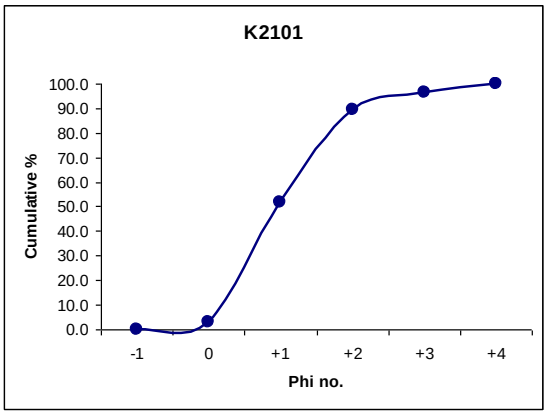

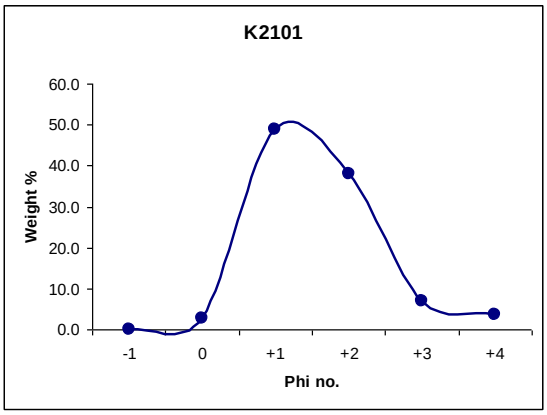

K2104

Strong brown (7.5YR 5/8) course to medium, very poorly sorted, sub- to well-rounded grains with moderate sphericity.

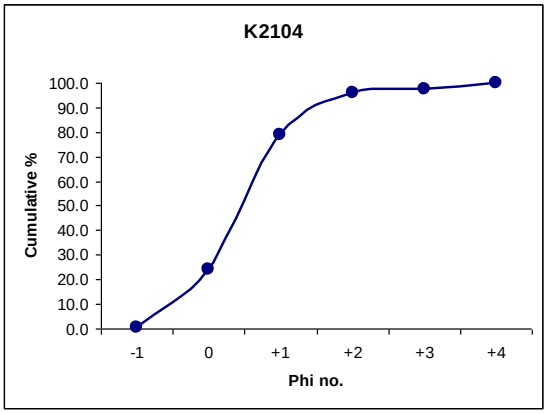

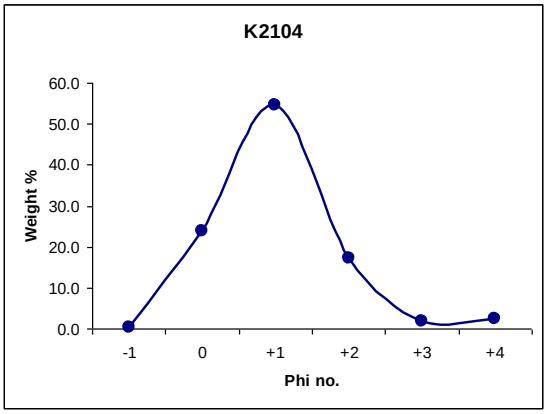

Thin sections

TS123 (near K2101)

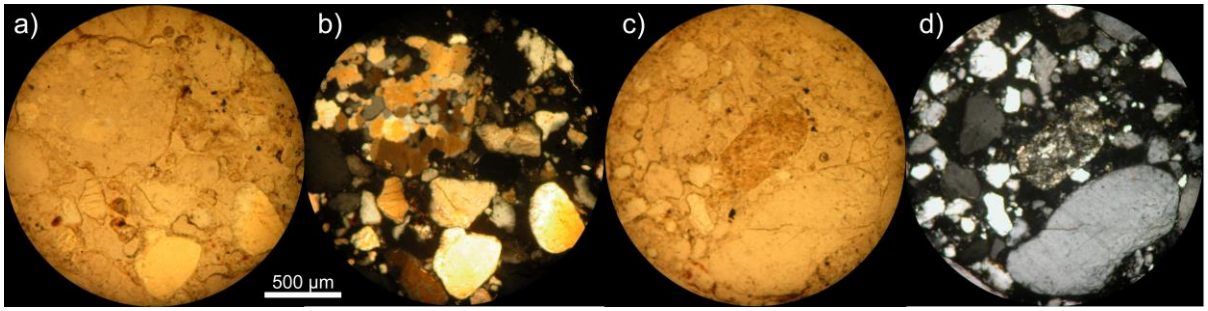

Poorly sorted <50 µm – 1mm. (mostly 200-400 µm), sub-rounded, quartz with moderate to low sphericity. Few thin/worn cutans, some cracked quartz with Fe stains. Some polycrystalline quartz grains. Large rounded grain in top left of a & b has quartzite-like fabric.

TS124

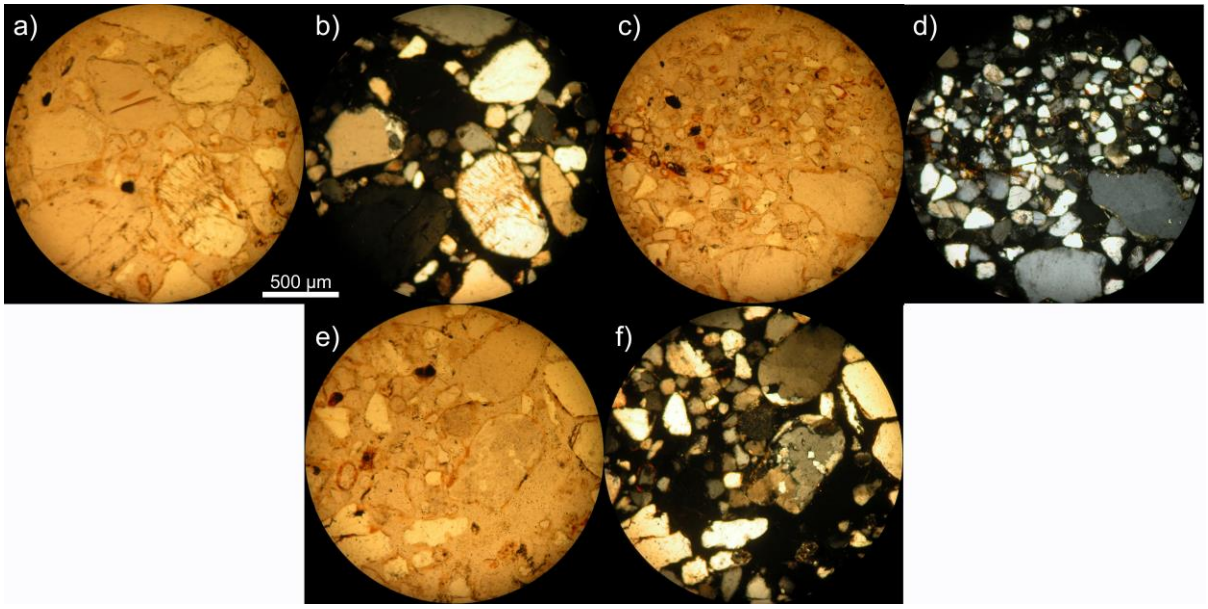

Poorly sorted 50 µm to 1mm. Sub-angular, moderate sphericity. Millimetre laminations of ~100 µm grains. Cutans thick and/or continuous but often partially removed, Some quartz cracked and some is polycrystalline.

Field observations

Laminated.

Summary Description

Stratigraphy

Laminated quartz sands. coarse to fine, with laminations defined by grainsize.

Pedostratigraphy

None

Biostratigraphy

None

Appendix C.2. Sediment descriptions from PR05 at BO07

Unit B

Loose sediments

K2115

Light yellowish-brown (10YR 6/4) medium to fine, moderately sorted, sub-rounded grains with moderate sphericity.

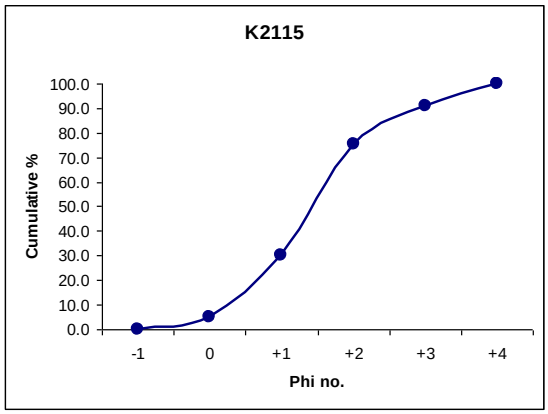

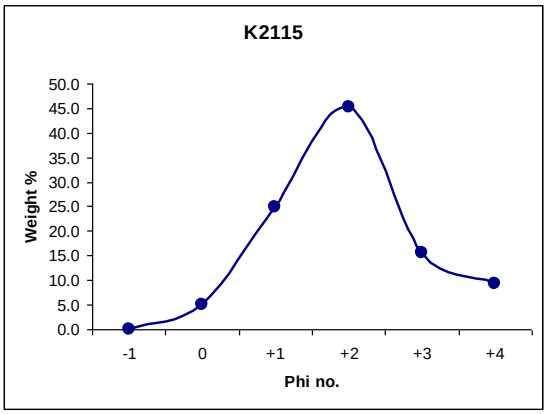

K5116

Light yellowish-brown (10YR 6/4) fine to silt, well sorted, sub-rounded grains with moderate sphericity.

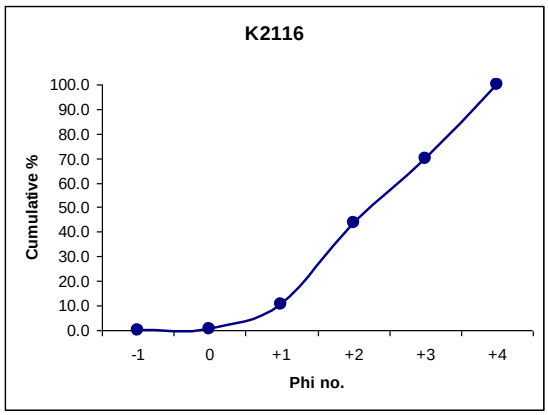

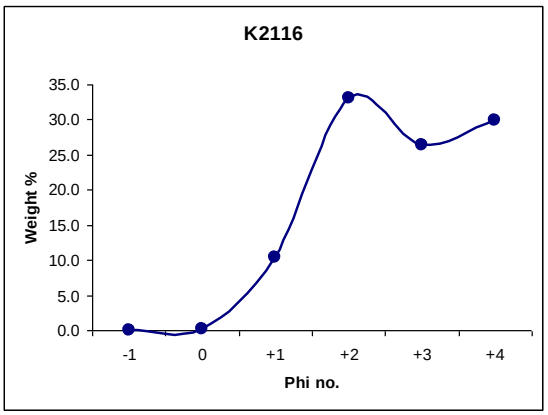

Thin sections

TS133 (near K2115)

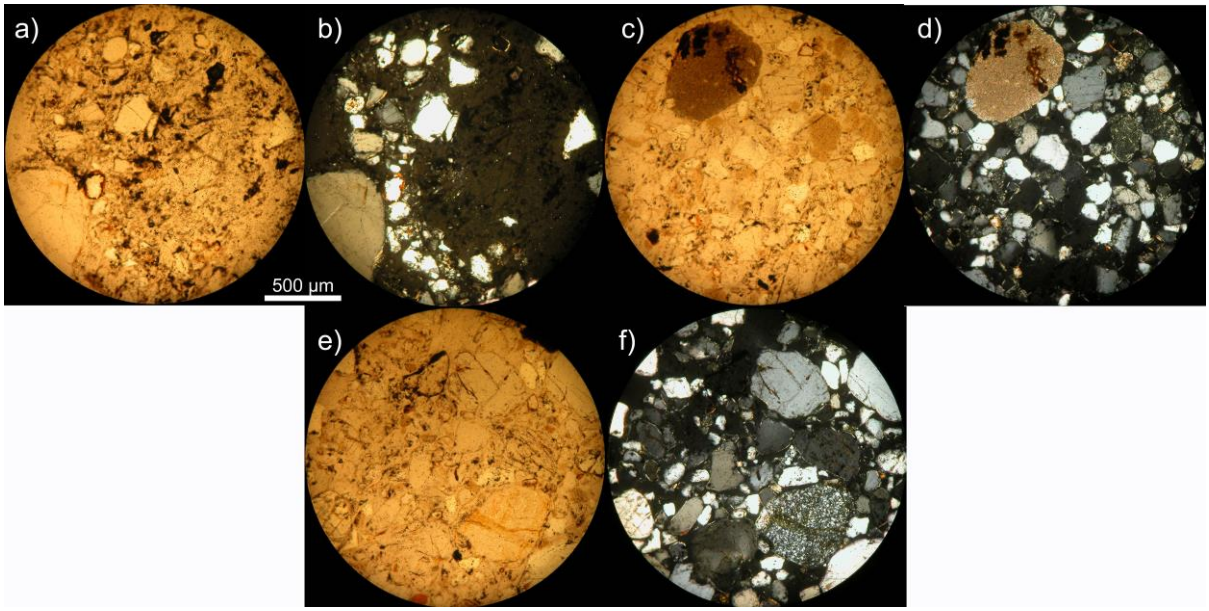

Sub- to well-rounded moderately sorted quartz 100-600µm. Some clay pellets and polycrystalline quartz. Opaque mineral coatings (thick clay?). Very well rounded grain of dense micritic carbonate in c/d. Microbialite, deposited as encrusting bio-induced carbonate in shallow water. Eroded, reworked and transported (well rounded). Minor quartz grains cemented into matrix and dendritic secondary Mn/Fe.

Field observations

Small exposure in centre of blowout

Summary Description

Stratigraphy

Fine grained, moderately sorted sand. Some clay pellets (reworked from above?)

Pedostratigraphy

None

Biostratigraphy

Unionid shell middens

Unit C

Loose sediments

K2114

Clay rich, yellowish brown (10YR 5/4) medium to silt, moderately poorly sorted, sub-rounded grains with moderate sphericity.

Thin sections

TS132 (near K2114)

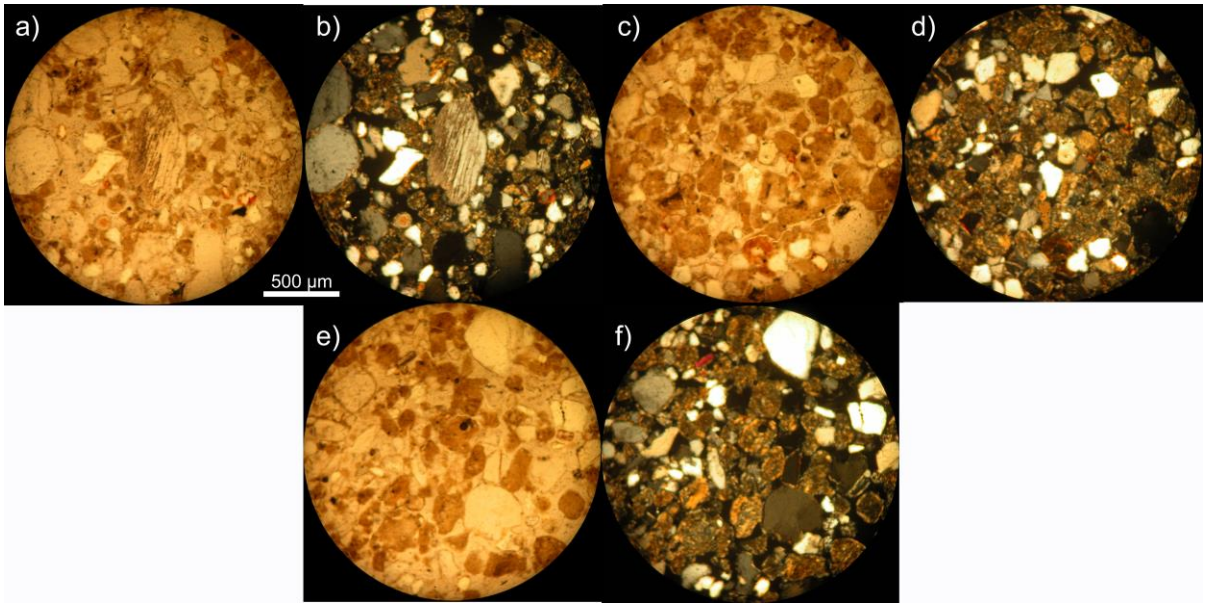

Peletal clay. Lots of rounded (transported) clay pellets with variable extinction patterns, including random flecks (bioturbated lake floor sediment) and strong domains (pedogenic modification? Some clay pellets slightly compacted. Sub-rounded quartz is moderately sorted 80-600 µm, (few >1mm, well rounded) some with Fe cutans and many with clay coatings. Hi relief mineral with laminations (cleavage or twinning) Some quartz with zoned extinction.

Field observations

Greenish-clay

Summary Description

Stratigraphy

Fine grained peletal clay with medium, sub-rounded sand

Pedostratigraphy

None

Biostratigraphy

None

Unit D

Loose sediments

K2111

Strong brown (7.5YR 5/6) medium to very fine, poorly sorted, sub-rounded grains with moderate sphericity.

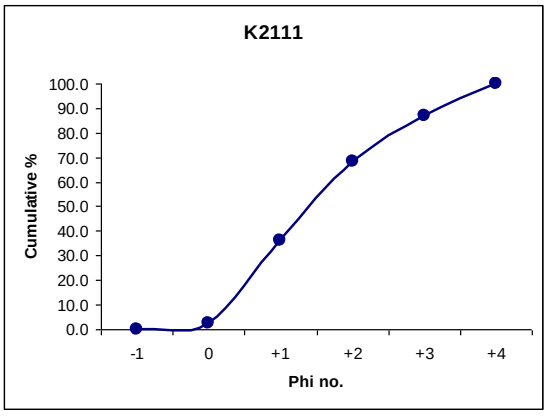

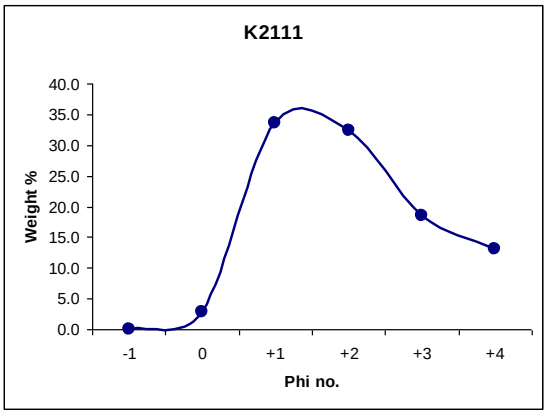

K2112

Light yellowish brown (10YR 6/4) medium to very fine, moderately poorly sorted, sub-rounded grains with moderate sphericity.

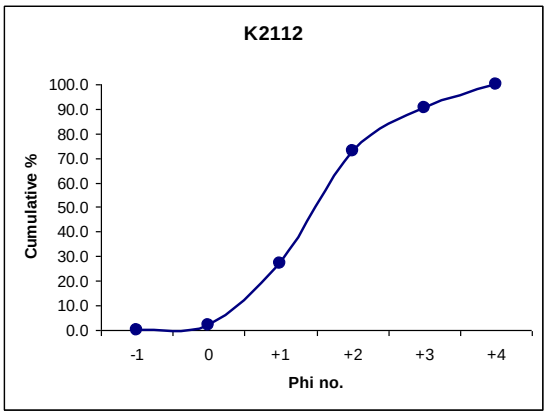

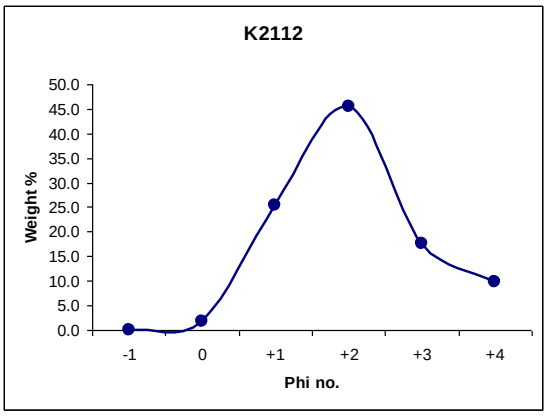

K2113

Light yellowish brown (10YR 6/4) medium to fine, moderately sorted, sub-rounded grains with moderate sphericity.

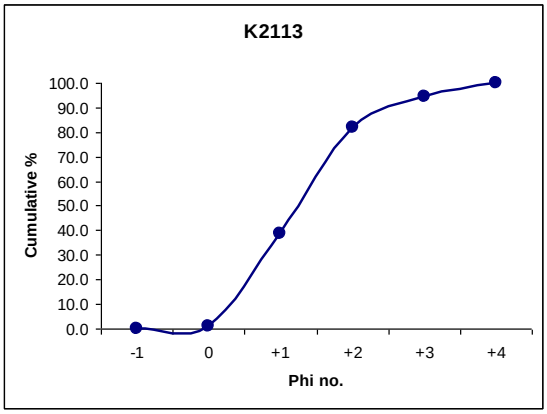

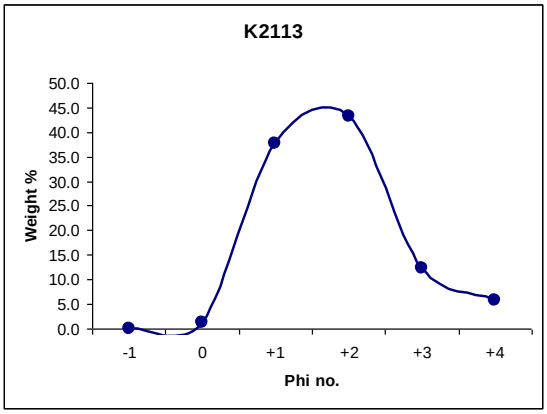

K2117

Light yellowish brown (10YR 6/4) medium to fine, moderately sorted sub-rounded grains with moderate sphericity.

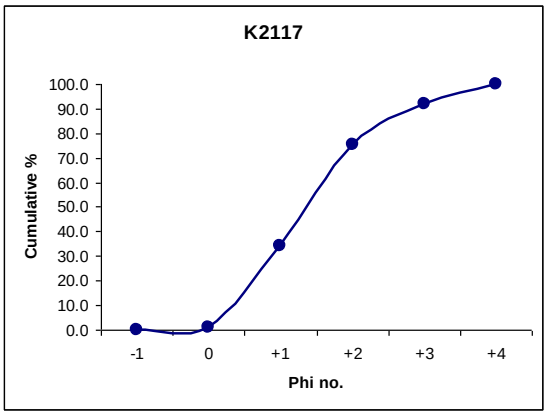

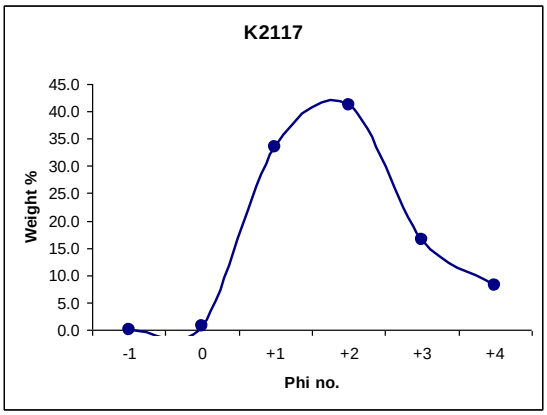

K2118

Light yellowish brown (10YR 6/4) very fine to silt, well sorted, sub-rounded, grains with moderate to high sphericity.

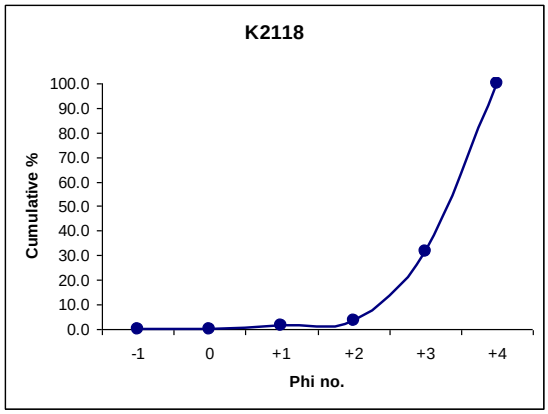

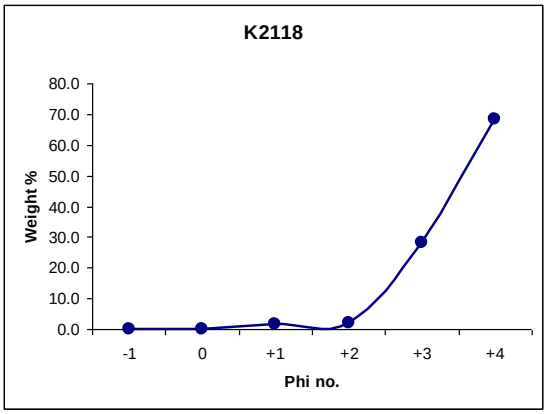

K2119

Light yellowish brown (10YR 6/4) fine to silt, well sorted, sub-rounded grains with low sphericity.

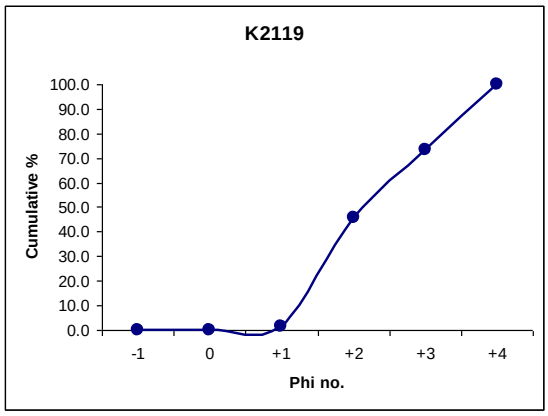

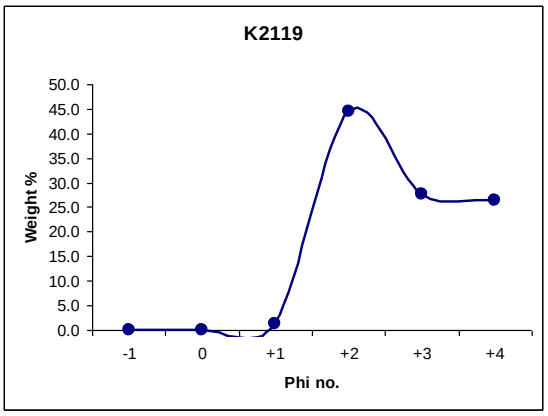

K2121

Reddish yellow (7.5YR 6/6) medium to very fine, moderately sorted, well rounded grains with moderate to high sphericity.

Thin sections

TS130 (near K2111)

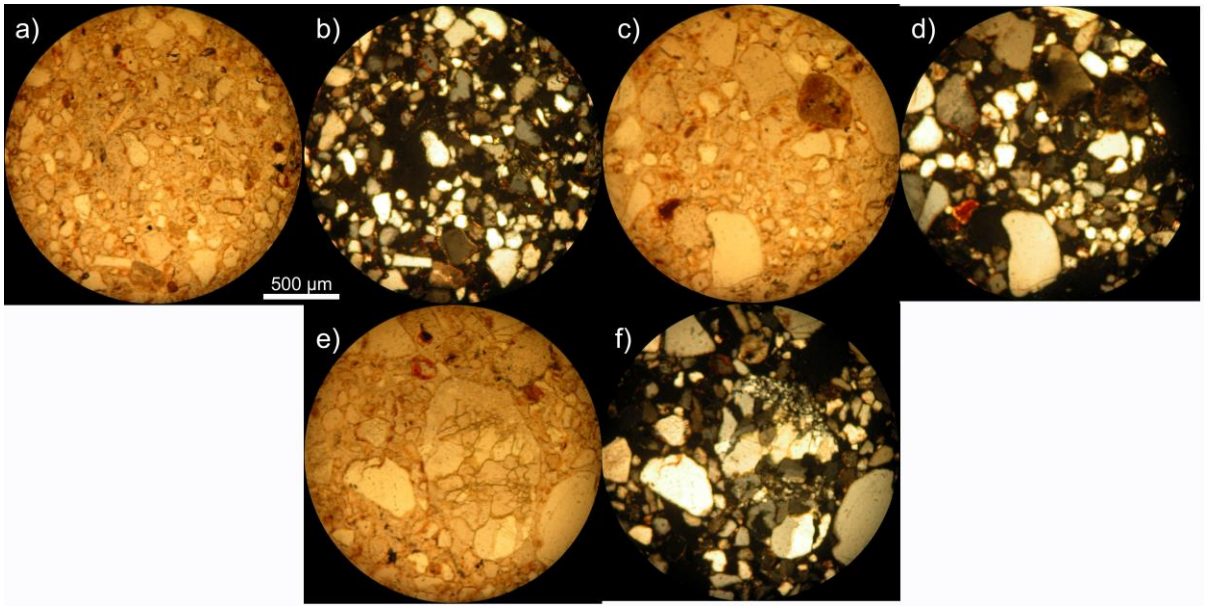

Poorly sorted, sub-rounded coarse to very fine 1mm - <50 µm quartz. Very coarse polycrystalline quartz in e/f. Large variation in thickness, redness and continuity of cutans (possibly *in situ* secondary cutans).

TS131 (near K2113)

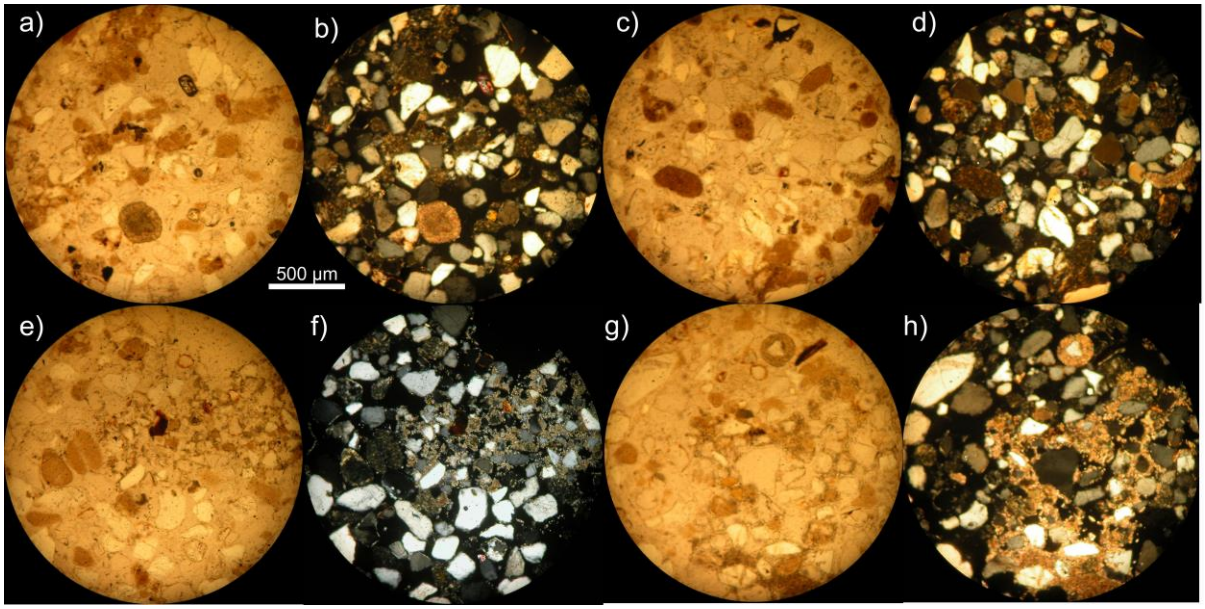

Moderately sorted sub-angular to sub-rounded quartz 100-500 µm. Well rounded clay pellets. Carbonate, some secondary cementation (e-h) (probably soil carbonate zone) plus ooids and shell fragment (beach zone indicators). The primary biogenic carbonate is probably the original source of secondary carbonate.

TS134 (near K2119)

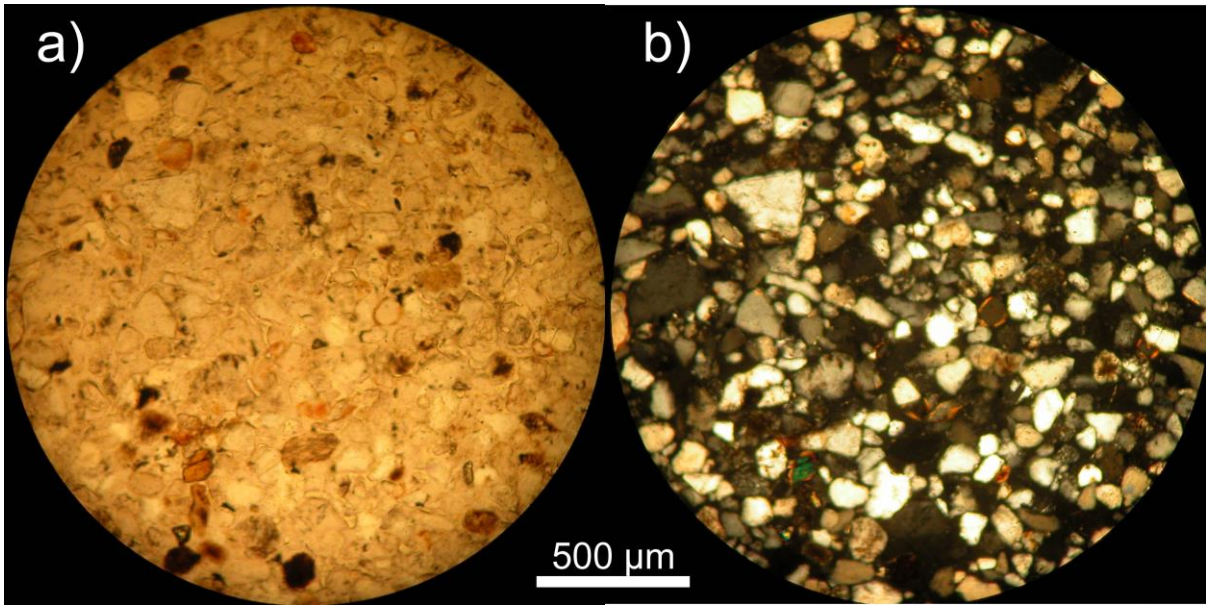

Well sorted fine to silt (<50-250 µm.), sub-angular to sub-rounded quartz with rare well rounded grains. Some cutans

TS136 (near K2121)

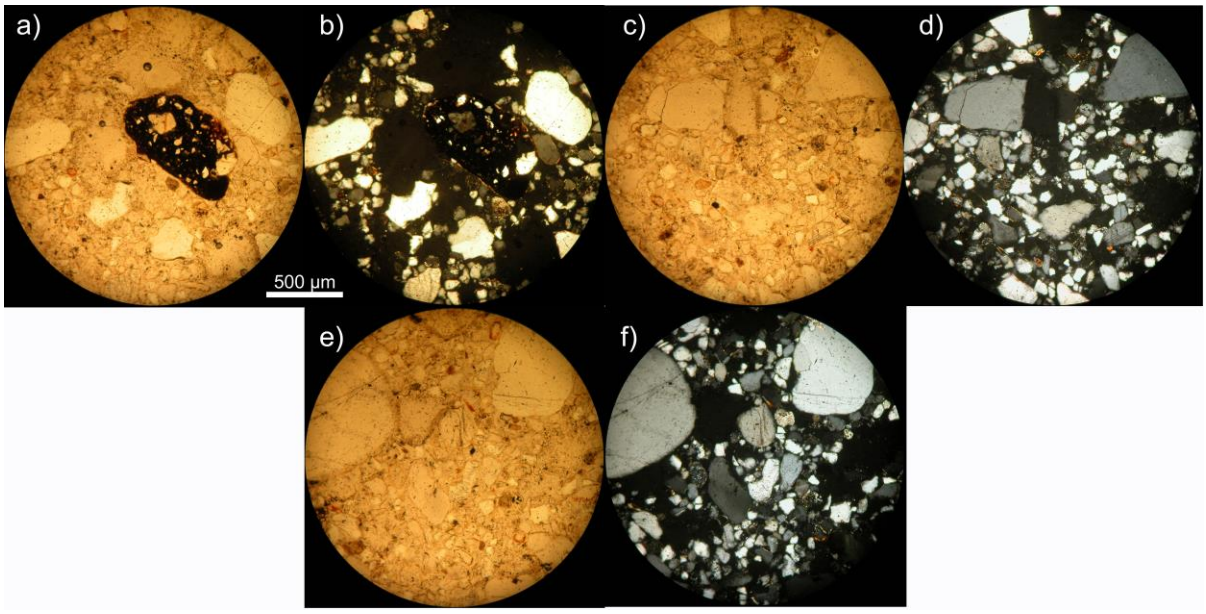

Moderatly sorted, sub-rounded, very fire to coarse (<50 µm – 1mm), high to low sphericity quartz. Bimodal population, 300-500 µm amd 30-50 µm. Few cutans, some polycrystalline quartz. Large opaque phase is iron-oxide cemented quartz sands. Probably originally formed as a dense soil nodule and now resistant enough to be reworked with the quartz sands.

Field observations

Apparent at front and up back of dune. Very fine, silt (blows in puffy clouds) at the front. Paleosol more apparent up the back. White at base, layer of calcrete nodules (forming a bench) then more red toward the top. Also has charcoal and burn marks in the red part near the top.

Summary Description

Stratigraphy

Yellowish-white, medium to silt sized quartz sand. Variation in grain size, though mostly moderately well sorted. Silt area in sheltered area at front of dune

Pedostratigraphy

Thick paleosol marked by calcification and rubification

Biostratigraphy

Unionid shell middens

Unit E

Loose sediments

K2107

Brownish yellow (10YR 6/6) fine to very fine, moderately sorted, sub-rounded grains with moderate sphericity.

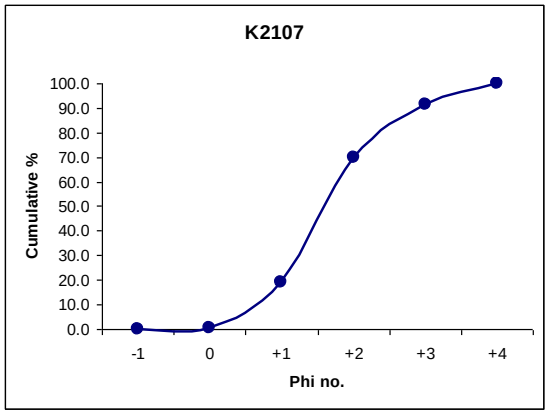

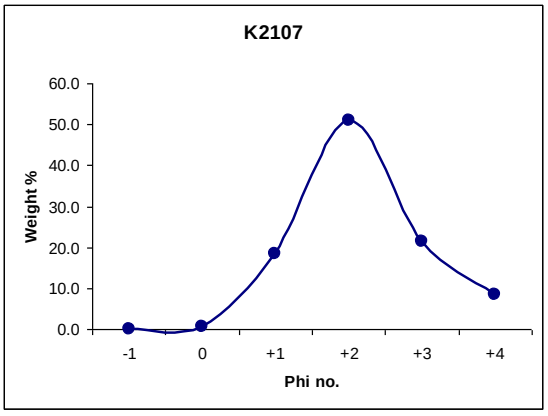

K2108

Yellowish Brown (10YR 5/8) course to very fine, Poorly sorted, well rounded grains with moderate sphericity.

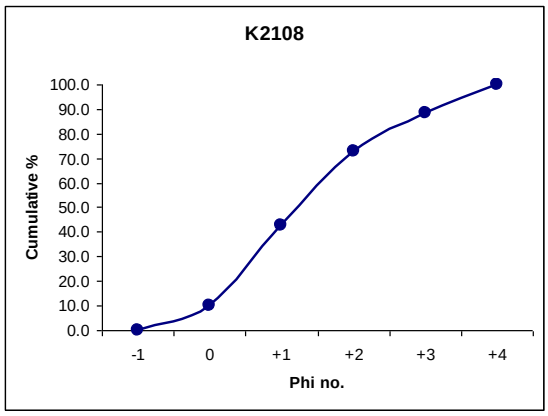

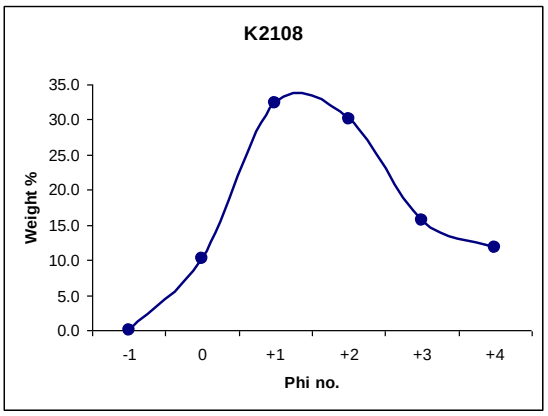

K2109

Reddish yellow (7.5YR 6/6) medium to very fine, poorly sorted, well-rounded grains with moderate sphericity.

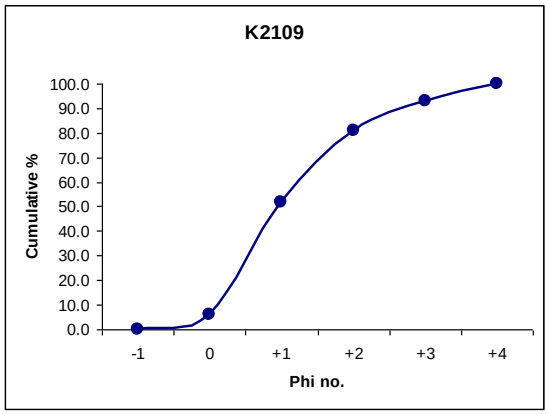

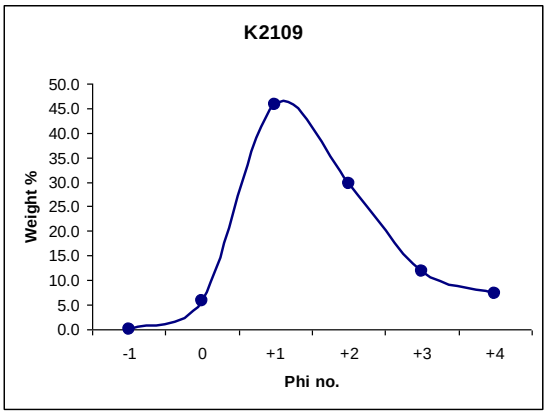

K2110

Reddish yellow (7.5YR 6/6) fine to very fine, well sorted, sub-rounded grains with moderate sphericity.

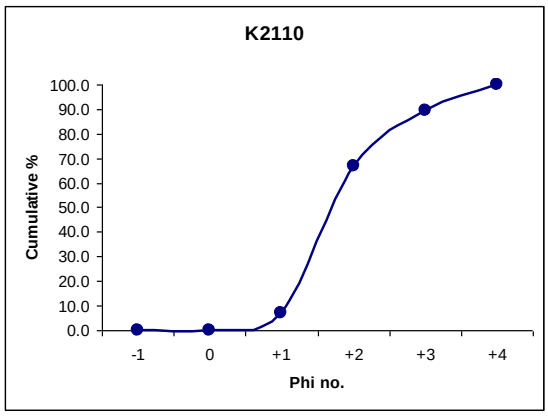

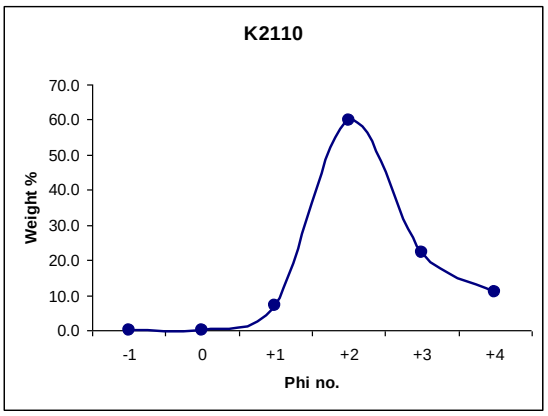

K2120

Light yellowish brown (10YR 6/4) fine to very fine, moderately sorted, sub-rounded grains with moderate sphericity.

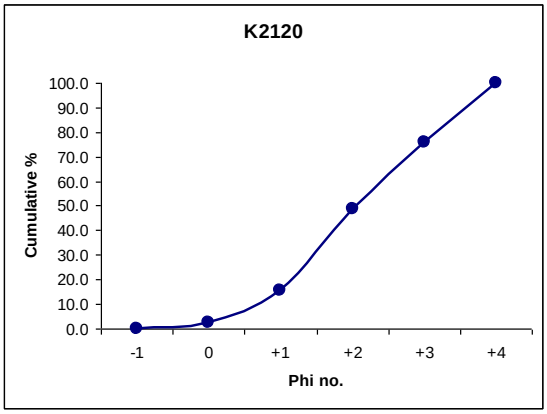

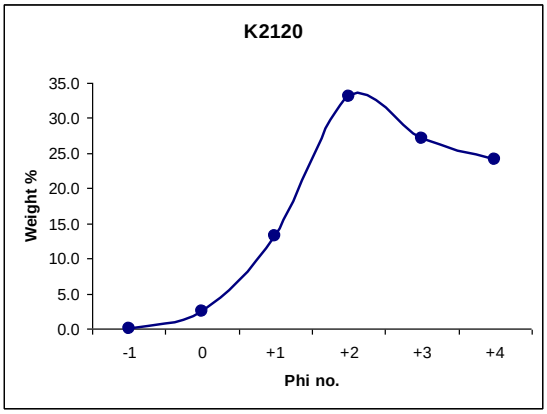

K2122

Light yellowish brown (10YR 6/4) coarse to very fine, very poorly sorted, sub-rounded grains with moderate to low sphericity.

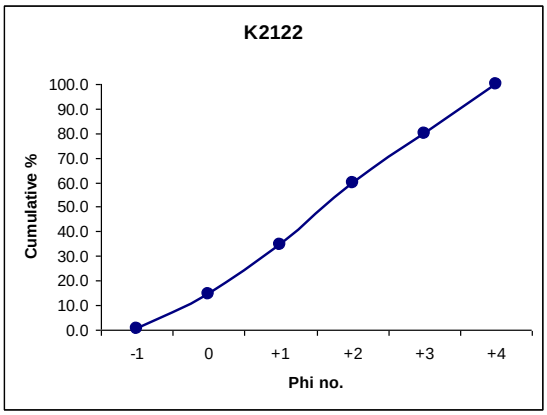

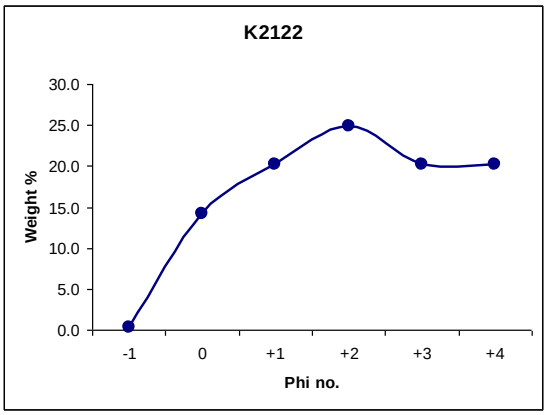

Thin sections

TS129 (near K2110)

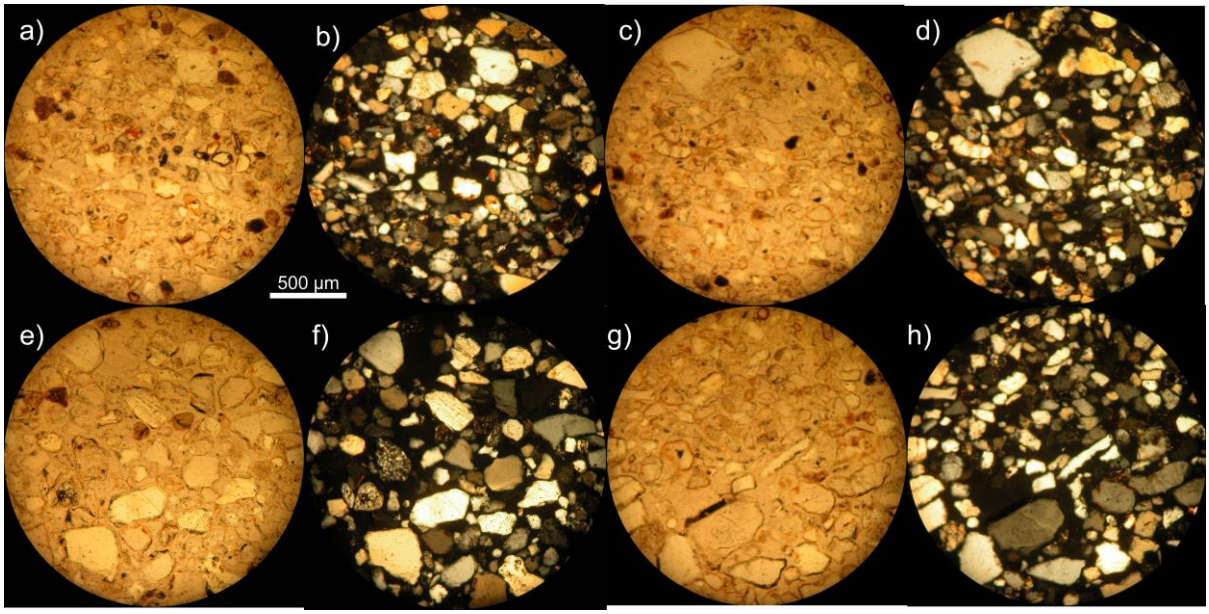

Laminated quartz layers. Fine layers 150-200 µm well sorted sub-angular grains. Coarse layers also include 0.5 – 1mm rounded grains with low sphericity (in addition to the fine component). Some imbrication parallel to bedding of elongate and tubular grains (in g/h) Polycrystalline quartz and possibly feldspar in e/f. Some occasional clay pellets, especially in a/b and e/f. Cutans.

TS135 (near K2120)

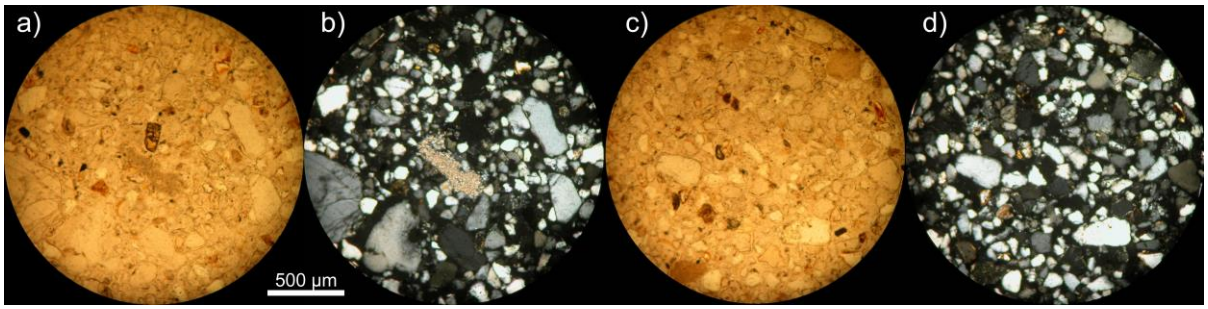

Moderately sorted, sub- to well-rounded, moderate to low sphericity quartz. Mostly ~200 µm, some <50-80 µm very few >1mm. Some carbonates plus few clay pellets. Also some thick ferri-argillans. Some fine grains may be wurstenquartz (top of a/b). Larger grains probably reworked out of a red soil.

TS137 (near K2122)

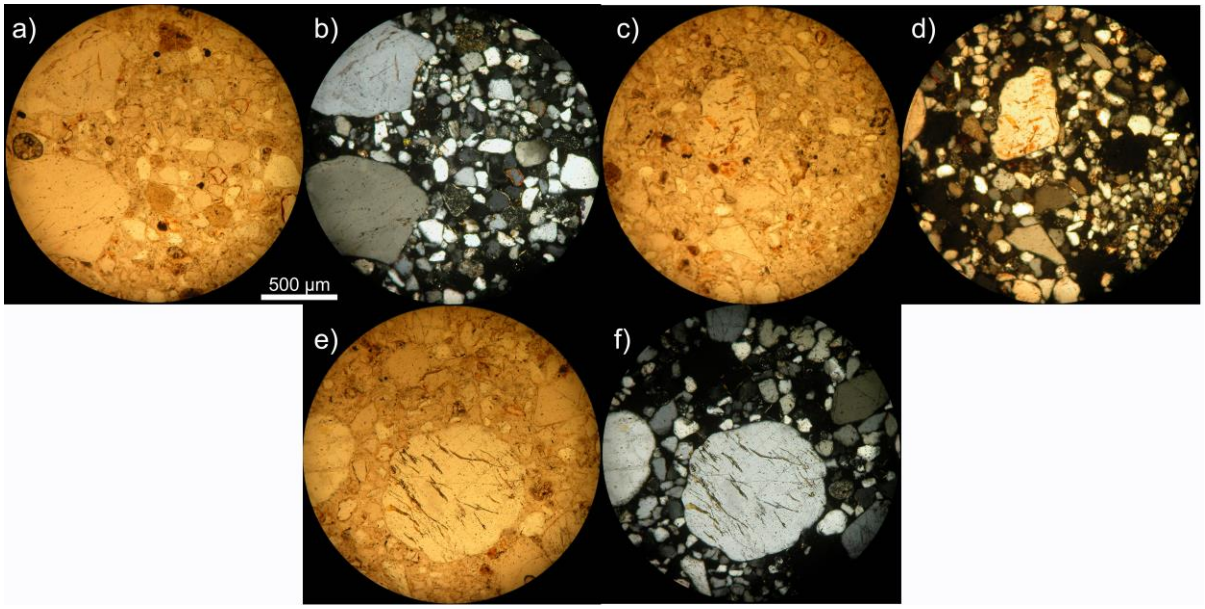

Very poorly sorted, <50 µm – 2 mm, sub-rounded, high sphericity. Some cutans and clay pellets. Fractured quartz. Biomodal texture. Some grains with ferri-argillans inherited from a red soil, thick coating in grain embayments but minimal or no coating on points. Some clay pellets also have inherited cutans, indicating reworking from a minimal soil zone: enough pedogenosis to generate cutans but not enough to break-down clay pellets.

TS149 (near K2127, 'beach edge' near PR05)

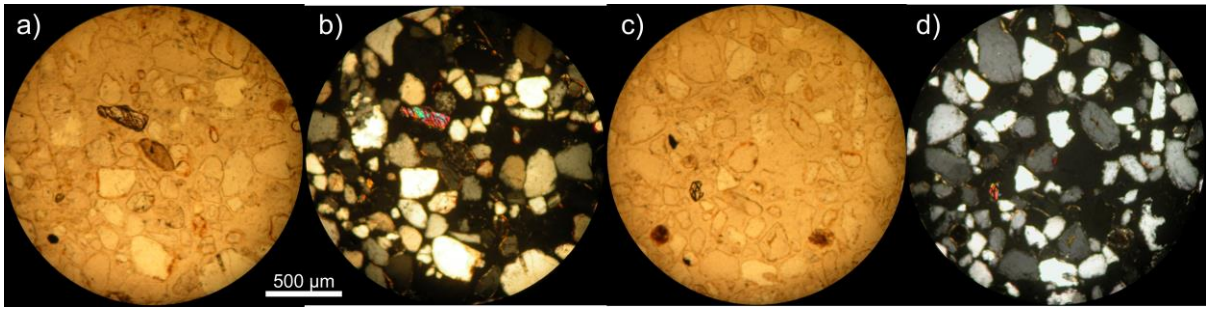

Medium to fine, 100-500 µm, sub-angular to sub-rounded well sorted quartz. Many with warn cutans some polycrystalline quartz and some dense clay pellets with cutans. A high bi-refringence, high relief phase.

Field observations

Thick, poorly consolidated sand mostly at rear, also a small amount at front of little foredune. Front to rear is connected along a ridge at eastern side of blowout, unconformably overlying all other units

Summary Description

Stratigraphy

Mostly poorly sorted, sometimes laminated, sometimes massive, quartz sand. Some clay pellets reworked from other units.

Pedostratigraphy

None

Biostratigraphy

None

Appendix C.3. Sediment descriptions from PR04 at MSE03

Unit A

Loose sediments

K2089

Clay-rich, reddish yellow (7.5YR 7/6), very fine to silt, poorly sorted, sub-rounded grains with moderate sphericity.

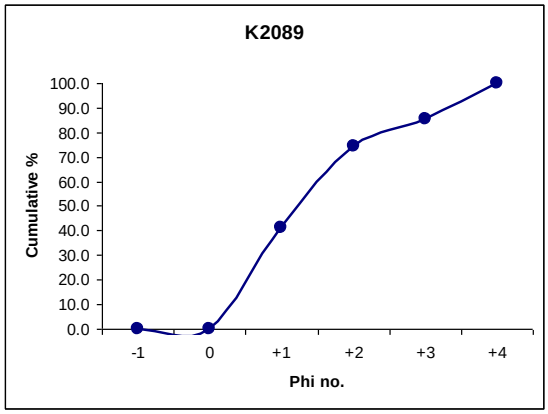

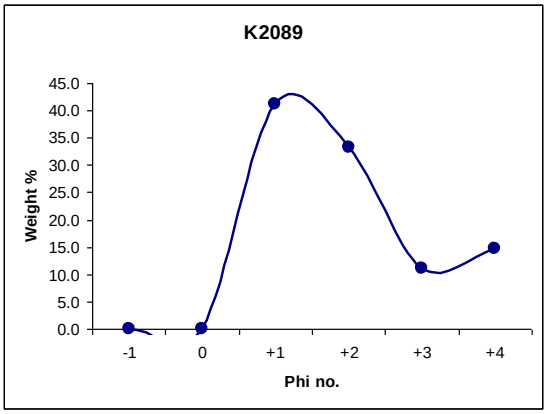

K2090

Clay and carbonate rich, strong brown (7.5YR 5/8), fine to silt, poorly sorted, sub-rounded grains with moderate sphericity.

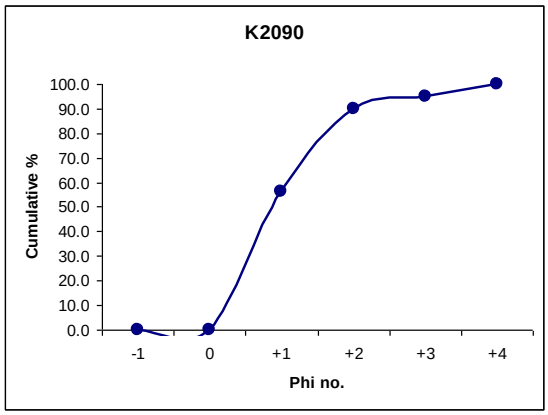

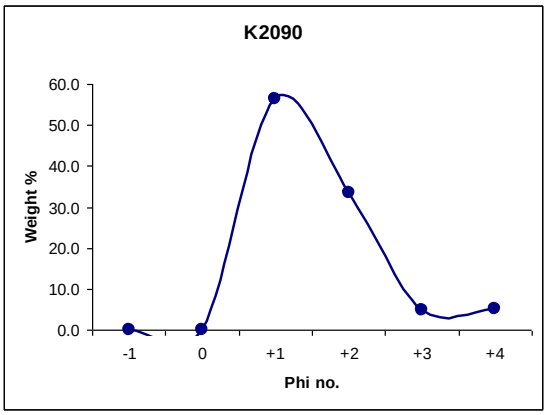

Thin sections

TS142 (between K2089 and K2090)

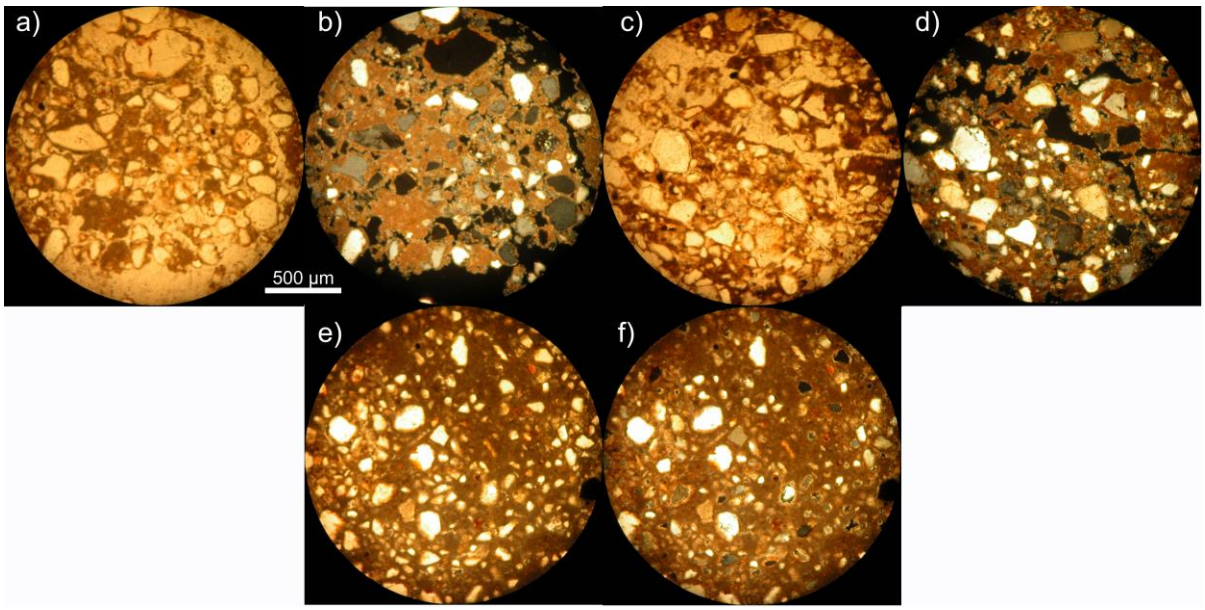

Clay and carbonate rich. Very dense matrix of clay impregnated with secondary carbonates. Disaggregated clay pellets that show up clearly in plane light and as cores in the carbonate rich matrix in crossed polarisers. Very poorly sorted medium to silt sized, sub-angular to sub-rounded quartz. Some polycrystalline quartz. Well cemented soil secondary carbonate zone.

Field observations

Reddish clayey-sand. Calcrete nodules. Very thick paleosol.

Summary Description

Stratigraphy

Sandy peletal clay. Very poorly sorted, sub-rounded, medium to silt sized grains with fine to medium sized clay pellets.

Pedostratigraphy

Thick paleosol present as calcification and rubification. Carbonate forms a matrix in some area and nodules in others.

Biostratigraphy

None

Unit B

Loose sediments

K2091

Strong Brown (7.5YR 5/6), fine, well sorted, sub-rounded grains with moderate sphericity.

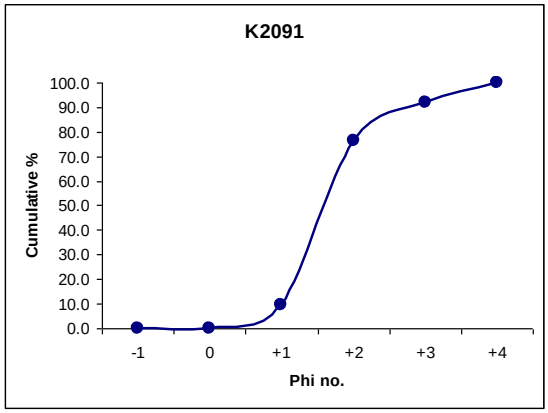

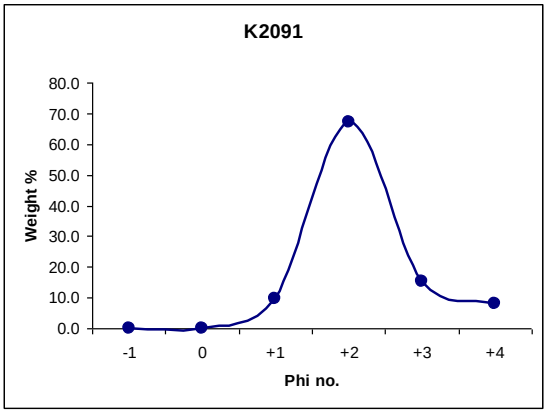

K2092

Reddish yellow (7.5YR 5/4), fine, well sorted, sub-rounded grains with moderate sphericity.

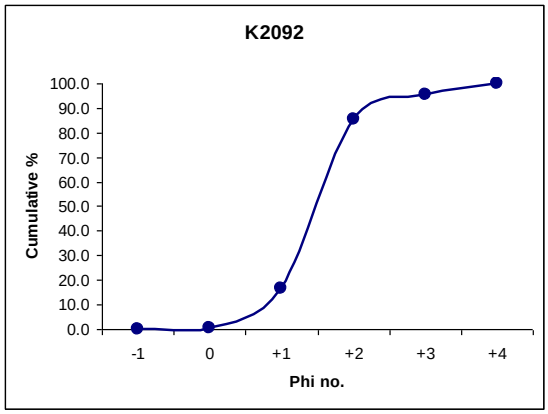

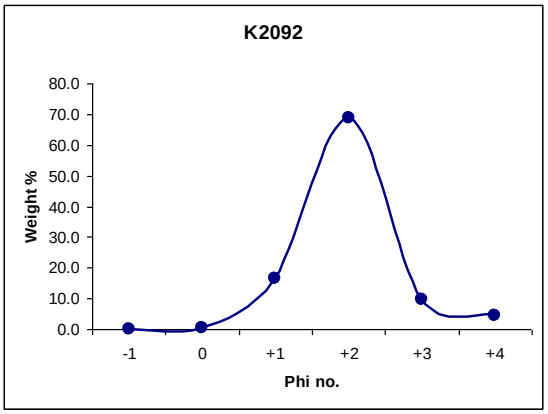

K2094

Yellow (10YR 5/4), medium, moderately well sorted, sub-rounded grains with moderate sphericity.

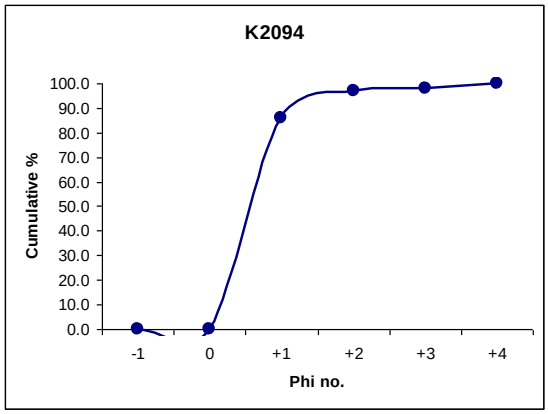

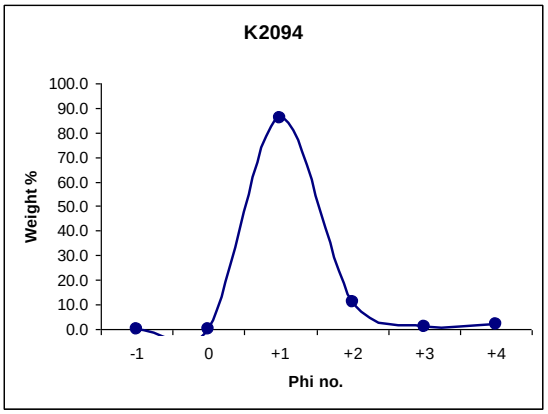

Thin sections

TS141 (between K2091 and K2092)

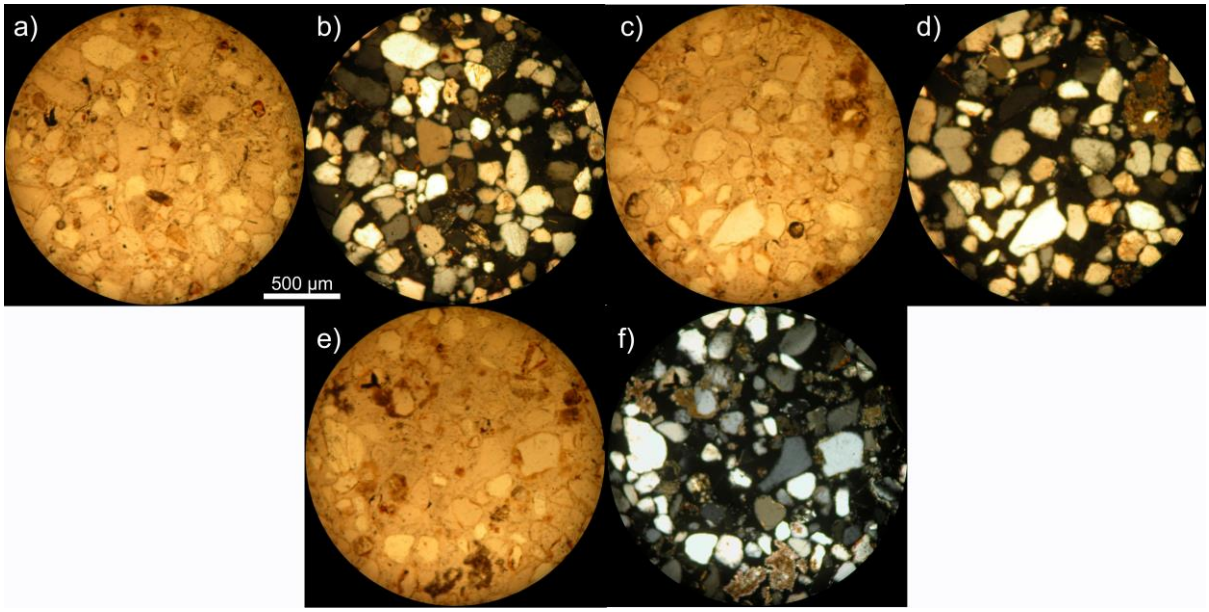

Moderately well sorted sub-rounded quartz, fine grained (mostly ~200 µm). Some polycrystalline quartz. Thick cutans on some grains, warn on others. Some carbonate nodules of dense secondary carbonate. Also a large soil nodule in upper right of c/d with reddish clay matrix containing quartz with Fe/Mn dendritic nodules.

TS139 (near K2094)

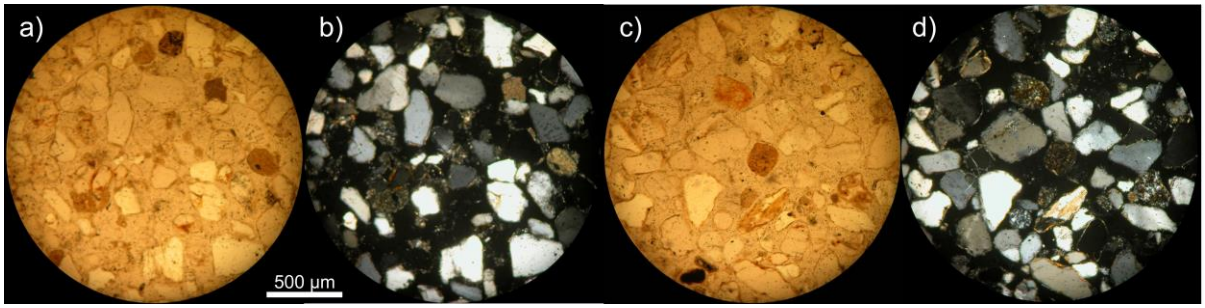

Medium grained (~300 μm) well-sorted sub-rounded quartz with thin cutans. Some rounded clay pellets.

Field observations

Orangey-sand with shell middens. At very base of unit (directly overlying unit A unconformity). Quite thick with greater degree of rubification nearer the top.

Summary Description

Stratigraphy

Well sorted sand. More coarse toward the top of the unit.

Pedostratigraphy

Evidence of paleosol through rubification. Partly removed through erosion.

Biostratigraphy

Unionid shell middens at base of unit.

Unit C

Loose sediments

K2093

Clay rich, yellowish brown (10YR 5/4), medium to fine, moderately poorly sorted, sub-rounded grains with moderate sphericity.

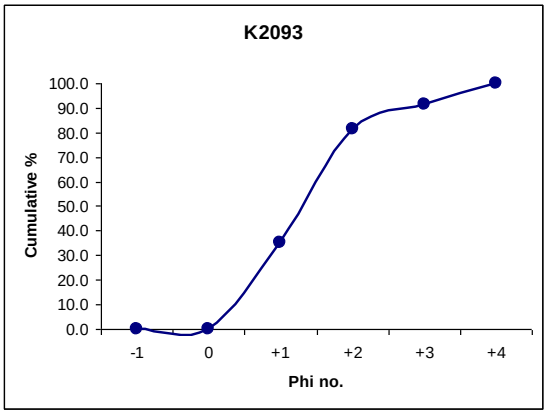

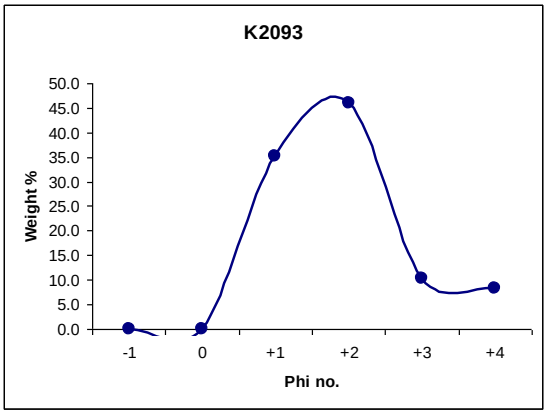

Thin sections

TS140 (near K2093)

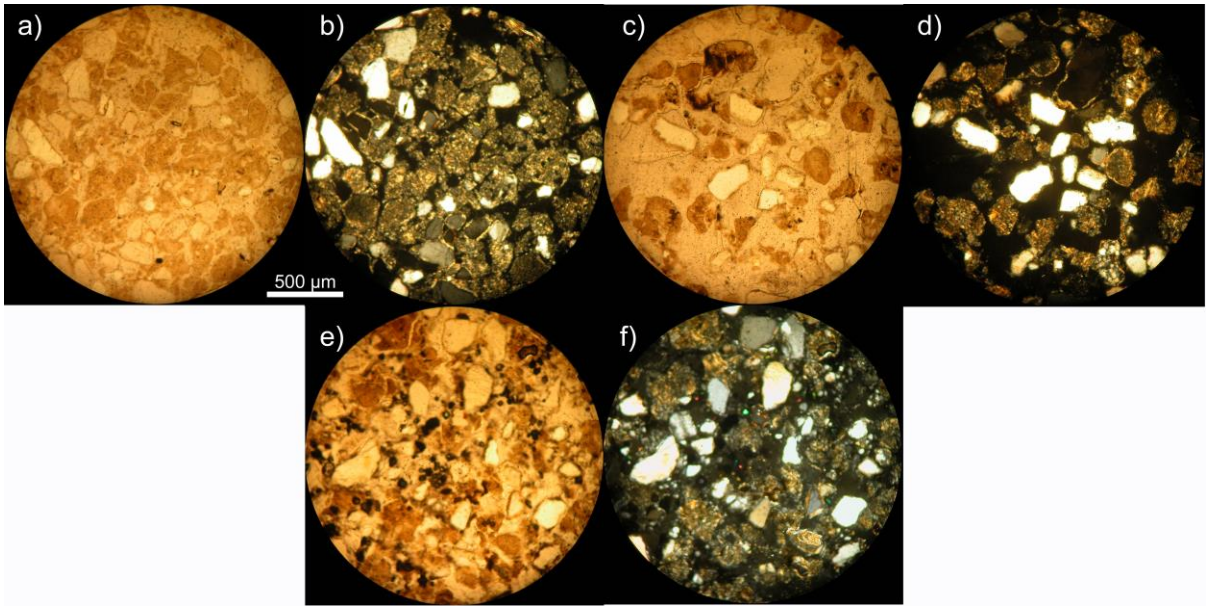

Clay pellets ~150 – 250 µm, many irregular and ragged, probably indicating minimal transport. Some have cutans and some don't. Quartz also medium to fine, sub-angular to sub-rounded with cutans. One area with many grains of very fine, high relief high birefringence, opaque phase (probably heavy minerals).

Field observations

Greenish-clay. Washing out to cover lower units. Contains gypsum rosettes. Heavily eroded away (only apparent at front of dune)

Summary Description

1.1.1.1.1. Stratigraphy

Medium to fine grained clay pellets with 15-20% medium to fine sand. Clumps of heavy minerals (possibly zircon) plus gypsum rosettes.

1.1.1.1.2. Pedostratigraphy

None

1.1.1.1.3. Biostratigraphy

None

Unit E

Loose sediments

K2095

Light yellowish brown (10YR 6/4) medium to fine, moderately well sorted, sub-rounded grains with moderate sphericity.

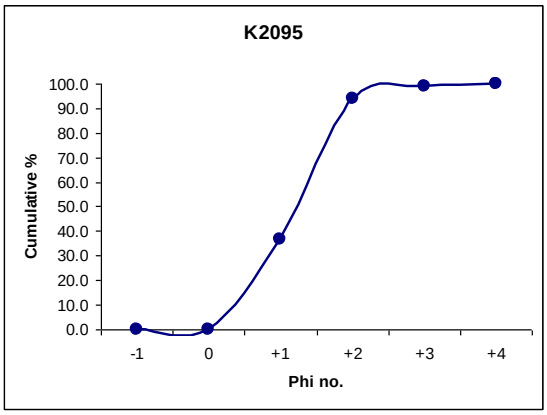

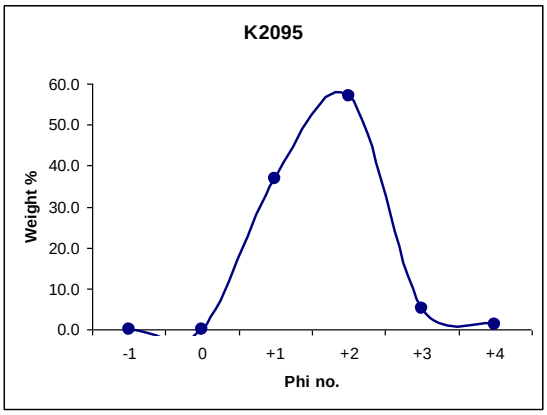

K2096

Light yellowish brown (10YR 6/4) medium to fine, well sorted, sub-rounded grains with moderate sphericity.

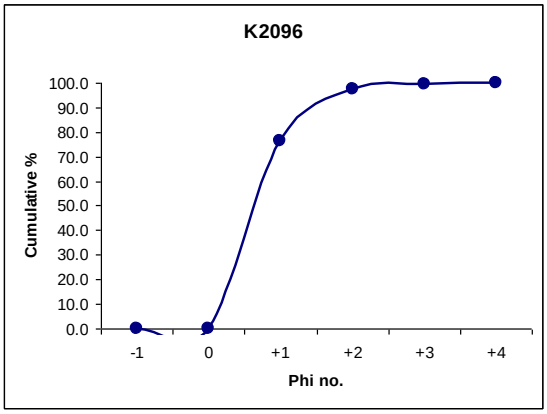

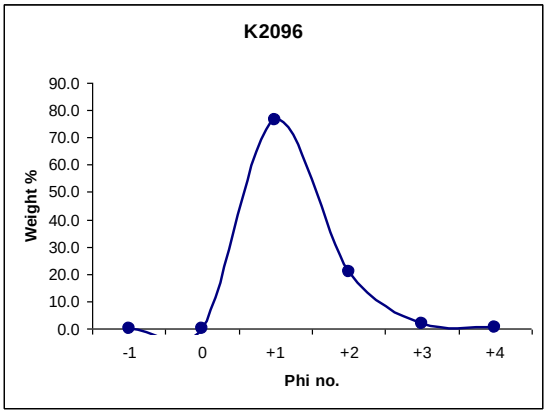

Thin sections

TS138 (between K2095 and K2096)

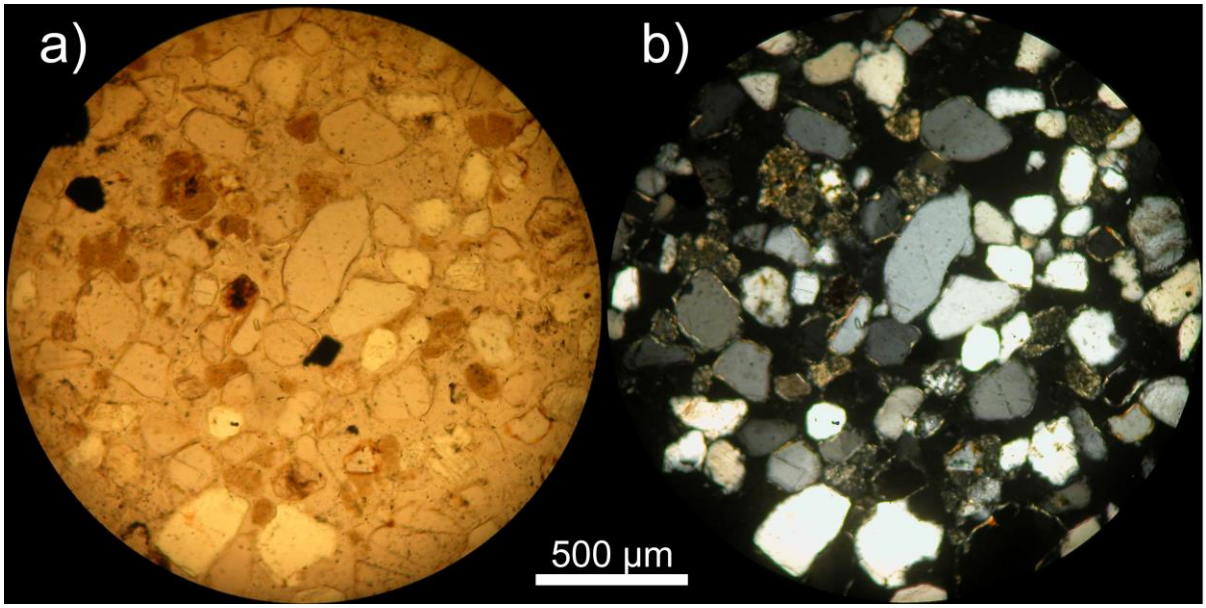

Fine to medium grained 150-300 µm, moderately well sorted, rounded quartz. Few clay pellets. Minimal cutans on some grains but absent on others and none on clay pellets.

Field observations

Lightly laminated by grainsize. Apparent contact within unit (slight but abrupt colour change). Eroding away, only apparent at rear of dune.

Summary Description

Stratigraphy

Laminated, medium to fine grained, poorly consolidated sands, also including re-worked clay pellets.

Pedostratigraphy

None

Biostratigraphy

None

Appendix C.4. Sediment descriptions from PR01 at BO29

Unit A

Loose sediments:

k2079

Clay rich, carbonate rich, Reddish Yellow (7.5YR 6/8), poorly sorted medium to silt sized, sub-angular grains with moderate to low sphericity.

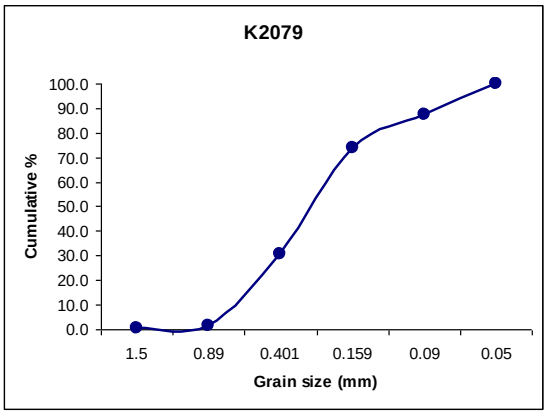

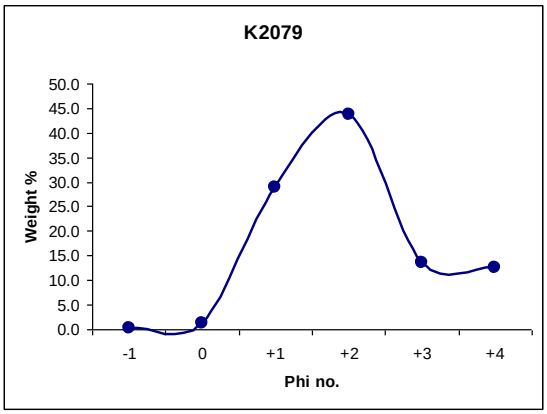

k2080

Clay rich, carbonate rich, Strong brown (7.5YR 4/6), poorly sorted medium to silt sized sub-rounded grains with moderate sphericity.

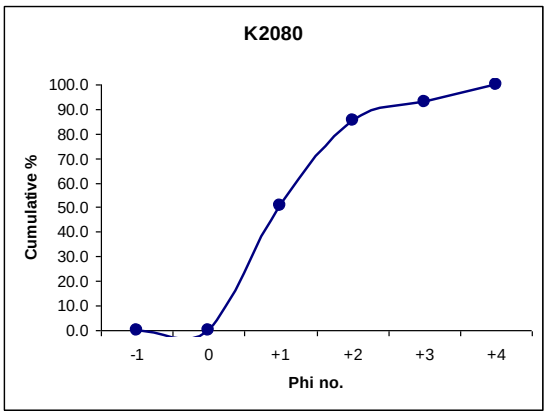

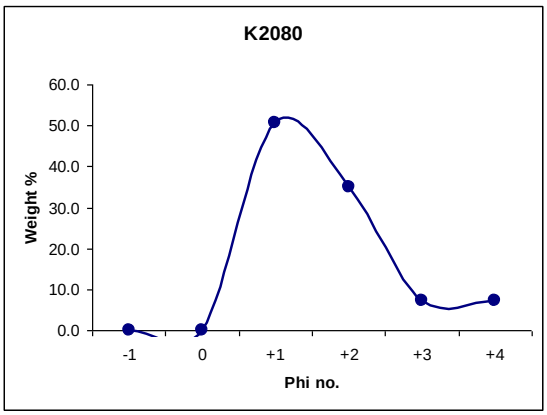

Thin sections

TS143 (near k2079)

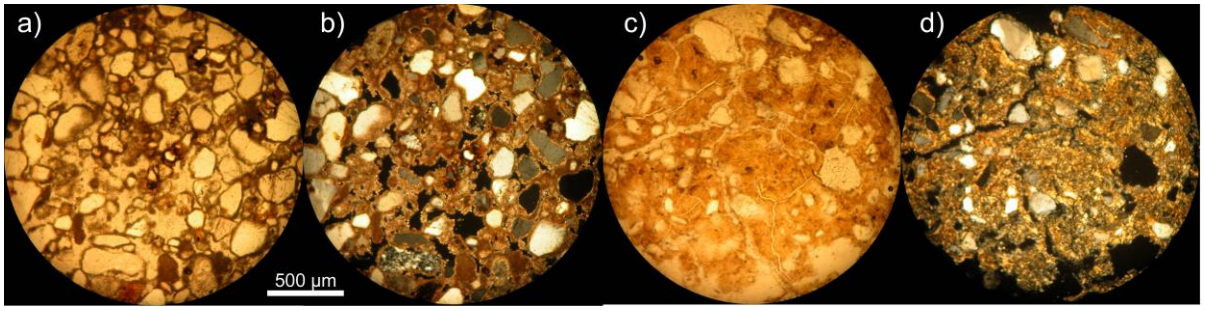

Quartz is poorly sorted (1 mm to < 50 µm, mostly > 200 µm), sub-angular with low sphericity. Few 80-250 µm clay pellets. A lot of secondary carbonate coating grains (including clay pellets) plus filling voids and impregnating the clay matrix (likely derived from dissagreagated pellets).

TS144 (near k2080)

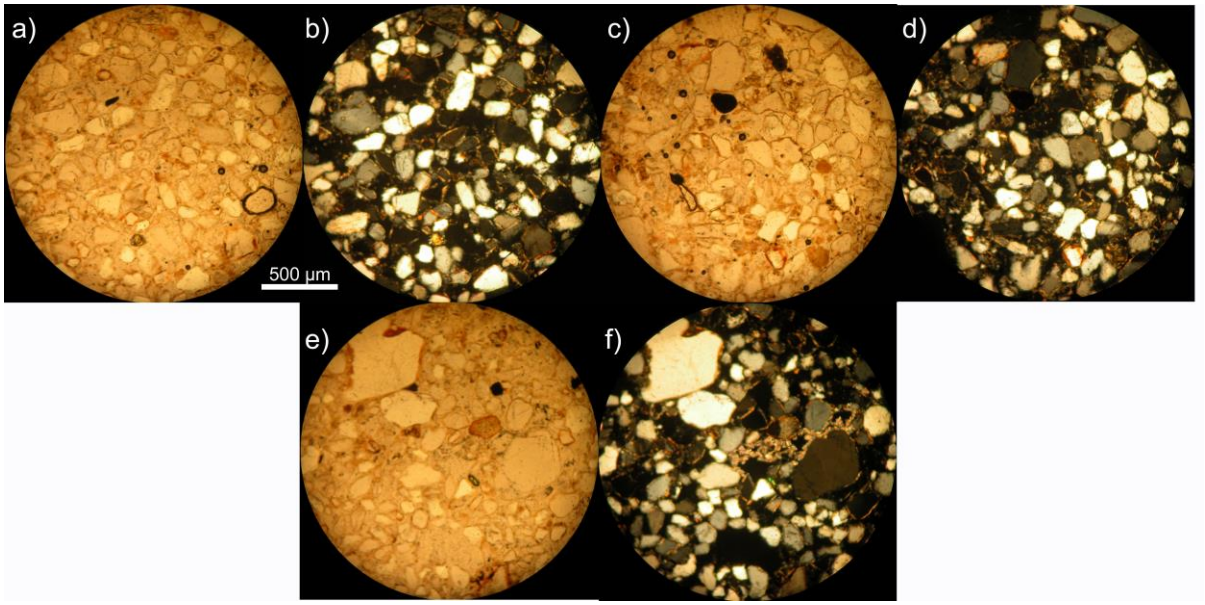

Quartz is poorly sorted (1 mm to < 50 µm, mostly > 200 µm), sub-rounded with moderate sphericity. Many with cutans, partly worn, irregular with a tendency to be thicker in embayments- indicating inheritance. Almost universal presence of cutans, suggests some *in situ* cutan formation. Few 80-250 µm clay pellets. Fine grained secondary carbonate matrix is in situ. Dark coating on grain in lower right of a/b may be micritic carbonate from shallow water zone.

Field observations

Reddish clayey sand. Calcrete benches, calcrete nodules. Gypsum rosettes present. Very thick paleosol.

Summary Description

Stratigraphy

Sandy peletal clays. Poorly sorted, medium to fine. More rounded and spherical and less carbonate matrix toward top of unit.

Pedostratigraphy

High levels of calcification and some cutan development.

Biostratigraphy

None

Unit B

Loose sediments:

K2081

Strong Brown (7.5YR 5/6), fine, well sorted, sub-rounded grains with low sphericity.

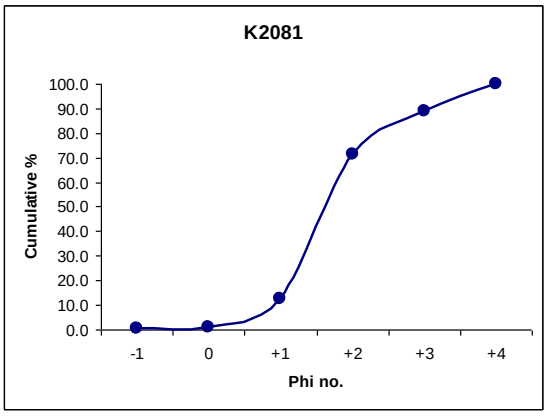

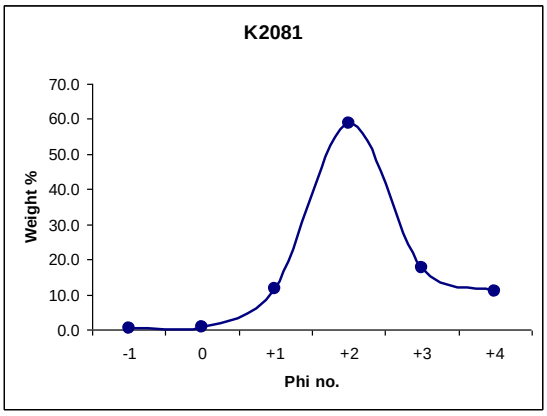

Unit D

Loose sediments:

K2082

Strong Brown (7.5YR 5/8), fine, well sorted, sub-rounded grains with moderate sphericity.

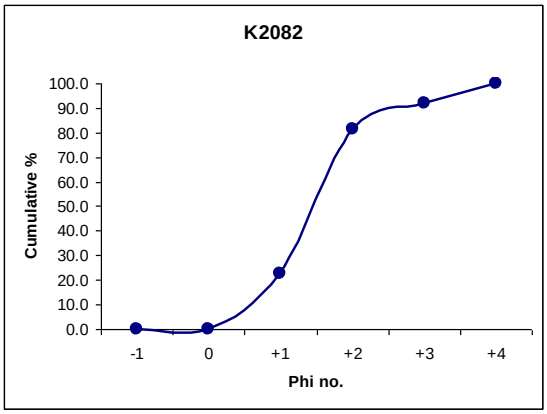

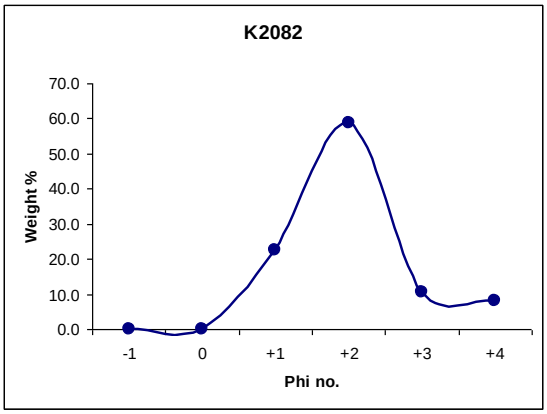

K2084

Strong Brown (7.5YR 5/8), medium to fine, moderately well sorted, sub-rounded grains with moderate sphericity.

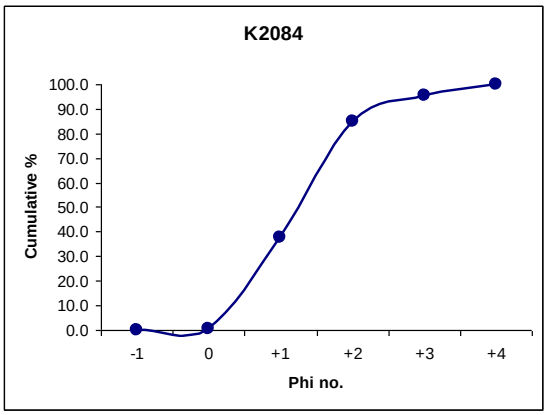

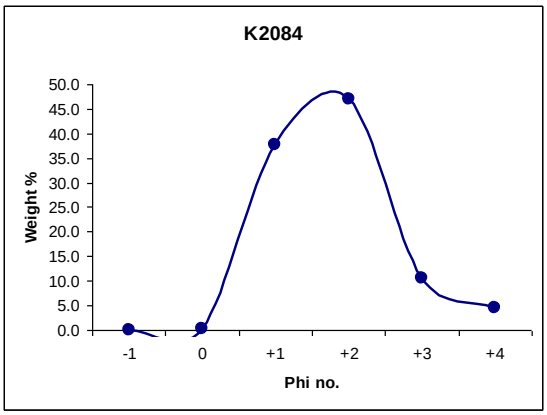

K2085

Clay rich, strong Brown (7.5YR 4/6), medium to very fine, moderately well sorted, sub-rounded grains with moderate sphericity.

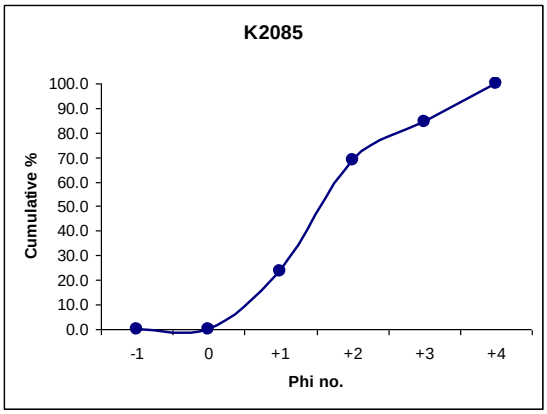

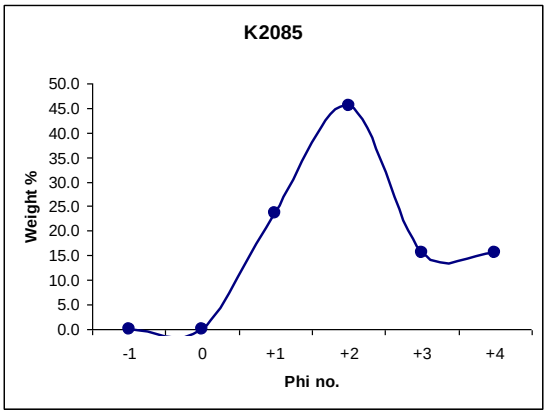

Thin sections

TS145 (near k2084)

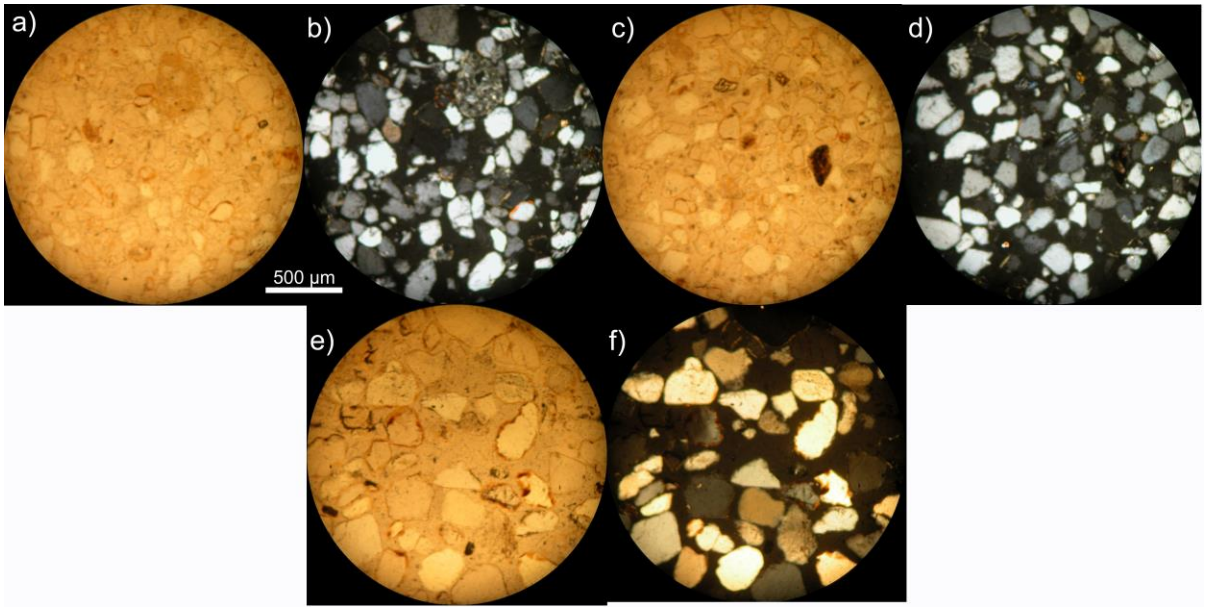

Very fine to medium 80-300µm sub-angular to sub-rounded, moderately well sorted quartz with moderate sphericity. Worn cutans on many grains. Reworked grains of carbonate impregnated clay soil. Some feldspars. High birefringence, high relief phase present in small amounts.

TS146 (near K2085)

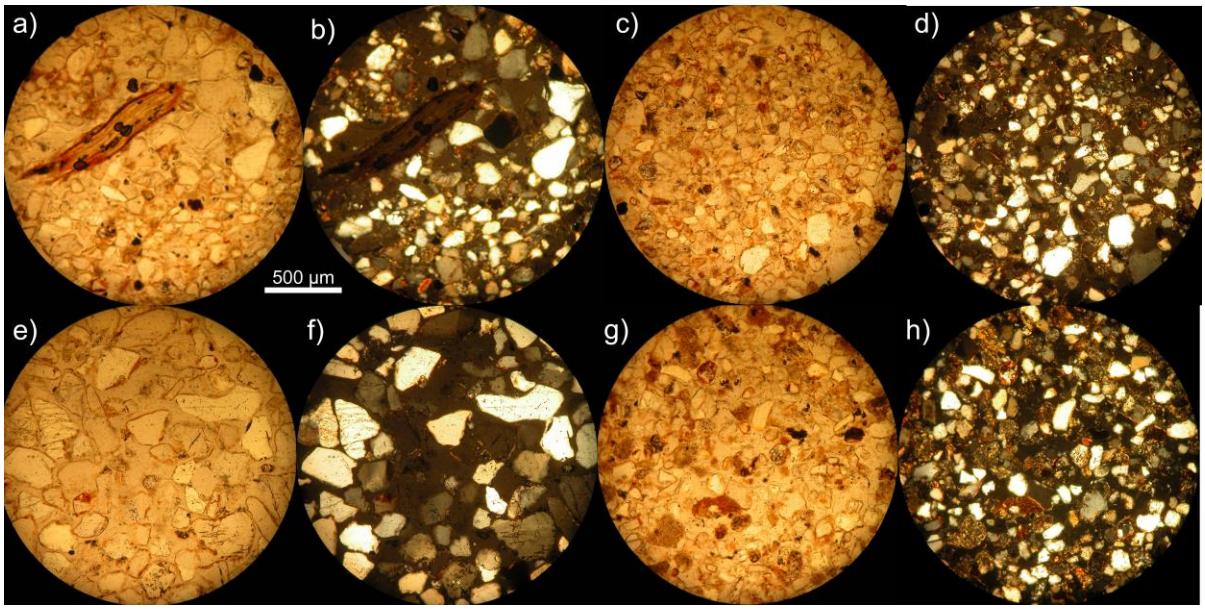

Very fine to silt, 50-200 μm, sub-angular to sub-rounded, well sorted quartz.. Wood/root in a/b. Slide includes clay rich region at top (clay pellets and very thick *in situ* cutans), medium, well sorted sand with worn cutans at bottom (similar to TS 145).

TS150 (near K2128, 'beach edge' near PR01)

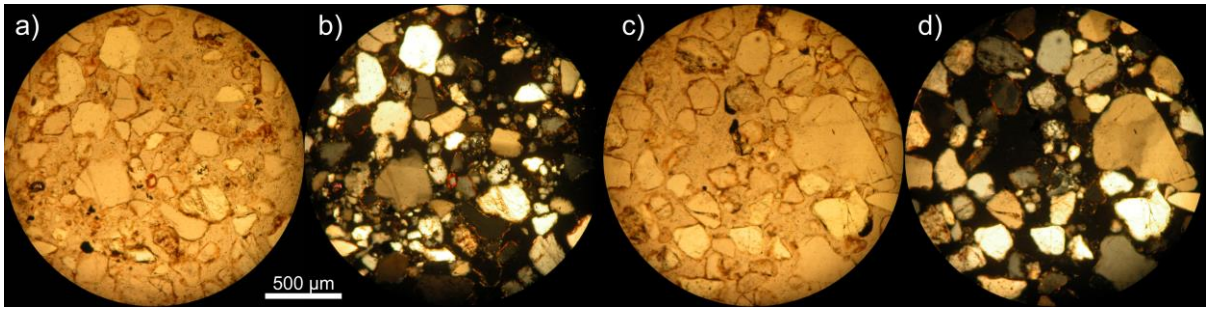

Mostly medium to fine, (some coarse grains) 600-150 μm, moderately to poorly sorted, sub-rounded to sub-angular quartz. Some with inherited cutans. Some polycrystalline quartz.

Field observations

Lots of carbonate rhizomorphs, some chalky. Middens with Unionid shells and Macquarie Perch otoliths. Charcoal and burnt stumps (burnt goat skull nearby). Clay layer marking top of unit can be easily traced around the edges of blow-outs.

Summary Description

Stratigraphy

Medium to fine poorly consolidated quartz sands

Pedostratigraphy

Thick (~10cm) clay overlaying highly rubified region. Lots of calcretions lower down.

Biostratigraphy

Carbonate rhizomorphs. Shell middens (with otoliths).

Unit E

Loose sediments

K2083

Reddish yellow (7.5YR 6/6), fine, well sorted, sub-rounded grains with moderate sphericity.

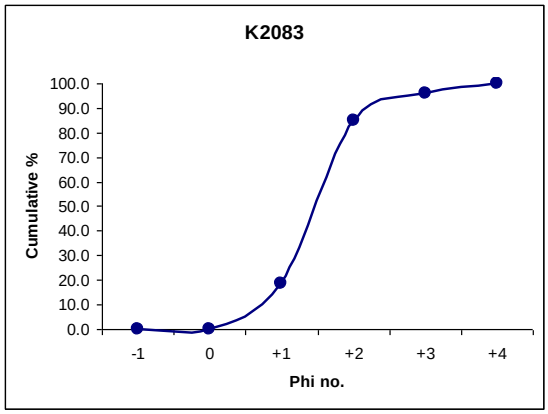

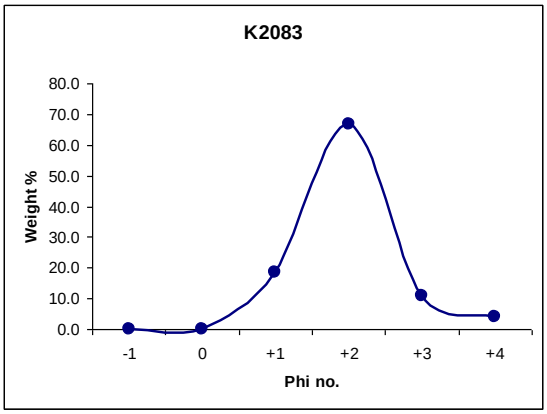

K2086

Strong Brown (7.5YR 5/6) medium to fine, well sorted, sub-rounded grains with moderate sphericity.

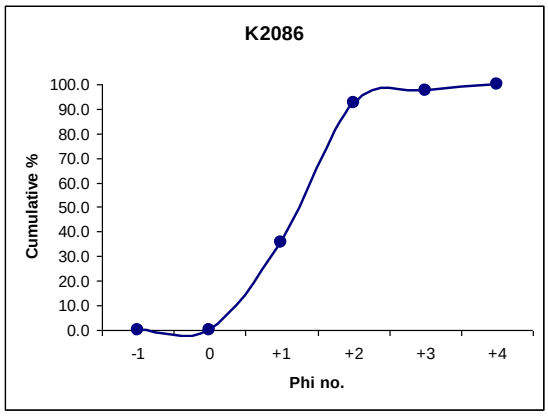

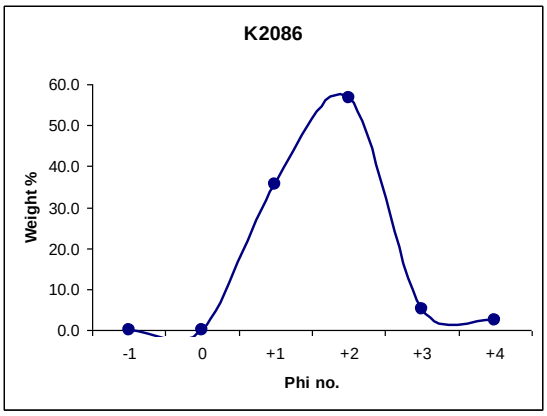

K2087

Reddish yellow (7.5YR 6/8), medium to fine, moderately well sorted, sub-rounded grains with moderate sphericity.

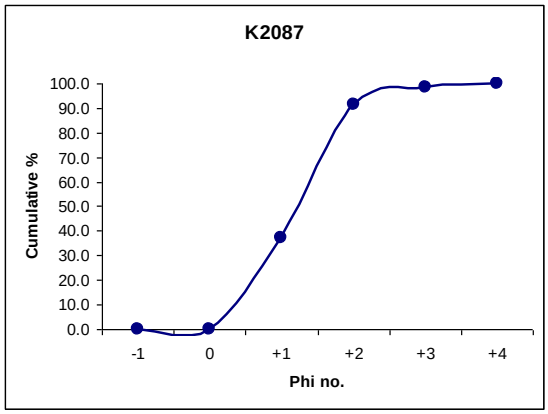

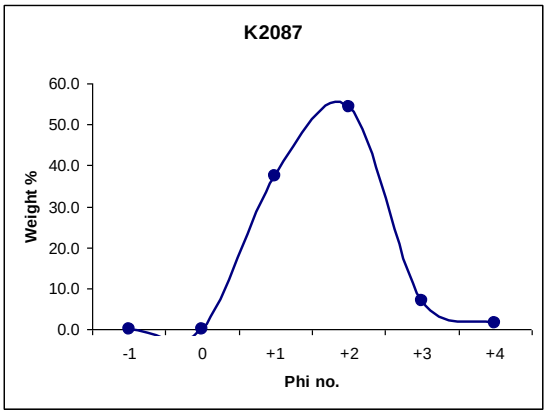

Thin sections

None

Field observations

Poorly consolidated, thick unit of laminated sands.

Summary Description

Stratigraphy

Laminated medium to fine sands, mostly well sorted. Laminations defined by grainsize. Highly eroded.

Pedostratigraphy

None

Biostratigraphy

Modern plant roots.

Appendix C.5. Sediment descriptions from SL11 at BG01

Unit C

Loose sediments

K2130

Yellowish brown (10YR 5/4) very fine to silt sized, moderately sorted, well rounded grains of moderate sphericity

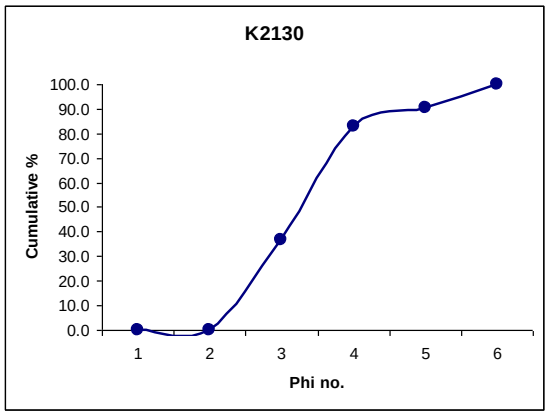

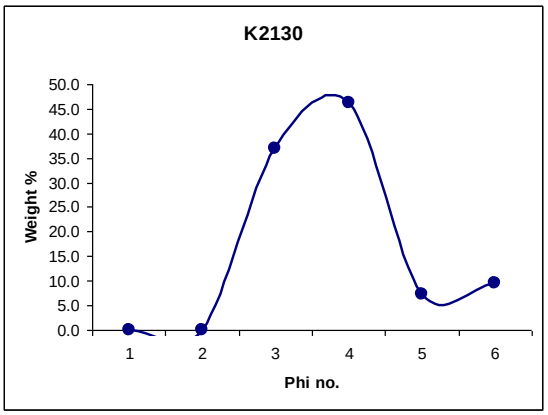

K2131

Strong brown (7.5YR 5/8) fine to silt sized, poorly sorted, sub-rounded grains of moderate sphericity

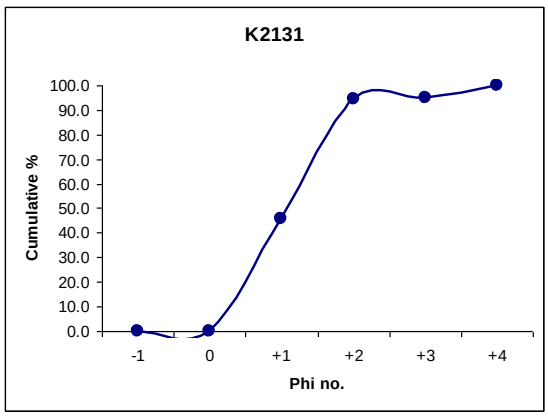

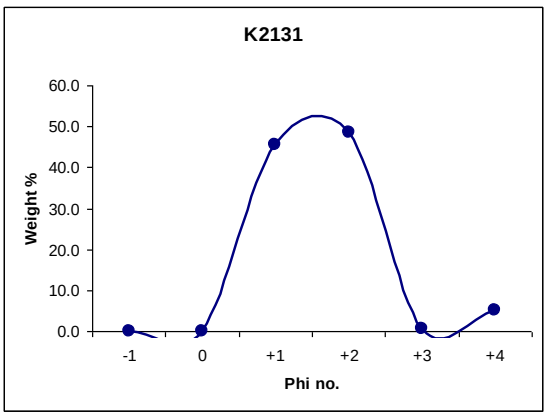

K2132

trong brown (7.5YR 5/6) very fine to silt sized, poorly sorted, sub-rounded grains of moderate sphericity

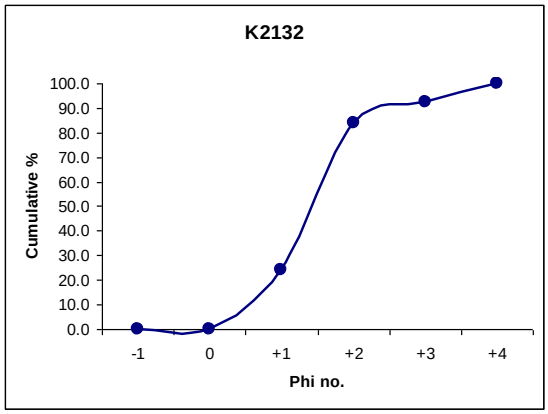

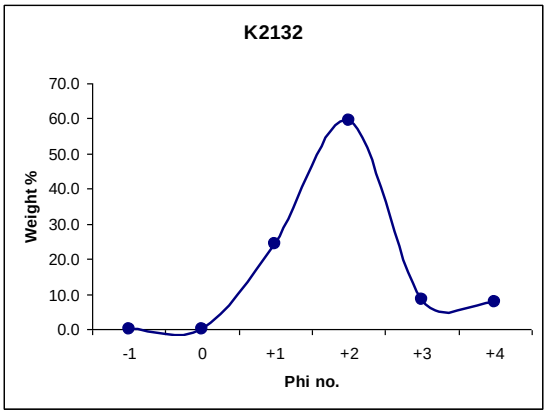

K2135

Strong brown (7.5YR 4/6) medium to silt sized, very poorly sorted, moderately rounded grains of moderate sphericity

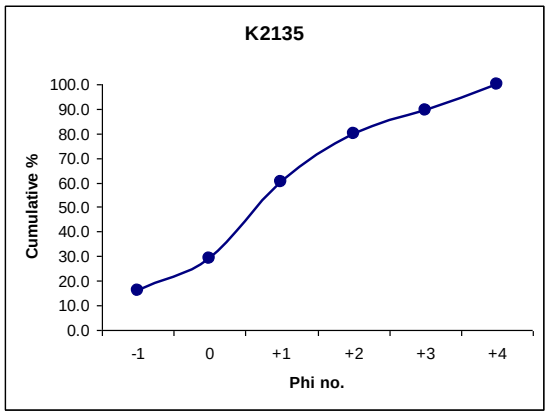

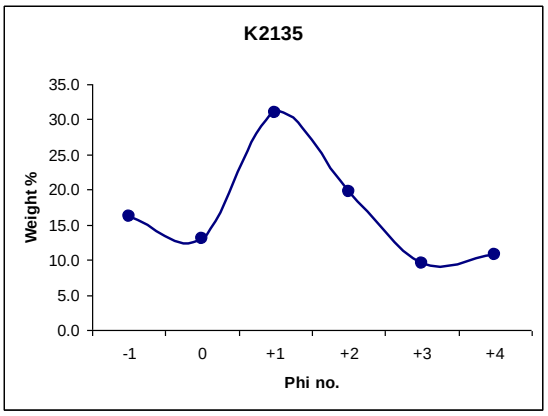

1.1.1.2. Thin sections

TS039 (above K2130, below and in same unit as K2131)

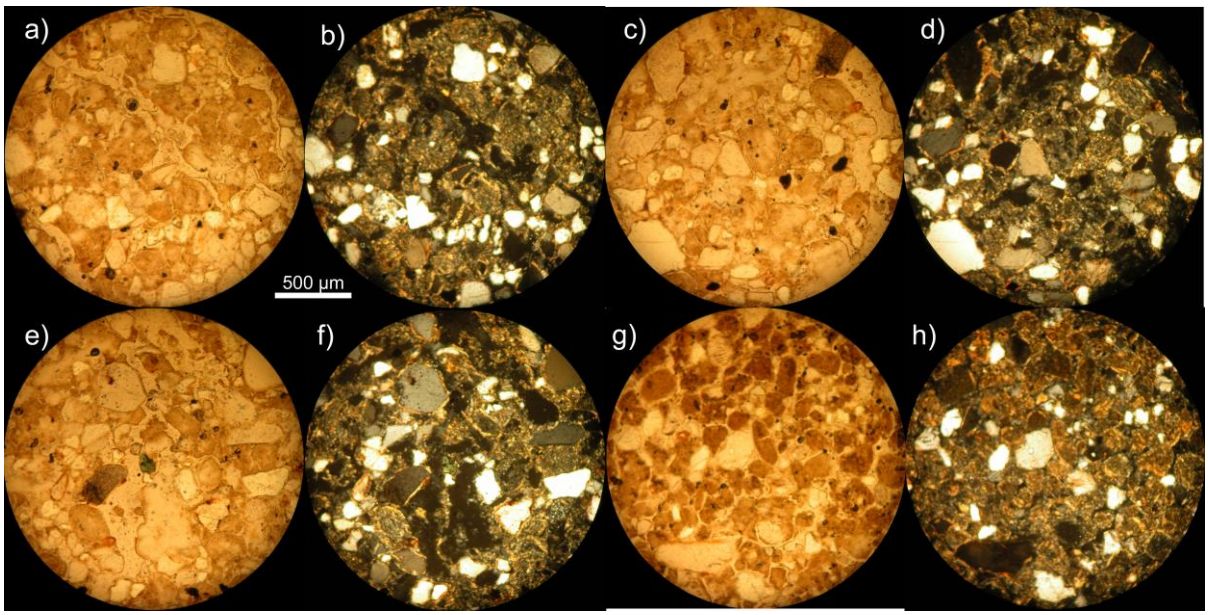

Sandy clay with moderately sorted, sub-angular quartz. Grainsize varies from very fine to medium, though most are in the 200-300 μm range. Rounded clay pellets are abundant, also 200-300 μm in size. Most show random flecked grains in cross-polarised light, while a few show illuminated domains. Both quartz grains and clay pellets have well developed clay cutans. A very fine grain of a high birefringence, high relief green pleochroic mineral is also present.

Clay pellets indicate a lake drying period. Well rounded pellets are indicative of transport and the difference in illumination between some grains indicates a mixed source. The grain with domains may have undergone pedogenesis before erosion and transport. The well-developed and ubiquitous clay cutans are probably illuvial and indicate *in situ* pedogenesis. The high-birefringence grain is probably detrital, possibly reworked out of the nearby Devonian sandstones.

TS040 (above and in same unit as **K2130**, below K2131)

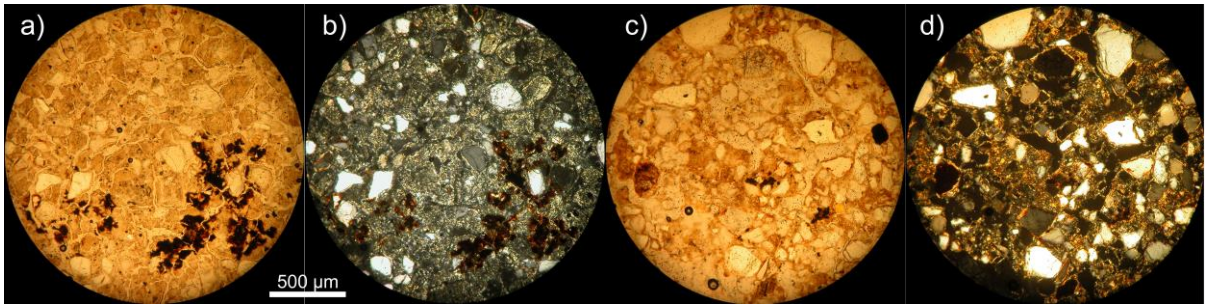

Sandy clay with moderately poorly sorted, sub-angular quartz. Grainsize varies from very fine to medium (50-500 μm). Rounded 200-300 μm clay pellets are abundant. Some large aggregates containing rounded 50 μm quartz grains. Many grains have clay cutans and interstitial Fe oxides are present in some areas.

Clay pellets indicate a lake drying period. Well rounded pellets are indicative of transport. The clay cutans are probably illuvial and indicate *in situ* pedogenesis, as do the iron oxides.

TS041 (above K2132, below K2135)

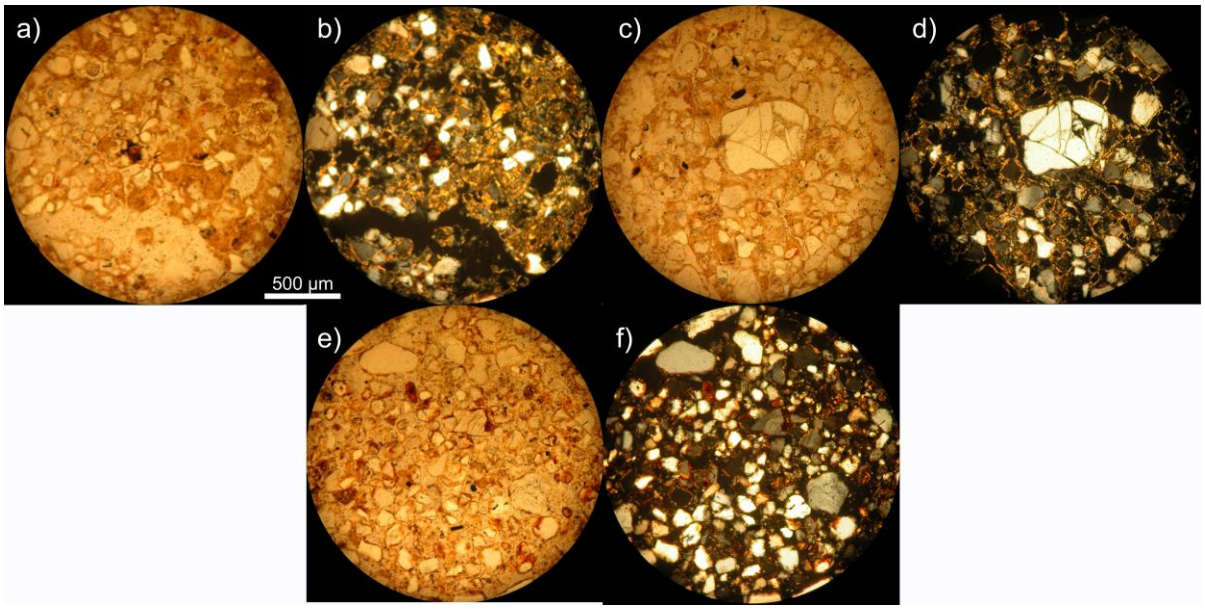

Sandy clay with moderately poorly sorted 50-500 µm (mostly 200 µm) sub-rounded quartz in a clay matrix. Some rounded clay pellets (a & b). Many grains have clay cutans. coarse quartz grain in c & d is fractured.

Clay pellets indicate a lake drying period. Well rounded pellets are indicative of transport. The clay cutans are probably illuvial and indicate *in situ* pedogenesis. Pedogenesis has also lead to the break down and coalescence of many of the clay pellets, resulting in the clay matrix. The coarse grain was probably fractured during thin-section making.

Field observations

Thick, malleable clay layer. Greeney-grey at base, more reddish higher up. Appear to be two paleosols.

Summary Description

Stratigraphy

Greenish grey sandy clay with poorly sorted medium – fine quartz

Pedostratigraphy

Two paleosols of darker red.

Biostratigraphy

None.

Unit E

Loose sediments

K2133

Strong brown (7.5YR 4/6) fine to very fine, moderately sorted, well-rounded grains of moderate sphericity.

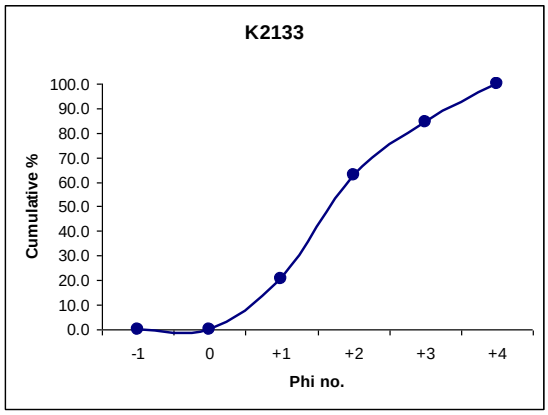

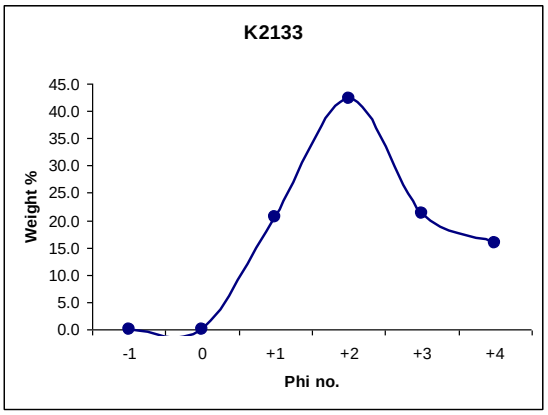

K2134

Reddish Yellow (7.5YR 6/6) very fine to silt sized, well sorted moderately rounded grains of moderate sphericity.

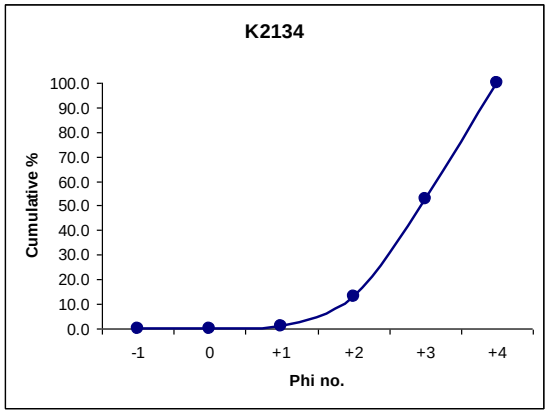

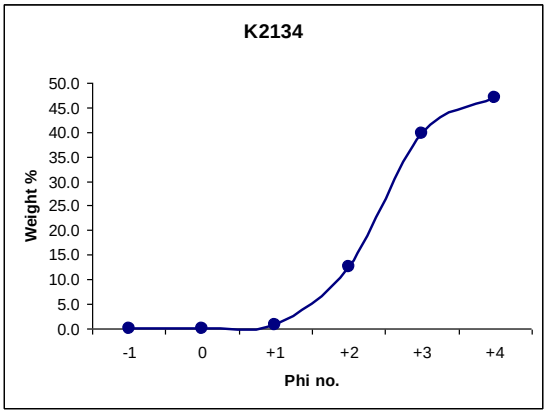

K2136

Reddish yellow (7.5YR 6/6) fine, well sorted, sub-rounded grains of moderate sphericity.

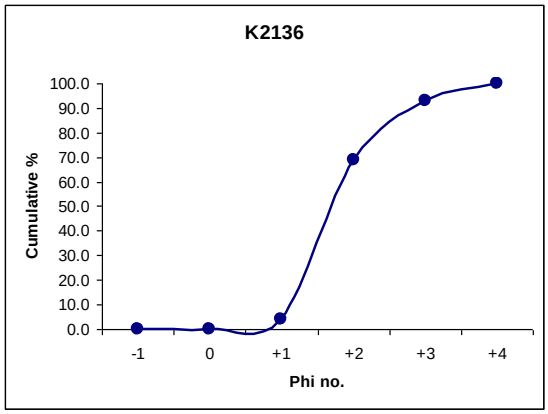

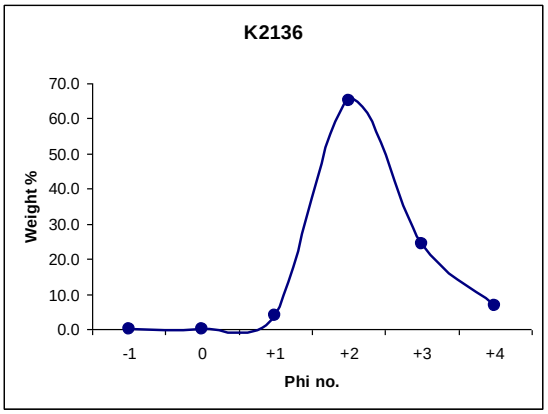

Thin sections

TS042 (below K2133)

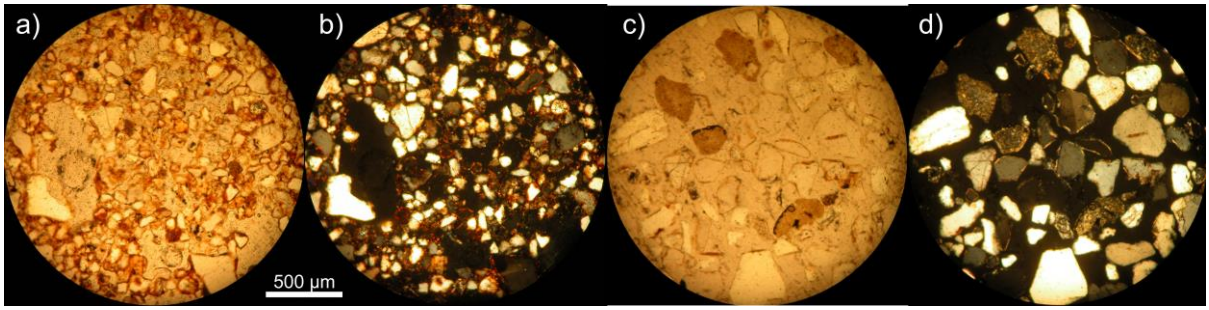

Sub-angular to sub-rounded, moderately poorly sorted medium quartz sand and silt. Bimodal grainsize with 200-500 µm quartz and a few clay pellets as well as 50 µm rounded quartz silt. Ferri-argillans are common.

Clay pellets indicate a lake drying period. There are rare in this sample, so may represent reworking. Ferri-argillans are illuvial and indicate *in situ* pedogenesis. The bimodal grain distribution represents a mixed source; possibly reworking of the lower unit mixed with aeolian silt of a more distant origin.

TS043 (above K2134 within laminations, below K2136)

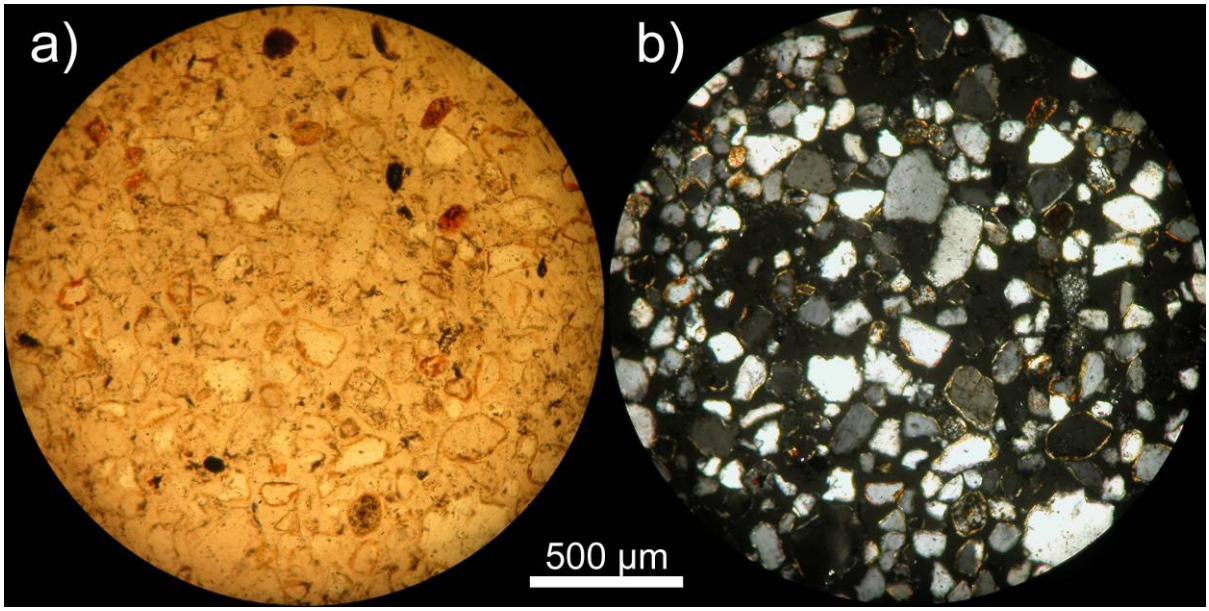

Well sorted, very fine to silt, sub-rounded quartz with clay cutans. Some rare clay pellets.

Field observations

Appears to have three sections, massive sand, then laminated for 20 cm then massive again to top.

Summary Description

Stratigraphy

Massive poorly sorted medium sand below laminated, well sorted fine sand

Pedostratigraphy

Some soil development

Biostratigraphy

Modern plant roots

Appendix C.6. Sediment descriptions from SL44 at RB03

Unit A

Thin sections

TS119 (between K2124 and K2125)

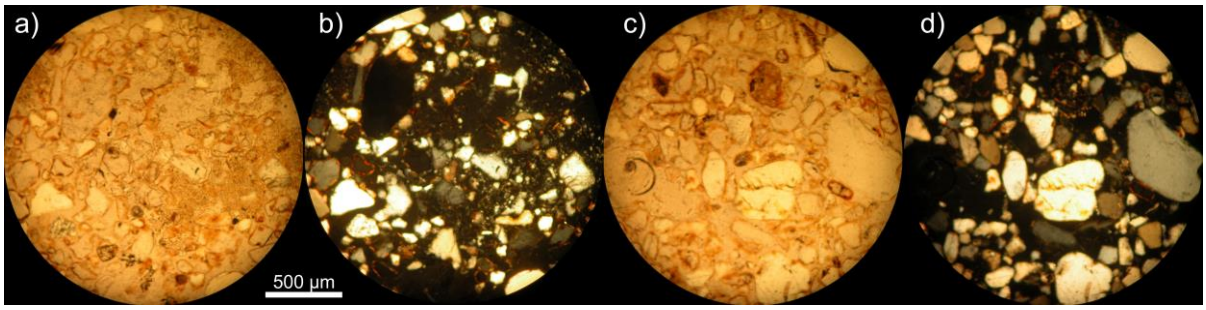

Moderately sorted, sub-angular, medium to very fine grains with moderate to low sphericity. Ferri-argillans are preferentially coating smaller grains. Some well-preserved cutans, though larger grains have remnant cutans in grain embayments.

Reworking of an older soil (remnant cutans) undergone paedogenesis in situ also (ferri-argillans and well-preserved cutans).

Field observations

Blowout has carbonate nodules in yellow sand at the base, grading in to red sand up the side.

Summary Description

Stratigraphy

Moderately sorted, medium to fine massive sand

Pedostratigraphy

Carbonate nodules and rubification

Biostratigraphy

None

Unit E

Field observations

Laminated medium to fine sands

Summary Description

Stratigraphy

Laminated medium to fine sands

Pedostratigraphy

Some modern soil development

Biostratigraphy

Modern plant roots

Appendix C. 7. Sediment descriptions from other locations

Shoreline and spit

Loose Sediments

K2127

Moderately sorted, sub-angular, fine to very fine brown sands with moderate sphericity.

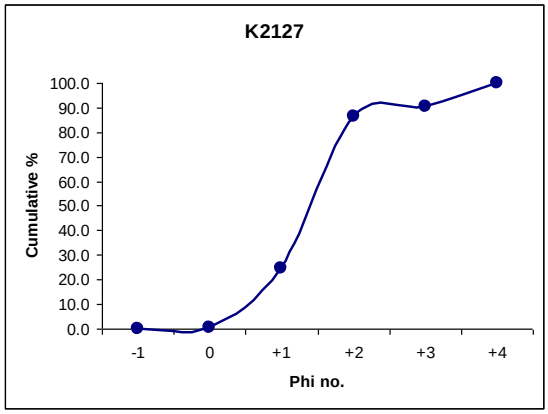

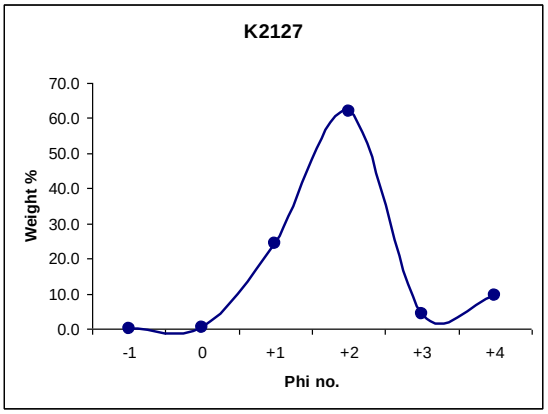

K2128

Moderately sorted, sub-angular, fine to very fine brown sands with moderate sphericity.

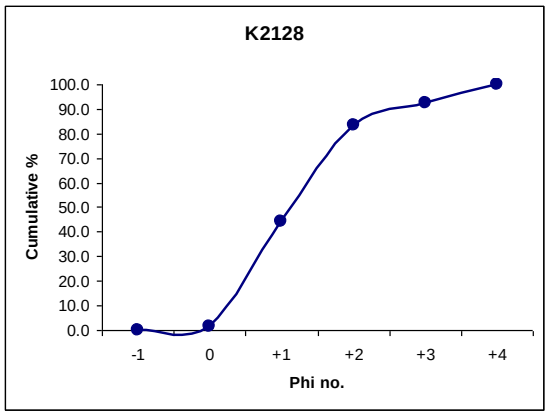

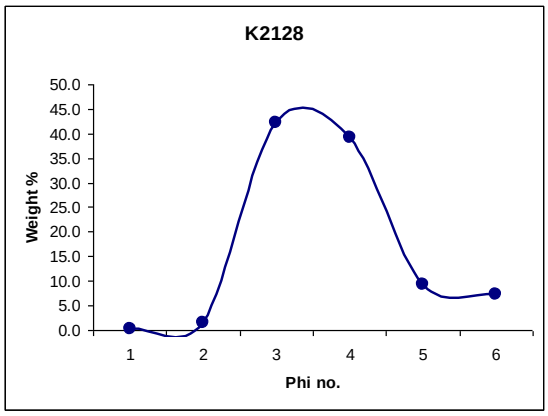

K2129

Poorly sorted, sub-rounded, course to very fine brown sands with moderate to low sphericity.

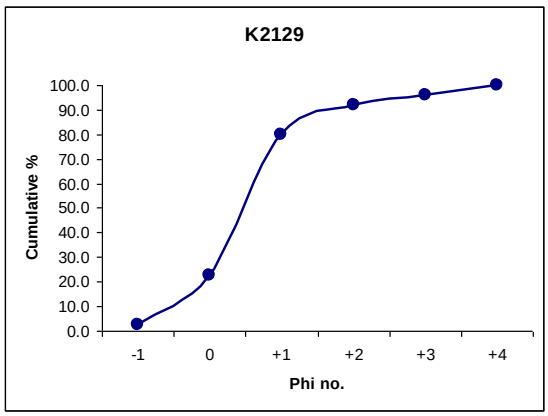

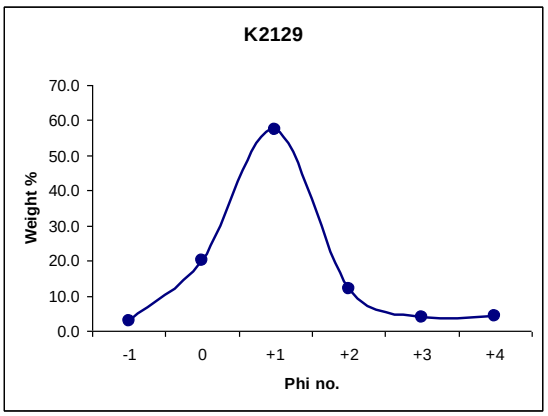

Thin Sections

TS151 (near K2129 the spit)

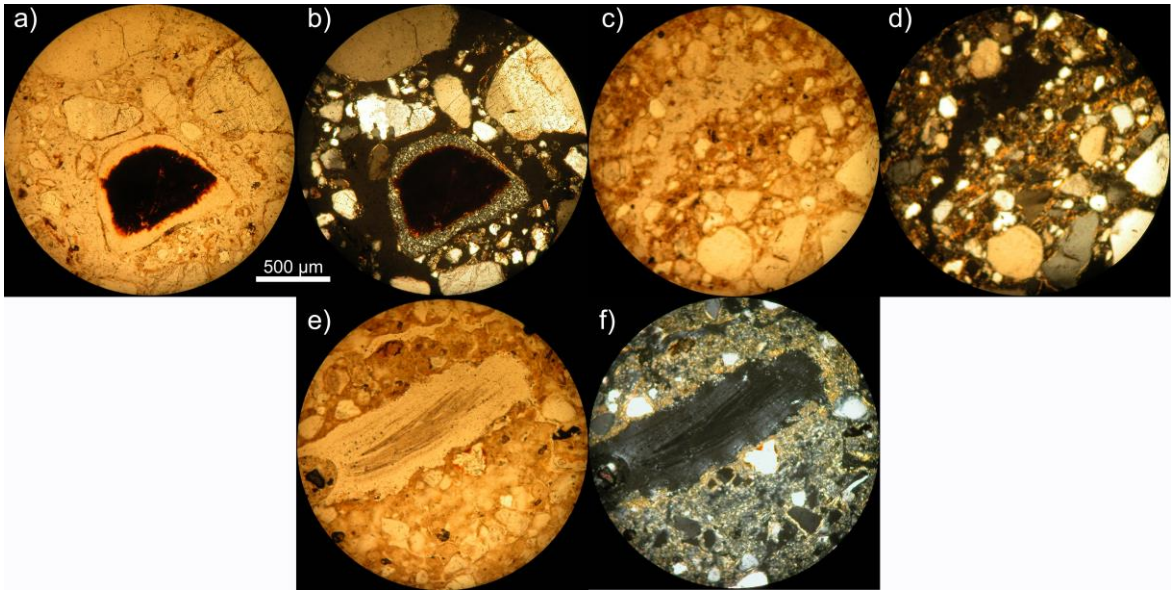

Coarse to very fine 2mm – 100 µm, poorly sorted, sub-rounded quartz. Some warn cutans Plus illuvial clay infilling between grains (oriented clay in e/f). Dark grain with the fine grained coating in a)/b) may be dense iron oxide with a coating of very fine polycrystalline quartz…symmetrical shape and even coating suggest a biogenic origin. Bone in e/f.

Other thin sections

TS049 (Gypsum 'rosettes' from A unit in the base of a gully)

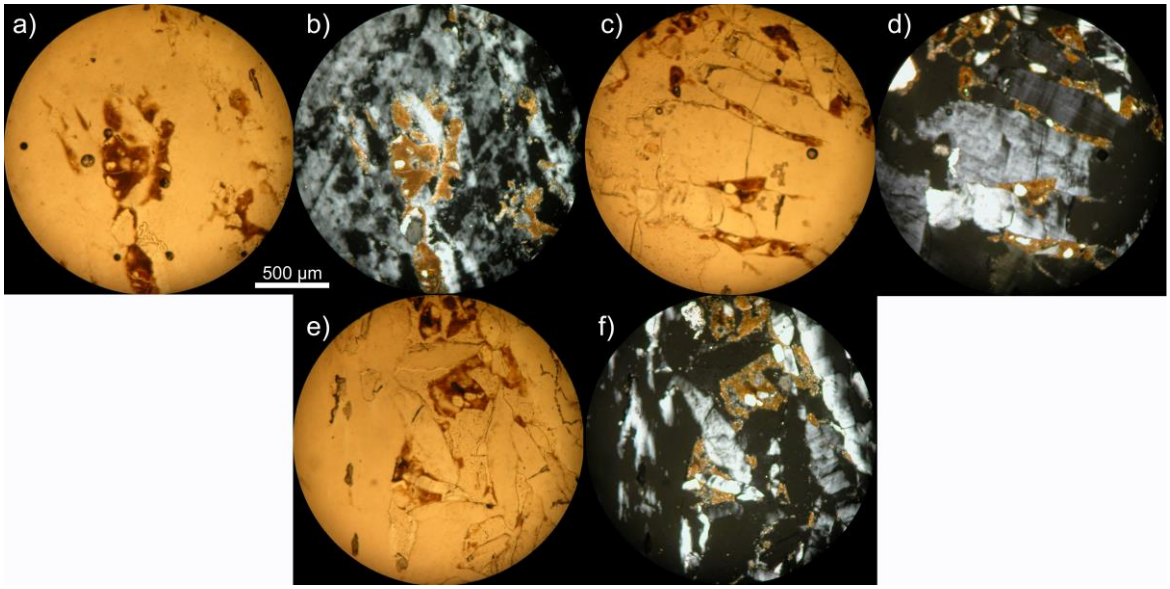

Euhedral to sub-hedral gypsum crystals with interstitial clay and fine carbonates.
Gypsum of pedogenic origin, having displaced the clay as it grew. Carbonate is also illuvial.

TS051 (carbonate nodule from A unit in the base of a gully).

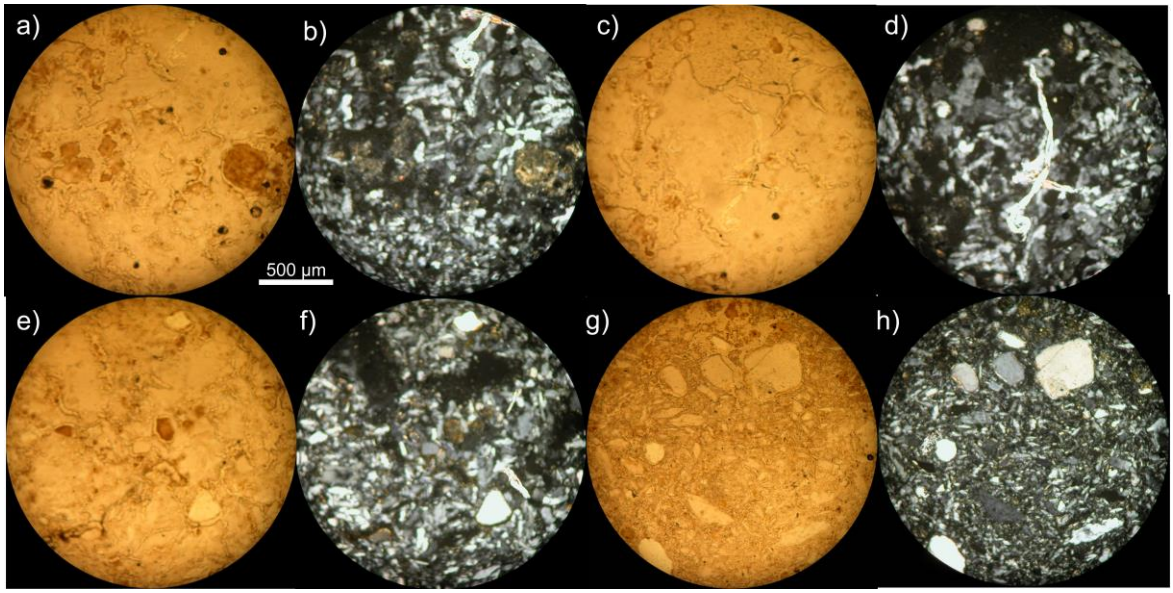

Fine grained carbonate intergrowths with quartz and clay inclusions. (Qtz 100-400 µm, rounded). Pedogenic carbonate nodule

Appendix D. Wombat enamel $\delta^{18}O$ results

Appendix D.1. Table of wombat enamel leaching test sample weights and $\delta^{18}O$ analysis results

Sample	Ag3PO4 mass (mg)	C mass (µg)	$\delta^{18}O$ (uncorr)	$\delta^{18}O$ Corrected
Empty	0.00	0.00	-913.57	
Beet 1	0.53	0.00	23.37	29.95
Beet 2	0.63	0.00	23.41	30.00
Beet 3	0.72	0.00	23.02	29.56
Beet 4	0.54	0.00	23.90	30.55
Beet 5	0.67	0.00	25.00	31.78
Beet 6	0.55	0.00	23.30	29.87
Beet 7	0.72	0.00	24.49	31.21
Beet 8	0.69	0.00	25.19	31.98
NH4_2 1	3.54	0.58	15.69	21.40
NH4_2 2	3.02	0.57	15.77	21.48
2ndFS 1	3.42	0.58	0.34	4.30
2nd FS 2	3.48	0.55	-0.96	2.85
Ma 1	2.69	0.57	11.89	17.16
Mb 1	2.91	0.58	13.62	19.09
Mb 2	3.38	0.69	15.06	20.70
Mc 1	3.21	0.50	16.21	21.98
Mc 2	2.87	0.70	16.33	22.11
Md 1	2.24	0.49	13.87	19.37
Md 2	3.78	0.55	14.72	20.32
Me 1	3.11	0.63	15.87	21.59
Me 2	3.17	0.62	16.06	21.81
Mf 1	3.58	0.55	17.12	22.99
Mf 2	3.67	0.63	17.15	23.02
Mg 1	4.27	0.51	16.55	22.36
Mh 1	2.83	0.50	16.10	21.85
Mh 2	2.33	0.49	15.65	21.35
Mi 1	1.55	0.45	14.13	19.66
NH4_2 1	3.47	0.52	16.11	21.87
NH4_2 2	3.67	0.58	16.04	21.79
2ndFS 1	3.20	0.48	-0.95	2.86
2nd FS 2	4.29	0.50	-3.21	0.34
Mj 1	2.92	0.47	15.29	20.95
Mj 2	2.83	0.65	16.74	22.57
Mk 1	2.88	0.56	16.24	22.01
Mk 2	2.80	0.54	16.40	22.19
F2a 1	2.80	0.49	18.39	24.40
F2a 2	2.68	0.68	18.70	24.75
F2b 1	2.82	0.56	16.17	21.93
F2b 2	2.95	0.47	16.69	22.51
F2c 1	2.99	0.60	19.02	25.10
F2c 2	3.45	0.67	19.91	26.10
F2d 1	2.90	0.46	19.73	25.90
F2d 2	3.79	0.63	19.63	25.78
F2F 1	2.51	0.66	19.68	25.85
F2f 2	4.04	0.57	20.38	26.62
F2g 1	3.29	0.75	19.86	26.05
F2g 2	3.40	0.53	19.65	25.81
NH4_2 1	3.38	0.65	16.39	22.18

Sample	Ag3PO4 mass (mg)	C mass (µg)	$\delta^{18}O$ (uncorr)	$\delta^{18}O$ Corrected
NH4_2 2	4.27	0.59	15.34	21.01
2ndFS 1	3.69	0.57	-0.42	3.46
2ndFS 2	3.98	0.64	-0.93	2.89
F2h 1	2.96	0.62	17.80	23.75
F2h 2	2.71	0.69	18.07	24.05
F2i 1	3.02	0.84	18.14	24.13
F2j 1	3.30	0.71	18.32	24.33
F2j 2	3.58	0.54	19.62	25.77
F2k 1	2.19	0.55	19.00	25.08
Fa 1	2.93	0.61	18.40	24.42
Fa 2	2.97	0.50	18.58	24.62
Fb 1	3.69	0.64	18.54	24.58
Fb 2	3.89	0.53	18.36	24.37
Fc 1	3.13	0.62	18.55	24.59
Fc 2	3.19	0.78	18.45	24.47
Fd 1	2.86	0.67	18.98	25.07
Fd 2	3.24	0.60	19.05	25.15
Fe 1	3.19	0.58	17.51	23.43
Fe 2	3.05	0.65	18.00	23.97
NH4_2 1	2.95	0.49	15.51	21.20
NH4_2 2	4.42	0.70	16.40	22.19
2ndFS 1	4.16	0.57	-0.36	3.52
2ndFS 2	2.87	0.69	-1.58	2.16
Ff 1	1.95	0.44	14.81	20.42
Fg 1	2.67	0.59	16.09	21.84
Fg 2	3.98	0.54	17.17	23.04
Fh 1	2.70	0.62	15.93	21.66
Fh 2	2.83	0.50	15.88	21.62
Fi 1	2.86	0.53	11.77	17.04
Fi 2	3.14	0.46	11.92	17.20
Fj 1	2.72	0.46	15.73	21.44
Fj 2	2.64	0.57	16.09	21.84
Fk 1	2.83	0.51	13.09	18.50
Fk 2	2.34	0.69	12.89	18.28
Empty	0.00	0.00	-858.97	
Beet 1	0.64	0.00	25.17	31.96
Beet 2	0.60	0.00	23.00	29.54
Beet 3	0.79	0.00	25.72	32.58
Beet 4	0.51	0.00	18.22	24.22
Beet 5	0.70	0.00	25.12	31.91
Beet 6	0.65	0.00	25.26	32.06
Beet 7	0.58	0.00	20.51	26.77
Beet 8	0.77	0.00	24.73	31.47
M2a 1	2.80	0.82	15.34	21.00
M2a 2	3.49	0.58	15.55	21.24
M2c 1	3.19	0.55	16.15	21.91
M2c 2	3.42	0.68	16.35	22.14
NH4_2 1	2.74	0.61	15.86	21.59
NH4_2 2	4.02	0.65	15.99	21.73
2ndFS 1	4.26	0.47	0.51	4.49
2ndFS 2	2.54	0.47	-1.37	2.40
M2d 1	2.40	0.68	13.39	18.83
M2e 1	3.39	0.66	16.45	22.24

Sample	Ag3PO4 mass (mg)	C mass (µg)	$\delta^{18}O$ (uncorr)	$\delta^{18}O$ Corrected
M2e 2	4.10	0.61	17.61	23.54
M2f 1	2.75	0.44	16.58	22.39
M2f 2	3.06	0.51	16.81	22.65
M2g 1	2.80	0.50	15.64	21.35
M2h 1	1.92	0.57	14.79	20.40
M2i 1	2.68	0.46	15.41	21.09
M2i 2	2.23	0.49	15.45	21.13
M2j 1	2.56	0.68	14.91	20.53
M2j 2	2.93	0.50	14.68	20.28
M2k 1	3.68	0.49	14.63	20.22
F3a 1	2.98	0.51	14.07	19.59
F3a 2	2.05	0.72	13.72	19.21
F3g 1	4.30	0.58	15.88	21.62
NH4_2 3	4.45	0.90	16.66	22.48
NH4_2 4	4.79	0.55	16.38	22.17
2ndFS 3	2.95	0.48	0.42	4.39
2ndFS 4	2.56	0.52	-1.07	2.73
F3h 1	2.53	0.52	14.03	19.54
F3i 1	2.91	0.60	16.56	22.37
F3i 2	3.79	0.52	17.80	23.75
F3j 1	2.67	0.55	17.26	23.14
F3j 2	2.76	0.57	17.67	23.60
F3k 1	2.78	0.57	18.69	24.74
F3k 2	3.09	0.51	19.10	25.20
S1a 1	2.70	0.61	11.76	17.02
S1a 2	2.38	0.61	11.76	17.02
S1b 1	1.97	0.60	9.87	14.92
S1c 1	2.44	0.51	9.21	14.18
S1d 1	1.83	0.53	9.23	14.21
S1e 1	3.36	0.58	9.59	14.60
S1f 1	3.29	0.47	12.23	17.54
S1f 2	3.21	0.53	10.78	15.93
NH4_2 1	3.07	0.70	13.91	19.42
NH4_2 2	3.28	0.49	15.23	20.89
2ndFS 1	4.00	0.54	0.14	4.08
2ndFS 2	3.28	0.47	0.36	4.33
S1g 1	1.59	0.55	7.16	11.89
S1h 1	1.35	0.63	7.49	12.26
S1i 1	3.11	0.49	10.95	16.12
S1i 2	3.03	0.46	10.51	15.63
S1j 1	3.11	0.61	9.32	14.30
S1k 1	3.69	0.49	11.67	16.92
S1k 2	4.34	0.55	12.09	17.39
S2a 1	2.98	0.69	2.90	7.15
S2a 2	3.44	0.63	1.88	6.01
S2b 1	3.45	0.47	1.91	6.05
S2b 2	2.70	0.57	1.85	5.98
S2c 1	3.15	0.52	1.25	5.31
S2c 2	3.64	0.46	1.46	5.55
S2d 1	1.93	0.59	1.93	6.07
S2f 1	3.02	0.56	1.24	5.30
NH4_2 1	2.81	0.56	8.76	13.68
NH4_2 2	3.32	0.48	10.33	15.42

APPENDIX D. WOMBAT ENAMEL $\delta^{18}O$ RESULTS

Sample	Ag3PO4 mass (mg)	C mass (µg)	$\delta^{18}O$ (uncorr)	$\delta^{18}O$ Corrected
2ndFS 1	3.69	0.48	0.65	4.65
2ndFS 2	4.10	0.45	-0.23	3.66
S2f 2	1.39	0.46	2.00	6.15
S2g 1	2.42	0.50	0.70	4.70
S2j 1	2.87	0.59	0.18	4.12

Appendix D.2. Table of sequential wombat enamel sample weights and $\delta^{18}O$ analysis results

Actual Sample	Mass Ag_3PO_4 (mg)	Mass sugar (mg)	Mass carbon (mg)	Uncorrected $\delta^{18}O$	Corrected $\delta^{18}O$
Beet 89 1		0.770		30.93	30.82
Beet 89 2		0.603		31.15	31.05
Beet 89 3		0.441		30.42	30.27
Beet 89 4		0.549		31.30	31.21
Beet 89 5		0.483		31.59	31.53
Beet 89 6		0.683		31.60	31.54
Beet 89 7		0.699		31.90	31.86
Beet 89 8		0.595		32.07	32.05
Beet 89 9		0.661		31.70	31.64
Beet 89 10		0.572		31.61	31.55
ANU 1		0.761		36.99	37.37
ANU 2		0.566		37.51	37.94
ANU 3		0.623		37.81	38.27
ANU 4		0.459		36.67	37.03
ANU 5		0.618		36.80	37.17
ANU 6		0.661		37.49	37.91
ANU 7		0.537		37.02	37.40
ANU 8		0.508		35.19	35.42
ANU 9		0.614		36.14	36.46
ANU 10		0.713		37.47	37.89
NH4_2 1	3.329		0.512	23.06	22.29
NH4_2 2	3.826		0.379	22.82	22.03
NH4_2 3	3.101		0.463	22.45	21.63
NH4_2 4	3.623		0.399	22.75	21.96
NH4_2 5	3.561		0.307	22.60	21.79
NH4_2 6	3.634		0.455	22.63	21.83
NH4_2 7	3.180		0.328	22.40	21.58
NH4_2 8	3.127		0.651	22.14	21.29
NH4_2 9	2.999		0.449	22.39	21.56
NH4_2 10	3.424		0.361	22.50	21.68
2ndFS 1	3.112		0.378	6.07	3.90
2ndFS 2	3.239		0.596	5.11	2.86
2ndFS 3	3.322		0.322	4.89	2.62
2ndFS 4	3.138		0.405	4.69	2.40
2ndFS 5	3.541		0.449	4.62	2.33
2ndFS 6	3.296		0.562	4.57	2.27
2ndFS 7	3.044		0.466	4.24	1.91
2ndFS 8	3.145		0.347	4.75	2.47
2ndFS 9	2.989		0.623	4.47	2.16
2ndFS 10	3.036		0.513	4.08	1.75
Wright 1	3.208		0.453	19.77	18.73
Wright 2	3.601		0.569	20.59	19.62
Wright 3	2.894		0.385	20.51	19.53
Wright 4	3.048		0.607	21.20	20.28
Wright 5	2.788		0.451	20.53	19.55
Wright 6	2.607		0.374	20.75	19.79
Wright 7	2.629		0.637	20.94	19.99
Wright 8	2.526		0.499	20.93	19.99

Actual Sample	Mass Ag_3PO_4 (mg)	Mass sugar (mg)	Mass carbon (mg)	Uncorrected $\delta^{18}O$	Corrected $\delta^{18}O$
Wright 9	2.819		0.461	20.73	19.77
Empty	0.000		0.000	-784.58	
W01-01	3.254		0.369	21.60	20.71
W01-02	3.445		0.523	14.17	12.67
W01-03	3.881		0.591	20.00	18.98
W01-04	3.138		0.550	21.59	20.70
W01-05	3.411		0.362	22.26	21.43
W01-06	3.303		0.442	24.36	23.70
W01-07	3.785		0.613	24.59	23.95
W01-08	3.700		0.370	24.02	23.33
W01-09	3.646		0.459	27.08	26.65
W01-10	3.118		0.524	24.80	24.18
W01-11	3.187		0.427	25.32	24.74
W02-01	3.729		0.381	26.62	26.15
W02-02	3.176		0.335	27.13	26.69
W02-03	3.289		0.379	23.42	22.68
W02-04	3.203		0.532	25.26	24.68
NH4_2 1	3.321		0.370	22.13	21.28
NH4_2 2	3.837		0.424	22.17	21.33
2nd FS 1	3.141		0.338	5.98	3.80
2nd FS 2	3.215		0.578	4.89	2.62
W02-05	3.472		0.393	23.47	22.74
W02-06	3.193		0.507	24.33	23.67
W02-07	3.297		0.577	24.25	23.58
W02-08	3.317		0.387	23.30	22.55
W02-09	3.454		0.645	22.76	21.97
W02-10	3.052		0.506	23.58	22.86
W03-01	3.480		0.393	21.45	20.55
W03-02	3.268		0.312	17.63	16.41
W03-03	3.127		0.420	22.96	22.19
W03-04	3.190		0.438	24.06	23.38
W03-05	3.064		0.455	20.67	19.70
W03-06	3.604		0.574	25.02	24.41
W03-07	3.609		0.335	26.09	25.58
W03-08	3.786		0.361	26.82	26.36
W03-09	3.268		0.318	27.03	26.59
NH4_2 1	3.515		0.403	22.37	21.55
NH4_2 2	3.417		0.306	22.16	21.32
2nd FS 1	4.074		0.402	5.60	3.38
2nd FS 2	3.295		0.350	4.92	2.65
Wright 1	3.452		0.353	19.48	18.41
Wright 1	3.592		0.456	20.17	19.16
W04-01	3.370		0.364	19.45	18.38
W04-02	3.298		0.356	23.14	22.38
W04-03	3.280		0.301	24.30	23.63
W04-04	3.111		0.339	23.17	22.41
W04-05	3.509		0.362	21.67	20.79
W04-06	3.573		0.354	23.24	22.49
W04-07	3.353		0.400	23.71	23.00
W04-08	3.291		0.300	24.13	23.45
W04-09	3.259		0.603	16.66	15.36
W04-10	3.256		0.442	19.60	18.55

Actual Sample	Mass Ag_3PO_4 (mg)	Mass sugar (mg)	Mass carbon (mg)	Uncorrected $\delta^{18}O$	Corrected $\delta^{18}O$
W05-01	3.227		0.444	19.94	18.91
W05-02	3.247		0.363	21.47	20.58
W05-03	3.444		0.403	23.03	22.26
W05-04	3.615		0.382	18.90	17.78
W05-05	3.315		0.405	20.24	19.24
NH4_2 3	3.305		0.306	21.56	20.67
NH4_2 4	3.163		0.396	21.51	20.61
2nd FS 3	3.232		0.655	4.93	2.66
2nd FS 4	3.305		0.367	5.88	3.69
W05-06	3.228		0.374	19.04	17.94
W05-07	3.614		0.371	21.29	20.37
W05-08	3.435		0.314	23.07	22.31
W06-01	3.069		0.346	16.28	14.95
W06-02	3.343		0.365	21.09	20.16
W06-03	3.094		0.322	20.88	19.93
W06-04	3.193		0.352	20.10	19.09
W06-05	3.266		0.342	22.52	21.71
W06-06	3.139		0.371	22.06	21.21
W06-07	3.192		0.682	17.57	16.35
W07-01	3.014		0.301	22.04	21.19
W07-02	3.447		0.303	22.71	21.92
W07-03	3.003		0.378	22.86	22.07
W07-04	3.009		0.381	22.16	21.32
W07-05	3.394		0.390	25.00	24.39
NH4_2 5	3.561		3.344	22.01	21.16
NH4_2 6	3.289		0.498	21.68	20.79
2nd FS 1	3.529		0.325	5.24	3.00
2nd FS 2	3.851		0.356	4.19	1.86
Wright 1	3.164		0.362	19.52	18.46
Wright 2	3.503		0.379	20.07	19.06
W07-06	3.318		0.377	17.81	16.60
W08-01	3.437		0.311	24.58	23.94
W08-02	3.240		0.420	17.86	16.66
W08-03	3.094		0.400	14.86	13.42
W08-04	3.495		0.426	20.67	19.70
W08-05	3.430		0.424	15.85	14.48
W08-06	3.409		0.382	26.26	14.93
W09-01	3.193		0.618	19.34	18.26
W09-02	3.383		0.391	19.49	18.43
W09-03	3.247		0.429	21.83	20.96
W09-04	3.571		0.448	23.39	22.65
W09-05	3.616		0.594	21.61	20.72
W09-06	3.160		0.460	23.28	22.53
W09-07	3.331		0.312	25.01	24.40
W09-08	3.065		0.367	25.94	25.41
NH4_2 1	3.832		0.290	21.49	20.59
NH4_2 2	3.091		0.343	22.10	21.25
Empty	0.000		0.000	-781.86	
Empty	0.000		0.000	-886.70	
Beet 1		0.479		30.42	30.26
Beet 2		0.413		31.28	31.20
Beet 3		0.470		30.16	29.98

Actual Sample	Mass Ag_3PO_4 (mg)	Mass sugar (mg)	Mass carbon (mg)	Uncorrected $\delta^{18}O$	Corrected $\delta^{18}O$
Beet 4		0.429		31.40	31.33
Beet 5		0.609		31.24	31.15
Beet 6		0.718		31.63	31.57
Beet 7		0.490		31.87	31.83
Beet 8		0.392		30.38	30.22
Beet 9		0.606		31.43	31.35
Beet 10		0.402		32.16	32.15
NH4_2 1	3.924		0.409	21.99	21.14
NH4_2 2	3.889		0.318	21.85	20.99
NH4_2 3	3.146		0.347	22.48	21.67
NH4_2 4	3.564		0.330	21.67	20.79
NH4_2 5	3.684		0.295	21.44	20.54
2nd FS 1	3.043		0.356	4.95	2.68
2ndFS 2	4.044		0.358	5.03	2.77
2ndFS 3	3.979		0.428	3.99	1.64
2ndFS 4	3.043		0.367	3.99	1.64
2ndFS 5	3.142		0.354	4.65	2.36
Wright 1	3.086		0.386	19.36	18.28
Wright 2	3.330		0.557	19.88	18.85
Wright 3	3.337		0.410	20.09	19.08
W09-09	3.156		0.532	23.33	22.59
W09-10	3.516		0.579	23.86	23.16
W10-01	3.779		0.323	25.96	25.43
W10-02	4.044		0.402	24.36	23.70
W10-03	3.254		0.732	21.94	21.08
W10-04	3.043		0.414	17.81	16.61
W10-05	3.710		0.432	16.43	15.11
W10-06	3.589		0.300	22.95	22.18
W11-01	3.479		0.299	16.99	15.72
W11-02	3.822		0.419	13.74	12.20
W11-03	3.375		0.548	18.87	17.76
W11-04	3.326		0.496	19.39	18.31
W11-05	4.102		0.344	15.31	13.90
W11-06	3.468		0.481	21.83	20.96
W11-07	3.653		0.338	18.32	17.16
NH4_2 1	3.783		0.343	20.94	20.00
NH4_2 2	3.141		0.559	21.03	20.09
2ndFS 1	3.301		0.323	6.68	4.55
2ndFS 2	3.605		0.477	4.17	1.84
W11-08	3.621		0.525	13.31	11.74
W11-09	3.237		0.464	18.48	17.33
W12-01	3.469		0.324	15.14	13.72
W12-02	3.280		0.298	19.23	18.14
W12-03	3.040		0.305	15.10	13.68
W12-04	3.451		0.797	19.09	18.00
W12-05	3.737		0.330	20.33	19.33
W12-06	3.233		0.407	24.03	23.34
W12-07	3.316		0.405	25.34	24.76
W13-01	3.669		0.533	15.86	14.50
W13-02	3.636		0.391	23.23	22.48
W13-03	3.402		0.493	19.31	18.24
W13-04	3.579		0.458	28.47	28.15

APPENDIX D. WOMBAT ENAMEL $\delta^{18}O$ RESULTS

Actual Sample	Mass Ag_3PO_4 (mg)	Mass sugar (mg)	Mass carbon (mg)	Uncorrected $\delta^{18}O$	Corrected $\delta^{18}O$
W13-05	3.459		0.436	26.48	25.99
W13-06	3.483		0.636	22.55	21.74
NH4_2 3	3.176		0.497	21.94	21.08
NH4_2 4	3.312		0.452	21.60	20.72
2ndFS 3	3.356		0.303	7.05	4.96
2ndFS 4	3.543		0.360	4.22	1.89
W13-07	3.722		0.383	29.19	28.93
W13-08	3.187		0.325	19.18	18.09
W14-01	3.511		0.371	18.29	17.13
W14-02	3.727		0.560	18.33	17.17
W14-03	3.284		0.346	26.37	25.87
W14-04	3.827		0.325	20.32	19.32
W14-05	3.107		0.529	25.64	25.09
W14-06	3.555		0.530	25.99	25.47
W14-07	3.473		0.435	27.70	27.32
W14-08	3.479		0.507	26.95	26.51
W14-09	3.030		0.528	25.05	24.45
W14-10	3.665		0.964	23.82	23.12
NH4_2 1	3.182		0.537	22.05	21.20
NH4_2 2	3.271		0.376	21.63	20.74
2ndFS 1	3.889		0.453	6.13	3.96
2ndFS 2	3.312		0.301	5.28	3.04

Appendix E. OxCal run code and output tables

Appendix E.1. Radiocarbon run code

```
Plot()
 {
  Curve("ShCal13","ShCal13.14c");
  Outlier_Model("General",T(5),U(0,4),"t");
  Sequence()
  {
   Boundary("Start B");
   Phase("B")
   {
    R_Date("SANU-10325", 32150, 370)
    {
     Outlier(0.05);
    };
    R_Date("SANU-10326", 32100, 360)
    {
     Outlier(0.05);
    };
    R_Date("SANU-10330", 28510, 250)
    {
     Outlier(0.05);
    };
    R_Date("SANU-10331", 34450, 470)
    {
     Outlier(0.05);
    };
    R_Date("SANU-10323", 26630, 190)
    {
     Outlier(0.05);
    };
    R_Date("SANU-10324", 26870, 200)
    {
     Outlier(0.05);
    };
    Interval("Interval B");
   };
   Boundary("End B");
   Interval("Interval B D");
   Boundary("Start D");
   Phase("D")
   {
    R_Date("SANU-10318", 200, 30)
    {
     Outlier();
    };
```

```
   R_Date("SANU-10319", 7360, 40)
   {
    Outlier();
   };
   R_Date("SANU-10327", 15930, 70)
   {
    Outlier(0.05);
   };
   R_Date("SANU-10329", 14840, 70)
   {
    Outlier(0.05);
   };
   R_Date("SANU-10332", 16470, 80)
   {
    Outlier(0.05);
   };
   R_Date("SANU-10321", 16210, 70)
   {
    Outlier(0.05);
   };
   Interval("Interval D");
  };
  Boundary("End D");
 };
};
```

Appendix E.2. Radiocarbon output table

Name	Unmodelled (BP)						Modelled (BP)								
	from	to	%	from	to	%	from	to	%	from	to	%	A	P	C
Curve ShCal13															
Outlier_Model															
General							-213	213	68.2	-1434	1897	95.3			99.7
T(5)	-1.135	1.135	68.2	-2.65	2.65	95.4									95.3
U(0,4)	3.99E-17	4	68.2	3.99E-17	4	95.4	5.38E-17	2.86	68.2	5.38E-17	3.824	95.4	100		99.5
Sequence															
Boundary Start B							41198	38451	68.1	44999	37148	95.4			94.3
Phase B															
R_Date SANU-10325	36390	35590	68.2	36938	35121	95.4	36399	35590	68.2	36975	35095	95.4	100.4	95.2	99.2
R_Date SANU-10326	36331	35566	68.2	36802	35110	95.4	36337	35562	68.2	36855	35082	95.4	100.3	95.3	99.2
R_Date SANU-10330	32841	31972	68.2	33210	31615	95.4	32844	31967	68.2	33228	31601	95.4	100.5	95.5	99.4
R_Date SANU-10331	39478	38461	68.2	40127	37864	95.4	39394	38302	68.2	39986	37229	95.4	94.2	93.7	98.7
R_Date SANU-10323	30989	30700	68.2	31114	30502	95.4	30995	30710	68.2	31127	30508	95.4	101.9	95.8	99.7
R_Date SANU-10324	31099	30838	68.2	31221	30695	95.4	31101	30840	68.2	31230	30691	95.4	101.4	96	99.8
Interval Interval B							8092	12857	68.2	6930	18499	95.4			97.8
Boundary End B							30896	28415	68.2	31016	24304	95.4			98.5
Interval Interval B D							7056	10791	68.1	2735	11091	95.4			98.5
Boundary Start D							21057	19679	68.2	24125	19557	95.4			98.5
Phase D															
R_Date SANU-10318	283	143	68.2	292	...	95.4	284	142	68.2	292	-2	95.3			99.9
R_Date SANU-	8177	8050	68.2	8282	8011	95.4	8177	8052	68.2	8284	8011	95.4		0.3	99.9

Name	Unmodelled (BP)						Modelled (BP)								
	from	to	%	from	to	%	from	to	%	from	to	%	A	P	C
10319 R_Date SANU-10327	19256	19020	68.2	19407	18942	95.4	19258	19019	68.2	19418	18937	95.4	100.7	96	99.8
R_Date SANU-10329	18103	17895	68.2	18236	17796	95.4	18126	17905	68.2	18290	17770	95.4	97.5	93.8	99.7
R_Date SANU-10332	19951	19688	68.2	20056	19580	95.4	19926	19660	68.2	20048	19560	95.4	100.4	95.9	99.8
R_Date SANU-10321	19626	19401	68.2	19739	19255	95.4	19627	19401	68.2	19743	19251	95.4	101.3	96.1	99.8
Interval Interval D							1804	4269	68.2	1441	9055	95.4			98.2
Boundary End D							18109	16829	68.2	19168	14048	95.4			96.8

Appendix E.3. OSL run code

Units A, B and D

```
Plot()
 {
  Outlier_Model("General",T(5),U(0,4),"t");
  Sequence()
  {
   Boundary("Start A");
   Phase("A")
   {
    C_Date("K2090", calBP(110150), 9786)
    {
     Outlier(0.05);
    };
    C_Date("K2123", calBP(91300), 7760)
    {
     Outlier(0.05);
    };
    C_Date("K2079", calBP(107260), 17240)
    {
     Outlier(0.05);
    };
    C_Date("K2124", calBP(31910), 3740)
    {
     Outlier();
    };
    C_Date("K2080", calBP(58890), 3763)
    {
     Outlier(0.05);
    };
    C_Date("K2125", calBP(120), 12)
    {
     Outlier();
    };
   Interval("Interval A");
  };
  Boundary("End A");
  Interval("Interval A to B");
  Boundary("Start B");
  Phase("B")
  {
   C_Date("K2091", calBP(81270), 5848)
   {
    Outlier(0.5);
   };
```

```
 C_Date("K2081", calBP(42440), 3155)
 {
  Outlier(0.05);
 };
 C_Date("K2116", calBP(52940), 3017)
 {
  Outlier(0.05);
 };
 C_Date("K2092", calBP(51550), 2627)
 {
  Outlier(0.05);
 };
 C_Date("K2094", calBP(54250), 4011)
 {
  Outlier(0.05);
 };
 C_Date("K2100", calBP(59730), 2657)
 {
  Outlier(0.05);
 };
 C_Date("K2099", calBP(46510), 3278)
 {
  Outlier(0.05);
 };
 C_Date("K2115", calBP(34370), 1819)
 {
  Outlier(0.05);
 };
 C_Date("K2098", calBP(32320), 2010)
 {
  Outlier(0.05);
 };
 Interval("Interval B");
};
Boundary("End B");
Interval("Interval B to D");
Boundary("Start D");
Phase("D")
{
 C_Date("K2117", calBP(28080), 1532)
 {
  Outlier(0.05);
 };
 C_Date("K2113", calBP(31600), 2183)
 {
  Outlier(0.05);
 };
```

```
   C_Date("K2118", calBP(27070), 1510)
   {
    Outlier(0.05);
   };
   C_Date("K2119", calBP(24270), 1347)
   {
    Outlier(0.05);
   };
   C_Date("K2082", calBP(17510), 1108)
   {
    Outlier(0.05);
   };
   C_Date("K2112", calBP(22430), 2302))
   {
    Outlier(0.5);
   };
   C_Date("K2121", calBP(17320), 925)
   {
    Outlier(0.05);
   };
   C_Date("K2084", calBP(5860), 577)
   {
    Outlier();
   };
   C_Date("K2111", calBP(1200), 1096)
   {
    Outlier();
   };
   C_Date("K2085", calBP(120), 15)
   {
    Outlier();
   };
   Interval("Interval D");
  };
  Boundary("End D");
 };
};
```

Unit C

```
Plot()
 {
  Outlier_Model("General",T(5),U(0,4),"t");
  Sequence("Sequence C")
  {
   Boundary("Start C");
   Phase("C")
   {
    C_Date("K2093", calBP(37520), 2480)
    {
     Outlier(0.05);
    };
    C_Date("K2114", calBP(25480), 1616)
    {
     Outlier(0.05);
    };
    C_Date("K2130", calBP(39820), 3532)
    {
     Outlier(0.05);
    };
    C_Date("K2131", calBP(22870), 1397)
    {
     Outlier(0.05);
    };
    C_Date("K2132", calBP(27750), 2207)
    {
     Outlier(0.05);
    };
    C_Date("K2135", calBP(1210), 214)
    {
     Outlier();
    };
    Interval("Interval C");
   };
   Boundary("End C");
  };
 };
```

Appendix E.4. OSL output tables

Units A, B and D

Name	Unmodelled (BP)						Modelled (BP)								
	from	to	%	from	to	%	from	to	%	from	to	%	A	P	C
Outlier_Model General							-25589	10308	68.3	-34343	34973	95.2			71.1
T(5)	-1.135	1.135	68.2	-2.65	2.65	95.4									52.9
U(0,4)	3.99E-17	4	68.2	3.99E-17	4	95.4	3.776	4	68.2	0.136	4	95.4	100		82.8
Sequence															
Boundary Start A							124039	95698	68.2	143347	88234	95.4			28.9
Phase A															
C_Date K2090	119925	100376	68.2	129677	90623	95.4	112330	91477	68.2	124853	80185	95.4	81.8	91.5	86.7
C_Date K2123	99050	83550	68.2	106785	75815	95.4	99168	83084	68.2	109677	72091	95.4	98.1	91.3	89.3
C_Date K2079	124477	90043	68.2	141661	72860	95.4	110550	83838	68.3	127087	68226	95.4	98.3	95.1	85
C_Date K2124	35646	28175	68.2	39374	24446	95.4	35832	27947	68.3	39223	24546	95.4			94.3
C_Date K2080	62649	55131	68.2	66399	51382	95.4	72783	58639	68.2	105223	56770	95.4	38.5	62.4	88.9
C_Date K2125	134	107	68.2	144	96	95.4	133	108	68.2	145	96	95.4			100
Interval Interval A							-4	64925	68.4	-4	81187	95.4			45.3
Boundary End A							69681	56860	68.2	105076	53868	95.4			94
Interval Interval A to B							-4	4865	68.2	-4	20819	95.4			90.9
Boundary Start B							64473	55750	68.2	84223	51168	95.4			95.

Name	Unmodelled (BP)						Modelled (BP)								
	from	to	%	from	to	%	from	to	%	from	to	%	A	P	C
															5
Phase B															
C_Date K2091	87112	75428	68.2	92939	69601	95.4	63939	49347	68.2	104876	33160	95.4	69.2	9.3	91.2
C_Date K2081	45592	39288	68.2	48735	36145	95.4	46067	38887	68.3	197885	32821	95.4	94.1	89.1	95.8
C_Date K2116	55954	49926	68.2	58961	46919	95.4	56134	49461	68.2	197786	42555	95.4	96.3	89.5	96.1
C_Date K2092	54175	48925	68.2	56793	46308	95.4	54502	48426	68.2	197886	42180	95.4	95.1	89.3	96.3
C_Date K2094	58257	50243	68.2	62254	46246	95.4	57701	49645	68.2	197876	41099	95.4	98.6	89.5	95.3
C_Date K2100	62385	57075	68.2	65033	54428	95.4	60901	54624	68.3	197832	42994	95.4	81.3	86.1	95.5
C_Date K2099	49786	43235	68.2	53052	39968	95.4	50280	42708	68.2	197823	35827	95.4	94.2	89.2	95.6
C_Date K2115	36189	32552	68.2	38000	30740	95.4	36978	33093	68.2	197137	30080	95.4	94.4	87.4	96.8
C_Date K2098	34330	30310	68.2	36330	28310	95.4	36187	31981	68.1	197880	29111	95.4	77.6	84	96.3
Interval Interval B							-4	32343	68.2	-4	43761	95.3			70.1
Boundary End B							34469	30503	68.2	104819	26893	95.4			98.1
Interval Interval B to D							-4	2611	68.2	-4	5772	95.4			91.8
Boundary Start D							32170	28385	68.2	36859	25337	95.4			97.8
Phase D															
C_Date K2117	29612	26548	68.2	31138	25023	95.4	29331	26108	68.2	32077	19602	95.4	97.4	89.6	96.8

Name	Unmodelled (BP)						Modelled (BP)								
	from	to	%	from	to	%	from	to	%	from	to	%	A	P	C
C_Date K2113	33782	29418	68.2	35957	27243	95.4	31036	26958	68.1	34404	16703	95.4	64.6	84.4	95.8
C_Date K2118	28580	25560	68.2	30085	24056	95.4	28536	25297	68.2	31486	20859	95.4	97.5	90	96.7
C_Date K2119	25618	22923	68.2	26958	21582	95.4	25838	22717	68.2	29253	18813	95.4	94.9	89.9	96.9
C_Date K2082	18618	16402	68.2	19722	15298	95.4	18988	16537	68.2	28484	14186	95.4	95.2	88.6	97.2
C_Date K2112	24731	20129	68.2	27023	17837	95.4	25808	19211	68.2	32373	12706	95.4	100.8	56.1	94.3
C_Date K2121	18245	16395	68.2	19165	15475	95.4	18638	16502	68.2	29553	14338	95.4	93.1	87.9	97.5
C_Date K2084	6438	5283	68.2	7012	4708	95.4	6433	5273	68.2	7009	4706	95.4		1.8	99.1
C_Date K2111	2296	104	68.2	3387	-987	95.4	2333	89	68.2	3387	-975	95.4		0.6	98.2
C_Date K2085	137	104	68.2	150	90	95.4	135	105	68.2	150	90	95.4		0.4	100
Interval Interval D							-4	17778	68.2	-4	23995	95.4			73.5
Boundary End D							17965	13228	68.3	18919	6565	95.4			69.4

Unit C

Name	Unmodelled (BP)						Modelled (BP)								
	from	to	%	from	to	%	from	to	%	from	to	%	A	P	C
Outlier_Model General							-364	367	68.2	-4221	4125	95.3			99.9
T(5)	-1.135	1.135	68.2	-2.65	2.65	95.4									99.4
U(0,4)	3.99E-17	4	68.2	3.99E-17	4	95.4	5.38E-17	3.74	68.3	5.38E-17	3.82	95.4	100		99.9
Sequence Sequence C															
Boundary Start C							46432	36537	68.1	59255	33655	95.4			84.3
Phase C															
C_Date K2093	39999	35041	68.2	42470	32570	95.4	39313	34442	68.3	41649	32041	95.4	99.9	95	97.5
C_Date K2114	27096	23865	68.2	28705	22255	95.4	27105	23897	68.2	28729	22421	95.4	101.7	95.2	98.3
C_Date K2130	43348	36292	68.2	46868	32773	95.4	41142	34462	68.1	44469	31424	95.4	95.1	94.9	96.3
C_Date K2131	24267	21473	68.2	25658	20083	95.4	24774	21896	68.4	26105	20486	95.4	97.9	95	98.3
C_Date K2132	29956	25544	68.2	32154	23346	95.4	30048	25507	68.1	32124	23480	95.4	100.8	95.1	97.8
C_Date K2135	1426	995	68.2	1638	783	95.4	1425	997	68.2	1639	784	95.4		3.8	99.7
Interval Interval C							14123	29673	68	10401	50182	95.4			86.3
Boundary End C							24233	16980	68.2	25686	4293	95.3			88.9

Appendix F. Additional ESR Data

Appendix F.1: Measured ESR sample values used in the DATA software

	WT01D 2493A	WT01G1 2496B	WT18 2526A	WT23F 2533A	WT23E 2534A	WT22A 2530A	WT26A 2538A	WT36A 2554A	WT13 2520A	WT14 2521A	WT10 2517A	WT17 2525A	WT01E 2494A	WT01F 2495B
De	6.53	3.62	24.23	88.91	76.51	12.26	15.28	7.31	45.48	18.41	129.36	30.87	3.91	25.77
De error (5%)	0.33	0.18	1.21	4.45	3.83	0.61	0.76	0.37	2.27	0.92	6.47	1.54	0.20	1.29
U content (ppm)	0.03	0.06	0.26	12.81	14.77	1.08	1.31	0.77	0.18	0.47	0.89	1.58	0.03	0.03
Alpha efficiency	0.13	0.13	0.13	0.13	0.13	0.13	0.13	0.13	0.13	0.13	0.13	0.13	0.13	0.13
Alpha efficiency error	0.02	0.02	0.02	0.02	0.02	0.02	0.02	0.02	0.02	0.02	0.02	0.02	0.02	0.02
U dentine 1 (ppm)	0.05	0.07	0.40	32.17	38.91	8.50	2.24	6.26	0.49	1.96	3.76	19.50	0.04	0.08
Water dentine (wgt%)	5	5	5	5	5	5	5	5	5	5	5	5	5	5
Water dentine error (wgt%)	2	2	2	2	2	2	2	2	2	2	2	2	2	2
Rn-loss (%)	0	0	0	0	0	0	0	0	0	0	0	0	0	0
total thickness (µmm)	397	391	530	420	425	413	380	453	502	437	568	392	423	445
Removed side 1 (µmm)	20	20	20	20	20	20	20	20	20	20	20	20	20	20
Removed side 2 (µmm)	20	20	20	20	20	20	20	20	20	20	20	20	20	20

	WT01D 2493A	WT01G1 2496B	WT18 2526A	WT23F 2533A	WT23E 2534A	WT22A 2530A	WT26A 2538A	WT36A 2554A	WT13 2520A	WT14 2521A	WT10 2517A	WT17 2525A	WT01E 2494A	WT01F 2495B
Density (g/cm^3)	2.99	2.99	2.99	2.99	2.99	2.99	2.99	2.99	2.99	2.99	2.99	2.99	2.99	2.99
Density error (g/cm^3)	0.07	0.07	0.07	0.07	0.07	0.07	0.07	0.07	0.07	0.07	0.07	0.07	0.07	0.07
U sediment (ppm)	0.36	0.36	0.38	0.37	0.37	0.45	0.51	0.35	0.20	0.37	0.20	0.35	0.36	0.36
Th sediment (ppm)	2.32	2.32	2.89	2.39	2.39	3.01	3.11	2.40	1.14	2.05	1.14	2.93	2.32	2.32
K sediment (%)	0.27	0.27	0.46	0.59	0.59	0.41	0.51	0.33	0.10	0.21	0.10	0.28	0.27	0.27
Water Sed (wgt%)	3	3	3	3	3	3	3	3	3	3	3	3	3	3
Water sed error (wgt%)	2	2	2	2	2	2	2	2	2	2	2	2	2	2
For β irr. only?	Yes	Yes	Yes	Yes	Yes	Yes	Yes	Yes	Yes	Yes	Yes	Yes	Yes	Yes
ext. gamma (μGy/a)	221	221	163	345	345	385	278	196	129	335	129	163	221	221
ext. gamma error (μGy/a)	3	3	3	3	3	4	3	3	2	3	2	3	3	3
Depth for cosmic (m)	0	0	0	0	0	0	0	0	0	0	0	0	0	0

Appendix F.2: All Early Uptake and Linear Uptake ESR results

Source	Sample name	Sample number	EU age (ka)	EU error (ka)	LU age (ka)	LU error (ka)
Measured	WT01D	2493A	8.0	4.0	8.0	0.4
Measured	WT01E	2494A	4.8	0.2	48.0	0.2
Measured	WT01F	2495A	31.0	1.0	31.0	1.0
Measured	WT01G1	2496A	4.4	0.2	4.4	0.2
Measured	WT10	2517A	144.0	9.0	182.0	10.0
Measured	WT13	2520A	75.0	4.0	78.0	4.0
Measured	WT14	2521A	18.8	1.0	19.9	1.0
Measured	WT17	2525A	23.0	1.3	29.2	1.6
Measured	WT18	2526A	8.3	1.6	12.8	2.5
Measured	WT22A	2530A	9.1	0.4	10.1	0.5
Measured	WT23F	2533A	24.9	2.3	38.0	3.0
Measured	WT23E	2534A	19.9	1.8	31.0	2.0
Measured	WT26A	2538A	12.3	0.6	13.4	0.7
Measured	WT36A	2554A	7.4	0.4	8.1	0.4
Extrapolated	WT01A	2490A	21.4	2.1	21.9	2.2
Extrapolated	WT01B	2491A	16.2	1.8	16.4	1.8
Extrapolated	WT01B	2491B	5.3	0.5	5.3	0.5
Extrapolated	WT01C	2492A	8.6	0.8	8.6	0.8
Extrapolated	WT01D	2493A	3.6	0.3	3.6	0.3
Extrapolated	WT01E	2494A	5.0	0.5	5.0	0.5
Extrapolated	WT01F	2495A	12.7	1.2	12.8	1.2
Extrapolated	WT01F	2495B	25.1	2.5	25.2	2.5
Extrapolated	WT01G1	2496A	4.0	0.4	4.1	1.4
Extrapolated	WT01G1	2496B	3.1	0.3	3.1	0.3
Extrapolated	WT02J	2508A	5.8	0.5	5.8	0.5
Extrapolated	WT02J	2508B	2.9	0.3	3.2	0.3
Extrapolated	WT02K	2509A	4.6	0.4	4.6	0.4
Extrapolated	WT02K	2509B	3.0	0.3	3.1	0.3
Extrapolated	WT02L	2510A	4.7	0.4	4.7	0.4
Extrapolated	WT02M	2511A	3.8	0.3	3.8	0.3
Extrapolated	WT02M	2511B	4.4	0.4	4.5	0.4
Extrapolated	WT03	2512A	23.2	2.3	29.7	3.0
Extrapolated	WT06	2513A	25.8	2.6	30.0	3.0
Extrapolated	WT07	2514A	28.0	3.0	30.0	3.0
Extrapolated	WT08	2515A	9.9	1.0	10.4	1.1

Source	Sample name	Sample number	EU age (ka)	EU error (ka)	LU age (ka)	LU error (ka)
Extrapolated	WT09	2516A	57.0	5.0	62.0	6.0
Extrapolated	WT10	2517A	66.0	7.0	80.0	8.0
Extrapolated	WT11	2518A	65.0	6.0	69.0	6.0
Extrapolated	WT12	2519A	83.0	8.0	86.0	8.0
Extrapolated	WT13	2520A	55.0	5.0	58.0	5.0
Extrapolated	WT14	2521A	22.9	2.3	24.3	2.4
Extrapolated	WT15	2522A	28.1	2.8	30.3	3.0
Extrapolated	WT16A	2524A	13.6	1.5	19.1	2.0
Extrapolated	WT17	2525A	26.1	2.7	33.0	3.0
Extrapolated	WT18	2526A	29.3	2.9	30.0	3.0
Extrapolated	WT19A	2527A	41.0	4.0	42.0	4.0
Extrapolated	WT20B	2528A	31.0	3.0	43.0	4.0
Extrapolated	WT21	2529A	32.0	3.0	36.0	3.0
Extrapolated	WT22A	2530A	12.8	1.3	14.3	1.4
Extrapolated	WT23A	2531A	42.0	5.0	66.0	8.0
Extrapolated	WT23C	2532A	47.0	6.0	74.0	9.0
Extrapolated	WT23F	2533A	24.7	3.1	38.0	4.0
Extrapolated	WT23E	2534A	21.2	2.6	33.0	3.0
Extrapolated	WT23G	2535A	20.2	2.4	29.5	3.3
Extrapolated	WT23M	2536A	33.0	3.0	47.0	5.0
Extrapolated	WT24B	2537A	9.1	1.1	13.5	1.5
Extrapolated	WT26A	2538A	13.7	1.4	15.1	1.5
Extrapolated	WT26B	2539A	8.5	1.0	11.6	1.2
Extrapolated	WT27A	2540A	8.3	0.8	10.9	1.1
Extrapolated	WT28A	2542A	6.7	0.6	8.4	0.8
Extrapolated	WT28C	2544A	4.4	0.5	6.3	0.6
Extrapolated	WT28D	2545A	4.6	0.5	6.6	0.7
Extrapolated	WT23B	2546A	138.0	14.0	186.0	19.0
Extrapolated	WT31	2547A	8.6	0.9	11.0	1.1
Extrapolated	WT32	2548A	4.8	0.5	6.3	0.6
Extrapolated	WT33	2549A	23.0	2.5	29.5	3.0
Extrapolated	WT34A	2550A	7.6	0.7	9.0	0.9
Extrapolated	WT34B	2551A	6.8	0.7	9.4	0.9
Extrapolated	WT34C	2552A	4.4	0.4	5.5	0.5
Extrapolated	WT35	2553A	26.9	2.7	31.0	3.0
Extrapolated	WT36A	2554A	8.2	0.8	9.1	0.9
Extrapolated	WT36B	2555A	6.7	0.6	7.8	0.7

Appendix G. Additional OSL data

Appendix G.1. Recycling ratios and recuperation in OSL aliquots.

Sample	Risø	Aliquot	Final D_e	Recyc ratio	Recyc error	Recyc. fractional dose offset	L_N/T_N	L_X/T_X (zero dose)	% Recoup.	Recup. fractional dose offset
K2079	A	1	191.43	1.00	0.04	0.41	11.67	0.038	0.33%	-0.11
K2079	A	5	12.88	1.00	0.03	-0.91	2.65	0.002	0.08%	-0.79
K2079	A	7	74.15	1.06	0.05	-0.45	8.35	0.020	0.24%	-0.34
K2079	A	9	180.89	1.03	0.04	0.33	14.35	0.028	0.20%	-0.47
K2079	A	11	107.91	0.98	0.04	-0.21	11.03	0.027	0.24%	-0.33
K2079	A	13	162.74	1.05	0.05	0.20	13.01	0.122	0.94%	1.57
K2079	A	15	189.28	0.99	0.04	0.39	14.88	0.035	0.24%	-0.36
K2079	A	17	246.45	1.03	0.04	0.81	17.07	0.025	0.15%	-0.60
K2079	A	19	52.69	0.98	0.04	-0.61	7.51	0.028	0.37%	0.02
K2079	A	23	96.59	1.05	0.04	-0.29	9.47	0.020	0.21%	-0.42
K2079	A	27	58.93	1.10	0.04	-0.57	9.32	0.139	1.49%	3.09
K2079	A	29	69.66	1.01	0.03	-0.49	9.97	0.038	0.38%	0.04
K2079	A	31	253.48	0.93	0.04	0.86	19.85	0.016	0.08%	-0.78
K2079	A	35	207.54	1.03	0.04	0.53	13.39	0.023	0.17%	-0.53
K2080	A	1	98.74	1.06	0.04	0.18	10.00	0.013	0.13%	-0.55
K2080	A	3	51.52	1.09	0.04	-0.39	8.45	0.017	0.20%	-0.31
K2080	A	5	61.86	0.98	0.03	-0.26	8.61	0.020	0.23%	-0.20
K2080	A	7	57.37	1.03	0.04	-0.32	7.94	0.027	0.34%	0.17
K2080	A	9	49.95	0.95	0.07	-0.40	7.05	0.006	0.09%	-0.71
K2080	A	11	115.91	1.07	0.04	0.38	11.18	0.024	0.21%	-0.26
K2080	A	13	44.69	1.11	0.06	-0.47	8.26	0.042	0.51%	0.75
K2080	A	15	78.84	1.04	0.03	-0.06	9.72	0.016	0.16%	-0.43
K2080	A	17	66.15	1.01	0.03	-0.21	7.71	0.041	0.53%	0.83
K2080	A	19	50.92	1.09	0.04	-0.39	7.63	0.038	0.50%	0.71
K2080	A	21	139.72	1.03	0.04	0.67	14.34	0.074	0.52%	0.77
K2080	A	23	103.81	1.01	0.04	0.24	7.13	0.016	0.22%	-0.23
K2080	A	25	67.13	1.02	0.03	-0.20	7.94	0.026	0.33%	0.13
K2080	A	27	73.18	1.00	0.04	-0.13	7.16	0.024	0.34%	0.15
K2080	A	29	71.23	1.01	0.03	-0.15	8.79	0.031	0.35%	0.21
K2080	A	31	223.43	1.01	0.03	1.66	15.87	0.027	0.17%	-0.42
K2080	A	33	72.79	1.05	0.04	-0.13	9.05	0.014	0.15%	-0.47
K2080	A	35	82.74	1.10	0.04	-0.01	10.05	0.025	0.25%	-0.14
K2081	A	1	52.78	0.99	0.03	-0.05	7.13	0.010	0.14%	-0.55
K2081	A	3	55.22	1.02	0.03	-0.01	7.25	0.057	0.79%	1.55
K2081	A	5	69.37	0.97	0.04	0.24	8.44	0.012	0.14%	-0.54
K2081	A	7	54.35	0.99	0.04	-0.03	6.31	0.011	0.17%	-0.43
K2081	A	9	45.08	0.99	0.03	-0.19	7.07	0.019	0.27%	-0.13
K2081	A	11	57.37	1.00	0.04	0.03	7.02	0.018	0.26%	-0.17
K2081	A	13	36.10	1.02	0.04	-0.35	6.08	0.037	0.61%	0.97
K2081	A	15	36.39	0.98	0.04	-0.35	5.77	0.018	0.31%	0.01
K2081	A	17	67.52	0.96	0.03	0.21	8.70	0.013	0.15%	-0.52
K2081	A	19	47.61	0.98	0.04	-0.15	5.90	0.039	0.66%	1.14
K2081	A	21	40.98	1.03	0.04	-0.27	6.85	0.023	0.34%	0.09
K2081	A	23	74.54	0.97	0.03	0.34	8.36	0.022	0.26%	-0.15
K2081	A	25	57.57	0.99	0.03	0.03	8.29	0.013	0.16%	-0.49
K2081	A	27	42.59	0.96	0.10	-0.24	6.08	0.032	0.53%	0.71
K2081	A	29	49.37	0.96	0.03	-0.12	7.94	0.014	0.18%	-0.43

Sample	Risø	Aliquot	Final D_e	Recyc ratio	Recyc error	Recyc. fractional dose offset	L_N/T_N	L_X/T_X (zero dose)	% Recoup.	Recup. fractional dose offset
K2081	A	31	60.20	0.96	0.03	0.08	7.12	0.020	0.28%	-0.09
K2081	A	33	61.47	1.00	0.04	0.10	6.90	0.007	0.10%	-0.67
K2081	A	35	96.40	1.01	0.04	0.73	13.73	0.029	0.21%	-0.32
K2082	A	1	18.15	0.97	0.04	0.05	3.45	0.011	0.32%	-0.83
K2082	A	3	8.46	1.06	0.04	-0.51	1.54	0.417	27.08%	13.34
K2082	A	5	16.14	0.97	0.04	-0.07	3.25	0.016	0.49%	-0.74
K2082	A	7	18.85	1.00	0.04	0.09	3.67	0.012	0.33%	-0.83
K2082	A	9	12.72	0.97	0.05	-0.26	2.60	0.028	1.08%	-0.43
K2082	A	11	20.79	0.95	0.05	0.20	4.06	0.011	0.27%	-0.86
K2082	A	13	15.59	0.99	0.04	-0.10	3.26	0.022	0.67%	-0.64
K2082	A	15	20.48	1.03	0.05	0.19	3.64	0.002	0.05%	-0.97
K2082	A	17	15.75	1.05	0.04	-0.09	3.18	0.016	0.50%	-0.73
K2082	A	19	20.25	1.06	0.05	0.17	3.56	0.003	0.08%	-0.96
K2082	A	21	17.38	1.03	0.05	0.01	3.68	0.007	0.19%	-0.90
K2082	A	23	15.90	1.00	0.05	-0.08	3.16	0.010	0.32%	-0.83
K2082	A	25	14.66	0.99	0.05	-0.15	3.01	0.011	0.37%	-0.81
K2082	A	27	21.88	1.06	0.04	0.27	3.98	0.009	0.23%	-0.88
K2082	A	29	15.44	1.00	0.05	-0.11	3.08	0.024	0.78%	-0.59
K2082	A	31	19.63	1.07	0.04	0.14	3.71	0.022	0.59%	-0.69
K2082	A	33	17.45	1.02	0.05	0.01	3.44	0.014	0.41%	-0.78
K2082	A	35	21.25	1.02	0.05	0.23	4.11	0.009	0.22%	-0.88
K2083	B	1	0.37	0.87	0.05	1.41	6.16	0.077	1.25%	-0.90
K2083	B	2	0.07	1.05	0.07	-0.53	1.31	0.250	19.08%	0.54
K2083	B	4	0.07	0.87	0.13	-0.57	1.20	-0.054	4.50%	-0.64
K2083	B	5	0.06	1.02	0.12	-0.59	1.15	0.394	34.26%	1.77
K2083	B	6	0.34	0.83	0.12	1.22	6.10	0.241	3.95%	-0.68
K2083	B	7	0.14	1.22	0.18	-0.11	2.51	0.609	24.26%	0.96
K2083	B	8	0.06	0.96	0.16	-0.62	0.92	0.117	12.72%	0.03
K2083	B	13	0.23	1.04	0.12	0.48	3.96	0.123	3.11%	-0.75
K2083	B	15	0.13	1.03	0.18	-0.15	2.39	0.143	5.98%	-0.52
K2083	B	16	0.14	0.85	0.14	-0.06	2.42	0.045	1.86%	-0.85
K2083	B	18	0.08	0.97	0.15	-0.47	1.45	0.364	25.10%	1.03
K2084	A	1	5.42	0.96	0.06	0.32	5.86	-0.019	0.32%	-0.25
K2084	A	3	3.58	0.99	0.07	-0.13	3.78	0.012	0.32%	-0.27
K2084	A	5	4.72	1.03	0.06	0.15	4.98	-0.010	0.20%	-0.54
K2084	A	7	3.33	1.06	0.05	-0.19	3.61	0.009	0.25%	-0.42
K2084	A	9	2.34	1.02	0.06	-0.43	2.69	-0.003	0.11%	-0.74
K2084	A	11	5.37	1.10	0.06	0.31	5.61	0.025	0.45%	0.03
K2084	A	13	7.66	1.02	0.04	0.87	7.66	0.014	0.18%	-0.58
K2084	A	15	2.97	1.11	0.08	-0.28	3.33	-0.015	0.45%	0.04
K2084	A	17	4.43	1.05	0.05	0.08	4.69	0.003	0.06%	-0.85
K2084	A	19	4.43	1.04	0.06	0.08	4.86	0.022	0.45%	0.05
K2084	A	21	6.22	0.94	0.04	0.52	6.61	0.034	0.51%	0.19
K2084	A	23	3.33	1.01	0.05	-0.19	3.64	0.025	0.69%	0.59
K2084	A	25	3.98	1.11	0.05	-0.03	4.32	0.026	0.60%	0.39
K2084	A	27	1.97	0.99	0.06	-0.52	2.20	0.016	0.73%	0.68
K2084	A	29	4.04	1.01	0.04	-0.01	4.51	0.025	0.55%	0.28
K2084	A	31	3.98	1.02	0.05	-0.03	4.18	0.030	0.72%	0.66
K2084	A	33	1.61	0.97	0.05	-0.61	1.82	0.019	1.04%	1.41
K2084	A	35	4.44	1.00	0.05	0.08	4.76	-0.007	0.15%	-0.66

Sample	Risø	Aliquot	Final D_e	Recyc ratio	Recyc error	Recyc. fractional dose offset	L_N/T_N	L_X/T_X (zero dose)	% Recoup.	Recup. fractional dose offset
K2085	B	1	0.20	0.96	0.04	0.00	0.40	0.030	7.50%	0.10
K2085	B	2	0.14	1.13	0.08	-0.30	0.28	0.049	17.50%	1.57
K2085	B	3	0.13	0.90	0.06	-0.32	0.30	0.047	15.67%	1.30
K2085	B	4	0.17	0.99	0.04	-0.15	0.35	0.011	3.14%	-0.54
K2085	B	5	0.17	0.93	0.05	-0.13	0.36	0.023	6.39%	-0.06
K2085	B	7	0.17	0.99	0.05	-0.15	0.34	0.011	3.24%	-0.52
K2085	B	9	0.15	0.86	0.06	-0.24	0.31	0.030	9.68%	0.42
K2085	B	10	0.15	1.01	0.05	-0.21	0.32	0.009	2.81%	-0.59
K2085	B	11	0.14	1.10	0.06	-0.31	0.29	0.002	0.69%	-0.90
K2085	B	12	0.17	1.07	0.07	-0.13	0.35	0.011	3.14%	-0.54
K2085	B	13	0.15	0.98	0.05	-0.24	0.31	0.018	5.81%	-0.15
K2085	B	14	0.16	1.06	0.05	-0.20	0.33	0.032	9.70%	0.43
K2085	B	15	0.11	1.03	0.05	-0.43	0.24	0.032	13.33%	0.96
K2085	B	16	0.14	1.01	0.04	-0.27	0.31	0.000	0.00%	-1.00
K2085	B	17	0.29	1.17	0.08	0.46	0.60	0.035	5.83%	-0.14
K2085	B	18	0.72	1.05	0.06	2.65	0.32	-0.014	4.38%	-0.36
K2086	B	1	0.11	0.91	0.16	-0.23	1.83	0.275	15.03%	0.72
K2086	B	3	0.08	0.97	0.22	-0.40	1.47	-0.184	12.52%	0.44
K2086	B	4	0.13	0.82	0.16	-0.09	2.41	0.147	6.10%	-0.30
K2086	B	5	0.07	1.27	0.20	-0.51	1.13	0.206	18.23%	1.09
K2086	B	6	0.04	1.11	0.12	-0.74	0.64	0.121	18.91%	1.17
K2086	B	7	0.15	1.06	0.25	0.06	2.63	0.133	5.06%	-0.42
K2086	B	11	0.03	1.16	0.21	-0.75	0.76	-0.004	0.53%	-0.94
K2086	B	12	0.08	0.98	0.12	-0.41	1.52	0.147	9.67%	0.11
K2086	B	13	0.36	1.03	0.11	1.58	5.61	0.211	3.76%	-0.57
K2086	B	15	0.03	0.97	0.12	-0.79	0.50	0.009	1.80%	-0.79
K2086	B	18	0.46	1.05	0.19	2.28	7.81	0.336	4.30%	-0.51
K2087	B	2	0.12	1.14	0.31	1.34	1.91	0.171	8.95%	-0.64
K2087	B	4	0.07	0.90	0.11	0.37	1.29	0.258	20.00%	-0.20
K2087	B	5	0.03	1.26	0.20	-0.38	0.67	0.180	26.87%	0.07
K2087	B	6	0.03	0.82	0.09	-0.33	0.72	0.203	28.19%	0.13
K2087	B	7	0.06	0.88	0.20	0.14	1.15	0.282	24.52%	-0.02
K2087	B	10	0.05	0.86	0.08	-0.05	0.79	0.133	16.84%	-0.33
K2087	B	11	0.03	1.04	0.19	-0.37	0.59	0.149	25.25%	0.01
K2087	B	12	0.01	1.09	0.23	-0.72	0.29	0.144	49.66%	0.98
K2088	B	2	0.11	0.87	0.09	-0.10	1.83	0.189	10.33%	0.38
K2088	B	7	0.07	0.97	0.20	-0.41	1.49	0.154	10.34%	0.38
K2088	B	12	0.14	0.88	0.10	0.16	2.33	0.067	2.88%	-0.62
K2088	B	13	0.09	0.98	0.11	-0.27	1.47	0.103	7.01%	-0.06
K2088	B	14	0.20	0.80	0.10	0.69	3.26	0.206	6.32%	-0.16
K2088	B	15	0.11	1.11	0.15	-0.06	1.72	0.138	8.02%	0.07
K2090	A	1	179.26	0.97	0.04	0.24	19.25	0.036	0.19%	0.01
K2090	A	3	118.67	0.98	0.04	-0.18	13.42	0.015	0.11%	-0.40
K2090	A	5	104.63	1.05	0.04	-0.28	11.83	0.018	0.15%	-0.18
K2090	A	9	117.90	1.01	0.04	-0.18	14.62	0.035	0.24%	0.29
K2090	A	11	104.44	0.99	0.03	-0.28	10.85	0.079	0.73%	2.92
K2090	A	13	104.25	0.99	0.03	-0.28	13.05	0.023	0.18%	-0.05
K2090	A	15	122.14	0.98	0.04	-0.15	14.43	0.012	0.08%	-0.55
K2090	A	17	124.25	1.00	0.04	-0.14	11.35	0.005	0.04%	-0.76
K2090	A	19	98.29	1.07	0.04	-0.32	11.40	0.040	0.35%	0.89

Sample	Risø	Aliquot	Final D_e	Recyc ratio	Recyc error	Recyc. fractional dose offset	L_N/T_N	L_X/T_X (zero dose)	% Recoup.	Recup. fractional dose offset
K2090	A	21	180.22	0.99	0.04	0.25	17.19	0.043	0.25%	0.35
K2090	A	23	255.42	0.99	0.04	0.77	26.03	0.019	0.07%	-0.61
K2090	A	25	109.06	0.96	0.03	-0.25	13.58	0.015	0.11%	-0.41
K2090	A	27	149.06	0.98	0.04	0.03	17.28	0.043	0.25%	0.34
K2090	A	29	145.60	0.98	0.04	0.01	16.85	0.014	0.08%	-0.55
K2090	A	31	200.99	0.98	0.04	0.39	19.14	0.030	0.16%	-0.16
K2090	A	33	234.46	1.01	0.04	0.62	23.07	0.016	0.07%	-0.63
K2090	A	35	107.13	1.02	0.03	-0.26	14.61	0.014	0.10%	-0.48
K2091	A	1	86.75	0.97	0.04	-0.22	10.31	0.040	0.39%	-0.05
K2091	A	3	120.41	1.00	0.04	0.08	8.79	0.011	0.13%	-0.69
K2091	A	5	98.86	1.01	0.03	-0.11	16.77	0.027	0.16%	-0.61
K2091	A	7	86.36	1.04	0.04	-0.22	10.25	0.032	0.31%	-0.24
K2091	A	9	70.20	0.99	0.03	-0.37	11.77	0.016	0.14%	-0.67
K2091	A	11	162.91	0.99	0.03	0.47	16.99	0.014	0.08%	-0.80
K2091	A	13	53.09	0.91	0.03	-0.52	8.56	0.342	4.00%	8.76
K2091	A	15	97.71	1.03	0.04	-0.12	9.56	0.012	0.13%	-0.69
K2091	A	17	76.94	1.03	0.04	-0.31	11.48	0.023	0.20%	-0.51
K2091	A	19	125.41	0.96	0.04	0.13	17.77	0.028	0.16%	-0.62
K2091	A	21	240.04	0.96	0.04	1.16	20.18	0.034	0.17%	-0.59
K2091	A	23	74.24	1.05	0.04	-0.33	10.01	0.013	0.13%	-0.68
K2091	A	25	107.52	1.06	0.04	-0.03	13.01	0.021	0.16%	-0.61
K2091	A	27	97.52	0.93	0.04	-0.12	13.21	0.021	0.16%	-0.61
K2091	A	29	174.65	1.03	0.04	0.57	18.98	0.012	0.06%	-0.85
K2091	A	31	94.05	1.04	0.04	-0.15	13.76	0.096	0.70%	0.70
K2091	A	33	91.36	1.04	0.04	-0.18	11.20	0.012	0.11%	-0.74
K2091	A	35	141.95	1.07	0.04	0.28	11.40	0.023	0.20%	-0.51
K2092	A	1	51.45	0.96	0.03	-0.17	8.62	0.008	0.09%	-0.72
K2092	A	3	48.18	1.02	0.04	-0.23	8.60	0.015	0.17%	-0.47
K2092	A	5	52.80	1.03	0.04	-0.15	7.89	0.015	0.19%	-0.42
K2092	A	7	46.74	1.01	0.04	-0.25	7.47	0.004	0.05%	-0.84
K2092	A	9	53.37	1.01	0.03	-0.14	7.17	0.011	0.22%	-0.33
K2092	A	11	59.72	1.02	0.04	-0.04	7.82	0.220	2.81%	7.62
K2092	A	13	47.22	0.95	0.04	-0.24	7.44	0.024	0.32%	-0.01
K2092	A	15	103.48	0.93	0.04	0.66	12.73	0.008	0.06%	-0.81
K2092	A	17	57.70	0.97	0.04	-0.07	9.21	0.005	0.05%	-0.83
K2092	A	19	105.79	1.07	0.04	0.70	15.48	0.052	0.34%	0.03
K2092	A	21	62.03	0.97	0.03	0.00	9.84	0.006	0.06%	-0.81
K2092	A	23	54.05	1.00	0.04	-0.13	8.06	0.019	0.24%	-0.28
K2092	A	25	40.87	1.02	0.04	-0.34	6.96	0.030	0.43%	0.32
K2092	A	27	38.85	1.02	0.04	-0.38	7.41	0.008	0.11%	-0.67
K2092	A	29	46.45	1.01	0.04	-0.25	7.31	0.027	0.37%	0.13
K2092	A	31	81.46	0.94	0.03	0.31	9.20	0.009	0.10%	-0.70
K2092	A	33	92.52	0.96	0.05	0.48	11.07	0.012	0.11%	-0.67
K2092	A	35	78.86	1.02	0.03	0.27	10.69	0.015	0.14%	-0.57
K2093	A	1	82.90	0.94	0.03	-0.15	9.47	0.025	0.26%	-0.04
K2093	A	3	117.52	0.95	0.04	0.21	14.37	0.046	0.32%	0.16
K2093	A	5	100.79	1.00	0.03	0.04	11.17	0.014	0.13%	-0.55
K2093	A	7	69.05	1.04	0.04	-0.29	9.37	0.013	0.14%	-0.50
K2093	A	9	69.05	1.05	0.04	-0.29	9.27	0.010	0.11%	-0.61
K2093	A	11	156.57	1.06	0.04	0.61	13.25	0.023	0.17%	-0.37

Sample	Risø	Aliquot	Final D_e	Recyc ratio	Recyc error	Recyc. fractional dose offset	L_N/T_N	L_X/T_X (zero dose)	% Recoup.	Recup. fractional dose offset
K2093	A	13	109.44	1.04	0.04	0.12	14.91	0.026	0.17%	-0.37
K2093	A	15	122.52	1.03	0.04	0.26	12.51	0.020	0.16%	-0.42
K2093	A	17	88.28	1.04	0.04	-0.09	12.69	0.018	0.14%	-0.49
K2093	A	19	86.36	1.05	0.04	-0.11	12.18	0.056	0.46%	0.67
K2093	A	21	77.51	1.09	0.04	-0.20	9.89	0.066	0.67%	1.42
K2093	A	23	65.59	1.04	0.04	-0.33	8.73	0.019	0.22%	-0.21
K2093	A	25	86.55	1.01	0.04	-0.11	11.24	0.005	0.04%	-0.84
K2093	A	27	63.28	1.02	0.04	-0.35	9.24	0.023	0.25%	-0.10
K2093	A	29	129.83	0.98	0.03	0.33	15.84	0.014	0.09%	-0.68
K2093	A	31	91.36	1.02	0.06	-0.06	13.50	0.153	1.13%	3.11
K2093	A	33	154.83	1.02	0.04	0.59	15.47	0.032	0.21%	-0.25
K2093	A	35	80.98	0.96	0.03	-0.17	13.08	0.038	0.29%	0.05
K2094	A	1	32.69	1.03	0.04	-0.19	5.86	0.020	0.34%	-0.18
K2094	A	3	39.22	1.03	0.05	-0.03	3.78	0.000	0.00%	-1.00
K2094	A	5	26.61	1.02	0.04	-0.34	4.98	0.035	0.70%	0.69
K2094	A	7	47.14	1.00	0.04	0.17	3.61	0.007	0.19%	-0.53
K2094	A	9	39.80	0.99	0.04	-0.01	2.69	0.010	0.37%	-0.10
K2094	A	11	51.67	1.03	0.04	0.28	5.61	-0.007	0.12%	-0.70
K2094	A	13	31.20	1.05	0.04	-0.23	7.66	0.028	0.37%	-0.12
K2094	A	15	28.39	1.06	0.04	-0.30	3.33	0.020	0.60%	0.45
K2094	A	19	44.16	1.01	0.04	0.10	4.69	0.009	0.19%	-0.54
K2094	A	21	32.80	1.05	0.04	-0.19	4.86	0.013	0.27%	-0.35
K2094	A	23	46.11	1.01	0.06	0.14	6.61	0.021	0.32%	-0.23
K2094	A	25	51.61	1.00	0.03	0.28	3.64	-0.004	0.11%	-0.74
K2094	A	27	71.28	1.01	0.05	0.77	4.32	0.014	0.32%	-0.22
K2094	A	29	31.20	1.02	0.08	-0.23	2.20	0.054	2.45%	4.92
K2094	A	31	32.23	1.03	0.04	-0.20	4.51	0.010	0.22%	-0.47
K2094	A	33	46.28	1.02	0.04	0.15	4.18	0.017	0.41%	-0.02
K2094	A	35	32.60	0.97	0.04	-0.19	1.82	-0.001	0.05%	-0.87
K2095	B	1	0.16	1.46	0.54	1.39	4.76	-0.072	1.51%	-0.88
K2095	B	2	0.04	1.32	0.27	-0.41	0.92	0.083	9.02%	-0.28
K2095	B	5	0.06	0.77	0.17	-0.03	1.12	0.150	13.39%	0.08
K2095	B	7	0.05	1.03	0.11	-0.25	0.84	-0.012	1.43%	-0.89
K2095	B	8	0.07	0.91	0.23	-0.01	1.03	0.244	23.69%	0.90
K2095	B	10	0.06	1.10	0.14	-0.02	1.09	0.287	26.33%	1.11
K2095	B	12	0.05	0.89	0.09	-0.26	0.85	0.121	14.24%	0.14
K2095	B	15	0.06	0.86	0.12	-0.02	1.12	0.135	12.05%	-0.03
K2095	B	17	0.07	1.19	0.22	-0.01	1.18	0.138	11.69%	-0.06
K2095	B	18	0.04	1.30	0.22	-0.38	0.82	0.092	11.22%	-0.10
K2096	B	1	0.04	0.80	0.10	-0.44	0.57	0.154	27.02%	0.07
K2096	B	2	0.04	1.00	0.11	-0.30	0.88	0.129	14.66%	-0.42
K2096	B	3	0.05	0.88	0.11	-0.26	0.84	-0.037	4.40%	-0.83
K2096	B	4	0.05	0.79	0.15	-0.25	0.84	0.327	38.93%	0.54
K2096	B	6	0.04	1.03	0.16	-0.44	0.59	0.206	34.92%	0.38
K2096	B	9	0.06	1.13	0.16	-0.01	1.05	0.302	28.76%	0.14
K2096	B	11	0.06	1.01	0.21	0.00	1.10	0.865	78.64%	2.11
K2096	B	12	0.03	1.15	0.09	-0.48	0.59	0.122	20.68%	-0.18
K2096	B	14	0.23	1.24	0.15	2.65	4.17	0.053	1.27%	-0.95
K2096	B	16	0.04	0.94	0.13	-0.33	0.74	0.070	9.46%	-0.63
K2096	B	17	0.05	1.32	0.24	-0.14	1.02	0.197	19.31%	-0.24

Sample	Risø	Aliquot	Final D_e	Recyc ratio	Recyc error	Recyc. fractional dose offset	L_N/T_N	L_X/T_X (zero dose)	% Recoup.	Recup. fractional dose offset
K2097	B	1	27.29	1.04	0.04	5.19	21.77	0.011	0.05%	-0.93
K2097	B	2	2.99	1.08	0.04	-0.32	3.11	0.014	0.45%	-0.34
K2097	B	3	2.03	1.00	0.04	-0.54	2.09	0.011	0.53%	-0.22
K2097	B	5	1.45	0.99	0.04	-0.67	1.55	0.006	0.39%	-0.43
K2097	B	6	1.76	0.95	0.05	-0.60	1.91	0.002	0.10%	-0.85
K2097	B	8	1.41	1.01	0.04	-0.68	1.48	0.005	0.34%	-0.50
K2097	B	9	3.46	0.91	0.07	-0.21	3.37	0.005	0.15%	-0.78
K2097	B	10	3.55	1.01	0.04	-0.19	3.56	0.004	0.11%	-0.83
K2097	B	11	0.44	0.98	0.06	-0.90	0.59	0.034	5.76%	7.51
K2097	B	12	1.10	0.92	0.08	-0.75	1.29	0.002	0.16%	-0.77
K2097	B	13	1.35	0.97	0.05	-0.69	1.44	0.009	0.63%	-0.08
K2097	B	14	1.39	0.98	0.05	-0.68	1.52	-0.005	0.33%	-0.51
K2097	B	15	2.89	0.95	0.04	-0.35	2.90	0.023	0.79%	0.17
K2097	B	16	4.00	1.07	0.05	-0.09	4.06	0.009	0.22%	-0.67
K2097	B	18	11.03	1.04	0.04	1.50	10.72	0.017	0.16%	-0.77
K2098	B	1	31.11	0.99	0.03	-0.04	5.13	0.028	0.55%	-0.10
K2098	B	2	26.89	1.01	0.04	-0.17	4.34	-0.012	0.28%	-0.55
K2098	B	3	30.30	1.01	0.04	-0.07	4.96	0.176	3.55%	4.84
K2098	B	4	26.69	1.02	0.04	-0.18	4.28	0.011	0.26%	-0.58
K2098	B	5	45.12	0.94	0.04	0.39	4.86	0.002	0.04%	-0.93
K2098	B	6	28.81	1.06	0.04	-0.11	5.24	0.018	0.34%	-0.43
K2098	B	7	36.16	0.98	0.03	0.12	5.74	0.006	0.10%	-0.83
K2098	B	8	37.98	0.97	0.03	0.17	5.04	0.015	0.30%	-0.51
K2098	B	9	32.60	1.03	0.04	0.01	5.25	0.005	0.10%	-0.84
K2098	B	10	35.96	1.01	0.03	0.11	5.70	0.007	0.12%	-0.80
K2098	B	11	31.62	1.02	0.04	-0.02	5.28	0.045	0.85%	0.40
K2098	B	12	30.92	1.00	0.03	-0.05	5.49	0.051	0.93%	0.53
K2098	B	13	28.42	1.00	0.03	-0.12	4.51	0.049	1.09%	0.79
K2098	B	14	33.92	0.99	0.04	0.05	5.05	0.009	0.18%	-0.71
K2098	B	15	31.68	0.99	0.03	-0.02	5.06	0.015	0.30%	-0.51
K2098	B	16	41.88	0.99	0.04	0.29	6.15	0.009	0.15%	-0.76
K2098	B	17	22.91	1.01	0.03	-0.29	3.89	0.010	0.26%	-0.58
K2098	B	18	30.69	1.03	0.04	-0.05	5.06	0.079	1.56%	1.57
K2099	B	1	25.61	1.03	0.03	-0.25	4.48	0.018	0.40%	0.02
K2099	B	2	30.70	1.03	0.04	-0.10	5.16	0.016	0.31%	-0.21
K2099	B	3	29.81	0.96	0.03	-0.13	5.24	0.057	1.09%	1.77
K2099	B	4	53.02	1.01	0.03	0.56	7.49	0.017	0.23%	-0.42
K2099	B	5	31.81	0.97	0.03	-0.07	5.68	0.019	0.33%	-0.15
K2099	B	6	34.34	1.03	0.04	0.01	5.86	0.028	0.48%	0.22
K2099	B	7	29.74	0.98	0.03	-0.13	5.20	0.025	0.48%	0.22
K2099	B	8	36.79	0.96	0.03	0.08	5.71	0.011	0.19%	-0.51
K2099	B	9	43.60	0.96	0.03	0.28	6.46	0.012	0.19%	-0.53
K2099	B	10	28.58	1.06	0.04	-0.16	4.46	0.021	0.47%	0.20
K2099	B	11	28.07	0.99	0.03	-0.18	4.92	0.009	0.18%	-0.53
K2099	B	12	36.80	1.01	0.03	0.08	6.03	0.011	0.18%	-0.54
K2099	B	13	34.41	0.96	0.03	0.01	6.26	0.019	0.30%	-0.23
K2099	B	14	34.78	1.10	0.04	0.02	5.11	0.009	0.18%	-0.55
K2099	B	15	38.04	1.02	0.03	0.12	5.61	0.011	0.20%	-0.50
K2099	B	16	33.68	1.01	0.03	-0.01	5.51	0.020	0.36%	-0.08
K2099	B	17	36.43	1.01	0.04	0.07	6.19	0.018	0.29%	-0.26

Sample	Risø	Aliquot	Final D_e	Recyc ratio	Recyc error	Recyc. fractional dose offset	L_N/T_N	L_X/T_X (zero dose)	% Recoup.	Recup. fractional dose offset
K2099	B	18	27.24	1.01	0.03	-0.20	4.54	0.055	1.21%	2.08
K2100	A	1	56.20	0.97	0.05	0.11	9.28	0.083	0.89%	3.27
K2100	A	3	56.66	0.98	0.04	0.12	7.00	0.011	0.16%	-0.25
K2100	A	5	52.85	1.01	0.03	0.05	7.88	0.019	0.24%	0.15
K2100	A	7	38.08	1.00	0.04	-0.25	6.25	0.007	0.11%	-0.47
K2100	A	9	47.43	1.05	0.04	-0.06	7.61	0.001	0.01%	-0.94
K2100	A	11	39.24	1.00	0.04	-0.22	6.33	0.007	0.11%	-0.47
K2100	A	13	44.20	0.99	0.04	-0.13	7.13	0.004	0.06%	-0.73
K2100	A	15	51.59	0.93	0.03	0.02	7.17	0.028	0.39%	0.86
K2100	A	17	50.09	1.01	0.04	-0.01	7.68	0.011	0.14%	-0.32
K2100	A	19	75.36	0.93	0.05	0.49	7.84	0.005	0.06%	-0.70
K2100	A	21	44.66	1.04	0.05	-0.12	7.34	0.039	0.53%	1.54
K2100	A	23	55.28	0.97	0.04	0.09	6.31	0.012	0.19%	-0.09
K2100	A	25	49.05	0.99	0.03	-0.03	7.61	0.007	0.09%	-0.56
K2100	A	27	69.13	0.97	0.04	0.37	10.55	-0.003	0.03%	-0.86
K2100	A	29	42.35	1.02	0.04	-0.16	7.25	0.024	0.33%	0.58
K2100	A	31	55.16	0.96	0.03	0.09	7.41	0.005	0.07%	-0.68
K2100	A	33	48.82	1.03	0.04	-0.03	7.24	0.013	0.18%	-0.14
K2100	A	35	34.04	0.98	0.03	-0.33	5.95	0.010	0.17%	-0.20
K2101	B	2	0.49	0.71	0.32	-0.16	7.06	0.564	7.99%	-0.44
K2101	B	3	0.07	0.86	0.21	-0.88	1.24	0.273	22.02%	0.54
K2101	B	10	0.39	1.16	0.20	-0.32	5.81	0.230	3.96%	-0.72
K2101	B	12	2.85	1.18	0.24	3.92	41.19	0.061	0.15%	-0.99
K2101	B	13	0.02	1.13	0.09	-0.96	0.41	0.107	26.10%	0.83
K2101	B	15	0.07	0.85	0.09	-0.88	1.45	0.381	26.28%	0.84
K2101	B	17	0.16	0.95	0.26	-0.72	2.70	0.359	13.30%	-0.07
K2102	B	1	5.32	1.03	0.03	0.12	1.12	0.028	2.50%	0.72
K2102	B	2	2.81	1.05	0.04	-0.41	0.60	0.037	6.17%	3.23
K2102	B	3	2.45	1.02	0.03	-0.48	0.53	0.009	1.70%	0.17
K2102	B	4	8.96	0.98	0.03	0.89	1.86	0.006	0.32%	-0.78
K2102	B	5	2.21	0.97	0.03	-0.53	0.48	0.007	1.46%	0.00
K2102	B	6	2.75	1.03	0.04	-0.42	0.59	0.003	0.51%	-0.65
K2102	B	7	3.52	0.98	0.03	-0.26	0.74	0.001	0.14%	-0.91
K2102	B	8	5.28	1.01	0.03	0.12	1.13	0.014	1.24%	-0.15
K2102	B	9	1.73	0.94	0.03	-0.63	0.40	0.013	3.25%	1.23
K2102	B	10	4.34	1.02	0.03	-0.08	0.95	0.013	1.37%	-0.06
K2102	B	11	5.49	1.02	0.03	0.16	1.18	0.011	0.93%	-0.36
K2102	B	12	7.90	1.02	0.03	0.67	1.68	0.008	0.48%	-0.67
K2102	B	13	3.21	0.99	0.03	-0.32	0.70	0.007	1.00%	-0.31
K2102	B	14	11.63	0.99	0.03	1.46	2.35	0.018	0.77%	-0.47
K2102	B	15	3.53	1.02	0.03	-0.25	0.77	0.017	2.21%	0.52
K2102	B	16	5.80	1.01	0.04	0.23	1.21	0.004	0.33%	-0.77
K2102	B	17	3.56	1.01	0.03	-0.25	0.77	0.009	1.17%	-0.20
K2102	B	18	4.73	1.03	0.04	0.00	1.01	0.007	0.69%	-0.52
K2103	B	1	0.06	1.06	0.15	0.50	1.01	0.152	15.05%	-0.51
K2103	B	2	0.01	0.92	0.10	-0.66	0.29	0.121	41.72%	0.35
K2103	B	4	0.05	1.02	0.08	0.41	1.23	0.746	60.65%	0.96
K2103	B	5	0.03	0.99	0.13	-0.26	0.60	0.142	23.67%	-0.24
K2103	B	6	0.11	1.04	0.17	1.86	1.93	0.162	8.39%	-0.73
K2103	B	7	0.02	1.13	0.16	-0.60	0.28	0.089	31.79%	0.03

Sample	Risø	Aliquot	Final D_e	Recyc ratio	Recyc error	Recyc. fractional dose offset	L_N/T_N	L_X/T_X (zero dose)	% Recoup.	Recup. fractional dose offset
K2103	B	8	0.04	1.16	0.21	0.01	0.62	0.147	23.71%	-0.23
K2103	B	9	0.02	0.80	0.11	-0.45	0.33	0.111	33.64%	0.09
K2103	B	10	0.01	0.99	0.08	-0.65	0.25	0.095	38.00%	0.23
K2103	B	11	0.01	1.03	0.14	-0.66	0.27	0.025	9.26%	-0.70
K2103	B	12	0.01	1.00	0.08	-0.66	0.24	0.172	71.67%	1.31
K2103	B	13	0.02	1.14	0.13	-0.56	0.30	0.105	35.00%	0.13
K2103	B	14	0.02	1.15	0.13	-0.52	0.40	0.269	67.25%	1.17
K2103	B	15	0.05	1.16	0.19	0.25	0.76	0.004	0.53%	-0.98
K2103	B	16	0.02	0.86	0.08	-0.47	0.36	0.109	30.28%	-0.02
K2103	B	17	0.14	1.06	0.07	2.47	2.38	0.123	5.17%	-0.83
K2104	B	1	0.03	1.24	0.27	-0.11	0.44	0.034	7.73%	-0.78
K2104	B	4	0.04	1.19	0.33	0.27	0.70	0.258	36.86%	0.04
K2104	B	5	0.05	1.25	0.16	0.79	0.92	0.516	56.09%	0.58
K2104	B	8	0.02	0.96	0.16	-0.28	0.33	-0.069	20.91%	-0.41
K2104	B	11	0.02	0.84	0.09	-0.35	0.31	0.058	18.71%	-0.47
K2104	B	12	0.03	0.94	0.11	-0.06	0.53	0.181	34.15%	-0.04
K2104	B	14	0.02	0.88	0.17	-0.12	0.47	0.259	55.11%	0.55
K2104	B	15	0.04	0.99	0.13	0.29	0.79	0.337	42.66%	0.20
K2104	B	17	0.02	0.88	0.08	-0.42	0.28	0.134	47.86%	0.35
K2105	B	3	0.09	0.86	0.11	0.81	1.52	0.380	25.00%	0.86
K2105	B	4	0.03	0.81	0.16	-0.28	0.57	-0.057	10.00%	-0.26
K2105	B	5	0.04	1.11	0.22	-0.22	0.80	0.012	1.50%	-0.89
K2105	B	6	0.04	0.85	0.26	-0.20	0.93	0.064	6.88%	-0.49
K2105	B	7	0.05	0.86	0.16	0.06	0.83	-0.052	6.27%	-0.53
K2105	B	8	0.05	0.96	0.06	0.07	0.92	0.070	7.61%	-0.43
K2105	B	10	0.05	0.87	0.08	0.11	0.86	0.114	13.26%	-0.01
K2105	B	14	0.05	0.94	0.13	0.07	1.05	0.245	23.33%	0.73
K2105	B	15	0.04	0.90	0.19	-0.26	0.58	0.229	39.48%	1.94
K2105	B	16	0.04	0.97	0.11	-0.12	0.73	0.078	10.68%	-0.21
K2105	B	17	0.05	0.86	0.08	-0.05	0.76	0.030	3.95%	-0.71
K2106	B	6	0.02	0.88	0.08	-0.46	0.48	0.353	73.54%	1.61
K2106	B	8	0.02	0.88	0.13	-0.41	0.39	-0.034	8.72%	-0.69
K2106	B	14	0.08	1.07	0.08	1.05	1.49	0.206	13.83%	-0.51
K2106	B	16	0.03	0.80	0.11	-0.18	0.60	0.100	16.67%	-0.41
K2107	B	1	0.04	1.46	0.45	0.41	0.58	0.522	90.00%	1.61
K2107	B	4	0.03	0.87	0.15	0.10	0.62	0.278	44.84%	0.30
K2107	B	6	0.03	1.16	0.19	-0.09	0.52	0.029	5.58%	-0.84
K2107	B	7	0.03	0.91	0.09	-0.14	0.41	0.161	39.27%	0.14
K2107	B	8	0.03	1.09	0.14	-0.07	0.54	0.020	3.70%	-0.89
K2107	B	10	0.04	0.86	0.06	0.26	0.69	0.146	21.16%	-0.39
K2107	B	11	0.03	1.03	0.14	0.13	0.55	0.159	28.91%	-0.16
K2107	B	15	0.02	1.07	0.16	-0.31	0.37	0.134	36.22%	0.05
K2107	B	16	0.02	1.04	0.08	-0.28	0.41	0.166	40.49%	0.17
K2108	B	1	1.37	1.23	0.24	1.39	20.27	-0.160	0.79%	-0.91
K2108	B	2	0.04	1.20	0.15	-0.93	0.73	-0.057	7.81%	-0.10
K2108	B	5	0.29	0.84	0.08	-0.50	4.77	0.133	2.79%	-0.68
K2108	B	9	2.18	1.14	0.11	2.81	35.33	0.089	0.25%	-0.97
K2108	B	11	0.21	1.06	0.10	-0.64	3.59	0.121	3.37%	-0.61
K2108	B	12	0.04	0.96	0.14	-0.93	0.72	0.335	46.53%	4.33
K2108	B	13	0.47	0.90	0.18	-0.17	7.20	0.232	3.22%	-0.63

Sample	Risø	Aliquot	Final D_e	Recyc ratio	Recyc error	Recyc. fractional dose offset	L_N/T_N	L_X/T_X (zero dose)	% Recoup.	Recup. fractional dose offset
K2108	B	16	0.30	0.82	0.09	-0.47	5.53	0.316	5.71%	-0.35
K2108	B	17	0.25	1.04	0.09	-0.56	4.50	0.362	8.04%	-0.08
K2109	B	1	0.04	0.93	0.14	-0.84	0.78	-0.023	2.95%	-0.48
K2109	B	2	0.05	0.86	0.13	-0.82	0.80	0.015	1.88%	-0.67
K2109	B	11	0.09	0.90	0.16	-0.68	1.85	0.182	9.84%	0.74
K2109	B	12	0.24	1.07	0.25	-0.10	4.21	-0.029	0.69%	-0.88
K2109	B	14	0.03	0.98	0.13	-0.90	0.53	0.042	7.92%	0.40
K2109	B	16	0.70	1.26	0.45	1.62	11.82	0.359	3.04%	-0.46
K2109	B	17	0.04	1.11	0.13	-0.84	0.73	0.116	15.89%	1.81
K2109	B	18	0.94	1.26	0.28	2.56	13.97	0.435	3.11%	-0.45
K2110	B	1	0.13	0.83	0.14	0.03	2.46	0.130	5.28%	-0.51
K2110	B	4	0.09	1.41	0.32	-0.31	1.58	0.148	9.37%	-0.14
K2110	B	6	0.13	1.01	0.23	0.07	2.17	0.413	19.03%	0.75
K2110	B	7	0.13	0.96	0.12	0.05	2.21	0.326	14.75%	0.36
K2110	B	8	0.12	1.07	0.15	-0.01	2.09	0.079	3.78%	-0.65
K2110	B	9	0.10	0.91	0.11	-0.19	2.03	0.459	22.61%	1.08
K2110	B	11	0.17	1.26	0.19	0.38	3.11	0.430	13.83%	0.27
K2110	B	12	0.13	1.07	0.13	0.07	2.33	0.333	14.29%	0.32
K2110	B	13	0.12	1.11	0.12	-0.07	1.95	0.239	12.26%	0.13
K2110	B	14	0.11	0.88	0.20	-0.08	1.83	-0.138	7.54%	-0.31
K2110	B	16	0.13	0.85	0.13	0.01	2.09	0.055	2.63%	-0.76
K2110	B	17	0.13	0.97	0.07	0.05	2.34	0.117	5.00%	-0.54
K2111	B	2	2.12	1.00	0.04	0.82	2.19	0.023	1.05%	-0.69
K2111	B	3	0.98	0.94	0.09	-0.16	1.11	0.052	4.68%	0.38
K2111	B	4	1.94	0.93	0.04	0.66	2.05	0.007	0.34%	-0.90
K2111	B	5	2.77	0.98	0.04	1.38	2.77	0.022	0.79%	-0.77
K2111	B	6	0.38	1.07	0.05	-0.68	0.40	0.041	10.25%	2.01
K2111	B	7	0.69	0.99	0.04	-0.41	0.70	0.012	1.71%	-0.50
K2111	B	8	1.18	0.87	0.05	0.01	1.22	0.227	18.61%	4.47
K2111	B	9	0.97	0.99	0.05	-0.17	0.95	-0.006	0.63%	-0.81
K2111	B	10	1.09	0.91	0.04	-0.06	1.08	0.015	1.39%	-0.59
K2111	B	11	1.54	0.98	0.04	0.32	1.57	0.007	0.45%	-0.87
K2111	B	13	0.53	0.93	0.04	-0.55	0.53	0.010	1.89%	-0.45
K2111	B	14	0.90	0.92	0.04	-0.23	0.85	0.001	0.12%	-0.97
K2111	B	16	0.52	0.97	0.03	-0.56	0.52	0.021	4.04%	0.19
K2111	B	17	1.32	0.94	0.04	0.13	1.31	0.026	1.98%	-0.42
K2111	B	18	0.59	0.89	0.05	-0.50	0.61	0.019	3.11%	-0.08
K2112	B	1	19.31	1.03	0.04	0.02	3.23	0.023	0.71%	0.23
K2112	B	2	35.14	0.98	0.03	0.86	5.60	0.005	0.09%	-0.85
K2112	B	3	14.21	0.99	0.03	-0.25	2.72	0.005	0.18%	-0.68
K2112	B	4	11.43	1.02	0.04	-0.39	2.25	0.013	0.58%	0.00
K2112	B	5	15.61	1.05	0.03	-0.17	2.93	0.017	0.58%	0.00
K2112	B	6	13.42	1.03	0.03	-0.29	2.55	0.020	0.78%	0.35
K2112	B	7	18.41	1.03	0.03	-0.02	3.68	0.010	0.27%	-0.53
K2112	B	8	17.09	1.06	0.04	-0.09	3.14	-0.004	0.13%	-0.78
K2112	B	9	12.97	1.03	0.04	-0.31	2.50	0.065	2.60%	3.49
K2112	B	10	21.82	0.99	0.03	0.16	3.83	0.046	1.20%	1.07
K2112	B	11	23.31	1.04	0.03	0.24	3.78	0.010	0.26%	-0.54
K2112	B	12	24.42	1.01	0.04	0.30	4.23	0.052	1.23%	1.12
K2112	B	13	21.21	1.02	0.03	0.13	3.93	0.008	0.20%	-0.65

Sample	Risø	Aliquot	Final D_e	Recyc ratio	Recyc error	Recyc. fractional dose offset	L_N/T_N	L_X/T_X (zero dose)	% Recoup.	Recup. fractional dose offset
K2112	B	14	18.77	1.01	0.03	0.00	3.63	0.011	0.30%	-0.48
K2112	B	15	13.99	1.00	0.03	-0.26	2.67	0.009	0.34%	-0.42
K2112	B	16	15.66	1.00	0.03	-0.17	3.05	0.005	0.16%	-0.72
K2112	B	17	26.25	1.00	0.03	0.39	4.78	0.013	0.27%	-0.53
K2112	B	18	16.20	0.99	0.03	-0.14	3.06	0.016	0.52%	-0.10
K2113	A	1	35.24	1.04	0.04	0.13	5.24	0.068	1.30%	1.15
K2113	A	3	29.09	0.96	0.03	-0.06	5.03	0.024	0.48%	-0.21
K2113	A	5	33.31	0.99	0.03	0.07	5.35	0.011	0.21%	-0.66
K2113	A	7	29.68	1.01	0.03	-0.04	4.98	0.008	0.16%	-0.73
K2113	A	9	31.26	0.99	0.03	0.01	5.31	0.010	0.19%	-0.69
K2113	A	11	29.68	1.01	0.04	-0.04	4.91	0.011	0.22%	-0.63
K2113	A	13	32.84	1.00	0.04	0.06	5.87	0.019	0.32%	-0.46
K2113	A	15	31.38	1.04	0.04	0.01	5.01	0.009	0.18%	-0.70
K2113	A	17	32.31	0.96	0.03	0.04	5.48	0.018	0.33%	-0.46
K2113	A	19	42.03	1.03	0.03	0.35	6.02	0.008	0.13%	-0.78
K2113	A	21	21.54	0.99	0.04	-0.31	3.79	0.171	4.51%	6.48
K2113	A	23	31.14	1.00	0.04	0.00	4.90	0.078	1.59%	1.64
K2113	A	25	31.73	1.04	0.04	0.02	4.95	0.017	0.34%	-0.43
K2113	A	27	26.11	0.97	0.03	-0.16	4.59	0.006	0.13%	-0.78
K2113	A	29	35.77	0.99	0.03	0.15	5.72	0.009	0.16%	-0.74
K2113	A	31	23.88	1.03	0.04	-0.23	4.18	0.005	0.12%	-0.80
K2113	A	33	31.90	1.04	0.04	0.03	5.06	0.012	0.24%	-0.61
K2113	A	35	30.21	1.01	0.03	-0.03	5.33	0.013	0.24%	-0.60
K2114	B	1	36.67	1.02	0.03	-0.17	5.92	0.015	0.25%	-0.57
K2114	B	2	33.54	1.07	0.04	-0.24	4.23	0.011	0.26%	-0.56
K2114	B	3	45.02	1.00	0.03	0.02	6.55	0.030	0.46%	-0.22
K2114	B	4	53.31	1.03	0.03	0.21	6.03	0.013	0.22%	-0.63
K2114	B	5	41.15	0.97	0.03	-0.07	5.09	0.018	0.35%	-0.40
K2114	B	6	56.45	1.01	0.03	0.28	6.69	0.021	0.31%	-0.47
K2114	B	7	45.03	0.98	0.03	0.02	6.59	0.018	0.27%	-0.53
K2114	B	8	29.05	0.98	0.05	-0.34	4.44	0.200	4.50%	6.67
K2114	B	9	43.09	1.01	0.03	-0.02	5.83	0.019	0.33%	-0.44
K2114	B	10	45.00	0.99	0.03	0.02	6.90	0.028	0.41%	-0.31
K2114	B	11	44.90	1.02	0.03	0.02	6.32	0.017	0.27%	-0.54
K2114	B	12	34.72	1.02	0.03	-0.21	5.93	0.012	0.20%	-0.66
K2114	B	13	44.13	1.03	0.03	0.00	5.92	0.063	1.06%	0.81
K2114	B	14	34.32	0.99	0.03	-0.22	5.73	0.031	0.54%	-0.08
K2114	B	15	59.88	1.02	0.03	0.35	7.07	0.023	0.33%	-0.45
K2114	B	16	56.12	1.01	0.03	0.27	6.43	0.008	0.12%	-0.79
K2114	B	17	44.14	1.00	0.03	0.00	6.20	0.030	0.48%	-0.18
K2114	B	18	48.92	0.98	0.03	0.11	6.65	0.013	0.20%	-0.67
K2115	A	1	31.55	1.01	0.04	0.18	5.79	0.012	0.21%	-0.44
K2115	A	3	23.06	1.05	0.04	-0.14	4.42	0.009	0.20%	-0.45
K2115	A	5	23.91	1.05	0.04	-0.10	4.91	0.031	0.63%	0.71
K2115	A	7	26.17	1.08	0.04	-0.02	4.70	0.014	0.30%	-0.19
K2115	A	9	26.02	1.08	0.04	-0.03	4.55	0.014	0.31%	-0.17
K2115	A	11	26.09	1.07	0.04	-0.02	4.65	0.043	0.92%	1.51
K2115	A	13	34.33	0.95	0.03	0.29	5.83	0.013	0.22%	-0.40
K2115	A	15	25.11	0.95	0.03	-0.06	4.91	0.019	0.39%	0.05
K2115	A	17	28.36	1.04	0.04	0.06	5.04	0.036	0.71%	0.94

Sample	Risø	Aliquot	Final D_e	Recyc ratio	Recyc error	Recyc. fractional dose offset	L_N/T_N	L_X/T_X (zero dose)	% Recoup.	Recup. fractional dose offset
K2115	A	19	22.22	0.98	0.04	-0.17	4.39	0.011	0.25%	-0.32
K2115	A	21	24.73	0.95	0.04	-0.07	4.72	0.034	0.72%	0.95
K2115	A	23	36.44	1.00	0.04	0.37	6.40	0.014	0.22%	-0.41
K2115	A	25	32.23	1.01	0.03	0.21	5.83	0.017	0.29%	-0.21
K2115	A	27	23.37	1.03	0.04	-0.12	4.33	0.008	0.18%	-0.50
K2115	A	29	23.61	1.01	0.03	-0.12	4.98	0.006	0.12%	-0.67
K2115	A	31	21.23	1.02	0.03	-0.20	4.33	0.009	0.21%	-0.44
K2115	A	33	28.55	1.01	0.03	0.07	5.55	0.015	0.27%	-0.27
K2115	A	35	23.55	0.95	0.03	-0.12	4.59	0.022	0.48%	0.30
K2116	A	1	75.40	1.05	0.04	0.38	11.00	0.041	0.37%	-0.08
K2116	A	3	45.47	1.07	0.04	-0.17	7.31	0.026	0.36%	-0.12
K2116	A	5	55.38	1.10	0.04	0.01	6.36	0.025	0.39%	-0.03
K2116	A	7	63.93	1.04	0.04	0.17	8.05	0.020	0.25%	-0.39
K2116	A	9	43.53	0.99	0.03	-0.20	7.05	0.057	0.81%	1.00
K2116	A	11	49.75	1.02	0.04	-0.09	7.29	0.033	0.45%	0.12
K2116	A	13	56.36	0.98	0.04	0.03	6.81	0.019	0.28%	-0.31
K2116	A	15	53.44	1.03	0.04	-0.02	6.24	0.024	0.38%	-0.05
K2116	A	17	49.55	1.07	0.04	-0.09	7.25	0.039	0.54%	0.33
K2116	A	19	52.66	1.06	0.04	-0.04	7.70	0.020	0.26%	-0.36
K2116	A	21	58.69	1.06	0.03	0.07	8.36	0.030	0.36%	-0.11
K2116	A	23	46.83	1.02	0.04	-0.14	7.29	0.021	0.29%	-0.29
K2116	A	25	48.58	1.03	0.04	-0.11	7.97	0.051	0.64%	0.58
K2116	A	27	60.05	1.04	0.04	0.10	7.76	0.012	0.15%	-0.62
K2116	A	29	60.63	1.04	0.03	0.11	8.87	0.020	0.23%	-0.44
K2116	A	31	56.36	1.05	0.04	0.03	8.13	0.038	0.47%	0.15
K2116	A	33	43.72	1.03	0.03	-0.20	7.14	0.026	0.36%	-0.10
K2116	A	35	63.16	1.00	0.03	0.16	8.12	0.057	0.70%	0.73
K2117	A	1	32.18	1.04	0.04	0.28	5.76	0.009	0.16%	-0.31
K2117	A	3	24.80	1.12	0.04	-0.01	4.62	0.005	0.11%	-0.52
K2117	A	5	26.58	1.03	0.04	0.06	4.37	0.008	0.18%	-0.19
K2117	A	7	26.35	1.04	0.04	0.05	4.70	0.008	0.17%	-0.25
K2117	A	9	27.13	1.09	0.04	0.08	4.61	0.013	0.28%	0.24
K2117	A	11	19.04	1.04	0.06	-0.24	3.54	0.009	0.25%	0.12
K2117	A	15	28.76	1.03	0.04	0.15	4.81	0.012	0.25%	0.10
K2117	A	17	24.95	1.03	0.03	0.00	4.71	0.012	0.25%	0.12
K2117	A	19	24.17	1.02	0.04	-0.04	4.08	0.009	0.22%	-0.03
K2117	A	21	33.11	1.00	0.04	0.32	5.43	0.013	0.24%	0.05
K2117	A	23	23.55	1.07	0.04	-0.06	4.15	0.006	0.14%	-0.36
K2117	A	25	20.44	0.97	0.03	-0.18	3.97	0.012	0.30%	0.33
K2117	A	27	31.95	1.02	0.04	0.27	4.62	0.006	0.13%	-0.43
K2117	A	29	21.38	1.02	0.04	-0.15	3.68	0.006	0.16%	-0.28
K2117	A	31	20.68	0.98	0.03	-0.17	4.15	0.019	0.46%	1.02
K2117	A	33	22.31	0.98	0.04	-0.11	4.12	0.010	0.24%	0.07
K2117	A	35	18.66	1.01	0.04	-0.26	3.63	0.011	0.30%	0.33
K2118	A	1	37.76	0.97	0.03	0.01	6.29	0.009	0.14%	-0.30
K2118	A	3	32.06	0.93	0.04	-0.14	5.52	0.017	0.31%	0.52
K2118	A	5	36.48	0.97	0.03	-0.02	5.86	0.006	0.10%	-0.50
K2118	A	7	35.90	0.93	0.03	-0.04	5.98	0.014	0.23%	0.15
K2118	A	9	43.46	0.97	0.03	0.16	6.70	0.012	0.18%	-0.12
K2118	A	11	35.43	0.94	0.03	-0.05	5.75	0.021	0.37%	0.80

Sample	Risø	Aliquot	Final D_e	Recyc ratio	Recyc error	Recyc. fractional dose offset	L_N/T_N	L_X/T_X (zero dose)	% Recoup.	Recup. fractional dose offset
K2118	A	13	38.17	0.96	0.03	0.02	6.29	0.011	0.17%	-0.14
K2118	A	15	38.34	0.96	0.03	0.03	5.89	0.010	0.17%	-0.16
K2118	A	17	34.09	0.96	0.03	-0.09	5.55	0.011	0.20%	-0.02
K2118	A	19	43.52	0.96	0.03	0.17	7.84	0.011	0.14%	-0.31
K2118	A	21	33.80	0.99	0.04	-0.09	5.36	0.007	0.13%	-0.36
K2118	A	23	32.64	0.95	0.03	-0.13	5.59	0.005	0.09%	-0.56
K2118	A	25	38.41	0.98	0.03	0.03	8.00	0.018	0.23%	0.11
K2118	A	27	29.41	1.02	0.04	-0.21	5.15	0.017	0.33%	0.63
K2118	A	29	34.03	0.98	0.03	-0.09	6.33	0.019	0.30%	0.48
K2118	A	31	43.49	1.01	0.03	0.16	6.77	0.015	0.22%	0.09
K2118	A	33	39.70	1.00	0.03	0.06	6.49	0.007	0.11%	-0.47
K2118	A	35	45.29	0.98	0.03	0.21	7.22	0.017	0.24%	0.16
K2119	A	1	25.30	0.99	0.04	-0.06	4.84	0.005	0.10%	-0.58
K2119	A	3	28.16	0.92	0.04	0.05	5.01	0.015	0.30%	0.20
K2119	A	5	26.93	1.06	0.05	0.00	4.03	0.002	0.05%	-0.80
K2119	A	7	25.59	1.05	0.04	-0.05	4.47	0.002	0.04%	-0.82
K2119	A	9	21.75	1.03	0.04	-0.19	4.09	0.011	0.27%	0.08
K2119	A	11	26.18	1.01	0.04		4.16	0.023	0.55%	
K2119	A	13	28.16	1.05	0.05	0.05	5.23	0.012	0.23%	-0.08
K2119	A	15	33.75	1.01	0.04	0.25	6.47	0.013	0.20%	-0.19
K2119	A	17	19.94	0.94	0.05	-0.26	3.96	0.019	0.48%	0.93
K2119	A	19	26.82	1.09	0.04	0.00	4.79	0.008	0.17%	-0.33
K2119	A	21	25.88	1.10	0.05	-0.04	4.21	0.019	0.45%	0.82
K2119	A	23	32.01	1.05	0.04	0.19	5.48	0.021	0.38%	0.54
K2119	A	25	24.89	1.03	0.04	-0.08	4.22	0.011	0.26%	0.05
K2119	A	27	25.88	1.01	0.04	-0.04	4.87	0.007	0.14%	-0.42
K2119	A	29	24.08	1.02	0.04	-0.11	4.53	0.010	0.22%	-0.11
K2119	A	31	29.27	1.02	0.04	0.09	5.17	0.018	0.35%	0.40
K2119	A	33	27.40	1.08	0.04	0.02	4.76	0.010	0.21%	-0.15
K2119	A	35	32.71	1.06	0.04	0.21	5.06	0.003	0.06%	-0.76
K2120	B	1	0.03	0.94	0.04	-0.36	0.08	0.018	22.50%	-0.05
K2120	B	2	0.03	0.98	0.04	-0.42	0.06	0.016	26.67%	0.13
K2120	B	3	0.04	0.94	0.04	-0.17	0.09	0.045	50.00%	1.12
K2120	B	4	0.03	0.96	0.04	-0.44	0.06	0.013	21.67%	-0.08
K2120	B	5	0.05	0.93	0.04	-0.03	0.10	0.026	26.00%	0.10
K2120	B	6	0.05	0.96	0.05	-0.03	0.10	0.006	6.00%	-0.75
K2120	B	7	0.04	0.95	0.04	-0.14	0.10	0.033	33.00%	0.40
K2120	B	8	0.03	0.97	0.04	-0.50	0.05	0.016	32.00%	0.36
K2120	B	9	0.04	1.04	0.04	-0.27	0.08	0.019	23.75%	0.01
K2120	B	10	0.03	0.99	0.04	-0.36	0.07	0.010	14.29%	-0.39
K2120	B	11	0.05	0.96	0.05	-0.03	0.15	0.058	38.67%	0.64
K2120	B	12	0.05	1.06	0.05	-0.11	0.10	0.023	23.00%	-0.03
K2120	B	13	0.19	1.02	0.04	2.63	0.42	0.007	1.67%	-0.93
K2120	B	14	0.06	0.93	0.04	0.13	0.13	0.047	36.15%	0.53
K2120	B	15	0.06	0.99	0.05	0.21	0.12	0.013	10.83%	-0.54
K2120	B	16	0.07	0.94	0.04	0.37	0.15	0.006	4.00%	-0.83
K2120	B	17	0.05	1.06	0.05	-0.11	0.09	0.030	33.33%	0.41
K2120	B	18	0.03	0.98	0.04	-0.36	0.08	0.017	21.25%	-0.10
K2121	B	1	13.64	1.01	0.03	-0.08	2.62	0.006	0.23%	-0.58
K2121	B	2	16.61	1.03	0.03	0.12	3.20	0.009	0.28%	-0.49

Sample	Risø	Aliquot	Final D_e	Recyc ratio	Recyc error	Recyc. fractional dose offset	L_N/T_N	L_X/T_X (zero dose)	% Recoup.	Recup. fractional dose offset
K2121	B	3	16.10	0.98	0.03	0.08	3.08	0.018	0.58%	0.07
K2121	B	4	12.82	1.01	0.03	-0.14	2.47	0.008	0.32%	-0.41
K2121	B	5	12.86	1.03	0.03	-0.14	2.40	0.085	3.54%	5.47
K2121	B	6	14.60	1.02	0.03	-0.02	2.84	0.007	0.25%	-0.55
K2121	B	7	15.57	1.01	0.03	0.05	3.01	0.010	0.33%	-0.39
K2121	B	8	12.69	1.01	0.03	-0.15	2.48	0.011	0.44%	-0.19
K2121	B	9	16.86	0.97	0.03	0.13	3.20	0.010	0.31%	-0.43
K2121	B	10	17.66	1.00	0.03	0.19	3.37	0.013	0.39%	-0.30
K2121	B	11	13.32	0.98	0.03	-0.10	2.61	0.019	0.73%	0.33
K2121	B	12	15.72	1.02	0.03	0.06	2.94	0.010	0.34%	-0.38
K2121	B	13	15.15	0.98	0.03	0.02	2.81	0.006	0.21%	-0.61
K2121	B	14	13.58	1.01	0.03	-0.09	2.68	0.013	0.49%	-0.11
K2121	B	15	14.55	0.99	0.03	-0.02	2.79	0.009	0.32%	-0.41
K2121	B	16	13.18	1.00	0.03	-0.11	2.52	0.007	0.28%	-0.49
K2121	B	17	13.96	1.01	0.03	-0.06	2.72	0.014	0.51%	-0.06
K2121	B	18	18.86	1.03	0.03	0.27	3.47	0.010	0.29%	-0.47
K2122	B	1	0.18	1.33	0.24	0.94	2.71	-0.059	2.18%	-0.74
K2122	B	2	0.10	0.87	0.05	0.10	1.70	0.125	7.35%	-0.11
K2122	B	3	0.05	0.95	0.16	-0.41	0.99	0.071	7.17%	-0.14
K2122	B	6	0.09	0.89	0.09	-0.02	1.49	0.114	7.65%	-0.08
K2122	B	8	0.07	0.91	0.09	-0.21	1.26	0.140	11.11%	0.34
K2122	B	10	0.08	0.95	0.12	-0.08	1.45	0.095	6.55%	-0.21
K2122	B	15	0.11	1.12	0.18	0.22	1.71	-0.012	0.70%	-0.92
K2122	B	16	0.06	0.87	0.09	-0.31	1.19	0.183	15.38%	0.85
K2122	B	17	0.07	1.13	0.14	-0.23	1.14	0.190	16.67%	1.01
K2123	A	1	76.17	0.96	0.04	-0.19	9.63	0.010	0.10%	-0.59
K2123	A	3	98.17	1.00	0.04	0.04	9.94	0.022	0.22%	-0.12
K2123	A	5	94.33	0.97	0.07	0.00	10.48	0.018	0.17%	-0.32
K2123	A	9	60.17	1.02	0.05	-0.36	7.51	0.103	1.37%	4.43
K2123	A	11	71.24	1.00	0.04	-0.24	11.06	0.023	0.21%	-0.18
K2123	A	13	102.02	1.00	0.04	0.09	13.37	0.033	0.25%	-0.02
K2123	A	15	110.33	1.06	0.04	0.17	11.24	0.024	0.21%	-0.15
K2123	A	17	89.56	0.97	0.04	-0.05	12.89	0.031	0.24%	-0.05
K2123	A	19	70.32	1.06	0.04	-0.25	9.11	0.020	0.22%	-0.13
K2123	A	21	100.02	0.95	0.03	0.06	11.69	0.019	0.16%	-0.36
K2123	A	23	110.79	0.97	0.04	0.18	11.09	0.009	0.08%	-0.68
K2123	A	25	112.64	1.05	0.04	0.20	10.31	0.027	0.26%	0.04
K2123	A	27	49.09	0.81	0.13	-0.48	8.11	-0.021	0.26%	0.03
K2123	A	29	67.24	1.02	0.04	-0.28	10.07	0.019	0.19%	-0.25
K2123	A	31	140.18	0.96	0.04	0.49	12.45	0.023	0.18%	-0.27
K2123	A	33	73.55	1.03	0.04	-0.22	11.88	0.012	0.10%	-0.60
K2123	A	35	171.57	1.01	0.04	0.83	15.76	0.009	0.06%	-0.77
K2124	B	1	22.96	0.94	0.03	-0.23	3.95	0.100	2.53%	4.31
K2124	B	2	16.41	0.97	0.03	-0.45	2.84	0.030	1.06%	1.22
K2124	B	3	18.32	0.91	0.04	-0.39	3.39	0.006	0.18%	-0.63
K2124	B	4	30.17	0.98	0.03	0.01	5.09	0.015	0.29%	-0.38
K2124	B	5	31.50	1.01	0.03	0.06	4.83	0.018	0.37%	-0.22
K2124	B	6	50.40	0.98	0.03	0.69	6.03	0.003	0.05%	-0.90
K2124	B	7	23.87	0.99	0.04	-0.20	3.88	0.012	0.31%	-0.35
K2124	B	8	35.07	0.97	0.03	0.17	5.73	0.010	0.17%	-0.63

Sample	Risø	Aliquot	Final D_e	Recyc ratio	Recyc error	Recyc. fractional dose offset	L_N/T_N	L_X/T_X (zero dose)	% Recoup.	Recup. fractional dose offset
K2124	B	9	30.92	1.00	0.03	0.04	5.09	0.006	0.12%	-0.75
K2124	B	10	36.56	0.94	0.03	0.22	6.76	0.024	0.36%	-0.26
K2124	B	11	11.61	1.03	0.04	-0.61	2.25	0.015	0.67%	0.40
K2124	B	12	15.25	1.01	0.03	-0.49	3.01	0.009	0.30%	-0.37
K2124	B	13	20.89	0.97	0.03	-0.30	3.74	0.014	0.37%	-0.21
K2124	B	14	16.50	1.00	0.03	-0.45	3.10	0.012	0.39%	-0.19
K2124	B	15	27.85	0.98	0.03	-0.07	4.58	0.018	0.39%	-0.18
K2124	B	16	22.47	0.98	0.03	-0.25	3.76	0.018	0.48%	0.00
K2124	B	17	46.17	0.96	0.03	0.55	6.39	0.027	0.42%	-0.11
K2124	B	18	80.24	1.04	0.04	1.69	10.02	0.012	0.12%	-0.75
K2125	B	1	0.08	1.11	0.11	-0.72	1.37	0.108	7.88%	-0.33
K2125	B	3	0.10	1.00	0.16	-0.65	1.52	0.187	12.30%	0.04
K2125	B	5	0.09	0.92	0.09	-0.67	1.75	0.060	3.43%	-0.71
K2125	B	8	0.09	1.09	0.13	-0.69	1.44	0.103	7.15%	-0.40
K2125	B	9	0.10	0.99	0.10	-0.65	1.71	0.196	11.46%	-0.03
K2125	B	10	0.04	0.84	0.17	-0.84	0.89	0.321	36.07%	2.04
K2125	B	12	0.04	1.00	0.15	-0.86	0.75	0.290	38.67%	2.26
K2125	B	14	0.27	0.91	0.12	-0.04	4.74	0.160	3.38%	-0.72
K2125	B	16	1.10	0.79	0.20	2.94	16.17	-0.130	0.80%	-0.93
K2125	B	17	1.13	1.00	0.14	3.07	18.43	0.163	0.88%	-0.93
K2125	B	18	0.03	1.00	0.08	-0.88	0.49	0.041	8.37%	-0.29
K2126	B	1	0.03	0.94	0.08	-0.97	0.55	0.204	37.09%	0.63
K2126	B	3	0.03	1.16	0.16	-0.97	0.49	0.116	23.67%	0.04
K2126	B	4	0.03	1.22	0.26	-0.97	0.53	-0.034	6.42%	-0.72
K2126	B	7	0.05	0.89	0.15	-0.95	0.84	0.258	30.71%	0.35
K2126	B	8	6.29	0.88	0.10	5.38	96.89	0.174	0.18%	-0.99
K2126	B	9	0.02	0.90	0.10	-0.98	0.38	0.080	21.05%	-0.07
K2126	B	11	0.03	1.10	0.10	-0.97	0.49	0.143	29.18%	0.28
K2126	B	12	0.04	0.92	0.08	-0.96	0.70	0.102	14.57%	-0.36
K2126	B	13	0.02	1.00	0.10	-0.98	0.30	0.199	66.33%	1.92
K2126	B	14	0.02	0.84	0.09	-0.98	0.35	0.145	41.43%	0.82
K2126	B	15	0.69	0.88	0.06	-0.30	11.71	0.226	1.93%	-0.92
K2126	B	16	6.49	1.00	0.09	5.58	66.64	0.309	0.46%	-0.98
K2126	B	17	0.03	1.13	0.16	-0.97	0.53	0.179	33.77%	0.49
K2126	B	18	0.06	0.90	0.13	-0.94	1.02	0.114	11.18%	-0.51
K2127	B	2	4.74	1.08	0.09	-0.37	4.51	0.051	1.13%	1.10
K2127	B	3	4.88	1.04	0.04	-0.35	4.91	0.014	0.29%	-0.47
K2127	B	4	5.24	1.07	0.05	-0.30	5.12	0.033	0.64%	0.20
K2127	B	5	5.37	0.95	0.04	-0.29	5.26	0.008	0.15%	-0.72
K2127	B	6	10.12	1.01	0.04	0.34	9.61	0.006	0.06%	-0.88
K2127	B	7	10.37	1.00	0.04	0.38	9.57	0.018	0.19%	-0.65
K2127	B	8	6.22	0.98	0.04	-0.17	6.13	0.005	0.08%	-0.85
K2127	B	9	3.20	1.09	0.09	-0.57	3.43	0.059	1.72%	2.20
K2127	B	10	3.66	1.10	0.08	-0.51	3.50	0.060	1.71%	2.18
K2127	B	11	5.54	0.94	0.04	-0.26	5.76	0.012	0.21%	-0.61
K2127	B	12	3.36	0.98	0.07	-0.55	3.32	0.027	0.81%	0.51
K2127	B	13	9.53	0.92	0.04	0.27	9.13	0.008	0.09%	-0.84
K2127	B	14	4.47	1.10	0.07	-0.41	4.55	0.035	0.77%	0.43
K2127	B	15	11.55	1.13	0.05	0.53	10.45	0.030	0.29%	-0.47
K2127	B	16	4.85	1.05	0.06	-0.36	4.88	0.042	0.86%	0.60

Sample	Risø	Aliquot	Final D_e	Recyc ratio	Recyc error	Recyc. fractional dose offset	L_N/T_N	L_X/T_X (zero dose)	% Recoup.	Recup. fractional dose offset
K2127	B	17	29.25	0.99	0.04	2.88	20.63	0.003	0.01%	-0.97
K2127	B	18	5.64	0.94	0.05	-0.25	5.35	0.007	0.13%	-0.76
K2128	B	1	1.65	1.01	0.06	-0.62	1.73	0.005	0.29%	-0.61
K2128	B	2	3.78	0.87	0.04	-0.12	3.65	0.007	0.19%	-0.74
K2128	B	4	13.11	0.94	0.04	2.04	11.95	0.013	0.11%	-0.85
K2128	B	5	0.95	0.96	0.07	-0.78	0.97	0.034	3.51%	3.71
K2128	B	6	6.44	0.98	0.05	0.49	6.37	0.029	0.46%	-0.39
K2128	B	7	2.73	0.87	0.04	-0.37	2.74	0.016	0.58%	-0.22
K2128	B	8	7.47	0.97	0.05	0.73	7.01	-0.019	0.27%	-0.64
K2128	B	9	1.77	0.92	0.05	-0.59	1.79	0.011	0.61%	-0.17
K2128	B	10	2.53	0.94	0.05	-0.41	2.71	0.028	1.03%	0.39
K2128	B	12	2.05	0.86	0.06	-0.53	2.17	0.017	0.78%	0.05
K2128	B	13	2.59	1.01	0.07	-0.40	2.77	0.001	0.04%	-0.95
K2128	B	14	6.54	1.01	0.06	0.52	6.05	0.025	0.41%	-0.44
K2128	B	15	8.99	1.04	0.11	1.08	7.63	-0.044	0.58%	-0.23
K2128	B	17	2.51	0.93	0.08	-0.42	2.49	0.046	1.85%	1.48
K2128	B	18	1.65	0.96	0.05	-0.62	1.76	0.008	0.45%	-0.39
K2129	B	1	3.71	0.98	0.03	-0.14	3.69	0.012	0.33%	-0.49
K2129	B	2	3.88	1.03	0.04	-0.10	3.81	0.020	0.52%	-0.18
K2129	B	3	7.52	1.00	0.04	0.74	6.96	0.013	0.19%	-0.71
K2129	B	4	5.23	1.02	0.03	0.21	5.00	0.011	0.22%	-0.65
K2129	B	5	3.04	1.02	0.04	-0.30	3.07	0.116	3.78%	4.93
K2129	B	6	7.19	1.03	0.04	0.66	6.73	0.008	0.12%	-0.81
K2129	B	7	3.86	0.96	0.04	-0.11	3.85	0.020	0.52%	-0.18
K2129	B	8	3.12	1.06	0.05	-0.28	3.09	0.014	0.45%	-0.29
K2129	B	9	2.50	0.93	0.04	-0.42	2.58	0.027	1.05%	0.64
K2129	B	10	3.73	0.99	0.04	-0.14	3.61	0.029	0.80%	0.26
K2129	B	11	2.54	0.97	0.03	-0.41	2.60	0.008	0.31%	-0.52
K2129	B	12	7.06	1.00	0.04	0.63	6.75	0.020	0.30%	-0.54
K2129	B	13	5.16	1.03	0.04	0.19	5.04	0.010	0.20%	-0.69
K2129	B	14	3.33	0.99	0.04	-0.23	3.33	0.023	0.69%	0.08
K2129	B	15	4.16	1.00	0.04	-0.04	4.15	0.012	0.29%	-0.55
K2129	B	16	4.90	0.98	0.03	0.13	4.93	0.016	0.32%	-0.49
K2129	B	17	4.55	0.94	0.03	0.05	4.48	0.046	1.03%	0.61
K2129	B	18	2.41	0.98	0.04	-0.44	2.50	0.009	0.36%	-0.44
K2130	A	1	64.86	1.02	0.04	-0.35	10.44	0.012	0.11%	-0.52
K2130	A	3	170.54	0.99	0.03	0.71	14.99	0.025	0.17%	-0.30
K2130	A	5	87.18	1.03	0.04	-0.13	8.73	0.021	0.24%	0.01
K2130	A	7	88.70	1.04	0.04	-0.11	9.86	0.017	0.17%	-0.28
K2130	A	9	142.31	1.03	0.04	0.42	10.49	0.013	0.12%	-0.48
K2130	A	11	98.81	0.99	0.04	-0.01	12.47	0.054	0.43%	0.81
K2130	A	13	104.92	1.00	0.03	0.05	13.12	0.048	0.37%	0.53
K2130	A	15	161.57	1.01	0.04	0.62	12.23	0.005	0.04%	-0.83
K2130	A	17	116.17	0.97	0.03	0.16	8.78	0.013	0.15%	-0.38
K2130	A	19	93.09	0.99	0.04	-0.07	10.11	0.133	1.32%	4.51
K2130	A	21	72.87	1.03	0.03	-0.27	11.40	0.014	0.12%	-0.49
K2130	A	23	135.44	1.08	0.06	0.35	14.82	0.014	0.09%	-0.60
K2130	A	25	84.89	1.03	0.03	-0.15	11.32	0.017	0.15%	-0.37
K2130	A	27	82.60	0.99	0.04	-0.17	11.90	0.015	0.13%	-0.47
K2130	A	29	66.58	0.99	0.03	-0.33	10.35	0.011	0.11%	-0.56

Sample	Risø	Aliquot	Final D_e	Recyc ratio	Recyc error	Recyc. fractional dose offset	L_N/T_N	L_X/T_X (zero dose)	% Recoup.	Recup. fractional dose offset
K2130	A	31	69.44	1.06	0.04	-0.31	10.01	0.018	0.18%	-0.25
K2130	A	33	85.40	0.98	0.04	-0.15	11.69	0.031	0.27%	0.11
K2130	A	35	73.86	0.98	0.04	-0.26	9.07	-0.012	0.13%	-0.45
K2131	A	1	50.07	0.95	0.04	0.25	7.21	0.013	0.18%	-0.39
K2131	A	3	42.92	0.95	0.03	0.07	7.28	0.008	0.11%	-0.63
K2131	A	5	36.53	1.01	0.04	-0.09	5.84	0.013	0.22%	-0.25
K2131	A	7	38.63	0.98	0.04	-0.03	7.08	0.009	0.13%	-0.57
K2131	A	9	43.21	0.98	0.04	0.08	6.36	-0.004	0.06%	-0.79
K2131	A	11	34.15	0.96	0.03	-0.15	6.20	0.016	0.26%	-0.13
K2131	A	13	51.70	1.01	0.04	0.29	8.16	0.015	0.18%	-0.38
K2131	A	15	35.58	0.92	0.04	-0.11	6.41	0.012	0.19%	-0.37
K2131	A	17	37.58	0.96	0.04	-0.06	6.10	0.005	0.08%	-0.72
K2131	A	19	43.21	1.05	0.05	0.08	5.92	0.009	0.15%	-0.49
K2131	A	21	51.22	0.95	0.04	0.28	7.94	0.013	0.16%	-0.45
K2131	A	23	33.19	1.03	0.04	-0.17	5.38	0.007	0.13%	-0.56
K2131	A	25	37.39	0.95	0.05	-0.06	6.77	0.024	0.35%	0.19
K2131	A	27	35.86	0.98	0.04	-0.10	6.33	0.027	0.43%	0.44
K2131	A	29	42.16	1.00	0.04	0.06	6.87	0.005	0.07%	-0.75
K2131	A	31	26.64	0.95	0.06	-0.33	5.21	0.008	0.15%	-0.48
K2131	A	33	47.70	0.95	0.03	0.19	7.43	0.014	0.19%	-0.37
K2131	A	35	31.26	0.98	0.04	-0.22	5.68	0.130	2.29%	6.71
K2132	A	1	30.79	0.97	0.03	-0.12	5.67	0.005	0.09%	-0.52
K2132	A	3	30.27	0.96	0.03	-0.13	5.50	0.008	0.15%	-0.21
K2132	A	5	31.07	0.97	0.03	-0.11	6.13	0.009	0.15%	-0.20
K2132	A	9	53.16	0.88	0.05	0.52	9.10	-0.005	0.05%	-0.70
K2132	A	11	28.73	0.94	0.04	-0.18	5.36	-0.001	0.02%	-0.90
K2132	A	13	37.26	1.00	0.04	0.07	5.59	0.030	0.54%	1.92
K2132	A	15	23.69	1.00	0.05	-0.32	4.05	-0.006	0.15%	-0.20
K2132	A	17	50.47	0.85	0.06	0.44	8.69	0.034	0.39%	1.13
K2132	A	19	40.69	0.96	0.03	0.16	7.00	0.009	0.13%	-0.30
K2132	A	21	30.79	0.98	0.03	-0.12	5.46	0.005	0.09%	-0.50
K2132	A	23	51.10	1.02	0.04	0.46	7.30	0.004	0.05%	-0.70
K2132	A	25	22.93	0.90	0.05	-0.34	4.72	-0.002	0.04%	-0.77
K2132	A	27	31.53	0.98	0.04	-0.10	5.58	0.019	0.34%	0.85
K2132	A	29	31.48	0.99	0.05	-0.10	6.16	0.052	0.84%	3.59
K2132	A	31	31.48	0.99	0.04	-0.10	4.94	0.000	0.00%	-1.00
K2132	A	33	42.96	1.01	0.04	0.23	6.61	0.005	0.08%	-0.59
K2132	A	35	25.93	1.01	0.04	-0.26	4.63	0.001	0.02%	-0.88
K2133	A	13	2.73	0.83	0.11	-0.36	2.88	0.015	0.52%	-0.26
K2133	A	15	1.41	1.06	0.11	-0.67	1.51	-0.006	0.40%	-0.43
K2133	A	19	6.66	1.19	0.24	0.56	5.85	0.053	0.91%	0.29
K2133	A	21	2.31	0.86	0.09	-0.46	2.42	0.052	2.15%	2.06
K2133	A	23	1.89	0.93	0.07	-0.56	2.08	-0.004	0.19%	-0.73
K2133	A	25	2.97	1.04	0.09	-0.30	3.42	0.021	0.61%	-0.13
K2133	A	27	12.83	0.87	0.24	2.01	11.76	-0.089	0.76%	0.08
K2133	A	35	3.30	1.18	0.09	-0.23	3.55	-0.003	0.08%	-0.88
K2134	B	3	0.13	0.99	0.19	-0.09	2.26	0.066	2.92%	-0.42
K2134	B	4	0.15	0.94	0.18	0.10	2.55	0.014	0.55%	-0.89
K2134	B	12	0.13	0.84	0.14	-0.09	1.93	0.169	8.76%	0.73
K2134	B	15	0.15	1.07	0.21	0.08	2.36	-0.188	7.97%	0.58

Sample	Risø	Aliquot	Final D_e	Recyc ratio	Recyc error	Recyc. fractional dose offset	L_N/T_N	L_X/T_X (zero dose)	% Recoup.	Recup. fractional dose offset
K2135	A	1	4.04	1.00	0.06	0.08	0.91	0.001	0.11%	-0.94
K2135	A	3	1.30	1.00	0.04	-0.65	0.30	0.003	1.00%	-0.48
K2135	A	5	1.98	1.05	0.04	-0.47	0.46	0.006	1.30%	-0.32
K2135	A	7	1.83	1.01	0.04	-0.51	0.41	0.008	1.95%	0.02
K2135	A	9	3.13	0.98	0.05	-0.16	0.70	0.005	0.71%	-0.63
K2135	A	11	21.14	1.05	0.05	4.66	4.45	0.014	0.31%	-0.84
K2135	A	13	2.82	1.02	0.06	-0.24	0.64	0.024	3.75%	0.96
K2135	A	15	1.37	1.02	0.05	-0.63	0.35	0.006	1.71%	-0.10
K2135	A	17	3.66	1.05	0.04	-0.02	0.82	0.002	0.24%	-0.87
K2135	A	19	1.83	1.07	0.05	-0.51	0.42	0.031	7.38%	2.86
K2135	A	21	1.14	1.05	0.04	-0.69	0.28	0.011	3.93%	1.05
K2135	A	23	3.82	1.15	0.09	0.02	0.80	0.035	4.38%	1.29
K2135	A	25	3.20	1.10	0.05	-0.14	0.78	-0.001	0.13%	-0.93
K2135	A	27	2.21	1.10	0.06	-0.41	0.50	0.006	1.20%	-0.37
K2135	A	29	6.71	0.97	0.05	0.80	1.54	0.014	0.91%	-0.52
K2135	A	31	2.15	1.08	0.05	-0.42	0.50	0.000	0.00%	-1.00
K2135	A	33	3.46	1.05	0.04	-0.07	0.77	-0.001	0.13%	-0.93
K2135	A	35	1.38	0.99	0.05	-0.63	0.36	0.019	5.28%	1.76
K2136	B	3	0.05	0.74	0.17	-0.42	0.90	0.305	33.89%	1.23
K2136	B	4	0.07	1.04	0.17	-0.16	1.25	0.066	5.28%	-0.65
K2136	B	5	0.09	0.93	0.10	0.01	1.47	0.195	13.27%	-0.13
K2136	B	6	0.12	1.18	0.28	0.38	1.67	0.103	6.17%	-0.59
K2136	B	7	0.11	1.15	0.11	0.24	1.85	-0.008	0.43%	-0.97
K2136	B	9	0.06	1.07	0.14	-0.29	1.28	0.175	13.67%	-0.10
K2136	B	10	0.08	1.37	0.34	-0.06	1.42	-0.094	6.62%	-0.56
K2136	B	11	0.08	1.03	0.15	-0.08	1.58	0.145	9.18%	-0.40
K2136	B	13	0.09	1.00	0.15	0.06	1.42	0.721	50.77%	2.35
K2136	B	15	0.11	1.09	0.13	0.33	2.19	0.274	12.51%	-0.18
K2079	A	7	68.45	1.06	0.06	0.06	32127	544	1.69%	0.06
K2079	A	27	58.38	1.10	0.05	-0.10	104606	3602	3.44%	-0.10
K2079	A	29	66.99	1.01	0.04	0.04	235629	2665	1.13%	0.04
K2080	A	1	98.93	1.06	0.04	0.36	209352	1415	0.68%	0.36
K2080	A	3	51.52	1.09	0.04	-0.29	219317	3274	1.49%	-0.29
K2080	A	5	61.86	0.98	0.04	-0.15	269735	2811	1.04%	-0.15
K2080	A	7	53.68	1.03	0.05	-0.26	46043	673	1.46%	-0.26
K2080	A	9	48.98	0.95	0.07	-0.32	9762	317	3.25%	-0.32
K2080	A	11	108.90	1.07	0.04	0.50	257013	1946	0.76%	0.50
K2080	A	13	45.50	1.11	0.07	-0.37	11375	484	4.25%	-0.37
K2080	A	15	74.03	1.04	0.04	0.02	656083	3195	0.49%	0.02
K2080	A	17	66.15	1.01	0.04	-0.09	165493	5952	3.60%	-0.09
K2080	A	19	50.95	1.09	0.04	-0.30	214718	6447	3.00%	-0.30
K2080	A	21	135.12	1.03	0.04	0.86	276691	3825	1.38%	0.86
K2080	A	25	64.88	1.02	0.04	-0.11	445153	4298	0.97%	-0.11
K2080	A	27	73.37	1.00	0.04	0.01	101505	2242	2.21%	0.01
K2080	A	29	71.23	1.01	0.04	-0.02	211559	4452	2.10%	-0.02
K2080	A	33	72.79	1.05	0.04	0.00	200272	1926	0.96%	0.00
K2080	A	35	82.74	1.10	0.05	0.59	206201	2785	1.35%	0.59
K2081	A	1	49.60	0.99	0.04	-0.05	169751	1036	0.61%	-0.05
K2081	A	5	66.70	0.97	0.04	0.28	89637	549	0.61%	0.28
K2081	A	7	49.90	0.99	0.04	-0.04	62571	610	0.97%	-0.04
K2081	A	9	44.03	0.99	0.04	-0.15	460272	4507	0.98%	-0.15

Sample	Risø	Aliquot	Final D_e	Recyc ratio	Recyc error	Recyc. fractional dose offset	L_N/T_N	L_X/T_X (zero dose)	% Recoup.	Recup. fractional dose offset
K2081	A	11	53.07	1.00	0.05	0.02	62693	892	1.42%	0.02
K2081	A	13	35.36	1.02	0.05	-0.32	75331	2614	3.47%	-0.32
K2081	A	15	34.84	0.98	0.04	-0.33	48851	1632	3.34%	-0.33
K2081	A	17	65.04	0.96	0.04	0.25	345798	1488	0.43%	0.25
K2081	A	19	42.44	0.98	0.04	-0.18	58424	2292	3.92%	-0.18
K2081	A	21	40.82	1.03	0.05	-0.21	42060	733	1.74%	-0.21
K2081	A	25	56.40	0.99	0.04	0.09	194710	1389	0.71%	0.09
K2081	A	29	47.98	0.96	0.04	-0.08	138849	1525	1.10%	-0.08
K2081	A	33	58.41	1.00	0.04	0.12	94784	719	0.76%	0.12
K2082	A	1	17.74	0.97	0.04	-0.02	116673	1587	1.36%	-0.02
K2082	A	7	18.35	1.00	0.04	0.01	67879	740	1.09%	0.01
K2082	A	11	20.16	0.95	0.04	0.11	70757	844	1.19%	0.11
K2082	A	13	15.44	0.99	0.04	-0.15	116905	2451	2.10%	-0.15
K2082	A	17	15.47	1.05	0.05	-0.15	21286	403	1.89%	-0.15
K2082	A	19	20.34	1.06	0.05	0.12	55781	332	0.60%	0.12
K2082	A	25	14.54	0.99	0.04	-0.20	49763	837	1.68%	-0.20
K2082	A	27	21.55	1.06	0.05	0.19	70622	1154	1.63%	0.19
K2082	A	29	15.33	1.00	0.04	-0.15	42581	1449	3.40%	-0.15
K2082	A	31	19.32	1.07	0.05	0.07	62786	2759	4.39%	0.07
K2082	A	35	21.19	1.02	0.05	0.17	23121	369	1.60%	0.17
K2083	B	11	0.07	0.87	0.13	-0.49	1498	870	58.08%	-0.49
K2083	B	4	0.07	1.02	0.12	-0.46	2735	1702	62.23%	-0.46
K2083	B	5	0.14	1.22	0.18	0.10	2593	1301	50.17%	0.10
K2083	B	7	0.06	0.96	0.16	-0.55	1042	675	64.78%	-0.55
K2083	B	8	0.38	0.66	0.19	1.96	2286	552	24.15%	1.96
K2083	B	9	0.09	1.25	0.12	-0.27	2976	856	28.76%	-0.27
K2083	B	10	0.08	1.23	0.11	-0.36	2999	874	29.14%	-0.36
K2083	B	11	0.06	0.71	0.12	-0.53	1663	800	48.11%	-0.53
K2083	B	12	0.23	1.04	0.12	0.78	4847	683	14.09%	0.78
K2083	B	13	0.13	1.03	0.18	0.00	1369	397	29.00%	0.00
K2083	B	15	0.14	0.85	0.14	0.12	2213	541	24.45%	

Appendix G.2. Primary variables used in OSL dose rate calculations

Sample	External gamma-dose (Gy/ka)	external gamma-dose error	% K	%K error	Th (ppm)	Th error (ppm)	U (ppm)	U error (ppm)	Depth (m)	Depth error (m)	Altitude (m asl)	Soft cosmic	Cosmic dose rate (Gy/ka)	Cosmic dose rate error	Moisture content	error	Total dose rate, Gy/ka	error
K2079	0.43	0.022	0.72	0.04	5.06	0.25	0.79	0.04	16.50	0.03	74.87	0.00	0.04	0.00	0.05	0.03	1.18	0.07
K2080	0.43	0.022	0.75	0.04	4.45	0.22	0.78	0.04	6.80	0.03	81.35	0.00	0.09	0.01	0.09	0.03	1.21	0.07
K2081	0.51	0.026	0.62	0.03	5.72	0.29	0.68	0.03	5.70	0.03	81.76	0.00	0.10	0.01	0.03	0.02	1.28	0.06
K2082	0.38	0.019	0.36	0.02	3.35	0.17	0.43	0.02	0.50	0.03	89.74	0.00	0.20	0.02	0.03	0.02	0.97	0.04
K2083	0.28	0.014	0.39	0.02	2.05	0.10	0.31	0.02	13.00	0.03	90.61	0.00	0.05	0.00	0.03	0.02	0.70	0.03
K2084	0.24	0.012	0.26	0.01	2.15	0.11	0.28	0.01	3.00	0.03	92.74	0.00	0.14	0.01	0.03	0.02	0.65	0.03
K2085	0.25	0.013	0.58	0.03	4.36	0.22	0.54	0.03	10.00	0.03	93.87	0.00	0.07	0.00	0.05	0.03	0.88	0.06
K2086	0.25	0.013	0.29	0.01	2.97	0.15	0.33	0.02	15.00	0.03	95.83	0.00	0.04	0.00	0.02	0.01	0.62	0.03
K2087	0.24	0.012	0.25	0.01	1.76	0.09	0.22	0.01	6.00	0.03	104.01	0.00	0.10	0.01	0.02	0.01	0.59	0.02
K2088	0.41	0.021	0.62	0.03	5.16	0.26	0.61	0.03	0.20	0.03	79.03	0.01	0.21	0.04	0.02	0.01	1.27	0.06
K2089	0.44	0.022	0.55	0.03	3.61	0.18	1.51	0.08	2.30	0.03	80.23	0.00	0.16	0.01	0.05	0.03	1.26	0.06
K2090	0.44	0.022	0.69	0.03	3.86	0.19	0.63	0.03	2.70	0.03	82.39	0.00	0.15	0.01	0.05	0.03	1.25	0.07
K2091	0.42	0.021	0.49	0.02	4.22	0.21	0.83	0.04	4.80	0.03	82.58	0.00	0.11	0.01	0.03	0.02	1.10	0.05
K2092	0.49	0.025	0.36	0.02	2.40	0.12	0.33	0.02	4.30	0.03	83.41	0.00	0.12	0.01	0.03	0.02	0.97	0.03
K2093	0.75	0.037	1.11	0.06	7.87	0.39	1.74	0.09	3.80	0.03	83.92	0.00	0.13	0.01	0.05	0.03	2.06	0.11
K2094	0.29	0.014	0.30	0.01	2.55	0.13	0.30	0.02	4.80	0.03	91.82	0.00	0.12	0.01	0.03	0.02	0.72	0.03
K2095	0.27	0.013	0.35	0.02	2.13	0.11	0.32	0.02	0.30	0.03	79.03	0.00	0.20	0.02	0.02	0.01	0.81	0.04
K2096	0.25	0.012	0.24	0.01	2.98	0.15	0.33	0.02	0.10	0.03	79.03	0.00	0.20	0.06	0.02	0.01	0.74	0.07
K2097	0.43	0.022	0.52	0.03	3.61	0.18	0.38	0.02	0.30	0.03	79.03	0.01	0.21	0.03	0.02	0.01	1.16	0.05
K2098	0.35	0.018	0.42	0.02	4.42	0.22	0.60	0.03	0.60	0.03	73.64	0.00	0.19	0.02	0.03	0.02	0.99	0.05
K2099	0.28	0.014	0.21	0.01	3.40	0.17	0.46	0.02	2.00	0.03	75.31	0.00	0.16	0.01	0.03	0.02	0.72	0.03
K2100	0.31	0.015	0.25	0.01	3.58	0.18	0.46	0.02	0.30	0.03	76.93	0.00	0.20	0.02	0.03	0.02	0.83	0.04
K2101	0.21	0.010	0.20	0.00	2.37	0.00	0.29	0.00	1.00	0.03	79.40	0.00	0.18	0.01	0.02	0.01	0.63	0.02
K2102	0.30	0.015	0.31	0.02	2.56	0.13	0.32	0.02	0.45	0.03	79.03	0.01	0.20	0.02	0.02	0.01	0.83	0.04
K2103	0.15	0.008	0.15	0.01	1.64	0.08	0.19	0.01	0.15	0.03	64.98	0.01	0.22	0.05	0.02	0.01	0.54	0.05
K2104	0.17	0.009	0.18	0.01	1.84	0.09	0.24	0.01	0.55	0.03	73.28	0.00	0.19	0.02	0.02	0.01	0.58	0.02
K2105	0.40	0.020	0.68	0.03	4.44	0.22	0.72	1.00	0.20	0.03	79.03	0.01	0.21	0.022	0.02	0.01	1.31	0.24
K2106	0.23	0.012	0.45	0.02	2.67	0.13	0.42	0.02	0.20	0.03	79.14	0.01	0.21	0.022	0.02	0.01	0.89	0.05

Sample	External gamma-dose (Gy/ka)	external gamma-dose error	% K	%K error	Th (ppm)	Th error (ppm)	U (ppm)	U error (ppm)	Depth (m)	Depth error (m)	Altitude (m asl)	Soft cosmic	Cosmic dose rate (Gy/ka)	Cosmic dose rate error	Moisture content	error	Total dose rate, Gy/ka	error
K2107	0.28	0.014	0.54	0.03	2.41	0.12	0.43	0.02	0.40	0.03	79.50	0.01	0.21	0.026	0.02	0.01	0.97	0.05
K2108	0.24	0.012	0.40	0.02	2.57	0.13	0.38	0.02	2.30	0.03	75.72	0.00	0.16	0.019	0.02	0.01	0.77	0.04
K2109	0.22	0.011	0.32	0.02	2.25	0.11	0.35	0.02	2.00	0.03	76.02	0.01	0.17	0.014	0.02	0.01	0.72	0.03
K2110	0.28	0.014	0.53	0.03	1.85	0.09	0.34	0.02	0.50	0.03	75.30	0.00	0.20	0.012	0.02	0.01	0.94	0.05
K2111	0.26	0.013	0.40	0.02	2.32	0.12	0.34	0.02	1.50	0.03	75.03	0.00	0.17	0.013	0.03	0.02	0.81	0.04
K2112	0.25	0.013	0.41	0.02	2.63	0.13	0.37	0.02	2.50	0.03	73.05	0.00	0.15	0.013	0.03	0.02	0.80	0.04
K2113	0.30	0.015	0.49	0.02	3.56	0.18	0.55	0.03	2.00	0.03	73.04	0.00	0.16	0.012	0.03	0.02	0.97	0.04
K2114	0.58	0.029	0.94	0.05	7.37	0.37	0.99	0.05	3.00	0.03	72.66	0.00	0.14	0.021	0.05	0.03	1.70	0.08
K2115	0.29	0.015	0.35	0.02	2.05	0.10	0.36	0.02	4.00	0.03	72.29	0.00	0.13	0.022	0.03	0.02	0.77	0.03
K2116	0.40	0.020	0.53	0.03	2.96	0.15	0.50	0.03	5.00	0.03	71.26	0.00	0.11	0.022	0.03	0.02	1.02	0.05
K2117	0.39	0.020	0.32	0.02	2.82	0.14	0.47	0.02	3.50	0.03	71.66	0.00	0.13	0.021	0.03	0.02	0.88	0.03
K2118	0.48	0.024	0.79	0.04	4.11	0.21	0.81	0.04	3.80	0.03	70.49	0.00	0.13	0.025	0.03	0.02	1.37	0.07
K2119	0.32	0.016	0.62	0.03	2.62	0.13	0.50	0.03	0.50	0.03	71.42	0.01	0.21	0.037	0.03	0.02	1.10	0.05
K2120	0.29	0.015	0.48	0.02	2.25	0.11	0.40	0.02	2.00	0.03	72.12	0.01	0.17	0.014	0.02	0.01	0.92	0.04
K2121	0.23	0.011	0.46	0.02	2.10	0.11	0.39	0.02	1.50	0.03	70.77	0.01	0.18	0.013	0.03	0.02	0.85	0.04
K2122	0.25	0.013	0.35	0.02	2.11	0.11	0.38	0.02	1.70	0.03	71.58	0.00	0.17	0.012	0.02	0.01	0.77	0.03
K2123	0.30	0.015	0.53	0.03	3.06	0.15	0.53	0.03	2.20	0.03	78.35	0.00	0.16	0.022	0.03	0.02	0.98	0.04
K2124	0.25	0.013	0.37	0.02	3.78	0.19	0.33	0.02	1.00	0.03	80.08	0.00	0.18	0.018	0.03	0.02	0.83	0.04
K2125	0.24	0.012	0.23	0.01	2.20	0.11	0.28	0.01	0.60	0.03	81.10	0.00	0.19	0.014	0.02	0.01	0.68	0.03
K2126	0.22	0.011	0.26	0.01	2.39	0.12	0.29	0.01	0.30	0.03	81.40	0.01	0.21	0.015	0.02	0.01	0.71	0.03
K2127	0.39	0.019	0.68	0.03	3.43	0.17	0.40	0.02	0.10	0.03	67.27	0.00	0.21	0.010	0.02	0.01	1.22	0.08
K2128	0.36	0.018	0.36	0.02	2.88	0.14	0.32	0.02	0.10	0.03	67.18	0.01	0.22	0.015	0.02	0.01	0.94	0.07
K2129	0.88	0.044	0.17	0.01	1.81	0.09	0.24	0.01	0.10	0.03	69.64	0.01	0.22	0.008	0.02	0.01	1.28	0.07
K2130	0.70	0.035	1.55	0.08	10.90	0.55	1.46	0.07	3.40	0.03	81.15	0.00	0.14	0.009	0.09	0.03	2.38	0.13
K2131	0.68	0.034	0.89	0.04	6.03	0.30	0.81	0.04	2.20	0.03	82.35	0.00	0.16	0.020	0.05	0.03	1.71	0.08
K2132	0.22	0.011	0.76	0.04	5.21	0.26	0.64	0.03	2.00	0.03	82.50	0.00	0.16	0.012	0.05	0.03	1.11	0.07
K2133	0.47	0.023	0.64	0.03	4.53	0.23	0.53	0.03	0.90	0.03	83.65	0.00	0.19	0.014	0.03	0.02	1.29	0.06
K2134	0.36	0.018	0.66	0.03	3.63	0.18	0.45	0.02	0.80	0.03	83.75	0.00	0.19	0.012	0.03	0.02	1.16	0.06
K2135	0.78	0.039	1.23	0.06	8.57	0.43	0.87	0.04	1.30	0.03	83.25	0.00	0.18	0.011	0.05	0.03	2.15	0.11
K2136	0.32	0.016	0.60	0.03	2.88	0.14	0.34	0.02	0.10	0.03	84.45	0.00	0.21	0.014	0.02	0.01	1.07	0.08

APPENDIX G. ADDITIONAL OSL DATA

All samples used the following average estimates:
Standard fractional error: 0.05
Average overburden density: 1.9±0.10 g/cm^3
Approximate latitude: -33.00
Approximate longitude 143.00

Appendix G.3. Supplementary variables used in OSL dose rate calculations

Laboratory code	K2079	K2080	K2081	K2082	K2083	K2084	K2085	K2086
Average beta-attenuation								
standard fractional error	0.050	0.050	0.050	0.050	0.050	0.050	0.050	0.050
Natural U	0.877	0.877	0.877	0.877	0.877	0.877	0.877	0.877
error	0.044	0.044	0.044	0.044	0.044	0.044	0.044	0.044
Th-232	0.822	0.822	0.822	0.822	0.822	0.822	0.822	0.822
error	0.041	0.041	0.041	0.041	0.041	0.041	0.041	0.041
K-40	0.946	0.946	0.946	0.946	0.946	0.946	0.946	0.946
error	0.047	0.047	0.047	0.047	0.047	0.047	0.047	0.047
Dose rate conversion (Gy/ka)								
standard fractional error	0.050	0.050	0.050	0.050	0.050	0.050	0.050	0.050
U (ppm)								
Beta	0.146	0.146	0.146	0.146	0.146	0.146	0.146	0.146
error	0.007	0.007	0.007	0.007	0.007	0.007	0.007	0.007
Gamma	0.112	0.112	0.112	0.112	0.112	0.112	0.112	0.112
error	0.000	0.000	0.000	0.000	0.000	0.000	0.000	0.000
Th (ppm)								
Beta	0.028	0.028	0.028	0.028	0.028	0.028	0.028	0.028
error	0.001	0.001	0.001	0.001	0.001	0.001	0.001	0.001
Gamma	0.048	0.048	0.048	0.048	0.048	0.048	0.048	0.048
error	0.000	0.000	0.000	0.000	0.000	0.000	0.000	0.000
K (%)								
Beta	0.798	0.798	0.798	0.798	0.798	0.798	0.798	0.798
error	0.040	0.040	0.040	0.040	0.040	0.040	0.040	0.040
Gamma	0.249	0.249	0.249	0.249	0.249	0.249	0.249	0.249
error	0.000	0.000	0.000	0.000	0.000	0.000	0.000	0.000
Cosmic dose								
Geomagnetic latitude	-42.7	-42.7	-42.7	-42.7	-42.7	-42.7	-42.7	-42.7
Dc (Gy/ka).	0.039	0.092	0.104	0.196	0.051	0.142	0.067	0.044
error	0.003	0.007	0.008	0.018	0.004	0.010	0.005	0.003
Moisture								
F	0.229	0.314	0.176	0.176	0.176	0.176	0.229	0.143
error	0.097	0.074	0.083	0.083	0.083	0.083	0.097	0.051
W	0.229	0.314	0.176	0.176	0.176	0.176	0.229	0.143
error	0.097	0.074	0.083	0.083	0.083	0.083	0.097	0.051
WF	0.053	0.099	0.031	0.031	0.031	0.031	0.053	0.020
error	0.032	0.033	0.021	0.021	0.021	0.021	0.032	0.010
Age uncertainties								
dDR/K	0.944	0.896	0.968	0.968	0.968	0.968	0.944	0.980
dDR/dC(B, K)	0.640	0.635	0.562	0.326	0.356	0.238	0.511	0.268
dDR/dA(K)	0.540	0.535	0.474	0.275	0.300	0.200	0.431	0.226
dDR/dTh	0.067	0.063	0.068	0.068	0.068	0.068	0.067	0.069
dDR/dC(B, Th)	3.902	3.255	4.526	2.651	1.622	1.701	3.362	2.380
dDR/dA(Th)	0.132	0.110	0.153	0.089	0.055	0.057	0.113	0.080
dDR/dU	0.225	0.214	0.231	0.231	0.231	0.231	0.225	0.234
dDR/dC(B, U)	0.823	0.781	0.844	0.844	0.844	0.844	0.823	0.855
dDR/dA(U)	0.108	0.101	0.095	0.060	0.043	0.039	0.074	0.047
dDR/dW	-0.311	-0.381	-0.233	-0.137	-0.121	-0.095	-0.248	-0.095
dDR/dF	-0.311	-0.381	-0.233	-0.137	-0.121	-0.095	-0.248	-0.095
dDR/C(G, K)	0.680	0.677	0.596	0.345	0.377	0.252	0.543	0.284
dDR/C(G, Th)	4.774	3.999	5.525	3.236	1.980	2.077	4.113	2.902
dDR/dC(G, U)	0.745	0.701	0.657	0.415	0.299	0.270	0.509	0.322
dDR/dCosmic	1.000	1.000	1.000	1.000	1.000	1.000	1.000	1.000
Dage/dDe	0.845	0.827	0.784	1.035	1.425	1.541	1.133	1.622
Dage/dDR	-90.697	-48.741	-33.323	-18.183	-0.258	-9.119	-0.203	-0.255

Laboratory code	K2087	K2088	K2090	K2091	K2092	K2093	K2094	K2095
Average beta-attenuation								
standard fractional error	0.050	0.050	0.050	0.050	0.050	0.050	0.050	0.050
Natural U	0.877	0.877	0.903	0.903	0.903	0.903	0.903	0.903
error	0.044	0.044	0.045	0.045	0.045	0.045	0.045	0.045
Th-232	0.822	0.822	0.856	0.856	0.856	0.856	0.856	0.856
error	0.041	0.041	0.043	0.043	0.043	0.043	0.043	0.043
K-40	0.946	0.946	0.964	0.964	0.964	0.964	0.964	0.964
error	0.047	0.047	0.048	0.048	0.048	0.048	0.048	0.048
Dose rate conversion (Gy/ka)								
standard fractional error	0.050	0.050	0.050	0.050	0.050	0.050	0.050	0.050
U (ppm)								
Beta	0.146	0.146	0.146	0.146	0.146	0.146	0.146	0.146
error	0.007	0.007	0.007	0.007	0.007	0.007	0.007	0.007
Gamma	0.112	0.112	0.112	0.112	0.112	0.112	0.112	0.112
error	0.000	0.000	0.000	0.000	0.000	0.000	0.000	0.000
Th (ppm)								
Beta	0.028	0.028	0.028	0.028	0.028	0.028	0.028	0.028
error	0.001	0.001	0.001	0.001	0.001	0.001	0.001	0.001
Gamma	0.048	0.048	0.048	0.048	0.048	0.048	0.048	0.048
error	0.000	0.000	0.000	0.000	0.000	0.000	0.000	0.000
K (%)								
Beta	0.798	0.798	0.798	0.798	0.798	0.798	0.798	0.798
error	0.040	0.040	0.040	0.040	0.040	0.040	0.040	0.040
Gamma	0.249	0.249	0.249	0.249	0.249	0.249	0.249	0.249
error	0.000	0.000	0.000	0.000	0.000	0.000	0.000	0.000
Cosmic dose								
Geomagnetic latitude	-42.7	-42.7	-42.7	-42.7	-42.7	-42.7	-42.7	-42.7
Dc (Gy/ka)	0.100	0.204	0.148	0.115	0.122	0.129	0.115	0.202
error	0.007	0.034	0.011	0.008	0.009	0.009	0.008	0.025
Moisture								
F	0.143	0.143	0.229	0.176	0.176	0.229	0.176	0.143
error	0.051	0.051	0.097	0.083	0.083	0.097	0.083	0.051
W	0.143	0.143	0.229	0.176	0.176	0.229	0.176	0.143
error	0.051	0.051	0.097	0.083	0.083	0.097	0.083	0.051
WF	0.020	0.020	0.053	0.031	0.031	0.053	0.031	0.020
error	0.010	0.010	0.032	0.021	0.021	0.032	0.021	0.010
Age uncertainties	1.000	1.000	1.000	1.000	1.000	1.000	1.000	1.000
dDR/K	0.980	0.980	0.957	0.981	0.981	0.957	0.981	0.994
dDR/dC(B, K)	0.227	0.569	0.626	0.454	0.331	1.000	0.274	0.324
dDR/dA(K)	0.192	0.480	0.519	0.376	0.274	0.828	0.227	0.269
dDR/dTh	0.069	0.069	0.067	0.069	0.069	0.067	0.069	0.070
dDR/dC(B, Th)	1.411	4.136	3.100	3.477	1.978	6.320	2.101	1.778
dDR/dA(Th)	0.048	0.139	0.100	0.113	0.064	0.205	0.068	0.058
dDR/dU	0.234	0.234	0.229	0.235	0.235	0.229	0.235	0.237
dDR/dC(B, U)	0.855	0.855	0.848	0.870	0.870	0.848	0.870	0.881
dDR/dA(U)	0.031	0.087	0.086	0.116	0.046	0.238	0.042	0.045
dDR/dW	-0.070	-0.185	-0.278	-0.197	-0.121	-0.517	-0.110	-0.096
dDR/dF	-0.070	-0.185	-0.278	-0.197	-0.121	-0.517	-0.110	-0.096
dDR/C(G, K)	0.241	0.602	0.653	0.472	0.345	1.043	0.285	0.337
dDR/C(G, Th)	1.720	5.043	3.642	4.076	2.318	7.425	2.463	2.082
dDR/dC(G, U)	0.215	0.596	0.594	0.802	0.319	1.642	0.290	0.313
dDR/dCosmic	1.000	1.000	1.000	1.000	1.000	1.000	1.000	1.000
Dage/dDe	1.704	0.788	0.800	0.913	1.028	0.485	1.396	1.230
Dage/dDR	-0.125	-0.070	-88.144	-74.243	-53.054	-18.220	-75.827	-0.092

Laboratory code	K2096	K2097	K2098	K2099	K2100	K2101	K2102	K2103
Average beta-attenuation								
standard fractional error	0.050	0.050	0.050	0.050	0.050	0.050	0.050	0.050
Natural U	0.903	0.903	0.877	0.877	0.877	0.903	0.903	0.903
error	0.045	0.045	0.044	0.044	0.044	0.045	0.045	0.045
Th-232	0.856	0.856	0.822	0.822	0.822	0.856	0.856	0.856
error	0.043	0.043	0.041	0.041	0.041	0.043	0.043	0.043
K-40	0.964	0.964	0.946	0.946	0.946	0.964	0.964	0.964
error	0.048	0.048	0.047	0.047	0.047	0.048	0.048	0.048
Dose rate conversion (Gy/ka)								
standard fractional error	0.050	0.050	0.050	0.050	0.050	0.050	0.050	0.050
U (ppm)								
Beta	0.146	0.146	0.146	0.146	0.146	0.146	0.146	0.146
error	0.007	0.007	0.007	0.007	0.007	0.007	0.007	0.007
Gamma	0.112	0.112	0.112	0.112	0.112	0.112	0.112	0.112
error	0.000	0.000	0.000	0.000	0.000	0.000	0.000	0.000
Th (ppm)								
Beta	0.028	0.028	0.028	0.028	0.028	0.028	0.028	0.028
error	0.001	0.001	0.001	0.001	0.001	0.001	0.001	0.001
Gamma	0.048	0.048	0.048	0.048	0.048	0.048	0.048	0.048
error	0.000	0.000	0.000	0.000	0.000	0.000	0.000	0.000
K (%)								
Beta	0.798	0.798	0.798	0.798	0.798	0.798	0.798	0.798
error	0.040	0.040	0.040	0.040	0.040	0.040	0.040	0.040
Gamma	0.249	0.249	0.249	0.249	0.249	0.249	0.249	0.249
error	0.000	0.000	0.000	0.000	0.000	0.000	0.000	0.000
Cosmic dose								
Geomagnetic latitude	-42.7	-42.7	-42.7	-42.7	-42.7	-42.7	-42.7	-42.7
Dc (Gy/ka)	0.207	0.202	0.194	0.161	0.202	0.184	0.198	0.206
error	0.064	0.025	0.017	0.012	0.025	0.014	0.019	0.044
Moisture								
F	0.143	0.143	0.314	0.176	0.176	0.176	0.176	0.229
error	0.051	0.051	0.074	0.083	0.083	0.083	0.083	0.097
W	0.143	0.143	0.314	0.176	0.176	0.176	0.176	0.229
error	0.051	0.051	0.074	0.083	0.083	0.083	0.083	0.097
WF	0.020	0.020	0.099	0.031	0.031	0.031	0.031	0.053
error	0.010	0.010	0.033	0.021	0.021	0.021	0.021	0.032
Age uncertainties	1.000	1.000	1.000	1.000	1.000	1.000	1.000	1.000
dDR/K	0.994	0.994	0.896	0.968	0.968	0.981	0.981	0.957
dDR/dC(B, K)	0.226	0.486	0.352	0.191	0.232	0.185	0.284	0.138
dDR/dA(K)	0.188	0.402	0.297	0.161	0.196	0.153	0.235	0.114
dDR/dTh	0.070	0.070	0.063	0.068	0.068	0.069	0.069	0.067
dDR/dC(B, Th)	2.487	3.013	3.233	2.691	2.833	1.953	2.109	1.317
dDR/dA(Th)	0.080	0.098	0.109	0.091	0.095	0.063	0.068	0.043
dDR/dU	0.237	0.237	0.214	0.231	0.231	0.235	0.235	0.229
dDR/dC(B, U)	0.881	0.881	0.781	0.844	0.844	0.870	0.870	0.848
dDR/dA(U)	0.047	0.054	0.078	0.065	0.065	0.041	0.045	0.026
dDR/dW	-0.088	-0.144	-0.264	-0.110	-0.121	-0.087	-0.113	-0.078
dDR/dF	-0.088	-0.144	-0.264	-0.110	-0.121	-0.087	-0.113	-0.078
dDR/C(G, K)	0.236	0.505	0.375	0.202	0.246	0.193	0.296	0.144
dDR/C(G, Th)	2.912	3.528	3.972	3.284	3.458	2.289	2.473	1.547
dDR/dC(G, U)	0.322	0.371	0.539	0.444	0.444	0.280	0.309	0.179
dDR/dCosmic	1.000	1.000	1.000	1.000	1.000	1.000	1.000	1.000
Dage/dDe	1.346	0.862	1.015	1.386	1.208	1.586	1.210	1.862
Dage/dDR	-0.096	-23.680	-34.620	-95.084	-0.277	-10.646	-0.042	-0.094

Laboratory code	K2104	K2105	K2106	K2107	K2108	K2109	K2110	K2111
Average beta-attenuation								
standard fractional error	0.050	0.050	0.050	0.050	0.050	0.050	0.050	0.050
Natural U	0.903	0.877	0.877	0.877	0.877	0.877	0.877	0.877
error	0.045	0.044	0.044	0.044	0.044	0.044	0.044	0.044
Th-232	0.856	0.822	0.822	0.822	0.822	0.822	0.822	0.822
error	0.043	0.041	0.041	0.041	0.041	0.041	0.041	0.041
K-40	0.964	0.946	0.946	0.946	0.946	0.946	0.946	0.946
error	0.048	0.047	0.047	0.047	0.047	0.047	0.047	0.047
Dose rate conversion (Gy/ka)								
standard fractional error	0.050	0.050	0.050	0.050	0.050	0.050	0.050	0.050
U (ppm)								
Beta	0.146	0.146	0.146	0.146	0.146	0.146	0.146	0.146
error	0.007	0.007	0.007	0.007	0.007	0.007	0.007	0.007
Gamma	0.112	0.112	0.112	0.112	0.112	0.112	0.112	0.112
error	0.000	0.000	0.000	0.000	0.000	0.000	0.000	0.000
Th (ppm)								
Beta	0.028	0.028	0.028	0.028	0.028	0.028	0.028	0.028
error	0.001	0.001	0.001	0.001	0.001	0.001	0.001	0.001
Gamma	0.048	0.048	0.048	0.048	0.048	0.048	0.048	0.048
error	0.000	0.000	0.000	0.000	0.000	0.000	0.000	0.000
K (%)								
Beta	0.798	0.798	0.798	0.798	0.798	0.798	0.798	0.798
error	0.040	0.040	0.040	0.040	0.040	0.040	0.040	0.040
Gamma	0.249	0.249	0.249	0.249	0.249	0.249	0.249	0.249
error	0.000	0.000	0.000	0.000	0.000	0.000	0.000	0.000
Cosmic dose								
Geomagnetic latitude	-42.7	-42.7	-42.7	-42.7	-42.7	-42.7	-42.7	-42.7
Dc (Gy/ka)	0.195	0.204	0.204	0.199	0.155	0.161	0.196	0.172
error	0.018	0.034	0.034	0.021	0.011	0.012	0.018	0.013
Moisture								
F	0.143	0.143	0.143	0.229	0.229	0.176	0.176	0.229
error	0.051	0.051	0.051	0.097	0.097	0.083	0.083	0.097
W	0.143	0.143	0.143	0.229	0.229	0.176	0.176	0.229
error	0.051	0.051	0.051	0.097	0.097	0.083	0.083	0.097
WF	0.020	0.020	0.020	0.053	0.053	0.031	0.031	0.053
error	0.010	0.010	0.010	0.032	0.032	0.021	0.021	0.032
Age uncertainties	1.000	1.000	1.000	1.000	1.000	1.000	1.000	1.000
dDR/K	0.994	0.980	0.980	0.944	0.944	0.968	0.968	0.944
dDR/dC(B, K)	0.172	0.631	0.415	0.477	0.352	0.292	0.480	0.358
dDR/dA(K)	0.143	0.533	0.350	0.402	0.297	0.247	0.405	0.302
dDR/dTh	0.070	0.069	0.069	0.067	0.067	0.068	0.068	0.067
dDR/dC(B, Th)	1.536	3.559	2.140	1.859	1.982	1.780	1.464	1.789
dDR/dA(Th)	0.050	0.120	0.072	0.063	0.067	0.060	0.049	0.060
dDR/dU	0.237	0.234	0.234	0.225	0.225	0.231	0.231	0.225
dDR/dC(B, U)	0.881	0.855	0.855	0.823	0.823	0.844	0.844	0.823
dDR/dA(U)	0.034	0.102	0.060	0.059	0.052	0.049	0.048	0.046
dDR/dW	-0.062	-0.193	-0.122	-0.199	-0.164	-0.111	-0.147	-0.159
dDR/dF	-0.062	-0.193	-0.122	-0.199	-0.164	-0.111	-0.147	-0.159
dDR/C(G, K)	0.179	0.669	0.440	0.507	0.374	0.310	0.509	0.380
dDR/C(G, Th)	1.798	4.339	2.609	2.274	2.425	2.173	1.787	2.189
dDR/dC(G, U)	0.235	0.704	0.410	0.406	0.358	0.338	0.328	0.321
dDR/dCosmic	1.000	1.000	1.000	1.000	1.000	1.000	1.000	1.000
Dage/dDe	1.735	0.765	1.123	1.031	1.291	1.396	1.068	1.231
Dage/dDR	-0.139	-0.020	-0.037	-0.298	-0.192	-0.242	-1.163	-27.443

Laboratory code	K2112	K2113	K2114	K2115	K2116	K2117	K2118	K2119
Average beta-attenuation								
standard fractional error	0.050	0.050	0.050	0.050	0.050	0.050	0.050	0.050
Natural U	0.877	0.877	0.877	0.877	0.877	0.877	0.877	0.877
error	0.044	0.044	0.044	0.044	0.044	0.044	0.044	0.044
Th-232	0.822	0.822	0.822	0.822	0.822	0.822	0.822	0.822
error	0.041	0.041	0.041	0.041	0.041	0.041	0.041	0.041
K-40	0.946	0.946	0.946	0.946	0.946	0.946	0.946	0.946
error	0.047	0.047	0.047	0.047	0.047	0.047	0.047	0.047
Dose rate conversion (Gy/ka)								
standard fractional error	0.050	0.050	0.050	0.050	0.050	0.050	0.050	0.050
U (ppm)								
Beta	0.146	0.146	0.146	0.146	0.146	0.146	0.146	0.146
error	0.007	0.007	0.007	0.007	0.007	0.007	0.007	0.007
Gamma	0.112	0.112	0.112	0.112	0.112	0.112	0.112	0.112
error	0.000	0.000	0.000	0.000	0.000	0.000	0.000	0.000
Th (ppm)								
Beta	0.028	0.028	0.028	0.028	0.028	0.028	0.028	0.028
error	0.001	0.001	0.001	0.001	0.001	0.001	0.001	0.001
Gamma	0.048	0.048	0.048	0.048	0.048	0.048	0.048	0.048
error	0.000	0.000	0.000	0.000	0.000	0.000	0.000	0.000
K (%)								
Beta	0.798	0.798	0.798	0.798	0.798	0.798	0.798	0.798
error	0.040	0.040	0.040	0.040	0.040	0.040	0.040	0.040
Gamma	0.249	0.249	0.249	0.249	0.249	0.249	0.249	0.249
error	0.000	0.000	0.000	0.000	0.000	0.000	0.000	0.000
Cosmic dose								
Geomagnetic latitude	-42.7	-42.7	-42.7	-42.7	-42.7	-42.7	-42.7	-42.7
Dc (Gy/ka)	0.152	0.161	0.142	0.126	0.112	0.134	0.129	0.196
error	0.011	0.012	0.010	0.009	0.008	0.010	0.009	0.018
Moisture								
F	0.176	0.143	0.143	0.143	0.176	0.176	0.176	0.143
error	0.083	0.051	0.051	0.051	0.083	0.083	0.083	0.051
W	0.176	0.143	0.143	0.143	0.176	0.176	0.176	0.143
error	0.083	0.051	0.051	0.051	0.083	0.083	0.083	0.051
WF	0.031	0.020	0.020	0.020	0.031	0.031	0.031	0.020
error	0.021	0.010	0.010	0.010	0.021	0.021	0.021	0.010
Age uncertainties	1.000	1.000	1.000	1.000	1.000	1.000	1.000	1.000
dDR/K	0.968	0.980	0.980	0.980	0.968	0.968	0.968	0.980
dDR/dC(B, K)	0.371	0.448	0.867	0.324	0.484	0.291	0.715	0.568
dDR/dA(K)	0.313	0.378	0.731	0.273	0.408	0.245	0.603	0.479
dDR/dTh	0.068	0.069	0.069	0.069	0.068	0.068	0.068	0.069
dDR/dC(B, Th)	2.081	2.853	5.907	1.643	2.342	2.232	3.252	2.100
dDR/dA(Th)	0.070	0.096	0.199	0.055	0.079	0.075	0.110	0.071
dDR/dU	0.231	0.234	0.234	0.234	0.231	0.231	0.231	0.234
dDR/dC(B, U)	0.844	0.855	0.855	0.855	0.844	0.844	0.844	0.855
dDR/dA(U)	0.052	0.078	0.141	0.051	0.070	0.066	0.114	0.071
dDR/dW	-0.135	-0.143	-0.279	-0.096	-0.170	-0.124	-0.251	-0.152
dDR/dF	-0.135	-0.143	-0.279	-0.096	-0.170	-0.124	-0.251	-0.152
dDR/C(G, K)	0.394	0.475	0.918	0.343	0.513	0.309	0.758	0.601
dDR/C(G, Th)	2.540	3.479	7.202	2.003	2.859	2.724	3.970	2.560
dDR/dC(G, U)	0.357	0.537	0.967	0.352	0.483	0.454	0.782	0.489
dDR/dCosmic	1.000	1.000	1.000	1.000	1.000	1.000	1.000	1.000
Dage/dDe	1.243	1.031	0.589	1.306	0.980	1.139	0.731	0.910
Dage/dDR	-47.397	-46.166	-15.032	-44.946	-51.916	-32.065	-19.836	-22.141

Laboratory code	K2120	K2121	K2122	K2123	K2124	K2125	K2126	K2127
Average beta-attenuation								
standard fractional error	0.050	0.050	0.050	0.050	0.050	0.050	0.050	0.050
Natural U	0.877	0.877	0.877	0.877	0.877	0.877	0.877	0.877
error	0.044	0.044	0.044	0.044	0.044	0.044	0.044	0.044
Th-232	0.822	0.822	0.822	0.822	0.822	0.822	0.822	0.822
error	0.041	0.041	0.041	0.041	0.041	0.041	0.041	0.041
K-40	0.946	0.946	0.946	0.946	0.946	0.946	0.946	0.946
error	0.047	0.047	0.047	0.047	0.047	0.047	0.047	0.047
Dose rate conversion (Gy/ka)								
standard fractional error	0.050	0.050	0.050	0.050	0.050	0.050	0.050	0.050
U (ppm)								
Beta	0.146	0.146	0.146	0.146	0.146	0.146	0.146	0.146
error	0.007	0.007	0.007	0.007	0.007	0.007	0.007	0.007
Gamma	0.112	0.112	0.112	0.112	0.112	0.112	0.112	0.112
error	0.000	0.000	0.000	0.000	0.000	0.000	0.000	0.000
Th (ppm)								
Beta	0.028	0.028	0.028	0.028	0.028	0.028	0.028	0.028
error	0.001	0.001	0.001	0.001	0.001	0.001	0.001	0.001
Gamma	0.048	0.048	0.048	0.048	0.048	0.048	0.048	0.048
error	0.000	0.000	0.000	0.000	0.000	0.000	0.000	0.000
K (%)								
Beta	0.798	0.798	0.798	0.798	0.798	0.798	0.798	0.798
error	0.040	0.040	0.040	0.040	0.040	0.040	0.040	0.040
Gamma	0.249	0.249	0.249	0.249	0.249	0.249	0.249	0.249
error	0.000	0.000	0.000	0.000	0.000	0.000	0.000	0.000
Cosmic dose								
Geomagnetic latitude	-42.7	-42.7	-42.7	-42.7	-42.7	-42.7	-42.7	-42.7
Dc (Gy/ka)	0.161	0.172	0.168	0.157	0.184	0.194	0.202	0.207
error	0.012	0.013	0.013	0.012	0.014	0.017	0.025	0.064
Moisture								
F	0.143	0.143	0.143	0.143	0.143	0.143	0.143	0.143
error	0.051	0.051	0.051	0.051	0.051	0.051	0.051	0.051
W	0.143	0.143	0.143	0.143	0.143	0.143	0.143	0.143
error	0.051	0.051	0.051	0.051	0.051	0.051	0.051	0.051
WF	0.020	0.020	0.020	0.020	0.020	0.020	0.020	0.020
error	0.010	0.010	0.010	0.010	0.010	0.010	0.010	0.010
Age uncertainties	1.000	1.000	1.000	1.000	1.000	1.000	1.000	1.000
dDR/K	0.980	0.980	0.980	0.980	0.980	0.980	0.980	0.980
dDR/dC(B, K)	0.443	0.429	0.321	0.487	0.341	0.209	0.241	0.624
dDR/dA(K)	0.374	0.362	0.271	0.410	0.288	0.176	0.204	0.526
dDR/dTh	0.069	0.069	0.069	0.069	0.069	0.069	0.069	0.069
dDR/dC(B, Th)	1.803	1.683	1.691	2.453	3.030	1.763	1.916	2.749
dDR/dA(Th)	0.061	0.057	0.057	0.083	0.102	0.059	0.065	0.093
dDR/dU	0.234	0.234	0.234	0.234	0.234	0.234	0.234	0.234
dDR/dC(B, U)	0.855	0.855	0.855	0.855	0.855	0.855	0.855	0.855
dDR/dA(U)	0.057	0.055	0.054	0.075	0.047	0.040	0.041	0.057
dDR/dW	-0.121	-0.117	-0.097	-0.143	-0.117	-0.074	-0.082	-0.167
dDR/dF	-0.121	-0.117	-0.097	-0.143	-0.117	-0.074	-0.082	-0.167
dDR/C(G, K)	0.469	0.454	0.340	0.515	0.361	0.221	0.256	0.661
dDR/C(G, Th)	2.199	2.052	2.062	2.990	3.694	2.150	2.336	3.352
dDR/dC(G, U)	0.391	0.381	0.371	0.518	0.322	0.274	0.283	0.391
dDR/dCosmic	1.000	1.000	1.000	1.000	1.000	1.000	1.000	1.000
Dage/dDe	1.090	1.181	1.300	1.019	1.202	1.462	1.401	0.821
Dage/dDR	-0.055	-20.530	-0.146	-93.056	-38.418	-0.267	-0.056	-4.229

Laboratory code	K2128	K2129	K2130	K2131	K2132
Average beta-attenuation					
standard fractional error	0.050	0.050	0.050	0.050	0.050
Natural U	0.877	0.877	0.877	0.877	0.877
error	0.044	0.044	0.044	0.044	0.044
Th-232	0.822	0.822	0.822	0.822	0.822
error	0.041	0.041	0.041	0.041	0.041
K-40	0.946	0.946	0.946	0.946	0.946
error	0.047	0.047	0.047	0.047	0.047
Dose rate conversion (Gy/ka)					
standard fractional error	0.050	0.050	0.050	0.050	0.050
U (ppm)					
Beta	0.146	0.146	0.146	0.146	0.146
error	0.007	0.007	0.007	0.007	0.007
Gamma	0.112	0.112	0.112	0.112	0.112
error	0.000	0.000	0.000	0.000	0.000
Th (ppm)					
Beta	0.028	0.028	0.028	0.028	0.028
error	0.001	0.001	0.001	0.001	0.001
Gamma	0.048	0.048	0.048	0.048	0.048
error	0.000	0.000	0.000	0.000	0.000
K (%)					
Beta	0.798	0.798	0.798	0.798	0.798
error	0.040	0.040	0.040	0.040	0.040
Gamma	0.249	0.249	0.249	0.249	0.249
error	0.000	0.000	0.000	0.000	0.000
Cosmic dose					
Geomagnetic latitude	-42.7	-42.7	-42.7	-42.7	-42.7
Dc (Gy/ka)	0.207	0.207	0.136	0.157	0.161
error	0.064	0.064	0.010	0.012	0.012
Moisture					
F	0.143	0.176	0.176	0.176	0.229
error	0.051	0.083	0.083	0.083	0.097
W	0.143	0.176	0.176	0.176	0.229
error	0.051	0.083	0.083	0.083	0.097
WF	0.020	0.031	0.031	0.031	0.053
error	0.010	0.021	0.021	0.021	0.032
Age uncertainties	1.000	1.000	1.000	1.000	1.000
dDR/K	0.980	0.968	0.968	0.968	0.944
dDR/dC(B, K)	0.331	0.152	1.414	0.814	0.676
dDR/dA(K)	0.279	0.128	1.193	0.686	0.570
dDR/dTh	0.069	0.068	0.068	0.068	0.067
dDR/dC(B, Th)	2.308	1.432	8.625	4.772	4.018
dDR/dA(Th)	0.078	0.048	0.291	0.161	0.135
dDR/dU	0.234	0.231	0.231	0.231	0.225
dDR/dC(B, U)	0.855	0.844	0.844	0.844	0.823
dDR/dA(U)	0.045	0.034	0.205	0.114	0.087
dDR/dW	-0.105	-0.069	-0.528	-0.299	-0.315
dDR/dF	-0.105	-0.069	-0.528	-0.299	-0.315
dDR/C(G, K)	0.350	0.161	1.499	0.863	0.718
dDR/C(G, Th)	2.815	1.748	10.529	5.825	4.915
dDR/dC(G, U)	0.313	0.232	1.410	0.782	0.604
dDR/dCosmic	1.000	1.000	1.000	1.000	1.000
Dage/dDe	1.064	0.779	0.419	0.583	0.900
Dage/dDR	-3.744	-2.463	-16.723	-13.379	-25.025

Laboratory code	K2133	K2134	K2135	K2136
Average beta-attenuation				
standard fractional error	0.050	0.050	0.050	0.050
Natural U	0.877	0.877	0.877	0.877
error	0.044	0.044	0.044	0.044
Th-232	0.822	0.822	0.822	0.822
error	0.041	0.041	0.041	0.041
K-40	0.946	0.946	0.946	0.946
error	0.047	0.047	0.047	0.047
Dose rate conversion (Gy/ka)				
standard fractional error	0.050	0.050	0.050	0.050
U (ppm)				
Beta	0.146	0.146	0.146	0.146
error	0.007	0.007	0.007	0.007
Gamma	0.112	0.112	0.112	0.112
error	0.000	0.000	0.000	0.000
Th (ppm)				
Beta	0.028	0.028	0.028	0.028
error	0.001	0.001	0.001	0.001
Gamma	0.048	0.048	0.048	0.048
error	0.000	0.000	0.000	0.000
K (%)				
Beta	0.798	0.798	0.798	0.798
error	0.040	0.040	0.040	0.040
Gamma	0.249	0.249	0.249	0.249
error	0.000	0.000	0.000	0.000
Cosmic dose				
Geomagnetic latitude	-42.7	-42.7	-42.7	-42.7
Dc (Gy/ka)	0.186	0.189	0.177	0.207
error	0.015	0.015	0.013	0.064
Moisture				
F	0.176	0.176	0.176	0.176
error	0.083	0.083	0.083	0.083
W	0.176	0.176	0.176	0.176
error	0.083	0.083	0.083	0.083
WF	0.031	0.031	0.031	0.031
error	0.021	0.021	0.021	0.021
Age uncertainties	1.000	1.000	1.000	1.000
dDR/K	0.968	0.968	0.968	0.968
dDR/dC(B, K)	0.587	0.600	1.125	0.550
dDR/dA(K)	0.495	0.506	0.949	0.464
dDR/dTh	0.068	0.068	0.068	0.068
dDR/dC(B, Th)	3.585	2.873	6.782	2.279
dDR/dA(Th)	0.121	0.097	0.229	0.077
dDR/dU	0.231	0.231	0.231	0.231
dDR/dC(B, U)	0.844	0.844	0.844	0.844
dDR/dA(U)	0.074	0.063	0.122	0.048
dDR/dW	-0.216	-0.203	-0.405	-0.176
dDR/dF	-0.216	-0.203	-0.405	-0.176
dDR/C(G, K)	0.623	0.637	1.193	0.583
dDR/C(G, Th)	4.376	3.506	8.278	2.782
dDR/dC(G, U)	0.512	0.435	0.840	0.328
dDR/dCosmic	1.000	1.000	1.000	1.000
Dage/dDe	0.777	0.864	0.465	0.938
Dage/dDR	-1.419	-0.106	-0.591	-0.070

Appendix H. OSL dating results in stratigraphic context

The dose distribution results for each sample, and the rational for determining the D_e results in Table 7.4, are provided for each sample in this section of the appendix. The results are grouped together by sampling site (i.e. profiles and stratigraphic logs), as the stratigraphic context plays a large role in identifying the D_e component most likely to relate to burial dose in the multi-component samples. The dose distribution images for each sample are provided alongside the description where possible, and sites are presented in order from north to south along the lunette. See section 3.3.3 for A3 versions of the transect images shown here.

Appendix H.1 OSL results at PR02

This section provides the OSL dating results from PR02, at the north end of the Mulurulu Lunette. See Section 3.3.3 for larger versions of the aerial photo and transect shown below. At PR02, Unit B spans an age of approximately 60 to 32 ka, while Unit E provides young age estimates, within the last 300 years. Both mussel shell samples provide ages of around 31 ka Cal. BP, which agrees within error with the overlying OSL date.

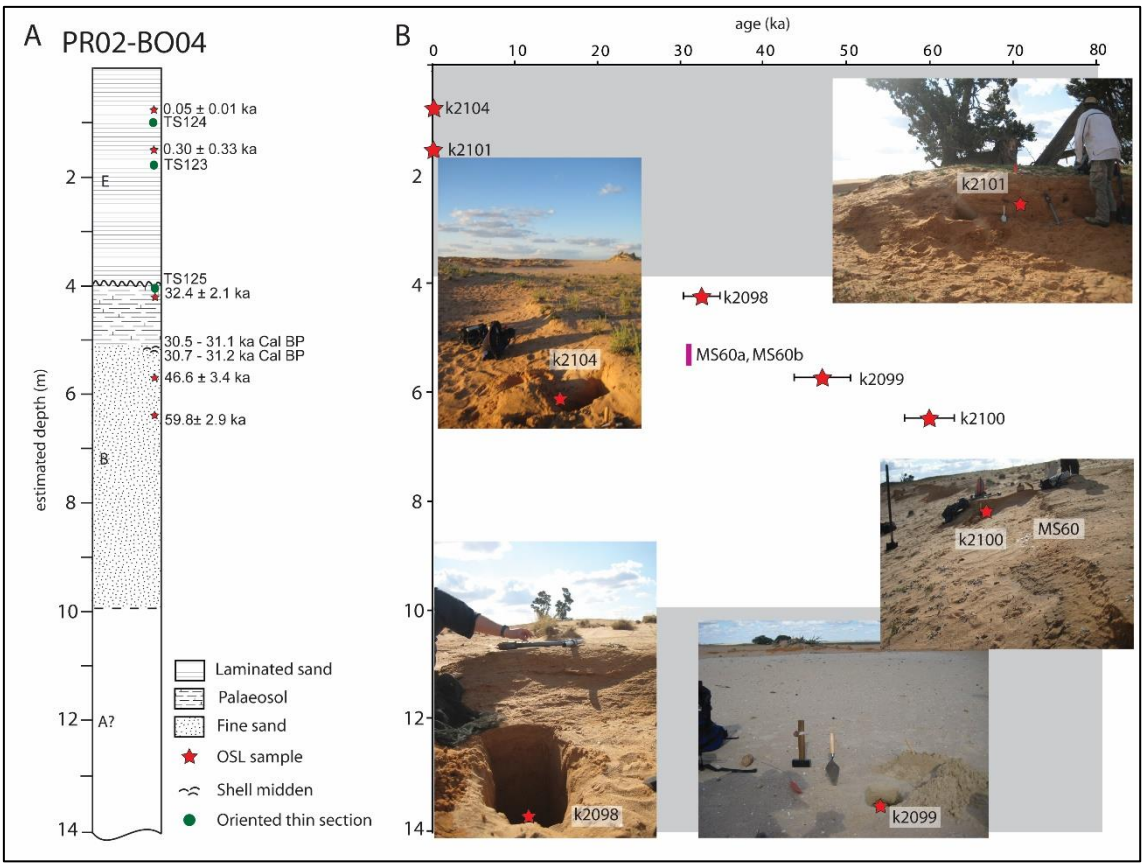

.

APPENDIX H. OSL DATING RESULTS

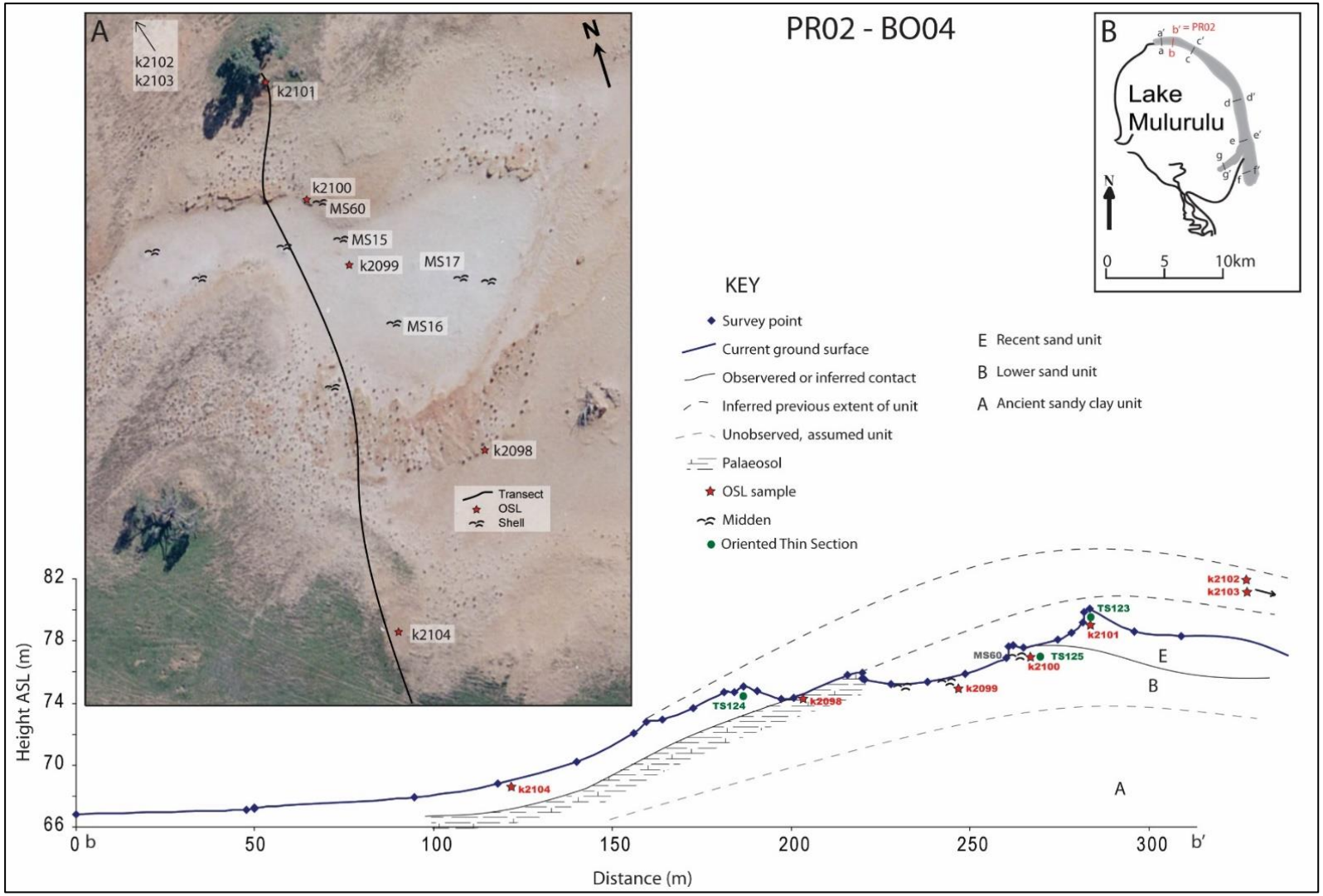

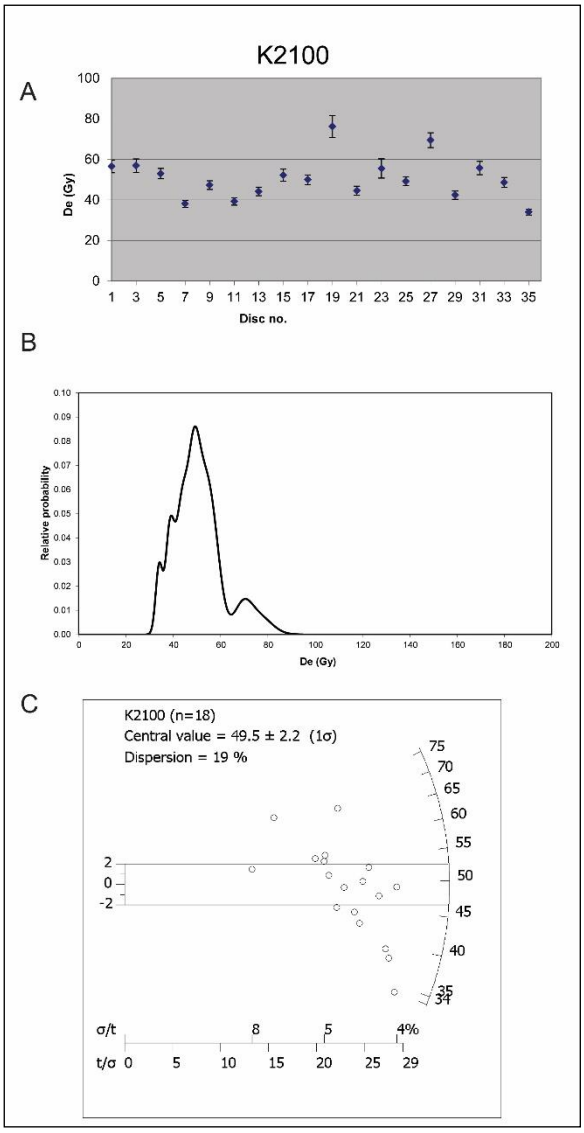

Sample K2100 was collected from Unit B in the side of a shallow blow out (BO04). As with the other Unit B samples from this site (K2098 and K2099) it has no rejected aliquots and a reasonably narrow dose distribution. This sample includes a few low precision higher D_e value aliquots, and some high precision lower ones, but removal of these has an insignificant effect on the CAM result. Even with all aliquots included, the overdispersion is less than 20%, resulting in a reliable D_e estimate, providing an age estimate of 32.38 ± 2.12 Gy.

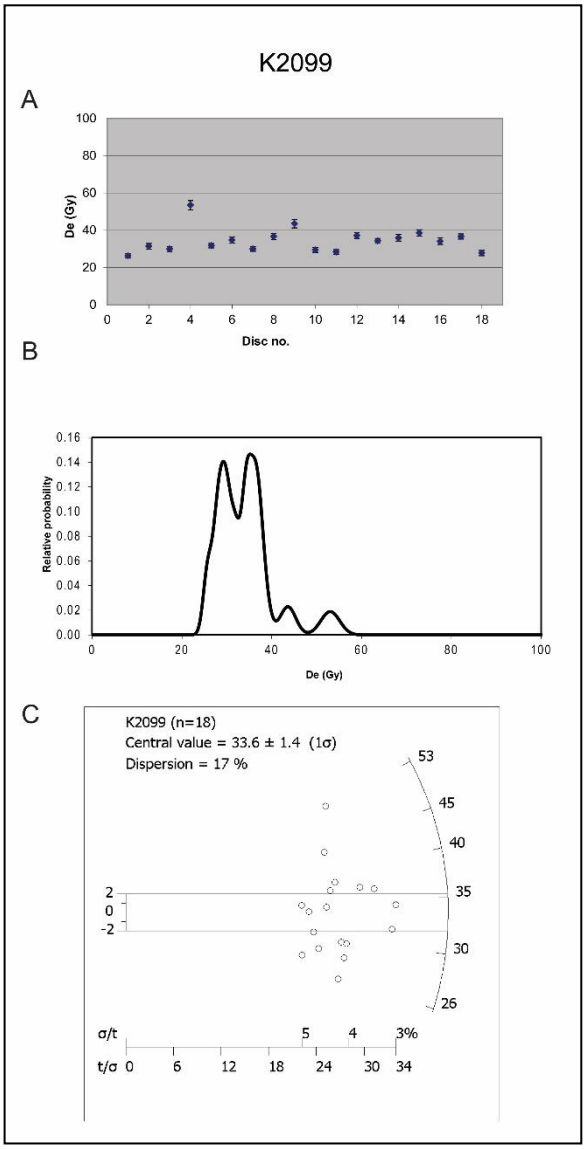

Sample K2099 was collected from Unit B. As with the other Unit B samples from this site (K2098 and K2100) it has no rejected aliquots and a reasonably narrow dose distribution. A couple of higher D_e value aliquots are clear on the radial plot and give the sample a small right 'shoulder' in the PD plot, but their removal has an insignificant effect on the CAM result. Even with all aliquots included, the overdispersion is less than 20%, resulting in a reliable CAM age estimate of .46.57 ± 3.41 ka.

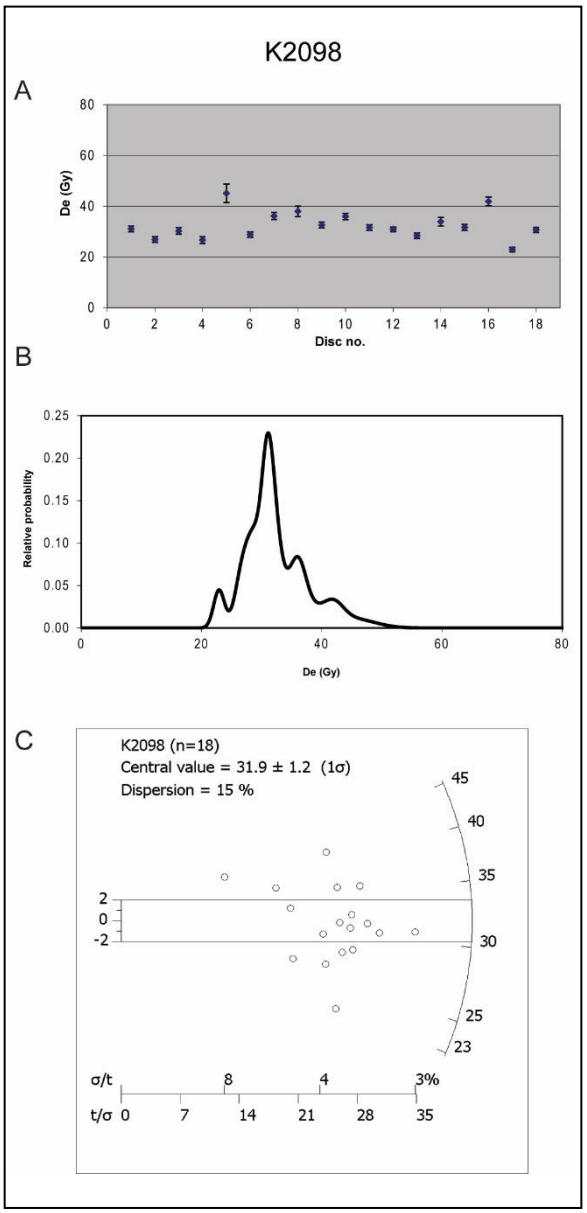

Sample K2098 was collected from Unit B. As with the other Unit B samples from this site (K2099 and K2100) it has no rejected aliquots and a reasonably narrow dose distribution. This sample has a very clear dominant central peak, regardless of a few low precision higher D_e value aliquots, the removal of which have an insignificant effect on the CAM result. Even with all aliquots included, the overdispersion is less than 20%, resulting in a reliable CAM age estimate of 32.38 ± 2.11 ka.

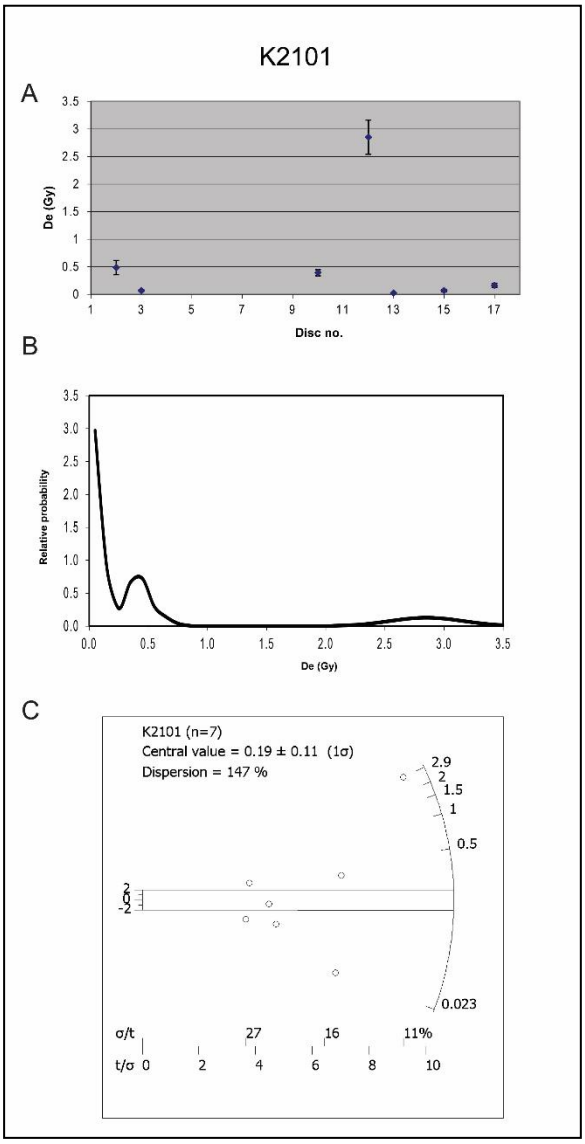

Sample K2101 was collected from within Unit E at the top of the lunette, and gives a very typical result, with high recuperation (>10%) and very high overdispersion (in this case >100%). Numerous aliquots were rejected from this sample, mostly due to poor recycling ratios (>10%), high palaeodose errors (>30%) or low signal to background ratios. The remaining aliquots mostly have very low D_e values (<0.5 Gy), with very low precision and high relative error. The one aliquot with a higher D_e value (~2.6 Gy) has a higher precision than the lower values and probably represents a small amount of mixing in this sample. The error on the age estimate (330 years) for this sample is greater than the age estimate (300 years) indicating that this sample can effectively be considered modern.

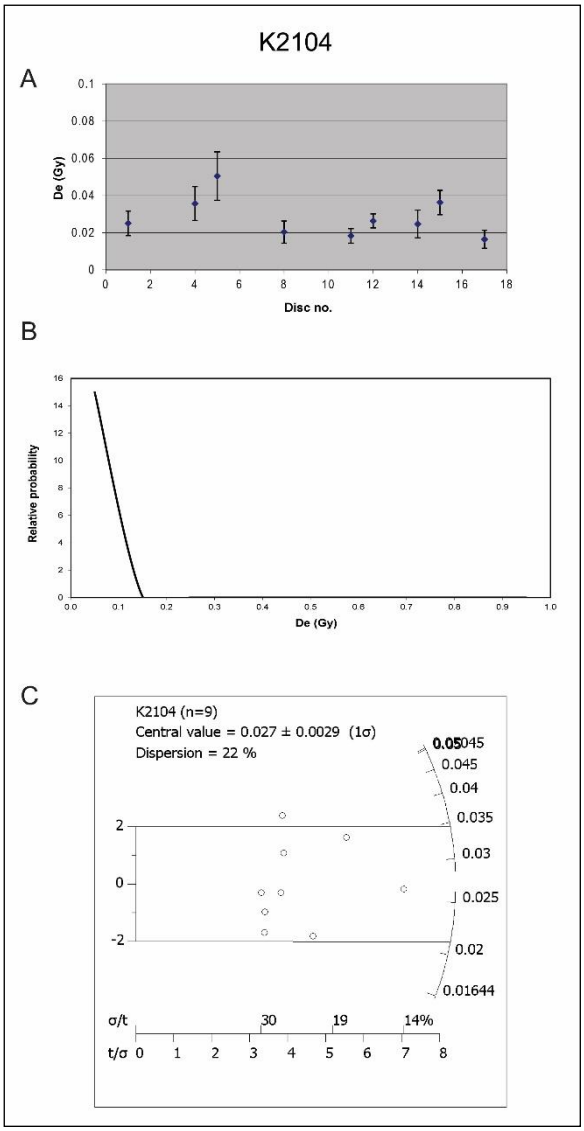

Sample K2104 was collected from within Unit E at the front of the lunette, and gives a fairly typical result, with high recuperation (>10%) though the overdispersion is only just over 20% in this case. Nine aliquots were rejected from this sample, seven due to poor recycling ratios (>10%) and two due to high palaeodose errors (>30%). The remaining nine aliquots have very low D_e values (<0.1 Gy), with low precision and high relative error. The age estimate of 50 ± 10 years indicates a very young age for this sample, and the high recuperation level means that even this is likely to be an overestimate.

APPENDIX H. OSL DATING RESULTS

Two additional samples were collected in the vicinity of PR02, which were not included in the stratigraphic log: K2102, below the modern ground surface behind a neighbouring dune, and K2103, within Unit E atop a neighbouring dune

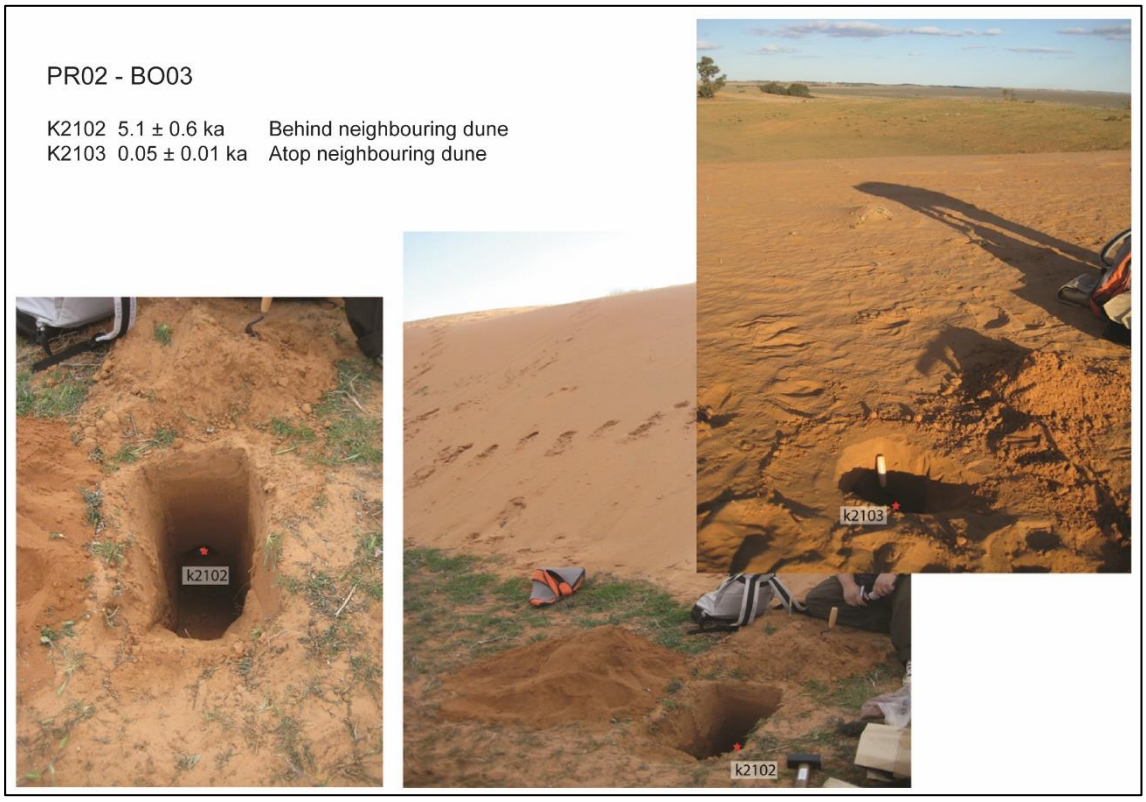

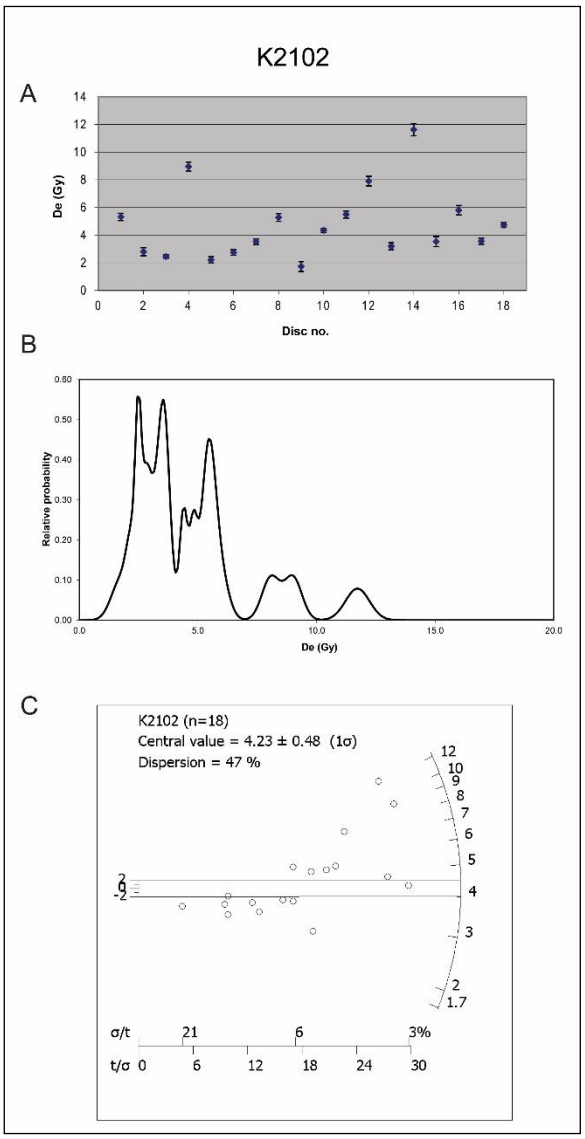

Sample K2102 was collected from beneath the ground surface, behind the lunette. No aliquots were rejected and the sample shows evidence of mixing, probably due to modern bioturbation. The sample was collected from 30 cm below the ground within the modern soil profile. The PD plot has multiple peaks and the radial plot is scattered with few data points within the 2σ error range. The age estimate of 5.12 ± 0.59 ka likely includes a very large modern component, mixed into the sediments by modern soil forming processes.

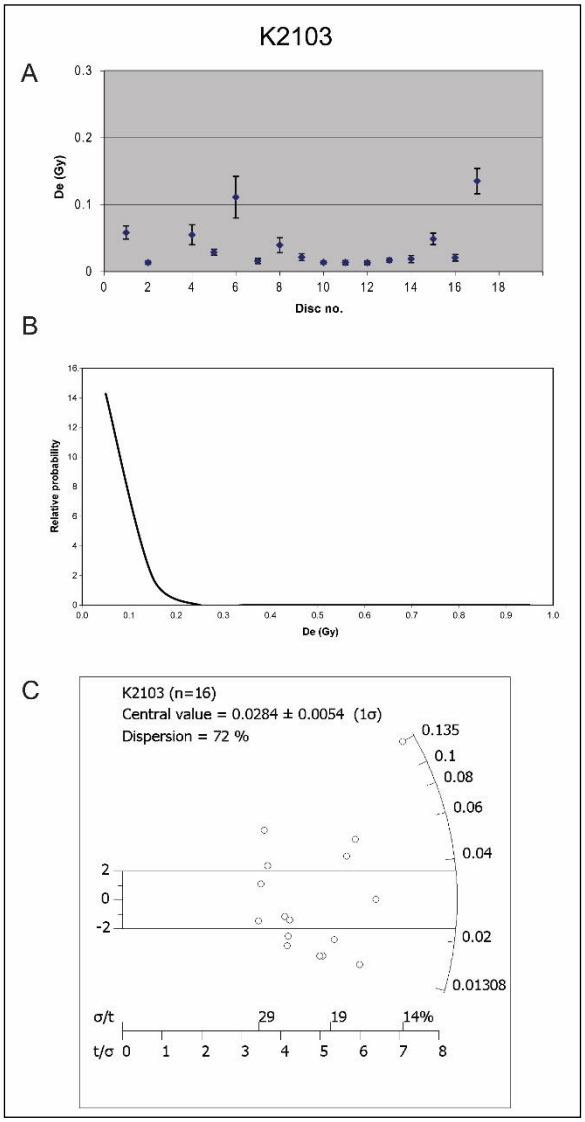

Sample K2103 was collected from the top of a dune neighbouring PR01. The sample gives a very typical Unit E result, with high recuperation (>10%) and very high over dispersion (>40%). Two aliquots were rejected from this sample, due to a poor recycling ratio (>10%) and a high palaeodose error (>30%). The remaining aliquots mostly have very low D_e values (<0.1 Gy), with very low precision and high relative error. The aliquot with the highest D_e value (~0.13 Gy) also has a higher precision than the lower values and probably represents a small amount of mixing in this sample. The specific age estimate of 50 ± 10 years is not highly reliable, and the high recuperation level means that this is likely to be an overestimate, thus the sample is likely to be relatively modern.

Appendix H.2 OSL Results at SL44

This section provides the OSL dating results from SL44, a stratigraphic log taken from the wall of RB03 (see Section 3.3.4). At SL44, the floor of the blow-out, within the Unit A palaeosol, gives an age of around 90 ka. K2124, from the wall of the blowout, part way up the Unit A palaeosol gives an age estimate of around 32 ka, which is likely to be an underestimate. Samples above and below the contact between Unit A and Unit E both give very young age estimates.

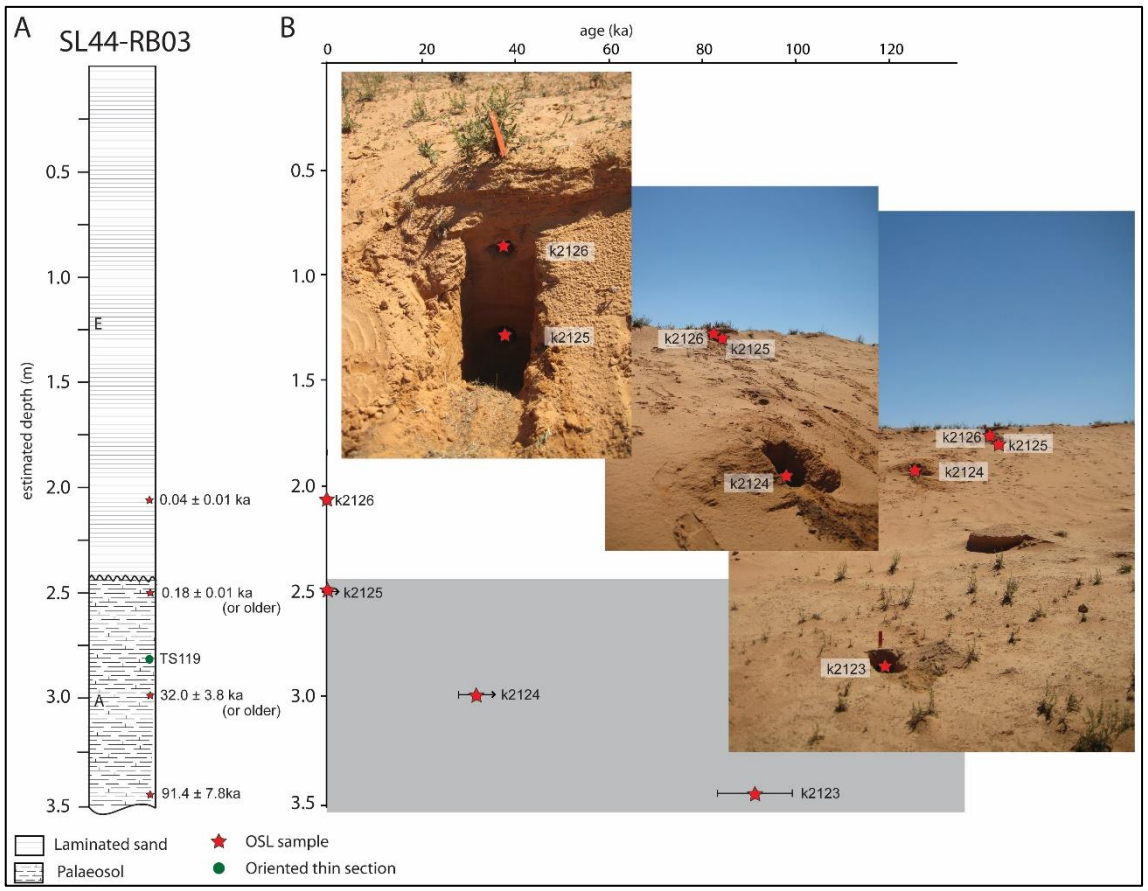

Sample K2123 was collected from the side of a small pit dug in the floor of the blowout. One aliquot was rejected, due to saturation. When a CAM estimate is made on the remaining aliquots, the overdispersion is a little high (>20%), and many data points fall outside the 2σ error on the radial plot. These data appear to be better described by at least two populations as implied by the bimodal distribution in the PD plot. There is also an older population in this sample, represented by the two aliquots over 140 Gy, plus the saturated sample. A three component mixture model applied to the data highlights this pattern. This model cannot reliably identify discrete components in these multi-grain aliquots, but it does indicate that multiple components are probably present. With no reliable argument for which population more accurately reflects the true depositional of the sample, the CAM on all un-rejected aliquots is used to provide the age estimate of 91.36 ± 7.97 ka.

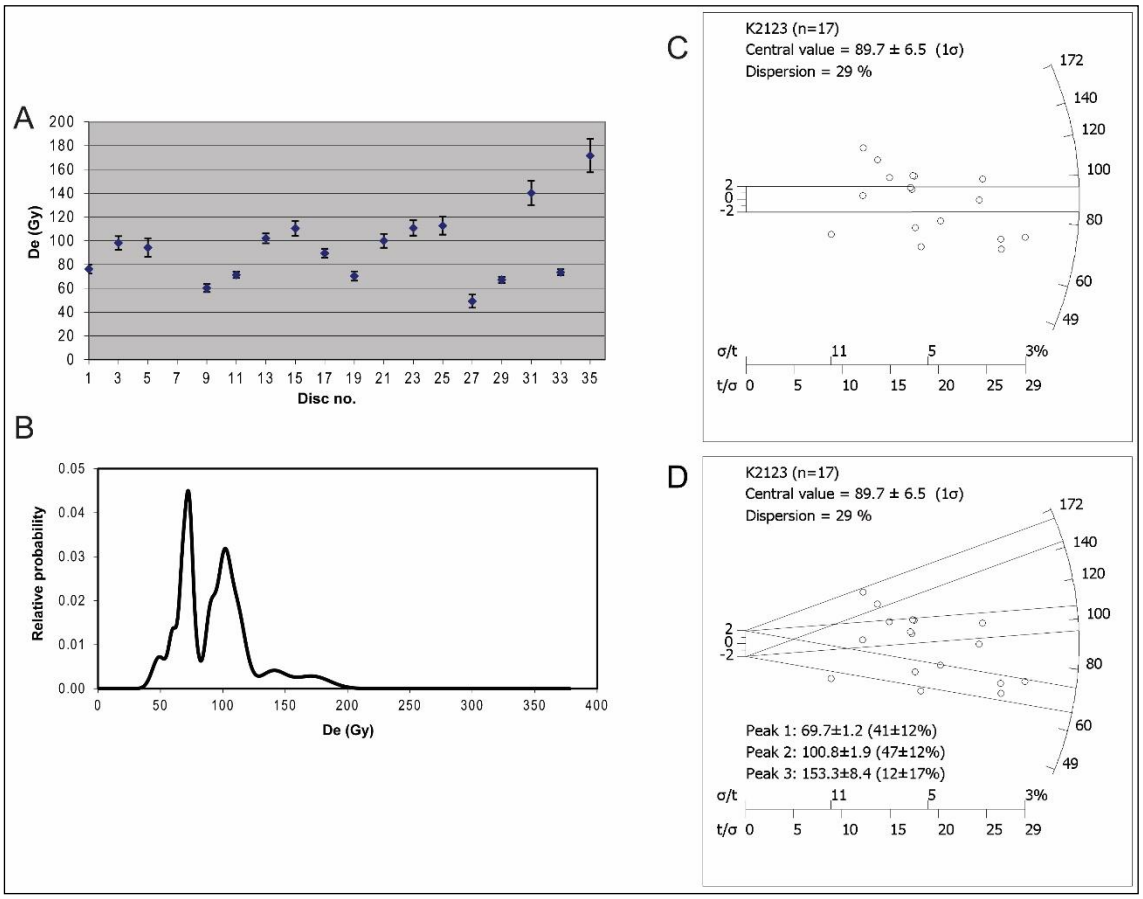

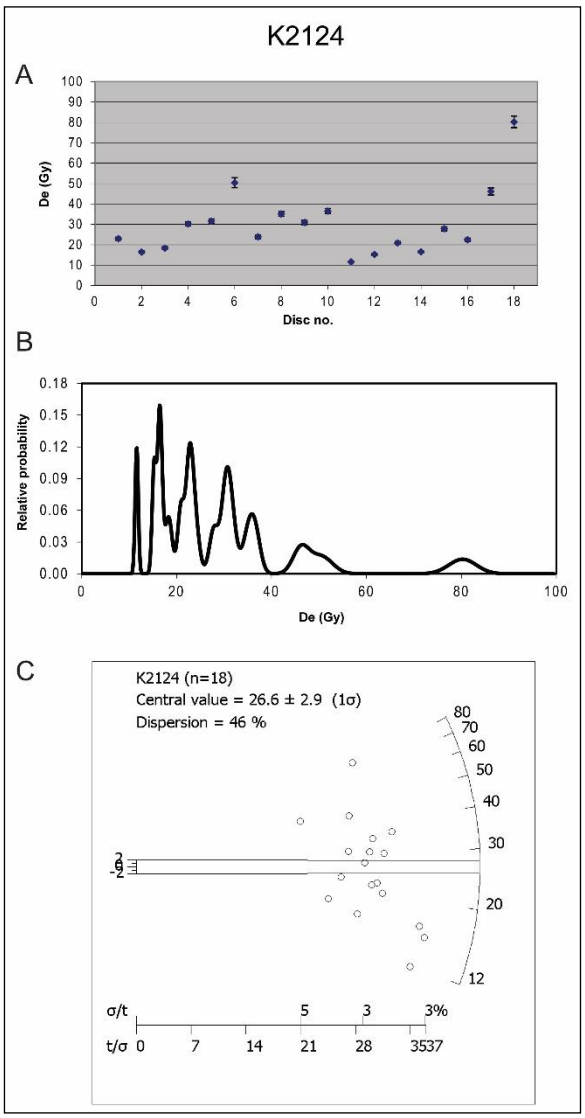

Sample K2124 was collected from part way up the wall of the RB02 blowout. No aliquots were rejected and the D_e results have a very scattered distribution. The PD plot has multiple peaks and the majority of aliquots fall outside the 2σ error in the radial plot. This may be an indication of post-depositional mixing, or a result of issues with microdosimetry. The thin section collected from just above this location (TS119) shows grains with cutans and ferri-argillans, indicative of soil development. Additionally, deep embayments on grain edges contain remnant cutans, indicating that the sand is from a reworked source. As such, the range of D_e values seen here may be due to partial bleaching of reworked sediments or in-situ bioturbation of the Unit A palaeosol. Either way, the CAM result, providing an age estimate of 31.97 ± 3.79 ka for this sample is very unlikely to represent the true depositional age of the sediments.

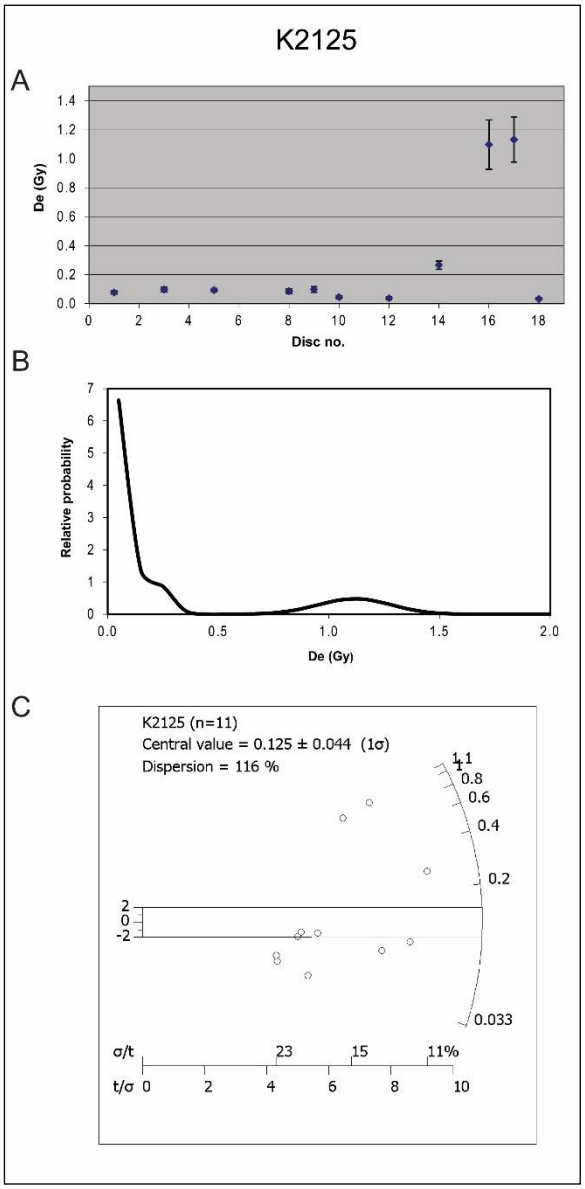

Sample K2125 (Figure 7.28) was collected from high in the side of the RB02 blow out. Seven aliquots were rejected, six due to poor recycling ratios (>10%) and one due to a high palaeodose error (>30%). The remaining aliquots provide a result fairly typical of Unit E sands, with very high overdispersion (>100% in this case), and mostly very low D_e values (<0.1 Gy). The presence of two aliquots >1 Gy, plus one >0.2 Gy indicate there is a population of very recent sands mixed with one or more older populations of sand from below, or grains that were only partially bleached upon deposition. The specific age estimate of 180 ± 10 years is not highly reliable and is not likely to represent the true age of deposition for the sample, but none-the-less the sample is likely to be relatively modern.

Sample K2126 was collected from within unit E, and gives a very typical result, with high recuperation (>10%). Four aliquots were rejected, one due to a poor recycling ratio (>10%) and three due to high palaeodose errors (>30%). The remaining aliquots mostly have very low D_e values (<0.1 Gy), with very low precision and high relative error. Three aliquots provide higher D_e values, one slightly higher at around ~0.7 Gy and two much higher, over 6 Gy. These probably represent a small amount of mixing in this sample. The removal of the three outliers results in a CAM age of 40 ± 10 years, which though not highly reliable, indicates the sample is likely to be relatively modern.

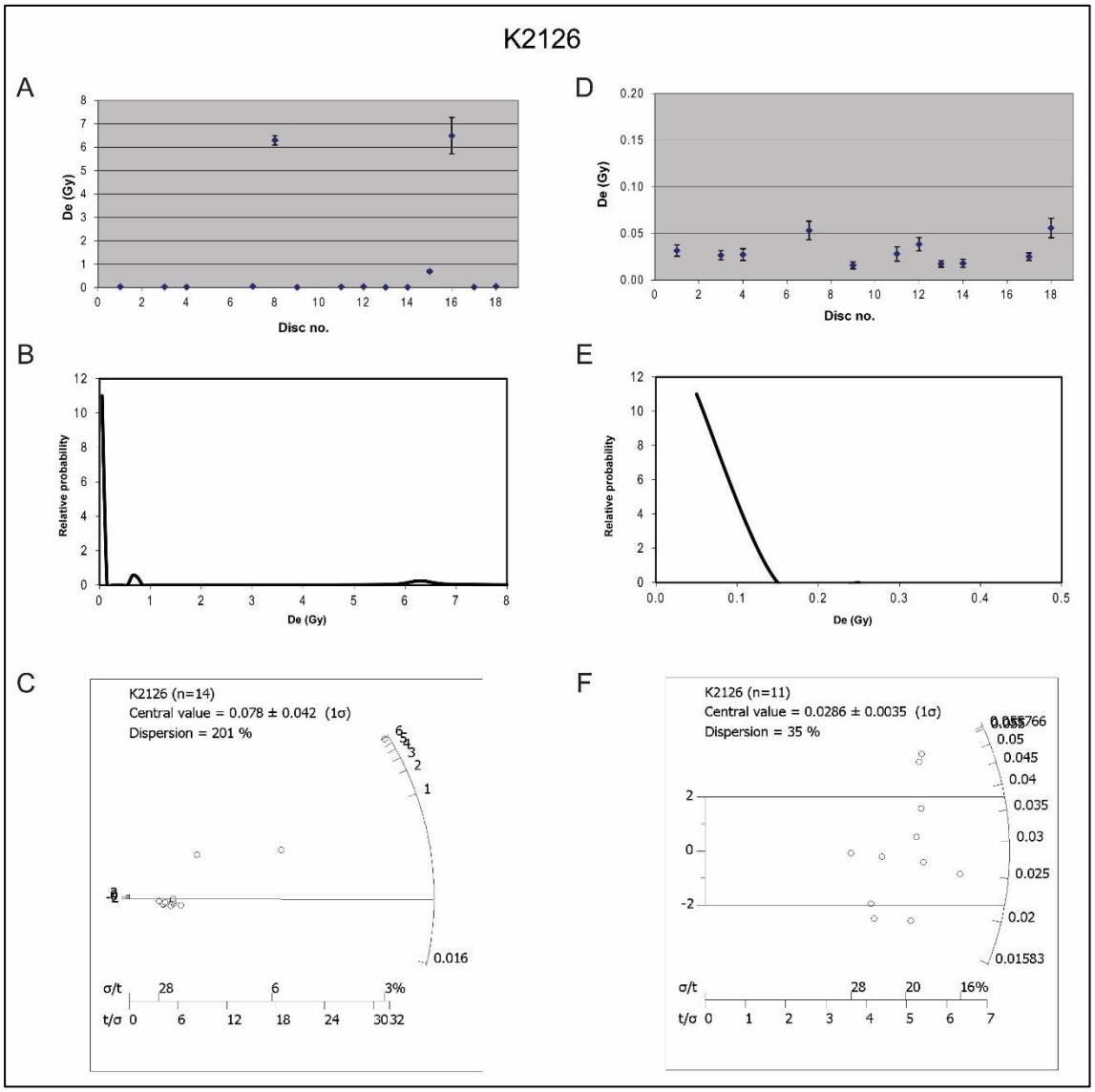

Appendix H.3. OSL results at PR05

This section provides the OSL dating results from PR05, See Section 3.3.3 for larger versions of the aerial photo and transect shown below. At PR05, the samples from Unit B date from around 53 to 34 ka, bracketing the mussel shells from MS63, which provide radiocarbon dates of 37-36 ka. The sample from Unit C dates to around 25 ka. One OSL sample from within the uppermost palaeosol of Unit D gives an age of only 1 ka, though this is likely to be an extreme underestimate. The other samples in the unit range from around 32 to 17 ka. Mussel shells from MS64 give younger calibrated radiocarbon ages than the overlying OSL age for K2119. Unit E once again provides age estimates within the last 200 years.

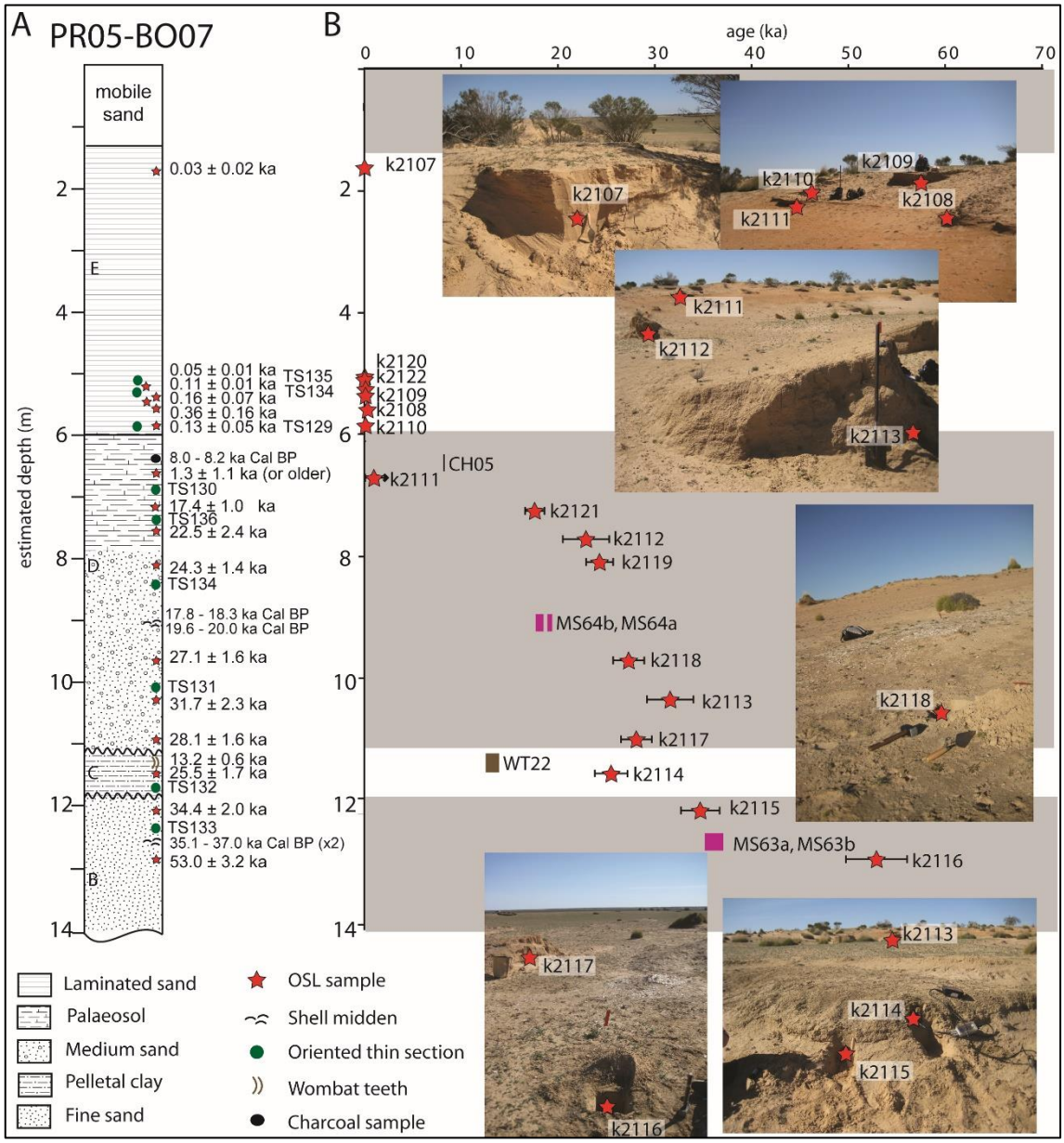

APPENDIX H. OSL DATING RESULTS

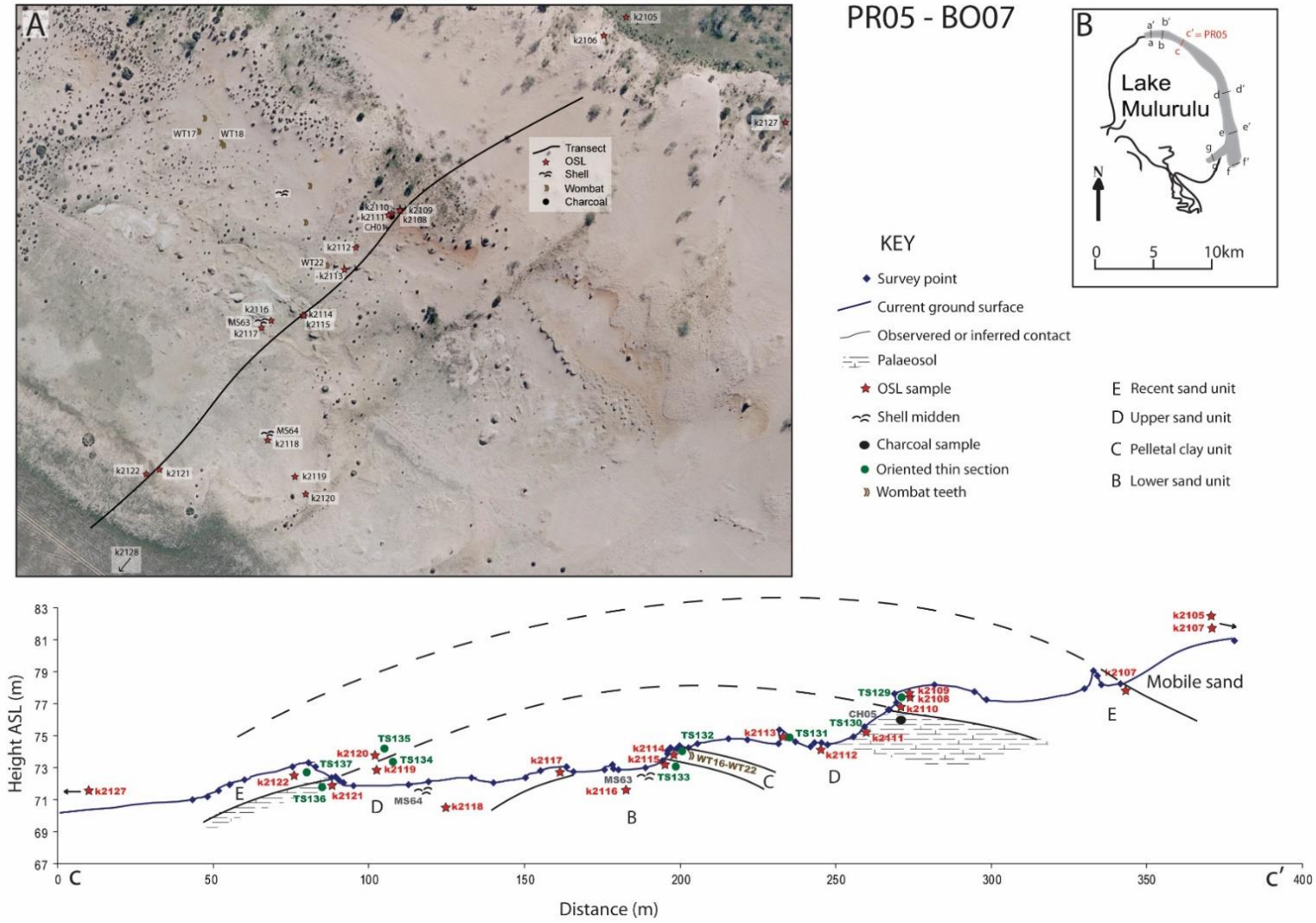

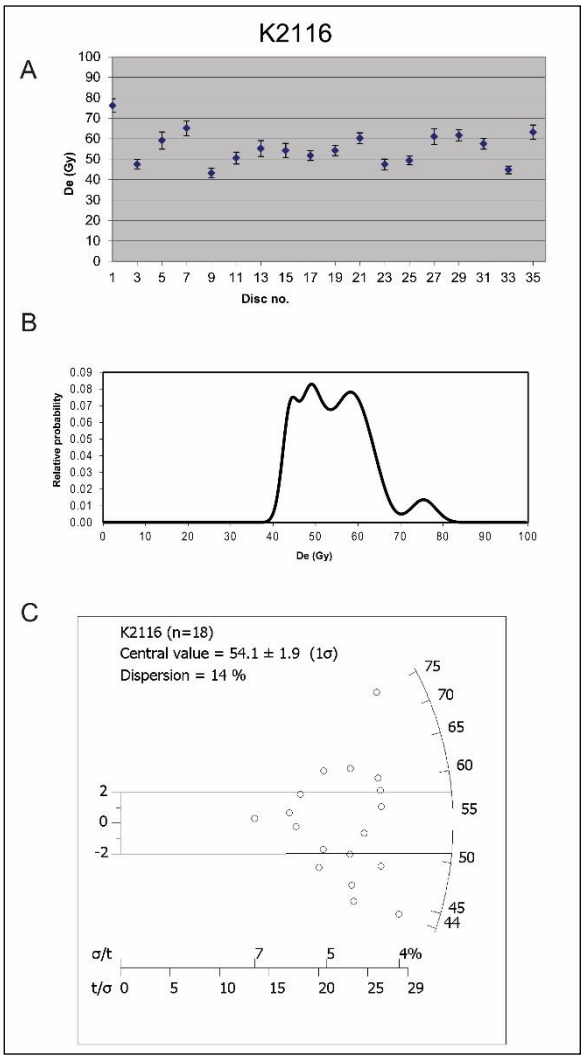

Sample K2116 was collected from stratigraphically below a shell midden (MS63) in Unit B. No aliquots were rejected from this sample. Although the dose distribution is a little broad about half the aliquots fall within the 2σ error on the radial plot. This, combined with the low overdispersion (<20%), result in a reasonably reliable CAM age estimate of 53.00±3.20 ka.

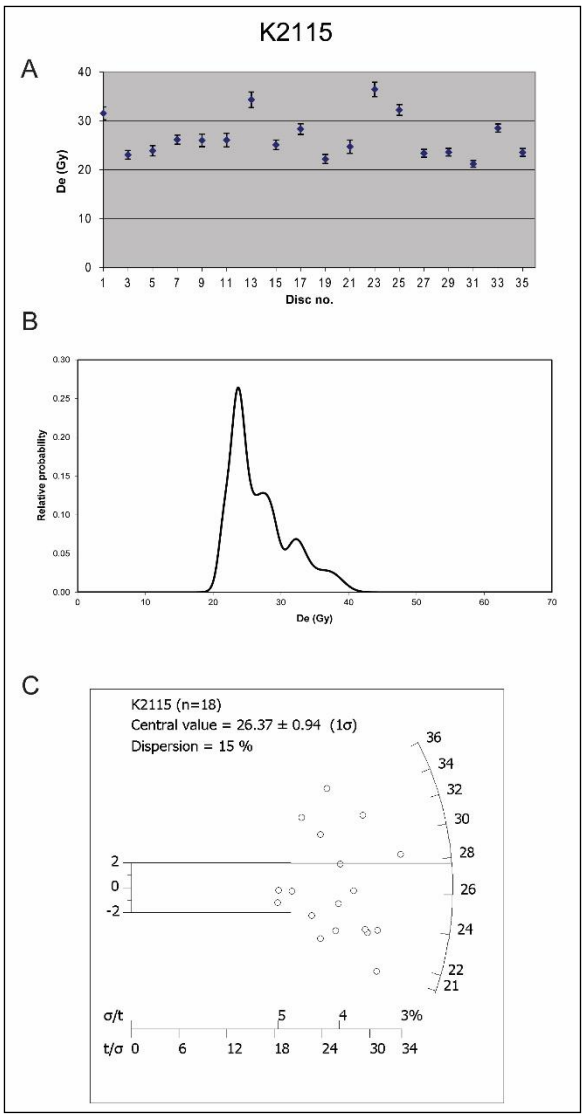

Sample K2115 was collected from above a shell midden (MS63) in unit B. No aliquots were rejected from this sample. The PD plot suggests a single dominant peak, with a small amount of right skew, which could suggest a little bigt of mixing with older material. Though a little scattered, most of the data in the radial plot falls within the 2σ error. The low overdispersion (<20%) results in a reliable CAM age estimate of 34.43 ± 1.95 ka.

Sample K2114 was collected from Unit C. No aliquots were rejected and about half the aliquots fall within or near the 2σ error range in the radial plot. Overdispersion is acceptable, at 18%. There do appear to be at least three D_e populations in this sample, as implied by the multimodal PD plot. When a mixture model is applied to the 18 aliquots three peaks are identified, with approximately 10 D_e between each peak. This mixing model is not reliable for identifying discrete populations in these multi-grained samples, but does highlight that multiple populations are likely to be present. Since the true depositional population cannot be isolated with this data, and because the overdispersion is acceptable, all 18 aliquots are used to determine a central measure of D_e, resulting in a CAM age estimate of 25.54 ± 1.69 ka.

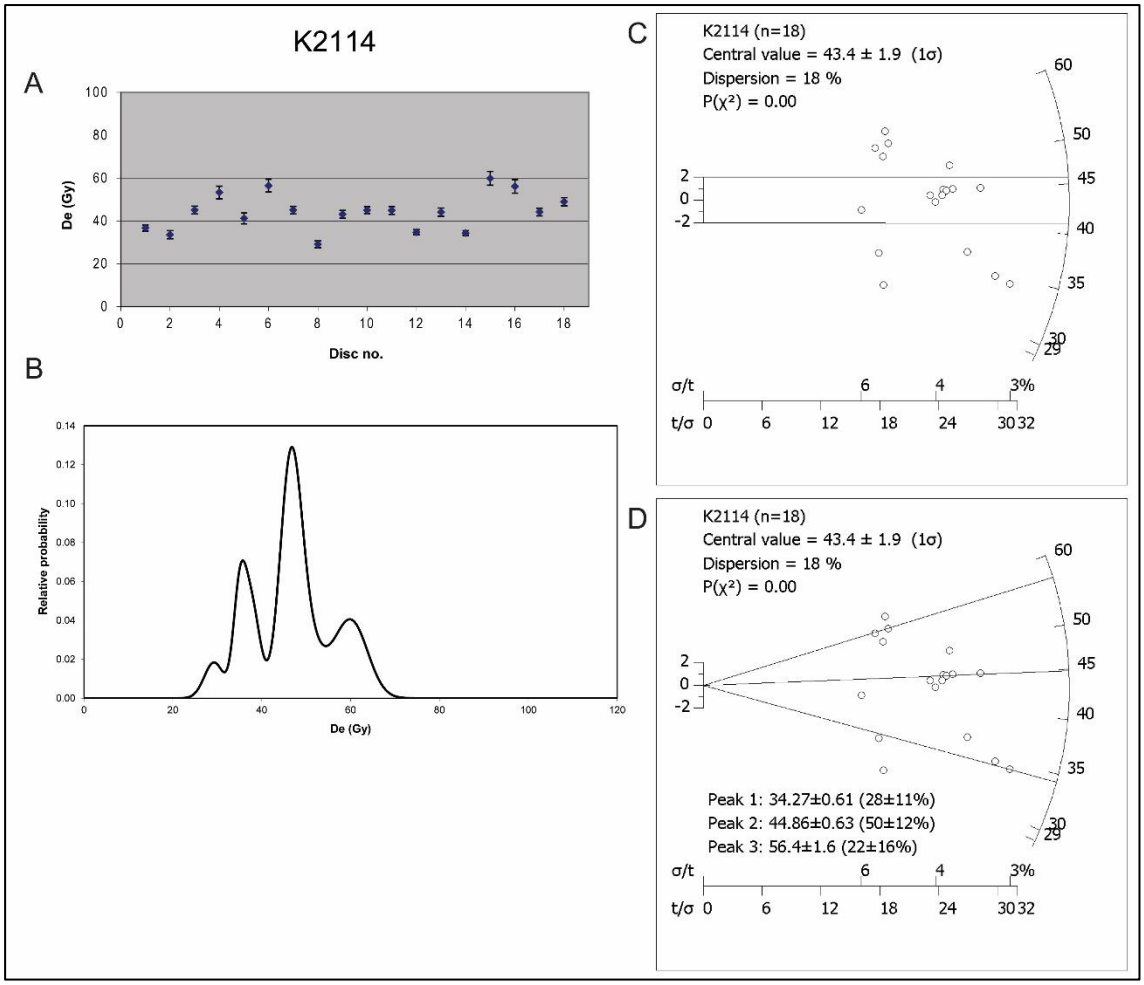

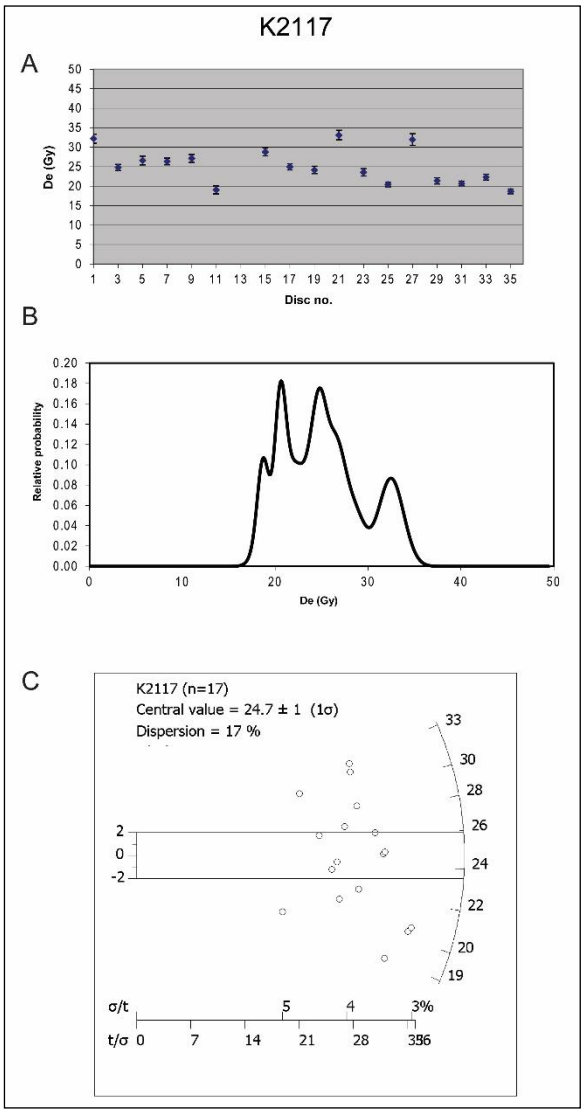

Sample K2117 was collected from Unit D immediately above the unconformable contact with Unit B. One aliquot was rejected due to a poor recycling ratio. Though it presents a relatively broad dose distribution with a scattered radial plot, the low overdispersion (<20%), suggests a reliable CAM age estimate of 28.14 ± 1.63 ka

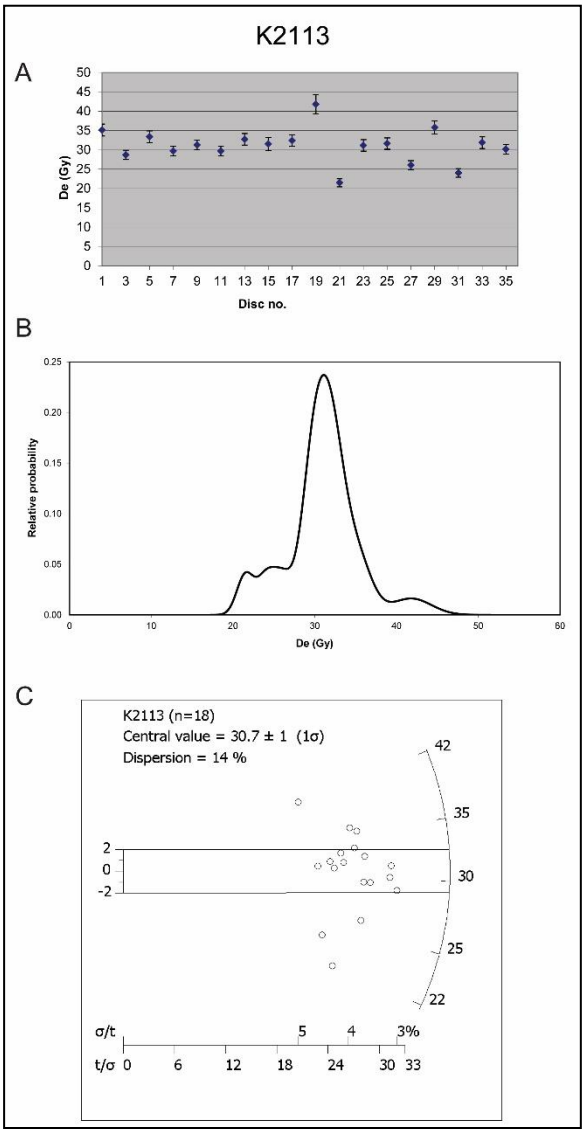

Sample K2113 was collected from within Unit D. No aliquots were rejected and the results form a PD plot that suggests a single dominant peak, a radial plot with most data falling within the 2σ error and a low overdispersion (<20%), resulting in a reliable CAM age estimate of 13.66 ± 2.36 ka.

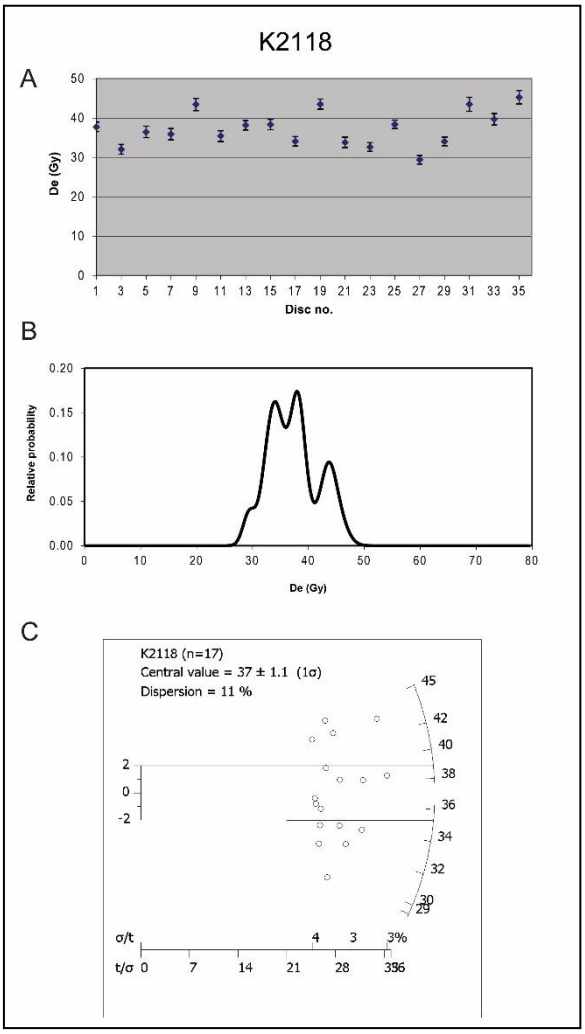

Sample K2118 was collected from stratigraphically below a shell midden (MS64), within Unit D. No aliquots were rejected. The dose distribution is relatively narrow, much of the data in the radial plot falls within the 2σ error and the overdispersion is low (<20%), resulting in a reliable CAM age estimate of 27.13 ± 1.60 ka.

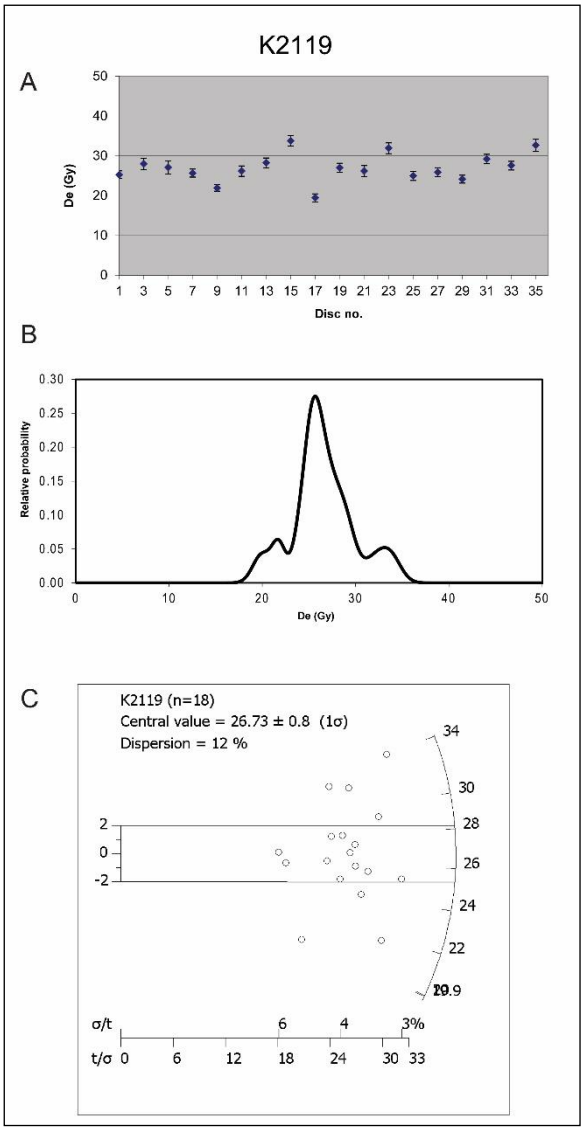

Sample K2119 was collected from above a shell midden (MS64) in Unit D. No aliquots were rejected. The PD plot suggests a single dominant peak, most of the data in the radial plot fall within the 2σ error and the overdispersion is low (<20%), resulting in a reliable CAM age estimate of 24.3 ± 1.43 ka.

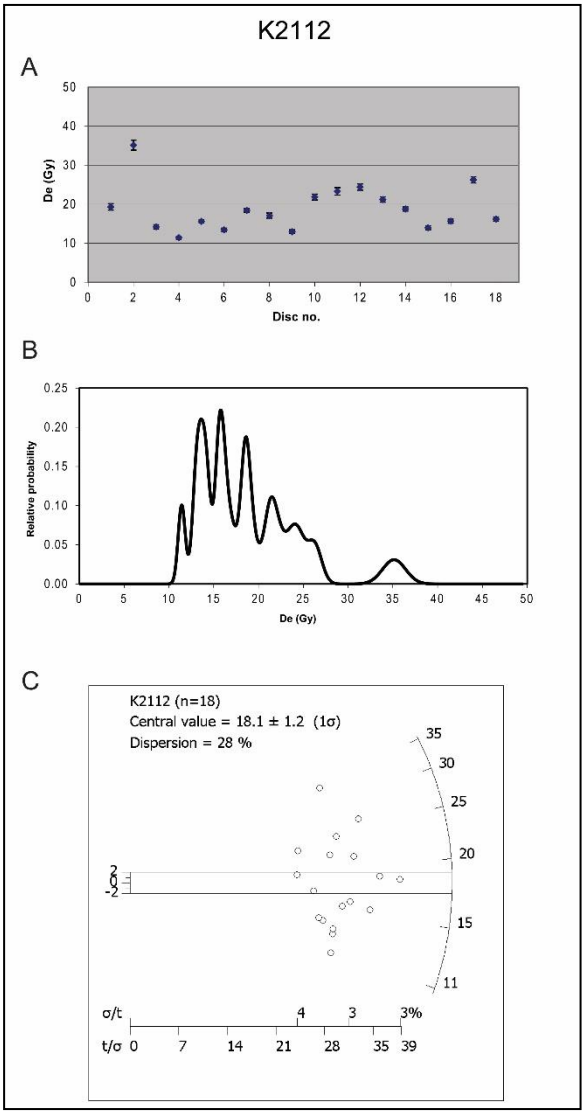

Sample K2112 was collected from the carbonate-rich region at depth within the Unit D palaeosol. No aliquots were rejected but the D_e results have a scattered distribution, resulting in a PD plot with multiple peaks and a radial plot in which the majority of aliquots fall outside the 2σ error of the CAM weighted mean. This may be an indication of post-depositional mixing, or a result of issues with microdosimetry. One aliquot has a much higher D_e than the others (~ 35 Gy, while the rest range from 11-26 Gy). Removing this outlier, however, does not alter the CAM D_e estimate from ~18 ± 1 Gy. The CAM age estimate of 22.5 ± 2 3 ka represents numerous grain populations in this sample, rather than the true depositional age of the unit.

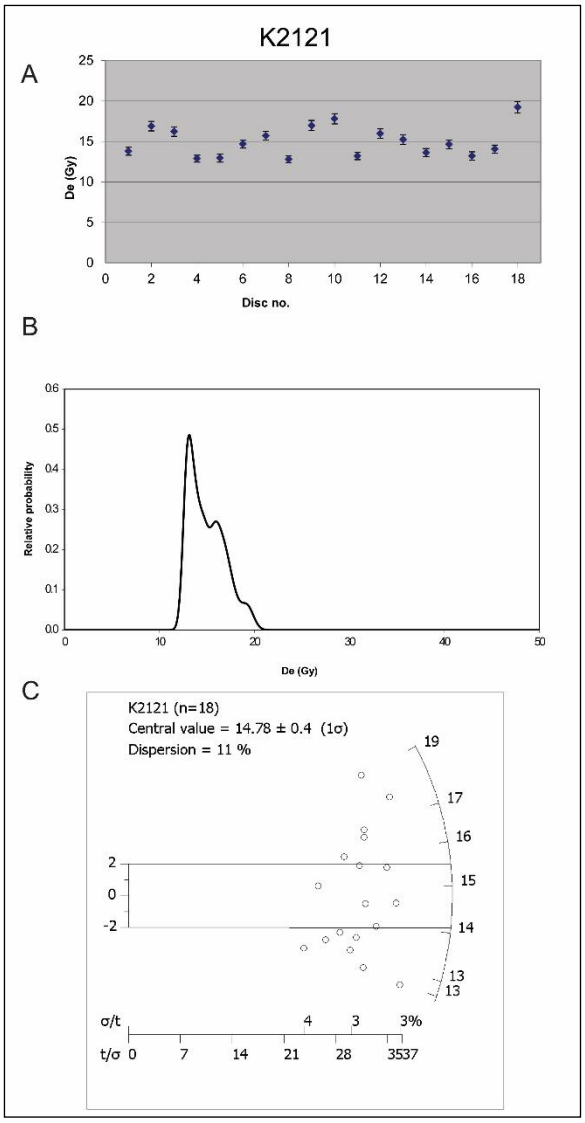

Sample K2121 was collected near the top of Unit D, below the contact with Unit E in the small sand ridge at the front of PR05. No aliquots were rejected. The dose distribution is narrow, the PD plot suggests a single dominant peak, much of the data in the radial plot falls within the 2σ error and the overdispersion is low (<20%), resulting in a reliable CAM age estimate of 17.38 ± 0.99 ka.

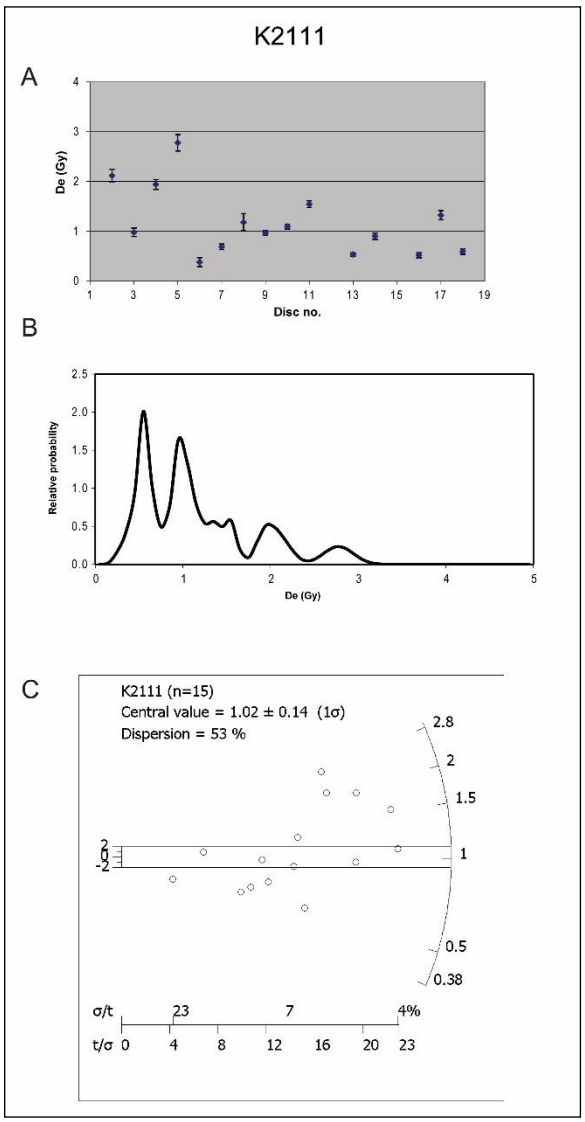

Sample K2111 was collected from within the rubified area at the top of Unit D, beneath the contact with Unit E. Three aliquots were rejected, due to poor recycling ratios (>10%) and the remaining D_e results have a scattered distribution, resulting in a PD plot with multiple peaks and a radial plot in which the majority of aliquots fall outside the 2σ error of the CAM weighted mean. This may be an indication of post-depositional mixing, or a result of issues with microdosimetry. The sample was collected from very close to the top of the unit, within the palaeosol, where bioturbation is likely to have occurred. The very young (and essentially modern) age estimate of 1.26 ± 1.12 ka is likely to include substantial contamination from the overlaying E layer and possibly modern material.

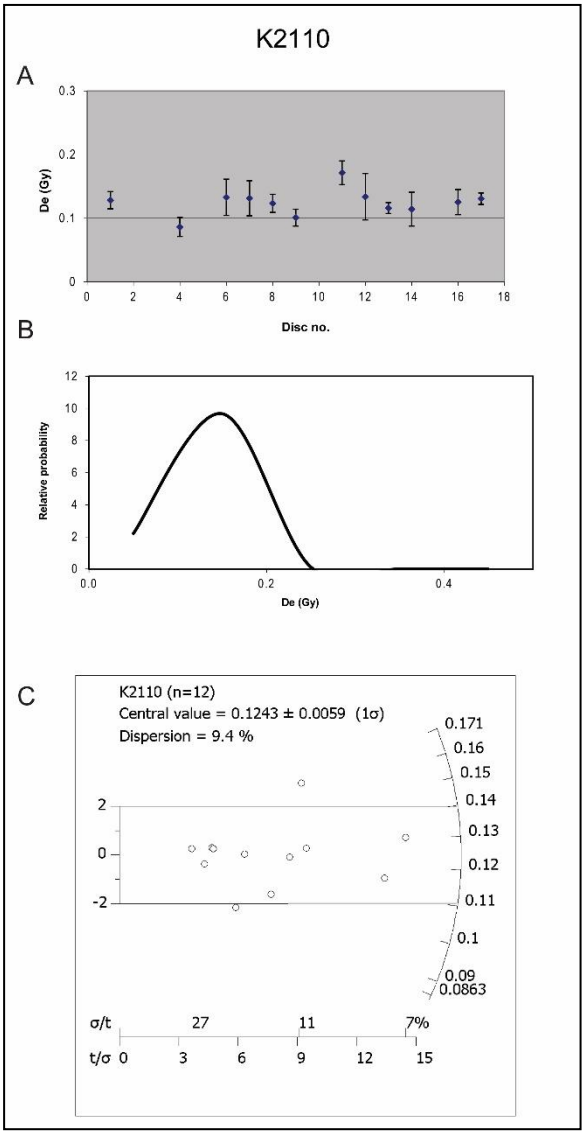

Sample K2110 was collected from the base of Unit E, just above the contact with Unit D. Six aliquots were rejected; five with poor recycling ratios (>10%) and one with a high palaeodose error (>30%). The remaining aliquots form a PD plot that suggests a single dominant peak, a radial plot with most data falling within the 2σ error and a low overdispersion (<20%), resulting in a reliable CAM age estimate of 130 ± 40 years.

Sample K2108 was collected from within a metre of the base of Unit E. Nine aliquots were rejected from this sample, one due to being out of range of the highest dose in the SAR (determined based on the DeLIA analysis of the sample), seven due to a poor recycling ratio (>10%) and one due to a high palaeodose error (30%). When a CAM analysis is applied to the remaining aliquots, the resultant overdispersion is very high, at 126%. The nine aliquots can be split in to three populations, each varying in D_e by an order of magnitude (<0.05, 0.2-0.5 and >1.0 Gy). The central value for the middle peak is the same as the CAM value for all aliquots, though with a much smaller error. With so few aliquots forming each population, it is difficult to determine whether they are true depositional populations and if they are, there is no argument as to which population represents the true depositional age of the unit. Thus the CAM result for all aliquots is used, which makes the results typical of Unit E, with high recuperation (>10%) and very high overdispersion (>40%). The specific age estimate of 360 ± 160 years is not highly reliable and given the indication of multiple populations, is not likely to represent the true age of deposition for the sample, but none-the-less the sample is likely to be relatively modern.

APPENDIX H. OSL DATING RESULTS

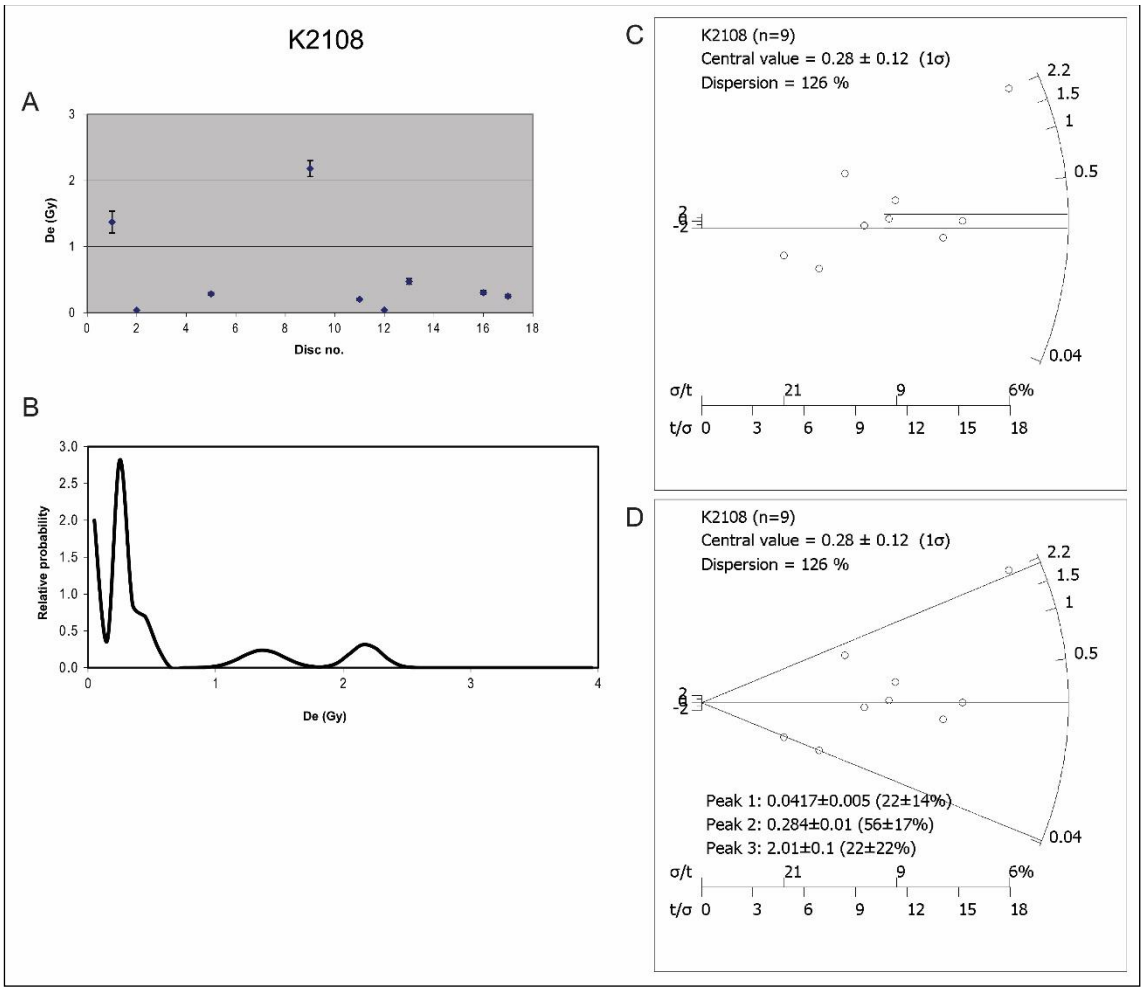

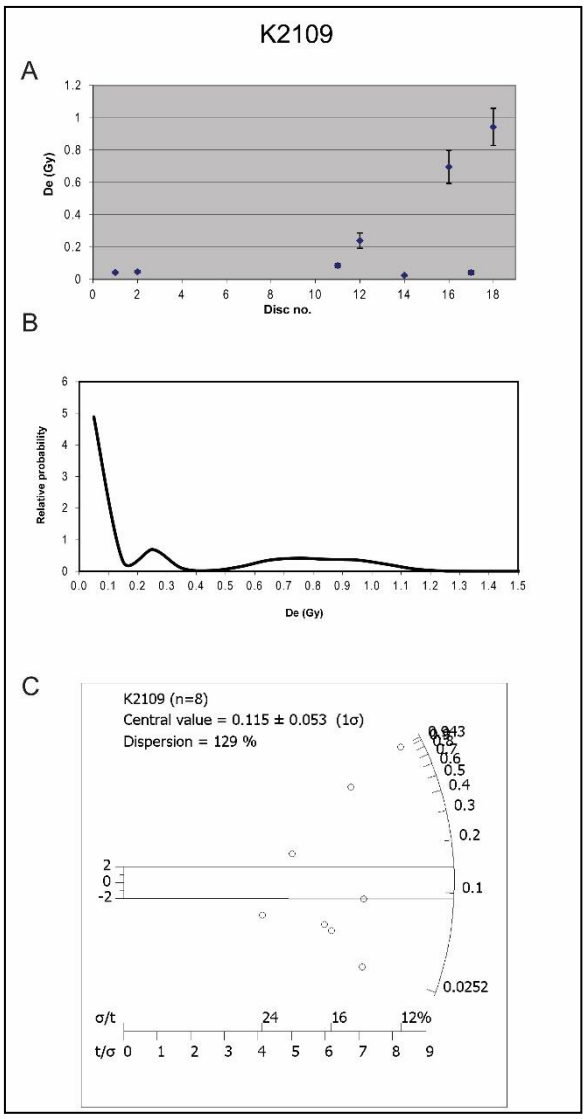

Sample K2109 was collected from within a metre of the base of Unit E. Ten aliquots were rejected from this sample, six due to a poor recycling ratio (>10%) and four due to a high palaeodose error (>30%). If a CAM analysis is applied to the remaining aliquots, the resultant overdispersion is nearly 130%. The extra peaks and long right tail suggested in PD plot, along with the scattered values in the radial plot, indicate a population of very recent sands mixed with one or more older populations of sand from below, or grains which were only partially bleached upon deposition. With no argument as to which population represents the true depositional age of the unit, the CAM result is used for this sample. The specific age estimate of 160 ± 70 years is not highly reliable and given the multiple populations, is not likely to represent the true age of deposition for the sample, but none-the-less the sample is likely to be relatively modern.

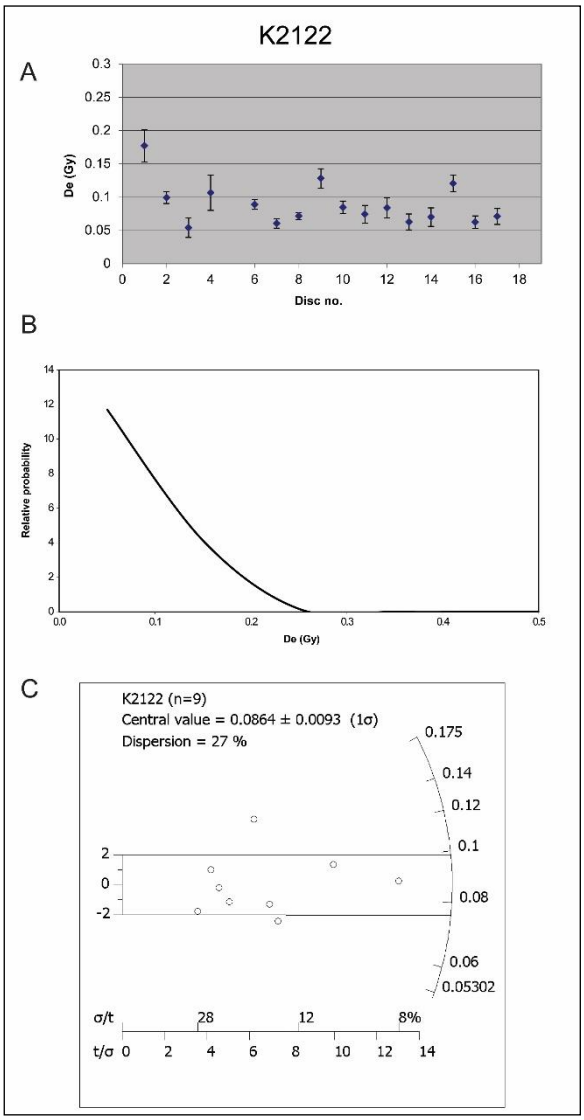

Sample K2122 was collected from the sands at the top of the small sand ridge at the front of PR05. Nine aliquots were rejected from this sample, due to poor recycling ratios (>10%). The results for the remaining nine aliquots are typical for Unit E sands, with high recuperation (>10%), very low D_e (<0.2 Gy) and most aliquots falling within the 2σ error on the radial plot. The overdispersion is relatively high (27%), though not as high as most Unit E samples (>40%). The specific age estimate of 110 ± 10 years is not highly reliable, though the sample is likely to be very modern.

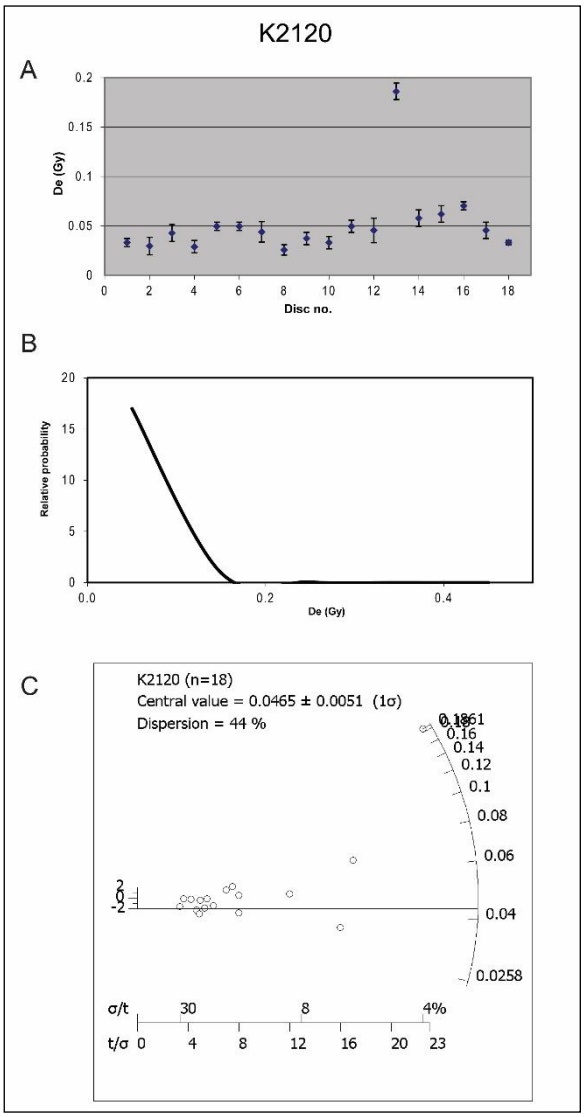

Sample K2120 (Figure 7.46) was collected from the sands at the in the small sand ridge to the side of PR05, within Unit E, just above the contact with Unit D. The results are typical of Unit E sands, with high recuperation (>10%), very low D_e (mostly <0.1 Gy) and most aliquots falling within the 2σ error on the radial plot. No aliquots were rejected from this sample and the overdispersion is relatively high (44%), though not as high as most Unit E samples (>40%). One aliquot has slightly higher D_e (>0.1 Gy), higher precision and lower relative error than the other aliquots, probably representing a small amount of mixing in this sample. The specific age estimate of 50 ± 10 years is not highly reliable, though the sample is likely to be very modern.

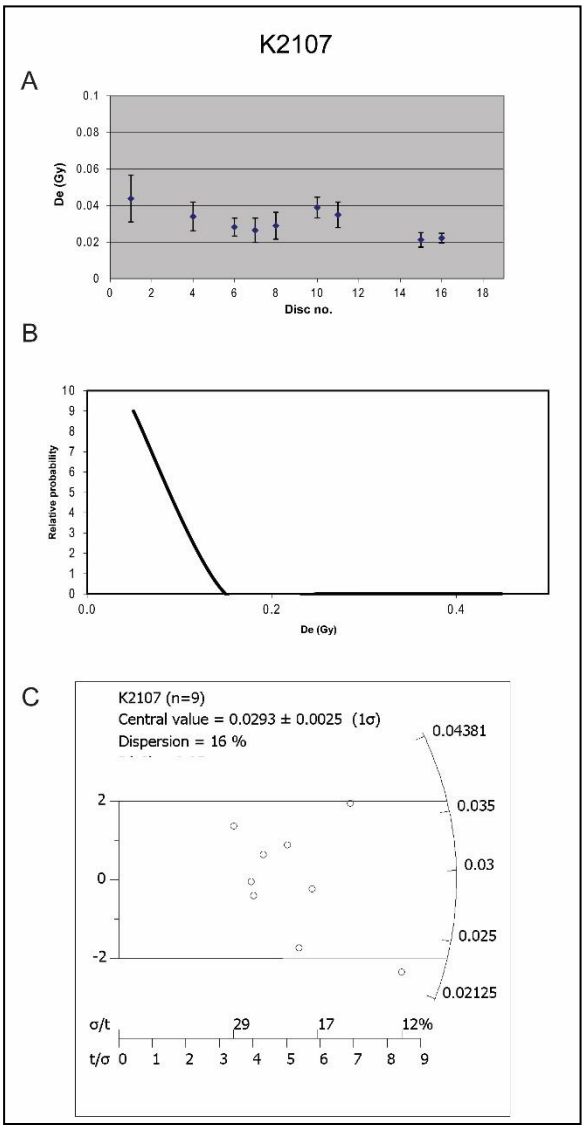

Sample K2107 was collected from the sands at the top of the lunette near PR05. The results are fairly typical of E Unit sands, with high recuperation (>10%), very low D_e (<0.1 Gy) and most aliquots showing low precision and falling within the 2σ error on the radial plot. Nine aliquots were rejected from this sample; five with a poor recycling ratio (>10%), one with a low signal to background ratio and three with high palaeodose errors (>30%). The overdispersion on the remaining nine aliquots is low, particularly for a Unit E sample, at 16%. The specific age estimate of 30 ± 10 years is not highly reliable, though the sample is certainly likely to be very modern.

APPENDIX H. OSL DATING RESULTS

Three additional samples were collected in the vicinity of PR05, which were not included in the stratigraphic log: K2105, below the modern ground surface behind the dune, K2106, half way up the back of the dune, and K2127, in the "beach ridge" at the front of the dune.

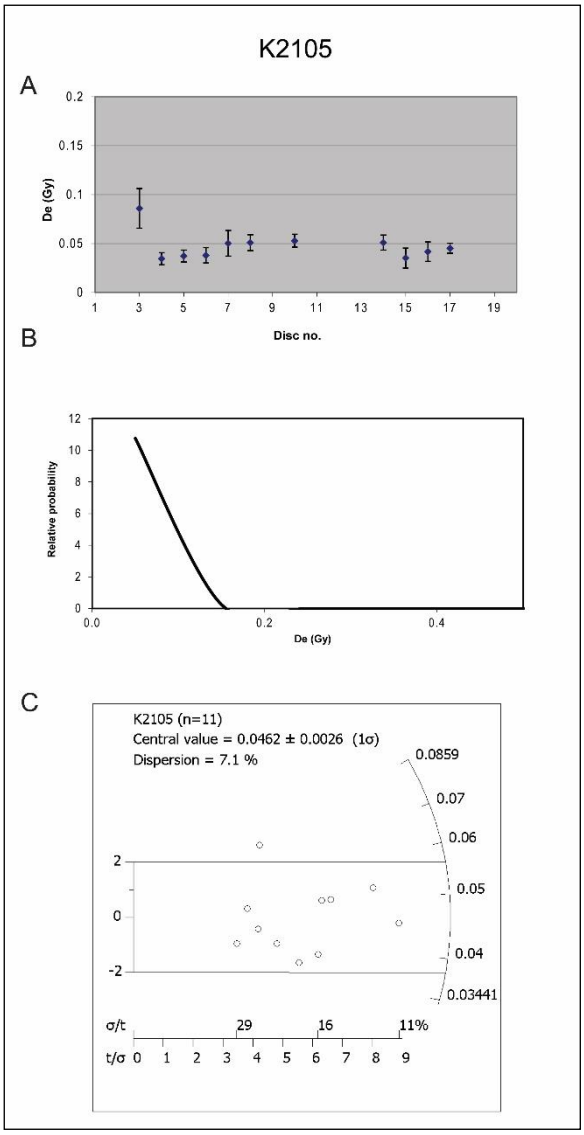

Sample K2105 was collected from beneath the current ground surface, behind the lunette at PR05. The results are more typical of Unit E sands however, with high recuperation (>10%), very low D_e (<0.1 Gy) and most aliquots falling within the 2σ error on the radial plot. Seven aliquots were rejected from this sample, five due to poor recycling ratios (>10%) and two due to high palaeodose errors (>30%). The remaining aliquots provide a CAM age estimate of 40 ± 6 years, indicating that the dated grains are actually very recently deposited sediments.

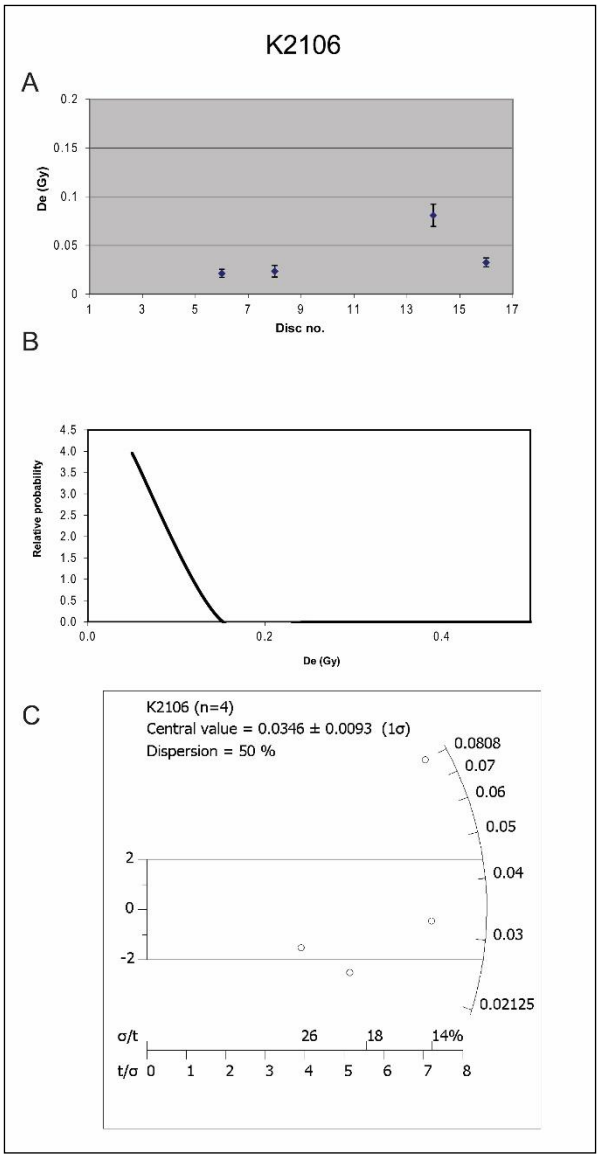

Sample K2106 was collected from the dune sands halfway up the rear of the lunette. Most aliquots were rejected from this sample, six due to a poor recycling ratio (>10%) and a futher eight due to a high palaeodose error (>30%). The results from the remaining four aliquots are typical of Unit E sands, with high recuperation (>10%), very high overdispersion (>40%), very low D_e (<0.1 Gy) and most aliquots showing low precision and falling within the 2σ error on the radial plot. One aliquot has slightly higher D_e (>0.04 Gy), higher precision and lower relative error than the other aliquots, probably representing a small amount of mixing in this sample. As it is based on only four aliquots, the specific age estimate of 40 ± 10 years is not highly reliable. Given its similarity to other young samples, however, the sample is likely to be very modern.

Sample K2127 was collected from within the beach ridge in front of the lunette and shows evidence of mixing, probably due to modern bioturbation. This sample was collected from only 10 cm below the current ground surface. One aliquot was rejected due to a poor recycling ratio (>10%). The PD plot suggests multiple peaks and the radial plot is scattered with few data points within the 2σ error range. The data in the radial plot appear to be explained by a three component mixture model. This mixing model is not reliable for identifying discrete populations in these multi-grained samples, but does, however, highlight that multiple populations are likely to be present. Since the true depositional population cannot be isolated with this data, and because the overdispersion is acceptable, all 18 aliquots are used to determine a central measure of D_e. The CAM age estimate of 5.2 ± 0.8 ka likely includes a large modern component, mixed into the sediments by modern soil forming processes.

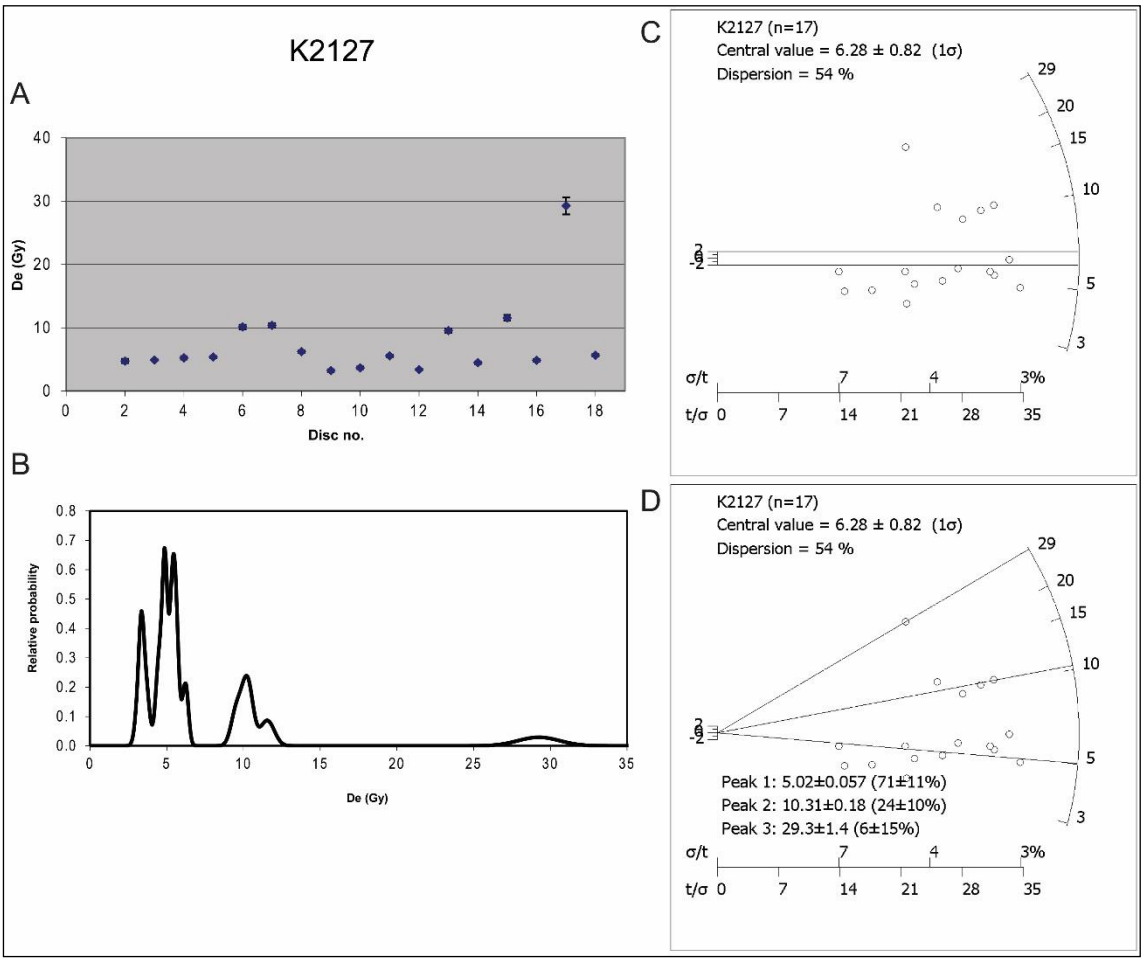

Appendix H.4. OSL Results at SL11

This section provides the OSL dating results from SL11, a stratigraphic log taken from the wall of BG01 (see Section **Error! Reference source not found.**). The lowermost sample from Unit C dates to around 40 ka. A slight age inversion is present at the lower palaeosol within Unit C, with the palaeosol dating to around 23 ka, while the sample immediately above dates to around 28 ka. The sample from within the upper palaeosol gives a much younger age estimate of about 1.3 ka. Unit E gives very young ages in both the laminated and upper, non-laminated section, though the lower, non-laminated sub-unit may date up to 2 ka.

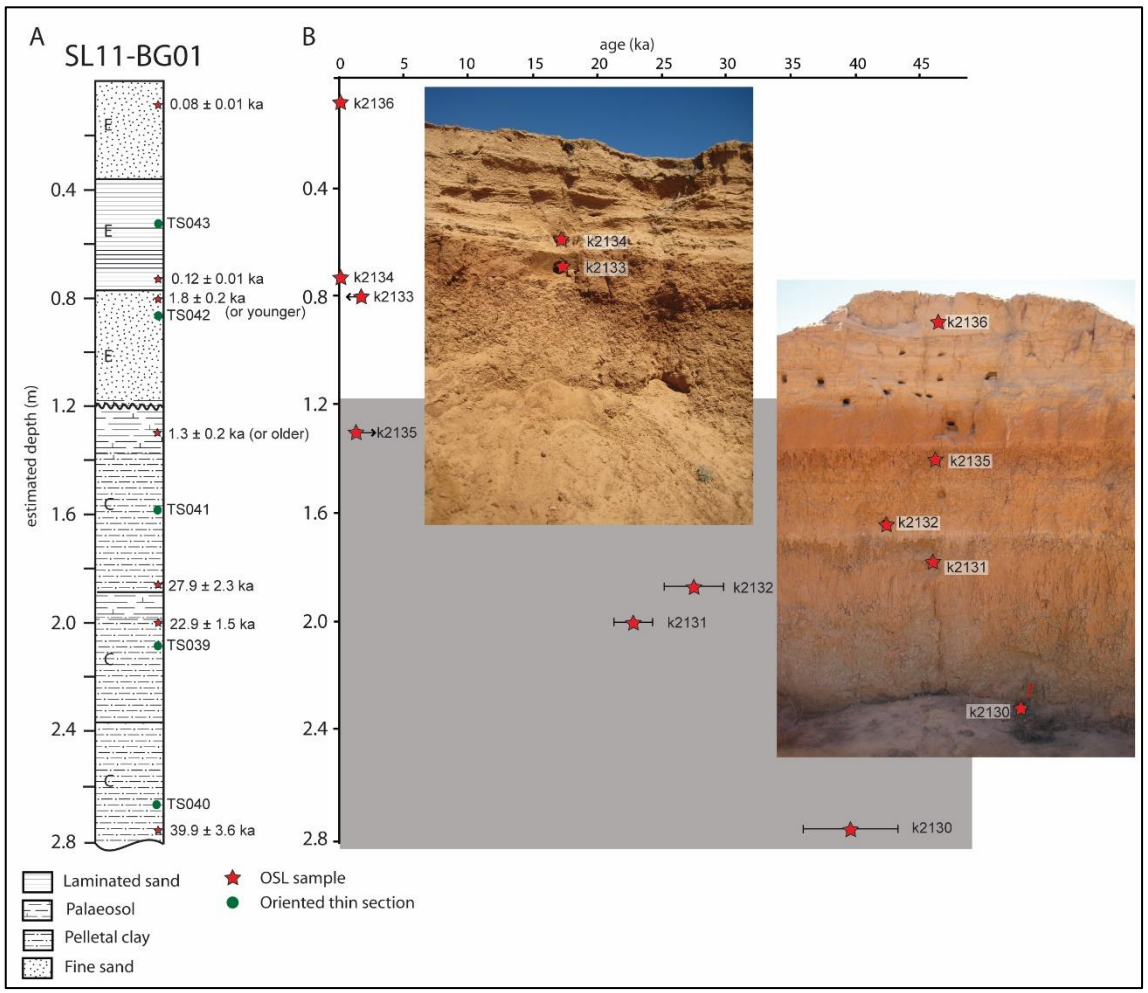

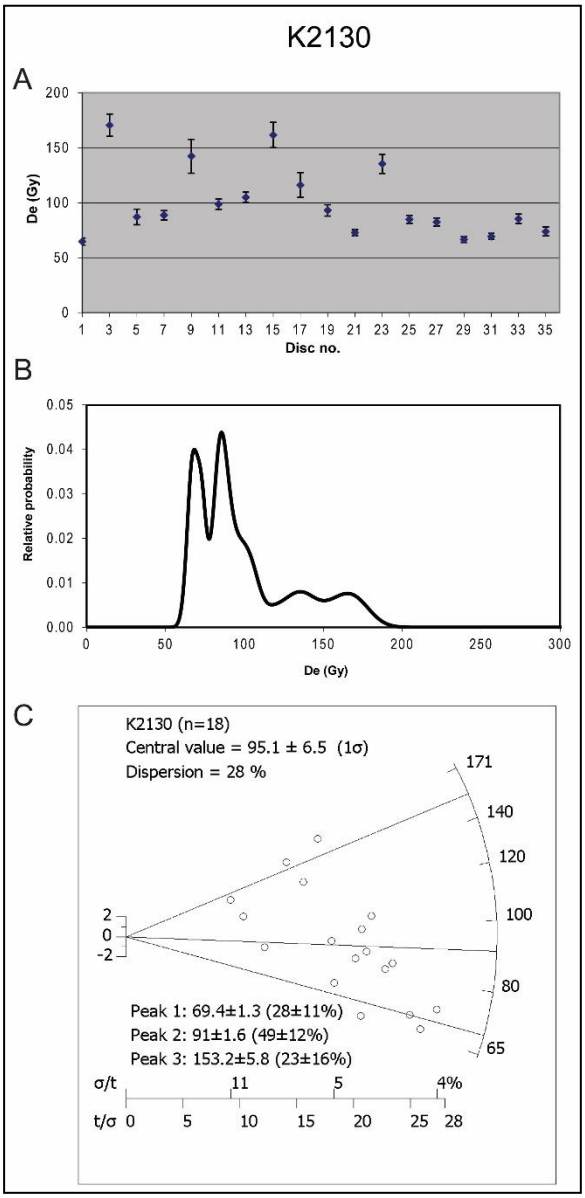

K2130 was collected from the green-grey clay at the base of the section. No aliquots were rejected from this sample, which appears to contain multiple grain populations. The data in the radial plot appear to be explained by a three component mixture model. This mixing model is not reliable for identifying discrete populations in these multi-grained samples, but does, however, highlight that multiple populations are likely to be present. The central measures of the three apparent populations range from ~70 Gy, to ~90 Gy to over 150 Gy. Since the true depositional population cannot be isolated with this data, all 18 aliquots are used to determine a central measure of D_e, resulting in a CAM age estimate of 39.88 ± 3.62 ka.

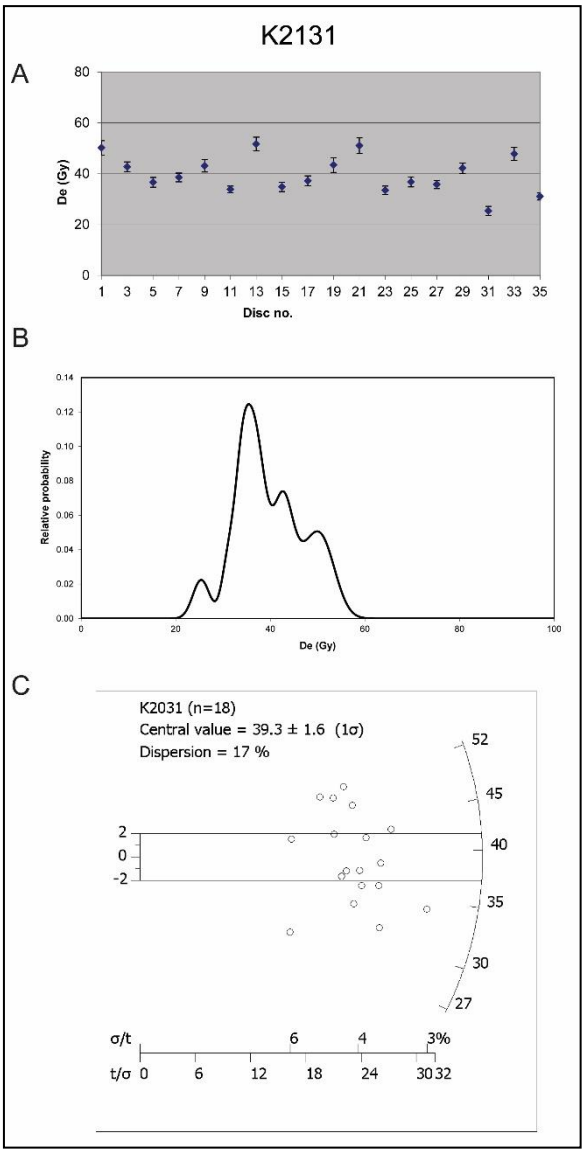

Sample K2131 was collected from further up the section than K2130, below the first palaeosol. No aliquots were rejected from this sample. The dose distribution is a little broad but suggests a central dominant peak and much of the data in the radial plot falls within the 2σ error. This, combined with the low overdispersion (<20%), result in a reliable CAM age estimate of 22.93 1.47 ka.

Sample K2132 was collected from partway up Unit C, just above the first palaeosol. One aliquot was rejected due to being out of range of the highest test dose in the SAR (determined based on the DeLIA analysis of the sample). The remaining aliquots form a PD plot that suggests a single dominant central peak and a right tail The highest peak in the tail is formed by three aliquots >50 Gy, which appear to represent a separate population, possibly introduced through sediment mixing. Removing these from the CAM analysis decreases the overdispersion from 24% to 17%. Given this improvement in overdispersion, and the clear dominant peak, the age estimate for this sample is calculated with the three outliers removed.

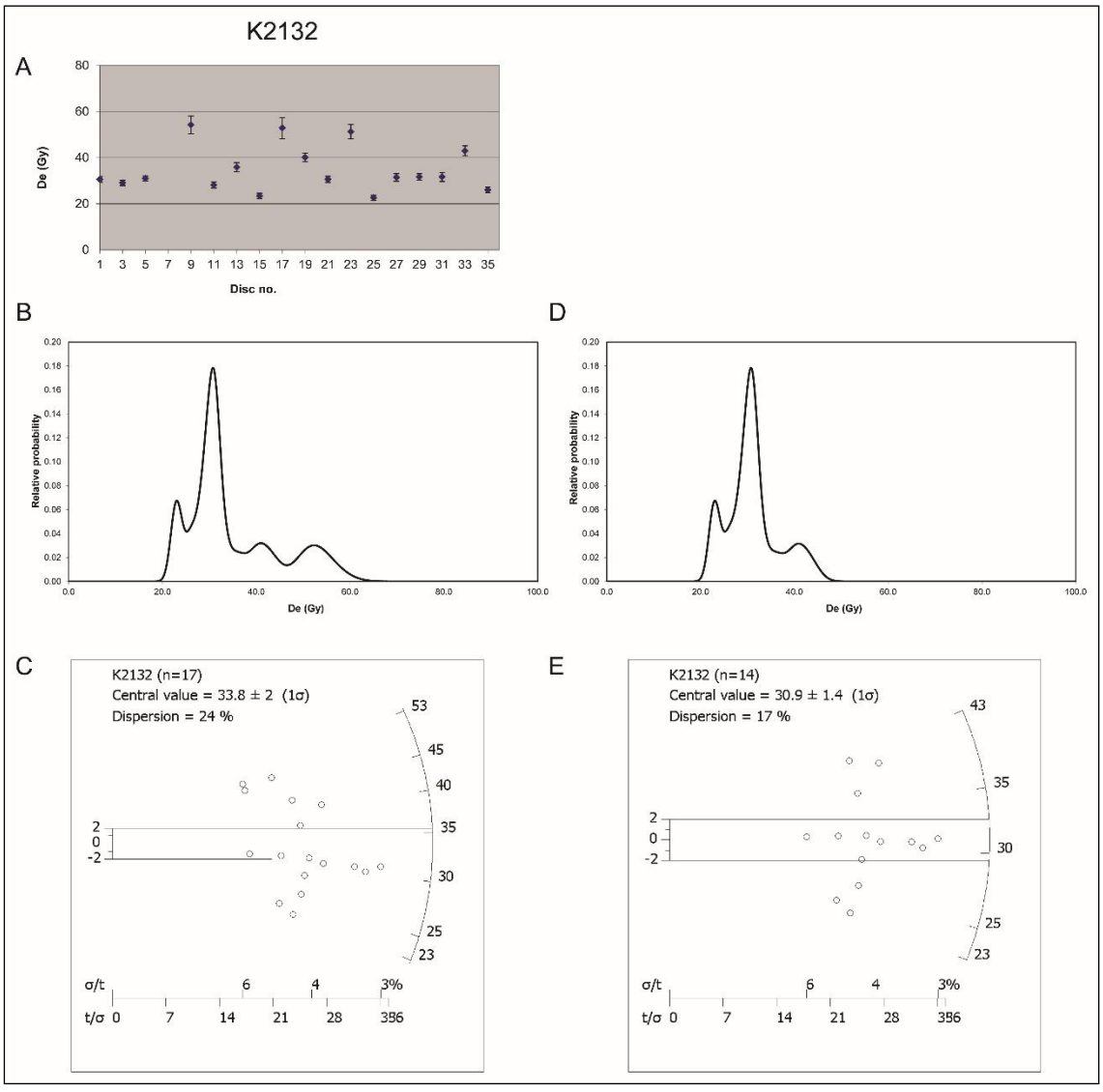

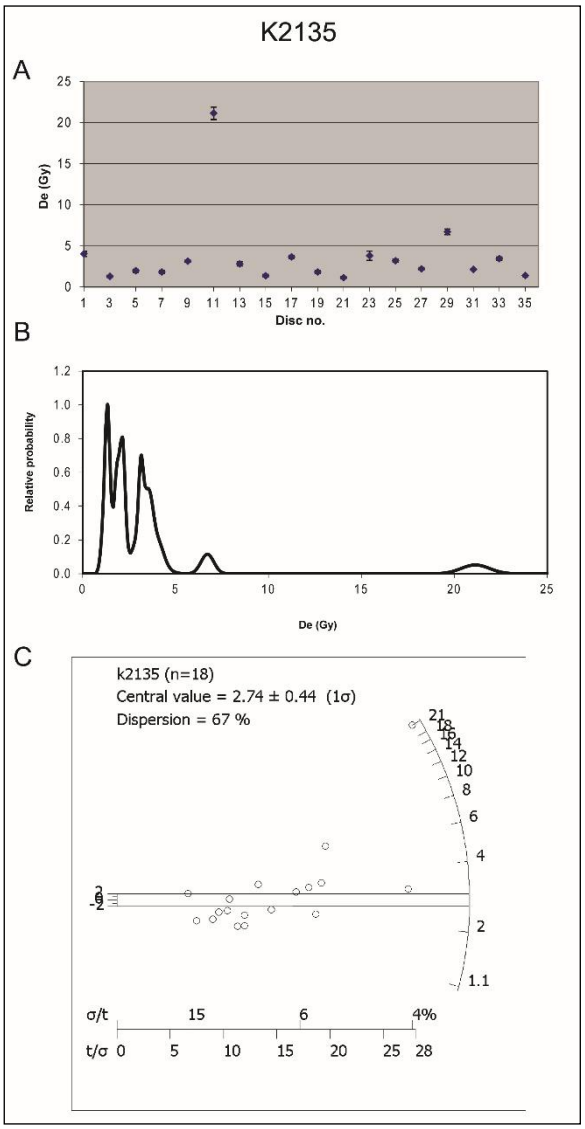

Sample K2135 was collected from within the upper palaeosol of Unit C. No aliquots were rejected from this sample, which has a PD plot that suggests multiple peaks and a radial plot in which the majority of aliquots fall outside the 2-σ error of the CAM weighted mean. One aliquot has a much higher D_e value (~21 Gy) than the other aliquots (mostly <5 Gy). Removing the outlying aliquot from the CAM calculation has only a minor effect on the age estimate (it remains within error), so all 18 aliquots are used to estimate an age for this sample. The scattered D_e distribution may be an indication of post-depositional mixing, or a result of issues with microdosimetry. The sample was collected from very close to the top of the unit, within the palaeosol, where bioturbation is likely to have occurred. It appears that a large amount of material has been incorporated into this layer when it was the ground surface, before deposition of Unit E, as the D_e values of the aliquots are very low (<5 Gy) compared to other samples from this unit (20-60 Gy). The age estimate of 1.27 ± 0.22 ka is therefore very unlikely to represent the true depositional age for these sediments.

Sample K2133 was collected from a rubified layer with in-situ ferri-argillans immediately overlying Unit C. Ten aliquots were rejected, nine due to poor recycling ratios (>10%) and one due to a high palaeodose error (>30%). Of the remaining eight aliquots, two are clear outliers, creating a right skew in the PD plot and a separate population in the radial plot. When those aliquots are removed from the CAM calculation the overdispersion decreases from 63% to 28%, but only two of the remaining six aliquots fall within the 2σ error on the radial plot. It is likely that the rubified sediments present in this sample represent re-worked material from the underlying Unit C palaeosol (as evidenced by in-situ ferri-argillans) and as such, some older material from Unit C is entrained with the Unit E sediments. Even after removing the two clear outliers, the age estimate of 1.83 ± 0.23 ka is unlikely to represent the true depositional age of the sediments.

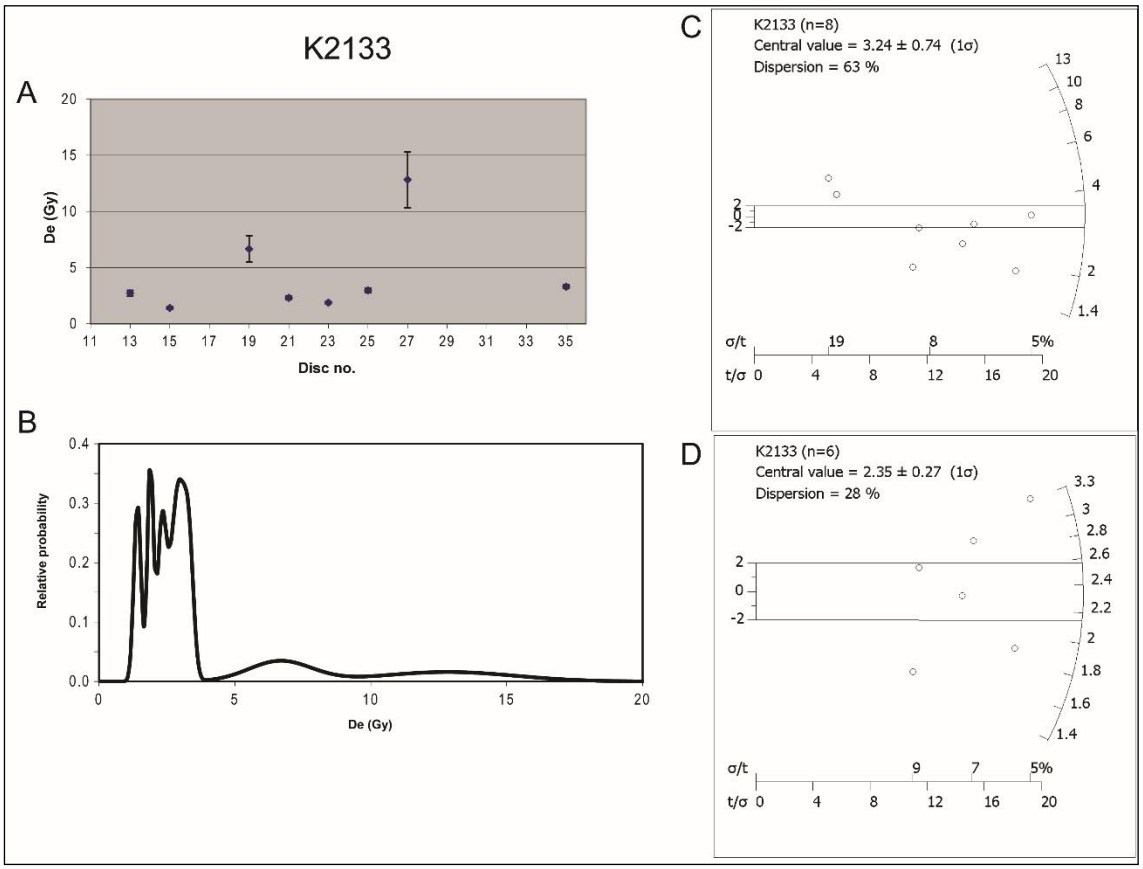

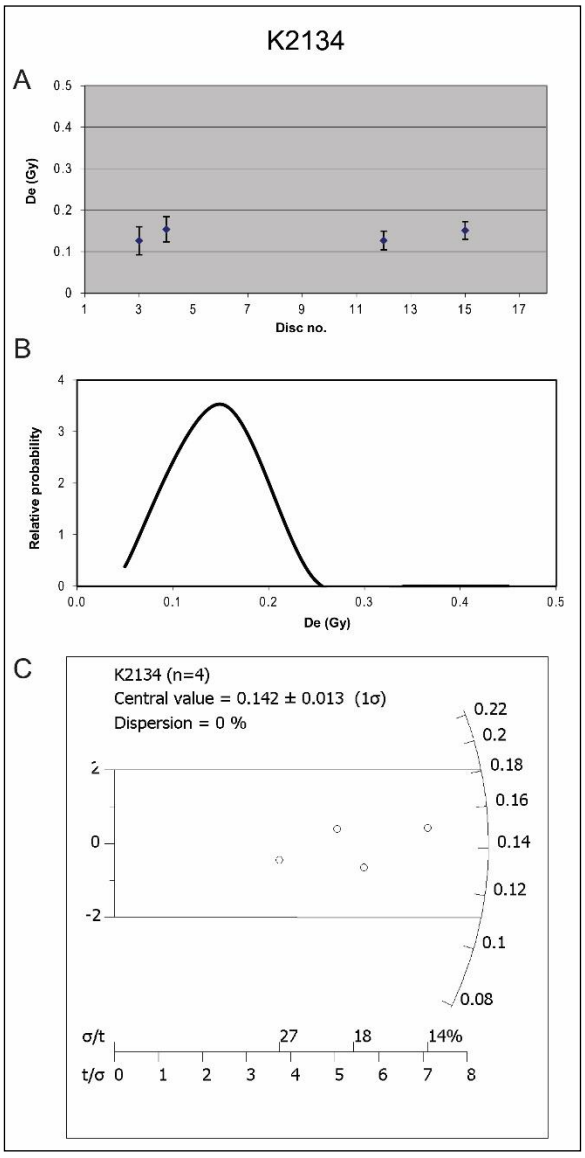

Sample K2134 was collected from within the laminated section of Unit E. Fourteen aliquots were rejected, due to a combination of poor recycling ratios, low signal to background ratios and high palaeodose errors. With only four remaining aliquots, the age estimate of 120 ± 10 years is highly unreliable, even though the PD plot forms a normal distribution, all data points fall within the 2σ error in the radial plot and overdispersion is very low.

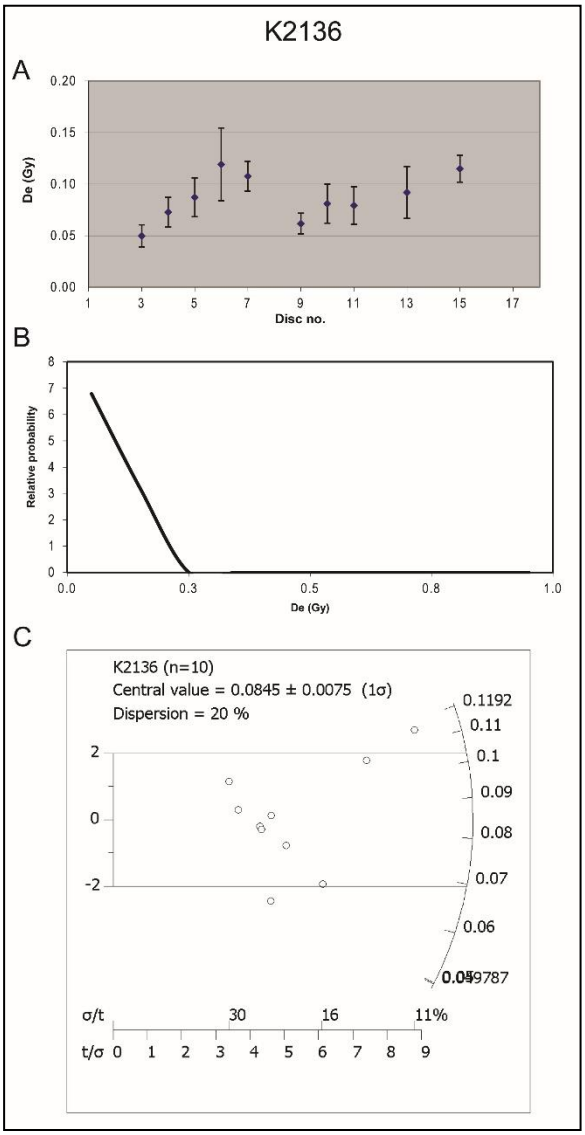

Sample K2136 was collected from within the top of Unit E, and gives a very typical result, with high recuperation (>10%). Eight samples were rejected, seven due to poor recycling ratios (>10%) and one due to a high palaeodose error (>30%). The remaining aliquots all have low D_e values (<0.2 Gy), mostly with very low precision and high relative error. As a result, the specific age estimate of 80 ± 10 years is not highly reliable, though the sample is likely to be relatively modern.

Appendix H.5. OSL results at PR04

This section provides the OSL dating results from PR04, See Section 3.3.3 for larger versions of the aerial photo and transect shown below. At PR04 the OSL ages do not show any inversions, though the calibrated radiocarbon ages for the mussel shells give younger ages than the OSL estimate for the immediately overlying sediments. The top of Unit A dates to at least 110 ka while the sample from lower in the unit (K2089) is fully saturated. The two mussel shells from Unit B give calibrated radiocarbon ages of around 33 ka and 40 ka, bracketed by sediments dated to approximately 52 ka (above) and 81 ka (below). The uppermost OSL sample from Unit B gave an age of around 54 ka. Unit C dates to about 38 ka while two samples from Unit E both give an age of approximately 70 years.

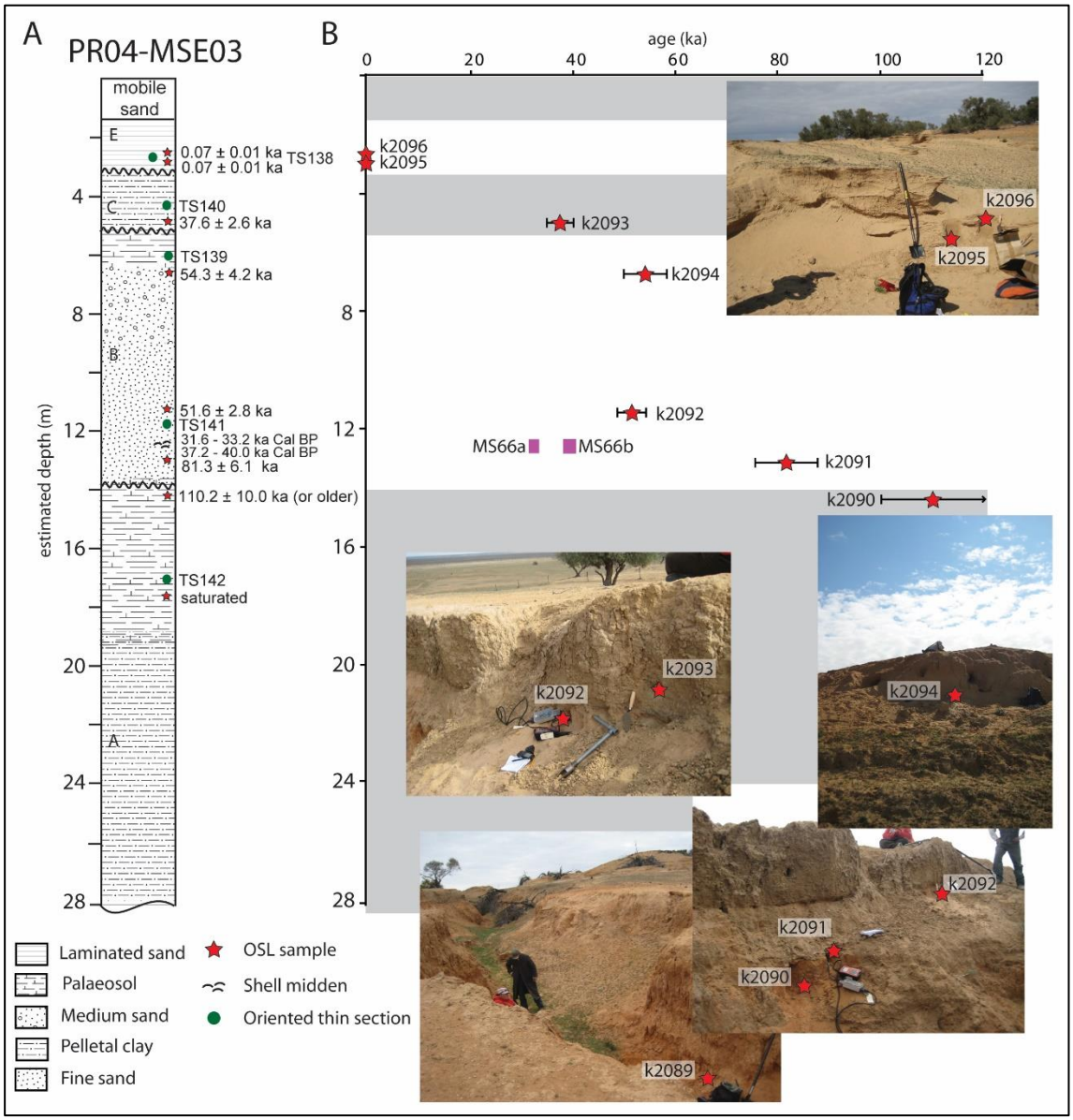

APPENDIX H. OSL DATING RESULTS

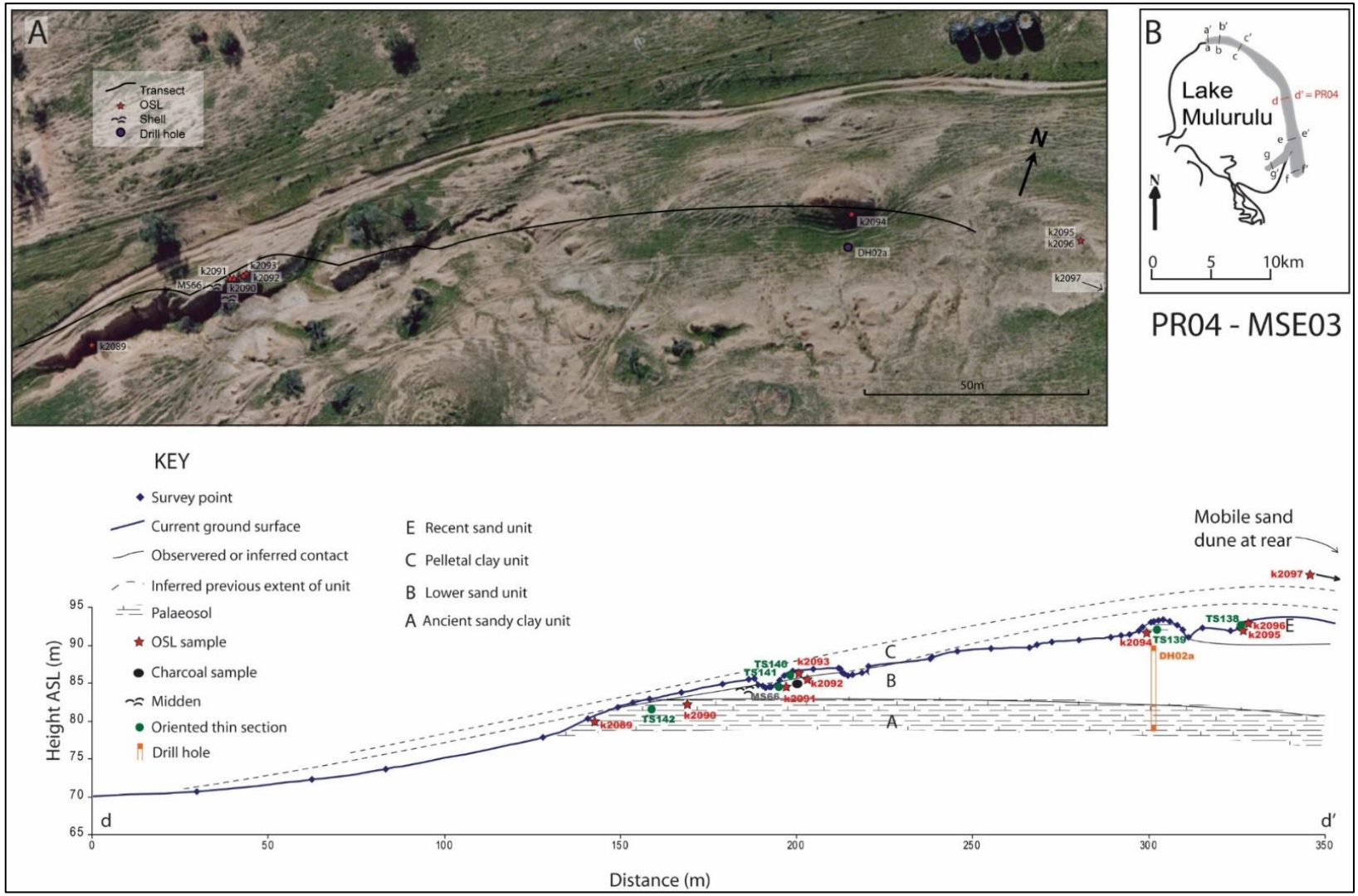

All aliquots of K2089, from deep within the palaeosol of Unit A, were rejected due to saturation. The highest dose step was 160 Gy, which for this sample would represent an age of 127 ka. This therefore represents a minimum age for this sample.

Sample K2090 was collected from near the top of Unit A. One aliquot was rejected, due to saturation. The remaining 17 aliquots form a PD plot that suggests a dominant peak around 100 Gy, plus at least two other, much older grain populations. Most of the data fall outside the 2σ error on the radial plot, and applying a mixture model suggests that four or more populations may be present. This mixing model is not reliable for identifying discrete populations in these multi-grained samples, but does, however, highlight that multiple populations are likely to be present. This scattered D_e distribution is likely a result of sediment mixing, as this sample was collected from within the palaeosol of this unit. Since the true depositional population cannot be isolated with this data, all 17 aliquots are used to determine a central measure of D_e, resulting in a CAM age estimate of 110.21 ± 10.03 ka, though the unit is probably older.

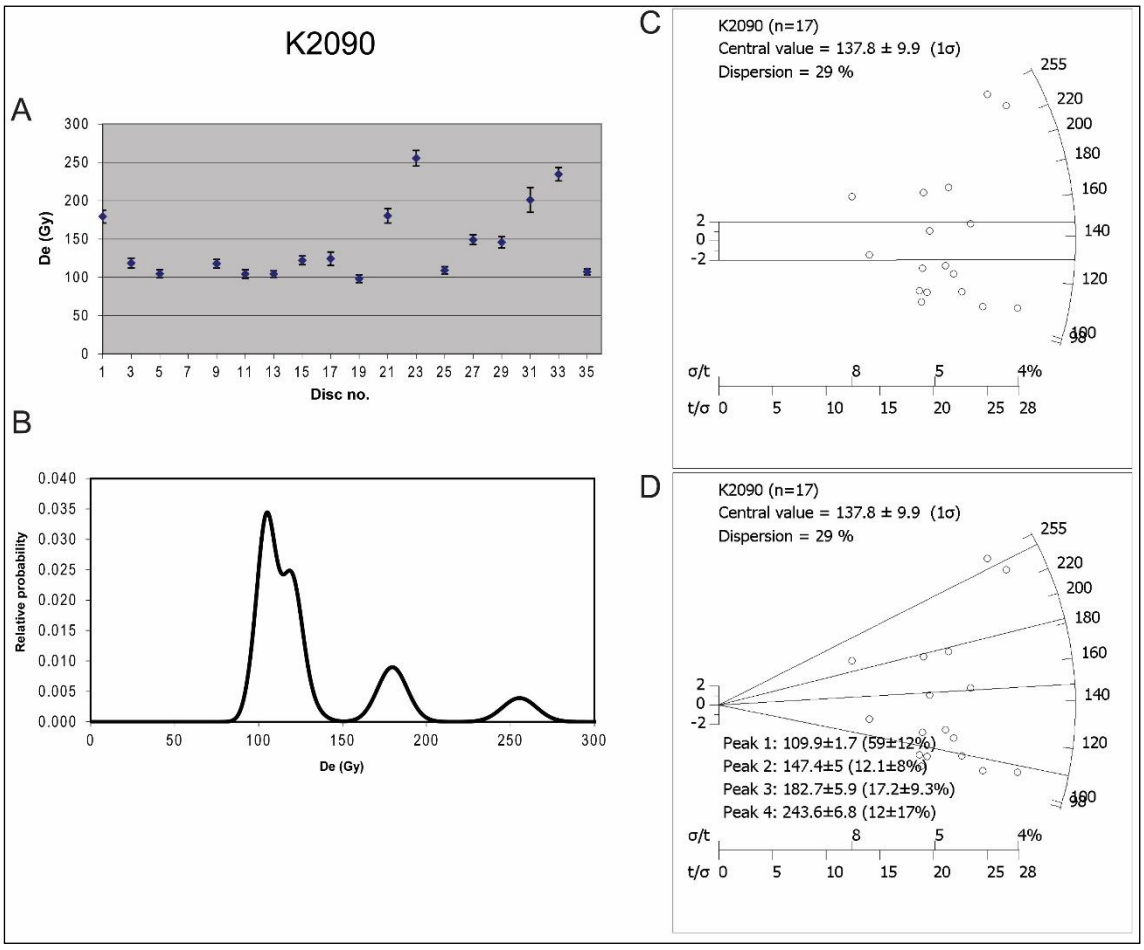

Sample K2091 was collected from Unit B, immediately above the contact with Unit A. No aliquots were rejected from this sample. Four aliquots are clear outliers, (>140 Gy) and form a right 'shoulder' on the PD plot. These outliers are within the range of the aliquots for the underlying sample K2090 (CAM = ~138 Gy). Removing these outliers from the CAM calculation results in a radial plot with much of the data falling within the 2σ error, brings the overdispersion to close to 20% and provdes an age estimate of 81.33± 6.07 ka.

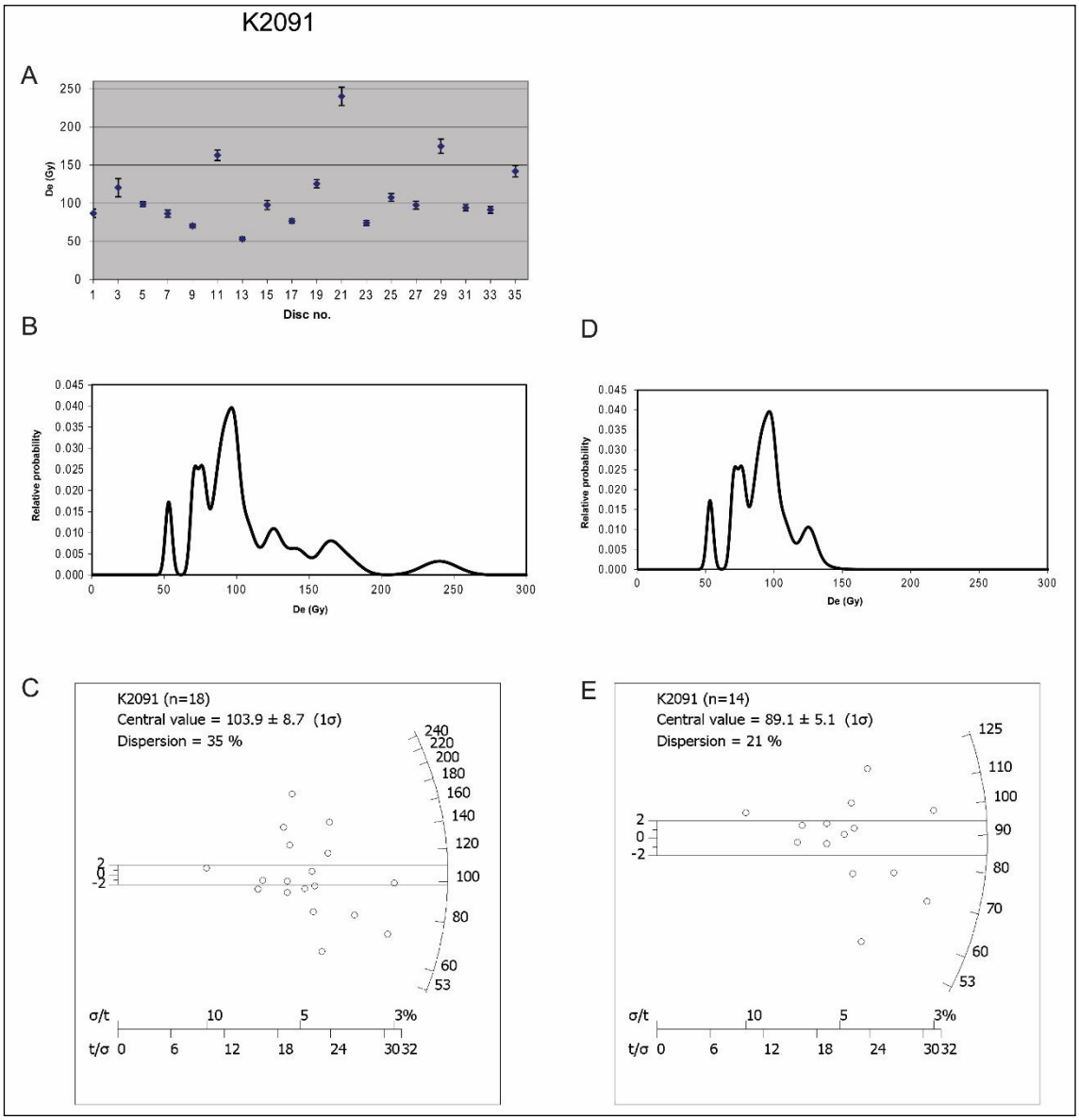

Sample K2092 was collected from Unit B, above a shell midden and thin section TS141. No aliquots were rejected from this sample. Five aliquots are outliers, (>78 Gy), forming discrete peaks on the PD plot and falling well above the 2σ error on the radial plot . These outliers are within the range of the aliquots for the underlying sample K2091 (CAM = ~89 Gy). Removing these outliers from the CAM calculation results in a radial plot with most data falling within the 2σ error, reduces the overdispersion to <20% and provides an age estimate of 51.61± 2.82 ka.

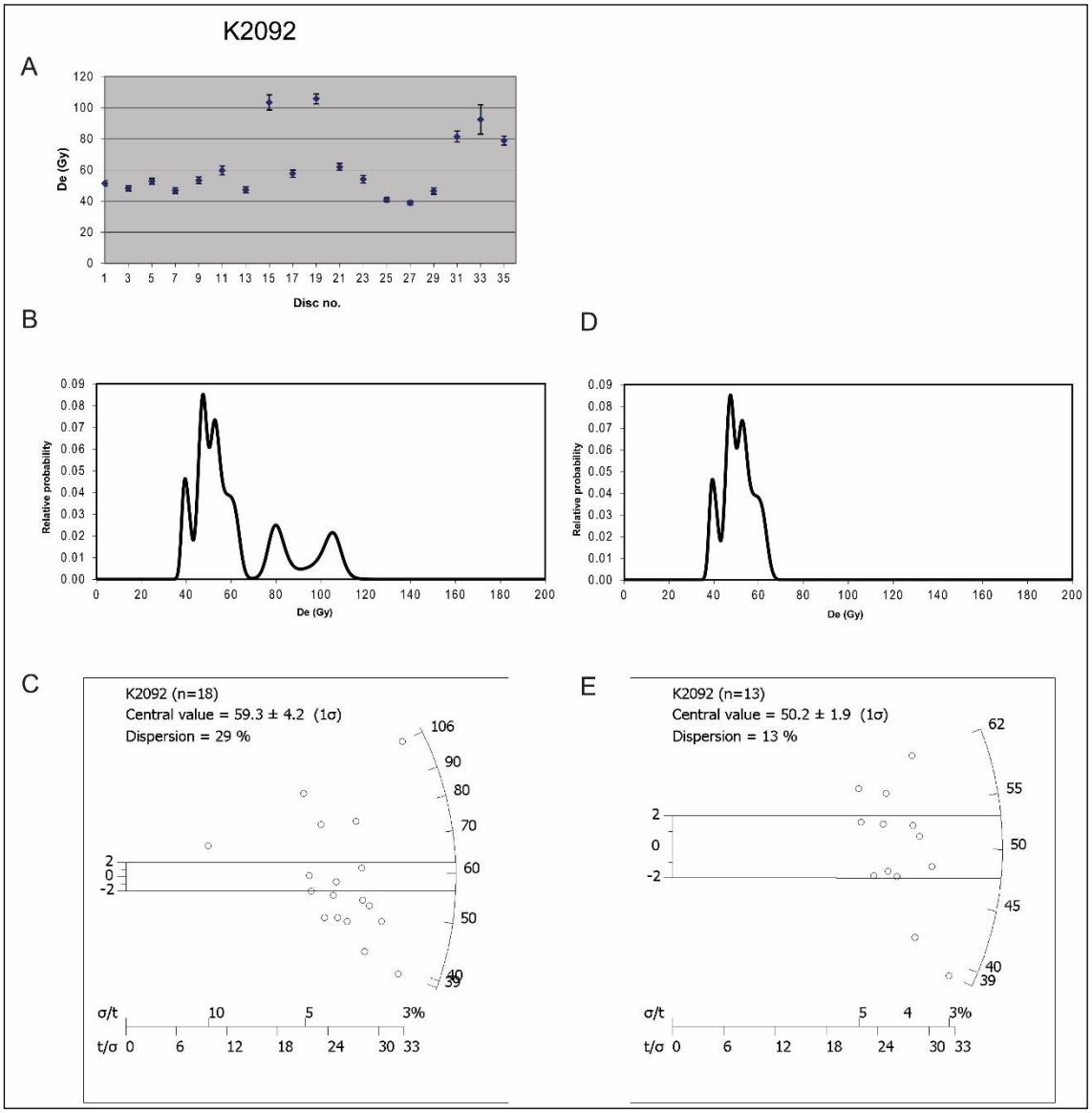

Sample K2094 was collected from atop a sand residual, within the rubified region of the Unit B palaeosol. One aliquot was rejected, due to saturation. The remaining aliquots from this sample provide multimodal relative probablity and radial plots. The mixing model shown here is not reliable for identifying discrete populations in these multi-grained aliquots, but does, however, highlight that multiple populations are likely to be present. Since the true depositional population cannot be isolated with this data and no argument can be made for why to accept one population over the other, the CAM is applied to all aliquots to determine an age estimate of 54.31 ± 4.16 ka for this sample, even though the overdispersion is slightly above 20%.

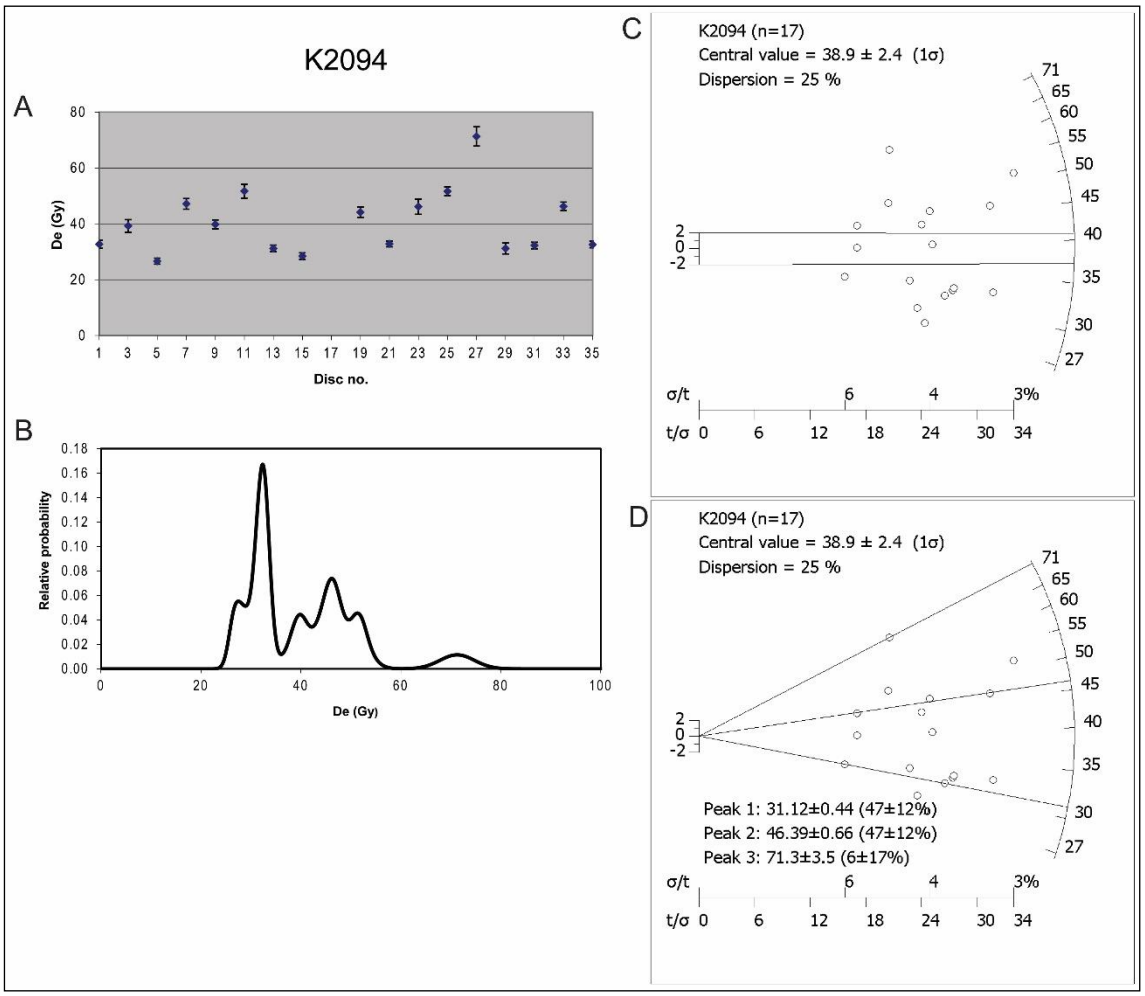

Sample K2093 was collected from within Unit C, from a gully wall exposure. No aliquots were rejected from this sample. With all aliquots included, the PD plot has a long right shoulder with two minor peaks. Removing the outlying aliquots, > 100 Gy, results in a much narrower, though bimodal, distribution, with most data falling within the 2σ error on the radial plot and brings the overdispersion below 20%. The CAM age estimate based on these aliquots is 37.58 ± 2.59 ka. The older population may have intruded in to this unit via dessication cracks, because although Unit C is stratigraphically overlying Unit B, the actual sampling site was downslope from the bulk of Unit B exposure.

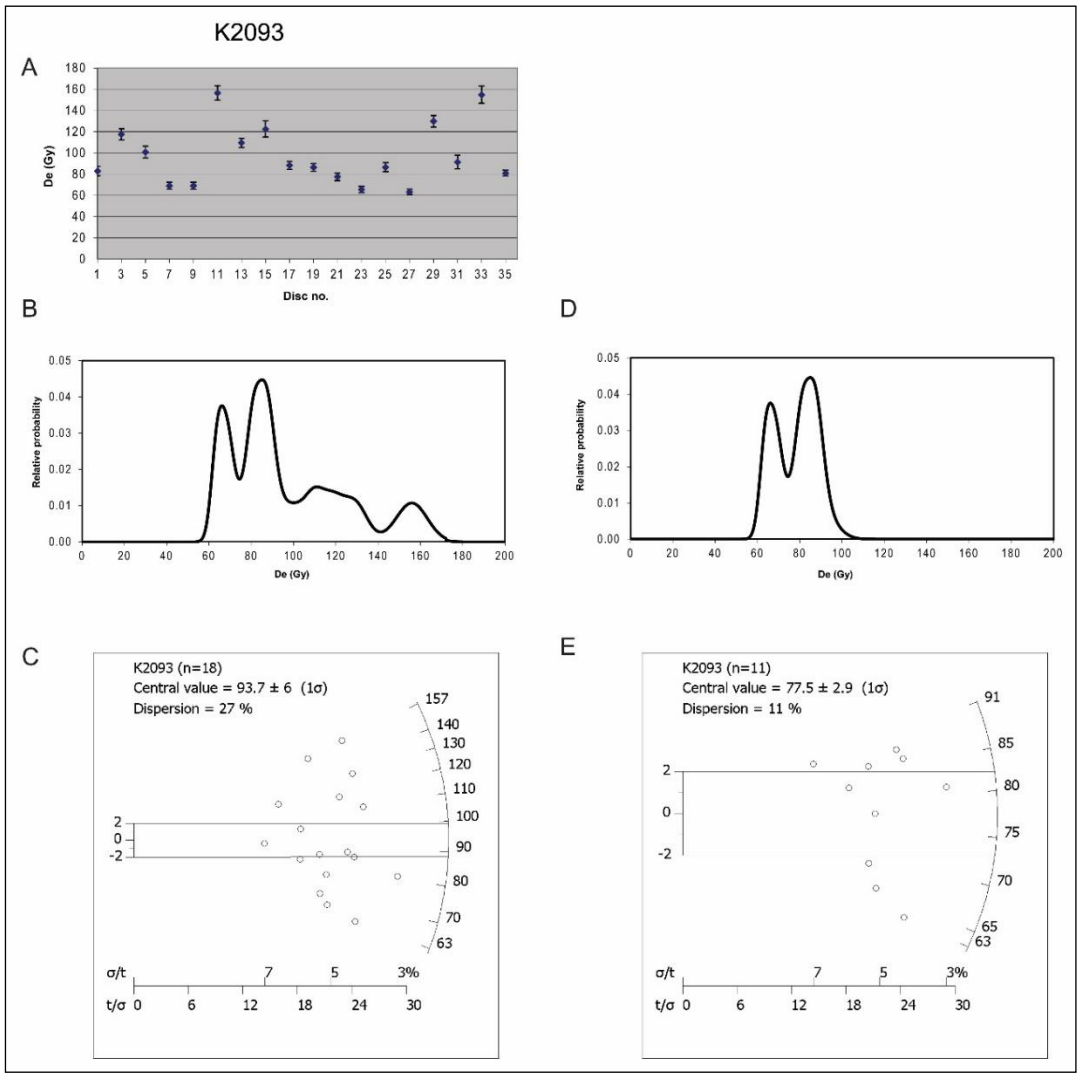

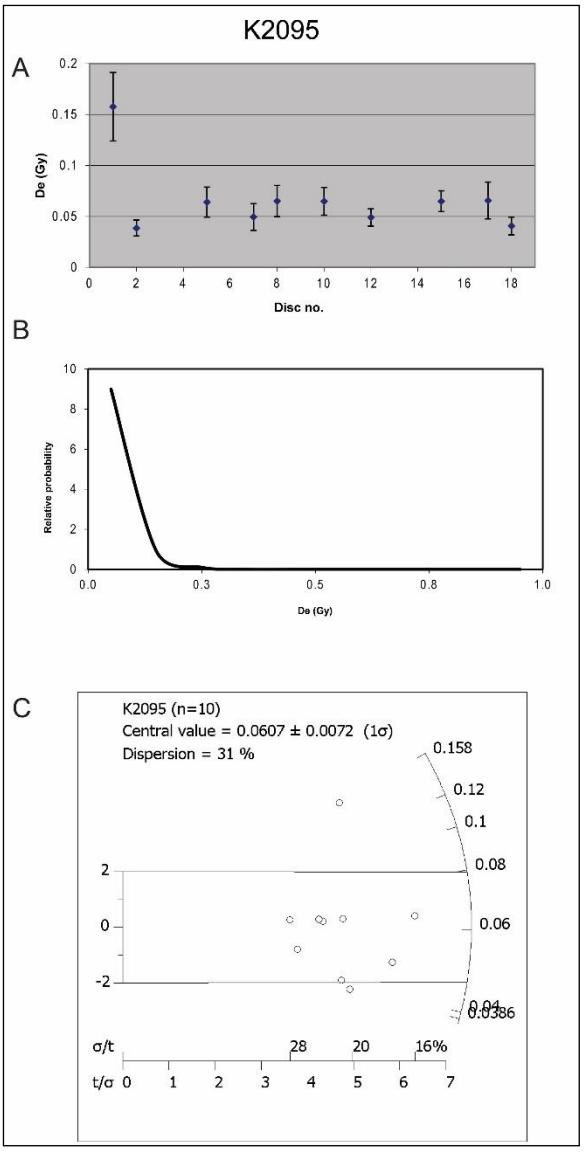

Sample K2095 was collected from within the sandy layers at the top of the lunette at PR04. The sample gives a very typical Unit E unit result, with high recuperation (>10%), and high overdispersion (>20%). Eight aliquots were rejected from this sample, five due to poor recycling ratios (>10%) and three due to high palaeodose errors. The remaining aliquots have very low D_e values (<0.1 Gy). One aliquot has slightly higher D_e (>0.2 Gy), probably representing a small amount of mixing in this sample. The specific age estimate of 70 ± 10 years is not highly reliable, though the sample is likely to be very modern.

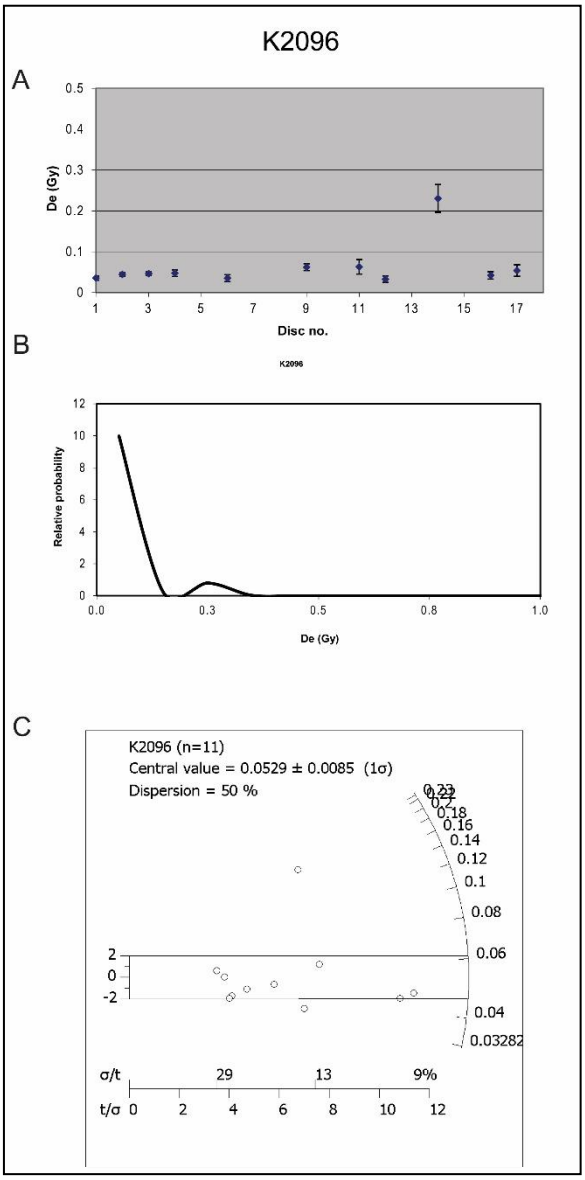

Sample K2096 was collected from within the sandy layers at the top of the lunette at PR04. The sample gives a very typical Unit E result, with high recuperation (>10%), very high overdispersion (>40%) and most aliquots falling within the 2σ error on the radial plot. Seven aliquots were rejected from this sample, three due to poor recycling ratios (>10%) and four due to high palaeodose errors. The remaining aliquots mostly have very low D_e values (<0.1 Gy), mostly with low precision and high relative error. One aliquot has slightly higher D_e (>0.2 Gy), probably representing a small amount of mixing in this sample. The specific age estimate of 70 ± 10 years is not highly reliable, though the sample is likely to be very modern.

One additional sample was collected in the vicinity of PR04, which was not included in the stratigraphic log: K2097, collected below the modern ground surface behind the dune

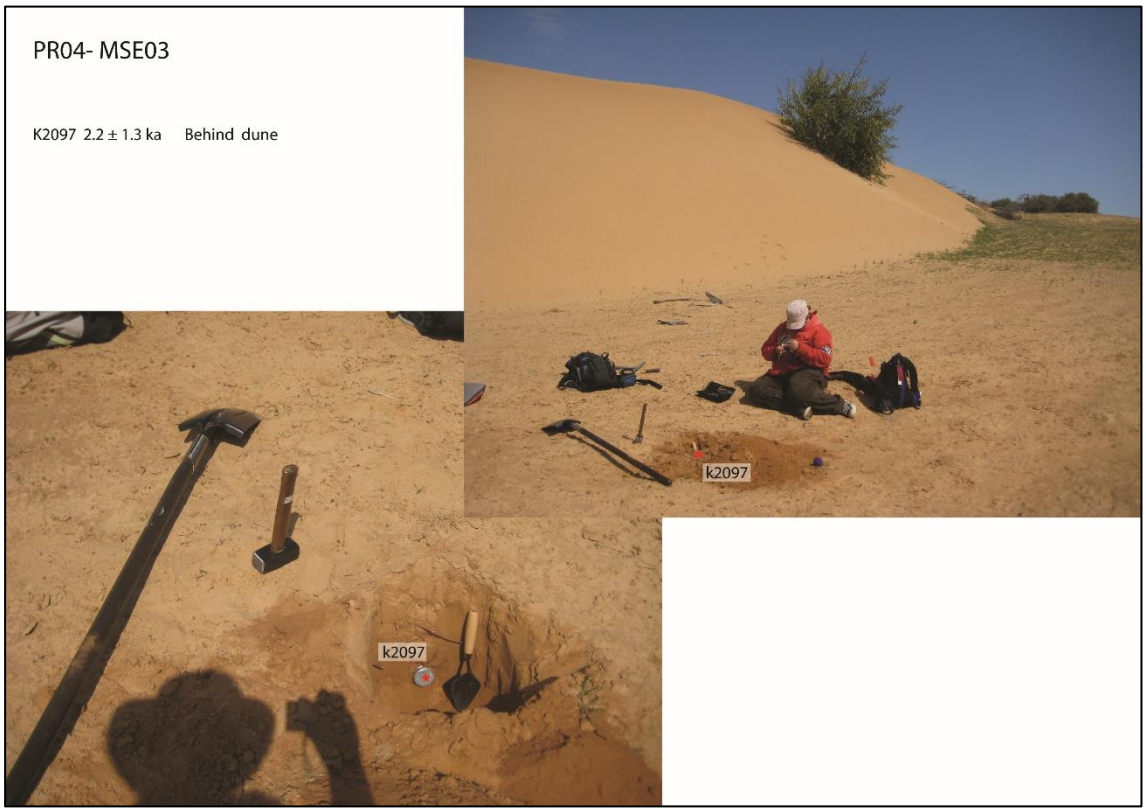

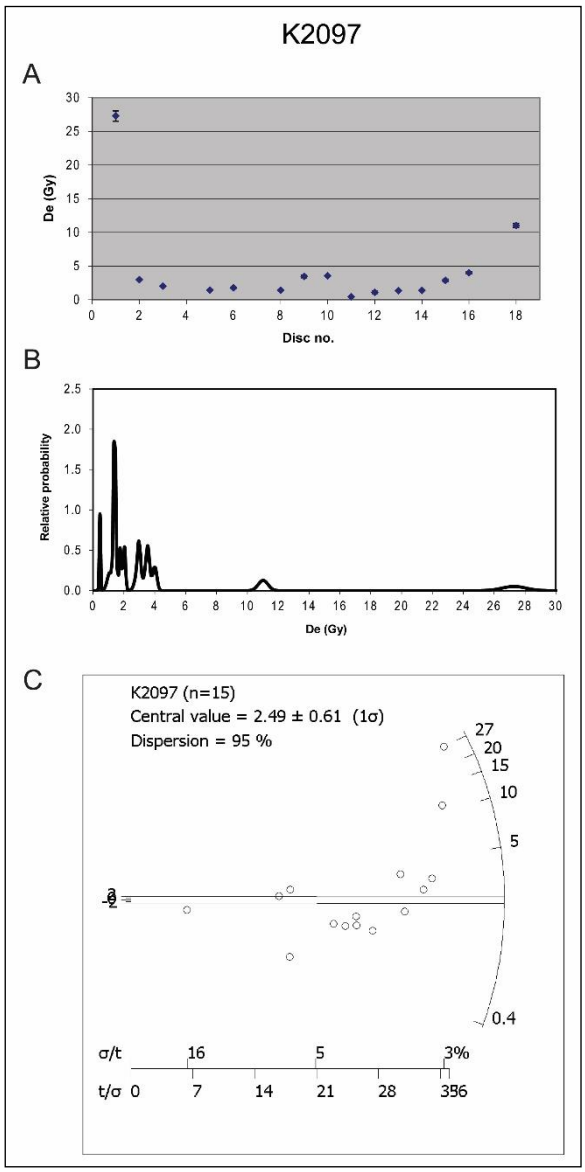

Sample K2097 was collected from beneath the ground surface, behind the lunette. Three aliquots were rejected, one due to giving a D_e value out of range of the dose steps applied, which were based on the preliminary DeLIA measurement results, and two due to poor recycling ratio (>10%). The sample shows evidence of mixing, probably due to modern bioturbation. It was collected from 30 cm below the ground within the modern soil profile. The PD plot has multiple peaks and the radial plot is scattered with few data points within the 2σ error range. The age estimate of 2.2 ± 1.3 ka likely includes a large modern component, mixed into the sediments by modern soil forming processes.

Appendix H.6. OSL Results at PR01

This section provides the OSL dating results from PR01. See Section 3.3.3 for larger versions of the aerial photo and transect shown below. At PR01, all ages are in stratigraphic order (increasing age with depth). The calibrated radiocarbon ages for the otoliths are in accordance with the OSL ages for the bracketing sediments. Unit A spans at least 100 to approximately 59 ka, while the single sample from Unit B gives an age of approximately 42 ka. The two samples near the top of Unit D (K2085 and K2084) give very young ages, but were sampled from within the palaeosol (see Section **Error! Reference source not found.**), the sample from below the palaeosol gives an age of approximately 18 ka, concordant with the underlying otoliths, dated to around 20-19 ka Cal. BP. The charcoal from within the Unit D palaeosol gives an apparently modern age of <300years cal. BP. Unit E provides young age estimates, within the last 200 years.

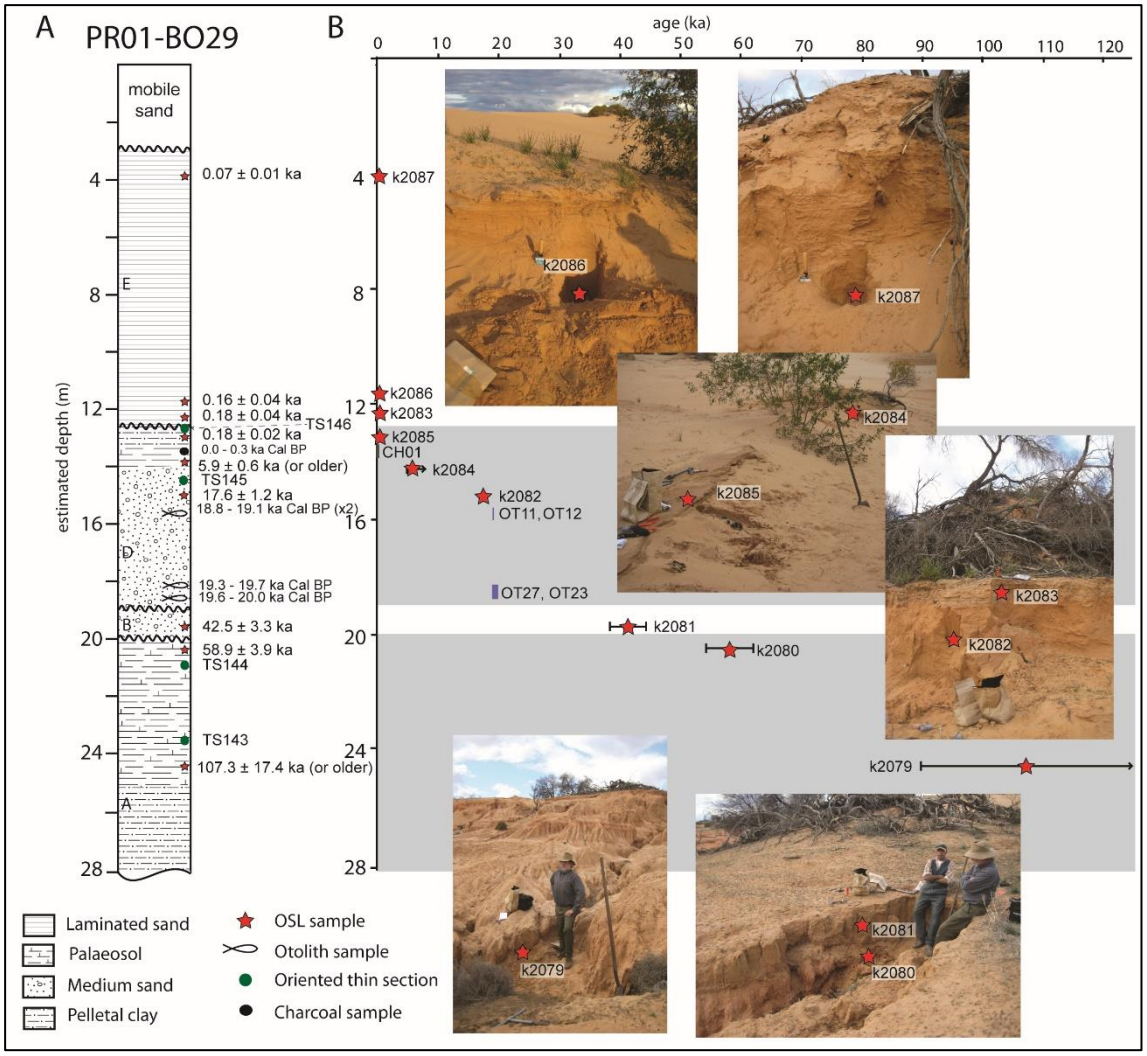

APPENDIX H. OSL DATING RESULTS

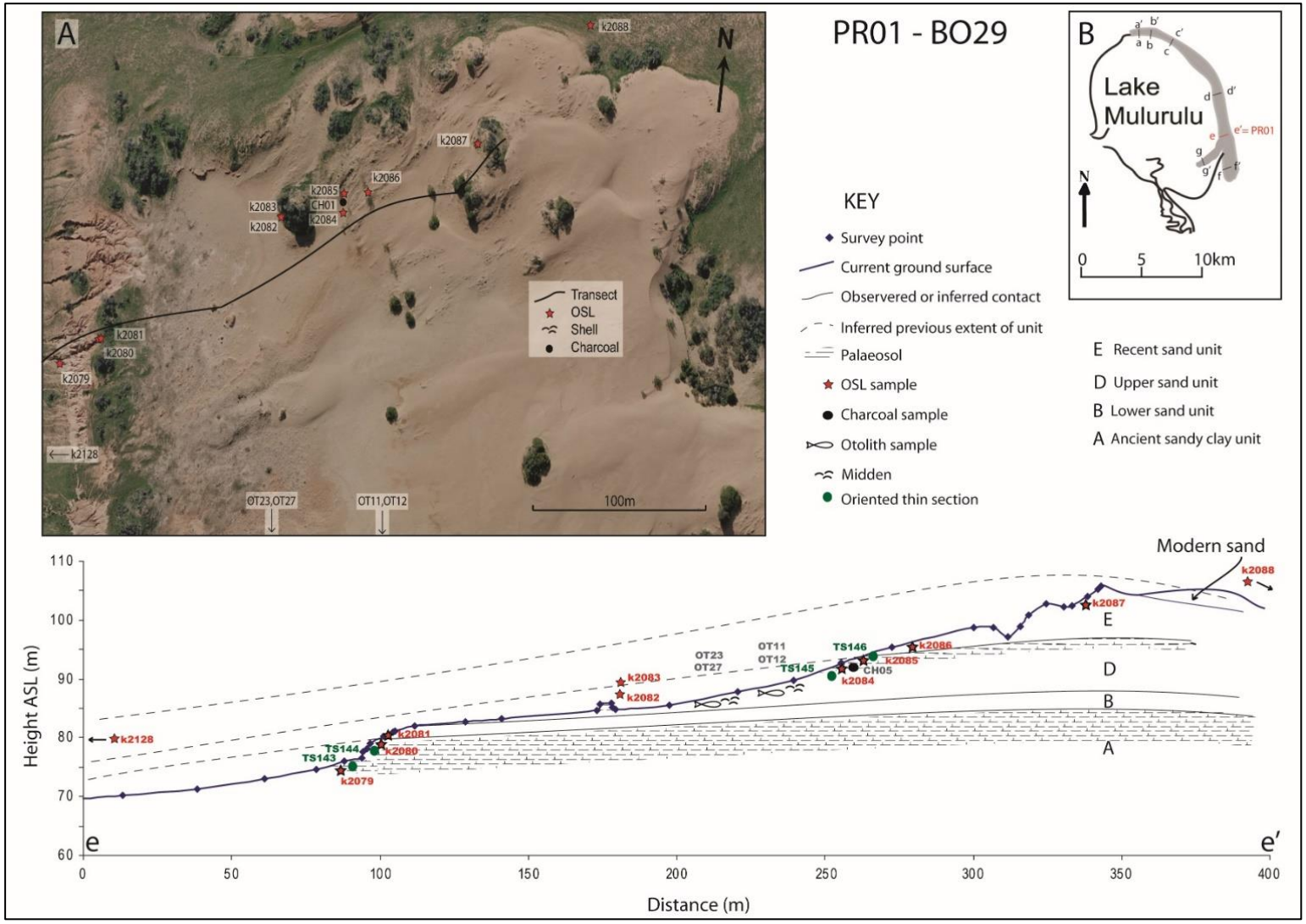

Sample K2079 was collected from within Unit A, where the lower part of the 3-4 m thick palaeosol is exposed in the base of a gully. Four aliquots were rejected from this sample, due to saturation. This implies that this is a relatively old sample, with many grains beyond the dating range. Examples of dose response curves for some of the saturated aliquots are shown below. The highest of the four dose steps equates to ~160 Gy, which in this sample would represent an age of approximately 135 ka.

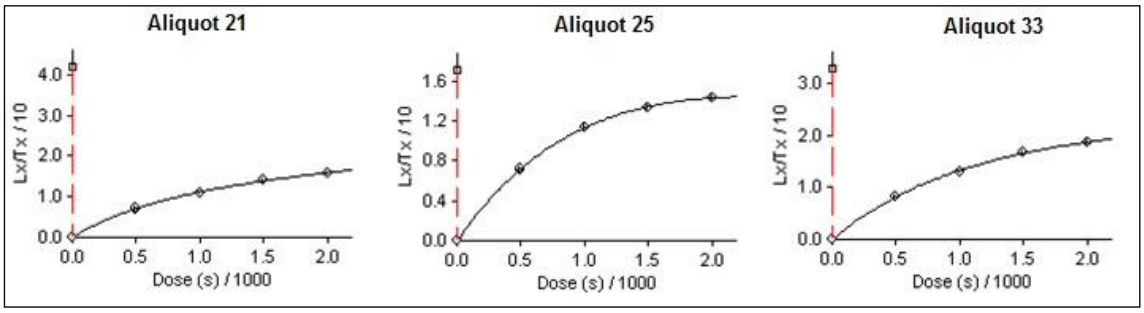

Of the remaining aliquots one gives a much lower D_e than the other 13 and is almost certainly a result of contamination. Having been collected from the base of a gully wall, there is ample opportunity for more recent material to be entrained with the older sediments.

Even disregarding this very young aliquot, there is a wide range of scatter in the radial plot and the PD plot appears multimodal, with a very broad D_e range, from ~50-280 Gy. In addition to young materials washed in to the gully, the sample was collected from within the base of a very thick palaeosol, so it is likely that a significant amount of post-deposition mixing is reflected in the D_e distribution. A central age model applied to the remaining 13 aliquots produces an age estimate of 107.3 ± 17.4 ka, while the minimum age estimate is 48.2 ± 4.1 ka. Even the CAM age is unlikely to represent the true age of deposition of the layer being dated, which is probably substantially older than this, and indeed, older than the 135 ka age represented by the highest regeneration step applied during the SAR protocol.

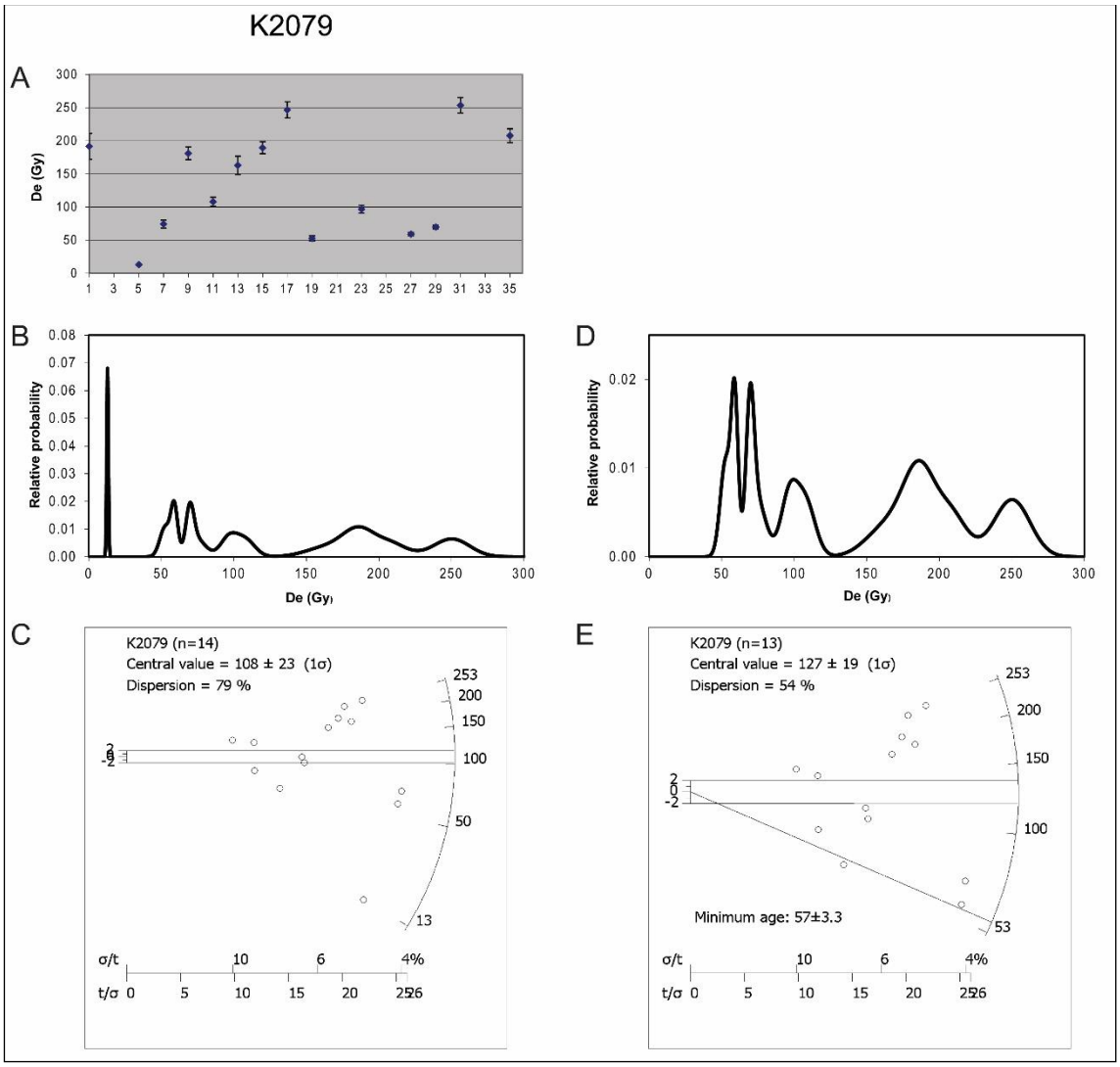

Sample K2080 was collected from near the top of unit A, within the thick palaeosol, where it is exposed in a gully wall. No aliquots were rejected from this sample, but five outlying aliquots at the higher end of the range give values over 95Gy. These aliquots most likely result from mixing in of sediments from below, possibly through bioturbation of the palaeosol. Removing these aliquots from the central age model changes the De estimate from 77 ± 7 Gy to 63 ± 3 Gy while the overdispersion reduces from 39% to 18%.

The data appear to be better represented by a bimodal distribution however. In this case, the five lower De values (44-55 Gy) may be due to inmixing of sediments from the Unit D layer above, making the population of eight higher D_e values (61-83 Gy) more representative of the depositional age. A CAM applied to just this population gives a central D_e of 71.3 ± 2.3 Gy, resulting in an age estimate of 59.0 ± 3.9 ka. This estimate is well within error of the age

estimate based on the CAM of all aliquots (63.6 ± 7.0 ka) though the overdispersion is much lower (7.6% rather than 39%)

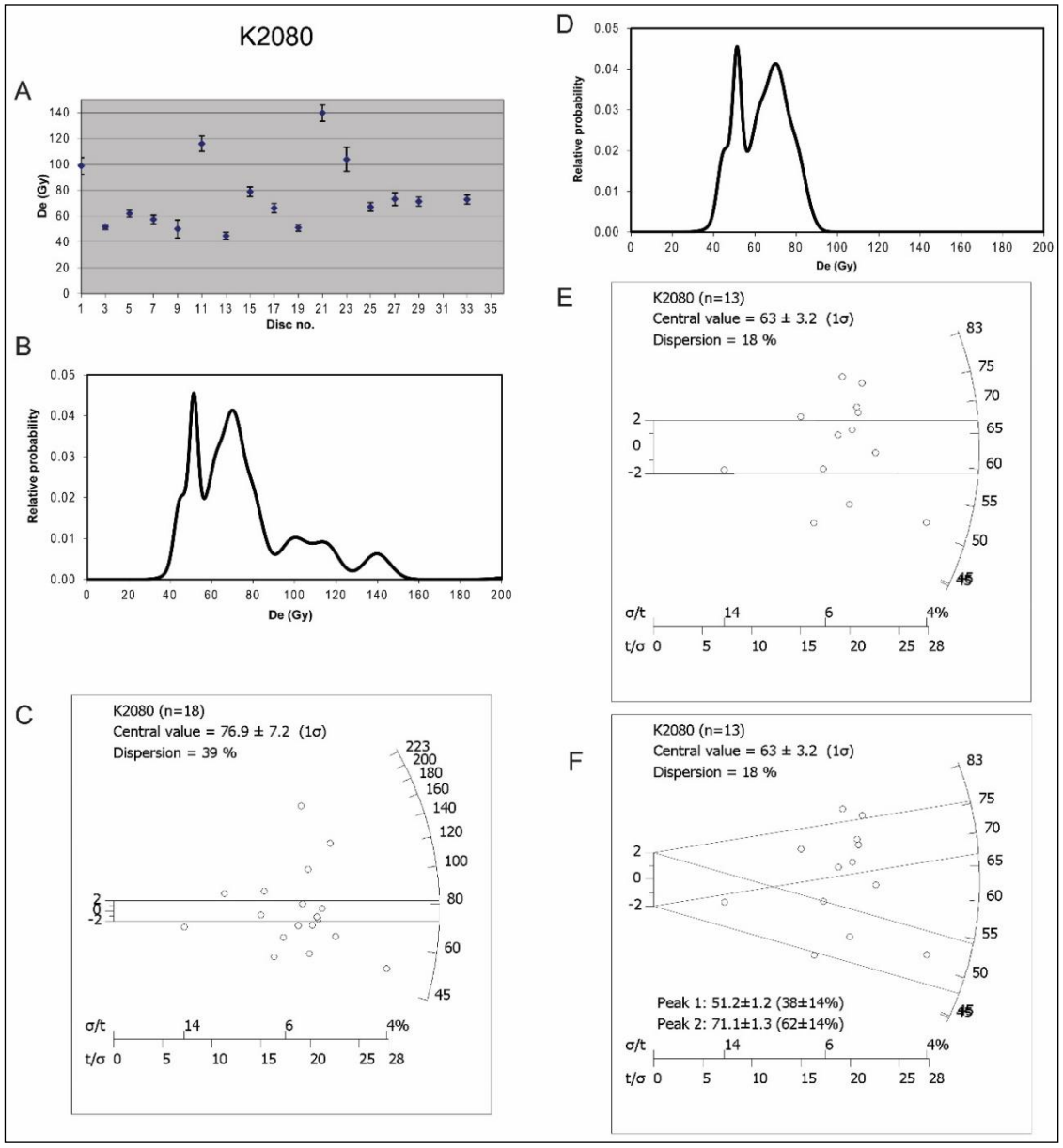

.

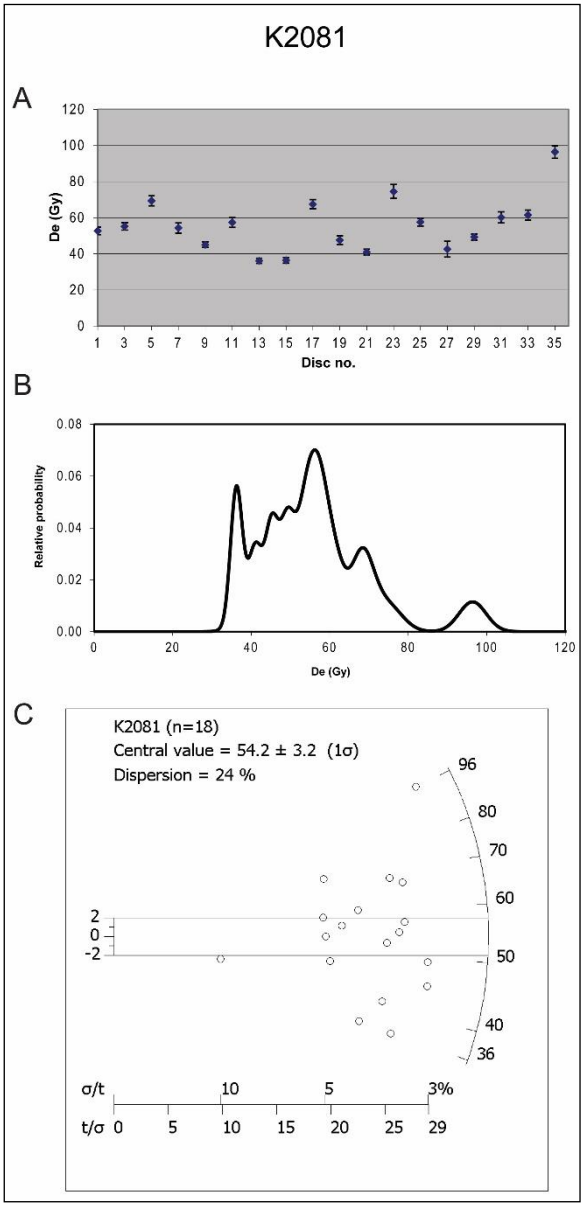

Sample K2081 was collected from the base of Unit B, immediately overlying Unit A. No aliquots were rejected and the D_e values provide a broad dose distribution, with just under half the aliquots falling within the 2σ error on the radial plot. Given that the overdispersion is not excessive, a CAM is used for this sample, resulting in an age estimate of 42.5 ± 3.3 ka.

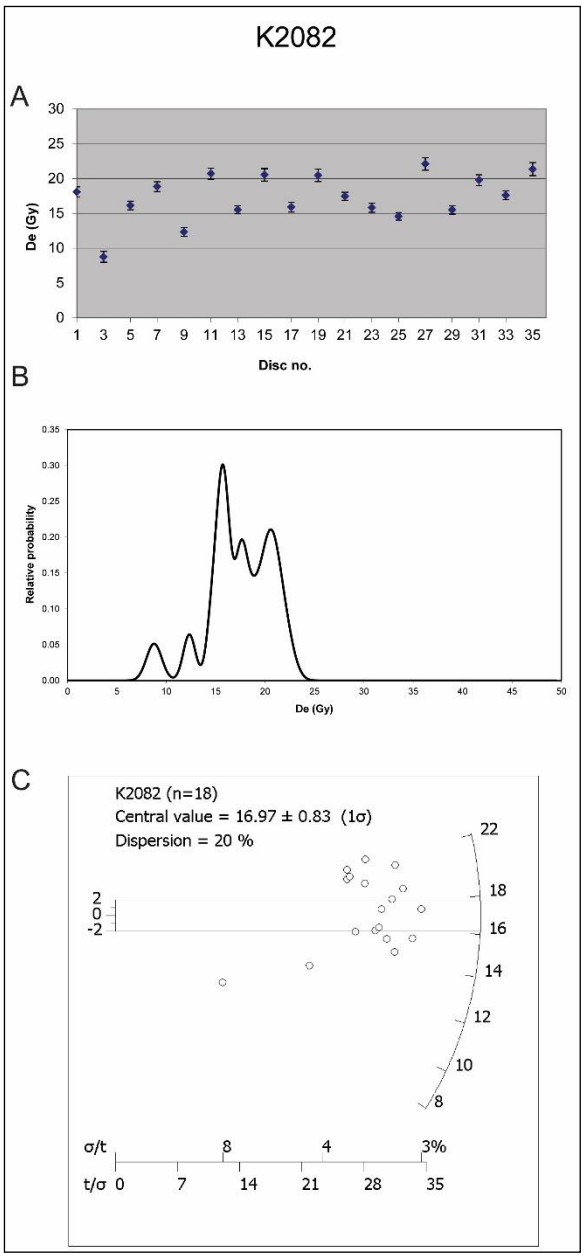

No aliquots were rejected from sample K2082. The sample was collected from Unit D, where it is exposed within a residual. Two aliquots provide slightly lower values than the rest of the population, however removing these from the CAM calculation does not significantly alter the estimate of D_e (it remains within error). Thus a CAM estimate for all accepted aliquots is used to provide the 17.57 ± 1.16 ka age for this sample.

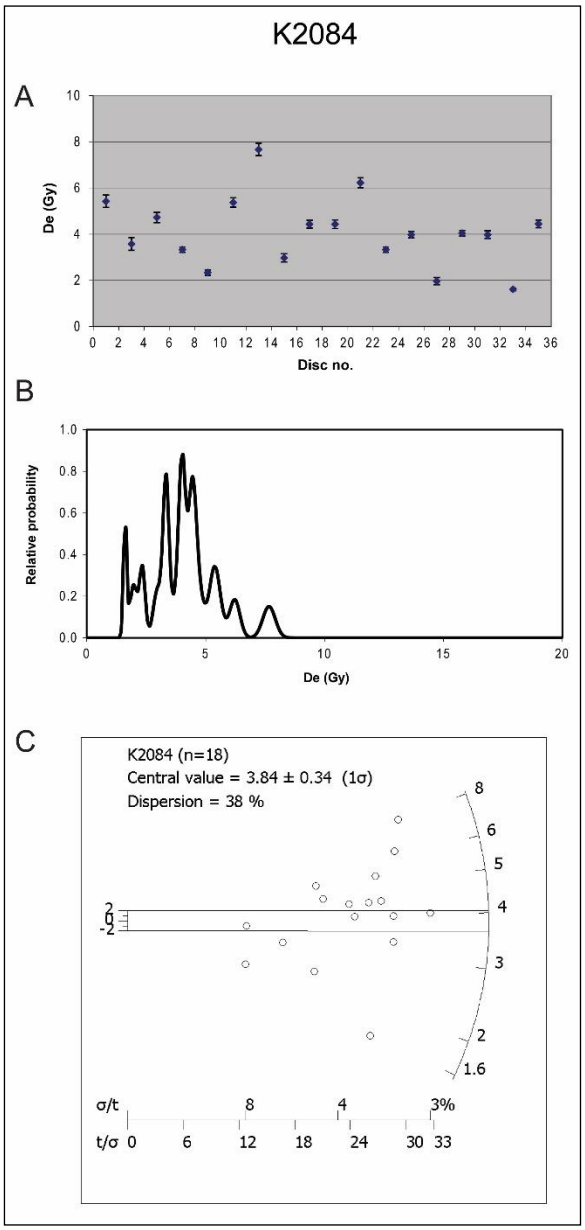

K2084 was collected from high in Unit D, immediately below the clay layer. No aliquots were rejected but the D_e results have a scattered distribution, resulting in a PD plot with multiple peaks and a radial plot in which the majority of aliquots fall outside the 2σ error of the CAM weighted mean. This may be an indication of post-depositional mixing, or a result of issues with microdosimetry. The sample was collected from very close to the top of the unit, within the palaeosol, where bioturbation is likely to have occurred. Additionally, the sample was taken from immediately below the clay layer capping the unit, so may have contained some clay pellets, resulting in differential exposure to beta radiation from potassium. The CAM age estimate for this sample is 5.92 ± 0.59 ka, but it is unlikely to represent the true depositional age. Thus, no reliable age for this sample can be determined from these results.

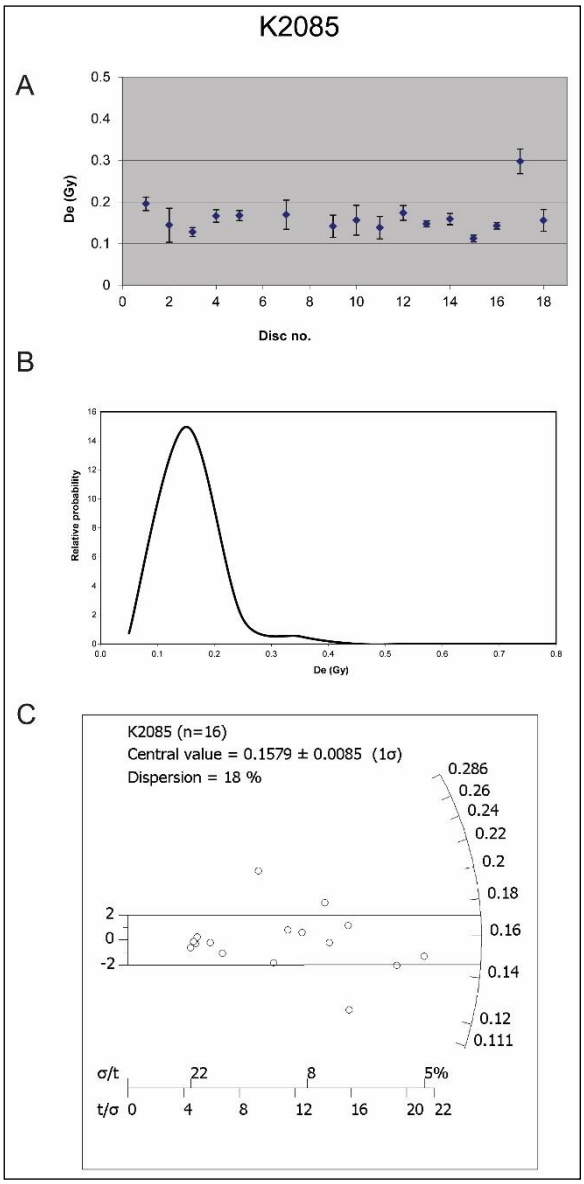

Sample K2085 was collected from the clay layer at the top of Unit D. Two aliquots were rejected from this sample, one due to a poor recycling ratio (>10%) and one due to a high palaeodose error. The PD plot forms a Gaussian curve with a small right shoulder due to one aliquot with a slightly higher D_e. The CAM result for this sample is 160 ± 10 years. This is a much younger age than expected from this pelletal clay. The clay is very dense with clay pellets and has a low proportion of quartz grains. It seems likely that the young age estimation is a result of contamination with quartz from the overlaying Unit E.

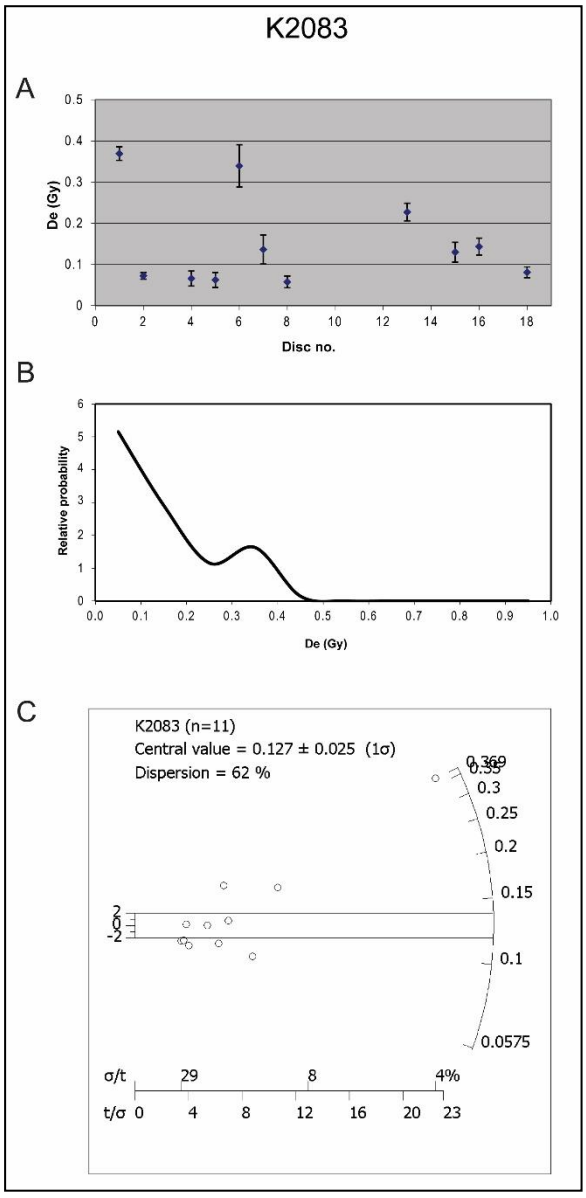

Sample K2083 was collected from within unit E, and gives a very typical result, with high recuperation (>10%) and very high overdispersion (>40%). Seven aliquots were rejected due to poor recycling ratio (>10%). The remaining aliquots all have low D_e values (<0.5 Gy), mostly with very low precision and high relative error. As a result, the specific age estimate of 180 ± 40 years is not highly reliable, though the sample is likely to be relatively modern and probably less than 200 years old.

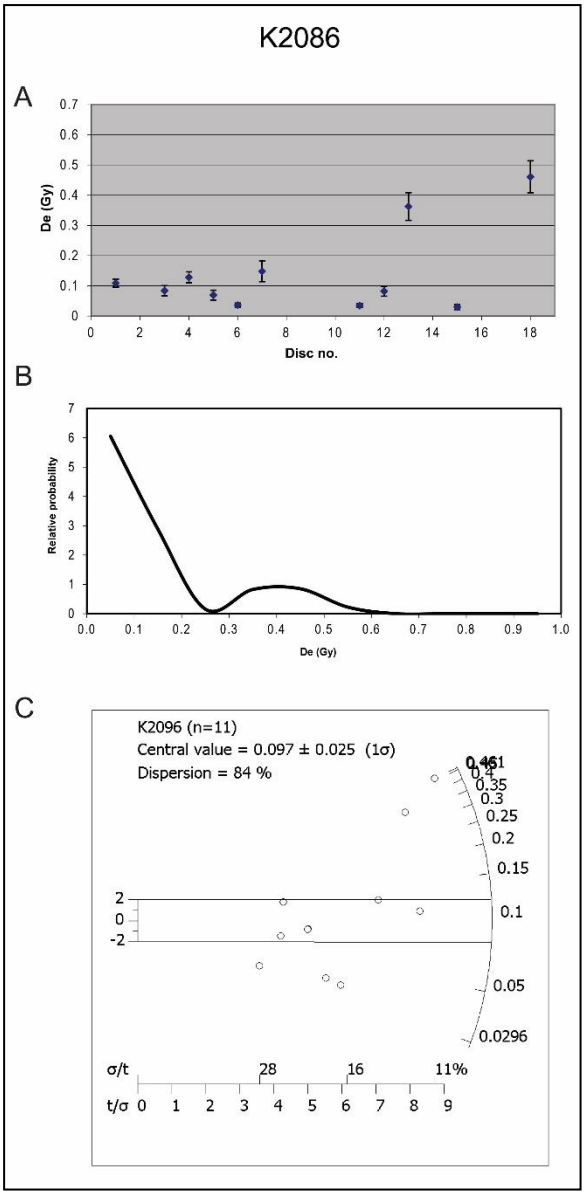

Sample K2086 was collected from within Unit E and gives a very typical result, with high recuperation (>10%) and very high over dispersion (>40%). Seven aliquots were rejected from this sample, one due to being out of range of the highest dose in the SAR (determined based on the DeLIA analysis of the sample), three due to poor recycling ratios (>10%) and three due to high palaeodose errors (>30%). The remaining aliquots mostly have low D_e values (<0.2 Gy), with very low precision and high relative error. The two aliquots that provide slightly higher D_e values (~0.3–0.5 Gy) also have a higher precision than the younger values and probably represent a small amount of mixing in this sample. As a result, the specific age estimate of 160 ± 40 years is not highly reliable, though the sample is likely to be relatively modern and probably less than 200 years old.

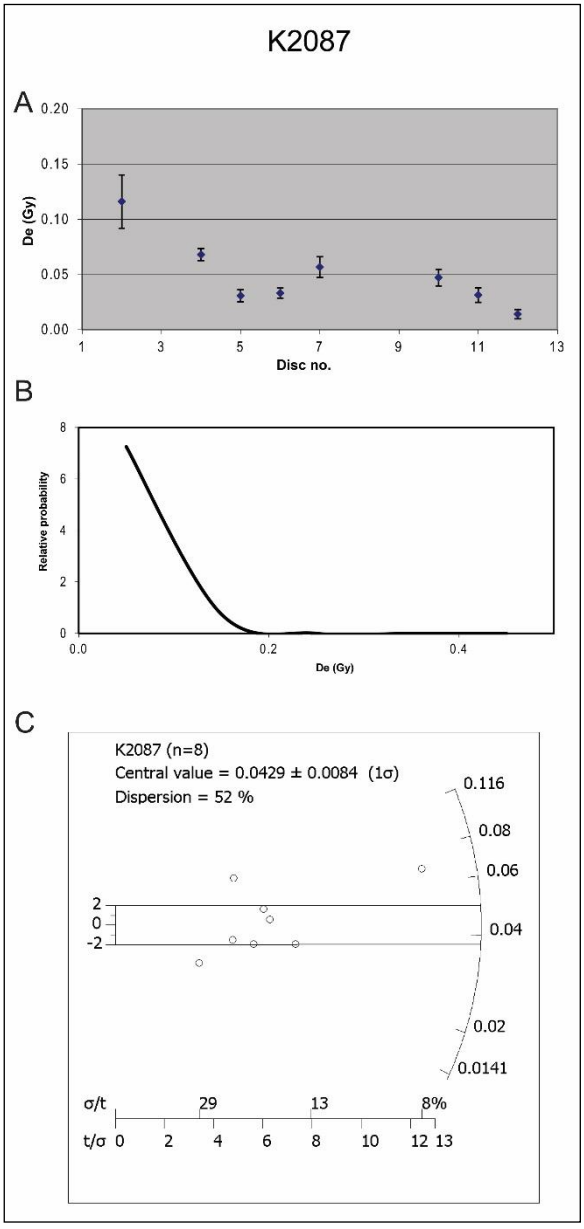

Sample K2087 was collected from within Unit E, and gives a very typical result, with high recuperation (>10%) and very high overdispersion (>40%). Ten aliquots were rejected from this sample, seven due to poor recycling ratios (>10%) and three due to high palaeodose errors (>30%). The remaining aliquots mostly have very low D_e values (<0.1 Gy), with very low precision and high relative error. As a result, the specific age estimate of 70 ± 10 years is not highly reliable, though the sample is likely to be relatively modern.

APPENDIX H. OSL DATING RESULTS

Two additional samples were collected in the vicinity of PR01, which were not included in the stratigraphic log: K2088, below the modern ground surface behind the dune, and K2128, in the "beach ridge" at the front of the dune

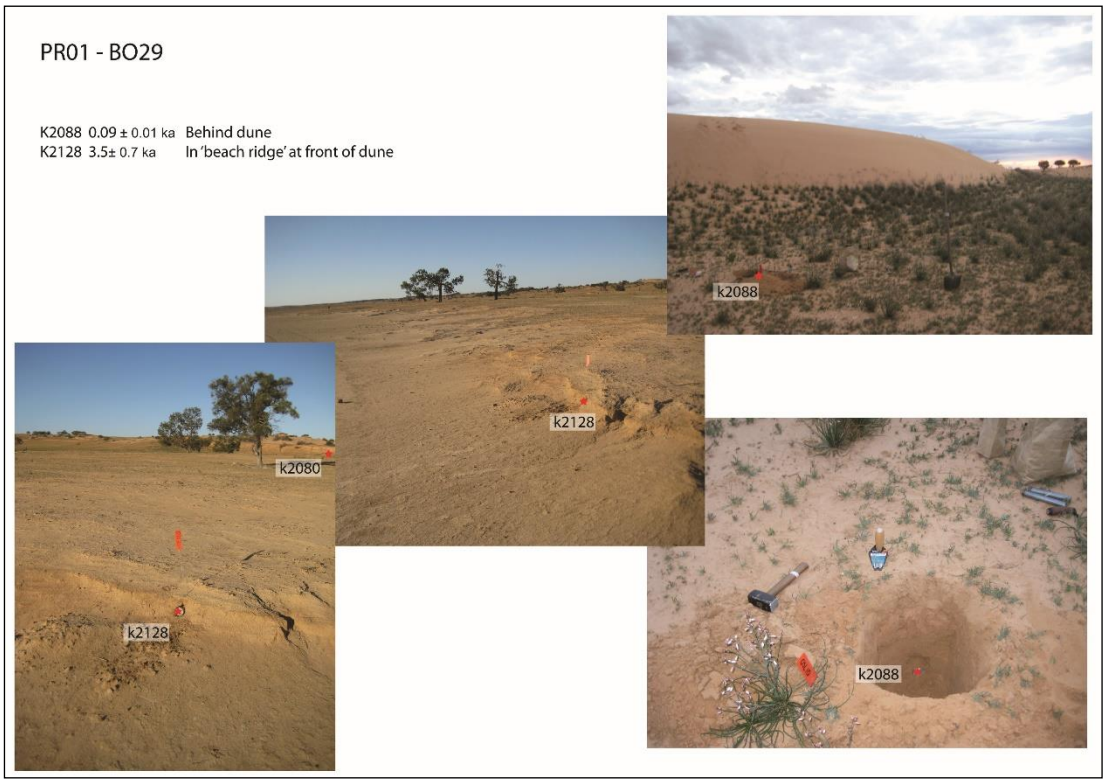

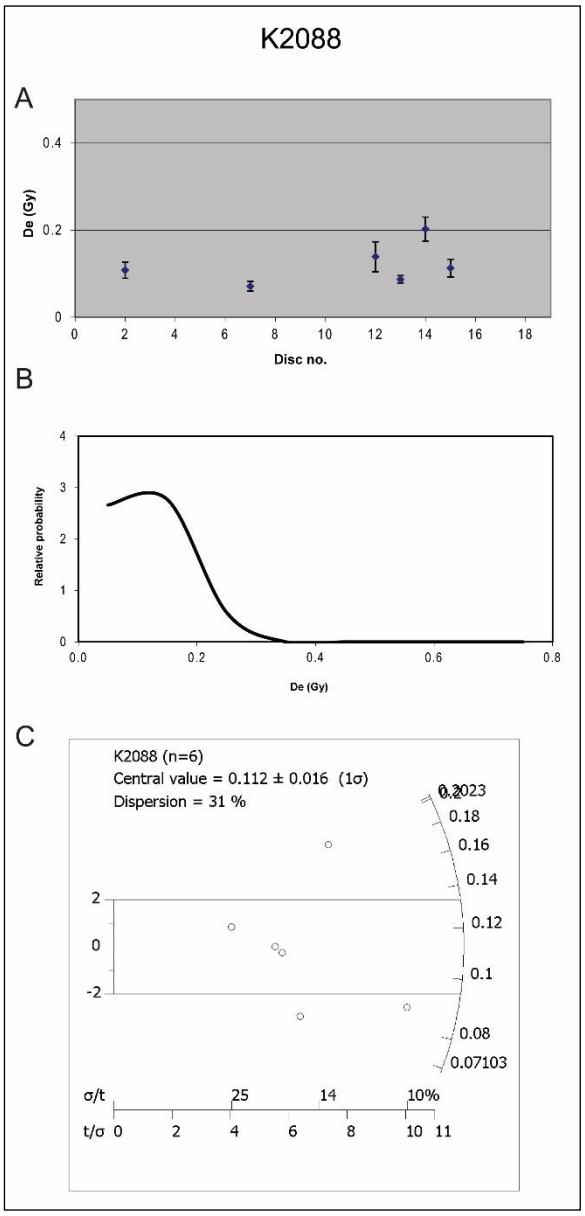

Sample K2088 was collected from below the ground surface behind the lunette, and gives a result similar to those typical of Unit E sands. Twelve aliquots were rejected from this sample, six due to poor recycling ratios (>10%), one due to a low signal to background ratio, and five due to high palaeodose errors (>30%). The remaining aliquots mostly have very low D_e values (<0.2 Gy), with very low precision and high relative error. This, combined with the low number of aliquots, means the specific age estimate of 90 ± 10 years is not highly reliable, though the sample is likely to be relatively modern and probably less than 200 years old.

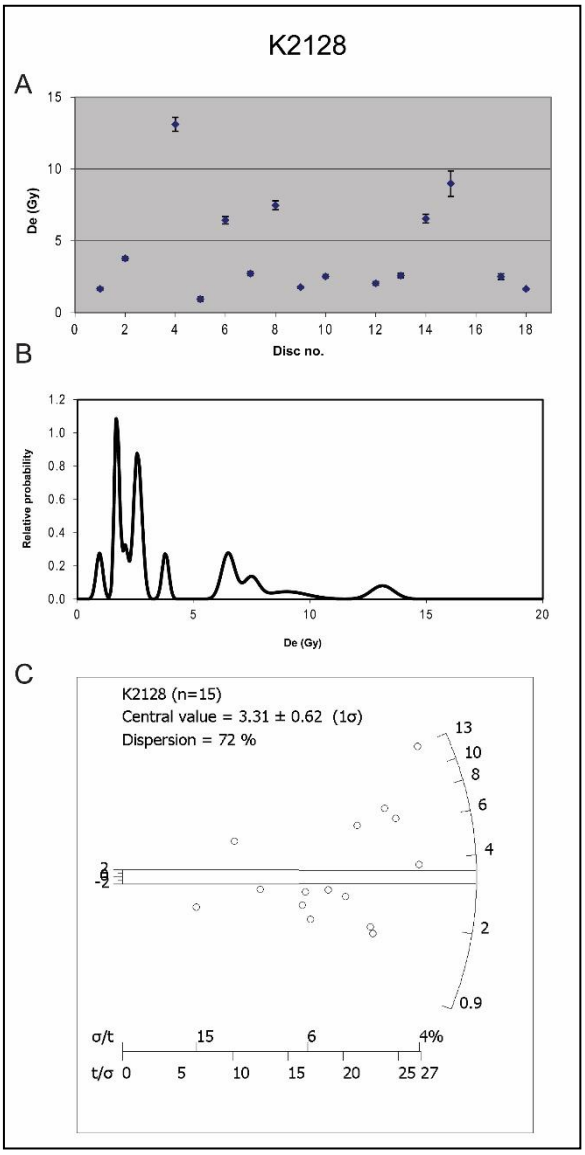

Sample K2128 was collected from within the beach ridge in front of the lunette and shows evidence of mixing, probably due to modern bioturbation. This sample was collected from only 10 cm below the current ground surface. Three aliquots were rejected from this sample, due to poor recycling ratios (>10%). The PD plot has multiple peaks and the radial plot is scattered with no data points within the 2σ error range. The CAM age estimate of 3.29 ± 0.60 ka almost certainly includes a large modern component, mixed into the sediments by modern soil forming processes.